Optically Designed Anodised Aluminium Surfaces: Microstructural and Electrochemical Aspects

Gudla, Visweswara Chakravarthy; Ambat, Rajan

Publication date:
2015

Document Version
Publisher's PDF, also known as Version of record

Optically Designed Anodised Aluminium Surfaces

Microstructural and Electrochemical Aspects

PhD Thesis

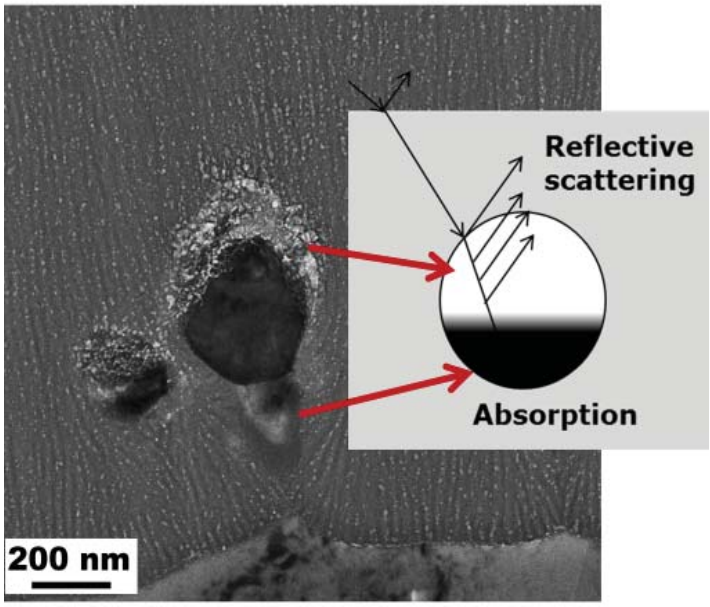

Visweswara Chakravarthy Gudla
July 2015

DTU Mechanical Engineering
Department of Mechanical Engineering

Optically Designed Anodised Aluminium Surfaces

Microstructural and Electrochemical Aspects

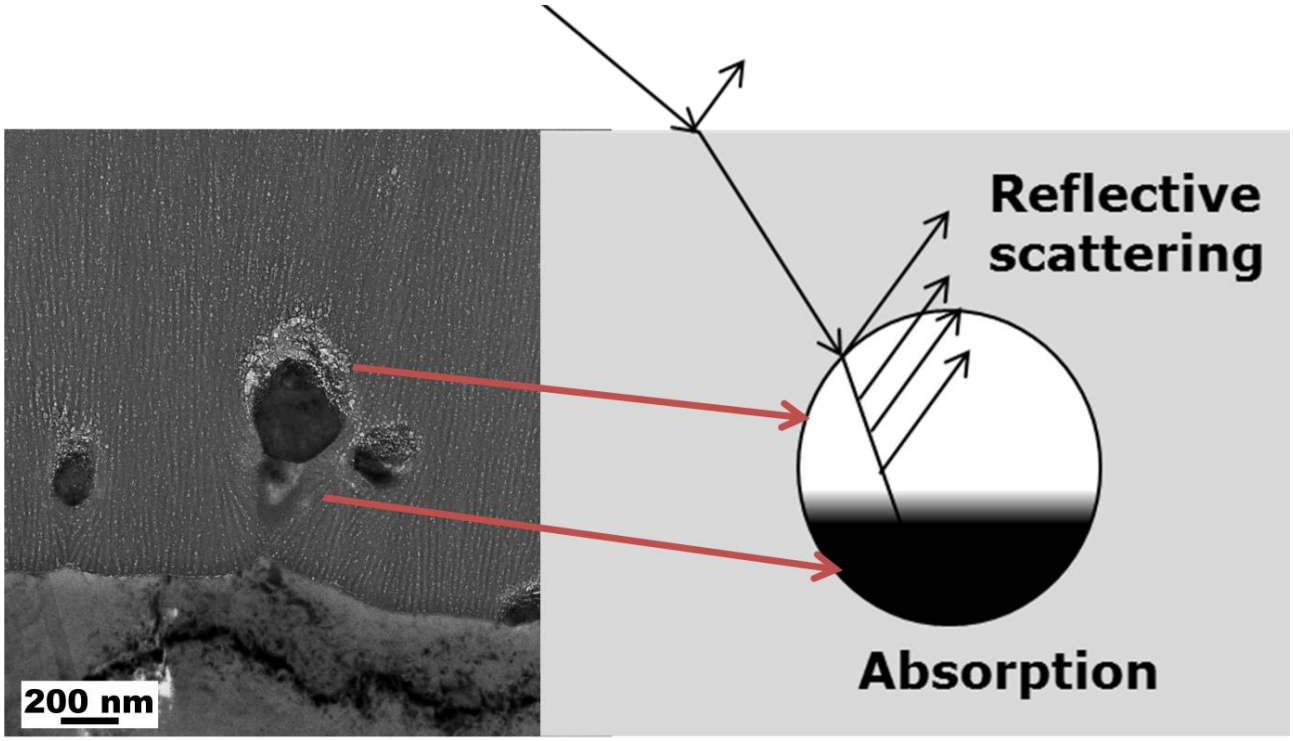

Visweswara Chakravarthy Gudla

Ph.D. Thesis
Department of Mechanical Engineering
Technical University of Denmark

July 2015

Title of the Thesis:

Optically Designed Anodised Aluminium Surfaces: Microstructural and Electrochemical Aspects

Ph.D. Student:

Visweswara Chakravarthy Gudla
E-mail: vichg@mek.dtu.dk
E-mail: chakri_gvc@yahoo.co.in, gvchakravarthy@gmail.com

Supervisor

Prof. Rajan Ambat
E-mail: ram@mek.dtu.dk

Address:

Department of Mechanical Engineering, Materials and Surface Technology
Technical University of Denmark
Produktionstorvet, Building 425
2800 Kgs. Lyngby, Denmark

Cover Image: Bright field transmission electron micrograph of anodised layer on Aluminium-TiO_2 composite and the proposed light interaction mechanism with the anodic layer.

Published by: Department of Mechanical Engineering, Section for Materials and Surface Engineering, Produktionstorvet, Building 425, 2800 Kgs. Lyngby, Denmark

All things are difficult before they become easy...

Preface

This thesis is submitted in partial fulfilment of the requirements for obtaining the degree of Ph.D. in Mechanical Engineering at Technical University of Denmark (DTU). The Ph.D. project was funded by the Danish National Advanced Technology Foundation (HTF, Højteknologi-fonden) through the project 'Optically Designed Anodised Aluminium Surfaces (ODAAS)'. It was carried out at the Department of Mechanical Engineering, Section of Materials and Surface Engineering (MTU) in DTU during the period 1st April, 2012 – 14th July, 2015 under the supervision of Professor Dr. Rajan Ambat.

Visweswara Chakravarthy Gudla
Kongens Lyngby, 15th July 2015

Abstract

This thesis presents the research work aimed at generating anodised aluminium surfaces with bright, white, and glossy decorative appearance. The aluminium surface finishing industry has been on the lookout for such surfaces due to their potential applications in aerospace, architecture, and design industry. Conventional colouring techniques applied to anodised aluminium surfaces cannot generate glossy white appearing surfaces due to the fundamental differences in the interaction with visible light that is required. Surfaces appearing as perfect white are due to the scattering of visible light providing high level of diffused reflection, which is similar to a mirror, but without the specular reflection component. Therefore the nature of the white surface should provide high scattering of light without significant absorption. Achieving white anodised surfaces using conventional dyeing techniques is not possible as the anodic pore sizes are an order of magnitude smaller than the traditional white pigments.

The approaches presented in this thesis focus on different techniques like modification of the aluminium microstructure, engineering of the aluminium surface, and application on non-conventional anodising processes. The idea behind the mentioned approaches is to enhance the scattering of visible light from the anodised aluminium surface and aluminium substrate interface for achieving high reflectance.

Magnetron sputtered coatings were employed to modify the Aluminium surface and tailor the microstructure in order to impart light scattering ability to the anodised layer. Coatings based on Al-Zr and Al-Ti binary system were studied for their anodising behaviour with and without heat treatment. The structure evolution of the Al-Zr sputtered coatings and the effect of Si during heat treatment was studied in-situ in a transmission electron microscope and also ex-situ using grazing incidence X-ray diffraction. The Al-Metal oxide surface composites based on TiO_2, Y_2O_3, and CeO_2 prepared by friction stir processing were employed to generate light scattering anodised surfaces by embedding oxide particles. Theoretical modelling and physical modelling of the anodised layer with TiO_2 particles were simulated using Polyurthenane-TiO_2 coatings and investigating the optical appearance.

The conventional DC anodising and high frequency pulse and pulse reverse pulse anodising were employed to generate bright-anodised surfaces. Effect of pulse frequency, anodic and cathodic cycle potential values was systematically investigated. Characterization of surfaces and substrates was performed using Scanning and Transmission Electron Microscopy, Grazing-Incidence X-ray Diffraction, Glow Discharge Optical Emission Spectroscopy, and Scanning Kelvin Probe Force Microscopy. Optical characterization was performed using integrating sphere measurements.

Combining the results and understanding obtained from anodising of magnetron sputtered coatings, Al-TiO_2 surface composites and their electrochemical behaviour under high frequency anodising, highly reflecting, bright and glossy white anodised aluminium surfaces were generated for the first time. Further, these white anodised surfaces were conventionally dyed to generate new appearances based on pastel colours.

The work presented in this thesis is mainly divided into two parts. The first part is based on magnetron sputter deposition, their heat treatment, characterization, and anodising behaviour (Chapter 5-8, 14). The second part of the thesis is based on Al-TiO_2 composites, their preparation characterization, and anodising behaviour (Chapter 9-13). The outcome of the work is presented in the last chapter (Chapter 15). The results from white anodising of the Al surfaces, which is the primary goal of this thesis and also the generation of a new set of pastel coloured anodised surfaces is presented. The optical characterization of these white anodised surfaces along with other reference white surfaces is presented and discussed.

Resumé

Denne ph.d. afhandling beskriver resultater og overvejelser fra et forskningsarbejde, der har haft til formål at udvikle anodiserede aluminiumsoverflader, der fremstår med en blank og dekorativ hvid farve. Sådanne overflader har store potentielle anvendelser inden for f.eks. transport-, fly- og rumfarts-, bygnings- og designindustrierne og har i lang tid været efterspurgt i brancherne. Konventionelle teknikker til at farve anodiseret aluminium kan ikke fremstille skinnende hvide overflader, idet den fysiske størrelse af porerne i det anodiserede lag ikke er store nok til at rumme pigment med hvid farve. En overflade fremstår perfekt hvid, hvis den spreder alt indkommende lys i det synlige spektrum, uden at der absorberes noget lys i materialet. Derfor er det et krav til overfladens optiske egenskaber, at al synligt lys spredes uden signifikant absorption.

I dette projekt er anvendt forskellige teknikker til at skræddersy aluminiumsoverfladen, f.eks. ved at ændre mikrostrukturen af og ved anvendelse af alternative anodiserings processer. Formålet med dette var at øge spredningen af synligt lys i det anodiserede lag og i grænselaget mellem basismaterialet og det anodiserede lag.

Belægninger fremstillet ved magnetronforstøvning blev optimeret, så lys vil spredes effektivt ved en efterfølgende anodisering. Egenskaberne ved anodisering af belægninger baseret på Al-Zr og Al-Ti binære systemer blev undersøgt, både med og uden efterfølgende varmebehandling. Udviklingen af mikrostrukturen af Al-Zr belagte overflader samt effekten af Si i grundmaterialet blev undersøgt in-situ ved transmission elektron mikroskopi og ex-situ ved røntgen spektroskopi.

Overflader af Al-metaloxid kompositter, baseret på TiO_2, Y_2O_3, og CeO_2, blev fremstillet ved friction stir processer og er anvendt til at skabe anodiserede overflader med integrerede partikler af metaloxider, der effektivt spreder synligt lys. De optiske egenskaber af anodiseret Al med inkorporerede TiO_2 partikler er modelleret ud fra teoretiske beregninger, og eftervist med fysiske modeller med Polyuretan-TiO_2.

Konventionel DC anodisering samt anodisering med højfrekvente puls mønstre er anvendt til at fremstille lyse, anodiserede overflader. Effekten af puls frekvensen og potentialerne af de anodiske og katodiske pulser, er undersøgt systematisk. De frembragte overflader og substrater er karakteriseret med scanningselektronmikroskopi (SEM), transmissionselektronmikroskopi (TEM), røntgendiffraktion (XRD), optisk emission spektroskopi (GDOES), og scanning kelvin probe force mikroskopi (SKPFM). Optisk karakterisering er foretaget med spektrofotometri (integrating sphere).

Ved at kombinere den viden, der blev opnået igennem de forskellige aspekter af forskningsprojektet, er det for første gang lykkedes at producere dekorativt skinnende hvide anodiserede aluminiumsoverflader. Herudover, er disse overflader farvet med konventionelle pigmenter, hvormed der er frembragt anodiserede aluminiumsoverflader med helt nye fremtoninger.

Resultaterne i afhandlingen er opdelt i to dele. Den første del omhandler magnetronforstøvede overflader, varmebehandling, anodisering og karakterisering af disse (Kapitel 5-8, 14). Den anden del omhandler Al-TiO_2 kompositter samt fremstilling, karakterisering og anodisering af disse (Kapitel 9-13). Det sidste kapitel (Kapitel 15) præsenterer resultater fra fremstillingen af hvid-anodisering af aluminium, hvilket var det primære mål i indeværende forskningsprojekt. Her gennemgås optisk karakterisering af hvid-anodiserede overflader, samt andre referenceoverflader.

Acknowledgements

First, I would like to thank my supervisor, Prof. Rajan Ambat (DTU-MEK), for giving me this opportunity to work with him and for his valuable time, supervision, inspiring ideas, enthusiasm and support throughout the course of the project. His unlimited engagement and passion for science and for bridging the gap between research and industry has been a great motivation for me.

I wish to thank Dr. Lars Pleth Nielsen (DTI, Århus) and Ib Kongstad (B&O, Struer) for their guidance and collaboration during the course of this project. I owe special thanks to Dr. Kirill Bordo (DTU-MEK) for his timely help in anodising, fruitful discussions on various matters and for day-to-day support throughout the project. I would like to acknowledge scientists Dr. Kai Dirscherl (DFM, Lyngby) for the scanning kelvin probe studies, Dr. Kristian Rechendorff (DTI, Århus) for the preparation of various sputter coatings and Dr. Stela Canulescu (DTU, Photonics) for optical characterization of the surfaces. In addition, I want to thank Assoc. Prof. Dr. Rajashekhara Shabadi (UMET, Univ. Lille1, France) for hosting me at his lab and for the TEM studies; and Asst. Prof. Dr. Aude Simar (iMMC, Univ. Catholique de Louvain, Belgium) for processing of various surface composites.

I am very grateful to Flemming Jensen (B&O, Struer) for the excellent work performed during his Master's thesis, for the help in arranging samples, performing anodising, valuable feedback and unending discussions and the good times throughout the duration of the project. Dr. Martin Aggerbeck (DTU-MEK) and Dr. Villads Johansen (DTU-MEK) are thanked for their help and collaboration. I would like to thank Adam Fuller, Zoltan Balogh and Dr. Takeshi Kasama (DTU-CEN) for their support with various microscopy techniques. I would also like to thank the various bachelors and masters students, Marcin and Serkan for their work and contribution to this project.

I am thankful to my colleagues in the section of Materials and Surface Engineering for their assistance during my PhD, and for making work a pleasant place. Especially I wish to thank my friend Dr. Rameez Ud Din for all the technical and more often non-technical discussions, collaboration and priceless entertainment. I would like to thank Dr. Daniel Minzari, Dr. Cecilia Kjartansdottir, Dr. Vadimas Verdingovas, Sunday Okoro and Dr. Federico Bottoli for their pleasant company.

Heartfelt thanks to my beloved Helene Conseil-Gudla for the joy, care, patience and untiring support during the entire PhD journey. Last but not the least, to my family who have always loved me, motivated me and extended all the support I need to succeed in all my endeavours.

List of Appended Papers

The following articles constitute a part of this thesis

1. **V.C. Gudla**, K. Rechendorff, Z.I. Balogh, T. Kasama, R. Ambat, *In-situ TEM investigation of microstructural evolution in magnetron sputtered Al–Zr and Al–Zr–Si coatings during heat treatment*, Mater. Des. 89 (2016) 1071–1078. doi:10.1016/j.matdes.2015.10.081.

2. **V.C. Gudla**, S. Canulescu, R. Shabadi, K. Rechendorff, K. Dirscherl, R. Ambat, *Structure of Anodized Al-Zr Sputter Deposited Coatings and Effect on Optical Appearance*, Appl. Surf. Sci. 317 (2014) 1113–1124. doi:10.1016/j.apsusc.2014.09.037.

3. **V.C. Gudla**, S. Canulescu, R. Shabadi, K. Rechendorff, J. Schou, R. Ambat*, Anodization and Optical Appearance of Sputter Deposited Al-Zr Coatings*, in: J. Grandfield, TMS (Eds.), Light Met. 2014, John Wiley & Sons, Inc., 2014: pp. 369–373. doi:10.1002/9781118888438.ch63.

4. M. Aggerbeck, A. Junker-Holst, D.V. Nielsen, **V.C. Gudla**, R. Ambat, *Anodisation of sputter deposited aluminium-titanium coatings: Effect of microstructure on optical characteristics*, Surf. Coatings Technol. 254 (2014) 138–144. doi:10.1016/j.surfcoat.2014.05.073.

5. **V.C. Gudla**, V.E. Johansen, S. Canulescu, J. Schou, R. Ambat, *Simulation of Reflectance From White Anodised Aluminium Surfaces Using Polyurethane-TiO_2 Composite Coatings*, J. Mater. Sci. 50 (2015) 4565–4575. doi:10.1007/s10853-015-9005-1.

6. **V.C. Gudla**, F. Jensen, S. Canulescu, A. Simar, R. Ambat, *Friction Stir Processed Al-Metal Oxide Surface Composites: Anodising and Optical Appearance*, in: T.S. Sudarshan, P. Vuoristo, H. Koivuluoto (Eds.), Surf. Modif. Technol. XXVIII, ValarDocs, Tampere, Finland, 2014: pp. 375–384.

7. **V.C. Gudla**, F. Jensen, A. Simar, R. Shabadi, R. Ambat, *Friction stir processed Al–TiO_2 Surface Composites: Anodising Behaviour and Optical Appearance*, Appl. Surf. Sci. 324 (2015) 554–562. doi:10.1016/j.apsusc.2014.10.151.

8. **V.C. Gudla**, F. Jensen, K. Bordo, A. Simar, R. Ambat, *Effect of High Frequency Pulsing on the Interfacial Structure of Anodized Aluminium-TiO_2*, J. Electrochem. Soc. 162 (2015) C303–C310. doi:10.1149/2.0311507jes.

9. **V.C. Gudla**, K. Bordo, F. Jensen, S. Canulescu, S. Yuksel, A. Simar, R. Ambat, *High Frequency Anodising of Aluminium-TiO_2 Surface Composites: Anodising Behaviour and Optical Appearance*, Surf. Coatings Technol. 277 (2015) 67–73. doi:10.1016/j.surfcoat.2015.07.035.

10. **V.C. Gudla**, K. Bordo, S. Engberg, K. Rechendorff, R. Ambat, *High frequency pulse anodising of magnetron sputtered Al–Zr and Al–Ti Coatings*, Mater. Des. 95 (2016) 340–347. doi:10.1016/j.matdes.2016.01.091.

The following intellectual property has been the outcome of the work carried out during the course of this thesis

1. **V.C. Gudla**, K. Bordo, R. Ambat, F. Jensen, I. Kongstad, *Highly reflecting anodised Aluminium surfaces with tailored diffuse and specular content*, 2016, *Patent pending.*

The following manuscripts have been co-authored during the course of the Ph.D. thesis but do not constitute a part of this thesis.

1. R.U. Din, **V.C. Gudla**, M.S. Jellesen, R. Ambat, *Accelerated growth of oxide film on aluminium alloys under steam: Part I: Effects of alloy chemistry and steam vapour pressure on microstructure*, Surf. Coatings Technol. 276 (2015) 77–88. doi:10.1016/j.surfcoat.2015.06.059.

2. R.U. Din, K. Piotrowska, **V.C. Gudla**, M.S. Jellesen, R. Ambat, *Steam assisted oxide growth on aluminium alloys using oxidative chemistries: Part I Microstructural investigation*, Appl. Surf. Sci. 355 (2015) 820–831. doi:10.1016/j.apsusc.2015.07.182.

3. R.U. Din, **V.C. Gudla**, M.S. Jellesen, R. Ambat, *Microstructure and corrosion performance of steam-based conversion coatings produced in the presence of TiO_2 particles on aluminium alloys*, Surf. Coatings Technol. 296 (2016) 1–12. doi:10.1016/j.surfcoat.2016.03.093.

List of Abbreviations

AA	Aluminium Alloy
AC	Alternating Current
AFM	Atomic Force Microscopy
B&O	Bang & Olufsen (DK)
CEN	Centre for Electron Nanoscopy (DTU-DK)
CIE	Commission Internationale de l'Eclairage (International Commission on Illumination)
DC	Direct Current
DFM	Danish Fundamental Metrology (DK)
DI	Deionised Water
DTI	Danish Technological Institute (DK)
DTU	Technical University of Denmark (DK)
EDS	Energy-Dispersive X-ray Spectroscopy
FCC	Face Centred Cubic
FEG	Field Emission Gun
FIB	Focused Ion Beam
FSP	Friction Stir Processing
FSW	Friction Stir Welding
GD-OES	Glow Discharge Optical Emission Spectroscopy
GI-XRD	Grazing Incidence X-Ray Diffraction
HT	Heat Treatment
ISRO	Indian Space Research Organisation
LOM	Light Optical Microscopy
MAO	Micro Arc Oxidation
NASA	National Aeronautics and Space Administration
PA	Pulse Anodising
PEO	Plasma Electrolytic Oxidation
PRPA	Pulse Reverse Pulse Anodising
PVD	Physical Vapour Deposition
SAA	Sulphuric Acid Anodising
SEM	Scanning Electron Microscopy
SK-PFM	Scanning Kelvin Probe Force Microscopy
TEM	Transmission Electron Microscopy
UV	Ultra Violet

Contents

1. Background

1.1 Aluminium

Aluminium (Al) and its alloys find extensive use across various technological applications. Industries such as architecture, automobile, aerospace, food packaging, consumer electronics etc. find use for Al and its alloys due to their excellent mechanical strength to weight ratio, inherent corrosion resistance, good electrical and thermal conductivity, and ability to be surface finished to generate beautiful and appealing decorative surfaces.

1.2 Anodised Aluminium

Anodising is one surface finishing treatment that allows the surface of Al to be electrochemically oxidised to generate a thick oxide layer. The oxide layer formed during conventional anodising is usually optically transparent and contains a self-ordered, hexagonal, nano-porous structure. This structure is later sealed usually by hydrothermal treatments to transform the porous oxide to a dense hydroxide. The increased mechanical hardness of the surface due to the formation of anodic oxide improves the wear and scratch resistance. In addition, corrosion resistance is enhanced due to the protective surface oxide layer. Anodising of Al finds use as a pre-treatment process for paint systems for better adhesion too.

1.3 Optical Appearance of Anodised Aluminium

Porous anodised Al surfaces, before sealing, are dyed to impart various colours, shades and hues to the surface allowing the material to be used in many applications such as window profiles, automobile exterior and interior parts, high end decorative consumer electronics such as audio and video systems.

Similar to a number of other material processing techniques, the quality and hence the optical appearance of the anodised Al surface highly depends on the composition, microstructure, prior processing history of the Al alloy in combination with the anodising parameters. Further, in recent years, due to the increased use of recycled Al alloys, the quality control of the anodised surface is becoming increasingly challenging. Over the years, a deep understanding has been developed in the scientific community as well as the surface finishing community on various factors influencing the anodising process and final surface finish resulting from the process on various Al alloys. In addition, the development of several surface analysis and microstructural characterization tools has thrown light on the underlying phenomenon of the anodising process.

It is generally known that the major effect on the optical appearance of anodised Al is due to the second phase particles or intermetallic phase particles that exist in almost all of the commercially available Al alloys. The specific behaviour of these intermetallic phases during anodising governs the final morphology and microstructure of the anodised layer. Depending on the electrochemical nature of the intermetallic phases, they can either be dissolved into the electrolyte or be oxidised during the anodising process and are incorporated as respective oxides into the anodic layer. If the oxide formation kinetics on the intermetallic phases is lower when compared to the Al matrix, they tend to be incorporated into the anodic layer either un-oxidised or partially oxidised state. On the other hand, if the intermetallic phases oxidise at a faster rate compared to the Al matrix, they are completely oxidised and in certain cases are also lost into the electrolyte. Each situation contributes to a certain optical appearance depending on how the particles are incorporated. In addition, type of the alloying element in the particles plays a role on the appearance of the anodised layer.

Optical appearance of anodised Al is an outcome of a complex phenomenon of interaction of light with the anodised surface. Reflectance of light from the surface of the anodised layer and interface between the anodic layer and Al substrate intertwining with scattering as well as absorption of light from within the anodic layer generates a specific optical appearance. Keeping these parameters in mind, surface finishers have been able to generate a wide variety of anodised surface appearances. They vary from highly metallic and glossy to very diffuse, and bright to dark black. However, preparation of decorative anodised Al surfaces with a bright,

white, and glossy finish has not been achieved to date. White anodised Al is of great interest to the surface finishing industries and users of anodised surfaces as it finds application in the consumer products design for pleasing aesthetics, aerospace, and deep space applications for high visibility surfaces and low solar absorption.

The reason for not being able to generate white anodised Al surfaces is that the fundamental physical phenomenon that generate colours from the anodised Al surface cannot be applied to generate white appearance. Colouring of anodised Al is based on absorptive colouring, but white appearance is obtained by light scattering. A white appearing surface is similar to a mirror, but producing full scattering of light unlike specular reflection from a mirror. Perfect scattering of light in a layer requires light scattering particles with optimum size range and refractive index. The diameter of the pores in anodic alumina layer limit the size of the light scattering pigments that can be incorporated into them, and hence limit the overall light scattering ability and the obtainable whiteness and brightness of the anodised surfaces.

1.4 Scope of the Current Thesis

The current PhD thesis attempts to understand the various factors affecting the decorative appearance of anodised Al. The knowledge gained and the knowhow from the existing scientific and industrial literature is combined with other aspects of materials science and technology such as mechanical processing of composites and vapour phase deposition processes along with post heat treatment to generate high reflectance anodised Al surfaces. The success criterion of this thesis is to achieve a bright, white, and glossy anodised Al surface with appealing decorative appearance based on a thorough scientific approach.

1.5 Scientific Approach

The approach presented in this thesis focuses on two main areas of surface engineering namely magnetron sputtered coatings and surface composites prepared by friction stir processing. The initial approach to understand the generation of optical appearance of anodised surfaces in a systematic way was to use a model Al alloy system. The microstructure of such a model alloy would be a dual phase structure, which is then anodised and then characterized for its optical appearance and anodising behaviour. Magnetron sputtering was employed for this purpose to produce binary coatings and heat treated to generate dual phase microstructures. The binary systems for coating were selected based on their physical metallurgy with respect to Al and the optical properties of their oxides when combined with anodised aluminium oxide layer. The morphology of the phases in the dual phase structure was studied by heating in a transmission electron microscope and attempts were made to modify the morphology of the second phases to enable highest interaction with light. Binary systems studied in this work include Al-Zr and Al-Ti coatings.

In order to achieve best scattering of light for white appearance of anodised Al, theoretical calculations and physical simulations were performed. This is done using polyurethane as the coating matrix on Al substrates as its refractive index is close to Al_2O_3, and TiO_2 as the light scattering particles. The results obtained on the optimum light scattering particle size, distribution, and refractive index was applied to prepare and anodise Al based composite surfaces. The observations and results obtained from anodising behaviour of Al based composites were correlated with the observations made from anodising behaviour of magnetron sputtered coating systems and also the theoretical calculations made. The surface composites studied are aluminium with TiO_2, CeO_2, and Y_2O_3 particles.

Finally, new anodising techniques were studied and the anodising process was optimised in order to generate the white anodised surfaces. The surfaces for anodising were engineered and designed based on the knowledge from the previous work. Several kinds of white appearing surfaces were generated. These surfaces were further coloured to generate different optical appearances based on pastel colouring systems.

1.6 Structure of the Thesis

The structure of the current thesis is based on the developmental steps in the work performed and the evolution of knowledge from the research work carried out in the project. Figure 1.1 shows the structure of the thesis as it is presented in the following chapters. The thesis is divided into 18 chapters. Chapters 1, 2 and 3 introduce the current thesis, the technology and the experimental methods used. The findings of the research work are presented as individual papers in Chapters 5-13. Among these papers Chapters 5-8 and 14, deal with magnetron sputtered coatings and Chapters 9-13 deal with the use of Al based surface composites for generating white appearance. The outcome of white anodised surfaces is presented in Chapter 15, however it does not provide all details and quantitative values due to the confidentiality of the process and intellectual property rights. A brief general discussion is presented in Chapter 16 and overall conclusions along with future prospects of this work are presented in Chapters 17 and 18.

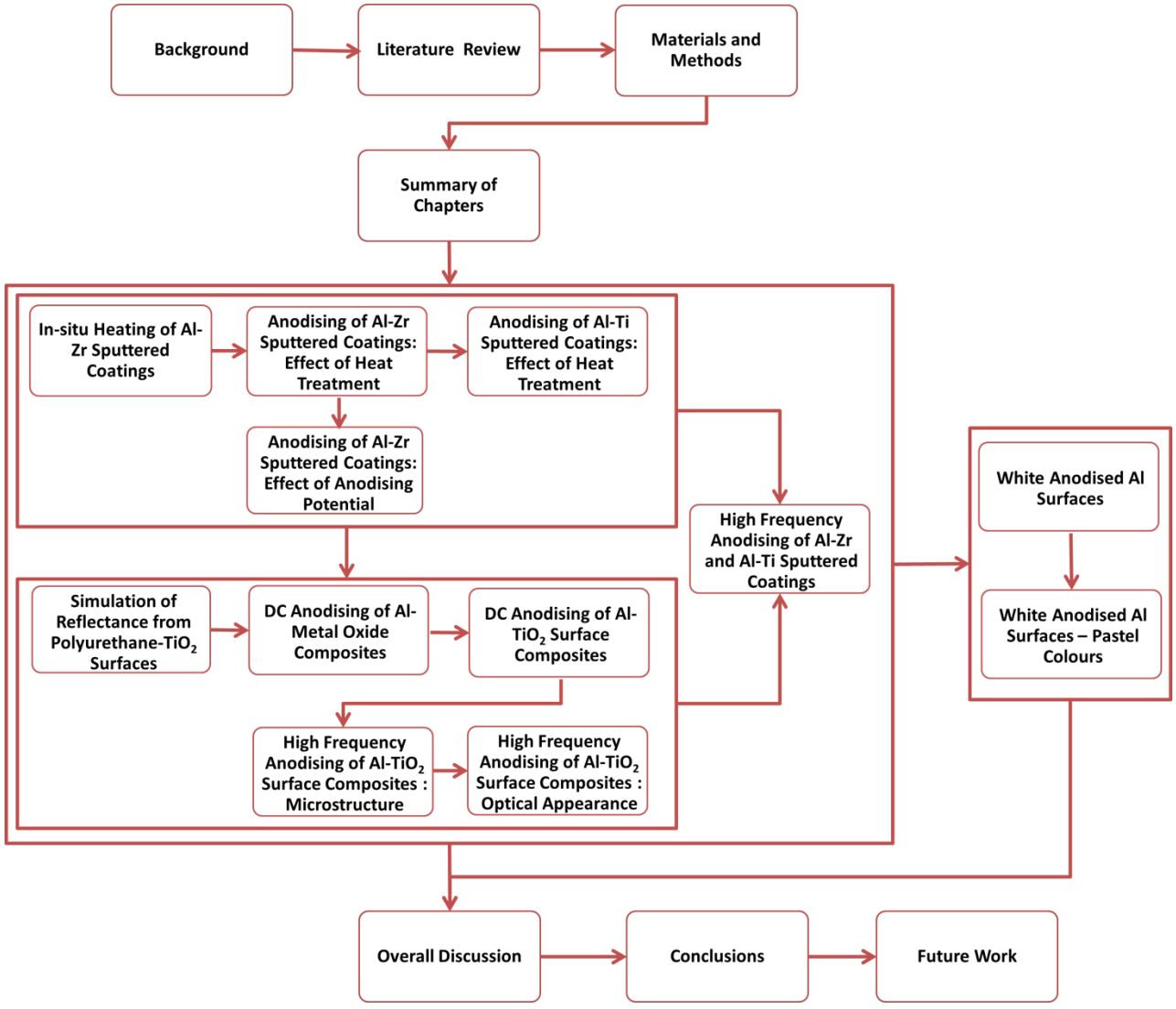

Figure 1.1: Structure of the Ph.D. thesis.

2. Introduction

2.1 Aluminium

Aluminium (Al) and aluminium alloys are widely used in today's industrial applications and are only second to Iron (Fe) and steel. They find use in different applications due to a combination of properties such as high strength to weight ratio, good ductility, excellent thermal and electrical conductivity, good inherent corrosion resistance, non-toxicity, and highly economic recyclability [1,2]. The primary Al consumption in the world and its use in various technological sectors in Europe is shown in Figure 2.1 and Figure 2.2. Today different aluminium alloys are used for various applications in the aerospace, automotive and transportation, building and construction, electrical and heat transfer applications, food packaging etc.

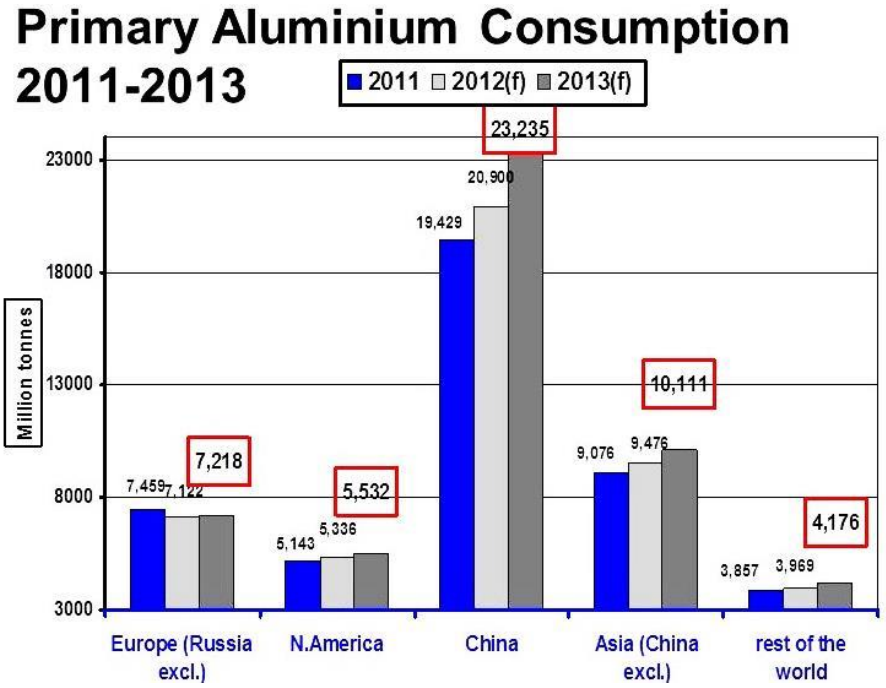

Figure 2.1: Total primary Aluminium consumption in the world, 2011- 2013 [3].

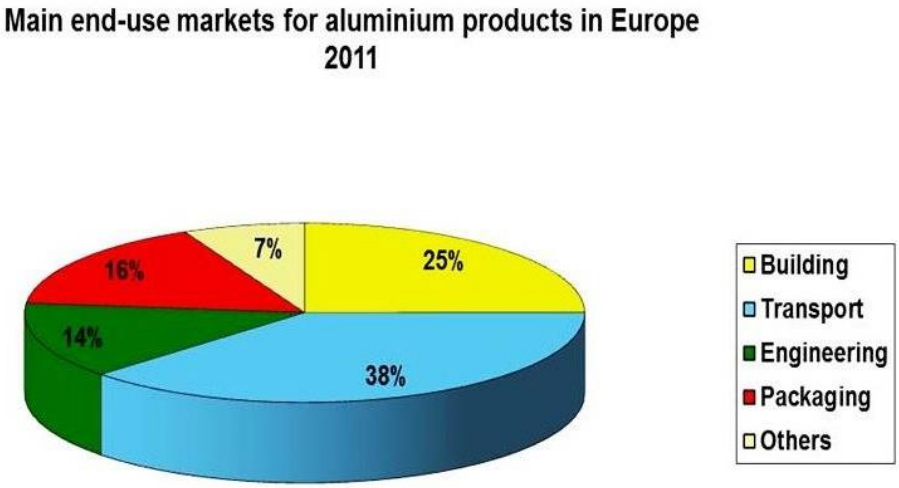

Figure 2.2: Main end-use markets for Al products in Europe, 2011 [4].

The wide ranged applications of Al are due to the ease with which it can be cast or shaped and also recycled. The energy requirements for recycling Al is only approx. 5 % compared to the production of primary aluminium [5]. Also the high strength to weight ratio of aluminium alloys makes them the first choice of material for use in applications requiring fuel efficiency such as in automotive and aerospace. In automotive industry use of Al is second only to steel in terms of the weight of materials used. The ability for generating decorative appearances with good corrosion and wear resistance obtained by electrochemical surface treatments like anodising make it a suitable candidate material for aesthetic and appealing surfaces that are widely used in various architectural and design industries thus adding value to the finished product.

2.1.1 Alloy Designation

The mechanical strength of pure Al can be substantially improved by cold working or alloying. Over the years various Al alloys have been developed with tailored properties to suit specific applications. The wide spectrum of aluminium alloys are classified and named based on the alloying elements used, manufacturing conditions, and heat treatments. The alloy classifications and designations for wrought Al were standardized by the Aluminium Association. It follows a four digit representation as shown in Table 2.1. The first digit signifies the alloy group, while second digit indicates modification or impurity limits. Last two digits indicate purity of the alloy for 1xxx series, while for other series the last two digits represents different alloys in the series. For example 1050 would indicate an Al purity of minimum 99.50 %, while for 2xxx and 8xxx series of Al alloys, the last two digits are used to identify the different Al alloys in the series.

Alloying of Al with Cu, Mn, Si, Zn, and Mg improve its mechanical properties by work and strain hardening, and also by precipitation hardening. The Al-Si alloys are mostly used as casting alloys. Usually addition of Ti and Zr to Al is performed for grain refinement. The individual alloy systems are briefly discussed below.

Table 2.1: Wrought Aluminium alloy designation and applications [6].

Aluminium, 99.0 % and greater	1xxx	Foils, Electrical Conducting Wires, Decorative applications
Copper	2xxx	Aircraft Industry
Manganese	3xxx	Utensils, Pressure Vessels, Cans, Buildings, Radiators
Silicon	4xxx	Food Handling Equipment, Heat Exchangers
Magnesium	5xxx	Cans, Transportation, Architectural Extrusions, Pipes
Magnesium and Silicon	6xxx	Transportation, Architectural Applications, Conductors
Zinc	7xxx	Aircraft Industry, Radiators
Other element	8xxx	Foils, Aircraft Industry
Unused series	9xxx	

Aluminium-Copper Alloys (2xxx Series): The maximum solubility of Cu in Al is 5.65 wt. % at approx. 550 °C, which reduces to 0.45 wt. % at 300 °C. Alloys containing 2.5-5 wt. % Cu have the best response to age hardening treatment. Hardening takes place by precipitation of theta (θ) phase which is close to the compound with formula $CuAl_2$. Minor alloying elements added to 2xxx series alloys include Si, Fe, Mn, Mg, Zn, and Cr.

Aluminium-Manganese Alloys (3xxx Series): The maximum solubility of Mn in Al at approx. 660 °C is 1.82 wt. %. Although the solubility decreases with temperature, Al-Mn alloys are not suitable for age hardening treatment.

Aluminium-Silicon Alloys (4xxx Series): The maximum solubility of Si in Al is 1.65 wt. % at approx. 580 °C. Aluminium – Silicon alloys are mostly cast or forged. Al-Si alloys have excellent castability and resistance to corrosion.

Aluminium-Magnesium Alloys (5xxx Series): The maximum solubility of Mg in Al at 450 °C is approx. 14.9 wt. % and decreases with temperature. Commercial wrought alloys contain generally up to 5 wt. % Mg and are not heat treatable, but usually strengthened by work hardening process. Al-Mg wrought alloys have good weldability, corrosion resistance, and moderate strength.

Aluminium-Magnesium-Silicon Alloys (6xxx Series): The Mg and Si combine to form Mg_2Si, which forms a simple eutectic system with Al. Precipitation of Mg_2Si phase in Al-Mg-Si wrought alloys allows them to be heat treatable to attain full strength. These alloys have good corrosion resistance and workability. In cast condition, Al-Mg-Si alloys have comparable strength with Al-Cu alloys.

Aluminium-Zinc Alloys (7xxx Series): The solubility of Zn in Al at approx. 275 °C is 31.6 wt. %, and decreases to 5.6 wt. % at 125 °C. Combined with Cu and Mg, 7xxx alloys have the highest tensile strengths among various Al alloys. Aluminium – Zinc alloys find application where good corrosion resistance and strength are required.

2.1.2 Temper Designation

In addition to the alloy designations, temper designations are provided for Al alloys to represent the basic treatments used to produce various alloys. The temper designation is usually shown followed by the alloy designations separated by a hyphen. The temper designations are summarized as follows in Table 2.2

Table 2.2: Temper designation of Al alloys

Designation	Temper Description
Basic temper designation	
F	As fabricated, no control over the amount of strain hardening, no mechanical property limits
O	Annealed and recrystallized. Temper with lowest strength and highest ductility
H	Strain hardened
T	Heat-treated to produce stable tempers
Strain-hardened subdivisions:	
H1	Strain hardened only. The degree of strain hardening is indicated by the second digit and varies from quarter hard (H12) to full Hard (H18) which is produced with approximately 75% reduction in area
H2	Strain hardened and partially annealed. Tempers ranging from quarter hard to full hard obtained by partial annealing of cold worked materials with strengths initially greater than desired. Tempers are H22, H24, H26 and H28.
H3	Strain hardened and stabilised. Tempers for age-softening Al-Mg alloys that are strain hardened and then heated at low temperature to increase ductility and stabilise the mechanical properties. H32, H34, H36 and H38.
Heat-Treated subdivisions:	
W	Solution Treated
T	Age Hardened

T1	Cooled from fabrication temperature and naturally aged
T2	Cooled from fabrication temperature, cold-worked and naturally aged
T3	Solution-treated, cold-worked and naturally aged
T4	Solution-treated, cold-worked and naturally aged
T5	Cooled from the fabrication temperature and artificially aged
T6	Solution-treated and artificially aged
T7	Solution-treated and stabilised by over-ageing
T8	Solution-treated, cold-worked and artificially aged
T9	Solution-treated, artificially aged and cold-worked
T10	Cooled from the fabrication temperature, cold-worked and artificially aged

2.1.3 Intermetallic Phases in Aluminium Alloys

Intermetallic phases are a characteristic of all Al alloys. The microstructure of Al alloys display a wide variety of intermetallic phases or intermetallic particles of varying composition, size, shape, number density, and morphology as seen in Figure 2.3.

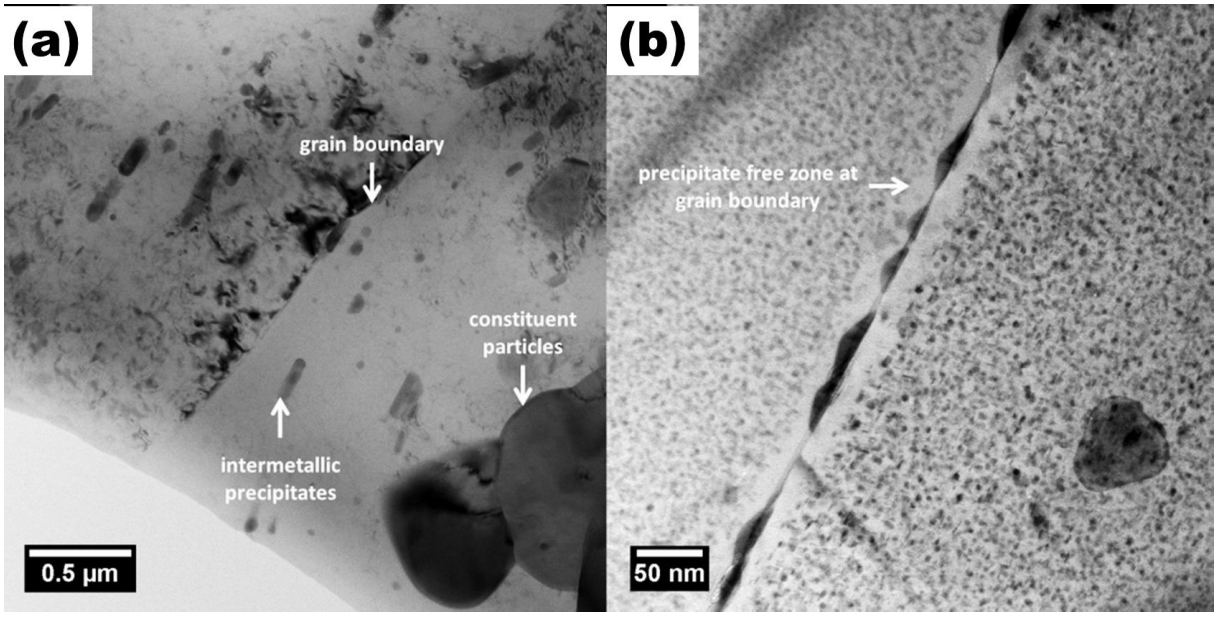

Figure 2.3: Bright field TEM micrograph showing typical microstructural variations in specimens of Al alloys: (a) AA2024-T3 and (b) AA7075-T76 [7].

The various intermetallic phases found in Al alloys contribute to the mechanical properties of Al alloys and can be classified as shown in Table 2.3.

Table 2.3: Classification of various intermetallic phases found in Al alloys [8,9].

Classification	Size Range	Morphology	Constituting Elements
Phases formed by precipitation, mostly from a super saturated solid solution that is subjected to low temperature ageing treatment	1 nm to 1 µm	Spherical, needle like, laths, plate like	Cu, Mg, Si, Zn and Li.
Phases formed during alloy solidification	few tenths of a µm to 10 µm	Large and irregularly shaped	Cu, Fe, Si and Mg
Phases that are insoluble in Al and termed as dispersoids. Generally found as segregates, clusters or nodules in solutionised state and most often responsible for grain refining	0.05 µm to 0.5 µm	Nodular or irregular	Cr, Zr, Ti and Mn

2.1.4 Electrochemistry of Aluminium

Aluminium is highly corrosion resistant due to a thin, adherent, dense and self-protecting natural oxide that forms immediately upon exposure to Oxygen [10]. This layer is invisible and is usually 3-5 nm thick. In strongly acidic or alkaline conditions, this native oxide layer is not sufficient to protect the Al surface and hence needs to be surface treated. Also, alloying of Al with various elements introduces microstructural heterogeneities at the surface, which alter its corrosion resistance.

Whilst Al and its alloys generally have good corrosion resistance, localized forms of corrosion can occur. There are two main factors which influence the general corrosion behaviour of Al. One is the type and aggressiveness of the environment and the second is its chemical and metallurgical structure. Environments can vary from outdoor atmospheres to media such as soil, water, building materials, chemicals etc. Industrial and marine environments are usually aggressive for Al due to the presence of sulphates and chlorides respectively. The corrosion resistance of aluminium decreases as its purity decreases and alloying elements are added. Copper lowers the resistance more than other elements, while magnesium has the least effect. Variations in thermal treatments of Al alloys can have big effects on its local chemistry and hence the resistance to localized corrosion. Generally, practices that result in a non-uniform microstructure will lower corrosion resistance especially if the microstructural effect is localized with electrochemical heterogeneity. Susceptibility to intergranular attack in some alloys (2xxx, 5xxx, with above 3% magnesium, and 7xxx) shows up as exfoliation and stress-corrosion cracking. Historically, the Al-Zn-Mg alloys have been the most susceptible to cracking. In addition, high- strength aluminium alloys are also susceptible to hydrogen embrittlement.

The following are few of the several ways to protect Al and its alloys from degradation due to corrosion [11]

- Surface treatment by application of Boehmite coatings, chemical conversion coatings, anodising or cladding.
- Surface coatings based on paint and lacquer.
- Use of inhibitors in the surrounding medium.

Of the above mentioned processes, anodising (specifically decorative anodising) is of interest to the current thesis and is explained in detail in the following sections.

2.2 Anodising of Aluminium

The process of converting the Al surface into thicker oxide using electrochemical methods in order to protect the surface from corrosion and wear was first introduced and patented in the early 1900s. The natural oxide on the Al surface was thickened with the help of a sulphuric medium containing iron sulphate. Shortly after, several other variants of the process evolved based on chromic acid, sulphuric acid, and oxalic acid.

Today there are various applications for anodising of aluminium, which include:

- decorative surfaces displaying pleasing aesthetics
- corrosion resistant surfaces
- surfaces with high hardness for increased wear resistance
- improved adhesion of top organic paint coats
- functional surfaces with tailored dielectric and optical properties

The decorative surfaces generated by anodising of Al have a very high aesthetic value and are very widely used in various applications. The current thesis aims at producing decorative anodised surfaces for Al enclosures applied in consumer electronic devices such as those shown in Figure 2.4.

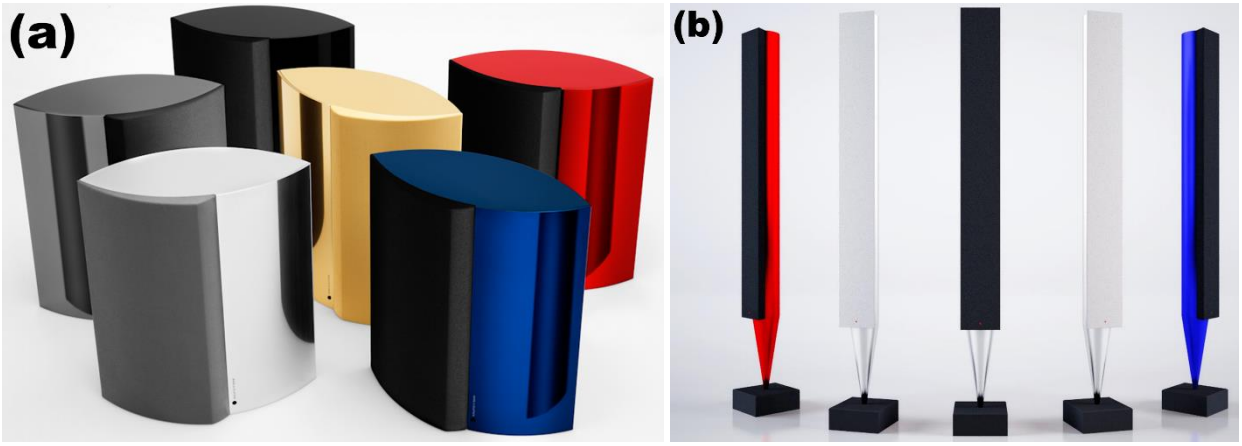

Figure 2.4: Some high-end design products produced by Bang and Olufsen A/S, Denmark: (a) BeoLab 4000™ speakers and (b) BeoLab 8000™ speakers that employ decorative anodising of Al for generating visually appealing surfaces.

2.2.1 Types of Anodising

A wide variety of anodising processes have been developed over the years. The processes have been optimised and tailored in order to achieve the functional properties that are specifically required for the application that they are intended for. A few of them are listed below [12].

- **Chromic acid anodising** - It is also known as Type 1 anodising and is commonly used in aerospace applications for 2xxx and 7xxx alloys. Anodic films produced are opaque, soft, and ductile and are harder to colour using dyes. This process may be applied as a pre-treatment before painting. Typical anodic layer thicknesses range from 0.5 µm to 18 µm.

- **Sulphuric acid anodising** - This process is also known as Type 2 and Type 3 anodising. It is the most widely used anodising process. Anodic film thicknesses are usually between 1.8 µm to 25 µm for Type 2. Type 3 anodising is called hard-coat, hard anodising or engineered anodising and anodic layer thicknesses are between 13 µm to 150 µm. They are typically used for protection against corrosion, good surface appearance, and for increased wear resistance.

- **Organic acid anodising** - This process is also known as integral colour anodising and can produce yellowish integral colours without dyes if it is carried out in weak acids with high voltages, high current densities, and strong refrigeration. Colour shades are limited to pale yellow, gold, deep bronze, brown, grey, and black. Using these processes anodic layer thicknesses of up to 50 µm can be achieved.

- **Phosphoric acid anodising** - This process is usually used as a surface preparation for adhesives.

- **Barrier type anodising** - This process is performed in borate or tartrate baths in which aluminium oxide is insoluble. The coating growth stops when the part is fully covered, and the thickness is linearly related to the voltage applied. Anodic layers are free of pores compared to the sulphuric and chromic acid processes. This type of coating is widely used to make electrolytic capacitors. Anodic layer thicknesses are in the range of 0.5 µm.

- **Plasma Electrolytic Oxidation** - This anodising process involves higher voltages during anodising. The high voltage causes sparks to occur, and results in more crystalline/ceramic type coatings with increased surface hardness.

The following schematic (Figure 2.5) shows the general sequence and steps involved in the anodising of Al alloys for decorative appearance using sulphuric acid (Type 2). The individual steps are discussed in detail in the following sections.

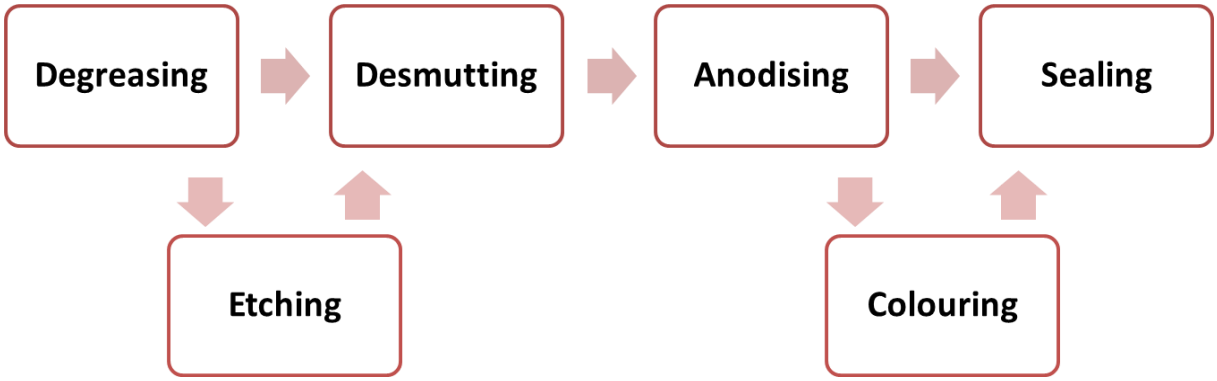

Figure 2.5: General steps involved in a decorative anodising process for Al.

2.2.2 Pre-treatments prior to Anodising

Prior surface finish of the alloy surface has huge effects on the nature of the final anodised surface in terms of its performance and appearance. The aluminium alloys are surface treated prior to anodising both for cleaning and degreasing as well as texturing for specific appearance or other properties. The pre-treatments commonly used for the decorative anodising purposes are usually a combination of mechanical, chemical, and electrochemical processes depending on the nature of the final anodised surfaces that are needed. Discussions below focus on the surface pre-treatments mainly used for the decorative applications as it is the focus of the present thesis.

Mechanical pre-treatments mostly include grinding, blasting, brushing, buffing, and polishing [12,13]. Grinding is one of the main pre-treatment processes used to remove the artefacts generated on the surface due to the manufacturing process. After grinding, the surfaces are subjected to diamond turning to impart a high gloss to the surface or polishing using buffing wheels. Polishing waxes based on Al_2O_3 as abrasive media are used to provide glossy surfaces. Blasting the surface using grit or glass beads provides rougher surface with a matte appearance. Similar appearances are achieved using heavy caustic (NaOH) etching of the surface [14,15].

Heavy caustic etching in general levels out the surface of the Al from any prior heterogeneities, the local composition differences, surface texture differences, and surface oxide inclusions [16,17]. A layer of smut

is usually formed on the surface of the alloy after being subjected to caustic etching. This smut is usually a mixture of the corrosion products formed from the alloying elements and impurities in the Al alloy some of which are insoluble in the caustic solution. This is due to difference in electrochemical dissolution of various alloying elements in the caustic media used for the etching process [8,9,18–20]. Timm [21] has categorized various intermetallic phases (Table 2.4) found in commercial Al alloys based on their behaviour during the alkaline etching treatment.

Table 2.4: Electrochemical behaviour of intermetallic particles during alkaline etching [21].

Cathodic (predominant attack of matrix)	Electroneutral	Anodic (predominant dissolution of particle)
Al_3Fe	$Al_6(Mn,Fe)$	Al_6Mn
$Al_6(Fe,Mn)$	$Al_{12}(Mn,Fe)Si$	Mg_2Si
$Al_{12}(Fe,Mn)Si$	Al_7Cr	Al_2Cu
$Al_9Fe_2Si_2$	Al_3Ni	
Mg_2Al_3		
Al_3Ti		

Removal of smut is performed by desmutting treatment, which involves immersion in concentrated HNO_3 for a few seconds. On the other hand, for surfaces which are prepared for high gloss, there is a highly deformed layer present on the surface due to the mechanical polishing and turning process [22]. This layer is known as Beilby layer [23] and contains impurities such as oxides and polishing medium in a fine grained or amorphous Al matrix, and causes a bad surface appearance after anodising [24–26]. In order to retain the gloss of the treated surface, but remove the deformed layer, the surface is degreased with a mild alkaline solution like Alficlean™ based on mild caustic and then desmutted.

2.2.3 The Anodising Process

2.2.3.1 Conventional DC Anodising

Anodising of Al is a controlled oxidation process of the metal surface generating an oxide layer up to a thickness of (12-20 µm for the decorative anodising). Anodising is an electrochemical process and it is usually applied to valve metals such as Al, Ti, Nb, and Ta. For Al and Al alloys, anodising process results in the formation of Aluminium oxide usually with self-assembled nano-porous structure. The process is usually performed in an electrochemical cell, where the work piece (in this case aluminium alloys) is the anode and the cathode material can be Al, Graphite, or Pt. The electrolyte is usually based on a mixture of oxidising inorganic acids, which also act as charge carriers.

Anodic films formed on Al are classified in to barrier type and porous type layers. Barrier type films are formed in electrolytes where the initially formed anodic oxide is insoluble. Examples of such electrolytes are neutral boric acid, ammonium borate, or tartrate aqueous baths. The pH values used for the above electrolytes for generating a barrier type anodic film is in the range of 5-7. Porous type anodic films are formed in electrolytes where the anodic oxide is slightly soluble, examples of which are sulphuric acid, phosphoric acid, chromic acid etc. The general differences between the two types of anodic oxides are outlined in Table 2.5.

Table 2.5: Classification of the two types of anodic oxide films that are formed on Aluminium [27].

	Barrier Type	Porous Type
Structure	Thin, compact, non-porous	Inner Layer - Thin, Compact barrier-type Outer layer – Thick and porous
Thickness	Voltage dependent, ~1.4 nm/V	Inner layer – voltage dependent, ~1 nm/V for sulphuric acid Outer layer – voltage independent, current density, time and temperature dependent
Typical Electrolytes	Solutions of Boric acid – Borax Citric acid – Citrate Ammonium tartrate	Sulphuric, Phosphoric, Chromic and Oxalic acid aqueous solutions

In the case of anodising for decorative applications, porous type films are used as they possess excellent corrosion and abrasion resistance. The porous oxide used for applications are also sealed, while a number of coloured anodised surfaces are produced by the dyeing process. Due to the presence of porosity, dye materials are incorporated into the porous structure during a post anodising process followed by sealing. Following reactions shows the mechanism of the oxide growth during anodising.

The overall anodising process can be described as:

Overall anodising reaction:

$$2Al + 3H_2O + 2Al^{3+} + 3O^{2-} \rightarrow 2Al_2O_3 + 3H_2 \qquad (2.1)$$

The anodic half reaction of Oxygen ions migrating to the Al metal-barrier oxide interface and Al ions migrating to barrier oxide-electrolyte interface can be shown as follows:

Anodic reaction at metal-oxide interface:

$$2Al + 3O^{2-} \rightarrow Al_2O_3 + 6e^- \qquad (2.2)$$

Anodic reaction at the oxide-electrolyte interface

$$2Al^{3+} + 3H_2O \rightarrow Al_2O_3 + 6H^+ \quad (2.3)$$

The cathodic half reaction resulting in the formation of Hydrogen gas can be shown as follows:

Cathodic half reaction

$$6H^+ + 6e^- \rightarrow 3H_2 \qquad (2.4)$$

The formation and evolution of porous anodic film structure has been of great interest and consequently extensive studies are available in the literature. It has been shown that the porous anodic films are comprised of a thin inner barrier layer and a thick outer porous layer. The thickness of the inner barrier

layer is dependent on the applied anodising potential and is expressed as anodising ratio (nm/V). The thickness of the barrier layer is affected by the concentration of electrolyte and the applied anodising potential [12]. For a given set of anodising parameters, the barrier layer thickness remains constant during the growth of the porous anodic film. It is proposed that the migrating cations and/or anions (as in half cell reactions in Equation 2.2 and 2.3) at the metal-barrier oxide interface and at the barrier oxide-electrolyte interface respectively forms the barrier layer. This barrier oxide is then converted to a porous oxide by other mechanisms (discussed in following sections) and thus the barrier layer thickness is maintained constant by the rate of conversion to the porous film.

The porous anodic layer usually shows a self-ordered and geometrically arranged hexagonal structure with a pore at the centre of every hexagon [28, 29]. The formation of this structure is suggested to occur by a purely chemical conversion process as the acidic conditions at the interface of barrier oxide-electrolyte are significantly different from that existing in the bulk of the electrolyte [30]. The phase constitution of the porous films has been investigated by many authors in detail and it mainly contains a mixture of amorphous alumina [31], $Al_2(SO_4)_3$, and boehmite (AlOOH), while additionally pseudo-boehmite [32] is formed during the hydrothermal sealing process.

The pore density, diameter, and wall thickness are affected by different parameters of anodising such as the anodising potential, anodising time, current density, type of electrolyte, and temperature of the electrolyte. Too long an anodising time usually results in pore widening at the top surface of the anodic layer as this is the region exposed to the electrolyte for the longest time. The pore diameter in this case would be higher than that found at the bottom of the porous film, leading to a conical geometry of the pores instead of cylindrical geometry. The reason for pore widening at the top surface is due to the dissolution of the oxide by the anodising electrolyte, and in most severe cases this effect is called “powdering effect” [33,34]. The mechanism of pore widening due to longer anodising times also introduces a limit on the maximum anodic film thickness obtainable for a given anodising potential. The anodic film growth ceases at a point when the pore diameter at the top of the anodic film is same as that of the oxide cell width. Continuing the anodising beyond this point may lead to dissolution of the already formed oxide and result in reduction of the anodic film thickness [35]. Increase in anodising potential increases the anodic film growth rate, increases the thickness of the barrier oxide layer, increases the pore diameter, and reduces the density of the pores. Low current densities generate a film with high pore density, but the hardness of the film is lower. Increase in the anodising temperature increases the growth rate, pore diameter, cell wall thickness, and pore density of the anodic oxide film.

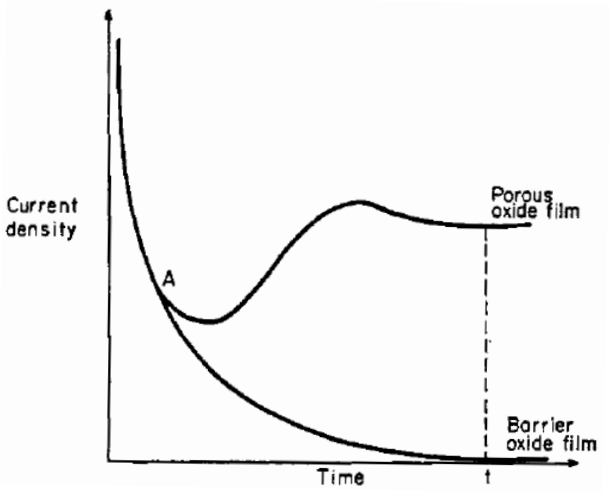

Figure 2.6: Current density-time transients for the formation of a barrier type and porous type anodic film on Al. Point A represents the point at which divergence of the two curves occurs, and hence may be related to the pore initiation phenomenon. Time *t* is typically 25 s for a 15 V application step to Al in 15 % Sulphuric acid [27,37].

The transition of anodic oxidation of Al from barrier type layer to porous type layer has been studied by various authors and several pore formation theories have been suggested [27]. The current density-time plot recorded for anodising of Al in 15 wt. % sulphuric acid is shown in Figure 2.6. Initially, as the barrier layer thickens, the electric field strength across the barrier layer and the current density decreases. As the anodising proceeds, the barrier layer current density reduces even further, while the porous layer current density continues to lower for a certain period of time and then increases. The barrier layer current density is mainly electronic, whereas the porous layer current is dominated by ion transport. Point A in Figure 2.6 shows the transition where the barrier to porous film transformation takes place. The thickness of the barrier layer decreases to a slight extent beyond this point and this facilitates the initiation of porous film. Keller et al. [28] have suggested that the pores initiate at weak spots in the already formed barrier layer. These weak spots correspond to areas of high current density leading to high joule heating, which leads to increased local dissolution of the barrier oxide. Another process proposed by Hoar et al. [36] states that the porous film forms due to a field assisted growth process involving the formation of OH^- ions due to alumina dissolution. These anions migrate across the barrier layer and combine with Al^{3+} to form alumina at the metal-barrier oxide interface.

Michelson [38] has reported that the conversion of the barrier layer to porous layer is influenced by the applied electric field. It was found that the time required to obtain a constant barrier layer thickness depended on the rate of change of the applied potential. Thompson et al. [39,40] provide a theory based on the pore formation theories presented above. It has been reported that both the Al^{3+} and the O^{2-}/OH^- ions are mobile during the anodic film growth, and the anions develop a solid film at the metal-barrier film interface by migrating inwards. The cation, Al^{3+}, migrates outward from the metal-barrier film interface to the barrier film-electrolyte interface and its contribution towards film growth is dependent on certain anodising parameters. In Figure 2.7 (a), the sequence of porous film formation is shown from an already formed anodic barrier film over the surface of Al. The oxide growth (barrier film) in its initial stages is assumed to grow uniformly. As time progresses, the migrating Al^{3+} from the metal surface to the top of barrier film get concentrated along certain regions and this results in localisation of the electric field. Consequently, lowering of the electric field in the surrounding regions takes place and a scalloped structure at the top surface of barrier film evolves due to the lower field assisted dissolution [41]. Here onwards, due to localised concentration of the electric field and ionic current across the barrier film, the anodic film growth proceeds by porous film formation. In Figure 2.7 (b), the evolution of anodising potential with time is shown for constant current anodising. The potential initially increases, corresponding to growth of the barrier type film. The potential then drops indicating the transition to porous film formation and then the potential value remains constant over time indicating a steady state growth of the porous film. The potential value corresponds mostly to the potential drop across the barrier film. The final structure of the porous anodic film is shown in Figure 2.8.

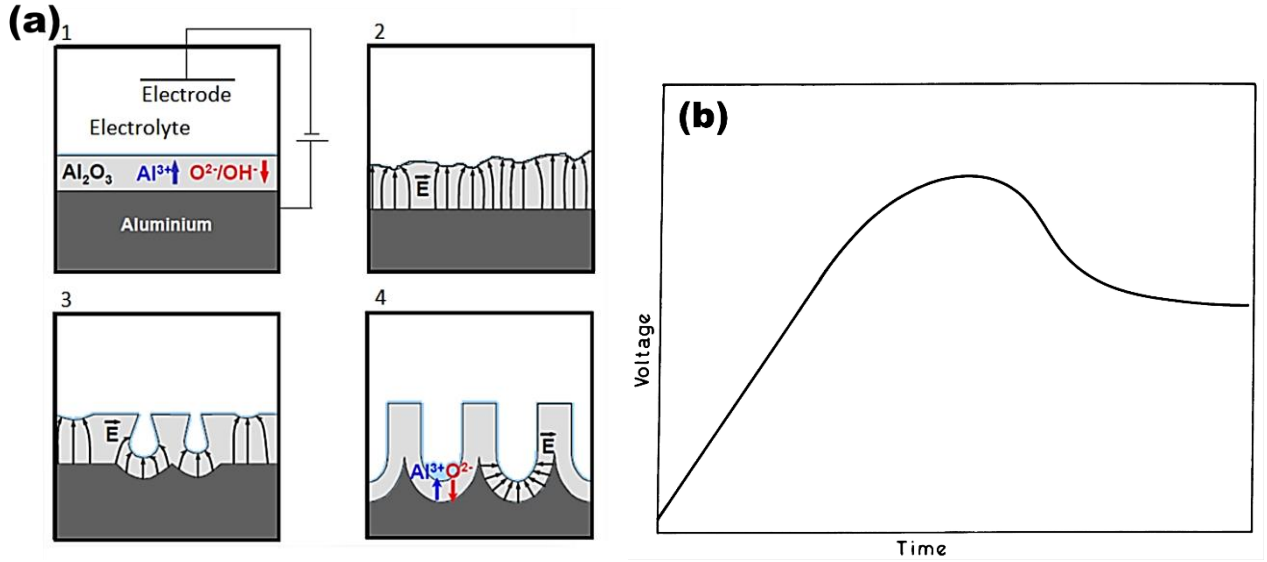

Figure 2.7: (a) Schematic showing pore development during anodising of Al in acid electrolyte, (b) Typical Voltage-Time curve for anodising of Al at constant current density in acid electrolyte [42,43].

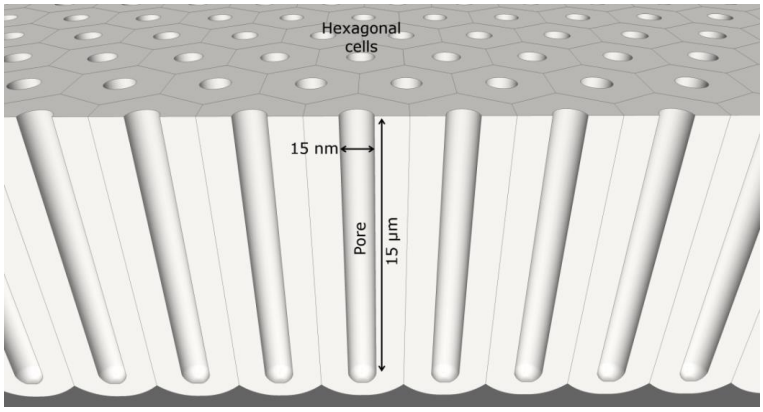

Figure 2.8: Ideal structure of a porous anodic layer (size of the pore is shown as an example) [44].

2.2.3.2 AC Anodising

Anodising using alternating current is of significant interest as it provides the possibility for the use of work pieces at both electrodes with anodising each of them in alternate cycles [45–47]. Alternating current (AC) anodising of Al provides anodic films with similar features as in conventional DC anodising [48]. The morphology of the anodic films, composition, and the role of parameters such as anodising current density, potential, and temperature are found to be comparable to DC anodising processes [49,50]. In general, AC anodising is used for obtaining thin anodic films, whereas producing thicker anodic films take longer times and therefore are softer than those obtained by DC anodising [51]. De Graeve et al. [48] studied the efficiency of the AC anodising in 20 wt.% H_2SO_4 for AA1050 alloy and reported that the charge efficiency is higher for the DC process (98 %) when compared to the AC process (90 %), whereas the oxide formation efficiency is the same (60 %). Also, it was observed that the charge as well as oxide forming efficiency reduced with increasing frequency from 10 Hz (98 %, 65 %) to 500 Hz (41 %, 44 %).

Zahavi [52] studied the structure of AC anodic films formed on Cu and Fe containing Al alloys using electron microscopy techniques. The local pore structure and incorporation of the partially oxidised intermetallic particles were investigated. The matrix was involved in anodic film formation and anodic current flow, whereas the intermetallic particles localised the cathodic current. Non-reactive intermetallic particles were

reported to be not affected by the cathodic current, while reactive intermetallic phases were covered with Cu deposited during the cathodic cycle.

In AC anodising, cathodic reactions such as sulphate reduction, sulphur deposition, and also hydrogen gas evolution result in yellowness of the anodic film making them unappealing for decorative purposes [48,50]. However, AC anodising in oxalic acid electrolytes has been reported to produce integral colours ranging from light to dark shades of gold and bronze in different Al alloys [45]. The cathodic reactions are reported to be localised at flaws or defects in the anodic layer such as the intermetallic particles, where the anodic film is disrupted due to oxygen evolution during the anodic cycle. This localisation of cathodic current and hydrogen evolution cause heterogeneities due to the preservation of the flaws [48].

The problem of yellow colouration and sulphur deposition in the anodic layer during AC anodising in sulphuric acid can be avoided by addition of modifying agents such as ferric ammonium oxalate, ferric sulphate, chloride or nitrate, nickel sulphate, and also sodium sulphate to the anodising electrolyte [53,54]. These modifying agents shift the reaction from reduction of sulphate to electrolysis of water and prevents the deposition of sulphur and its compounds in the pores [55,56]. Barbosa et al. [57] studied the distribution and incorporation of one such modifier (ferric sulphate) into the anodic oxide formed in 10 vol.% H_2SO_4. Results showed no significant difference between the maximum sulphur content (5 - 6 wt. %) for thin and thick anodic films, and also no direct relationship between the sulphur content and anodising conditions. Ferric sulphate was not found to be incorporated into the anodic layer. Another variation of AC anodising is to use pulses of current or voltage in a process known as pulse anodising which is discussed in the following section.

2.2.3.3 Pulse Anodising

Pulse anodising technique involves cyclic varying of the potential between two different values [58,59]. This technique has been introduced by Yokoyama et al. [60,61] in order to provide thick and dense anodic films by applying high current density at room temperature, therefore avoiding the “burning and powdering effect”. Burning of anodic films takes place at high anodic current densities and at very low anodising temperatures. This is due to the metallic Al projections from the substrate into the barrier layer, which cause localisation of anodic current density. This creates joule heating, which leads to non-uniformity in the anodic layer and locally enhanced dissolution of the barrier oxide (burning). This can be prevented by anodising at higher temperatures, but results in powdering of the anodic layer due to higher chemical dissolution by the anodising electrolyte [33].

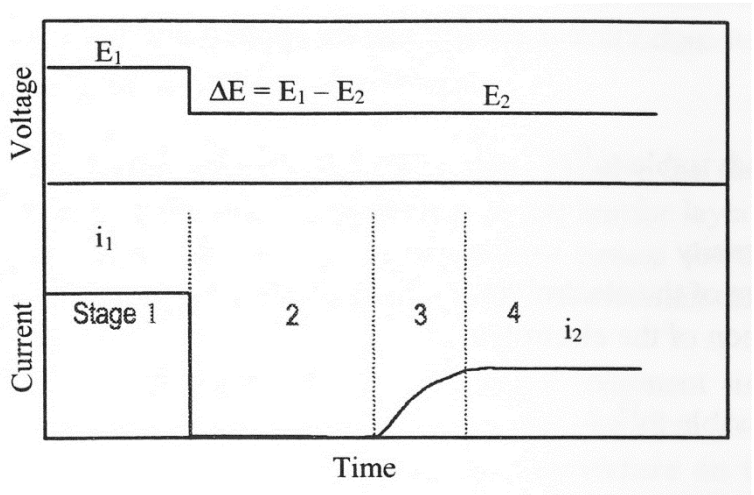

Figure 2.9: Anodising potential and corresponding current vs. anodising time showing the recovery effect [62,63].

Pulse anodising by applying high and low anodic potential to Al substrates introduces a related change in the anodic current due to “recovery effect” [38] as shown in Figure 2.9. The processes taking place during

the current recovery have been studied by Takahashi et al. [62] using electron microscopy of ultra-thin anodic sections (see Figure 2.10). It has been observed that the current initially drops from a stable value (Stage 1) to a very low value (Stage 2) when the anodising potential is dropped, which then increases gradually (Stage 3). This drop in current was correlated to the lowering of the electric filed across the already formed barrier layer. During this period, thinning of the barrier film takes place due to chemical dissolution by the electrolyte [33,34]. The electric field across the barrier film increases once again due to the reduction in thickness. Corresponding increase in the anodising current with time was observed due to the field enhanced dissolution of the barrier layer [41], which reaches a steady value corresponding to the new anodising potential E_2 (Stage 4). A new set of hemispherical barrier type oxide forms and evolution of a new set of pores takes place leading to anodic pore structure corresponding to the lowered anodising potential.

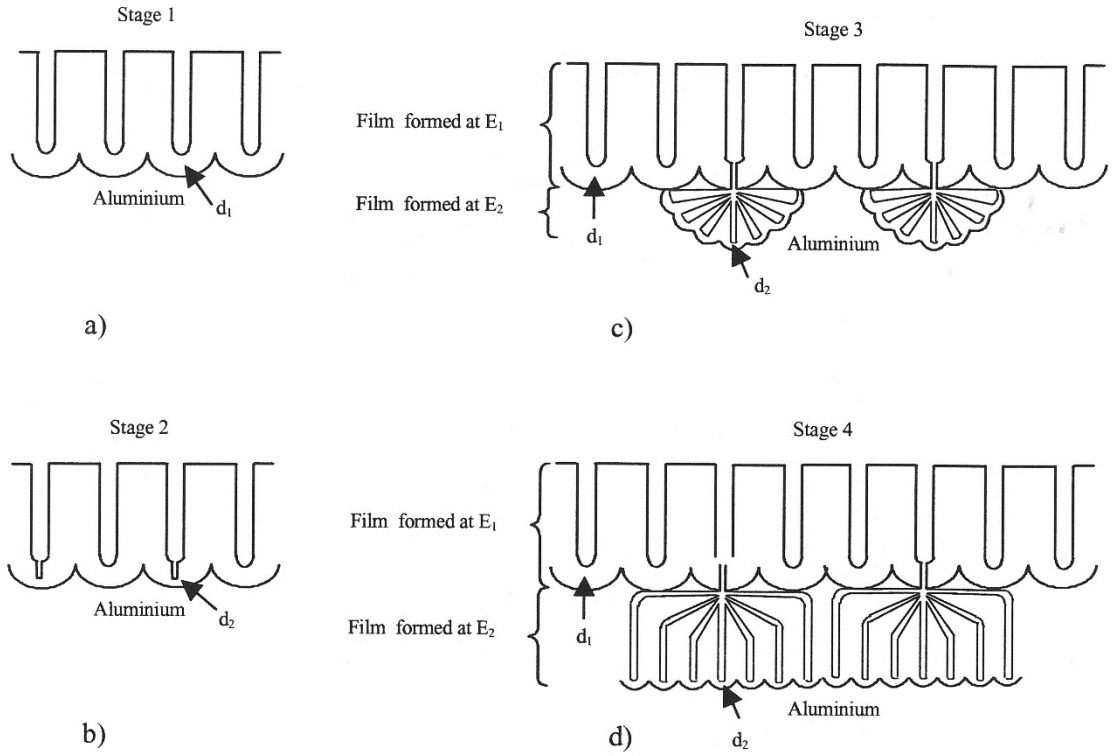

Figure 2.10: Schematic showing the structure of anodic oxide layer evolution during recovery period [62,63].

Pulse anodising is reported to be suitable for anodising in electrolytes which generate natural-coloured anodic oxides like oxalic acid on Al substrates that are prone to burning or containing a considerable amount of Si (cast alloys). The structure of anodic layers formed on AA6063 and AA7075 by pulse anodising was studied by Komisarov et al. [64]. A clear distinction between the pores formed at high current density and low current density (see Figure 2.11) was observed when the difference between the pulse amplitudes was higher.

Juhl [63] has investigated the effect of pulsing on the anodised structure of cast and extruded Al alloys. Three main variations of pulse anodising were investigated namely: (i) low frequency pulse anodising, (ii) high frequency pulse anodising, and (iii) high frequency pulse reverse pulse anodising. It was observed that for extruded AA60603 alloy (20 µm of anodic layer thickness), none of the processes showed any superior behaviour when compared with conventional DC anodising in terms of wear resistance, hardness, colour, and sealing test. However, for cast Al alloys containing Si, the properties of the anodic layer were poorer for high Si alloys compared to the alloys with low silicon content. Fratila-Apachitei et al. [65,66] have studied the effect of low temperature pulse anodising using various current and potential waveforms as shown in Figure 2.12 on pure Al, AlSi10, and AlSi10Cu3 cast alloys. The pulse frequency was 0.0125 Hz (low frequency pulse anodising) and the duty cycle was 75%. Results did now any significant difference between the anodic layer

properties achieved using the six different waveforms. Slightly better anodic layer hardness and growth rate were obtained for ramp-down spike (rds) current waveform at the cost of increased surface roughness.

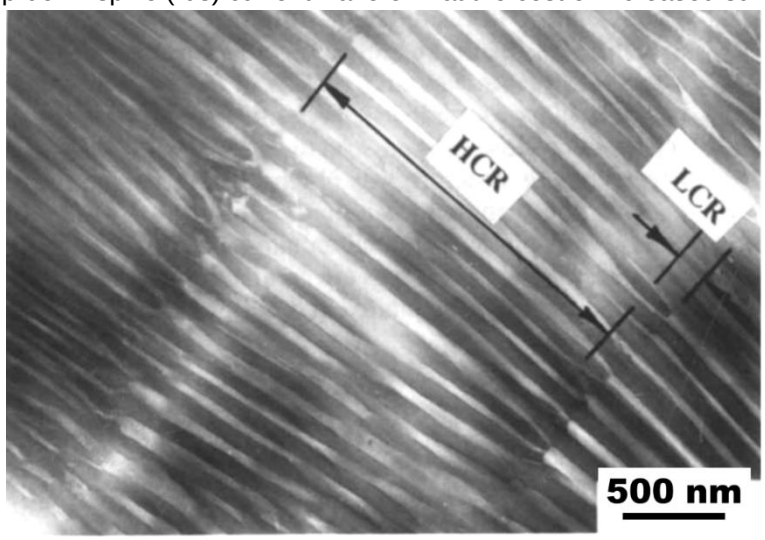

Figure 2.11: Cross section of pulse anodised porous alumina layer on AA6063. LCR: Low current density region, HCR: High current density region [64].

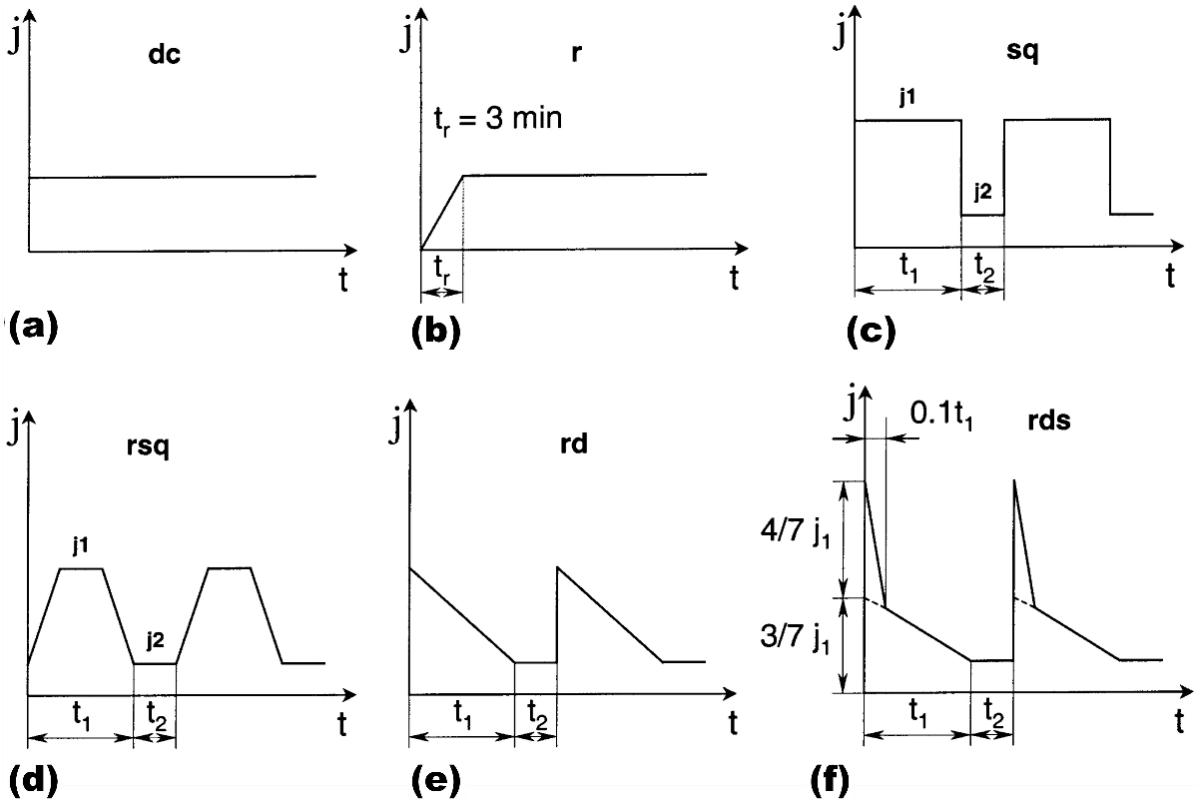

Figure 2.12: Schematic representation of current waveforms: (a) Direct Current, DC; (b) Ramped Current, r; (c) Square Pulses, sq; (d) Ramp-Square Pulses, rsq; (e) Ramp-Down Pulses, rd; and (f) Ramp-Down Spike Pulses, rds. Current density j_1 = 3 A/dm^2 and 4.2 A/dm^2; $j_2 = ¼\, j_1$ [65].

High frequency pulse reverse anodising (PRPA) (at 13.3 Hz) in oxalic acid and sulphuric acid was applied to AA1080 by Okubo et al. [67,68]. The effect of duty cycle, temperature, and anodising time on the obtained anodic layer thickness and hardness was investigated. Thicker coatings could be obtained by

controlling the negative current density and hardness improved with increasing negative current density, decreasing temperature, and anodising time. Increasing the duty cycle resulted in the increase of coating thickness and an optimum value for hardness and coating ratio was observed at 86-95 % duty cycle. Similar results were observed by Kanagaraj et al. [69] for pulse anodising in oxalic acid electrolyte. Comparative studies in different electrolytes like sulphuric, oxalic, and chromic acid were also performed using pulse reverse pulse anodising [70]. The cell size and pore structure was found to be uniform for sulphuric acid electrolyte, whereas for oxalic acid electrolyte, the degree of pore branching increased with decreasing duty cycle. Chromic acid and oxalic acid anodising showed similar anodic pore structures. It was observed that the cathodic reactions like hydrogen gas evolution weakened and destroyed the barrier oxide during negative cycle and reduced the resistance of the barrier layer for the subsequent anodic or positive cycle.

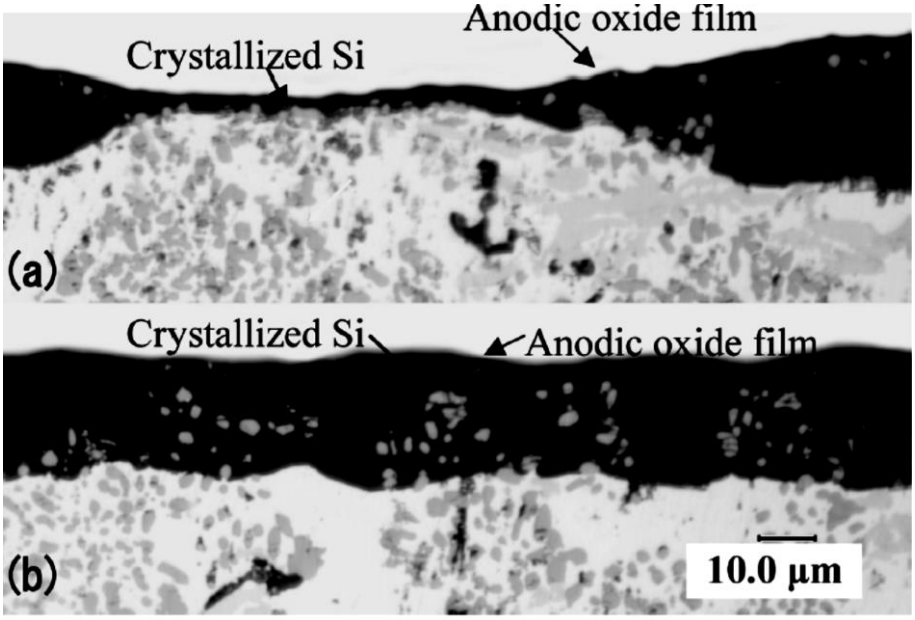

Figure 2.13: Micrographs of cross-section of anodic oxide films formed by: (a) conventional DC anodising at 2.5 A/dm^2 for 1200 s and (b) high frequency pulse reverse pulse anodising at 46 V with 30 µs/cycle (33.3 kHz) for 240 s on cast Al-Si (AC8A) alloy[71].

Pulse anodising using low to very high frequency (0.01 to 100 Hz) in sulphamic acid for AA1100 showed increasing anodic film thickness, hardness, and coating ratio with increasing pulse frequency, current density, and duty cycle [72]. Yamamoto et al. [71] and Fujita et al. [73] applied very high frequency pulse reverse pulse anodising (approx. 2 kHz to 47 kHz) to a cast Al-Si alloy (AC8A). It was shown that the anodic film obtained was far more uniform under high frequency anodising compared to the conventional DC anodising as the cathodic cycle electrolysis resulted in the entrapment of primary Si phase and pore branching (see Figure 2.13 and Figure 2.14).

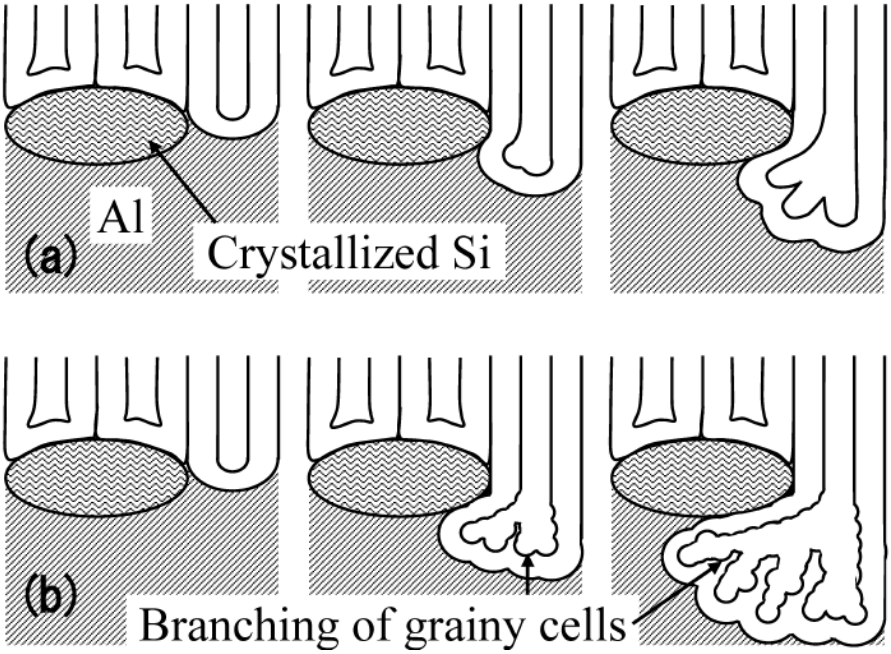

Figure 2.14: Proposed schematic diagram showing cross section of anodic films formed by: (a) conventional DC anodising and (b) high frequency pulse reverse pulse anodising on cast Al-Si (AC8A) alloy [71].

2.2.3.4 Plasma Electrolytic Oxidation (PEO)

Plasma electrolytic oxidation (PEO) is also known as micro arc oxidation (MAO), micro plasma electrolysis, anode spark electrolysis or plasma electrolytic anode treatment [74]. It is a special anodising treatment combining the electrochemical anodising process with plasma process. It is often applied to Al, Nb, Mg, and Ti [75–77]. The mechanical properties of the PEO coatings such as hardness, wear resistance, and chemical resistance are very good, however the surface after PEO treatment is extremely rough compared to the conventional anodising [78–80]. Hardness levels up to 1500 HV can be obtained using this technique and the coatings have an exceptional fatigue life due to the inherent compressive stresses in the coating [81]. Build-up of the anodic layer on Al substrates during this process takes place at very high temperatures (2000 °C) generated by the local arcing at the anode. Electrochemically formed boehmite transforms to alumina (Corundum) due to the higher temperature at the anode generated by the sparking or arcing

The surface of the plasma anodised materials show a typical pin hole type morphology, which correspond to micro channels where the arcing or plasma discharge takes place [82]. The micro-arcs or plasma discharges owing to their high energy generate local heating, melting the anodic boehmite to form crystalline α-, β- and γ-Al_2O_3 [83]. The anodic film formation mechanism during PEO has been of great interest and general understanding is that due to high temperature at the micro channels Al from the substrate melts and is ejected out through the micro channels. Rapid cooling combined with electrochemical oxidation takes place once the molten Al reaches the anodic layer – electrolyte interface [84]. Very thick anodic layers can be achieved by this process as the anodic layer growth continues as long as the micro channels are open to the substrate unlike conventional anodising where the migration of species across the barrier layer is the rate limiting step [79]. Plasma electrolytic oxidation can be performed under AC or DC conditions and the usual voltage range is between 100-900 V [85]. The electrolytes used are acidic [86] and more often alkaline [83] with addition of some salts.

2.2.4 Anodising Behaviour of Intermetallic Phases

The relationship between the anodising parameters and the structure of the anodic layer produced described above hold true only for anodising of pure Al. However, the commercial Al alloys, which often have various phases and heterogeneous microstructures behave in a different manner depending on the electrochemical behaviour of different phases and also the anodising process used. Timm [21] has classified (see Table 2.6) various intermetallic phases based on their behaviour during sulphuric acid anodising when compared to the surrounding Al matrix.

Table 2.6: Behaviour of intermetallic phases during anodising in sulphuric acid [21].

A Unchanged and incorporated into the oxide films	B Oxidised and incorporated (or dissolved) at a rate comparable or slower than Al	C Oxidised and incorporated (or dissolved) at a rate faster than Al
Si $Al_6(Mn, Fe)$	$Al_{12}(Fe, Mn)_3$ Si * Al_3Fe	$Al_{12}(Fe, Mn)_3$ Si * Mg_2Al_3
Al_3Ti	Al_6Fe	Mg_5Al_8
	$Al_6(Fe, Mn)$	Mg_2Si
	$Al_9Fe_2Si_2$	Al_7Cr
		Al_2Cu

* dependent on particle size

Fratila-Apachitei et al. [87,88] have reported that the precipitates based on Si anodise at a lower rate than the surrounding Al. Jariyaboon et al. [89] using FIB-SEM showed that the Fe and Si based second phases behave in a similar manner. Iron bearing intermetallic phases such as Al_3Fe and Al_6Fe were studied for their anodising behaviour by Shimizu et al. [90]. It was found that the oxidation rate is higher for Al_3Fe phases when compared to Al_6Fe phases (0.44 times that of Al matrix). In general, Fe and/or Si bearing intermetallic phases have been shown to oxidize at a slower rate than the Al matrix. Intermetallic phases containing Cu and Mg are anodised at a rate faster than the Al matrix [8,9,20]. This difference in anodising behaviour of the intermetallic phases has been found to alter the local structure of the anodic porous film and also results in incorporation of partially oxidised intermetallic phases or voids due to preferential dissolution of the phases [91,92]. Saenz de Miera et al. [93] have studied various model intermetallic phase particles and found that the formation of a stable oxide over the intermetallic phases (like Cu and Fe containing) during anodising lowers their oxidation rate. For phases containing Mg, absence of a stable oxide during the anodising causes them to readily oxidise when compared to the surrounding Al matrix.

2.2.5 Post-treatments

2.2.5.1 Colouring

Sulphuric acid anodising (SAA) is considered to provide anodised surfaces that are best for colouring/dyeing for the decorative appearance. As mentioned earlier, SAA provides a nano-porous anodic film where the pores extend from the surface to throughout the thickness of the anodic layer up to the barrier layer. Also, the anodised layer in itself is colourless and transparent to visible light and hence makes it easy to impart colours to the surface [12,13]. There are three main techniques **(see** Figure 2.15**)** for colouring the anodised layer on Al.

- Adsorption Colouring/Dyeing
- Electrolytic Colouring
- Integral Colouring

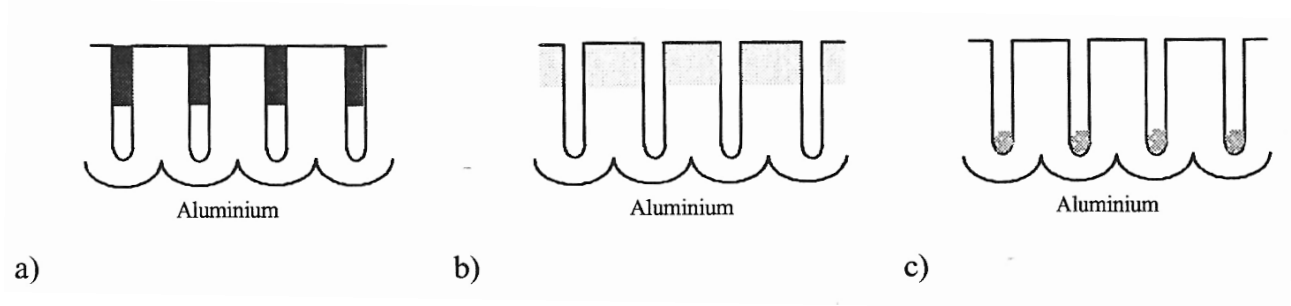

Figure 2.15: Schematic showing three different types of colouring: (a) Adsorption colouring, (b) Integral colouring, and (c) Electrolytic colouring[63].

2.2.5.1.1 Adsorption Colouring/Dyeing

In adsorption colouring, the dye used can be organic or inorganic in nature. Colours are imparted to the surface by immersing the anodised surface into the dye solution or by spraying followed by sealing. Colouring takes place due to the adsorption of the dye solution into the pores of the anodic layer by capillary effect. Various colours and shades can be imparted to the surface using this technique, but the lightfastness (UV stability) of the obtained colours is of prime concern in the case of organic dyes [94,95]. Factors such as thickness of the anodic film, inherent colour of the anodic film, and defects in the anodic film due to microstructural heterogeneities are to be considered for colouring a porous anodic film by this technique. Anodised surfaces obtained using electrolytes like Oxalic acid (slightly yellow or gold) or Chromic acid (usually grey and opaque) are not usually recommended for colouring [27]. Time and temperature of dyeing along with volume of dye solution to oxide film weight ratio, pH and concentration of the dye solution are important factors that affect the degree of dye adsorption and hence the colour shades that can be imparted to the porous anodic film [96].

2.2.5.1.2 Integral Colouring

Colouring of anodic layer by this technique, as the name implies, takes place by imparting colour to the anodic layer itself. The process is performed during the anodising step using an electrolyte that is engineered for addition of one or more salts or/and by use of a special grade of Al alloy. Colours from light bronze to black can be imparted using this technique [96].

2.2.5.1.3 Electrolytic Colouring

Electrolytic colouring of SAA surfaces is usually performed by AC treatment in a bath containing metal salts of Tin, Nickel, Cobalt, and other metals. Colours produced by this method ranges from bronze to black, blue, green, burgundy, and gold [96]. Colouring takes place by the cathodic deposition of metals at the bottom of the anodic pores. The colours obtained by this method are more resistant to UV.

2.2.5.2 Sealing

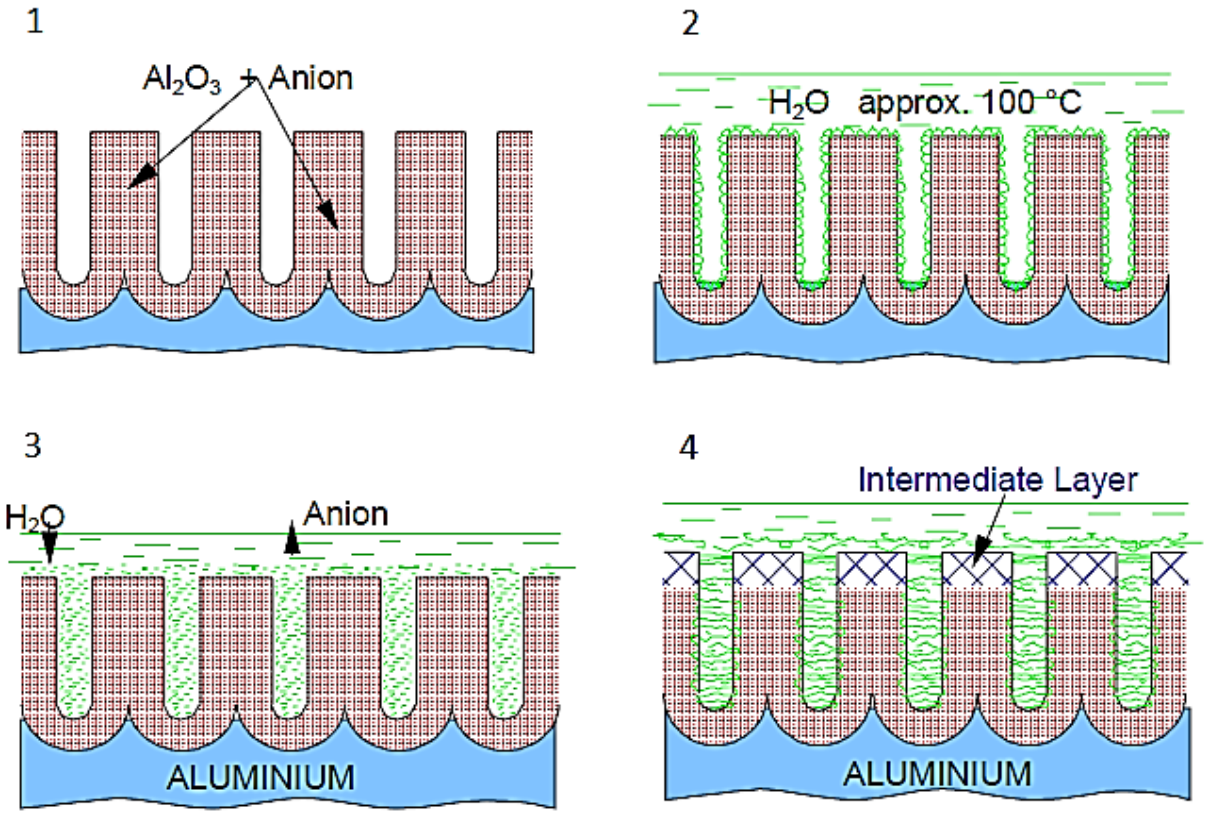

Figure 2.16: Schematic diagram of dynamic sealing process [42,63,97].

Anodised Al is seldom used in as-anodised condition and is often sealed before being put into service to enhance its corrosion resistance, and to prevent leaching out and increasing the UV resistance of the dyes. Sealing is usually the last step in the surface finishing process using anodising. The most common sealing process is immersing the anodised Al in a bath containing de-ionized boiling water (hot water sealing or hydrothermal sealing). Other solutions used for sealing are nickel acetate, nickel fluoride, sodium silicate, and di-chromate based solutions [97]. During the sealing treatment, the porous anodic layer produced by sulphuric, phosphoric or oxalic acid absorbs the water. The process is often referred to as hydrothermal sealing, as the water at this temperature reacts with the anodic alumina (barrier and porous type) to form Boehmite, AlO(OH) (or $Al_2O_3.H_2O$) [98,99]. It is proposed that the anodic alumina undergoes a hydration process at the pore walls to form a pseudo-boehmite gel, which later crystallizes to form boehmite [100,101]. The sequential transformation steps in hydrothermal sealing are shown in Figure 2.16.

The quality of the sealed anodic layer depends on the pH, purity, and temperature of the bath along with the sealing time and also parameters of anodising. Optimal sealing bath parameters for hydrothermal sealing are 95-96 °C and pH of 5.5-6.5 [102]. Optimum sealing time is dependent on the porous film thickness and is usually around 2- 3 min/µm [97]. During sealing of the porous anodic films, the barrier layer also undergoes hydration, but it is limited and occurs only when the pore mouth is still open allowing the water to diffuse to the bottom of the pores [103,104]. There is a volume increase of approx. 25 % after sealing of porous anodic films as the density of alumina is reported to be 3.2 g/cc and that of boehmite is only 3.0 g/cc [102]. The volume increase during the sealing process combined with the long term ageing of the sealed anodic film leads to stress increase in the film making longer sealing times harmful [105].

The porous anodic films formed using oxalic acid (OAA) and phosphoric (PAA) acid can be sealed using hydrothermal sealing process [106]. However, sealing of phosphoric acid anodised films are slower when compared to that of sulphuric acid and oxalic acid anodised films [27]. The slower hydration process for

phosphoric acid anodised films is due to the presence of phosphate ions [97,107,108]. In general, hydrothermal sealing is slow and costly process and also requires a stringent control on the parameters such as purity to prevent unappealing appearance to the decorative anodised surface. Alternatively, steam sealing is reported to be 2-4 times faster than the hydrothermal sealing and is less sensitive to pH of the sealing bath [44,97]. This increase in rate of sealing is a result of higher operating temperatures of 110 – 150 °C and increased diffusivity of the species at elevated temperatures. However, the sealed films obtained after steam sealing are found to be softer when compared to those obtained by the hydrothermal sealing. Nickel acetate sealing involves deposition of nickel hydroxide in the pores formed by hydrolysis. Dichromate/chromate sealing involves the absorption of chromate ion at low pH and hydration at high pH [109].

2.2.6 Properties of Anodised Surfaces

The decorative appearance, mainly of the transparent and clear anodic porous alumina films formed under conventional sulphuric acid DC anodising has been of great interest to surface finishers, architects, and designers. Apart from the pleasing appearance, anodised Al surfaces are characterised by improved mechanical and tribological properties and enhanced corrosion resistance. Some of the key properties are listed below in Table 2.7.

Table 2.7: Key properties of anodised Al surfaces.

Hardness	65 to 70 Rockwell C, 850 to 900 HV/10
Colour	Clear transparent to ceramic off-white
Coating Thickness	A few µm to approx. 200 µm
Dielectric	Non-conductive and will withstand 800 V per 0.001" thickness.
Machining	Can be ground, lapped, honed or polished.
Dyeing	Dyed by most colours
Resistivity	between 10^6 to 10^{12} Ohm-cm

The optical properties and appearance of anodised Al that are of interest to this thesis are discussed in detail in the following section. The fundamentals of optics, colour of materials, and various factors influencing the optical appearance are discussed.

2.3 Optical Properties and Appearance of Materials

The optical appearance of a material is an outcome of complex phenomenon resulting from the interaction of light with the material [110]. Features such as the surface topography, the size, and geometry of the metal along with its chemical composition affect the optical properties as well as the perceived optical appearance of the metal. This section deals with a few basic phenomena affecting the optical properties of a material. Factors influencing the optical appearance of Al and anodised Al surfaces are presented and discussed in the next section.

2.3.1 Colour

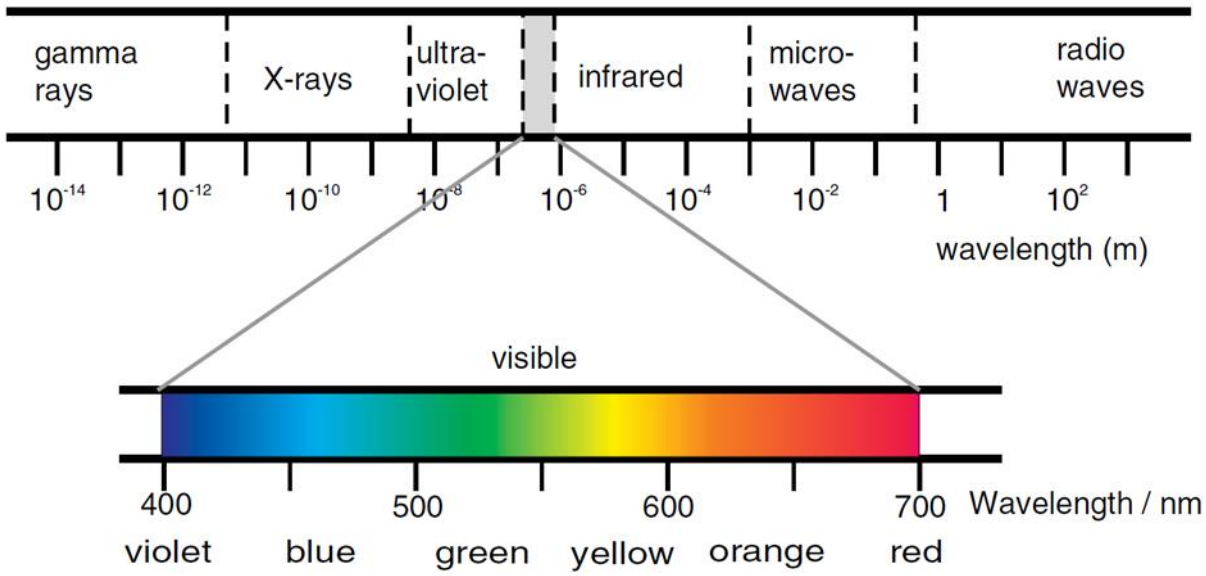

Figure 2.17: The electromagnetic spectrum. Historically, different regions have been given different names. The boundaries between each region are not sharply defined, but grade into one another. The visible spectrum occupies only a small part of the total spectrum [111].

The visible light is part of the electromagnetic spectrum (Figure 2.17) and is generally defined from a wavelength range of 350 nm (violet) to 750 nm (red). Colour, perceived by the human eye from a material is due to the interaction of this light with the cells in the human eye. A single wavelength or a mixture of them gives rise to various colours due to colour mixing – Additive colour mixing and Subtractive colour mixing. Colours are usually defined by three parameters namely: Hue – Corresponds to wavelength or frequency of the radiation; Saturation – Corresponds to the amount of white light mixed with the hue and allows pale 'washed out' colours to be described; and Lightness, brightness and value – Describes the intensity of the colour, which depends on the number of photons reaching the eye.

Colour and appearance perceived from a surface is due to reflection, absorption, and scattering of light. A beam of light incident on a surface undergoes reflection at the surface. The light passing through the material undergoes absorption or scattering. Light absorbed due to attenuation or extinction can lead to rise in temperature of the absorbing material or be re-emitted as fluorescence. Scattered light may be absorbed later or re-emitted from the material surface. The light leaving the material is called transmitted light (see Figure 2.18). The initial intensity of light is then the sum of intensity of light that is reflected, scattered, absorbed, and transmitted.

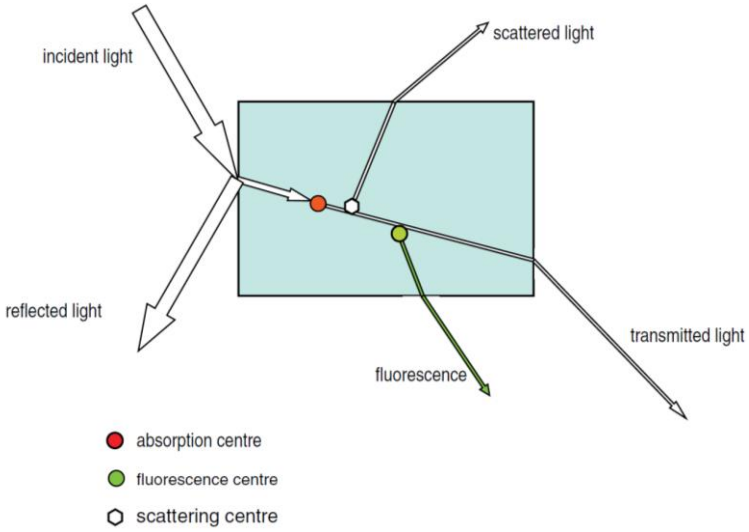

Figure 2.18: The interaction of light with a transparent material. The light can be reflected, absorbed or scattered. Some absorption centres are able to re-emit light as fluorescence or luminescence. All of the processes labelled are wavelength dependent and can lead to colour production [111].

2.3.2 Appearance and Transparency

Reflection from a smooth surface is said to be specular and from a rough surface is said to be diffuse (see Figure 2.19 (a)). The gloss of a surface is the measure of the relative amounts of diffuse to specular reflection. A material is said to be transparent if there is no absorption or scattering of visible light when light passes through it. An example of a transparent material is glass, which is a solidified liquid. As there are no internal boundaries in the material, therefore there is no scattering of light. However, even the slightest amount of crystallization in glass can lead to scattering. The glass is then no more transparent, but will appear as translucent. The transmitted light then comprises of diffuse and specular light (Figure 2.19 (b)). Increasing the number of scattering centres to a very high density makes the glass opaque. The amount of transmitted light is then zero and the scattered light is reflected from the surface making it appear white when there is no selective absorption in the visible wavelength region.

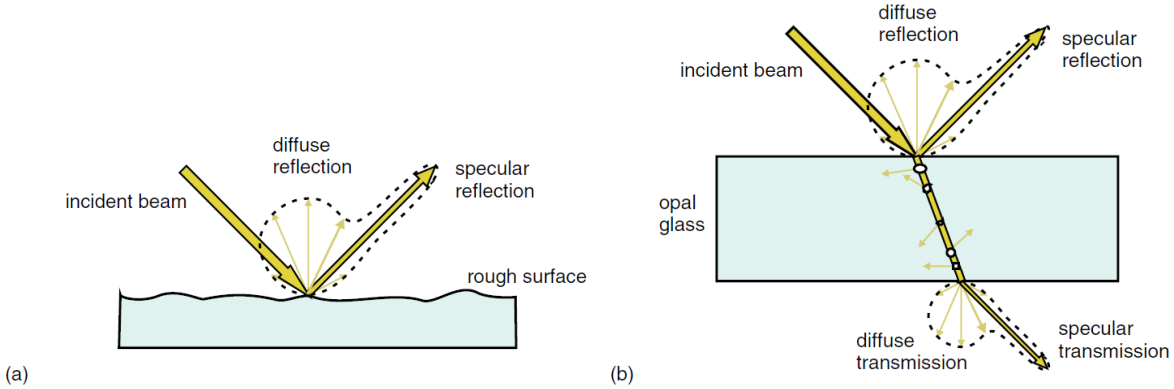

Figure 2.19: (a) Reflection of light from a rough surface consists of two components, diffuse reflection and specular reflection. The ratio of diffuse reflection to specular reflection increases as the surface roughness increases. The ratio is an indication of surface gloss. (b) The passage of light through a translucent material containing many scattering centres gives rise to both surface reflection and transmitted light with diffuse and specular components [111].

2.3.3 Refractive Index

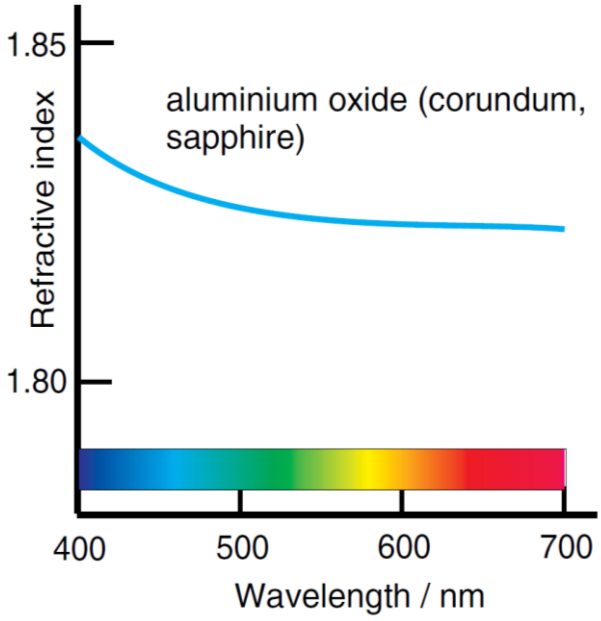

Figure 2.20: Dispersion curve for corundum, Al_2O_3. In the case of corundum, the refractive index depends upon direction and the average values are plotted [112].

A beam of light entering a transparent medium appears to bend. This is called refraction. The extent of bending of the beam at the interface is governed by the difference in the refractive index of the two medium, which is due to the difference in the velocity of light in the media. Generally, the refractive index of a transparent solid material is positive. The refractive index of transparent, opaque, and translucent materials is expressed as a complex function *N*. The complex refractive index is then given as $N = n + ik$; where *n* is the refractive index and *k* is the extinction or absorption index. Both are optical constants of a material, and a function of wavelength and density of the material (see Figure 2.20). The real part, *n,* deals with non-absorbing part of the medium and the imaginary part, *k,* deals with the absorbing part of the medium. For completely non-absorbing materials the complex part, *k* is zero.

2.3.4 Scattering

Scattering of light is interaction of light beam with small particles such as dust or water droplets. The intensity of light traversing in a medium reduces in the incident direction as light gets scattered into other directions. The intensity of light lost due to scattering can be written as

$$I = I_0 \exp(-\alpha_s l) \quad (2.5)$$

Where I_0 is the incident beam intensity, *l* is the distance travelled in the medium and α_s is the linear scattering coefficient which is dependent on:

- number of scattering centres present,
- ratio of particle diameter to the wavelength of light,
- ratio of refractive indices of the scattering particle and the surrounding medium,
- shape of the particle

When all the parameters are held constant, the relative scattering coefficient is found to be maximum at a scattering particle size that is somewhat half the wavelength of the incident light (see Figure 2.21).

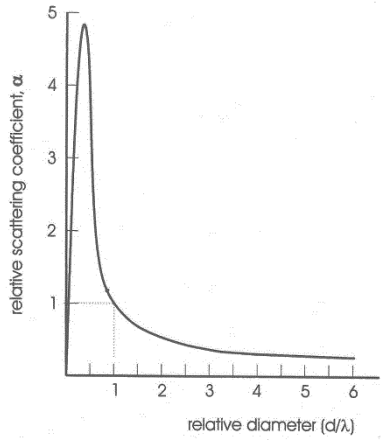

Figure 2.21: Schematic illustration of the effect of particle size, expressed as relative diameter (particle diameter, d/ wavelength of light, λ) on the relative scattering coefficient, α, expressed as the ratio of the scattering coefficient α_s at the relative diameter of 1.0 to that at other relative diameters. The maximum scattering occurs when the particle diameter is about half the wavelength of light [113].

2.3.4.1 Rayleigh Scattering

Rayleigh scattering is applied to scattering from particles that have a diameter that is less than one tenth of wavelength of the visible light. It is strongest in the direction of propagation (forward and backward) and only has an effect when the scattering particles are widely spaced (see Figure 2.22 (a)). Shorter wavelengths are scattered more strongly than the longer wavelengths. The blue colour of a clear sky and the red colour of a sunset is an example of the Rayleigh scattering by gas molecules in the upper atmosphere.

2.3.4.2 Mie Scattering

Mie scattering is applied to particles that are larger than those for which Rayleigh scattering is applied. The mathematics of the theory was formulated by Gustav Mie in 1908 [114]. Generally, the particle sizes involved are in the range of one third of the wavelength of light or more. As the scattering particle size increases, the forward scattering dominates over backward scattering (see Figure 2.22 (b). Upon further increase in particle size, the forward scattering part still increases and side bands appear and the position of which is dependent on the wavelength and hence it gives a colour at definite angles (see Figure 2.22 (c)).

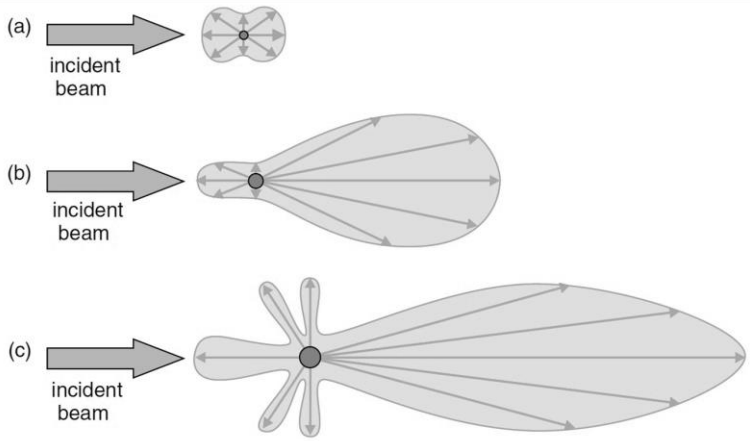

Figure 2.22: Light scattering by small particles: (a) Rayleigh scattering from particles much smaller than the wavelength of light. (b) Particles approaching the wavelength of light; the scattering becomes

pronounced in the forward direction. (c) Particles larger than the wavelength of light; lobes appear which are wavelength dependent and so give rise to colours at specific viewing angles [113].

The scattered intensity under Mie scattering is a function of wavelength, particle size, and refractive index of the particle. However, Mie scattering theory allows the calculation of cross sections for absorption, scattering, and extinction. Many industrial paints are made opaque by using materials such as TiO_2 in a low refractive index medium. The TiO_2 particles however are colourless and appear white in powder form in air due to surface reflection and scattering. Opacity of a paint film arises due to the scattering from these particles at size ranges of 200 nm, by Mie scattering. Also, TiO_2 absorbs UV radiation and hence it is used in sunscreens. Lower particle sizes are used here to prevent any opacity from the particles and UV absorption takes place by Rayleigh scattering.

2.3.5 Colour of Metals

The colour of solids is mostly governed by their band structure. In metals, the uppermost energy band is only partially filled. The band gap of metals is zero. The higher empty electronic energy levels of a metal are close to the uppermost filled levels, therefore there is a continuous band of allowed energies. This allows electrons to absorb any wavelength that is incident upon the metal and would result in all metals to appear black. However, each electron can fall back from its excited state emitting exactly the same energy that was absorbed. Thus a flat piece of metal reflects the entire incident light falling on it and hence is very reflective. On the other hand fine metal powders appear black, as the emitted light is reabsorbed by nearby metal particles and are observed by the eye at the angle of reflection. The characteristic feature of metals is that they have a very high extinction coefficient. Metal nanoparticles are shown to have brilliant colours when suspended in a solution. This colour of these colloids arises from a phenomenon known as surface plasmon resonance [115,116].

2.4 Optical Appearance of Aluminium and Anodised Aluminium

Aluminium in its pure condition is a highly reflective metal in the visible region. It can be seen from Figure 2.23 that the reflectivity of pure Al surpasses Silver, which has been widely used for high reflecting applications. Gold and Copper also show high reflectivity, but as their band gap lies in the lower wavelength region of visible light they absorb the UV and blue part of the spectrum and hence appear yellowish and reddish respectively [116].

Nyce et al. [117] studied the refractive index for bulk polycrystalline and single crystal Al along with sputter coated Al at a wavelength of 632.8 nm and found that the value of *n* varied from 1.4-1.7 and the extinction coefficient *k* varied from 6.5-7.9. Premendra et al. [22,118] and Buytaert et al. [119,120] studied the effect of mechanical processing of Al alloy and observed that high impurities in Al alloys along with rolled in oxides, inclusions, and deformed sub-surface layers reduced the total reflectance of the Al alloys (see Figure 2.24).

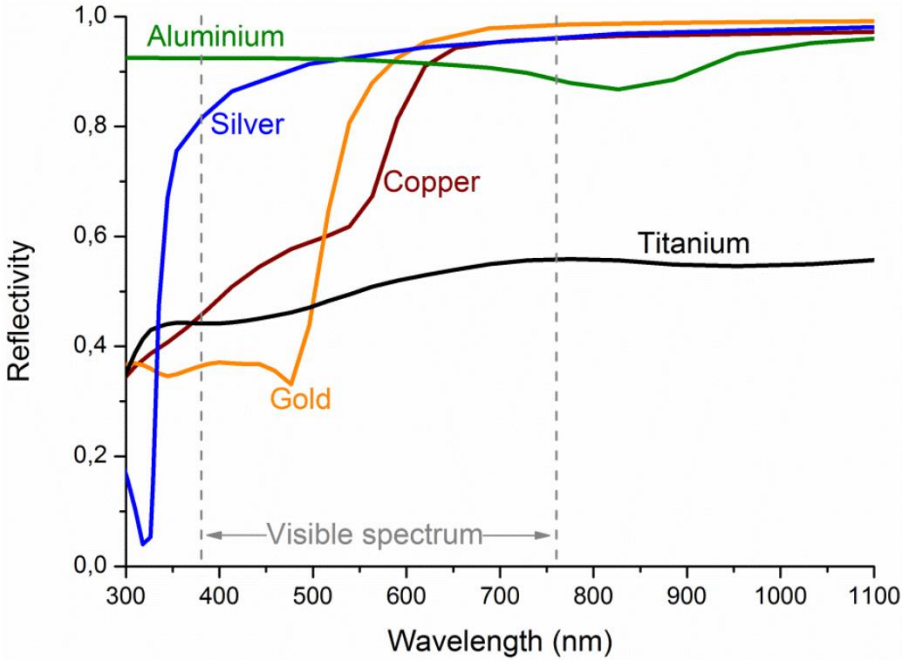

Figure 2.23: Reflectivity of silver, aluminium, titanium, copper, and gold [44,121].

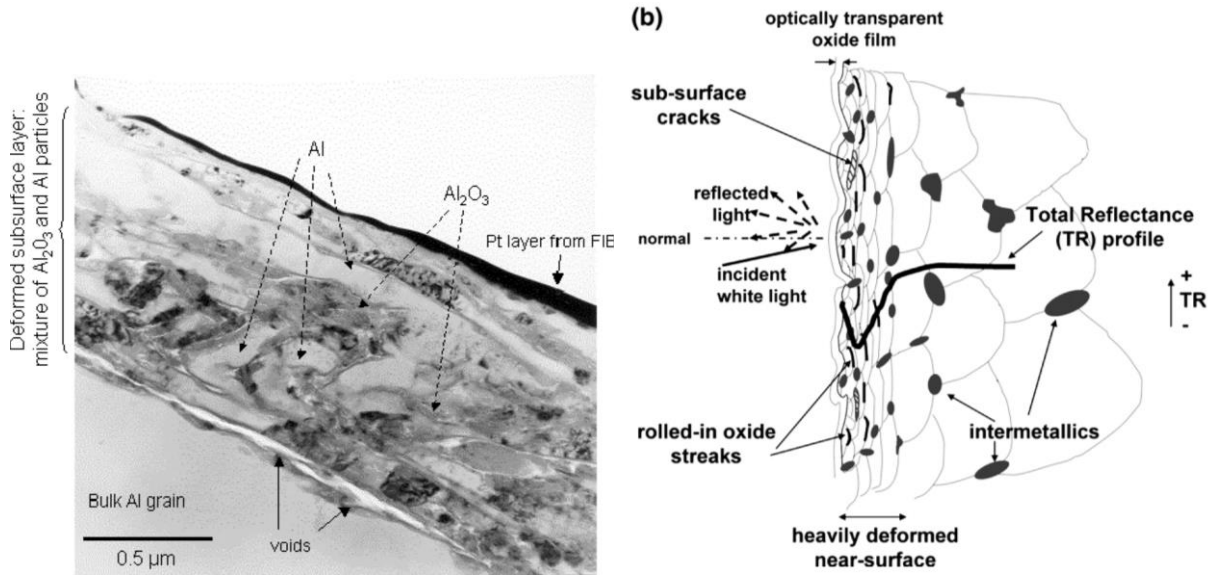

Figure 2.24: (a) Bright field TEM image of subsurface of hot rolled and annealed AA1050, (b) Schematic of the surface layer and its influence on the Total Reflectance (TR) profile of hot rolled Al alloy [22,119].

Anodising of Al, using sulphuric acid, provided anodic alumina films with a refractive index, *n* that varied between 1.2 – 1.7 and extinction coefficient, *k* varied between $1x10^{-2}$ – $1.5x10^{-2}$ (see Figure 2.25). It was observed that the optical properties were a function of the anodising parameters such as the current density and the anodic pore density along with the anodic film thickness. Khan et al. [122] studied the optical properties of anodic alumina films formed on AA1050 alloys, which is then stripped to get the film alone. The refractive index of the film, *n* reduced from 1.8 to 1.6 as the wavelength changes from 200 nm to 800 nm.

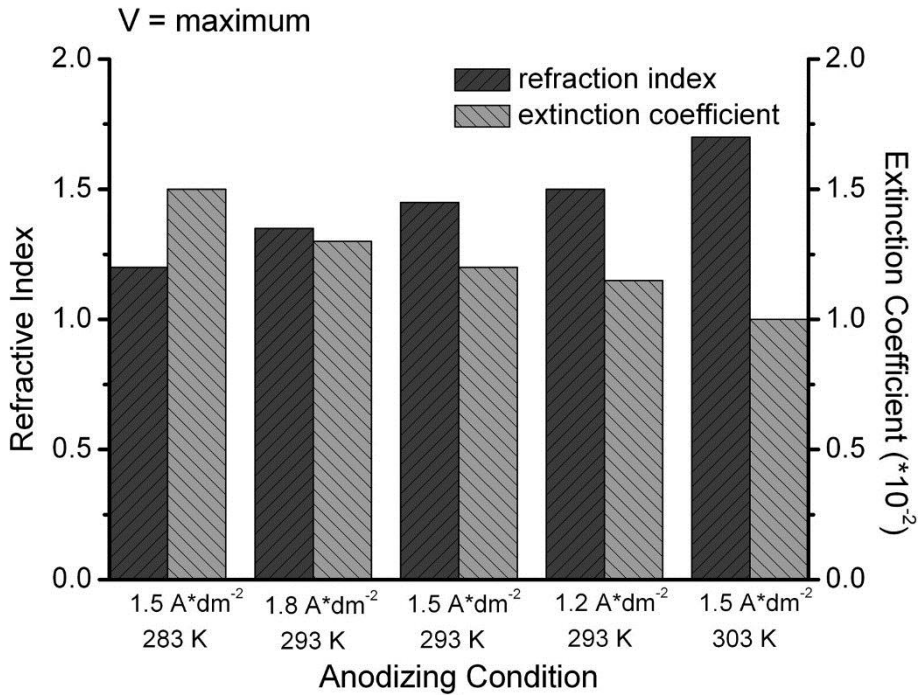

Figure 2.25: Optical properties of AAO films formed in 15% w/w sulphuric acid: (a) with various current density at 20 °C; (b) with various bath temperatures at 1.5 A dm^{-2} [123].

Generally, the optical appearance of decorative anodised surfaces is shown to be a function of the surface morphology of the substrate, the type of pre-treatments performed, the purity of the Al substrate, the type of alloying elements, the anodising parameters used, and the post-treatment parameters [12,13].

Zhu et al. [14,124,125] studied the origin of streak defects after anodising of AA6xxx alloys and reported that the inhomogeneous distribution of such surface impurities and the imperfections caused formation of etching pits, grain boundary groves, and grain etching steps. These features modified the localised diffuse and specular reflectance from the surface, which led to varying optical effects. Figure 2.24 shows the imperfections caused from the manufacturing process. In addition, the presence of intermetallic phases introduce local deformation resistance during the extrusion of alloys, which leads to localized surface roughness variations during etching. This can create streaking after the anodising process [15,19,126]. In general the etching of Al causes surface roughening, which is highly dependent on the grain orientation, grain size, presence of intermetallic particles etc. in the Al substrate [16,18]. Aggerbeck et al. [17] studied the effect of alloy composition, prior surface finish, and sealing after anodising for different Al alloys. It was observed that the major contribution to the difference in the anodised appearance was from hardness of the alloy material and sealing which reduces the heterogeneities in the anodised surface. Similar results were reported by Tabrizian et al. [127] for AA6060 who observed that the reflectance was lower for surfaces after heat treatment compared to the non-heated surfaces.

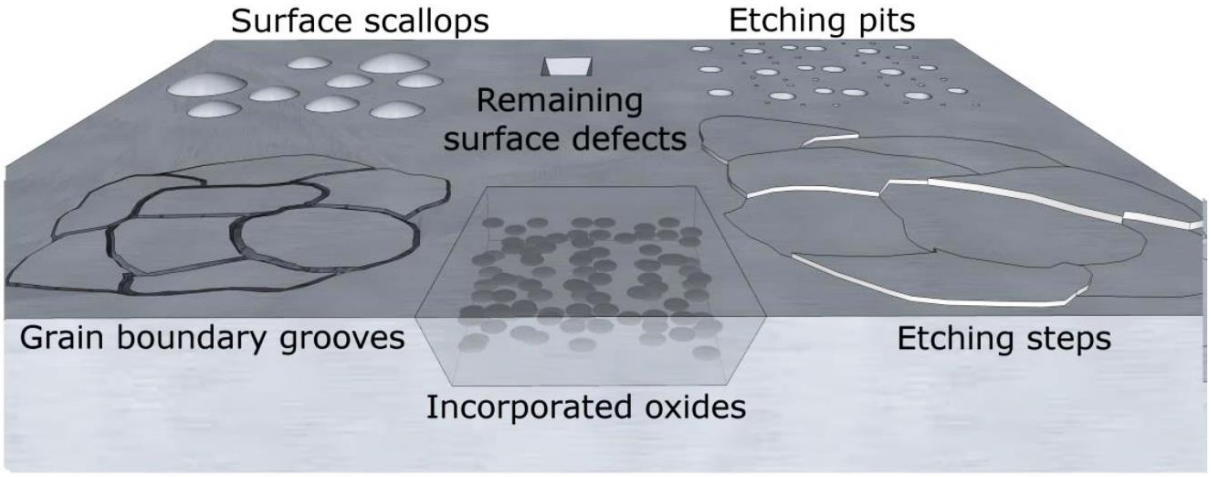

Figure 2.26: Surface structures affecting the visual appearance, created before or during etching and anodising [44].

Intermetallic phases in the Al substrate, due to their varying electrochemical nature not only affect the surface topography and morphology during caustic etching pre-treatment, but also affect the structure and hence the optical appearance of the anodised Al surfaces. Timm [21] reported the effect of Fe and Si containing intermetallic phases on anodising behaviour of Al alloys. A clear relationship was observed between the size, shape, and distribution of $Al_6(Fe,Mn)$ phases on the resulting anodised appearance, which varied from transparent to dark grey. The incorporation of the intermetallic phases into the anodic layer was the key factor in the darkening and reduced reflectance of the anodic layer. Saito [128,129] studied the effect of un-oxidised Al phase incorporated into the anodic layer on pure Al alloys and AA5052 using optical and chemical analysis techniques. For a given thickness of the anodic layer, it was seen that as the current density increased, the anodic films grew darker. Using theoretical considerations, mainly the refractive index, *n,* of dielectrics such as anodic alumina and metals like Al along with their extinction coefficient, *k*, it was shown that even a small amount of metallic Al in anodic alumina matrix can lead to darkening of the anodised layers. Recently, Ma et al. [130] studied the darkening on AA6063 alloy profiles and suggested that abnormal anodising conditions and overaged microstructures are a prerequisite for darkening after anodising. These results can be explained using the studies on un-oxidised Al, where overaged microstructures tend to result in higher amount of un-anodised metallic phases into the anodic layer. This effect is also enhanced by the higher current densities

observed during the abnormal anodising conditions. A simpler theory put forward by Hultquist [131] states that under certain anodising conditions, particles of Al metal get incorporated into the anodic alumina and act as pigmentation, which was theoretically and experimentally presented by Chang et al. [132].

The effect of various alloying elements and impurities in the Al alloy on the appearance of decorative anodised surfaces is summarized and listed below [85].

- Iron - Leads to grey or black colour at very small amounts, high Fe/Si ratio (>7) also leads to darkening.
- Silicon - High Si concentration (>5 wt. %) leads to grey or black appearance after anodising, while no effect if dissolved in the solid solution.
- Titanium - Similar effects as that of Iron.
- Magnesium - Up to 0.3 wt.% gives clear and transparent coatings
- Copper - Acceptable up to 2 wt. % in the solid solution state, however higher levels cause discolouration.
- Manganese – Up to 1 wt.% will lead to spots and brown anodised surfaces,
- Zinc – Up to 5 wt. % leads to good protective layer, however if distribution is not homogenous leads to brown and marbled surfaces.
- Chromium – Yellowness of anodised surface at 0.3 wt. %.

2.5 White Anodising of Aluminium

White appearing anodised Aluminium has been of great interest to researchers and industrial surface finishers as well as designers and architects for the last couple of decades. Several attempts have been made in this direction and a few reports are found in the literature in terms of patented processes and equipment or research articles. However, white anodised Al with a glossy decorative appearance has not been found in literature or commercially. Decorative anodised Al owing to its porous structure can be coloured as mentioned in the previous sections by conventional dyeing and integral or electrolytic colouring. But, white appearance requires very high scattering of light and without any selective absorption of particular wavelengths of visible light [113,133]. The most efficient light scattering is provided by scatterers with size close to half the wavelength of visible light in diameter, approx. 150-200 nm as shown in Figure 2.27 for TiO_2 (rutile).

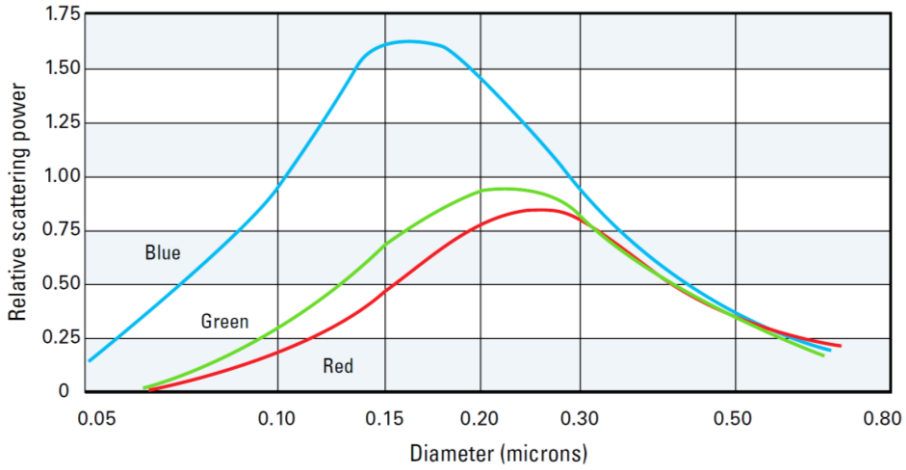

Figure 2.27: Relative light scattering power versus TiO_2 (Rutile) particle size [134].

Decorative anodised Al, generated using sulphuric acid anodising, produces transparent anodic films where the anodic pore size is approx. 20-50 nm in diameter. The dye molecules used in conventional dyeing process are very small compared to the pore diameters and hence can be adsorbed into the pores very easily. But, on the other hand, to obtain white anodised Al, using dyeing by white pigments like TiO_2 is not possible as the size of the light scattering pigments is an order of magnitude higher than the average pore diameters (see Figure 2.28).

One process patented by Reynold Metals [136] is reported to generate white appearing anodised surfaces with 70-80 % reflectivity, and is used by the National Aeronautics and Space Administration (NASA) for the thermal control of spacecraft. The electrolyte used was a combination of titanium lactate, glycerol, sulphuric acid, and lactic acid. The white surface for these applications was intended to provide necessary degree of whiteness and brightness for optical and visual tracking, while at the same time also a high degree of corrosion resistance along with control of ambient temperature [76]. Other variations, for similar applications at Indian Space Research Organisation (ISRO) has been reported by Siva Kumar et al. [137,138]. However, no data on the intensity of diffuse reflectance and specular reflectance of the anodised surfaces achieved using the process is reported.

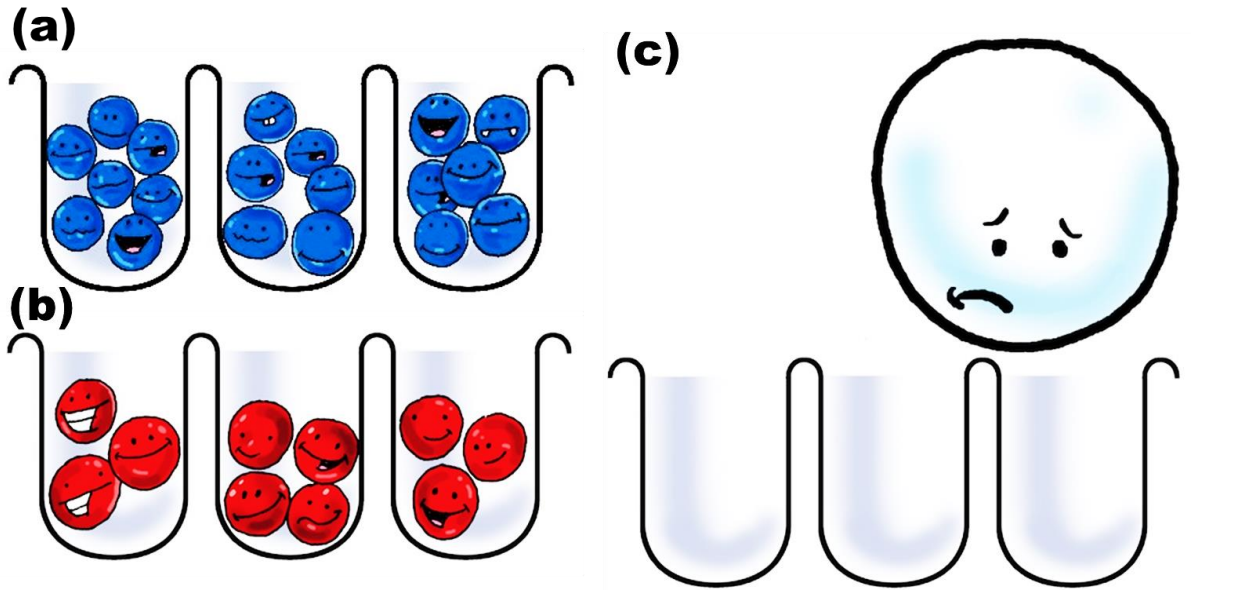

Figure 2.28: Schematic showing the relative sizes of: (a), (b) organic dye molecules used for colouring decorative anodised alumina and (c) light scattering TiO_2 particles with respect to average pore diameters of decorative anodic alumina [135].

There has been a considerable amount of patented research aimed at white anodising of Al. Different white anodised surfaces were reported by different companies like Showa Aluminium (Chromic acid and glycerol mixture, opaque enamel), Honey Chemicals [139] (mixture of amine and inorganic oxy acid under AC anodising conditions), Nikkei Aluminium (mixture of oxalic acid and triethanolamine; or alkali metal phosphates and citric or tartaric acid), Sankyo Aluminium (electrolytic colouring in neutral or alkaline solutions of Ba or Ca salts), and Pilot Pen [140] (dipping in or electrolytic deposition of salts of Ca, Mg, Ba, Sr, Zn, Pb Ti or Al) using a combination of various electrolyte mixtures providing either white appearance by integral colouring or due to deposition of compounds in a dipping step after anodising [13].

Plasma electrolytic oxidation (PEO), as mentioned in the earlier section, also generate white appearing anodised surfaces, but the reflectance from the surface is completely diffuse with no specular content (no gloss) [85]. Therefore, the coatings are not aesthetically pleasing and cannot be used for decorative applications. In order to achieve highly reflecting white appearing anodised surfaces, in this thesis new novel design approaches are attempted, that are discussed in the following sections.

2.5.1 Designing White Anodised Aluminium

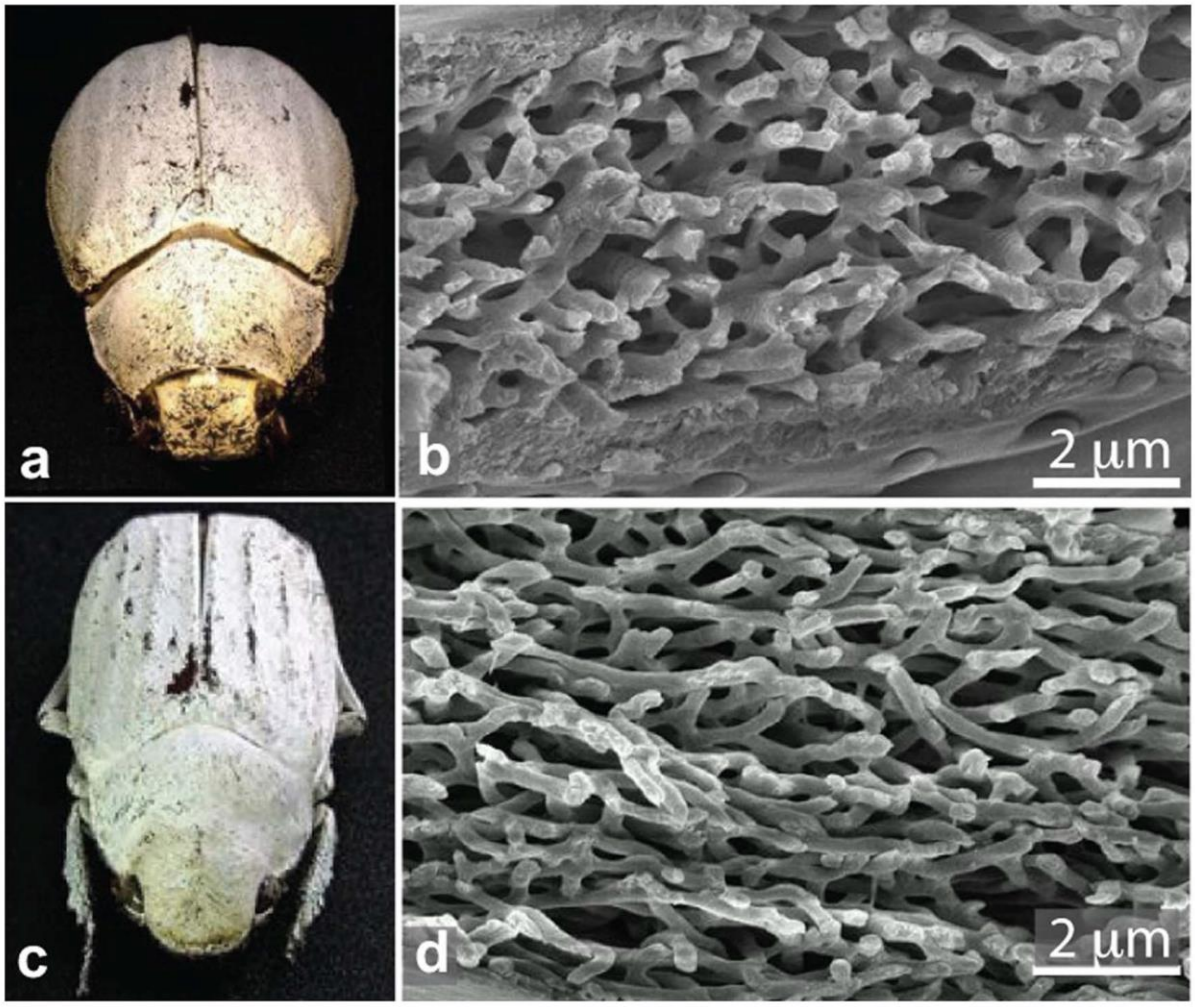

Figure 2.29: White reflection from beetle scales: (a), (c), Images of Cyphochilus and Lepidiota stigma beetles, respectively. (b), (d), Scanning electron micrographs (SEM) of the cross-section of the scales of the respective species [141].

In nature, white appearance arises from efficient multiple scattering of light without any absorption. For example, the brilliant whiteness observed in bright white-beetles arises from diffuse and broadband reflection of light by optical scattering in a randomly structured network of high refractive index chitin [141]. In order to provide efficient scattering of light for the decorative anodised surfaces, the requirement therefore is to present such high refractive index light scattering centres in a certain size, shape, and distribution. As explained in the earlier section, introducing light scattering particles of required size to the anodic pores is not possible due to size limitations. However, alternative approaches for incorporation or in-situ creation of scattering centres into the anodic alumina can be attempted. Two main possible approaches are listed and discussed below

- In-situ creation of scattering centres during anodising
- Incorporation of scattering centres prior to anodising

For both approaches, the process is designed to provide high diffuse reflectance from the anodised surface using light scattering from within the anodic alumina matrix and a required amount of specular reflectance (gloss) arising from the smoothness/flatness of the anodic alumina surface.

2.5.1.1 In-situ Creation of Scattering Centres during Anodising

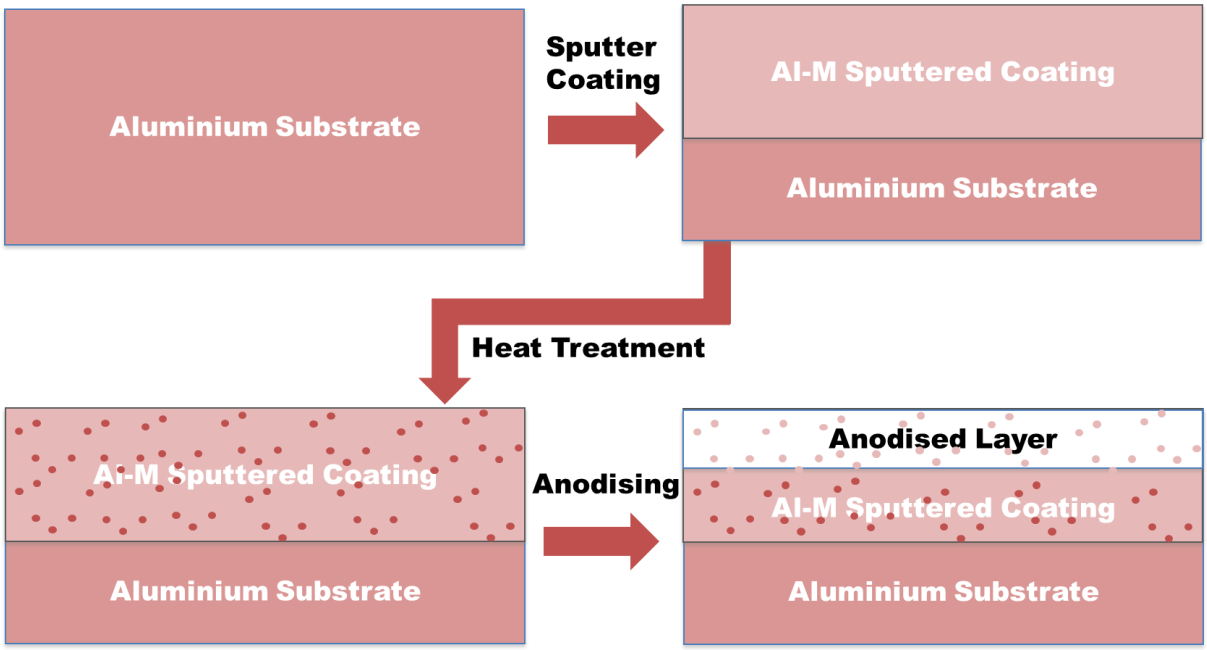

Figure 2.30: Process schematic showing involved steps in generating white anodised surfaces using magnetron sputtered coatings.

Light scattering centres in anodic alumina based on high refractive index metal oxides are created during anodising of the Al surface. In order to achieve a final anodic structure containing metal oxide particles in an anodic alumina matrix, the prior microstructure of the substrate is designed to contain Al-M (M = metal) phases in an Al matrix. The Al-M phases (like intermetallic phases) upon anodising would transform to Al-M-O mixed oxides, which are incorporated into the anodic alumina matrix. This structure would then scatter incident light due to the difference in refractive index of the anodic alumina and the Al-M-O phases, which are created in-situ during anodising. The design considerations for the microstructure of the Al surface for being able to scatter the light efficiently prior to the anodising are as follows

- Optimum size, shape, and distribution of Al-M phases for efficient light scattering
- Al-M-O phase should have a high refractive index
- Al-M phase should be able to be oxidised under normal decorative anodising conditions

In order to achieve a microstructure satisfying above considerations, vapour phase deposition processes like DC magnetron sputtering can be employed to coat the Al surface with a binary Al-M system. Heat treatment of this coating would result in the formation of Al-M phases in the Al matrix due to the phase transformations dictated by the thermodynamic considerations. Figure 2.30 shows a schematic of the steps involved in this approach and the following section will elaborate on the processes used for preparation.

2.5.1.2 Incorporation of Scattering Centres Prior to Anodising

In this approach, one could aim to obtain a white appearing anodised surface using an Al substrate that already contains incorporated light scattering centres (like a composite). Anodising of such an Al composite would result in incorporation of the (electrochemically inert) light scattering centres into the anodic alumina matrix for light scattering. Particles such as metal oxides (M-O) having high refractive index would be incorporated into the Al matrix using mechanical processing techniques. The resulting Al/M-O composite would be then anodised. The design considerations for such an Al based composites are as follows:

- Optimum size, shape, and distribution of M-O particles for efficient light scattering
- M-O phase should have a high refractive index
- M-O phase should be stable under normal decorative anodising conditions

In order to obtain the Al/M-O metal matrix composites, friction stir processing was employed in the present investigation. This method provides a surface metal matrix composite, which can be later anodised for obtaining high light scattering and white appearance (see Figure 2.31).

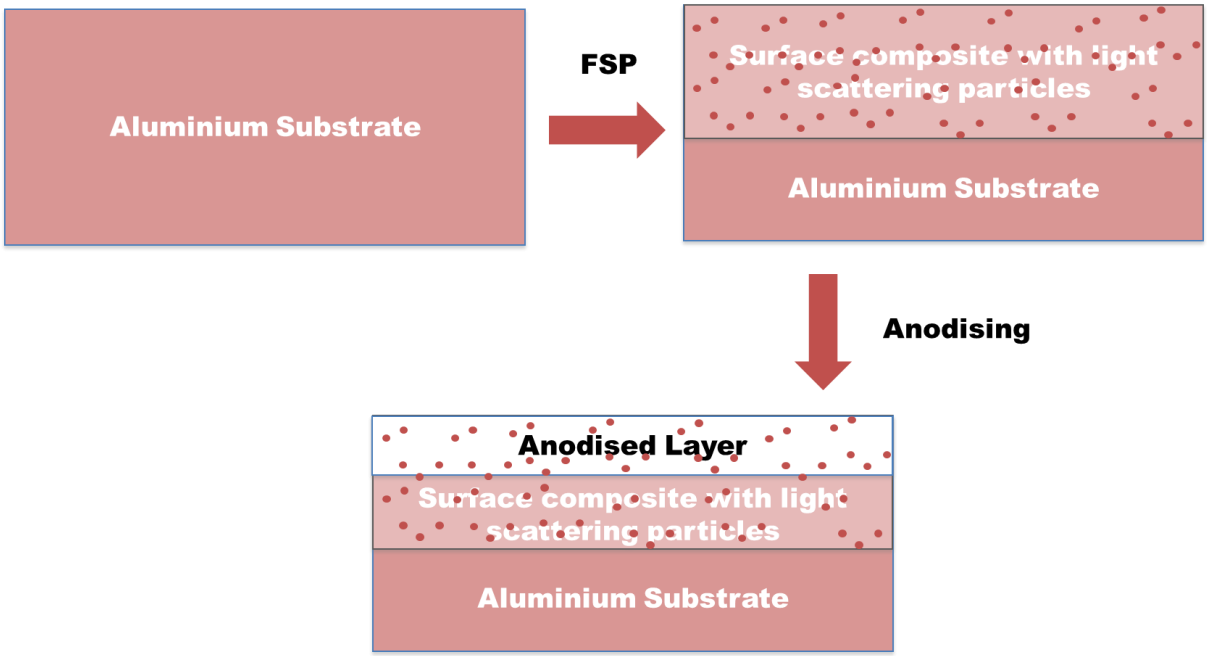

Figure 2.31: Schematic of the process showing involved steps in generating surface with high diffused reflection aiming at white anodised surfaces using FSP surface composites containing light scattering particles.

2.6 Magnetron Sputter Coating

Sputter coating is a vapour deposition process that is carried out in a vacuum chamber. A target (or cathode) plate is bombarded by high energy ions from glow discharge plasma in the vicinity of the target. This bombardment removes or sputters the target material in the form of atoms or sometimes cluster of atoms which may get deposited or condensed on the substrate as a thin film [85]. The plasma is maintained by the secondary electrons generated from the bombardment process. This process is limited by low deposition rates, low ionisation efficiencies in the plasma, and high heating of the substrate [142]. Magnetron sputtering and unbalanced magnetron sputtering have been developed to overcome these limitations. In this process, magnets are arranged in such a way that there is a magnetic field that traps the electrons in the vicinity of the target enhancing the ionisation efficiency and therefore results in increased sputtering and deposition rates (see Figure 2.32) [143,144].

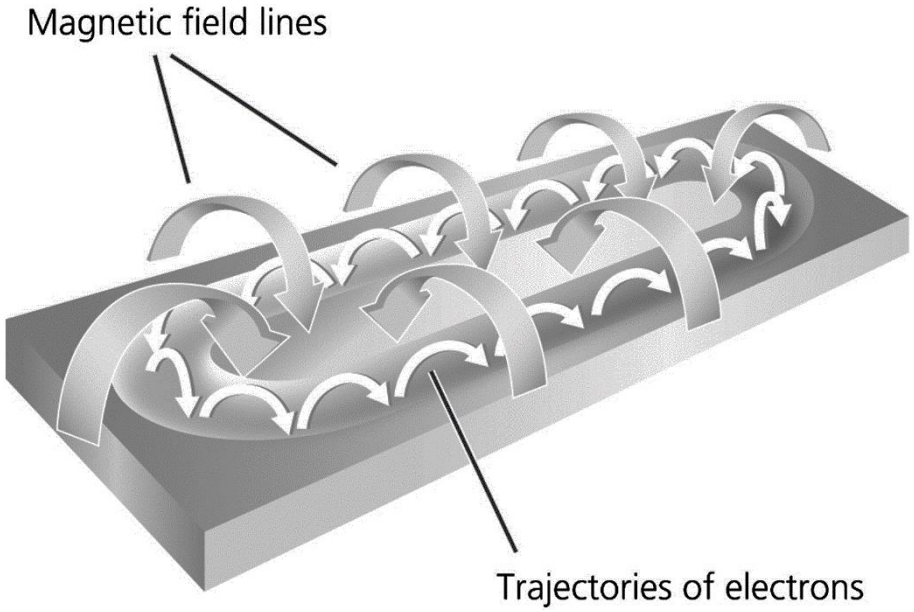

Figure 2.32: The principle of magnetron sputtering. Electrons are trapped by the Lorentz force in an inhomogeneous magnetic field, resulting in an enhanced ionisation of argon atoms [143].

The glow discharge (plasma) can also be operated at lower operating pressures and voltages. Typical operating parameters for magnetron sputtering is with a chamber pressure of $1\text{-}10^{-3}$ Pa and voltage of -500 V [142]. Very often a bias voltage is applied to the substrates, which needs to be coated. This helps in sputter cleaning or plasma cleaning of the substrate surface by bombardment with the gas ions thus removing impurities and surface oxides. Sputter cleaning of the substrate will improve adhesion of the coating to the substrate. Prior to sputter cleaning, the chamber is heated to remove the adsorbed volatile phases and moisture [85]. Binary or multi element coatings can be deposited using two or more cathodes of pure elements or targets of alloys operating at different powers, which are experimentally optimized for a certain composition ratio.

2.6.1 Structure of Sputtered Coatings

The general structure of sputter deposited coatings was proposed by Thornton [145–147], who classified it into zones according to the ratio between the substrate temperature (T) and melting temperature of the coating material (T_m), and the process pressure as shown in Figure 2.33.

Zone 1: Coarse columnar growth due to low mobility of the species, high degree of intergranular porosity.

Zone T: This is an intermediate zone where the coating morphology is dependent on the process pressure; lower pressure increases the density of the coating.

Zone 2: Dense and coarse columnar type morphology

Zone 3: Equiaxial crystals due to high thermal energy enabling equilibrium type of growth independent of pressure.

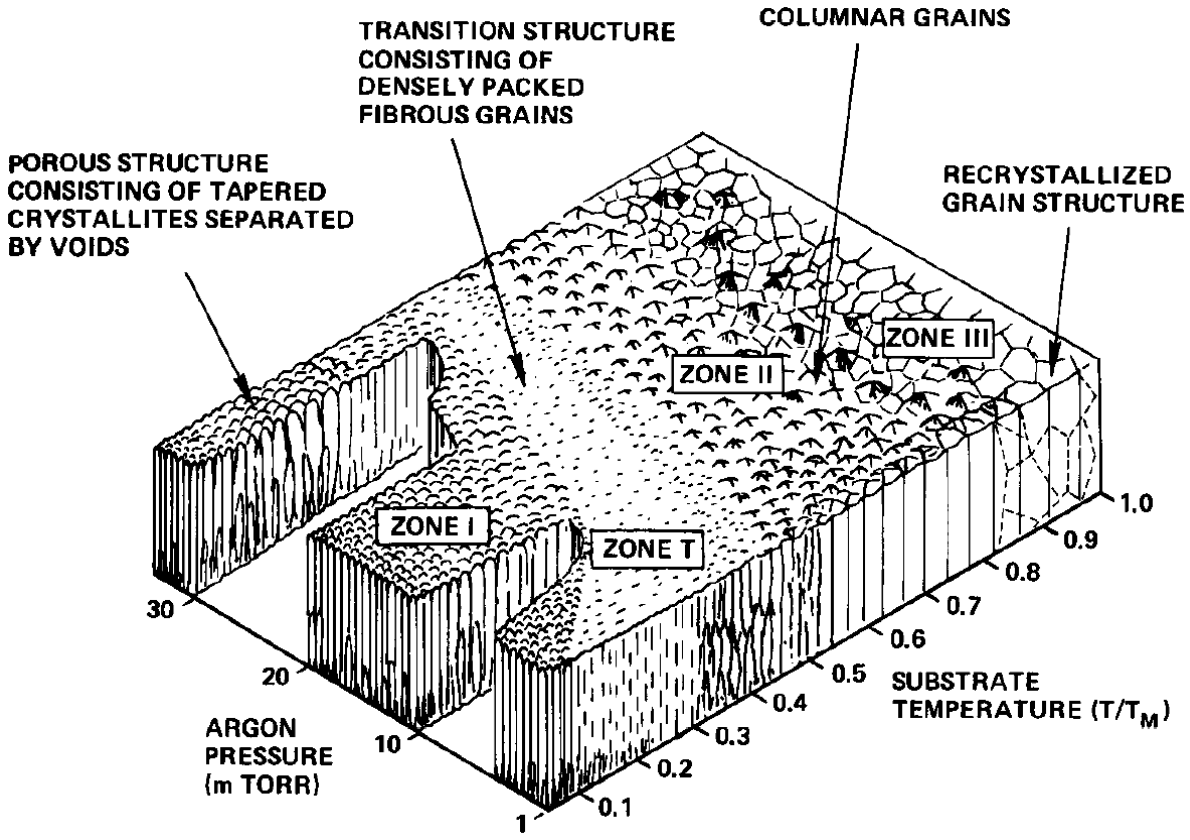

Figure 2.33: Influence of substrate temperature and Ar pressure on microstructure of sputtered metallic coatings [147].

The dependence of the structure on the T/T_m is largely due to the interplay of three mechanisms: shadowing, diffusion and surface recrystallization, and grain growth [147,148]. Shadowing is due to peaks in the coatings receiving more coating flux than the valleys causing porosity at the boundaries in Zone 1. As the temperature of the substrate is increased, diffusion takes place and the structures in Zone T have lower porosity. Upon further increase in substrate temperature, the diffusion is enough to overcome shadowing and the effect of surface recrystallization is visible in Zone 2. Further increase in temperature causes bulk recrystallization of the coating and hence equiaxed structures with large and oriented grains are observed in Zone 3.

Magnetron sputter coatings have been widely used in the past decade for studying various phenomenon such as anodising behaviour, tribology, functional properties, electrochemistry, and corrosion

resistance. Magnetron sputtering can provide meta-stable coatings with very high and well-defined concentrations of alloying elements in Al compared to conventional melt and cast techniques. This allows them to be used as model alloys for systematic and controlled studies. Coatings based on Al-Cu [149–151], Al-Mn [152], Al-Mg [153], Al-Zn [154], Al-Fe [155], and Al-Ti [156] have been studied for their anodising and electrochemical polarization behaviour.

2.6.2 Design of Coatings

As mentioned in the earlier section, for the present work Al-M binary coatings were produced using magnetron sputtering for further heat treatment and anodising. Elements such as Zr and Ti were selected as the alloying element owing to the fact that the oxides of Zr (n = 2.2) and Ti (n = 2.65) [157] have a high refractive index when compared to that of anodic alumina (n = 1.7) [123]. Besides, Zr and Ti also have a very low solubility in Al at room temperature making it easier to precipitate Al-Zr and Al-Ti phases from a super saturated solid solution of Al-Zr and Al-Ti (see Figure 2.34 and Figure 2.35) [158].

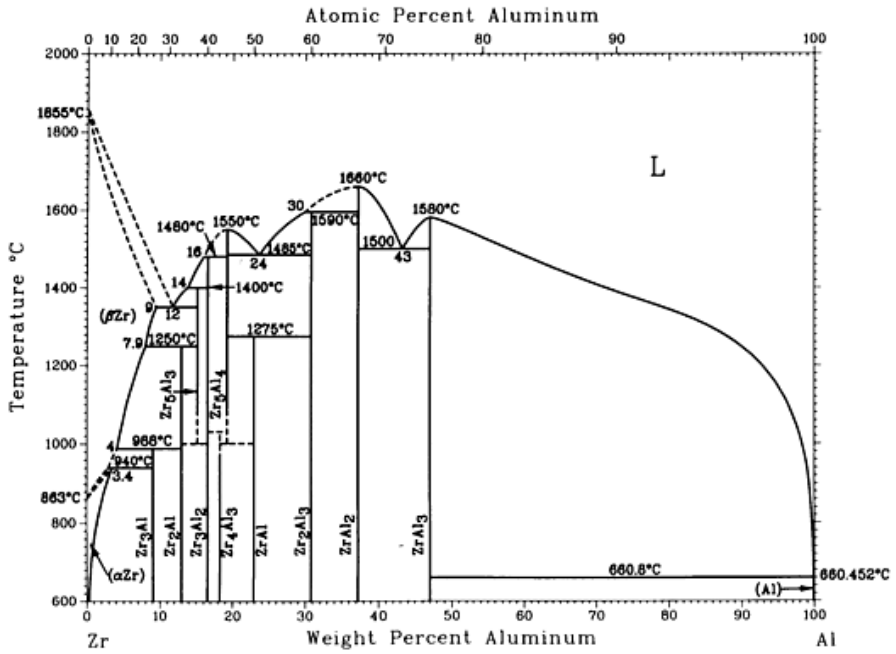

Figure 2.34: The binary Al-Zr phase diagram [158].

The binary equilibrium phase diagram of Al-Zr in Figure 2.34 shows that the Zr has very low solubility in Al. Alloys containing Zr concentrations of up to 53 wt. % would show a dual phase microstructure containing Al_3Zr phases in α-Al. Accordingly, Zr concentrations of up to 25 wt.% were chosen for magnetron sputter coating. Similar phases are observed in Al-Ti system (see Figure 2.35) where the dual phase region of Al_3Ti and α-Al exists up to 37 wt. % Ti. Coatings containing up to 16 wt. % Ti were therefore chosen for the sputter deposition.

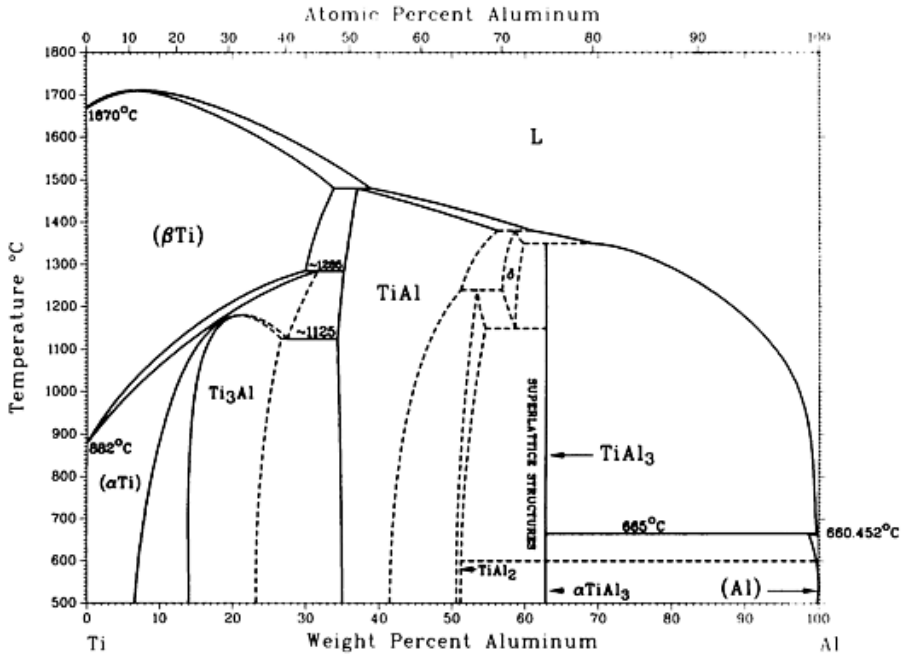

Figure 2.35: The binary Al-Ti phase diagram [158].

2.7 Friction Stir Processing

Friction Stir Processing (FSP) is a mechanical processing technique which has been developed based on the concept of Friction Stir Welding (FSW) [159,160]. This technique allows for processing of materials with high superplasticity [161,162], microstructural refinement and homogenization [163], and preparation of metal matrix composites including surface composites [164,165]. Friction stir processing has been employed to generate reinforced surface composites and metal matrix composites containing different fillers. The main advantage of FSP is that it is a solid phase mechanical processing technique and therefore significantly reduces interfacial reaction between the filler material and the matrix phase. Such interfacial reactions cannot be controlled or avoided when using other composite processing techniques such as casting, plasma spraying, and laser melting etc. for which at least one phase is in the liquid state. For investigations in the thesis, obtaining an Al/M-O surface composite by FSP is highly favourable compared to bulk composite processing methods as the anodising process is applicable only to the surface. Also, the FSP is a fast process for producing surface composites, which can be used as model systems for studying the anodising behaviour.

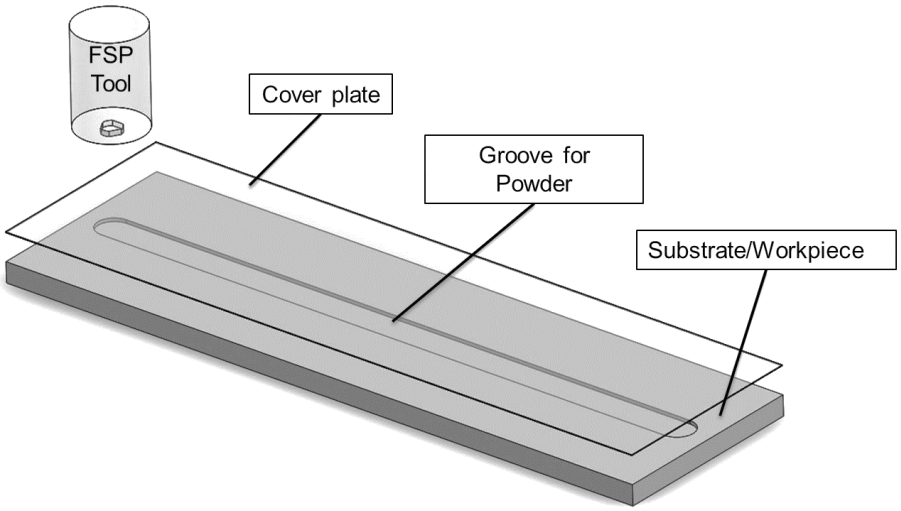

Figure 2.36: Schematic showing processing of surface composites using FSP.

The basic mechanism of FSP is that a non-consumable rotating tool with a pin and shoulder (see Figure 2.36) is plunged into the surface of a monolithic work piece and then traversed along the work length. The friction between the tool and the work piece generates heat and the movement produces the flow of material from the front of the pin to the back. Surface composites are prepared by application of the filler material in the form of a fine layer at the top of the metal work piece [166] or by filling in a grove milled into the surface of the work piece [167]. Homogenization of the surface composite can be performed by repeating the FSP processing over the same region multiple times with or without an offset of the processing tool from the centre of the processed zone [164,168]. The depth of the processed zone depends on the pin length of the tool and the width of the processed zone depends on the diameter of the tool shoulder. The traverse speed of the tool also affects the homogeneity and bonding of the surface composite to the underlying metal work piece or substrate [159].

2.7.1 Design of Surface Composites

Model surface composites were prepared using FSP of Al substrates with different filler powders. The particle size, shape, morphology, and type were chosen based on their refractive index, chemical stability in Al, and mechanical properties. Powders of Y_2O_3, CeO_2, and TiO_2 (rutile) were chosen for this purpose due to their higher refractive index compared to anodic alumina. Refractive index of Y_2O_3 is $n = 1.95$ [169], CeO_2 is $n = 2.3$ [170] and TiO_2 is $n = 2.7$ [157].

References

[1] Organisation of European Aluminium Refiners and Remelters (OEA), European Aluminium Association (EAA), Aluminium Recycling in Europe, Eur. Alum. Assoc. Brussels. (2006) 52. http://scholar.google.com/scholar?hl=en&btnG=Search&q=intitle:Aluminium+recycling:+the+road+to+high+quality+products#0 (accessed May 21, 2014).

[2] J. Cui, H.J. Roven, Recycling of automotive aluminum, Trans. Nonferrous Met. Soc. China. 20 (2010) 2057–2063. doi:http://dx.doi.org/10.1016/S1003-6326(09)60417-9.

[3] European Aluminium Association (EAA), Primary Aluminium Consumption in World Regions, (n.d.). doi:http://www.alueurope.eu/consumption-primary-aluminium-consumption-in-world-regions/.

[4] European Aluminium Association (EAA), Consumption - End-use markets for aluminium products 2011, (n.d.). doi:http://www.alueurope.eu/consumption-end-use-markets-for-aluminium-products-2010/.

[5] C. Vargel, M. Jacques, M.P. Schmidt, Aluminium and Its Alloys, in: C.V.J.P.B.T.-C. of A. Schmidt (Ed.), Elsevier, Amsterdam, 2004: pp. 1–5. doi:http://dx.doi.org/10.1016/B978-008044495-6/50005-7.

[6] S.H. Avner, Introduction to Physical Metallurgy, Second, McGraw-Hill, Singapore, 1974.

[7] S.R.K. Malladi, In-Situ TEM Studies : Heat-Treatment and Corrosion, Delft University of Technology, 2014. doi:10.4233/uuid:33ff5f84-7100-407a-b387-2623e0954ae9.

[8] N. Birbilis, R.G. Buchheit, Electrochemical Characteristics of Intermetallic Phases in Aluminum Alloys: An Experimental Survey and Discussion, J. Electrochem. Soc. 152 (2005) B140–B151. doi:10.1149/1.1869984.

[9] R.G. Buchheit, A Compilation of Corrosion Potentials Reported for Intermetallic Phases in Aluminum Alloys, J. Electrochem. Soc. 142 (1995) 3994. doi:10.1149/1.2048447.

[10] C. Vargel, M. Jacques, M.P. Schmidt, Chapter B.1 - The Corrosion of Aluminium, in: C.V.J.P.B.T.-C. of A. Schmidt (Ed.), Elsevier, Amsterdam, 2004: pp. 81–109. doi:http://dx.doi.org/10.1016/B978-008044495-6/50011-2.

[11] C. Vargel, M. Jacques, M.P. Schmidt, Chapter B.5 - Protection Against Corrosion, in: C.V.J.P.B.T.-C. of A. Schmidt (Ed.), Elsevier, Amsterdam, 2004: pp. 185–207. doi:http://dx.doi.org/10.1016/B978-008044495-6/50015-X.

[12] P.G. Sheasby, R. Pinner, The Surface Treatment and Finishing of Aluminium and Its Alloys, Volume 1, 6th ed., ASM International; Finishing Publications, 2001.

[13] P.G. Sheasby, R. Pinner, The Surface Treatment and Finishing of Aluminium and Its Alloys, Volume 2, 6th ed., ASM International; Finishing Publications, 2001.

[14] H. Zhu, X. Zhang, M.J. Couper, A.K. Dahle, Effect of primary intermetallic particles on surface microstructure and appearance of aluminium extrusions, Mater. Chem. Phys. 113 (2009) 401–406. doi:10.1016/j.matchemphys.2008.07.109.

[15] G. Vander Voort, B. Suárez Peña, J. Asensio Lozano, Microstructure Investigations of Streak Formation in 6063 Aluminum Extrusions by Optical Metallographic Techniques, Microsc. Microanal. 19 (2013) 276–284. doi:10.1017/S143192761300010X.

[16] G. Buytaert, B. Kernig, H.J. Brinkman, H. Terryn, Influence of surface pre-treatments on disturbed rolled-in subsurface layers of aluminium alloys, Surf. Coatings Technol. 201 (2006) 2587–2598. doi:10.1016/j.surfcoat.2006.05.004.

[17] M. Aggerbeck, S. Canulescu, K. Dirscherl, V.E. Johansen, S. Engberg, J. Schou, et al., Appearance of anodised aluminium: Effect of alloy composition and prior surface finish, Surf. Coatings Technol. 254 (2014) 28–41. doi:10.1016/j.surfcoat.2014.05.047.

[18] A.J. Dowell, Metal structure and composition effects in the alkaline etching of Aluminium, Trans. Inst. Met. Finish. 65 (1987) 147–151.

[19] H. Zhu, X. Zhang, M.J. Couper, A.K. Dahle, Effect of initial microstructure on surface appearance of anodized aluminum extrusions, Metall. Mater. Trans. A Phys. Metall. Mater. Sci. 40 (2009) 3264–3275. doi:10.1007/s11661-009-9976-0.

[20] R. Akeret, H. Bichsel, E. Schwall, E. Simon, M. Textor, Influence of chemical composition and fabrication procedures on the properties of anodised aluminium surfaces, Trans. Inst. Met. Finish. 68 (1990) 20–28.

[21] J. Timm, Influence of Fe and Si Containing Phases on the Anodisation Behaviour, Key Eng. Mater. 44-45 (1990) 219–232. doi:10.4028/www.scientific.net/KEM.44-45.219.

[22] J.H. Chen, F.D. Tichelaar, H. Terryn, J.H.W. deWit, L. Katgerman, Optical and transmission electron

microscopical study of the evolution of surface layer on recycled aluminium along the rolling mills, Surf. Coatings Technol. 201 (2007) 4561–4570. doi:10.1016/j.surfcoat.2006.09.090.
[23] G.M. Scamans, M.F. Frolish, W.M. Rainforth, Z. Zhou, Y. Liu, X. Zhou, et al., The ubiquitous Beilby layer on aluminium surfaces, Surf. Interface Anal. 42 (2010) 175–179. doi:10.1002/sia.3204.
[24] C.H. Desch, Aggregation and flow of solids. By Sir G. Beilby. Pp. xv.+256. (London: Macmillan and Co., Ltd. 1921.) Price 20s. net, J. Soc. Chem. Ind. 41 (1922) R20–R20. doi:10.1002/jctb.5000410116.
[25] S.G.T. Beilby, Aggregation and Flow of Solids: Being the Records of an Experimental Study of the Micro-structure and Physical Properties of Solids in Various States of Aggregation, 1900-1921, Macmillan and Company, limited, 1921. http://books.google.dk/books?id=JGVDAAAAIAAJ.
[26] A. Smithells, Aggregation and Flow of Solids: Being the Records of an Experimental Study of the Micro-structure and Physical Properties of Solids in Various States of Aggregation, 1900–1921, Nature. 109 (1922) 262–265. doi:10.1038/109262a0.
[27] J.W. Diggle, T.C. Downie, C.W. Goulding, Anodic oxide films on aluminum, Chem. Rev. 69 (1969) 365–405. doi:10.1021/cr60259a005.
[28] F. Keller, M.S. Hunter, D.L. Robinson, Structural Features of Oxide Coatings on Aluminum, J. Electrochem. Soc. 100 (1953) 411. doi:10.1149/1.2781142.
[29] G.C. Wood, J.P. O'Sullivan, B. Vaszko, The Direct Observation of Barrier Layers in Porous Anodic Oxide Films, J. Electrochem. Soc. 115 (1968) 618–620. http://jes.ecsdl.org/content/115/6/618.abstract.
[30] M.S. Hunter, P. Fowle, Factors Affecting the Formation of Anodic Oxide Coatings, J. Electrochem. Soc. 101 (1954) 514. doi:10.1149/1.2781147.
[31] J.D. Edwards, F. Keller, The structure of anodic oxide coatings, Trans. AIME, Inst. Met. Div. 156 (1944) 288–300. http://scholar.google.com/scholar?hl=en&btnG=Search&q=intitle:The+Structure+of+Anodic+Oxide+Coatings#4 (accessed November 8, 2013).
[32] S. Feliu, M.J. Bartolomé, J.A. González, S. Feliu, XPS Characterization of Porous and Sealed Anodic Films on Aluminum Alloys, J. Electrochem. Soc. 154 (2007) C241–C248. http://jes.ecsdl.org/content/154/5/C241.abstract.
[33] M. Nagayama, K. Tamura, H. Takahashi, Dissolution of porous anodic oxide films on Al in (COOH)2 solutions, Corros. Sci. 10 (1970) 617–627. doi:http://dx.doi.org/10.1016/S0010-938X(70)80055-5.
[34] M. Nagayama, K. Tamura, Dissolution of the anodic oxide film on aluminium in a sulphuric acid solution, Electrochim. Acta. 12 (1967) 1097–1107. doi:http://dx.doi.org/10.1016/0013-4686(67)80105-1.
[35] F. Liechti, W.D. Treadwell, Zur Kenntnis elektrolytisch erzeugter Oxydschichten auf Aluminium, Helv. Chim. Acta. 30 (1947) 1204–1218. doi:10.1002/hlca.19470300515.
[36] T.P. Hoar, N.F. Mott, A mechanism for the formation of porous anodic oxide films on aluminium, J. Phys. Chem. Solids. 9 (1959) 97–99. doi:http://dx.doi.org/10.1016/0022-3697(59)90199-4.
[37] M.S. Hunter, P. Fowle, Determination of Barrier Layer Thickness of Anodic Oxide Coatings, J. Electrochem. Soc. 101 (1954) 481–485. http://jes.ecsdl.org/content/101/9/481.abstract.
[38] C.E. Michelson, The Current-Voltage Characteristics of Porous Anodic Oxides on Aluminum, J. Electrochem. Soc. 115 (1968) 213–219. http://jes.ecsdl.org/content/115/2/213.abstract.
[39] G.E. Thompson, Y. Xu, P. Skeldon, K. Shimizu, S.H. Han, G.C. Wood, Anodic oxidation of aluminium, Philos. Mag. B (Physics Condens. Matter, Electron. Opt. Magn. Prop. 55 (1987) 651–667.
[40] G. Thompson, R.C. Furneaux, G.C. Wood, J.A. Richardson, J.S. Goode, Nucleation and growth of porous anodic films on aluminium, Nature. 272 (1978) 433–435. doi:10.1038/272433a0.
[41] M. Nagayama, K. Tamura, On the mechanism of dissolution of porous oxide films on aluminium during anodizing, Electrochim. Acta. 13 (1968) 1773–1783. doi:http://dx.doi.org/10.1016/0013-4686(68)80085-4.
[42] F. Jensen, Investigation on the Optical Appearance of Anodised Layer on Aluminium Containing TiO2 Particles, Technical University of Denmark, 2013.
[43] G.. Thompson, Porous anodic alumina: fabrication, characterization and applications, Thin Solid Films. 297 (1997) 192–201. doi:10.1016/S0040-6090(96)09440-0.
[44] M. Aggerbeck, Tailored Aluminium based Coatings for Optical Appearance and Corrosion Resistance, Technical University of Denmark, 2014.
[45] J.M. Kape, Anodising with Alternating Current, Trans. Inst. Met. Finish. 55 (1977) 25–30.
[46] J.M. Kape, AC Anodizing, Met Finish J. 20 (1974) 80–84.
[47] J.M. Kape, Further developments in the AC anodizing of aluminium in sulphuric acid electrolytes, Trans. Inst. Met. Finish. 63 (1985) 90–97.
[48] I. De Graeve, H. Terryn, G.E. Thompson, AC-Anodising of Aluminium: Contribution to Electrical and Efficiency Study, Electrochim. Acta. 52 (2006) 1127–1134. doi:10.1016/j.electacta.2006.07.010.

[49] M.A. Barbosa, D.R. Gabe, D.H. Ross, I. Sutherland, A Contribution to the Understanding of AC Anodizing of Aluminium, J. Appl. Electrochem. 19 (1989) 829–838. doi:10.1007/BF01007930.
[50] J.A. Treverton, N.C. Davies, XPS Studies of DC and AC Anodic Films on Aluminium Formed in Sulphuric Acid, Electrochim. Acta. 25 (1980) 1571–1576. doi:http://dx.doi.org/10.1016/0013-4686(80)80006-5.
[51] J.M. Kape, Comparison of AC and DC sulphuric acid based anodizing processes, Trans. Inst. Met. Finish. 66 (1988) 41–46.
[52] J. Zahavi, A-C Anodizing Processes of Aluminum Alloys, J. Electrochem. Soc. 129 (1982) 1572. doi:10.1149/1.2124211.
[53] D.R. Gabe, I.H. Dowty, A.C. Anodizing of Aluminium Alloys, Surf. Coatings Technol. 30 (1987) 309–316. doi:10.1016/0257-8972(87)90088-0.
[54] L. Li, AC Anodization of Aluminum, Electrodeposition of Nickel and Optical Property Examination, Sol. Energy Mater. Sol. Cells. 64 (2000) 279–289. doi:10.1016/S0927-0248(00)00229-4.
[55] V. Balasubramanian, S. John, B.A. Shenoi, Influence of Addition Agents for A.C. Anodizing in Sulphuric Acid Electrolytes, Surf. Technol. 19 (1983) 293–303. doi:10.1016/0376-4583(83)90034-1.
[56] D.A.L. Nicklen, D.R. Gabe, A.C. Anodizing of Aluminium in Sulphuric Acid, Surf. Technol. 7 (1978) 353–359. doi:10.1016/0376-4583(78)90033-X.
[57] M.A. Barbosa, D.R. Gabe, D.H. Ross, I. Sutherland, A Contribution to the Understanding of A.C. Anodizing of Aluminium, J. Appl. Electrochem. 19 (1989) 829–838. doi:10.1007/BF01007930.
[58] C. Colombini, Using Pulse Rectifiers for Aluminium Anodizing, Finishing. 12 (1988) 34–38.
[59] V. Raj, M.R. Rajaram, G. Balasubramanian, S. Vincent, D. Kanagaraj, Pulse Anodizing - An Overview, Trans. Inst. Met. Finish. 81 (2003) 114–121.
[60] K. Yokoyama, H. Konno, H. Takahashi, M. Nagayama, Advantages of Pulse Anodizing, Plat. Surf. Finish. 69 (1982) 62–65.
[61] K. Yokoyama, H. Konno, H. Takahaski, M. Nagayama, Anodic Oxidation of Aluminum Utilizing Current Recovery Effect, AES Int. Symp. Pulse Plat. (American Electroplat. Soc. (1981).
[62] H. Takahashi, M. Nagayama, H. Akahori, A. Kitahara, Electron-microscopy of Porous Anodic Oxide Films on Aluminium by Ultra-thin Sectioning Technique: Part 1. The Structrual Change of the Film during the Current Recovery Period, J. Electron Microsc. (Tokyo). 22 (1973) 149–157. http://jmicro.oxfordjournals.org/content/22/2/149.abstract.
[63] A. Deacon Juhl, Pulse anodising of extruded and cast aluminium alloys, Technical University of Denmark, 1999.
[64] V. Komisarov, A.R. Thölén, TEM investigation of pulse anodized porous films formed on aluminium alloys, Mater. Sci. Eng. A. 151 (1992) 197–203. doi:10.1016/0921-5093(92)90208-I.
[65] L.. Fratila-Apachitei, J. Duszczyk, L. Katgerman, AlSi(Cu) anodic oxide layers formed in H2SO4 at low temperature using different current waveforms, Surf. Coatings Technol. 165 (2003) 232–240. doi:10.1016/S0257-8972(02)00733-8.
[66] L.E. Fratila-Apachitei, J. Duszczyk, L. Katgerman, Voltage transients and morphology of AlSi(Cu) anodic oxide layers formed in H2SO4 at low temperature, Surf. Coatings Technol. 157 (2002) 80–94. doi:10.1016/S0257-8972(02)00144-5.
[67] K. Okubo, Y. Sakura, Anodic oxidation on aluminum in oxalic acid by pulse current with a negative current component., J. Met. Finish. Soc. Japan. 39 (1988) 751–755. doi:10.4139/sfj1950.39.751.
[68] K. Okubo, S. Toba, Y. Sakura, Studies of High-Temperature, High Speed Anodic Oxidation on Aluminum by the Pulse Current With Negative Current Component, J. Met. Finish. Soc. Japan. 39 (1988) 512–516. doi:10.4139/sfj1950.39.512.
[69] D. Kanagaraj, V. Raj, S. Vincent, B.P. Kumar, A.S. Kumar, S.V. Iyer, Pulse anodizing of AA1100 aluminium alloy in oxalic acid electrolyte, Bull. Electrochem. 17 (2001) 285–288. http://cecri.csircentral.net/1232/ (accessed May 22, 2014).
[70] K. Okubo, S. Suyama, Y. Sakura, Studies of Microstructure of Anodic Oxide Films on Aluminum by Pulse Current with a Negative Component, J. Surf. Finish. Soc. Japan. 40 (1989) 1366–1371. doi:10.4139/sfj.40.1366.
[71] T. Yamamoto, H. Tanaka, M. Fujita, H. Asoh, S. Ono, Effect of high-frequency switching electrolysis on film thickness uniformity of anodic oxide film formed on AC8A Aluminum alloy, J. Japan Inst. Light Met. 60 (2010) 602–607. doi:10.2464/jilm.60.602.
[72] D. Kanagaraj, V. Raj, S. Vincent, S.V. Iyer, Effect of Pulse Frequency on Pulse Anodising of AA1100 Aluminium Alloy in Sulphamic Acid, Bull. Electrochem. 17 (2001) 523–526.
[73] M. Fujita, H. Tanaka, H. Muramatsu, T. Yamamoto, H. Asoh, S. Ono, Effect of High Frequency Switching Electrolysis on Structure of Anodic Oxide Film Formed on Aluminum Alloy, J. Surf. Finish.

Soc. Japan. 62 (2011) 346–350.
[74] A.L. Yerokhin, X. Nie, A. Leyland, A. Matthews, S.J. Dowey, Plasma electrolysis for surface engineering, Surf. Coatings Technol. 122 (1999) 73–93. doi:10.1016/S0257-8972(99)00441-7.
[75] Y.Z. Deng, F.H. Wang, Y.W. Shao, Y.Q. Wang, New sealing treatment of microarc oxidation coating, Surf. Eng. 30 (2014) 31–35. doi:10.1179/1743294413Y.0000000195.
[76] A.K. Sharma, Surface engineering for thermal control of spacecraft, Surf. Eng. 21 (2005) 249–253. doi:10.1179/174329405X50118.
[77] Z. Yao, B. Hu, Q. Shen, A. Niu, Z. Jiang, P. Su, et al., Preparation of black high absorbance and high emissivity thermal control coating on Ti alloy by plasma electrolytic oxidation, Surf. Coatings Technol. 253 (2014) 166–170. doi:10.1016/j.surfcoat.2014.05.032.
[78] U. Malayoglu, K.C. Tekin, U. Malayoglu, S. Shrestha, An investigation into the mechanical and tribological properties of plasma electrolytic oxidation and hard-anodized coatings on 6082 aluminum alloy, Mater. Sci. Eng. A. 528 (2011) 7451–7460. doi:10.1016/j.msea.2011.06.032.
[79] L. Rama Krishna, K.R.. Somaraju, G. Sundararajan, The tribological performance of ultra-hard ceramic composite coatings obtained through microarc oxidation, Surf. Coatings Technol. 163-164 (2003) 484–490. doi:10.1016/S0257-8972(02)00646-1.
[80] M. Sieber, T. Mehner, D. Dietrich, G. Alisch, D. Nickel, D. Meyer, et al., Wear-resistant coatings on aluminium produced by plasma anodising – a correlation of wear properties, microstructure, phase composition and distribution, Surf. Coatings Technol. 240 (2013) 96–102. doi:10.1016/j.surfcoat.2013.12.021.
[81] J.M. Wheeler, J.A. Curran, S. Shrestha, Microstructure and multi-scale mechanical behavior of hard anodized and plasma electrolytic oxidation (PEO) coatings on aluminum alloy 5052, Surf. Coatings Technol. 207 (2012) 480–488. doi:10.1016/j.surfcoat.2012.07.056.
[82] V. Dehnavi, B.L. Luan, X.Y. Liu, D.W. Shoesmith, S. Rohani, Correlation between plasma electrolytic oxidation treatment stages and coating microstructure on aluminum, Surf. Coat. Technol. (2014). doi:10.1016/j.surfcoat.2014.11.007.
[83] N. Godja, N. Kiss, C. Löcker, a. Schindel, a. Gavrilovic, J. Wosik, et al., Preparation and characterization of spark-anodized Al-alloys: Physical, chemical and tribological properties, Tribol. Int. 43 (2010) 1253–1261. doi:10.1016/j.triboint.2010.01.007.
[84] J.A. Curran, T.W. Clyne, Thermo-physical properties of plasma electrolytic oxide coatings on aluminium, Surf. Coatings Technol. 199 (2005) 168–176. doi:10.1016/j.surfcoat.2004.09.037.
[85] P. Møller, L. Pleth Nielsen, Advanced surface technology Vol. 1-2, Møller & Nielsen, 2013.
[86] E. Matykina, R. Arrabal, A. Pardo, M. Mohedano, B. Mingo, I. Rodríguez, et al., Energy-efficient PEO process of aluminium alloys, Mater. Lett. 127 (2014) 13–16. doi:http://dx.doi.org/10.1016/j.matlet.2014.04.077.
[87] L.E. Fratila-Apachitei, H. Terryn, P. Skeldon, G.E. Thompson, J. Duszczyk, L. Katgerman, Influence of substrate microstructure on the growth of anodic oxide layers, Electrochim. Acta. 49 (2004) 1127–1140. doi:10.1016/j.electacta.2003.10.024.
[88] L.. Fratila-Apachitei, F.D. Tichelaar, G.E. Thompson, H. Terryn, P. Skeldon, J. Duszczyk, et al., A transmission electron microscopy study of hard anodic oxide layers on AlSi(Cu) alloys, Electrochim. Acta. 49 (2004) 3169–3177. doi:10.1016/j.electacta.2004.02.030.
[89] M. Jariyaboon, P. Møller, R.E. Dunin-Borkowski, R. Ambat, FIB-SEM investigation of trapped intermetallic particles in anodic oxide films on AA1050 aluminium, Anti-Corrosion Methods Mater. 58 (2011) 173–178. doi:10.1108/00035591111148885.
[90] K. Shimizu, G.M. Brown, K. Kobayashi, P. Skeldon, G.E. Thompson, G.C. Wood, Ultramicrotomy-a route towards the enhanced understanding of the corrosion and filming behaviour of aluminium and its alloys, Corros. Sci. 40 (1998) 1049–1072. doi:10.1016/S0010-938X(98)00006-7.
[91] E. Senel, M. Hallenstvet, Effect of Alloying Elements on the Colour Development of Anodised Al-Mg-Si Alloys, Mater. Sci. Forum. 794-796 (2014) 247–252. doi:10.4028/www.scientific.net/MSF.794-796.247.
[92] M. Saenz De Miera, M. Curioni, P. Skeldon, G.E. Thompson, Preferential anodic oxidation of second-phase constituents during anodising of AA2024-T3 and AA7075-T6 alloys, Surf. Interface Anal. 42 (2010) 241–246. doi:10.1002/sia.3191.
[93] M. Saenz de Miera, M. Curioni, P. Skeldon, G.E. Thompson, The behaviour of second phase particles during anodizing of aluminium alloys, Corros. Sci. 52 (2010) 2489–2497. doi:10.1016/j.corsci.2010.03.029.
[94] P.G. Sheasby, The weathering of anodized aluminium, Alum. 2000. (1990) 8–28.
[95] L. Section, J. Blair, H.C. Guu, The Dyeing of . Anodised Aluminium, (1937).
[96] C.A. Grubbs, Anodizing of Aluminum, Met. Finish. 105 (2007) 397–412. doi:10.1016/S0026-

0576(07)80359-X.
[97] L. Hao, B.R. Cheng, Sealing processes of anodic coatings—Past, present, and future, Met. Finish. 98 (2000) 8–18. doi:10.1016/S0026-0576(01)80002-7.
[98] W.J. Bernard, J.J. Randall, The Reaction between Anodic Aluminum Oxide and Water, J. Electrochem. Soc. 108 (1961) 822–825. doi:10.1149/1.2428230.
[99] H. Puderbach, H.J. Göhausen, Investigation on anodized aluminium, Spectrochim. Acta Part B At. Spectrosc. 39 (1984) 1547–1551. doi:10.1016/0584-8547(84)80180-9.
[100] K. Wefers, Mechanism of Sealing of Anodic Oxide Coatings on Aluminium, Aluminium. 49 (1973) 622–625.
[101] T.P. Hoar, G.C. Wood, The sealing of porous anodic oxide films on aluminium, Electrochim. Acta. 7 (1962) 333–353. doi:10.1016/0013-4686(62)87009-1.
[102] Technical proceedings of 44th Annual Convention of American Electroplaters' Society, Am. Electroplat. Soc. -- Annu. Conv. -- Proc. (1957) 24–156.
[103] Wood, Marron, Studies of the sealing of anodized aluminium using ac impedance techniques and electron probe microanalysis: I. sealing in typical salt solutions, Trans. Inst. Met. Finish. 45 (1967) 17–26.
[104] Wood, Marron, Studies of the sealing of anodized aluminium using a.c. impedance techniques and electron probe microanalysis. II. Influence of film porosity, dyeing and colouring and corrosion, Trans. Inst. Met. Finish. 45 (1967) 107–114.
[105] C.E. Michelson, Thermal crazing of anodic coatings on aluminum, Soc. Automot. Eng. -- Pap. (1965).
[106] V. López, E. Otero, a Bautista, J.. González, Sealing of anodic films obtained in oxalic acid baths, Surf. Coatings Technol. 124 (2000) 76–84. doi:10.1016/S0257-8972(99)00626-X.
[107] M.S. Hunter, P.F. Towner, D.L. Robinson, Hydration of anodic oxide films, Am. Electroplat. Soc. -- Tech. Proc. (1959) 220–225.
[108] C.J. Amore, J.F. Murphy, Sealing of anodized aluminum, Met. Finish. 63 (1965).
[109] Chromate sealing of anodic films, Light Met. 9 (1946) 22–35.
[110] R. Tilley, Colour and The Optical Properties of Materials: An Exploration of the Relationship Between Light, the Optical Properties of Materials and Colour, 2010. http://www.pilkington.com/products/bp/bybenefit/specialapplications/tecglass/ (accessed November 4, 2013).
[111] R.J.D. Tilley, Light and Colour, in: Colour Opt. Prop. Mater., John Wiley & Sons, Ltd, 2010: pp. 1–48. doi:10.1002/9780470974773.ch1.
[112] R. Tilley, Colours due to Refraction and Dispersion, in: Colour Opt. Prop. Mater., 2011: pp. 49–90. http://onlinelibrary.wiley.com/doi/10.1002/9780470974773.ch2/summary (accessed May 22, 2014).
[113] R.J.D. Tilley, Colour due to Scattering, in: Colour Opt. Prop. Mater., John Wiley & Sons, Ltd, 2010: pp. 175–196. doi:10.1002/9780470974773.ch5.
[114] G. Mie, Beitraege zur Optik trueber Medien, speziell kolloidaler Metallloesungen, Ann. Phys. 25 (1908) 377–445. doi:10.1002/andp.19083300302.
[115] M. Faraday, The Bakerian Lecture: Experimental Relations of Gold (and Other Metals) to Light, Philos. Trans. R. Soc. London. 147 (1857) 145–181. doi:10.1098/rstl.1857.0011.
[116] R. Tilley, Colour in Metals, Semiconductors and Insulators, in: Colour Opt. Prop. Mater., 2011: pp. 419–489.
[117] A.C. Nyce, L.P. Skolnick, Optical constants of bulk and thin-film aluminum at 6328 A, J. Opt. Soc. Am. 65 (1975) 792–796. doi:10.1364/JOSA.65.000792.
[118] Premendra, B.S. Tanem, J.M.C. Mol, H. Terryn, J.H.W. DeWit, L. Katgerman, A combined TEM and SKPFM investigation of the surface layers on rolled AA5050 aluminium alloy using ultra-microtomy, Surf. Interface Anal. 40 (2008) 1157–1163. doi:10.1002/sia.2857.
[119] G. Buytaert, H. Terryn, S. Van Gils, B. Kernig, B. Grzemba, M. Mertens, Investigation of the (sub) surface of commercially pure rolled aluminium alloys by means of total reflectance, r.f. GDOES, SEM/EDX and FIB/TEM analysis, Surf. Interface Anal. 38 (2006) 272–276. doi:10.1002/sia.2205.
[120] G. Buytaert, H. Terryn, S. Van Gils, B. Kernig, B. Grzemba, M. Mertens, Study of the near-surface of hot- and cold-rolled AlMg0.5 aluminium alloy, Surf. Interface Anal. 37 (2005) 534–543. doi:10.1002/sia.2046.
[121] D.R. (ed.). Lide, W.M. (ed.). Haynes, CRC handbook of chemistry and physics : a ready-reference book of chemical and physical data, CRC Press, 2010.
[122] I. Khan, J. Leach, N. Wilkins, The thickness and optical properties of films of anodic aluminium oxide, Corros. Sci. 6 (1966) 483–497. doi:10.1016/S0010-938X(66)80065-3.
[123] T.S. Shih, P.S. Wei, Y. Sen Huang, Optical properties of anodic aluminum oxide films on Al1050 alloys,

Surf. Coatings Technol. 202 (2008) 3298–3305. doi:http://dx.doi.org/10.1016/j.surfcoat.2007.12.002.
[124] H. Zhu, M.J. Couper, A.K. Dahle, Effect of process variables on the formation of streak defects on anodized aluminum extrusions: An overview, High Temp. Mater. Process. 31 (2012) 105–111. doi:10.1515/htmp-2012-0024.
[125] H. Zhu, T. Wei, M.J. Couper, A.K. Dahle, Effect of extrusion profile on surface microstructure and appearance of aluminum extrusions with different Fe contents, JOM. 65 (2013) 618–624. doi:10.1007/s11837-013-0581-8.
[126] H. Zhu, T. Wei, M.J. Couper, A.K. Dahle, Effect of Fe-rich particles on the formation of die streaks on anodized aluminum extrusions, Jom. 64 (2012) 337–345. doi:10.1007/s11837-012-0252-1.
[127] N. Tabrizian, H.N. Hansen, P.E. Hansen, R. Ambat, P. Møller, Influence of annealing and deformation on optical properties of ultra precision diamond turned and anodized 6060 aluminium alloy, Surf. Coatings Technol. 204 (2010) 2632–2638. doi:10.1016/j.surfcoat.2010.02.002.
[128] M. Saito, Unoxidized Aluminum Particles in Anodic Alumina Films, J. Electrochem. Soc. 140 (1993) 1907. doi:10.1149/1.2220737.
[129] M. Saito, Y. Shiga, M. Miyagi, K. Wada, O. Sachiko, Optical Transmittance of Anodically Oxidized Aluminum Alloy, Jpn. J. Appl. Phys. 34 (1995) 3134. http://stacks.iop.org/1347-4065/34/i=6R/a=3134.
[130] Y. Ma, X. Zhou, G.E. Thompson, J.O. Nilsson, M. Gustavsson, A. Crispin, Anodizing of AA6063 aluminium alloy profiles: Generation of dark appearance, Surf. Interface Anal. 45 (2013) 1479–1484. doi:10.1002/sia.5219.
[131] A.E. Hultquist, On the Nature of Burned Anodic Coatings, J. Electrochem. Soc. 111 (1964) 1302. doi:10.1149/1.2425989.
[132] R. Chang, W.F. Hall, On the correlation between optical properties and the chemical /metallurgical constitution of multi-phase thin films, Thin Solid Films. 46 (1977) L5–L8. doi:10.1016/0040-6090(77)90068-2.
[133] E. Hecht, Optics, Addison Wesley, 2002.
[134] DuPont, DuPont ™ Ti-Pure titanium dioxide - Titanium Dioxide For Coatings, 2007.
[135] http://www.bluebuddhaboutique.com/blog/2011/09/no-white-anodized-aluminum/, (2015). http://www.bluebuddhaboutique.com/blog/2011/09/no-white-anodized-aluminum/ (accessed March 9, 2015).
[136] D.K. Howard, Anodizing Aluminum, US3524799 A, 1970. http://www.google.com/patents/US3524799.
[137] C. Siva Kumar, S.M. Mayanna, K.N. Mahendra, A.K. Sharma, R. Uma Rani, Studies on white anodizing on aluminum alloy for space applications, Appl. Surf. Sci. 151 (1999) 280–286. doi:10.1016/S0169-4332(99)00290-1.
[138] C. Siva Kumar, A.K. Sharma, K.N. Mahendra, S.M. Mayanna, Studies on anodic oxide coating with low absorptance and high emittance on aluminum alloy 2024, Sol. Energy Mater. Sol. Cells. 60 (2000) 51–57. doi:10.1016/S0927-0248(99)00062-8.
[139] S. Yoshida, Y. Ito, Y. Sakasita, T. Kobata, Coloring methods for aluminum and aluminum alloys, US4024039 A, 1977. http://www.google.com/patents/US4024039.
[140] H. Watanabe, I. Shimamura, M. Abe, M. Mizusawa, Surface treatment of aluminum or aluminum alloys, US4659439 A, 1987. http://www.google.com/patents/US4659439.
[141] M. Burresi, L. Cortese, L. Pattelli, M. Kolle, P. Vukusic, D.S. Wiersma, et al., Bright-white beetle scales optimise multiple scattering of light., Sci. Rep. 4 (2014) 6075. doi:10.1038/srep06075.
[142] P.J. Kelly, R.D. Arnell, Magnetron sputtering: A review of recent developments and applications, Vacuum. 56 (2000) 159–172. doi:10.1016/S0042-207X(99)00189-X.
[143] G. Bräuer, B. Szyszka, M. Vergöhl, R. Bandorf, Magnetron sputtering – Milestones of 30 years, Vacuum. 84 (2010) 1354–1359. doi:http://dx.doi.org/10.1016/j.vacuum.2009.12.014.
[144] M. Ohring, Chapter 3 - Physical Vapor Deposition, in: M.B.T.-T.M.S. of T.F. Ohring (Ed.), Academic Press, San Diego, 1992: pp. 79–145. doi:http://dx.doi.org/10.1016/B978-0-08-051118-4.50009-8.
[145] J.A. Thornton, Influence of apparatus geometry and deposition conditions on the structure and topography of thick sputtered coatings, J. Vac. Sci. Technol. 11 (1974) 666. doi:10.1116/1.1312732.
[146] J.A. Thornton, The microstructure of sputter-deposited coatings, J. Vac. Sci. Technol. A Vacuum, Surfaces, Film. 4 (1986) 3059. doi:10.1116/1.573628.
[147] J.A. Thornton, Influence of substrate temperature and deposition rate on structure of thick sputtered Cu coatings, J. Vac. Sci. Technol. 12 (1975) 830–835. doi:10.1116/1.568682.
[148] B.A. Movchan, A. V. Demichishin, Study of the Structure and Properties of Thick Vacuum Condensates of Nickel, Titanium, Tungsten, Aluminum Oxide and Zirconium Dioxide, Fiz Met. I Met. 28 (1969) 653–660.
[149] H.H. Strehblow, C.M. Melliar-Smith, W.M. Augustyniak, Examination of Aluminum-Copper Films during

the Galvanostatic Formation of Anodic Oxide, J. Electrochem. Soc. 125 (1978) 915. doi:10.1149/1.2131590.
[150] H. Habazaki, X. Zhou, K. Shimizu, P. Skeldon, G.E. Thompson, G.C. Wood, Mobility of copper ions in anodic alumina films, Electrochim. Acta. 42 (1997) 2627–2635. doi:10.1016/S0013-4686(96)00454-9.
[151] S.J. Garcia-Vergara, K. El Khazmi, P. Skeldon, G.E. Thompson, Influence of copper on the morphology of porous anodic alumina, Corros. Sci. 48 (2006) 2937–2946. doi:10.1016/j.corsci.2005.10.017.
[152] A.C. Crossland, G.E. Thompson, C.J.E. Smith, H. Habazaki, K. Shimizu, P. Skeldon, Formation of manganese-rich layers during anodizing of Al-Mn alloys, Corros. Sci. 41 (1999) 2053–2069. doi:10.1016/S0010-938X(99)00025-6.
[153] Y. Liu, P. Skeldon, G.. Thompson, H. Habazaki, K. Shimizu, Anodic film growth on an Al–21at.%Mg alloy, Corros. Sci. 44 (2002) 1133–1142. doi:10.1016/S0010-938X(01)00115-9.
[154] X. Zhou, H. Habazaki, K. Shimizu, P. Skeldon, G.E. Thompson, G.C. Wood, Enrichment-dependent anodic oxidation of zinc in Al-Zn alloys, Corros. Sci. 38 (1996) 1563–1577. doi:10.1016/0010-938X(96)00051-0.
[155] H. Habazaki, Development of Iron-Rich Layers during Anodic Oxidation of Sputter-Deposited Al-4 atom % Fe Alloy, J. Electrochem. Soc. 146 (1999) 2502. doi:10.1149/1.1391962.
[156] V.C. Nettikaden, H. Liu, P. Skeldon, G.E. Thompson, Porous anodic film formation on Al-Ti alloys in sulphuric acid, Corros. Sci. 57 (2012) 49–55. doi:10.1016/j.corsci.2011.12.035.
[157] E.D. Palik, Chapter 2 - Refractive Index, Handbook of Optical Constanst of Solids, in: Handb. Opt. Constants Solids, Academic Press, Burlington, 1997: pp. 5–114. doi:http://dx.doi.org/10.1016/B978-012544415-6.50149-7.
[158] ASM Handbook - Alloy Phase Diagrams - Volume 3, ASM International, 1992.
[159] R.S. Mishra, Z.Y. Ma, Friction stir welding and processing, Mater. Sci. Eng. R Reports. 50 (2005) 1–78. doi:10.1016/j.mser.2005.07.001.
[160] Z.Y. Ma, Friction Stir Processing Technology: A Review, Metall. Mater. Trans. A. 39 (2008) 642–658. doi:10.1007/s11661-007-9459-0.
[161] R.S. Mishra, M.W. Mahoney, S.X. McFadden, N.A. Mara, A.K. Mukherjee, High strain rate superplasticity in a friction stir processed 7075 Al alloy, Scr. Mater. 42 (1999) 163–168. doi:http://dx.doi.org/10.1016/S1359-6462(99)00329-2.
[162] J.Q. Su, T.W. Nelson, C.J. Sterling, A new route to bulk nanocrystalline materials, J. Mater. Res. 18 (2003) 1757–1760.
[163] R.S. Mishra, M.W. Mahoney, Friction stir processing: A new grain refinement technique to achieve high strain rate superplasticity in commercial alloys, Mater. Sci. Forum. 357-359 (2001) 507–514.
[164] P.B. Berbon, W.H. Bingel, R.S. Mishra, C.C. Bampton, M.W. Mahoney, Friction stir processing: A tool to homogenize nanocomposite aluminum alloys, Scr. Mater. 44 (2001) 61–66. doi:10.1016/S1359-6462(00)00578-9.
[165] Z.Y. Ma, R.S. Mishra, Friction stir surface composite fabrication, TMS Annu. Meet. (2003) 243–250.
[166] R.S. Mishra, Z.Y. Ma, I. Charit, Friction stir processing: A novel technique for fabrication of surface composite, Mater. Sci. Eng. A. 341 (2003) 307–310. doi:10.1016/S0921-5093(02)00199-5.
[167] M.N. Avettand-Fènoël, a. Simar, R. Shabadi, R. Taillard, B. de Meester, Characterization of oxide dispersion strengthened copper based materials developed by friction stir processing, Mater. Des. 60 (2014) 343–357. doi:10.1016/j.matdes.2014.04.012.
[168] P.K.J. and R.J. Rajashekhara Shabadi, Marie Noëlle Avettand-Fènoël, Aude Simar, Roland Taillard, Thermal Conductivity in Yttria Dispersed Copper, Mater. Des. 65 (2015) 869–877. doi:http://dx.doi.org/10.1016/j.matdes.2014.09.083.
[169] Y. Nigara, Measurement of the Optical Constants of Yttrium Oxide, Jpn. J. Appl. Phys. 7 (1968) 404. http://stacks.iop.org/1347-4065/7/i=4/a=404.
[170] G. Hass, J.B. Ramsey, R. Thun, Optical Properties and Structure of Cerium Dioxide Films, J. Opt. Soc. Am. 48 (1958) 324. doi:10.1364/JOSA.48.000324.

3. Materials and Methods

3.1 Materials

Pure Al (Reinal™, AA1090) in cast condition as well as rolled Al alloys of AA6060 and AA6401 were used in this study as substrates for magnetron sputter deposition. Rolled plates of Peraluman706™ (P706) were used as substrates for friction stir processing (FSP) to prepare surface composites. Standard composition of these alloys is listed in the Table 3.1.

Table 3.1: Chemical composition (in wt.%) of different Al alloys used in this study.

	Mg	Si	Fe	Cu	Mn	Zn	Ti	Cr
Reinal™	<0.01	<0.07	<0.07	<0.02	<0.01	<0.03	<0.01	
AA6060	035-0.6	0.30-0.6	0.1-0.3	<0.1	<0.1	<0.15	<0.1	<0.05
AA6401	0.35-0.7	0.35-0.7	<0.04	0.05-0.2	<0.03	<0.04	<0.01	
P706™	0.3-0.8	0.2	0.2	0.03-0.1	0.05	0.05	0.03	0.02

Powders for preparing surface composites and for polymer composites were based on the oxides of Ti, Ce and Y. The TiO_2 powders in rutile phase of different size distributions were obtained from DuPont Titanium Technologies, Belgium (Ti-Pure™ R900, R960, R796). The TiO_2 powders in anatase phase of average particle size 14 nm were obtained from Evonik Industries, Germany (Aeroxide™ P90). The CeO_2 particles of 250 nm average size were obtained from Nano-Oxides Inc, USA. The Y_2O_3 powders of average size 750 nm were obtained from Skyspring Nanomaterials Inc, USA. For spin coating of composites onto Al substrates, a polyurethane clear coat based on acrylic resin (Sigmavar WS Satin™) was obtained from Sigma coatings.

3.2 Pre-treatments

Surface preparation of the Al alloys was performed by rough grinding of the surface followed by wheel polishing using an alumina abrasive paste of different size grades. Fine polishing was performed using a soft polishing disc for obtaining the high gloss surfaces. The surfaces were then cleaned in ethanol for removing the polishing residues. To obtain rough matte surfaces, caustic etching was performed on the surfaces by immersion in 10 % NaOH solution at 60 °C in an ultrasonic bath for 10 min. Desmutting was performed after caustic etching by immersion in a 69 vol.% HNO_3 solution for 10 s. Samples were then cleaned in ethanol and then under running deionised water.

3.3 Processing of Surfaces

3.3.1 Magnetron Sputtering

The binary Al-Zr and Al-Ti as well as ternary Al-Zr-Si coatings were deposited by DC magnetron sputtering at the Tribology Centre, Danish Technological Institute, Denmark. An industrial scale CemeCon CC800/9 machine with multiple cathodes was employed for deposition of the coatings. The cathodes faced the substrates which were mounted on a planetary rotating table in the middle of the chamber to ensure a homogenous deposition. The deposition chamber was initially evacuated to a base pressure of 6 mPa. During sputtering, a constant argon flow of 200 mL/min was used providing a typical argon pressure of 500 mPa. The distance between the targets and sample was about 100 mm, and the bias voltage on the substrates was fixed at -50 V. The maximum temperature during deposition was between 150 °C and 200 °C as measured using a bi-metal thermometer during the deposition. AA6060, AA6401 and AA1090 substrates (Erbslöh Aluminium GmbH, Germany) with dimensions 200 mm x 40 mm x 5 mm were coated with constant compositions and composition gradients of varying Zr/Ti content along the length of the specimen.

The binary coatings were produced using one target of Al and another target of Al with cylindrical Zr/Ti inserts of 1 cm in diameter. For ternary Al-Zr-Si coatings, an extra target of commercial Si wafer was used. The Al target was operated at 2000 W and the Al-Zr/Ti target was operated at varying power optimized for the required concentration of alloying elements. For the gradient coatings, the targets were displaced with respect to the centre of the chamber. Thereby, the Zr/Ti content in the deposition flux varies throughout the chamber and the resulting coating on the relatively long substrate has a varying composition. This method was employed as it is very practical for screening purposes as a single deposition on substrate will provide different compositions for testing. The alloy content of the coatings and the thicknesses are mentioned in the individual chapters where the specific samples are investigated.

3.3.2 Friction Stir Processing

Friction stir processing was performed to prepare surface composites and was carried out at the Catholic University of Louvain, Belgium. The processing was performed using a Hermle milling machine equipped with a steel tool having 20 mm shoulder diameter and 1.5 mm pin length with a M6 thread. The backwards tilt angle of the tool was maintained at 1˚. A groove of 0.5 mm deep, 10 mm wide, and 180 mm long was milled into the Al plates (Peraluman 706) and was completely filled with the filler powder (see Figure 3.1). The filled plates were then covered by the same Al sheet rolled down to a thickness of 0.25 mm to prevent loss of the powder during the initial FSP pass. The rotational speed of the tool was 1000 rpm and the advancing speed was 200 mm/min for the first pass to ensure correct closure of the groove and 1000 mm/min for the next six passes. A surface of 175 mm length x 20 mm width was processed for each pass with a total processing time of roughly 2 min. All seven passes were performed one over the other without any shift. For comparison, reference samples without any powders were also produced using the same FSP parameters.

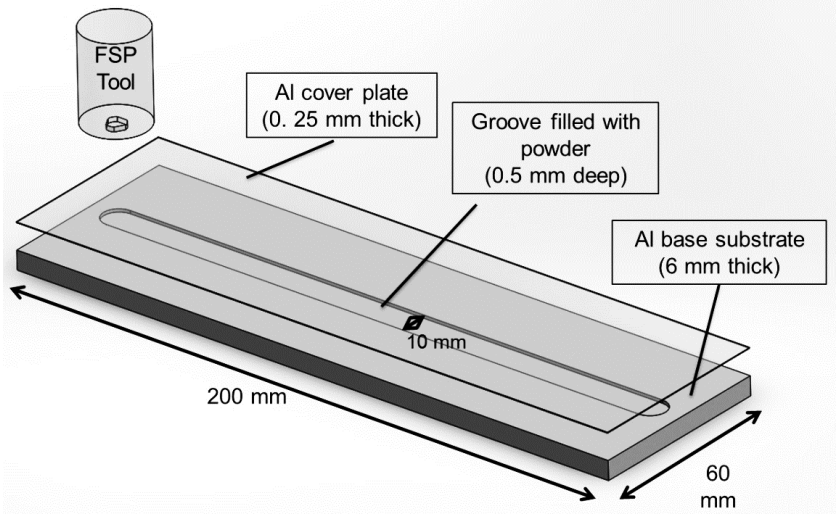

Figure 3.1: Schematic of the sample geometry with groove used for FSP process.

3.4 Anodising

Anodising of the material was performed using conventional DC anodising and high frequency Pulse Anodising. Conventional DC anodising was performed at Bang and Olufsen A/S, Denmark in the anodising line whereas the high frequency anodising was performed at Technical University of Denmark at a lab scale. The details of these processes are described below.

Conventional DC anodising:

- Alkaline cleaning in AlfiClean™ from AluFinish at 60 °C for 2 min – 6.5 min with rough agitation.
- Cleaning (in deionised water).
- Desmutting in 6 wt. % HNO_3 at 27.5 °C – 28.0 °C for approximately 4 min.
- Cleaning in DI water.
- Anodising in 190 g/L H_2SO_4 at 17.9 °C with mild agitation at a constant voltage of 12.6 V ± 0.5 V and a current density of about 1 A/dm^2.
- Cleaning in DI water.
- Sealing in 2 g/L – 3 g/L AlfiSeal™ from AluFinish at 96 °C.
- Drying at 74 °C – 78 °C for 3 min – 5 min.

High Frequency Pulse Anodising:

- Alkaline cleaning in AlfiClean™ from AluFinish at 60 °C for 5 min with rough agitation.
- Cleaning (in deionised water)
- Desmutting in 69 % HNO_3 at 27.5 °C – 28.0 °C for approximately 10 s.
- Cleaning in DI water.
- Anodising in 190 g/L H_2SO_4 at 10/20 °C with mild agitation using a voltage profile varying from -5 V to 0 V at cathodic cycle and +10 V to + 20 V at anodic cycle at 2 kHz frequency and 30-70% duty cycle.
- Cleaning.
- Sealing in deionised water at 96 °C.
- Drying in warm air.

3.5 Reflectance Spectroscopy

Reflectivity of the samples was investigated in detail using a spectrally resolved optical reflectance method comprising of an integrating sphere-spectrometer setup as shown in Figure 3.2. The samples were illuminated with a collimated beam from a deuterium tungsten-halogen light source (type DH2000 from Ocean Optics) at an incidence angle of 8˚ to the normal. The scattered light inside the sphere was collected using an optical fibre coupled to an optical spectrometer (QE65000 from Ocean Optics). Each reflectance spectrum was recorded over the wavelength range from 350-750 nm and was averaged for 4 s. Diffuse reflectance of a sample can be measured directly using a gloss trap coated with a dark absorbing material in the specular light port of the sphere. The specular reflectance spectrum is then obtained by subtracting the diffuse reflectance from total reflectance spectrum. The spectrophotometer was calibrated using high diffuse reflectance standards.

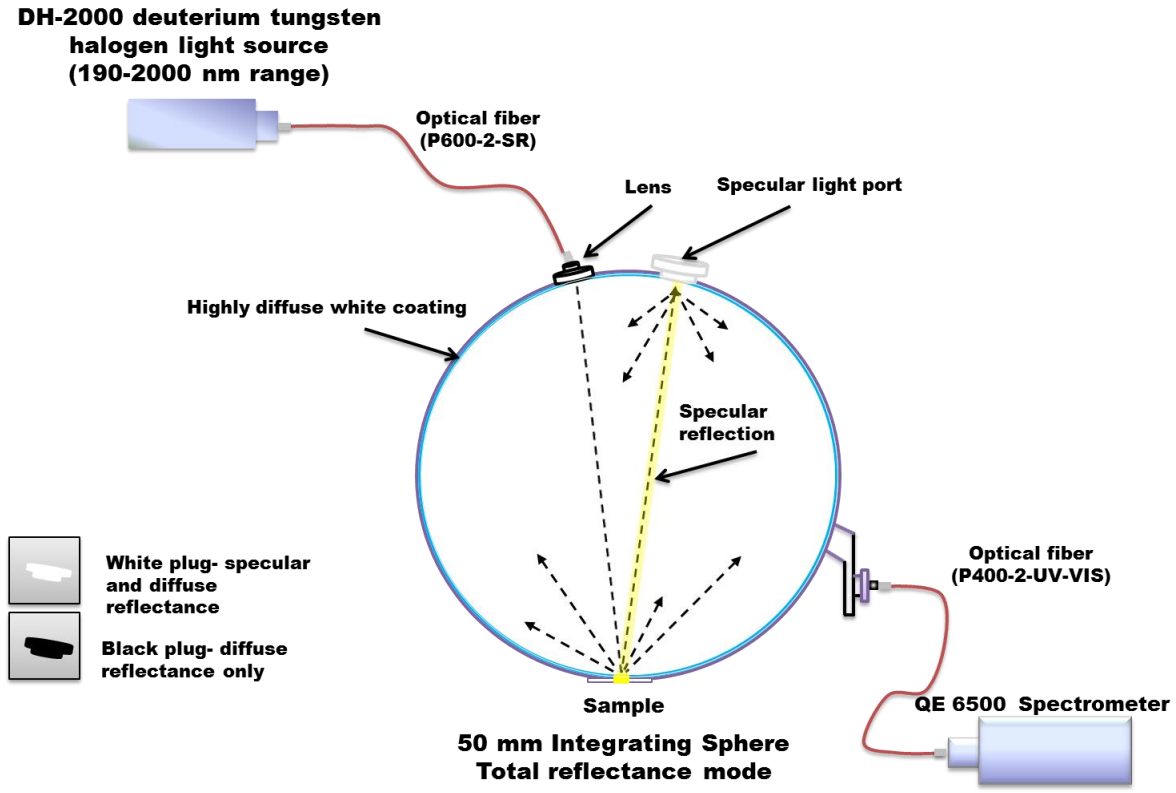

Figure 3.2: Schematic showing the integrating sphere-spectrometer setup used to measure the surface reflectance.

3.6 Atomic Force Microscopy and Scanning Kelvin Probe Force Microscopy

Scanning Kelvin Probe Force Microscopy (SKPFM) measurements were performed using an Atomic Force Microscope (AFM, Model Bruker, Multimode™ 5). Commercially available silicon tips (Nanosensors, PPP-EFM) coated with approx. 25 nm of chromium and platinum iridium on both sides of the cantilever were used. The tips have a resonance frequency of approximately 75 kHz and the tip radius is approximately 5 nm. The scans were performed using a line-wise two-pass lift mode over an area of 20 x 20 μm^2 with a scan rate of 0.2 Hz. During the first pass, the topography was measured using the mechanical intermittent AFM mode. During the second pass, the tip was lifted approximately 10 nm above the surface, and retraced the previous topography while simultaneously measuring the Volta potential. Measurements were carried out in air at ambient temperature and humidity. Samples were mechanically polished and degreased in acetone prior to performing the measurements.

3.7 Chemical Composition and Phase Analysis

3.7.1 X-Ray Diffraction

Phase analysis of the samples was performed in both Bragg-Brentano condition (bulk analysis) and also in Grazing incidence mode (thin film analysis) using an X-ray diffractometer (Model Bruker Discover D8™) using Cu K_α radiation at 40 kV and 40 mA.

3.7.2 Radio Frequency Glow Discharge Optical Emission Spectroscopy (RF GDOES)

Compositional analysis of the samples in bulk as well as a function of depth was performed using Radio Frequency Glow Discharge Optical Emission Spectroscopy (RF-GDOES, Model GD-Profiler 2, Horiba Jobin Yvon). The instrument is equipped with a radiofrequency (RF) generator, a standard discharge source

with an anode of 4 mm internal diameter, a monochromator and polychromator optical spectrometers, and Quantum XP™ software. Calibration of the GD-OES profiler was carried out at optimized discharge condition of 850 Pa pressure and RF power of 40 W by sputtering the sample surface for a specific time and then measuring depth of the resulting crater using a surface profilometer. The instrument was coupled with a software package (Quantum XP™) for analysing and quantifying the data.

3.8 Microstructural Characterization

3.8.1 Scanning Electron Microscopy

The microstructure and morphology of the samples was observed using a scanning electron microscope (SEM) (Model Quanta 200™ ESEM FEG, FEI) equipped with an energy dispersive spectrometer (EDS) (Oxford Instruments 80 mm^2 X-Max™). For observing cross section of coatings and anodised layers, the samples were initially cut in transverse direction, and later embedded into an epoxy and polished. A thin layer of gold (~3 nm) was sputter coated to prevent charging of the samples during electron imaging. The atomic number contrast (Z-contrast) images were obtained using a Quad - solid-state back scatter detector (BSED) and the topographical images were obtained using a Everhart-Thornley detector (ETD).

3.8.2 Transmission Electron Microscopy

The high-resolution microstructural analysis was carried out on the sample cross sections using a transmission electron microscope (TEM) (Model Tecnai™ G2 20) operating at 200 keV. Compositional analysis was performed in S-TEM mode using an EDS (Oxford Instruments 80 mm^2 X-Max™) coupled to an Inca™ software package. Thin film lamella for TEM analysis were prepared using in-situ focused ion beam (FIB-SEM) lift out (Model Quanta 200 3D™ DualBeam, FEI) and were further thinned for electron transparency in a FIB-SEM (Helios Nanolab™ DualBeam, FEI). For studying the microstructural evolution of samples, in-situ heating of the lamella was performed in the TEM using a Tantalum holder with a resistive heating stage. The temperature was measured using a thermocouple that was built into the holder and placed next to the sample. The temperature was controlled using a hot stage controller (Gatan SmartSet™ Model 901).

3.8.3 Focused Ion Beam – Scanning Electron Microscopy

Focused Ion Beam – Scanning Electron Microscopy (Dual Beam FIB-SEM, FEI Helios Nanolab EBS3™) was used to observe the cross-sections of the samples and to prepare thin site-specific lamella (~150 nm thick) for transmission electron microscopy. The microscope was equipped with a field emission gun electron source and a Ga^+ ion source, Everhart-Thornley detector (ETD), Gas injection systems (GIS) for tungsten and platinum deposition, and in-situ Omniprobe™ micromanipulator for the lift out of thin lamella. The technique for site-specific milling and insitu lift out of thin lamella for the TEM analysis using FIB-SEM is explained below.

3.8.3.1 FIB-SEM in-situ lamella lift out

Lift out techniques developed for TEM lamella are ex-situ and in-situ lift out. Ex-situ lift out uses a micromanipulator under an optical microscope to lift the lamella. In-situ technique does the same inside the specimen chamber of the FIB-SEM. The FIB enables the preparation of samples having dissimilar materials in combination. Unlike in mechanical thinning where there is a difference in the thickness obtained for different materials, sections made by FIB provide uniform thickness across the sample. The basic steps followed for the TEM lamella in-situ lift out using a FIB-SEM (Dual beam) are as follows:

- Deposit a protective layer (Pt or W) over the area of interest using electron beam (approx. 5 keV, 5 nA) and followed by ion beam (52° tilt, approx. 30 keV, 0.3 nA) induced deposition (see Figure 3.3 (a)).
- Rough milling on either side of the deposit using the ion beam (approx. 52° tilt, 30 keV, 7 nA) (see Figure 3.3 (b)).
- Fine milling is then performed on external faces of the two trenches using the ion beam (52° tilt, approx. 30 keV, 5 nA) (see Figure 3.3 (c)).
- Fine milling allows first to reconcile the non-parallelism induced by the Gaussian shape of the ion beam and secondly to eliminate the amorphous layer generated by the high energy ions used in rough milling.

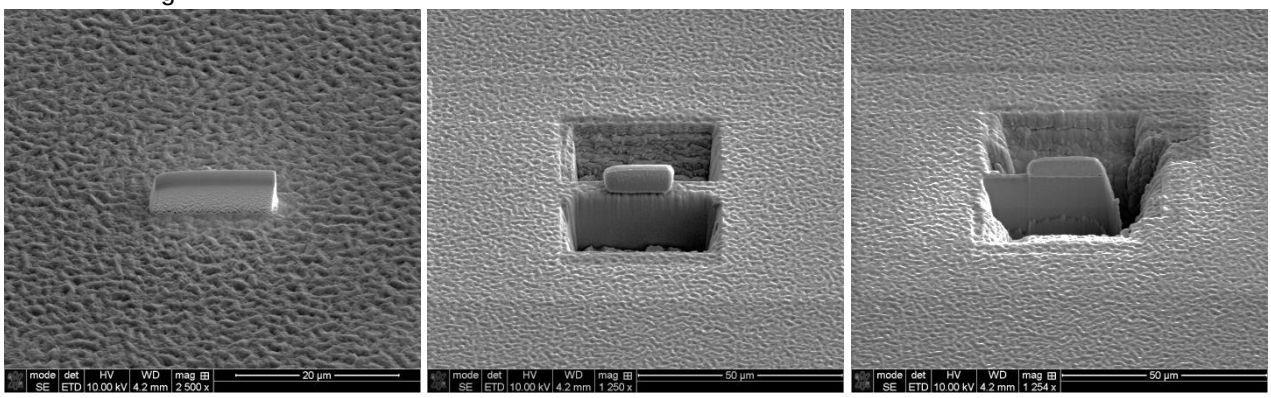

Figure 3.3: Electron micrographs of TEM lamella lift out using FIB showing: (a) protective Pt layer deposition, (b) rough milling and (c) fine milling of trenches around the area of interest.

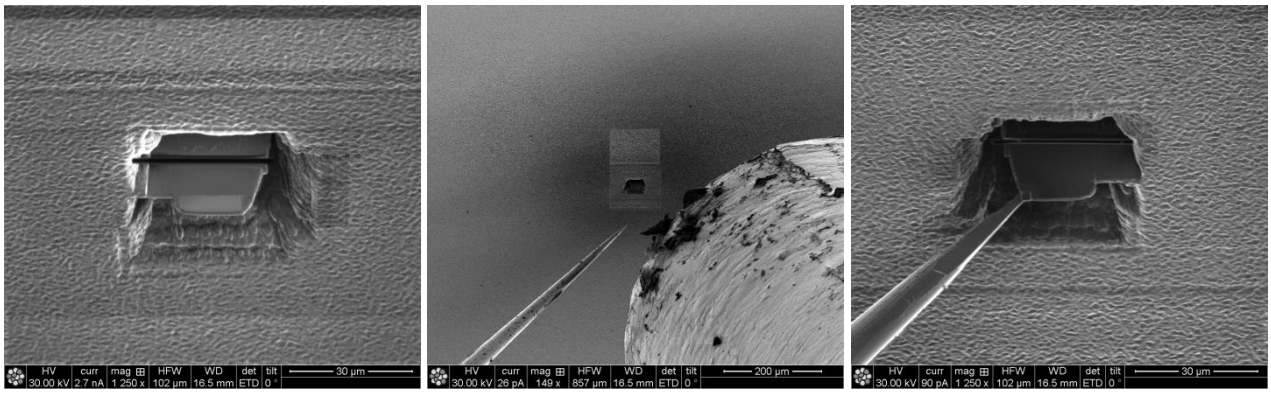

Figure 3.4: Electron micrographs of TEM lamella lift out using FIB showing: (a) milling of undercuts, (b) positioning of GIS and Omniprobe micromanipulator, and (c) welding of Omniprobe™ micromanipulator to the lamella using Pt deposition.

- The undercut is then milled below the lamella using the ion beam (approx. 30 keV, 0.5 nA). The sample is rotated 180° in between the cuts on either sides of the lamella (see Figure 3.4 (a)).
- The gas injection needle is inserted and then the Omniprobe™ is brought close to the lamella. This is done in dual beam mode (ion beam, approx. 30 keV, 10 pA) (see Figure 3.4 (b)).
- The Pt deposition (~1 µm) is performed to weld the lamella to the Omniprobe™ tip using ion beam (approx. 30 keV, 0.3 nA) (see Figure 3.4 (c)).
- The anchor holding the lamella to the specimen is then milled to release the lamella using the ion beam (approx. 30 keV, 1 nA) (see Figure 3.5 (a)).
- After the milling and making sure that the lamella is completely free from the substrate, the stage is lowered using the Z control of the stage (see Figure 3.5 (b)).

- A TEM grid is then placed on the stage and then the chamber is evacuated for further processing (see Figure 3.5 (c)).

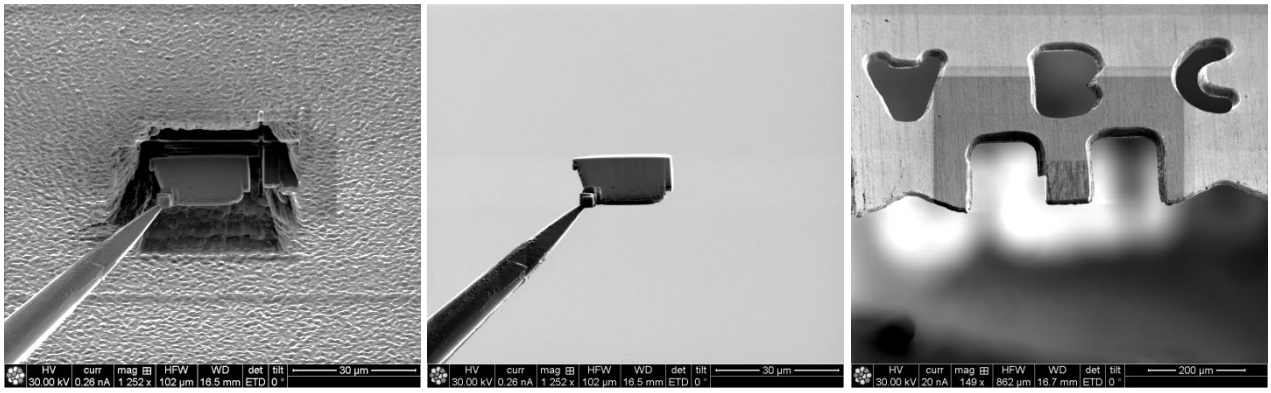

Figure 3.5: Electron micrographs of TEM lamella lift out using FIB showing: (a) milling of anchor to release the lamella from the sample, (b) in-situ lift out of the lamella by lowering the sample stage and (c) Cu/Mo TEM grid for welding the lamella.

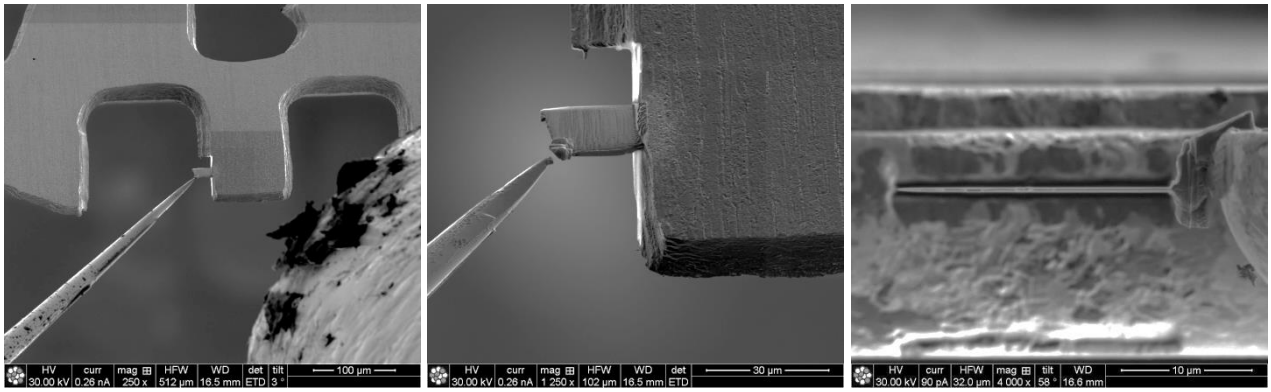

Figure 3.6: Electron micrographs of TEM lamella lift out using FIB showing: (a) transfer of the lamella to TEM grid and welding using Pt deposition, (b) milling of anchor to release the lamella from the micromanipulator, and (c) final TEM lamella after thinning.

- The Omniprobe™ is then brought close to the TEM grid and Pt deposition is performed to weld the lamella to the grid using ion beam (approx. 30 keV, 0.3 nA) (see Figure 3.6 (a)).
- Free the specimen from the manipulator tip using the ion beam (approx. 30 keV, 1 nA) (see Figure 3.6 (b)).
- Reprocess the specimen (thinning) with the ion beam to produce the TEM lamella of required thickness (see Figure 3.6 (c)).

4. Summary of Chapters

This section summarizes the key findings of the scientific papers arising from the PhD research work. Each paper is presented as an individual chapter. The overall goal of the project is to achieve anodised aluminium surfaces with high reflectance and white appearance.

The first four papers deal with magnetron sputtered coatings based on model Al-Zr and Al-Ti systems. The idea is to heat treat binary Al-alloy systems and achieve a multiphase microstructure of Al_3M (M = Zr, Ti) precipitates in an α-Al matrix, which can be subsequently anodised for decorative purposes. In order to understand the microstructural evolution and the morphology of the phases that are formed in the sputtered coatings during heat treatment, in-situ heating of the sputtered coatings was performed in a transmission electron microscope (discussed in Chapter 5 (Paper 1)). The binary model alloy system of Al-Zr was investigated initially. It was observed that upon heating, the Al-Zr sputtered coating initially shows fine spherical precipitates of Al_3Zr phase with 30-40 nm in diameter corresponding to $L1_2$ (cubic) structure at 500 °C. As temperature is further increased to 550 °C, the $L1_2$ phase transforms to the thermodynamically stable tetragonal DO_{23} structure with needle like morphology. The crystal structures were analysed partly using X-ray diffraction and using Selective Area Electron Diffraction (SAED) during the in-situ heating in TEM. Addition of Si to the Al-Zr sputtered coating modified the morphology of the precipitates and formed Al-Zr-Si phase with DO_{22} structure and approx. stoichiometry of $Al_{2.6}Si_{0.4}Zr$. This phase displayed a spheroidal morphology instead of the needle like morphology of the DO_{23}-Al_3Zr (see Figure 4.1).

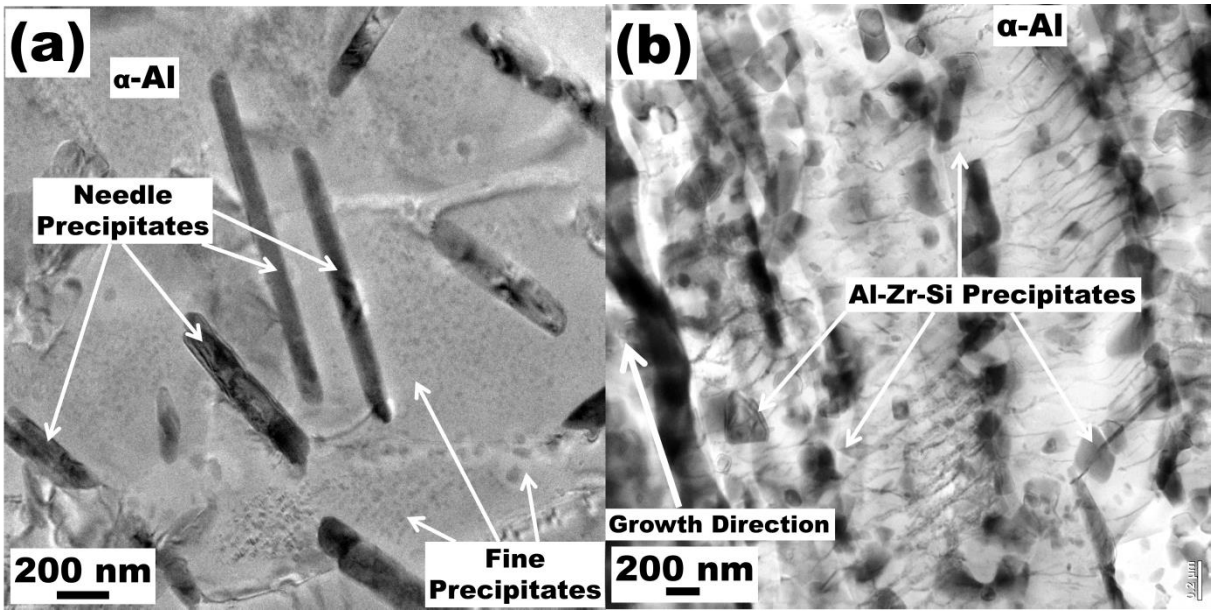

Figure 4.1: TEM bright field image of: (a) Al-Zr coating at RT after in-situ heat treatment at 500 °C for 3 h showing the needle like precipitates (DO_{23}-Al_3Zr) and fine precipitates ($L1_2$-Al_3Zr) formed in the coating matrix, and (b) Al-Zr-Si coating at RT after in-situ treatment at 545 °C showing precipitates with nodular morphology (DO_{22}-$Al_{2.6}Si_{0.4}Zr$).

Chapter 6, 7 & 8 (Paper 2, 3 and 4) focus on the anodising behaviour of binary Al-Zr and Al-Ti magnetron sputtered coatings. The coatings were deposited on different grades of Aluminium (AA6060 and AA1090) alloys using DC magnetron sputtering technique. The composition on Zr and Ti were varied within 4-25 wt. % as measured by Energy Dispersive X-ray Spectroscopy (EDS) and Rutherford Backscatter Spectroscopy (RBS). Anodising of non-heat treated coatings resulted in clear and transparent anodised layers. However, the heat treated surfaces after anodising displayed a wide range of shades of dark grey. For AA6060 substrates (Chapter 6 (Paper 2)), grazing incidence X-ray diffraction (GI-XRD) revealed that the Si in the substrate promoted the formation of DO_{22}- $Al_{2.6}Si_{0.4}Zr$ phase after heat treatment. However, when pure Al

(AA1090) substrates were used (Chapter 7 (Paper 3)), DO_{23}-Al_3Zr precipitated in the sputtered coating upon heat treatment as was observed from the in-situ heating experiments (Chapter 5 (Paper 1)). For Al-Ti sputtered coatings (Chapter 8 (Paper 4)), Al_3Ti phase was formed after heat treatment. Scanning Kelvin Probe Force Microscopy (SK-PFM) of the heat-treated surface showed that the Al-Zr-Si precipitates are cathodic compared to the surrounding Al matrix. The difference in their electrochemical behaviour caused the Al-Zr-Si and the Al-Ti based precipitates to undergo only partial oxidation during the anodising process, whereas the surrounding Al matrix undergoes complete oxidation. Transmission electron microscopy of the anodised layer showed partially oxidized Al-Zr-Si and Al-Ti phases incorporated into the amorphous anodic Al-O matrix in a crystalline metallic phase (see Figure 4.2). This specific situation of crystalline metallic phases in a dielectric medium such as anodic Al-O leads to high attenuation and absorption of incident light by the metal particles.

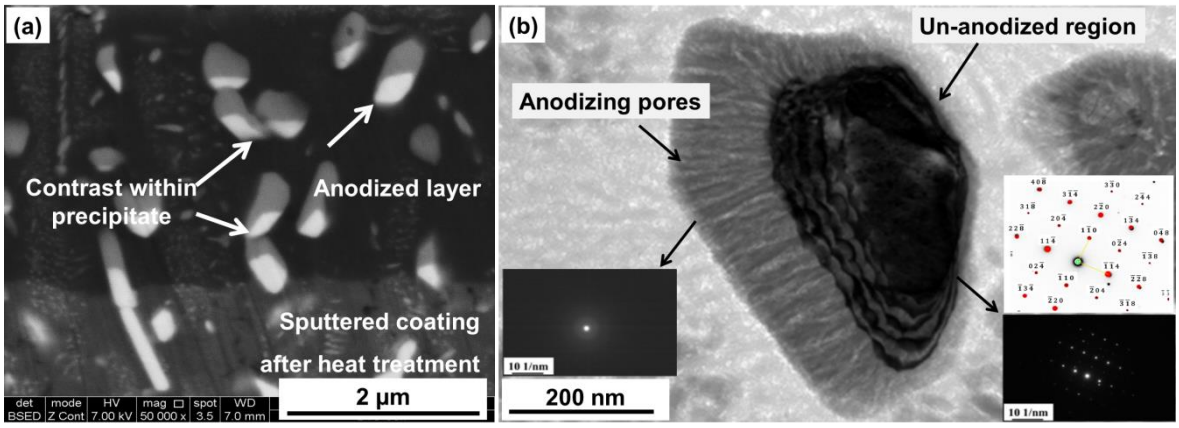

Figure 4.2: (a) Back scattered electron (BSE) image of Al-11 wt. % Zr coating in cross section on AA6060 substrate after heat treatment and anodising and (b) individual Al-Zr based second phase in anodised region with SAED showing partial oxidation of intermetallic phases.

Attempts were made to achieve complete oxidation of the second phases by increasing the DC potential during anodising (Chapter 7 (Paper 3)). Anodising of the heat-treated Al-Zr coating resulted in slightly grey appearing surfaces at higher anodising potential compared to that at lower potentials. Key learnings of this study are that metallic phases in crystalline nature when present in an anodised matrix lead to darkening of the otherwise transparent anodic layer. The incorporated metallic phase in an anodic alumina matrix (which is a dielectric) causes efficient attenuation of incident light due to its high extinction coefficient (*k*). This results in darkening of the anodic layer. This study clearly explains the various defects in the optical appearance observed after anodising of recycled Al alloys, which contain higher amount of intermetallic phases having tendency for partial oxidation during anodising.

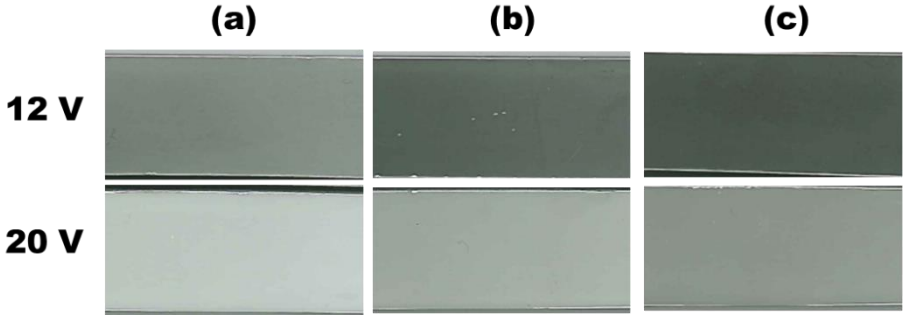

Figure 4.3: Optical images showing appearance of the anodised layer on Al-Zr coatings for Zr concentrations of: (a) 9 wt. %, (b) 15 wt. % and (c) 21 wt. % after heat treatment and anodising at different voltage.

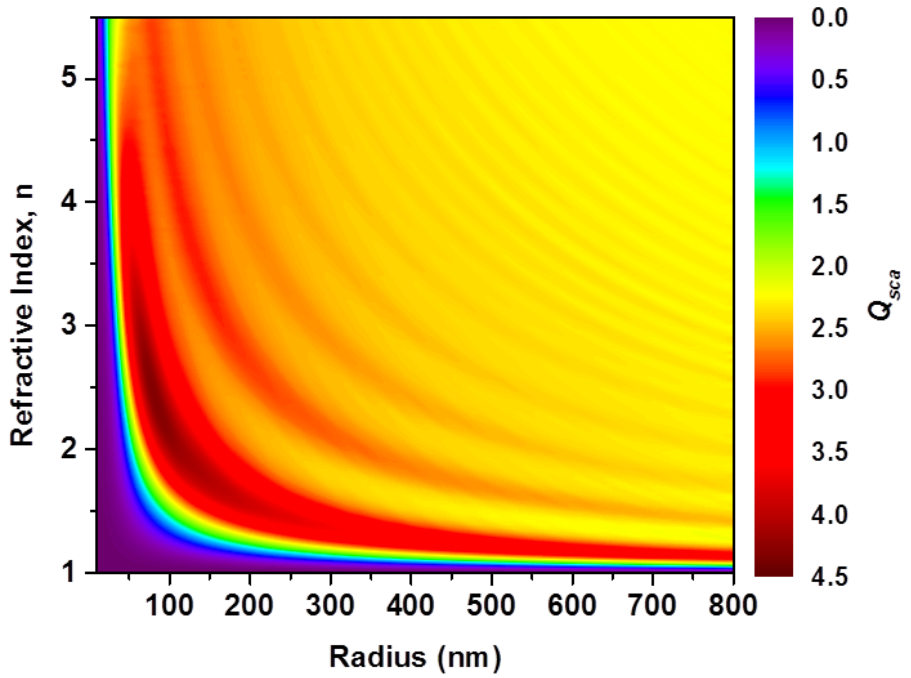

Figure 4.4: Scattering efficiency of a particle suspended in PU averaged over the visible spectrum.

With the aim of obtaining white appearing, highly reflecting anodised Al surfaces, inspiration was taken from naturally occurring nanostructures such as the white beetle and from the commercial white paint formulations, which use a white pigment in a transparent polymer matrix. In both the cases, white appearance arises from multiple scattering of light due to structures that are composed of materials with different refractive indices. In Chapter 9 (Paper 5), theoretical calculations were performed for obtaining scattering efficiencies of TiO_2 particles (in rutile phase) dispersed in a Polyurethane matrix that has similar optical properties as anodised alumina layer. Experimental measurements were performed for total and diffuse reflectance on the Polyuretahne-TiO_2 composite coatings and correlated with the theoretical calculations. The optimal size, distribution, and concentration were predicted for obtaining highly reflecting and glossy appearing white anodised surfaces (see Figure 4.4).

Chapter 10 (Paper 6) is based on anodising of Al composites containing oxides of Ti, Ce, and Y. The oxide particle size, distribution, density, and refractive index of these metal oxides was chosen based on the theoretical modelling and calculations arrived using Kubelka-Munk approach and Mie scattering for the optimum light scattering and reflectance (Chapter 9 (Paper 5)). Model Al metal matrix composite surfaces were obtained using multiple pass friction stir processing. The prepared surface composites were mechanically polished, degreased, and then subjected to conventional decorative DC anodising (see Figure 4.5). Promising results were observed for Al-TiO_2 composites when anodised at a higher DC potential. Anodising of Al-Y_2O_3 and Al-CeO_2 did not show good reflectance values as the Y_2O_3 particles were lost from the Al matrix during anodising and the CeO_2 was transformed to a low refractive index amorphous phase.

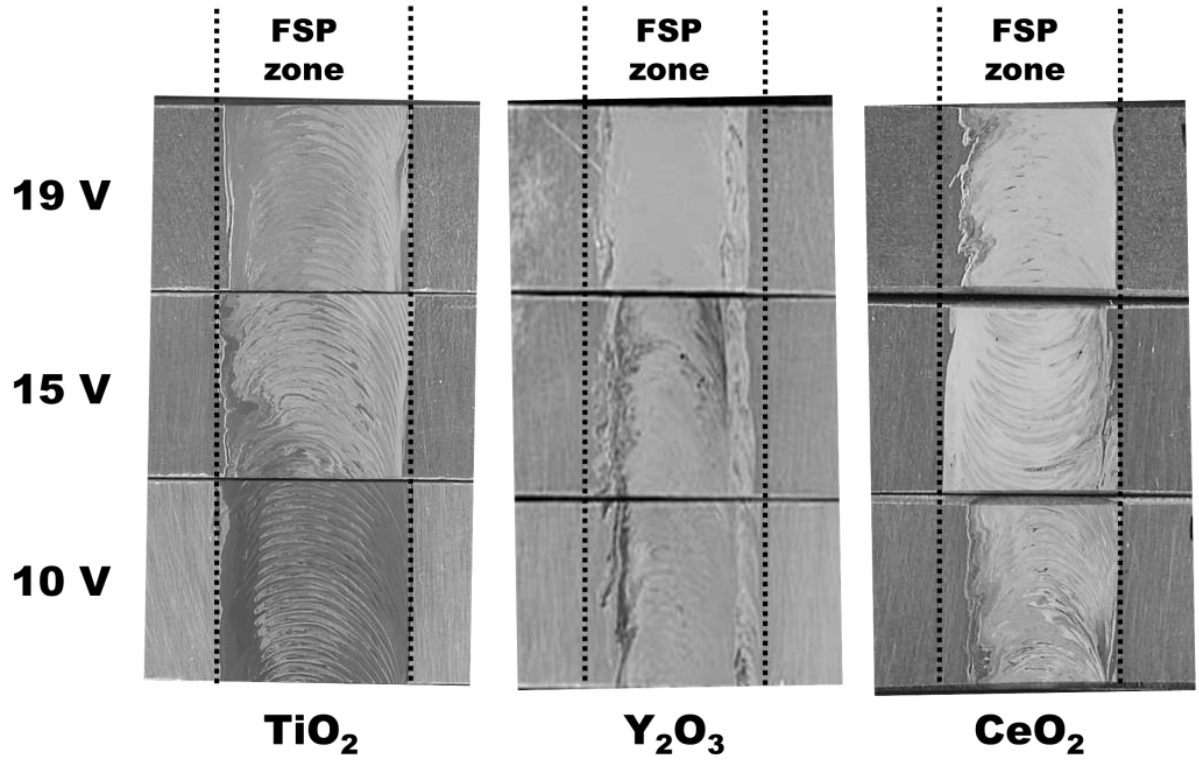

Figure 4.5: Visual appearance of the friction stir processed samples with different powders after sulphuric acid anodising at different voltages.

In order to understand better, the Al-TiO_2 anodised composite surfaces were subjected to further studies and phase analysis using GI-XRD and microstructural characterization using TEM (Chapter 11 (Paper 7)). Results showed that at lower anodising potentials, the TiO_2 phase transformed to Oxygen deficient Magneli phases of the general formula Ti_nO_{2n-1}. This was attributed to the effect of SO_4^{2-} in the sulphuric acid electrolyte that dissolves the TiO_2. In addition, it was seen that as the anodising potential is increased, the TiO_2 transforms from a crystalline phase to a completely amorphous phase (see Figure 4.6). Lower anodising potential leads to electrochemical shadowing of underlying Al and results in un-oxidized Al trapped in anodic alumina leading to darkening of anodic layer (as seen in Chapter 6, 7 & 8 (Paper 2, 3 and 4)). Also, literature suggested that Magneli phases in themselves are coloured from a range of blue to grey shades. The findings led to the efforts in optimizing the anodising process to prevent the formation of Magneli phases and transformation of TiO_2 to amorphous phase along with obtaining complete oxidation of the Al to anodic Al-oxide thus preventing the anodic layer darkening.

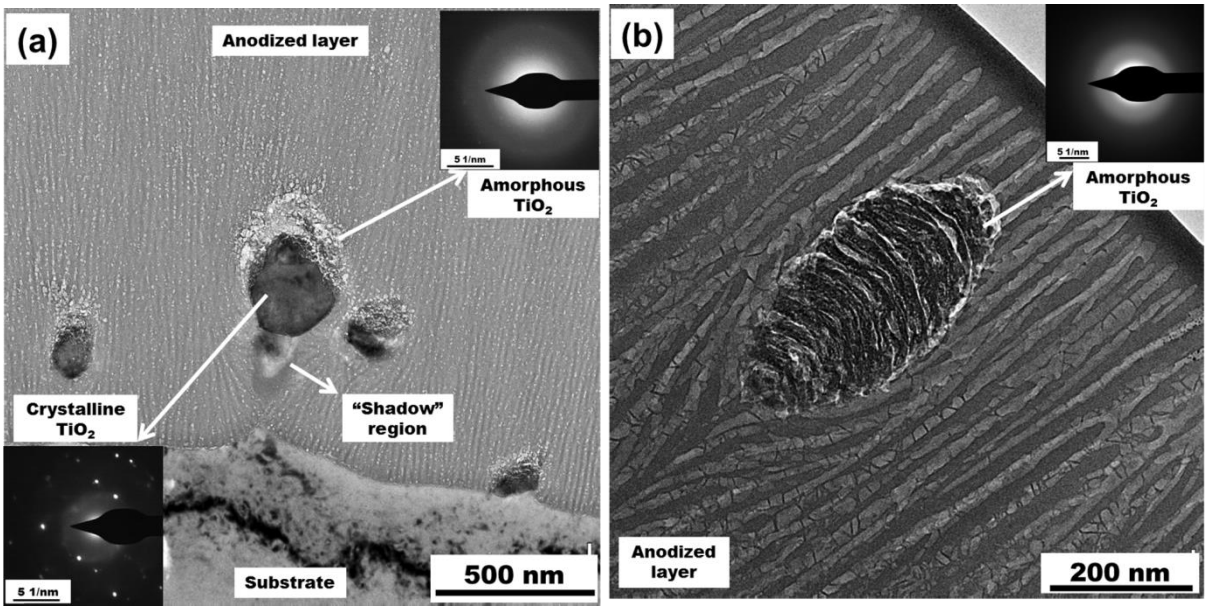

Figure 4.6: TEM bright field image and selected area electron diffraction (SAED) showing anodised layer cross section of the Al-TiO_2 samples anodised at: (a) 9.6 V and (b) 18.9 V in a sulphuric acid electrolyte.

In recent years, AC/Pulse anodising techniques have been gaining wide interest and applications due to their ability to provide uniform and homogenous anodic oxide layers and also due to their higher anodising speeds and efficiencies. Keeping this in mind, high frequency anodising of Al-TiO_2 composites was performed with varying anodising parameters presented in Chapter 12 & 13 (Paper 8 & 9). The effect of varying anodic cycle and cathodic cycle potential values was investigated. Primarily, it was observed that the higher reflectance values were achievable using high frequency pulse anodising when compared to conventional DC anodising (Paper 9). Further characterization of surfaces using TEM showed that the anodic structure of the Al-TiO_2 composites surfaces was highly dependent on the cathodic cycle potential applied (Chapter 12 (Paper 8)). Heterogeneities such as tortuous porosity, anodic pore branching, and loss of TiO_2 particles from anodic matrix were observed when a negative potential was applied during cathodic cycle or low voltage cycle compared to 0 V. This was attributed to the combined effect of increased conductivity of TiO_2 due to oxygen defects (Magneli phases, Ti_nO_{2n-1}). The increased conductivity leads to phenomenon such as current localization at TiO_2 - Anodic alumina - Al substrate interfaces during cathodic cycle. This results in localised cathodic reactions such as electrolysis of water causing vigorous evolution of H_2 at these interfaces. Subsequent mechanical weakening of the interfaces takes place leading to easy access of anodising electrolyte at the weakened and degraded interfaces during the next anodic cycle (see Figure 4.7). This causes pore branching and loss of TiO_2. Effect of pulse frequency, anodising temperature, anodising time, and thickness (see Figure 4.8) were investigated for Al-TiO_2 composite surfaces (Chapter 13 (Paper 9)).

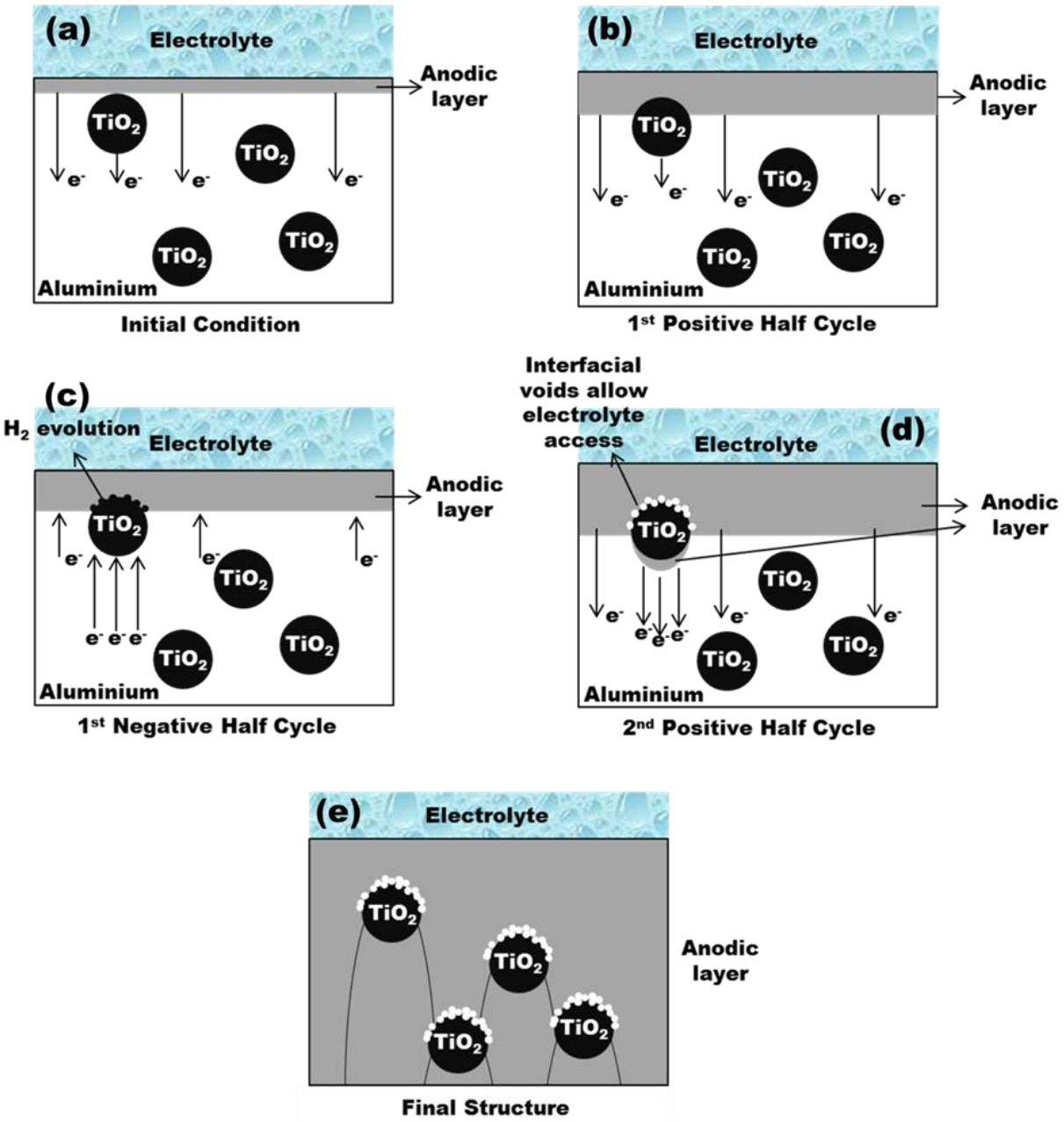

Figure 4.7: Schematic showing the: (a) to (e) stepwise anodic film growth on Al-TiO_2 composite and successive incorporation of TiO_2 particles during high frequency pulse reverse pulse anodising (PRPA).

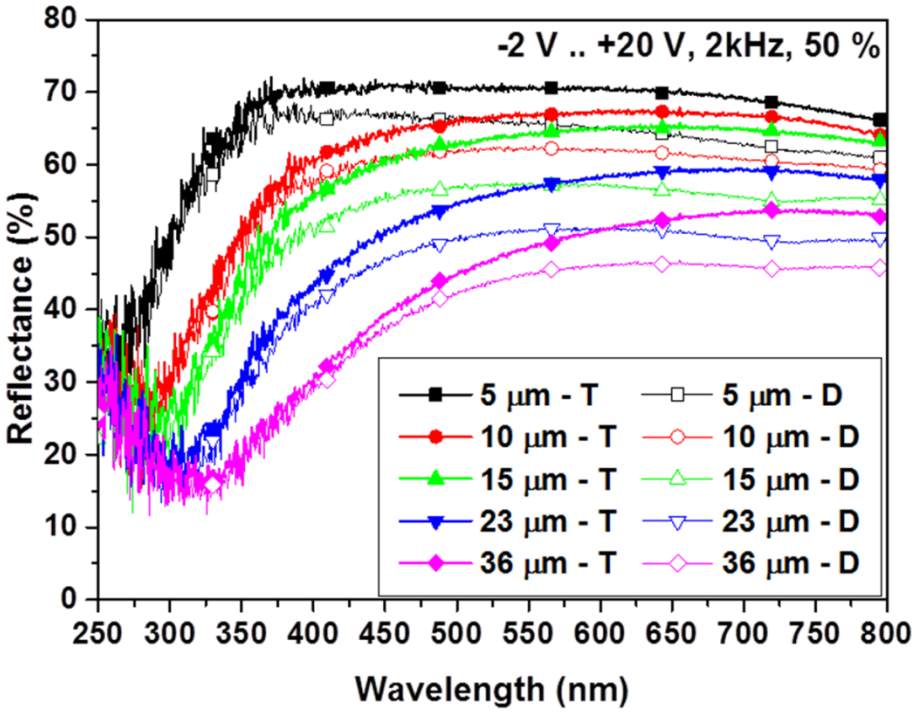

Figure 4.8: Total and diffuse reflectance of the high frequency anodised surfaces as a function of the anodic layer thickness (T- Total reflectance, D – Diffuse reflectance).

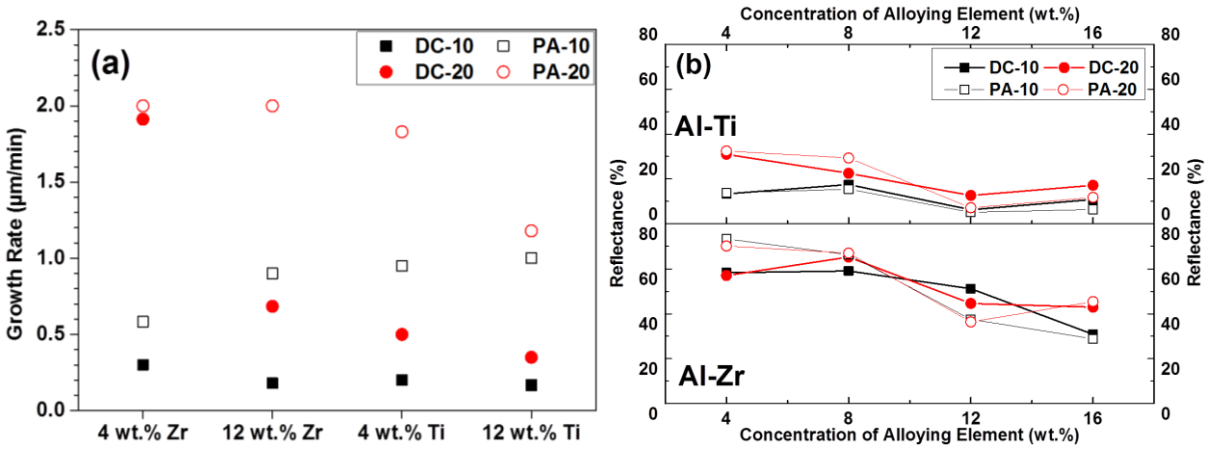

Figure 4.9: (a) Anodic film growth rate and (b) Total reflectance values at 555 nm for the magnetron sputtered and heat treated Al-Zr and Al-Ti surfaces after conventional DC and high frequency pulse anodising in sulphuric acid.

The high reflectance values obtained by high frequency pulse anodising inspired to study the applicability of this technique to sputter deposited and heat treated Al-Zr and Al-Ti coatings in Chapter 14 (Paper 10). The electrochemical behaviour differences and resulting optical appearance were compared to conventional DC anodising. In all the cases, brighter surfaces and faster growth rates were achieved using high frequency pulse anodising compared to conventional DC anodising (Figure 4.9).

The technique of high frequency pulse anodising was thoroughly studied and optimised for Al-TiO_2 composites and white appearing highly reflecting anodised surfaces were generated. The optimisation process and the key process parameters are not reported here due to confidentiality reasons; however the optical appearance of the obtained surfaces after optimising the process is presented and discussed in Chapter 15. The white anodising process developed was further used as a precursor for obtaining unique pastel colours developed by dyeing the white anodised surfaces (see Figure 4.10).

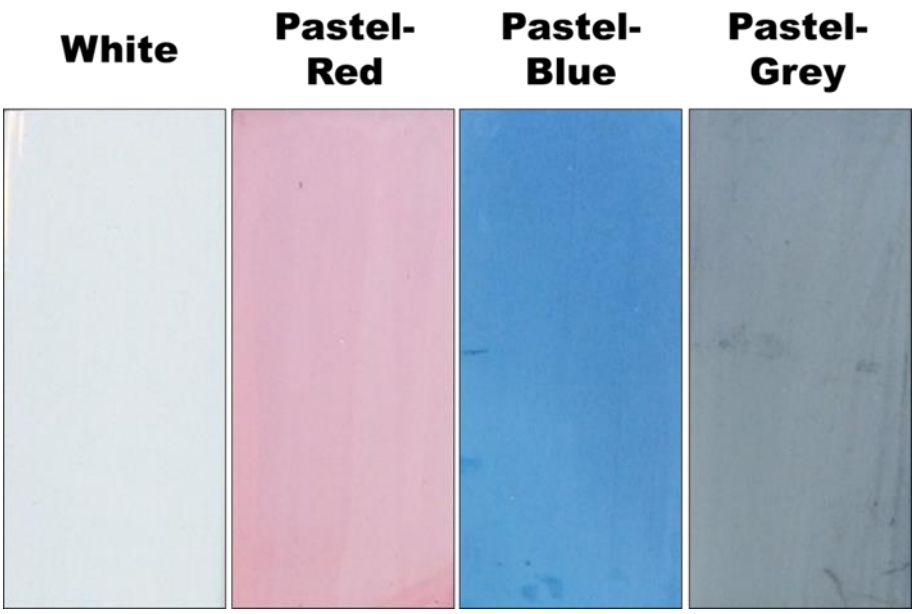

Figure 4.10: Representative optical images of white anodised Aluminium surface and pastel colours obtained after conventional dyeing of the white anodised surfaces.

5. In-Situ TEM Investigations (Paper 1)

In-Situ TEM Investigation of Microstructural Evolution in Magnetron Sputtered Al-Zr and Al-Zr-Si Coatings during Heat Treatment*

Abstract

The magnetron sputtered Al-Zr and Al-Zr-Si coatings were heat treated in-situ in a transmission electron microscope as well as ex-situ to observe the phase transformations. The samples were heated up to a temperature of 550 °C and then cooled to room temperature. A layered structure with alternating layers of Al and Zr/Si rich Al was found for the as deposited sputter coatings. During in-situ heat treatment, the phases formed in the coatings were analysed using selective area electron diffraction and energy dispersive X-ray spectroscopy. For Al-Zr sputtered coatings, metastable $L1_2$-Al_3Zr nucleated initially by splitting of Zr rich Al layers followed by transformation to equilibrium DO_{23}-Al_3Zr. Addition of Si to the Al-Zr sputtered coating resulted in the formation of DO_{22}-$Al_{2.6}Si_{0.4}Zr$ phase instead of the DO_{23}-Al_3Zr phase. The lattice parameters and compositions of different phases formed are measured and presented.

Keywords: In-situ TEM; Heating; Magnetron Sputtering; Al-Zr; XRD.

**Published as V.C. Gudla, K. Rechendorff, Z.I. Balogh, T. Kasama, R. Ambat, In-Situ TEM Investigation of Microstructural Evolution in Magnetron Sputtered Al-Zr and Al-Zr-Si Coatings during Heat Treatment, Mater. Des. 89 (2016) 1071–1078.*

5.1 Introduction

Magnetron sputtered coatings have been used extensively for various applications requiring corrosion and wear resistance, low friction coefficient, decorative appearance, and for achieving other specific functional properties [1]. The method is also used for making coatings of metallic alloys as model systems for various studies due to the possibility of synthesizing non-equilibrium compositions. These include investigations related to the effect of higher levels of alloying elements in aluminium on the electrochemical behaviour such as polarization [2–6], anodising [7–10], mechanical properties [11,12], functional property of mixed oxides such as band gap measurements, optical reflectance etc. [13–17]. The advantage of using magnetron sputtering process to produce model systems is that the composition of the alloying elements can be precisely controlled and varied while maintaining a single phase, which is not possible by other methods. Therefore, a number of non-equilibrium microstructures can be produced by the magnetron sputtering process. Microstructures obtained by the magnetron sputtering can vary from completely amorphous to crystalline. Coating morphology depends on the process temperature with respect to the melting point of the coating material (T/T_m) as well as the energy of the ions bombarding the film during growth [18]. Also, the specific geometry of the targets and the substrates has been reported to result in non-uniform microstructure for the sputter coatings.

The sputtered coatings are often studied as model alloys under as-deposited condition. Gudla et al. [15,16] and Aggerbeck et al. [17] have used Al-Zr and Al-Ti based sputtered coatings for understanding the effect of Zr and Ti on the anodising behaviour of aluminium with and without heat treatment. The anodising behaviour of the coating was found to be strongly dependant on the structure of the magnetron sputtered coatings before and after the heat treatment including the formation of the second phase particles. Zirconium is added to the aluminium alloys as grain pinning agent to control the grain growth and therefore it is used in thermally stable precipitation-strengthened alloys [19]. Zirconium has a very limited equilibrium solid solubility in α-Al and low diffusivity [20]. Ageing behaviour of the super-saturated Al-Zr alloys shows formation of low lattice mismatch cubic Al_3Zr phase initially, which will age to equilibrium tetragonal Al_3Zr after 100 to 1000 hours at temperatures >450 °C [21]. Addition of Si to the Al-Zr system has been shown to promote formation of Al-Zr-Si phases with varying stoichiometry as observed for diffusion couples [22].

In order to understand the microstructural changes in the sputtered coating as a function of temperature, present work focus on in-situ heating of Al-Zr and Al-Zr-Si magnetron sputtered coatings in a transmission electron microscope (TEM). In-situ heating allows observation of the reactions and phase transformations in real time and events such as nucleation or nullification of voids [23]. Magnetron sputtering was used to deposit Al-Zr based coatings with and without Si on an Al substrate for investigation. In-situ focused ion beam scanning electron microscope (FIB-SEM) lift out was performed on the sputtered coating surface to prepare lamellae for TEM. Results from in-situ TEM were compared with the results from ex-situ analysis using X-ray diffraction.

5.2 Experimental

5.2.1 Sputter Deposition

The coatings were deposited by DC magnetron sputtering using an industrial scale CemeCon CC 800/9 machine with four cathodes. The oppositely placed cathodes facing the substrates were mounted on a planetary rotating table in the middle of the chamber to ensure a homogeneous deposition (see Figure 5.1). For Al-Zr deposition, two cathodes of pure aluminium (99.99 % purity) were used, while the other two cathodes were pure Zr (purity 99.9 %). For depositing Al-Zr-Si coating, two cathodes made of pure Al (99.99 % purity), one Zr target (purity 99.9 %), and one Si target (purity 99.999 %) were used. The composition of the coating was aimed at 10-12 wt. % Zr and 2 wt. % Si, and was obtained by adjusting the power on the targets. The deposition chamber was initially evacuated to a base pressure of 1 mPa. During sputtering, constant argon flow of 200 mL/min was used providing a typical Ar pressure of about 180 mPa. The distance between the targets and sample was about 100 mm. No additional heating was used during the deposition and the maximum temperature during deposition was about 270 ˚C. For all depositions, pure Al substrates (Reinal™, Alcan Rolled Products, Germany) with dimensions of 100 mm x 40 mm x 5 mm were used.

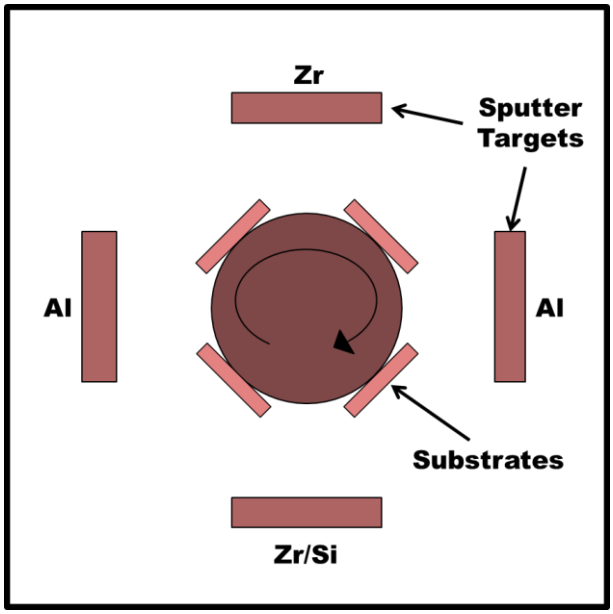

Figure 5.1: Schematic showing the relative positions of the substrates and targets used for sputter deposition of Al-Zr and Al-Zr-Si coatings.

5.2.2 Electron Microscopy

Thin film lamellae from the sputtered coating were prepared using in-situ focused ion beam (FIB) lift-out (Quanta 200 3D™ DualBeam, FEI) and were further thinned for electron transparency in a FIB-SEM (Helios Nanolab™ DualBeam, FEI). TEM analysis was carried out on the lamella using a TEM (Tecnai T20™, FEI) operating at 200 keV. In-situ heating of the lamella was carried out using a tantalum holder with a resistive heating stage. The temperature was measured using a thermocouple that was built into the holder and placed next to the sample. The temperature was controlled using a hot stage controller (Gatan Smartset Model 901).

5.2.3 Grazing Incidence X-Ray Diffraction

Grazing incidence X-ray diffraction (GI-XRD) (Bruker Discover D8™) was performed using Cu Kα radiation at 40 keV and 40 mA for the phase analysis of the deposited and heat-treated coatings. Diffraction patterns were recorded in the 2θ range from 15° to 100° with an incidence angle of 3°, step size of 0.03°, and a scan step time of 8 s.

5.3 Results and Discussion

5.3.1 As-deposited coatings

The bright field TEM images in Figure 5.2 show the structure of the as-deposited magnetron sputtered Al-Zr (Figure 5.2 (a) and (b)) and Al-Zr-Si (Figure 5.2 (c) and (d)) coatings. The cross-section of the coating in Figure 5.2 (a) shows a columnar structure and does not show any porosity or voids. A closer look at the cross section images in Figure 5.2 (b) and (d) shows a fine repeating structure of alternative bright and dark layers in the structure of the coating. The layers are parallel to the sample surface and perpendicular to the growth direction. The layered structure with different contrast is due to the difference in the concentration of Zr in the sputter deposited coating across the thickness. The relative positions of the samples and the sputter targets (see Figure 5.1) during the sputter deposition process results in the evolution of fine layered structure with variation in composition. As the sample stage revolves around its own axis, the sample surfaces are exposed to an alternating flux of Al atom flux, and Zr rich Al atom flux in the sputter chamber. Similar structural features were also observed by Asami et al. [24] while depositing Al-Ta coatings using the magnetron sputtering process.

In Figure 5.2 (d), the layered structure in the Al-Zr-Si sputtered deposited coating is observable and also some particles with approximate size of 200 nm are present. These particles are aggregates of elemental Si that are sputtered from the Si target during the sputter deposition process. As can be observed, the degree of homogeneity for the repetitive layered structure is higher for the Al-Zr coatings, whereas for the Al-Zr-Si sputtered coatings, it is not clearly demarcated. This could be due to the aggregates of Si particles that are sputtered from the targets during deposition, which cause a roughness in the sputtered coating. These local sputtered crystals of Si, cause shadowing effects, as the deposition process is a line of sight process [25,26]. Also, these crystals of Si can act as nucleation sites and accelerated growth of relative to the matrix can take place locally. This increased local growth and shadowing effects, results in the heterogeneity in the Al-Zr-Si coating when compared to the Al-Zr sputter deposited coating where no such sputtered crystals are observed (see Figure 5.2 (a) and (b)) [27,28]. The composition of the sputtered coatings measured using EDS analysis is presented in Table 5.1.

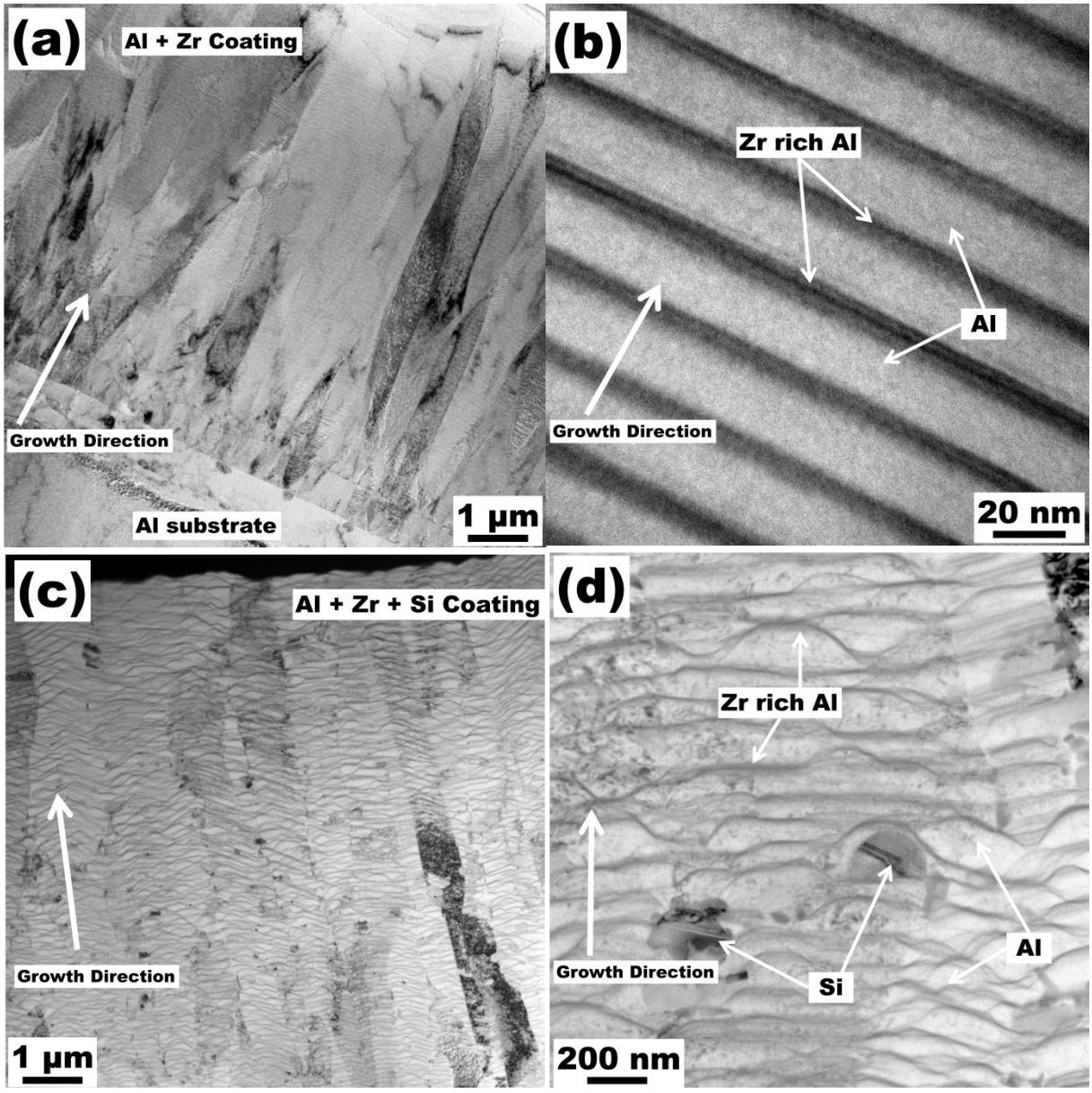

Figure 5.2: Bright field TEM images of: (a) Al-Zr sputter coating in cross-section, (b) showing alternate layers of Al and Zr rich Al and (c) Al-Zr-Si sputter coating in cross-section and (d) showing alternating layers of Al and Zr rich Al, along with Si crystallites.

Table 5.1: Representative EDS compositional analysis of the sputter deposited Al-Zr and Al-Zr-Si coatings in wt. %.

Coating Type	O (wt. %)	Al (wt. %)	Si (wt. %)	Zr (wt. %)
Al-Zr	1.34±0.41	88.0±3.39	-	10.66±3.15
Al-Zr-Si	1.08±0.46	84.70±1.69	1.93±0.7	12.30±1.29

5.3.2 In-situ heating

Figure 5.3 shows the typical images from the in-situ observation under TEM showing the evolution of the microstructure as a function of temperature. The cross-section images show the alternate layers of Al and Zr rich Al, which changes in morphology during heating. The sample was heated gradually from room temperature (Figure 5.3 (a)) to nearly 550 °C. There was no significant changes to the structure until the temperature reaches up to 400 °C (Figure 5.3 (b) and (c)). Some contrast differences observed in the images is due to the diffraction contrast in the TEM. Further increase in temperature has caused significant change in the microstructure across the cross-section.

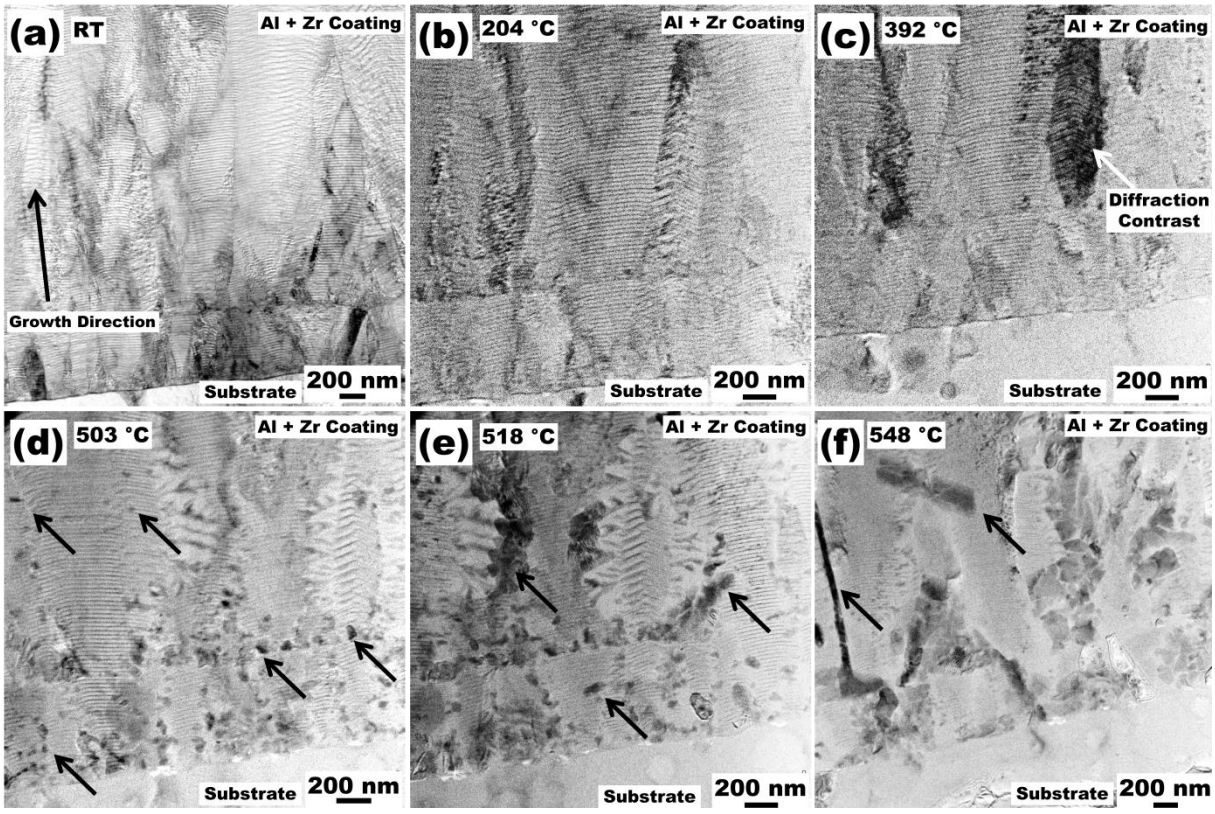

Figure 5.3: Bright field TEM image of Al-Zr sputter coating at: (a) RT, (b) 204 °C, (c) 392 °C, (d) 503 °C, (e) 518 °C and (f) 548 °C. Image contrast variation seen in figure (a) to (c) is a result from a small change in diffraction condition.

Upon heating above 450 °C, precipitates of size approx. 30-40 nm are found to form (marked with arrows in Figure 5.3 (d)) primarily at the columnar grain boundaries of the sputtered coating. Some of the precipitates grow larger in size with increase in temperature (Figure 5.3 (e)). The alternating bright and dark contrast lines of Al and Zr rich Al are reduced with gradual increase of temperature and disappear eventually (Figure 5.3 (d) to (f)). The number density of the precipitates at 548 °C (Figure 5.3 (f)) is lower than the initial density observed at 502 °C (Figure 5.3 (d)). The resulting structure after holding the sample at 550 °C for the

extended period of time (approx. 3 h) is shown in Figure 5.4 (a). The large precipitates exhibited a needle or parallelepiped morphology with a high aspect ratio. The parallelepiped nature of the precipitates can be seen clearly in Figure 5.4 (b) where the facets of one such precipitate are clearly visible. Finer precipitates are also observed of the size of 20-30 nm that are distributed within the coating matrix.

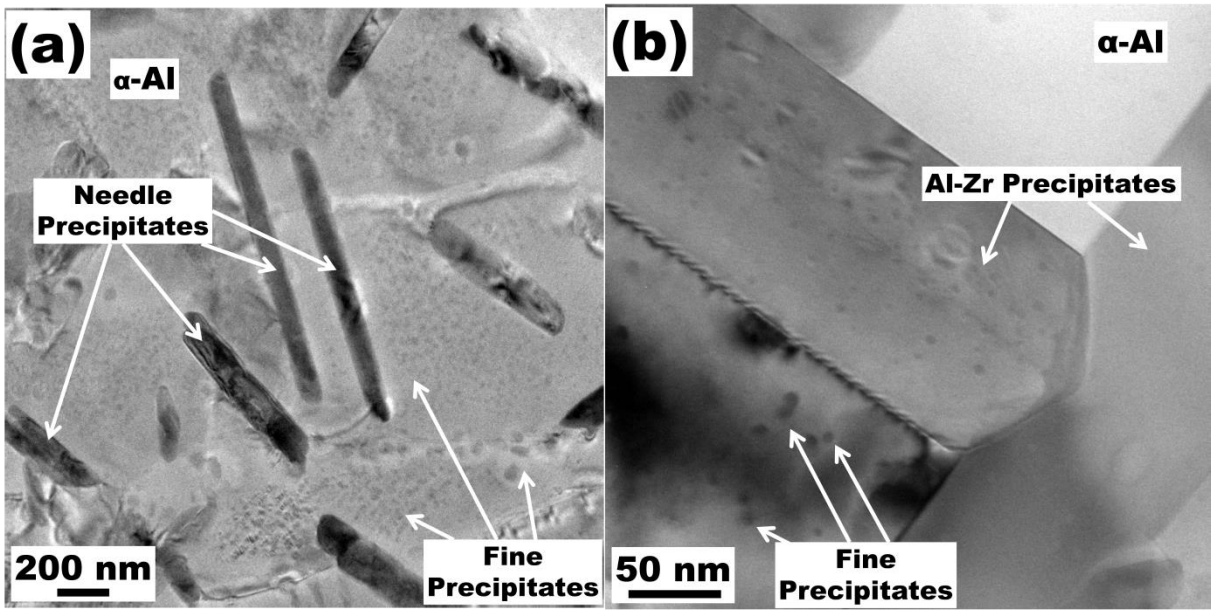

Figure 5.4: TEM bright field image of the Al-Zr coating at RT after in-situ heat treatment at 500 °C for 3 h showing: (a) the needle like precipitates and fine precipitates formed in the coating matrix, and (b) precipitates at high magnification.

Figure 5.5 shows the structure of the coating when held at 550 °C for 1 h. The growth of a needle like precipitate in the coating matrix containing finer precipitates can be observed as a time lapse series. It can be seen that the alternating continuous layers of Al and Zr rich Al have now transformed into fine precipitates dispersed in a matrix and distribution of fine precipitates follow the Zr rich regions of the initial sputtered coating. The needle like Al-Zr precipitate grows with the parallelepiped morphology and shows a pyramidal end. The growth of this needle like precipitate takes place across the alternating layers of fine precipitates and the fine precipitates are consumed for the growth of needle-like precipitate. The presence of fine particles within the needle like particle is due to the thickness of the sample, which allows the fine particles to be present above or below the needle like precipitate.

The Al-Zr-Si sputtered coating showed similar behaviour upon heating up to 550 °C in the TEM. However, the morphology of the precipitates formed was nodular or spherical, which is different from the needle-like structure found for the Al-Zr coating. The formation of the precipitates in the Al-Zr-Si coating is shown as a function of temperature in Figure 5.6. At RT there is no observable evidence of any precipitation (Figure 5.6 (a)). Upon gradually increasing the temperature to 450 °C, nucleation of nodular phases at the columnar grain boundaries (Figure 5.6 (b)) takes place followed by growth in size with temperature (Figure 5.6 (c)). The size of the precipitates in the coating after holding at 550 °C for 3 h is approx. 250 nm.

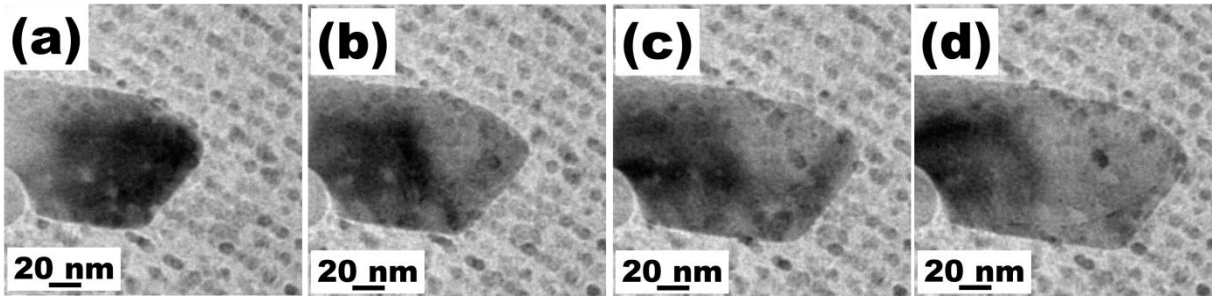

Figure 5.5: A time-lapse series of TEM bright field images showing growth of needle type Al-Zr precipitate in the sputter coating matrix containing fine precipitates after 1 h at 550 °C. Time interval is approx. 30 s between each captured image.

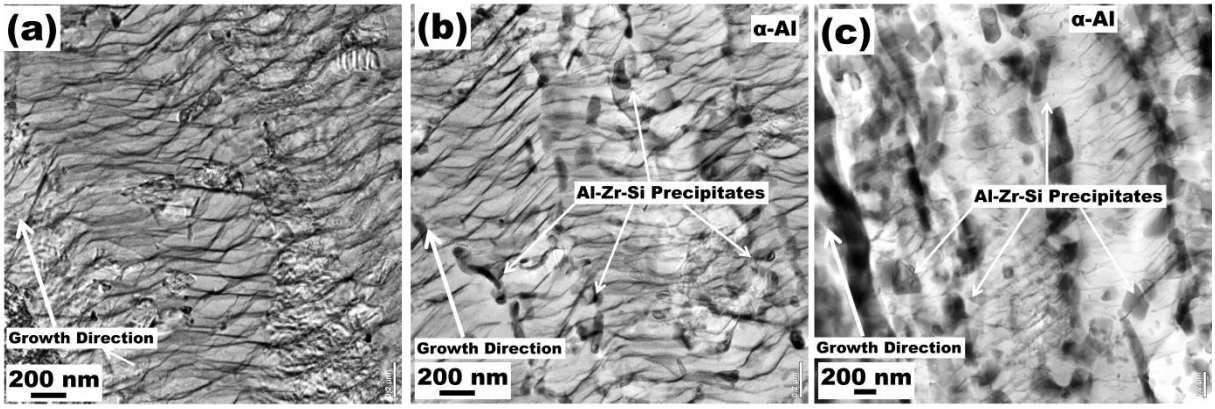

Figure 5.6: Bright field TEM image of Al-Zr-Si sputter coating at: (a) RT, (b) 450 °C, and (c) 545 °C showing precipitates with nodular morphology.

5.3.3 Phase Identification

The selected area electron diffraction (SAED) and EDS analysis were performed on various features observed in the Al-Zr and Al-Zr-Si sputtered coatings during in-situ heat treatment. The needle-like precipitates formed in the Al-Zr coatings showed a tetragonal structure (SG: I4/mmm) corresponding to the equilibrium DO_{23}-Al_3Zr phase (a = 4.005 Å, c = 17.285 Å [29,30]) (see Figure 5.7). The elongation axis corresponds to its <110> direction. The needle like precipitates do not contain significant defects such as stacking faults. Presence of Si in the sputtered coating, resulted in the formation of a different phase, which was indexed to $(Al_2Si)Zr$ with tetragonal structure (SG: I4/mmm, a = 3.899 Å, c = 9.008 Å [31]) (see Figure 5.8). This phase is closely related to the DO_{22}-Al_3Zr (c ~ 2a). The GI-XRD results (see Figure 5.9) of the Al-Zr-Si sputtered coating after ex-situ heat treatment show that the structure contains a phase based on Al-Zr-Si indexed to the τ_1 ($Al_{0.45}Si_{0.21}Zr_{0.34}$, [31]) phase (JCPDS File no.: 14-0625) in an Al matrix. This is in agreement with the results observed from the electron diffraction. Apart from the DO_{23}-Al_3Zr in Al-Zr coating after heat treatment, another phase corresponding to a different structure was observed. This phase was indexed to the JCPDS File no. 26-0041[32] which corresponds to metastable $L1_2$-Al_3Zr phase with a cubic structure (SG: Pm3m, a = 4.093 Å [33]).

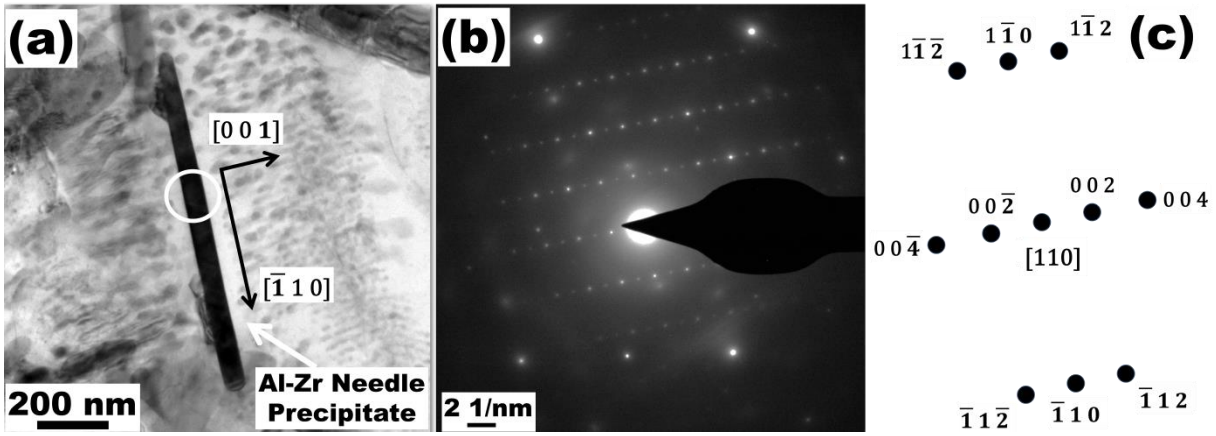

Figure 5.7: Bright field TEM image of Al-Zr sputtered coating after heating to 550 °C showing: (a) needle like Al-Zr precipitate and (b) SAED pattern from the needle like precipitate, and (c) simulated SAED pattern of DO_{23}-Al_3Zr [110]. Absence of fine precipitates around the needle like precipitate is evidence that Zr diffuses to form the needle like precipitate.

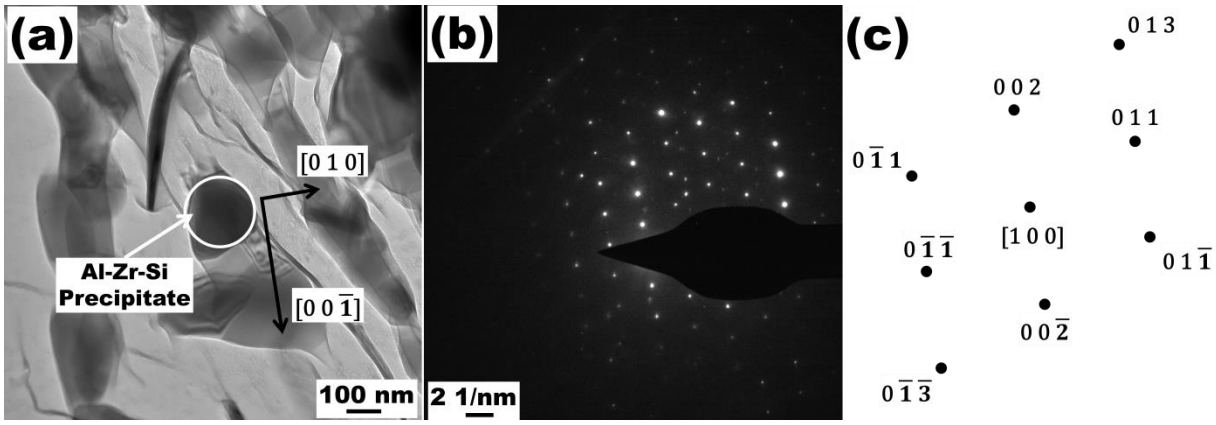

Figure 5.8: Bright field TEM image of Al-Zr-Si sputtered coating after in-situ heating to 550 °C showing: (a) nodular Al-Zr-Si precipitate and (b) SAED pattern from the nodular precipitate, and (c) simulated SAED pattern of $Al_{0.45}Si_{0.21}Zr_{0.34}$ [1 0 0].

Srinivasan et al. [34] studied the evolution of Al-Zr phases in rapid solidified Al-Zr alloys and observed that the $L1_2$-Al_3Zr phases precipitates out from the quenched structure initially at 400 °C, but for the Al-Zr sputtered coatings in as-deposited condition similar phase was not observed (Figure 5.9). However, presence of Si in the Al-Zr sputtered coatings showed the presence of the cubic $L1_2$-Al_3Zr phase in as-deposited coating (as shown in Figure 5.9). The measured temperature of the specimen surface during sputter deposition of Al-Zr-Si coatings reached maximum 270 °C. This suggests that the addition of Si reduces the precipitation temperature for the $L1_2$-Al_3Zr phase to at least 270 °C. The broadness of the peaks for this phase observed in the GI-XRD pattern is from their very fine size as also seen in the TEM images. The Si particles observed in the Al-Zr-Si (see Figure 5.2 (c) and (d)) were also observed in the GI-XRD spectra of the as-received sputtered coating.

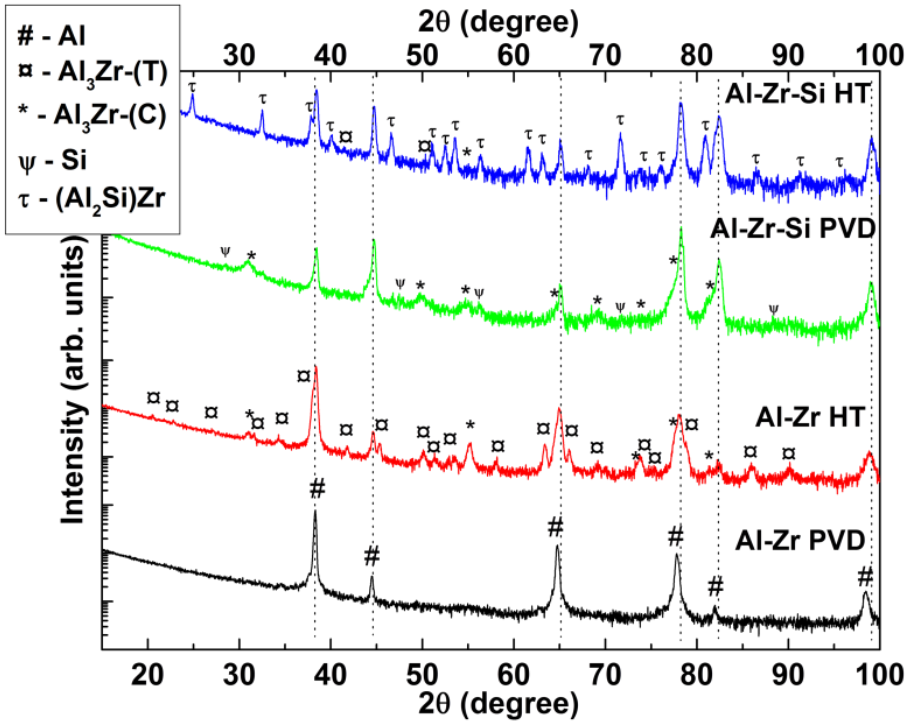

Figure 5.9: Grazing Incidence XRD patterns recorded from the sputter coated Al-Zr and Al-Zr-Si coatings in as-deposited condition (Al-Zr PVD and Al-Zr-Si PVD) and after ex-situ heat treatment at 550 °C for 4 h (Al-Zr HT and Al-Zr-Si HT). Al_3Zr-(T) is Tetragonal and Al_3Zr-(C) is Cubic.

Table 5.2: Representative TEM-EDS elemental analysis (in wt. %) and the lattice parameters (in Å) calculated from the GI-XRD patterns of the various phases observed in Al-Zr and Al-Zr-Si sputtered coating after in-situ heat treatment.

	Morphology	Al (wt.%)	Zr (wt.%)	Si (wt.%)	Others (Cu, Ti, Ga, Fe)	Lattice parameter (Å)
DO_{23}-Al_3Zr	Needle	39.86 ± 0.27	53.14 ± 0.3	-	Rest	*a* = 3.999, *c* = 17.281
Al matrix	-	84.36 ± 0.52	8.38 ± 0.47	-	Rest	*a* = 4.058
$L1_2$-Al_3Zr	Fine spheroids	57.96 ± 0.47	32.26 ±0.51	-	Rest	*a* = 4.109
DO_{22}-$(Al_2Si)Zr$ (τ_1)	Coarse spheroids	42.01 ± 0.13	50.83 ± 0.21	7.14 ± 0.06	Rest	*a* = 3.892, *c* = 8.992

The composition of the different phases as measured by EDS and their lattice parameters measured from the GI-XRD data is given in
Table 5.2. The needle-like precipitates show relative composition of Al and Zr, which suggest at Al_3Zr phase. However, the relative composition of Al, Si, and Zr in the nodular precipitates suggests a higher ratio of Al to Si hinting at $Al_{2.6}Si_{0.4}Zr$ [35] instead of $(Al_2Si)Zr$ as mentioned in the crystallographic data files [31]. The fine precipitates of $L1_2$-Al_3Zr in Al-Zr sputtered coating showed a relatively lesser amount of Zr when compared to Al. However this might be attributed to the Al matrix surrounding the fine precipitates in the relatively thick sample of approx. 100 nm, while the fine precipitates are only approx. 30-40 nm. Another explanation for the deviation from the stoichiometric ratio is that the metastable $L1_2$ phase is not completely ordered [36].

The sequential bright field TEM images in Figure 5.5 show that initially the Al-Zr sputtered coating forms a dual microstructure of α-Al and $L1_2$-Al_3Zr by splitting the Zr rich layers. Further increase in temperature (> 450 °C) causes the growth of DO_{23}-Al_3Zr, which increases in size at the cost of the $L1_2$-Al_3Zr phase. The $L1_2$-Al_3Zr phase is the primary metastable phase at room temperature for the Al-Zr system and the high temperature phase is the equilibrium DO_{23}-Al_3Zr phase. As the lattice mismatch is lower between $L1_2$ and FCC-Al, the $L1_2$ phase precipitates easily [20]. The transition temperature (using differential scanning calorimetry) from $L1_2$ to DO_{23} was observed at approx. 570 °C for the mechanically alloyed powders [37]. However, Al-Zr sputtered coatings subjected to ex-situ heat treatment at 550 °C showed the formation of DO_{23}-Al_3Zr and also presence of the $L1_2$-Al_3Zr, which are in accordance with the findings of Srinivasan et al [38]. The proposed mechanism for microstructural coarsening of Al-Zr system was set in four stages. Stage 1 showed formation of very fine, < 5 nm spheroidal $L1_2$-Al_3Zr precipitates, which coarsen in stage 2, further coarsening to ellipsoidal $L1_2$-Al_3Zr (stage 3), and finally transform to equilibrium DO_{23}-Al_3Zr discs in stage 4 [21]. The isochronal aging of conventionally solidified Al-Zr alloys did not show the presence of DO_{23}-Al_3Zr phase at 450 °C and even after heating at 575 °C the $L1_2$-Al_3Zr phase still existed untransformed. The onset of transformation to DO_{23}-Al_3Zr was observed to be approx. 500 °C. Similar evolution of structures is observed for magnetron sputtered coatings, where initially $L1_2$-Al_3Zr spheroids of approx. 20 nm form and coarsen to form DO_{23}-Al_3Zr needles. The onset of transformation from $L1_2$-Al_3Zr to equilibrium DO_{23}-Al_3Zr was observed at approx. 445 °C and the DO_{23}-Al_3Zr phase coarsened to approx. 200 – 500 nm in length within 2 – 3 hour of ageing at 550 °C.

Table 5.3 Various phases and related temperature range observed for Al-Zr and Al-Zr-Si sputtered coatings in as-deposited condition and during heating.

Sputtered Coating System	As-Deposited	Heating	
	RT	400 - 450 °C	500 - 550 °C
Al-Zr	Al + (Zr)	α-Al + $L1_2$-Al_3Zr	α-Al + $L1_2$-Al_3Zr + DO_{23}-Al_3Zr
Al-Zr-Si	Al + $L1_2$-Al_3Zr + Si	α-Al + $L1_2$-Al_3Zr	α-Al + $L1_2$-Al3Zr + DO_{22}-$Al_{2.6}Si_{0.4}Zr$

The presence of Si in Al-Zr sputter coating enhances the precipitation of cubic $L1_2$-Al_3Zr phase and also lowers the precipitation temperature. Spherical or nodular precipitates of DO_{22} structure are formed instead of needle like precipitates of DO_{23} in the Al-Zr coatings upon addition of Si. The size of the DO_{22} nodular precipitates is found to be max. 200-300 nm, while that for DO_{23} precipitates is approx. 1 µm upon holding at 550 °C for 3 h. Similar behaviour was observed by Sato et al. [39] during ex-situ heat treatment of Al-Zr alloys with and without Si/Ti additions prepared by chill casting. It can be reasonably stated that the addition of Si prevents the over-ageing and growth of the Al-Zr precipitates during heat treatment at 550 °C. The observed phases and their related temperature ranges in the sputter coating system are summarized in Table 5.3.

5.4 Conclusions

- Magnetron sputter coated model alloy systems combined with in-situ TEM studies have been successfully applied for studying recrystallization and precipitation of binary and ternary systems.
- Magnetron sputtering of Al-Zr binary coatings resulted in alternating layers of Al and Zr rich Al due to the geometry arrangement and rotation of the samples and targets during the deposition.
- In-situ heating in TEM showed splitting of the Zr rich layers initially to form precipitates of cubic $L1_2$-Al_3Zr type (fine precipitates) and later equilibrium tetragonal DO_{23}-Al_3Zr type (needle like morphology).

- Addition of Si to the Al-Zr coating resulted in the precipitation of tetragonal DO_{22}-Al-Zr-Si (τ_1) precipitates with measured composition close to $Al_{2.6}Si_{0.4}Zr$ upon heating.
- Presence of Si enhances the formation of cubic $L1_2$ phase at temperatures as low as 270 °C during sputter deposition.
- Formation of the DO_{23}-Al_3Zr and DO_{22}-$Al_{2.6}Si_{0.4}Zr$ precipitates takes place by nucleation mostly at the columnar grain boundaries and growth by consumption of the $L1_2$-Al_3Zr phase.

References

[1] P.J. Kelly, R.D. Arnell, Magnetron sputtering: A review of recent developments and applications, Vacuum. 56 (2000) 159–172. doi:10.1016/S0042-207X(99)00189-X.

[2] J.R. Scully, D.E. Peebles, A.D. Romig, D.R. Frear, C.R. Hills, Metallurgical factors influencing the corrosion of aluminum, Al-Cu, and Al-Si alloy thin films in dilute hydrofluoric solution, Metall. Trans. A. 23 (1992) 2641–2655. doi:10.1007/BF02658068.

[3] H. Yoshioka, Q. Yan, H. Habazaki, A. Kawashima, K. Asami, K. Hashimoto, Passivity and its breakdown on sputter-deposited amorphous Al-early transition metal alloys in 1 M HCl at 30°C, Corros. Sci. 31 (1990) 349–354. doi:10.1016/0010-938X(90)90130-W.

[4] Y. Liu, M.A. Arenas, P. Skeldon, G.E. Thompson, P. Bailey, T.C.Q. Noakes, et al., Anodic behaviour of a model second phase: Al-20at.%Mg-20at.%Cu, Corros. Sci. 48 (2006) 1225–1248. doi:10.1016/j.corsci.2005.05.007.

[5] E. Akiyama, H. Yoshioka, J.H. Kim, H. Habazaki, A. Kawashima, K. Asami, et al., The effect of magnesium on the corrosion behavior of sputter-deposited amorphous Al-Mg-Ti ternary alloys in a neutral chloride solution, Corros. Sci. 34 (1993) 27–40. doi:10.1016/0010-938X(93)90256-G.

[6] D. Kek Merl, P. Panjan, J. Kovač, Corrosion and surface study of sputtered Al-W coatings with a range of tungsten contents, Corros. Sci. 69 (2013) 359–368. doi:10.1016/j.corsci.2013.01.002.

[7] X. Zhou, H. Habazaki, K. Shimizu, P. Skeldon, G.E. Thompson, G.C. Wood, Enrichment-dependent anodic oxidation of zinc in Al-Zn alloys, Corros. Sci. 38 (1996) 1563–1577. doi:10.1016/0010-938X(96)00051-0.

[8] H. Habazaki, K. Shimizu, P. Skeldon, G.E. Thompson, G.C. Wood, Formation of amorphous anodic oxide films of controlled composition on aluminium alloys, Thin Solid Films. 300 (1997) 131–137. doi:http://dx.doi.org/10.1016/S0040-6090(96)09491-6.

[9] H. Habazaki, K. Shimizu, P. Skeldon, G.E. Thompson, G.C. Wood, X. Zhou, Nanoscale enrichments of substrate elements in the growth of thin oxide films, Corros. Sci. 39 (1997) 731–737. doi:10.1016/S0010-938X(97)89339-0.

[10] H. Habazaki, P. Skeldon, K. Shimizu, Anodic film formation on a sputter-deposited Al-30at% Mo alloy, Corros. Sci. 31 (1995) 1497–1509. http://www.sciencedirect.com/science/article/pii/0010938X9500061N (accessed May 22, 2014).

[11] L. Cunha, M. Andritschky, Residual stress, surface defects and corrosion resistance of CrN hard coatings, Surf. Coatings Technol. 111 (1999) 158–162. doi:10.1016/S0257-8972(98)00731-2.

[12] J. Kovac, H.R. Stock, B. Köhler, H. Bomas, H.W. Zoch, Tensile properties of magnetron sputtered aluminum-scandium and aluminum-zirconium thin films: A comparative study, Surf. Coatings Technol. 215 (2013) 369–375. doi:10.1016/j.surfcoat.2012.05.147.

[13] S. Canulescu, K. Rechendorff, C.N. Borca, N.C. Jones, K. Bordo, J. Schou, et al., Band gap structure modification of amorphous anodic Al oxide film by Ti-alloying, Appl. Phys. Lett. 104 (2014) 121910. doi:10.1063/1.4866901.

[14] S. Van Gils, T. Dimogerontakis, G. Buytaert, E. Stijns, H. Terryn, P. Skeldon, et al., Optical properties of magnetron-sputtered and rolled aluminum, J. Appl. Phys. 98 (2005). doi:10.1063/1.2085315.

[15] V.C. Gudla, S. Canulescu, R. Shabadi, K. Rechendorff, J. Schou, R. Ambat, Anodization and Optical Appearance of Sputter Deposited Al-Zr Coatings, in: J. Grandfield, TMS (Eds.), Light Met. 2014, John Wiley & Sons, Inc., 2014: pp. 369–373. doi:10.1002/9781118888438.ch63.

[16] V.C. Gudla, S. Canulescu, R. Shabadi, K. Rechendorff, K. Dirscherl, R. Ambat, Structure of anodized Al-Zr sputter deposited coatings and effect on optical appearance, Appl. Surf. Sci. 317 (2014) 1113–1124. doi:http://dx.doi.org/10.1016/j.apsusc.2014.09.037.

[17] M. Aggerbeck, A. Junker-Holst, D.V. Nielsen, V.C. Gudla, R. Ambat, Anodisation of sputter deposited

aluminium-titanium coatings: Effect of microstructure on optical characteristics, Surf. Coatings Technol. 254 (2014) 138–144. doi:10.1016/j.surfcoat.2014.05.073.
[18] J.A. Thornton, Influence of apparatus geometry and deposition conditions on the structure and topography of thick sputtered coatings, J. Vac. Sci. Technol. 11 (1974) 666. doi:10.1116/1.1312732.
[19] K.E. Knipling, D.C. Dunand, D.N. Seidman, Criteria for developing castable, creep-resistant aluminum-based alloys – A review, Zeitschrift Für Met. 97 (2006) 246–265. doi:10.3139/146.101249.
[20] K.E. Knipling, D.C. Dunand, D.N. Seidman, Nucleation and Precipitation Strengthening in Dilute Al-Ti and Al-Zr Alloys, Metall. Mater. Trans. A. 38 (2007) 2552–2563. doi:10.1007/s11661-007-9283-6.
[21] K.E. Knipling, D.C. Dunand, D.N. Seidman, Precipitation evolution in Al–Zr and Al–Zr–Ti alloys during aging at 450–600 °C, Acta Mater. 56 (2008) 1182–1195. doi:http://dx.doi.org/10.1016/j.actamat.2007.11.011.
[22] J.K. Jain, S.P. Gupta, Intermetallic compound formation in the Zr-Al-Si ternary system, Mater. Charact. 49 (2002) 139–148. doi:10.1016/S1044-5803(02)00343-1.
[23] Z.L. Wang, Transmission Electron Microscopy of Shape-Controlled Nanocrystals and Their Assemblies, J. Phys. Chem. B. 104 (2000) 1153–1175. doi:10.1021/jp993593c.
[24] K. Asami, H. Yoshioka, K. Hashimoto, K. Shimizu, K. Kobayashi, Superlattice-like structure of sputter-deposited amorphous aluminum-heavy element alloys, J. Non. Cryst. Solids. 110 (1989) 258–264. doi:10.1016/0022-3093(89)90266-4.
[25] P. Panjan, M. Čekada, M. Panjan, D. Kek-Merl, F. Zupanič, L. Čurković, et al., Surface density of growth defects in different PVD hard coatings prepared by sputtering, Vacuum. 86 (2012) 794–798. doi:10.1016/j.vacuum.2011.07.013.
[26] M. Čekada, P. Panjan, D. Kek-Merl, M. Panjan, G. Kapun, SEM study of defects in PVD hard coatings, Vacuum. 82 (2007) 252–256. doi:http://dx.doi.org/10.1016/j.vacuum.2007.07.005.
[27] P. Panjan, M. Čekada, M. Panjan, D. Kek-Merl, Growth defects in PVD hard coatings, Vacuum. 84 (2009) 209–214. doi:http://dx.doi.org/10.1016/j.vacuum.2009.05.018.
[28] P. Panjan, P. Gselman, D. Kek-Merl, M. Čekada, M. Panjan, G. Dražić, et al., Growth defect density in PVD hard coatings prepared by different deposition techniques, Surf. Coatings Technol. 237 (2013) 349–356. doi:http://dx.doi.org/10.1016/j.surfcoat.2013.09.020.
[29] G. Brauer, Über die Kristallstruktur von TiAl3, NbAl3, TaAl3, und ZrAL3, Zeitschrift Für Anorg. Und Allg. Chemie. 242 (1939) 1–22. doi:10.1002/zaac.19392420101.
[30] N.J. Clark, E. Wu, Hydrogen absorption in the Zr-Al system, J. Less Common Met. 163 (1990) 227–243. doi:http://dx.doi.org/10.1016/0022-5088(90)90589-C.
[31] O. Schob, H. Nowotny, F. Benesovsky, Strukturbestimmung an einigen Phasen in den Systemen: Zr-Al-Si und Hf-Al-Si{ZrAl3(Si); ZrSi(Al), Hf(Si, Al); Zr3Si2; Hf3Si2}, Monatshefte fur Chemie. 92 (1961) 1218–1226. doi:10.1007/BF00914988.
[32] T. Ohashi, R. Ichikawa, A new metastable phase in rapidly solidified Al-Zr alloys, Metall. Trans. a (Physical Metall. Mater. Sci. 3 (1972) 2300–2302. doi:10.1007/BF02643251.
[33] P.B. Desch, R.B. Schwarz, P. Nash, Formation of metastable L 12 phases in Al3Zr and Al-12.5%X-25%Zr (X≡Li,Cr,Fe,Ni,Cu), J. Less-Common Met. 168 (1991) 69–80. doi:10.1016/0022-5088(91)90035-3.
[34] D. Srinivasan, K. Chattopadhyay, Metastable phase evolution and hardness of nanocrystalline Al-Si-Zr alloys, Mater. Sci. Eng. A. 304-306 (2001) 534–539. doi:10.1016/S0921-5093(00)01510-0.
[35] A. Raman, K. Schubert, Uber den aufbau einiger zu TiAl3 verwandter legierungsreihen .2. Untersuchungen in einigen T-Al-Si und T4...6-in-systemen, Zeitschrift Fur Met. 56 (1965) 44–52.
[36] K.S. Vecchio, D.B. Williams, Convergent beam electron diffraction study of Al3Zr in Al-Zr AND Al-Li-Zr alloys, Acta Metall. 35 (1987) 2959–2970. doi:http://dx.doi.org/10.1016/0001-6160(87)90295-1.
[37] S. Srinivasan, P.B. Desch, R.B. Schwarz, Metastable phases in the Al3X (X = Ti, Zr, and Hf) intermetallic system, Scr. Metall. Mater. 25 (1991) 2513–2516. doi:http://dx.doi.org/10.1016/0956-716X(91)90059-A.
[38] D. Srinivasan, K. Chattopadhyay, Non-equilibrium transformations involving L12-Al3Zr in ternary Al-X-Zr alloys, Metall. Mater. Trans. A. 36 (2005) 311–320. doi:10.1007/s11661-005-0304-z.
[39] T. Sato, A. Kamio, G.W. Lorimer, Effects of Si and Ti additions on the nucleation and phase stability of the L12-type Al3Zr phase in Al-Zr alloys, Mater. Sci. Forum, Mater Sci Forum. 217-222 (1996) 895–900.

6. Anodising of Al-Zr Coatings: Effect of Heat Treatment (Paper 2)

Structure of Anodised Al-Zr Sputter Deposited Coatings and Effect on Optical Appearance*

Abstract

The mechanism of interaction of light with the microstructure of anodised layer giving specific optical appearance is investigated using Al-Zr sputter deposited coating as a model system on an AA6060 substrate. Differences in the oxidative nature of various microstructural components result in the evolution of typical features in the anodised layer, which are investigated as a function of microstructure and correlated with its optical appearance. The Zr concentration in the coating was varied from 6 wt.% to 23 wt.%. Heat treatment of the coated samples was carried out at 550 ˚C for 4 h in order to evolve Al-Zr based second phase precipitates in the microstructure. Anodising was performed using 20 wt.% sulphuric acid at 18 ˚C with an intention to study the effect of anodising on the Al-Zr based precipitates in the coating. Detailed microstructural characterization of the coating and anodised layer was carried out using high resolution scanning and transmission electron microscopy, grazing incidence X-ray diffraction analysis, glow discharge optical emission spectroscopy, and optical appearance using spectrophotometry. The evolution of microstructure in the anodised layer as a function of anodising parameters and their influence on the interaction of light is investigated and the results in general are applicable to discolouration of anodised layer on recycled aluminium alloys due to intermetallics.

Keywords: Magnetron sputtering; aluminium; microstructure; anodising; optical appearance; TEM.

Published as **V.C. Gudla, S. Canulescu, R. Shabadi, K. Rechendorff, K. Dirscherl, R. Ambat, Structure of anodised Al-Zr sputter deposited coatings and effect on optical appearance, Appl. Surf. Sci. 317 (2014) 1113–1124.*

6.1 Introduction

The optical transparency and therefore the appearance of the anodised layer on aluminium alloy surfaces depends on the micro- and nano-scale morphology of the anodised layer which is evolved on the basis of the substrate microstructure consisting of different phases with varying oxidative nature. This is usually the case for recycled aluminium alloys for which the presence of higher levels of intermetallics in the microstructure due to impurity elements results in discolouration of the anodised layer [1–5]. The effect is due to the presence of partially or fully oxidized intermetallics in the anodised layer based on their chemical composition and reactivity, the resulting nano-scale morphology, and its interaction with the visible light spectrum [6–8].

Decorative anodising of aluminium is usually carried out to obtain an oxide film of thickness 10-15 µm with pleasing appearance for which transparency of the film is most important to achieve bright or matte finish [9,10]. Anodising of pure aluminium results in a porous anodic aluminium oxide structure with a band gap of ~7.3 eV [11]. The large band gap of anodic aluminium oxide is responsible for the clear and transparent nature of the anodised layer through which the underlying substrate surface is visible [12,13]. The surface appearance of anodised aluminium is therefore largely controlled by the substrate-oxide interface morphology resulting in diffuse or specular reflection of light [14–17]. On the other hand, morphology of the interface is largely controlled by the prior surface treatments like polishing, degreasing and etching, which are influenced by the surface impurities and second phase precipitates [18–21]. For example, a highly polished surface gives rise to a glossy appearance to the anodised layer, while anodising of sand blasted or chemically etched surfaces will result in a matte appearance [12].

Although, anodising of high purity Al results in a transparent oxide layer, this seldom is the situation for Al alloys. The heterogeneous microstructure of commercial Al alloys, especially recycled alloys [22,23], gives rise to differences in anodising behaviour [24–26], and results in incorporation of partially anodised second phase precipitates or intermetallics into the anodised layer [27]. Presence of fully or partially oxidized phases in the anodised layer modifies the transparency of the anodic film depending on the optical properties (refractive index) of the local oxide structure and un-oxidized metallic regions [28,29]. This results in modified absorption or scattering of light [14,15].

Anodising behaviour of various second phases based on Mg, Fe, Cu, and Si in Al alloys has been studied earlier by Miera et al. [30]. It was observed that Mg based second phases are oxidized readily when compared to those containing Fe as they lacked a protective and stable oxide film. For second phases containing elements that support a stable oxide, like Cu, it was seen that the increase in Cu content enhances the rate of oxidation of the second phase. Fratila-Apachitei et al. [31] studied the effect of Fe, Si, and Cu based second phases during anodising of cast Al substrates, where occlusion of Al-Fe and Al-Fe-Si second phases into the anodised layer and modification of surrounding pore structure was observed. Other studies about darkening and discolouration of anodised appearance in wrought Al alloys were also focused on incorporated second phases in the anodised layer and localized modification of anodic layer morphology [32–35].

In general, the degree of oxidation of various intermetallic or second phase particles present in aluminium alloys during anodising depends on the constituting elements and their electrochemical nature. Phases consisting of Si, Fe, and Ti in general are incorporated in an unchanged or partially oxidized form (like primary Si, $Al_6(Mn,Fe)$, Al_3Ti), while second phase precipitates with Mg, Cr, and Cu etc. (like Mg_2Al_3, Mg_2Si, Al_7Cr, Al_2Cu) are found to dissolve completely [36]. The presence of the former set of phases results in an anodised layer with embedded particles fully in the metallic state or with an oxide crust covering the metallic core, while the latter set leaves a void in the anodised layer due to active dissolution of the precipitate. Light interaction with the anodised layer is modified in both cases depending on the refractive index of the local structure and absorption by the remaining metallic fraction.

In summary, three kinds of effects related to the second phase particles in Al alloys can modify the interaction of the anodised layer with light: (i) direct incorporation into the anodised layer with different degree of oxidation, (ii) varying behaviour during the pre-treatment process (etching) and (iii) locally changing the morphology of the anodic layer (pore density, voids). However, the exact underlying physical phenomenon

relating the darkening and discolouration of an anodised surface to the incorporated second phase precipitates in anodic layer is not clearly understood in terms of interaction with light.

In order to understand this physical phenomenon, sputter coatings based on binary and ternary Al based model alloys are used as they enable us to investigate the electrochemical and anodising behaviour as a function of microstructural and compositional change. Many authors have used sputter coating techniques to deposit Al based alloy systems which were then anodised in order to understand their corrosion [37–40] and anodising behaviour [41–46]. These sputter coating techniques provide flexibility to obtain surfaces with a wide range of compositions which cannot be obtained by conventional melting and casting. Furthermore, the methods are applicable on any type of substrate [47]. The anodising behaviour of different alloy systems like Al-Cu [48–50], Al-Mg [51], Al-Mn [52] and Al-Zn [53] produced by sputter coating have been investigated earlier in terms of morphology of the anodised layer, enrichment and migration of alloy species, adhesion and delamination of anodic films. Investigations based on optical properties have been performed for pure sputter coated Al [54], however, the optical appearance for Al based alloy sputtered coatings after heat treatment and anodising has not yet been studied in detail.

This paper is focused on model magnetron sputtered Al-Zr binary system coating for understanding the correlation between micro- and nano-structure of the substrate, the resulting nano-scale morphology and optical properties of the anodised layer. The substrate used for the coating was an AA6060 alloy, while the Zr concentration in the Al-Zr coating was varied from 6 wt.% to 23 wt.%. The coated samples were further heat treated to generate microstructure with Zr based second phase precipitates, followed by anodising. Use of Zr as a model element is based on the fact that oxide of Zr in its crystalline form has a high refractive index of 2.2, and as a result, upon anodising precipitates containing Zr in anodised layer may interact with light more strongly [23], making it an interesting phase to study. Spectrophotometry technique used for analysing the surface appearance quantifies the total and diffuse reflectance of incident light from the surface. High resolution scanning electron microscopy coupled with transmission electron microscopy was used to understand the microstructure of the coatings, especially the incorporated precipitates and nano-scale morphology of the anodised layer. Glow discharge optical emission spectroscopy was employed to measure the composition of the deposited and heat treated coatings before and after anodising in sulphuric acid.

6.2 Experimental

6.2.1 Materials and methods

Coatings were deposited by DC magnetron sputtering using an industrial scale CemeCon CC800/8 machine with two cathodes. The opposite placed cathodes faced the substrates which were mounted on a planetary rotating table in the middle of the chamber to ensure a homogeneous deposition. The deposition chamber was initially evacuated to a base pressure of 6 mPa. During sputtering constant argon flow of 200 mL/min was used, leading to a typical argon pressure of 500 mPa. The distance between the targets and sample was about 100 mm, and the bias voltage on the substrates was fixed at -50 V. The maximum temperature during deposition was between 150 °C and 200 °C, as measured by a bi-metal thermometer during the deposition. AA6060 substrates (Erbslöh Aluminium GmbH, Germany) with dimensions 200 mm x 40 mm x 5 mm were coated with Al-Zr gradient of varying Zr content along the length of the specimen. Coatings were produced using one target of aluminium and one of aluminium with cylindrical zirconium inserts of 1 cm in diameter. The aluminium target was operated at 2000 W and the Al-Zr target was operated at 300 W and the targets were displaced with respect to the centre of the chamber. Thereby, the zirconium content in the deposition flux varies throughout the chamber and the resulting coating on the relatively long substrate has a varying composition. This method is very practical for screening purposes, as a single deposition will give different compositions. The zirconium content of the coating varied from 6 wt. % in one end to 23 wt. % in the other, with thicknesses of the coating varying from 16 µm to 14 µm.

Heat treatment of the coated samples was performed in a muffle furnace at a temperature of 550 ˚C for 4 h. Samples were then removed from the furnace and air cooled. The heat treated and the as coated samples were then mechanically polished, buffed, and degreased in a mild Alficlean™ solution at 60 ˚C.

Desmutting was performed by immersing the samples in diluted HNO_3 followed by rinsing with demineralised water. This process resulted in the removal of 5-6 µm of the sputtered coating thickness. Anodising was carried out in a 20 wt.% sulphuric acid bath maintained at 18 ˚C and 12.5 V for 30 min followed by rinsing with demineralized water. Sealing of the anodised layer was performed in a hot water bath maintained at 96 ˚C for 25 min followed by drying with hot air.

6.2.2 Optical Appearance

The visual optical appearance of the samples was recorded using an office document scanner. Reflectivity of the samples was investigated in detail using a spectrally resolved optical reflectance method comprising of an integrating sphere-spectrophotometer setup [55]. The samples were illuminated with a collimated beam from a deuterium tungsten-halogen light source (type DH2000 from Ocean Optics) at an incidence angle of 8˚ to the normal. The scattered light inside the sphere was collected using an optical fibre coupled to an optical spectrometer (QE65000 from Ocean Optics). Each reflectance spectrum was recorded over a the wavelength range from 350-750 nm and averaged for 4 s. Diffuse reflectance of a sample can be measured directly using a gloss trap coated with a dark absorbing material in the specular light port of the sphere. The specular reflectance spectrum is then obtained by subtracting the diffuse reflectance from total reflectance spectrum. The spectrophotometer was calibrated using high diffuse reflectance standards.

6.2.3 High Resolution Electron Microscopy

High-resolution structure and morphology of the sputtered coatings and anodised layer was observed using a scanning electron microscope (SEM) (Model Quanta 200™ ESEM FEG, FEI) equipped with an energy dispersive spectrometer (EDS) (Oxford Instruments 80 mm^2 X-Max™). The samples were first cut in transverse direction and then mounted in an epoxy and polished to reveal the cross section. Transmission electron microscopy analysis was carried out on the sample cross section in the anodised as well as non-anodised regions using a transmission electron microscope (TEM) (Model Tecnai G2 20™) operating at 200 keV. The lamellas for TEM were prepared using insitu-focussed ion beam (FIB) lift out (Model Quanta 200 3D™ DualBeam, FEI) and were further thinned in a FIB-SEM (Helios Nanolab™ DualBeam, FEI).

6.2.4 Grazing Incidence X-Ray Diffraction

Grazing incidence X-ray diffraction (GI-XRD) (Model Bruker Discover D8™) was performed using Cu K_α radiation at 40 kV and 40 mA for the phase analysis of deposited and heat treated coatings before and after anodising. Diffraction patterns were recorded in the 2θ range from 20° to 100° with an incidence angle of 1˚, step size of 0.03° and a scan step time of 4 s.

6.2.5 Radio Frequency Glow Discharge Optical Emission Spectroscopy (RF GDOES)

Compositional depth profiling of the coated, heat treated, and anodised samples was performed using RF-GDOES (Model GD-Profiler 2, Horiba Jobin Yvon). The instrument was coupled with a software package (Quantum XP™) for analysing and quantifying the data.

6.2.6 Atomic Force Microscopy and Scanning Kelvin Probe Force Microscopy

Scanning Kelvin Probe Force Microscopy (SKPFM) measurements were performed using an Atomic Force Microscope (AFM, Model Bruker, Multimode 5). Commercially available silicon tips (Nanosensors, PPP-EFM) coated with approx. 25 nm of chromium and platinum iridium on both sides of the cantilever were used. These tips have a resonance frequency of approximately 75 kHz. The tip radius is approximately 5 nm. The scans were performed using a line-wise two-pass lift mode, over an area of 20 x 20 $µm^2$ with a scan rate of 0.2 Hz. During the first pass, the topography was measured using the mechanical intermittent AFM mode. During the second pass, the tip was lifted approx. 10 nm above the surface, and retraced the previous topography while simultaneously measuring the Volta potential. Measurements were carried out in air, at

ambient temperature and humidity. Samples were mechanically polished and degreased in acetone prior to performing the measurements. As the mapping technique is a nulling method, the data obtained needs to be inverted in sign to get real potential values [56]. However, the data presented in the results section of this paper are not modified and hence electrochemically more active regions would appear more positive in the potential scale and are measured relative to the scanning probe used.

6.3 Results

6.3.1 Visual Appearance

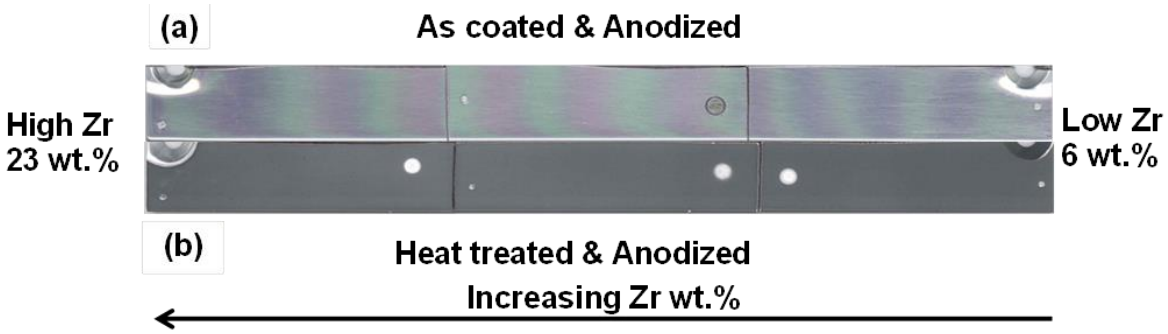

Figure 6.1: Scanned images of Al-Zr coated samples of varying composition in: (a) as coated, polished and anodised, (b) heat treated, polished, and anodised condition. The Zr concentration in the coatings decreases from left to right, bright circular spots are sputtered areas where composition was measured using RF-GDOES.

Figure 6.1 shows the appearance of the coated samples after anodising with and without heat treatment. The as coated and heat treated samples after mechanical polishing have a metallic lustre as expected. The samples that were anodised in as coated condition after polishing retain their metallic appearance, but are more diffuse (Figure 6.1 (a)). The colour fringes appearing on the surface are due to interference from a transparent anodised layer and a smooth metallic substrate [57] [58]. However, the heat treated sample after anodising (Figure 6.1 (b)) looks grey and dull throughout the range of Zr concentrations.

6.3.2 Scanning Electron Microscopy

Figure 6.2 (a) shows the cross section of the sputtered coating containing ~11 wt.% Zr after mechanical polishing and anodising. The thickness of the coating after the surface preparation process is ~10 µm out of which the anodised layer thickness is ~4 µm. During the characterization of this sample, some bright striations were observed in the coatings, which are not clearly visible (marked with arrows), in the captured image. TEM analysis was performed on these coatings to get a more detailed view of the coating structure. The heat treated coating shows formation of secondary phases with different morphology, size, and distribution (Figure 6.2 (b)). One type of precipitates is in the size range of 300-400 nm, which are homogenously distributed across the coating, and the others are in the nanometer size range (< 100 nm). The nanometre sized precipitates are segregated along certain regions and seem to have a lamellar structure as in Figure 6.2 (d). The EDS data (not shown here) of these second phases revealed that they are composed of Al, Zr, and Si. The presence of Si in the sputtered coating after heat treatment may be attributed to the diffusion from AA6060 substrate containing Si. The microstructure of the coating after heat treatment is similar throughout the compositional range of Zr consisting of nano and submicron sized precipitates. Anodising of these samples resulted in an anodised layer that has a thickness of ~3 µm (Figure 6.2 (b)). It can be seen that in the anodised layer, the submicron sized second phases are only partially affected or anodised (Figure 6.2 (b), (c) & (d)) which is reflected in the brightness contrast in individual precipitates. The nano-sized precipitates are completely anodised, as there is no observable contrast in the appearance of these precipitates within the anodised layer. The EDS analysis (not shown here) of the partially anodised precipitates does not show any

appreciable changes in the relative concentration of the constituting elements, but the presence of oxygen is detected. BSE images taken from a Zr concentration of ~17 wt.% are shown in Figure 6.3. From Figure 6.3 (a) & (b), it is confirmed that the microstructural features are similar to that observed in the Figure 6.2.

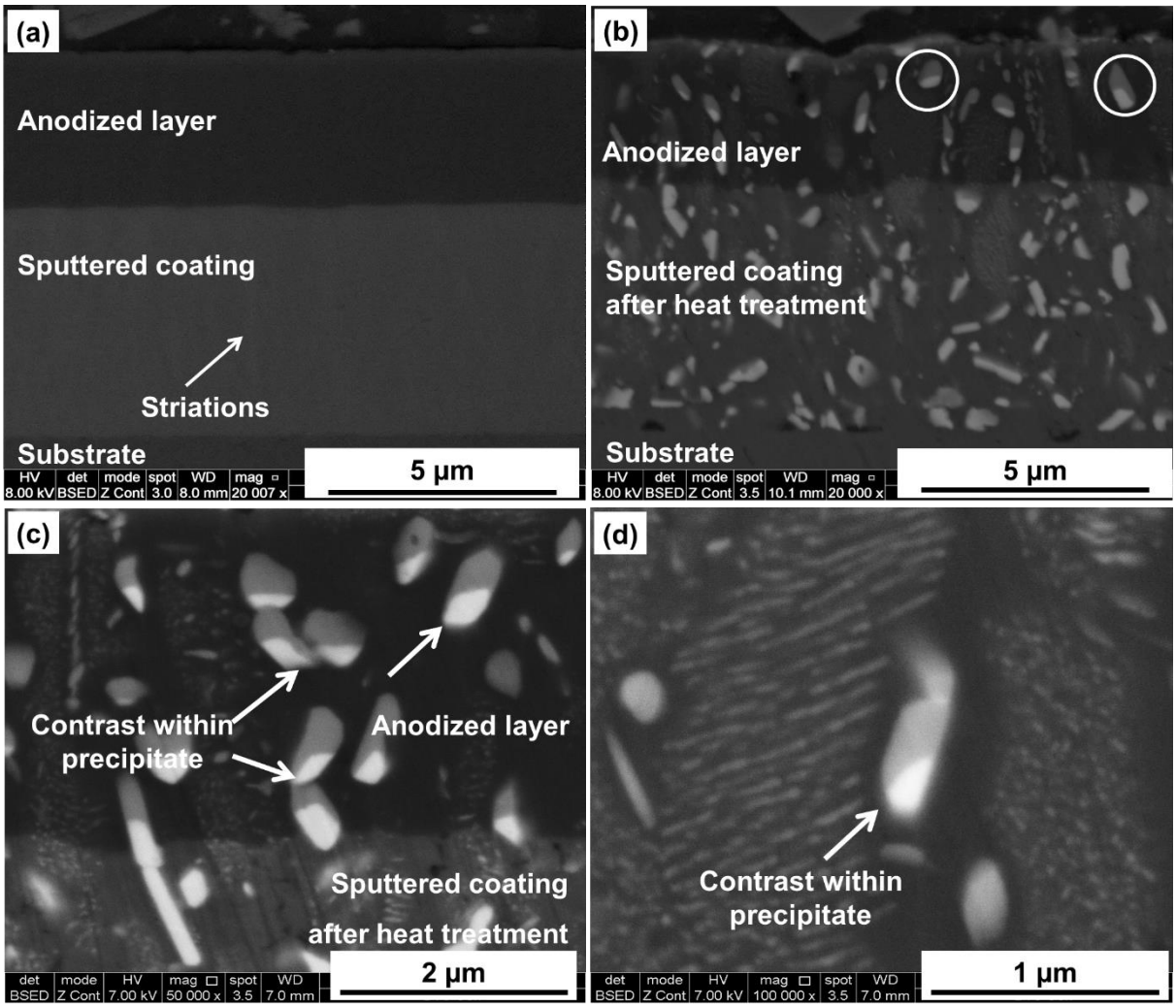

Figure 6.2: Back scattered electron (BSE) images of Al-11 wt.% Zr coatings cross section on AA6060 substrate in: (a) as coated and anodised, (b), (c) and (d) heat treated and anodised. Precipitates formed in the sputtered coating after heat treatment are found to have a brightness contrast after anodising.

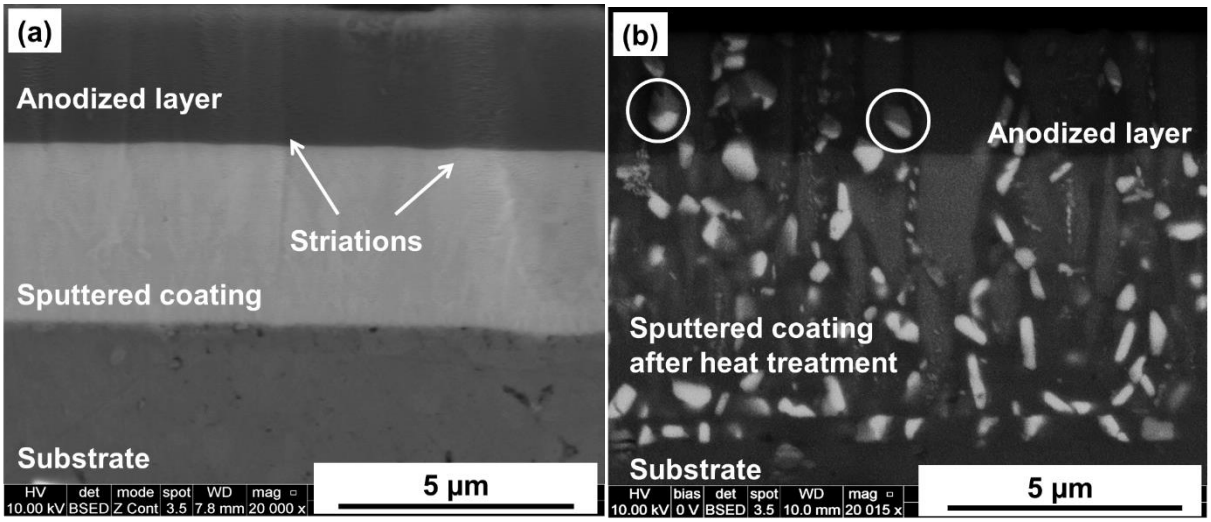

Figure 6.3: Back scattered electron images of Al-17 wt.% Zr coatings cross section on AA6060 in: (a) as coated and anodised and (b) heat treated and anodised condition. Precipitates formed in the sputtered coating after heat treatment, are found to have a brightness contrast after anodising.

6.3.3 Grazing Incidence X-Ray Diffraction

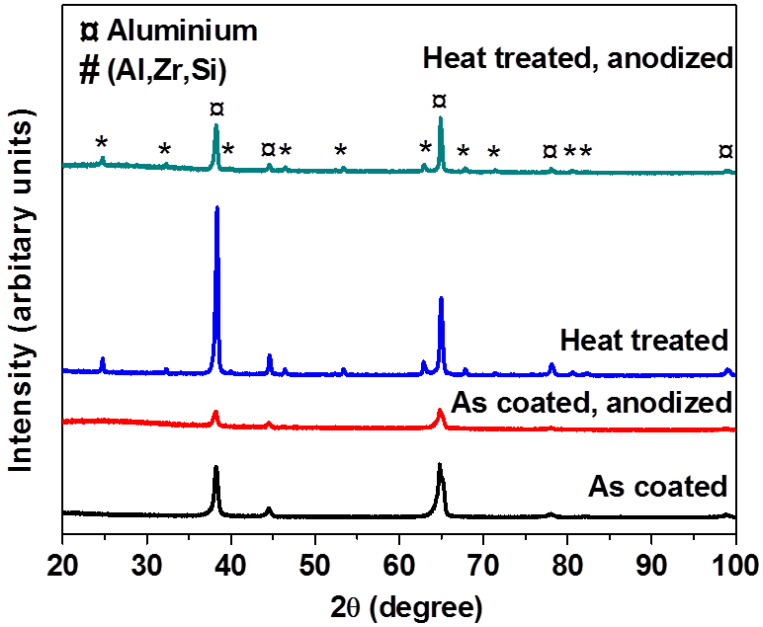

Figure 6.4: GI-XRD pattern of the samples in as coated and anodised condition with and without heat treatment. The Zr content is ~15 wt.%.

The GI-XRD patterns of the as coated, heat treated, and anodised samples are shown in Figure 6.4. The diffraction pattern from the as-coated samples show peaks which correspond to pure Al which are broad and asymmetric. There are no separate peaks which correspond to Zr or related phases, implying that all the sputtered Zr is dissolved into the Al matrix, which also explains the asymmetry in the Al peaks. The diffraction pattern of the heat treated sample shows sharp peaks corresponding to Al and a phase which was indexed from the JCPDS database as (Al, Zr, Si) (Pattern No. 14-0625). This is in accordance with the compositional data obtained from EDS results. It can also be observed that the anodising process transforms the surface to an amorphous oxide anodised layer.

6.3.4 RF-GDOES

The RF-GDOES compositional analysis for the sputtered coating before and after heat treatment is shown in Table 6.1. Concentration of Si in the sputtered coating after heat treatment has increased considerably along with the Mg content. As mentioned earlier, the increased content of Si and Mg in the sputtered coating after heat treatment is due to diffusion from the AA6060 substrate which is an Al-Mg-Si alloy.

Table 6.1: Composition analysis of sputtered coating before and after heat treatment at ~9 wt.% Zr.

	Si (wt.%)	Fe (wt.%)	Cu (wt.%)	Mg (wt.%)	Zn (wt.%)	Zr (wt.%)	Others (wt.%)	Al (wt.%)
As coated	0.08 ± 0.01	0.20 ± 0.02	0.02 ± 0.01	0.01 ± 0.01	0.12 ± 0.03	9.24 ± 0.58	1.11	Rest
After Heat treatment	1.28 ± 0.04	0.23 ± 0.02	0.01 ± 0.005	0.38 ± 0.05	0.09 ± 0.02	8.64 ± 0.72	1.30	Rest

6.3.5 Spectrophotometry

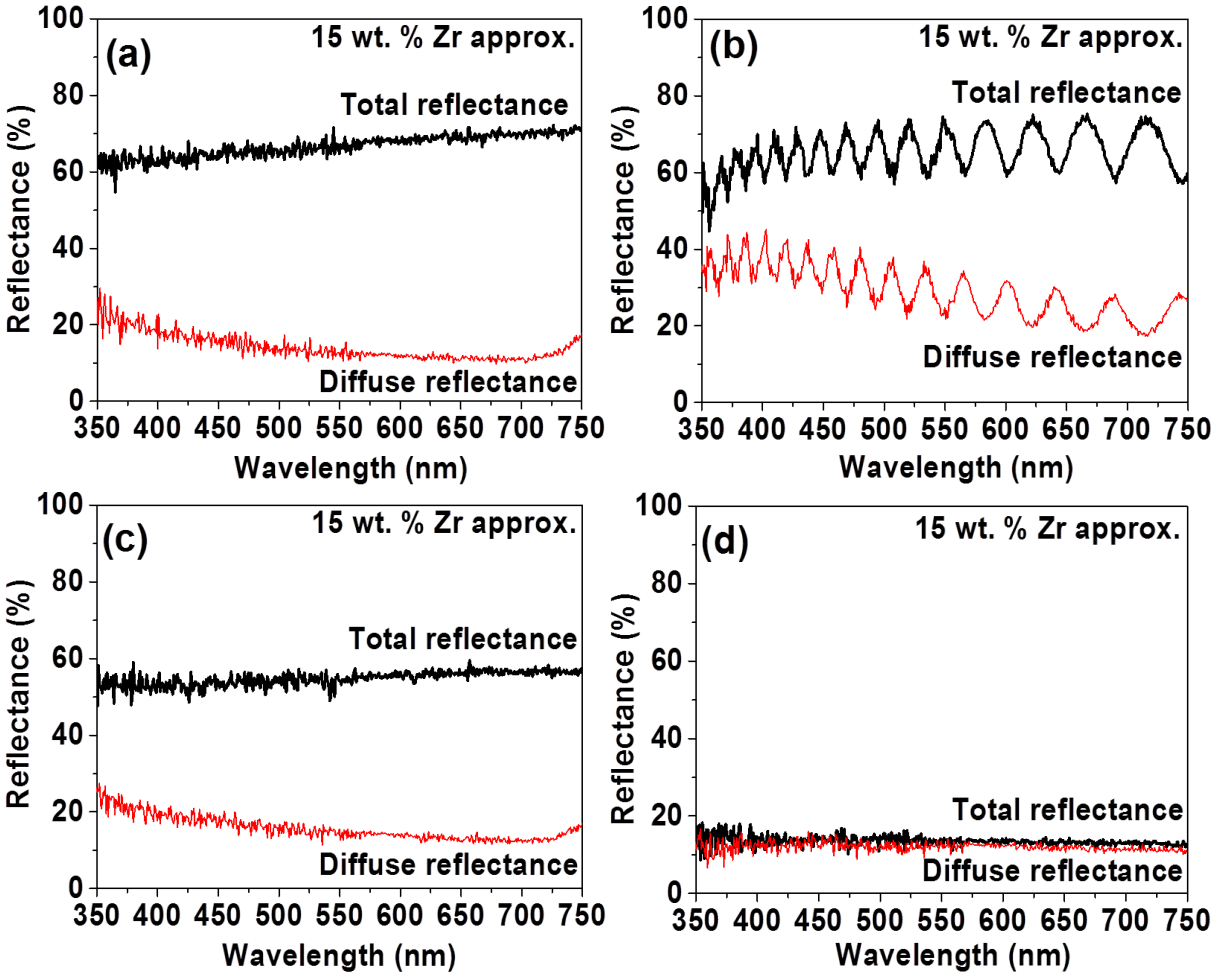

Figure 6.5: Reflectance spectra of ~Al-15 wt. % Zr coatings on AA6060 substrate in: (a) as coated, (b) as coated and anodised, (c) heat treated and (d) heat treated and anodised condition

The diffuse and total reflectance spectra of the samples taken at a location corresponding to a Zr concentration of ~15 wt.% are shown in Figure 6.5. It can be observed that the as coated sample (Figure 6.5 (a)) after mechanical polishing has a high total reflectance and a diffuse reflectance value corresponding to approximately one third of the total reflectance value. The specular reflectance of these samples is the difference between the total and diffuse reflectance and is hence the remaining two thirds of total reflectance in this case. After anodising Figure 6.5 (b)) the total reflectance remains the same, but a wavy reflectance pattern observed in the spectra is due to interference from difference in refractive index of the non-anodised and the anodised coating along with the low anodised layer thickness (~4 µm) [58]. The heat treated samples (Figure 6.5 (c)) have a similar total and diffuse reflectance spectra as the as coated samples. Upon anodising, the heat treated sample (Figure 6.5 (d)) has a reduced total and diffuse reflectance which can be correlated with dark visual appearance of the surface (see Figure 6.1 (b)). Also, the diffuse reflectance is dominant, implying that the samples lose their glossy metallic appearance. Similar reflectance spectra were measured across all Zr concentrations. The total and diffuse and reflectance values at 532 nm were plotted as a function of Zr content and are shown in Figure 6.6 (a) and (b). The wavelength of 532 nm was chosen by convention and it corresponds to a stable level in the visible spectral range.

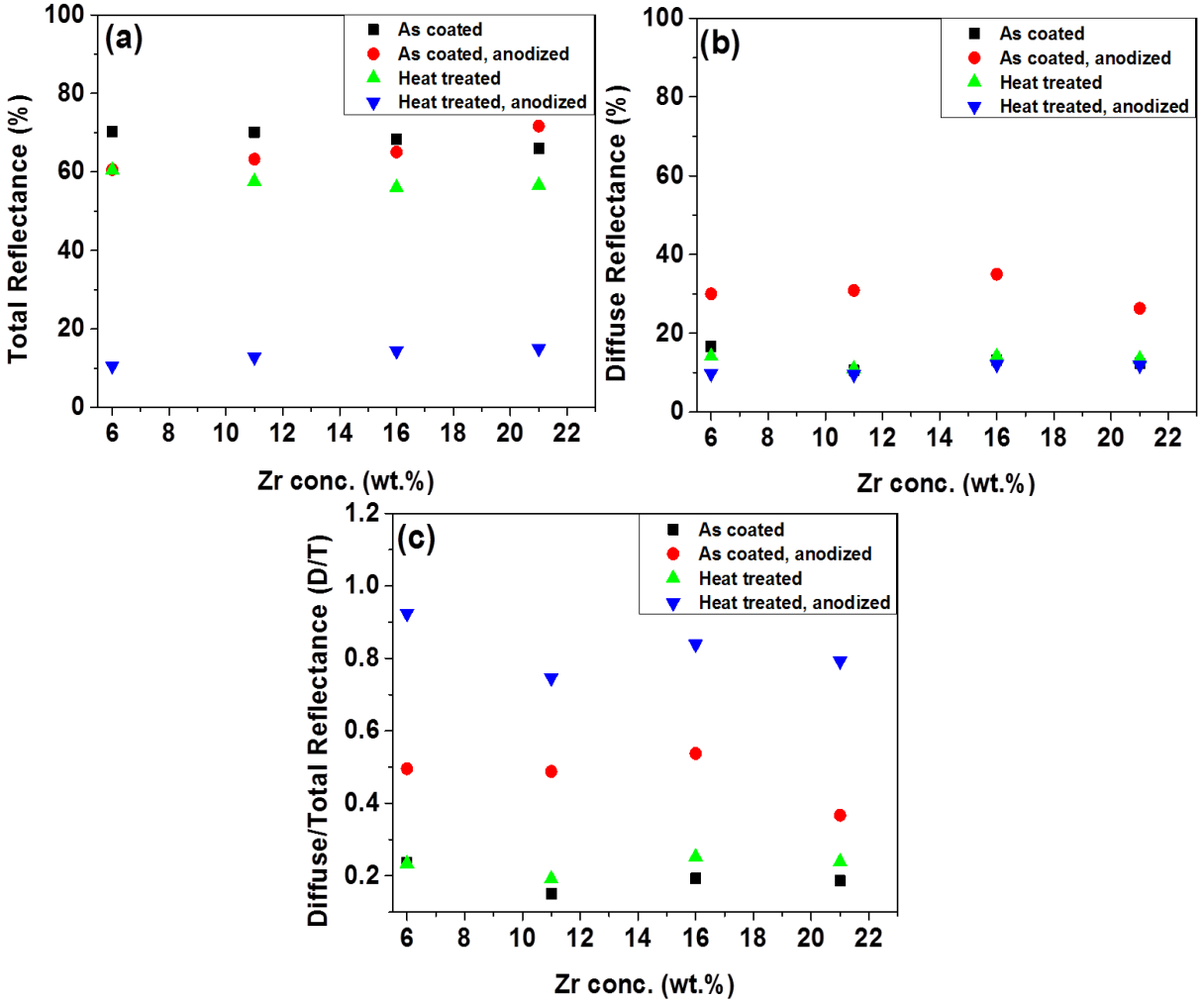

Figure 6.6: Total (a) and diffuse (b) reflectance values at a wavelength of 532 nm plotted as a function of Zr content. The ratio between total and diffuse reflectance values as a function of Zr content is shown in (c).

It is evident that reflectance depends only weakly on the Zr content. Total and diffuse reflectance values do not change significantly with Zr content (see Figure 6.6 (a) and (b)). However, the fraction of diffused scattered light varies significantly from the metallic Al-Zr coating to the anodised Al-Zr coating, as shown in

Figure 6.6 (c). This indicates that the pores and surface roughness formed in the anodising process act as scattering centres for light. Furthermore, the heat treated and anodised coatings show the highest fraction of diffuse reflectance (diffuse/total ratio ~0.9).

6.3.6 Transmission Electron Microscopy

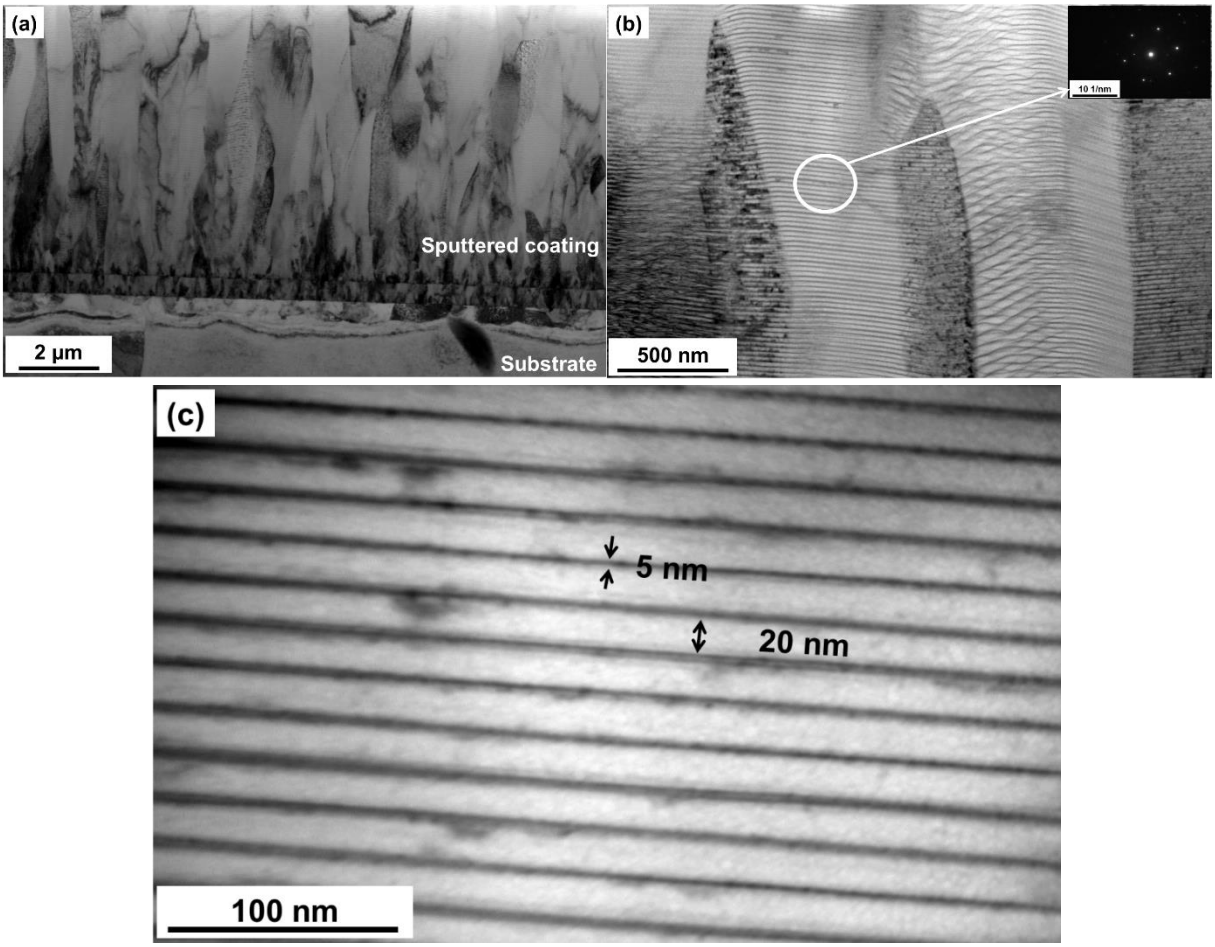

Figure 6.7: TEM bright field images of the Al-Zr sputtered coating: (a) cross section, (b) magnified view with selected area electron diffraction (SAED) and (c) at high magnification showing sputtered layers.

Figure 6.7 (a) shows the bright field TEM image of lamella prepared by FIB milling and lift out from the sputtered Al-Zr coating surface. The striations in the sputtered coating were also observed in the SEM images (Figure 6.2 (a) & (b)). The difference in the morphology and contrast between individual columnar grains is confirmed to be an effect due to their overlapping and orientations in the FIB lamella. Structure of the sputter deposited coating along with a selected area diffraction pattern is shown in Figure 6.7 (b) and the diffraction pattern shows that the columnar grains are crystalline. Figure 6.7 (c) shows at high magnification, the structure from the region where diffraction pattern was recorded. It can be observed that the sputtered coating has deposited in the form of multilayers which are observed as alternative bright (~20 nm thick) and dark (~5 nm thick) regions in the image. The bright regions contain a high Al content and the dark regions a high Zr content.

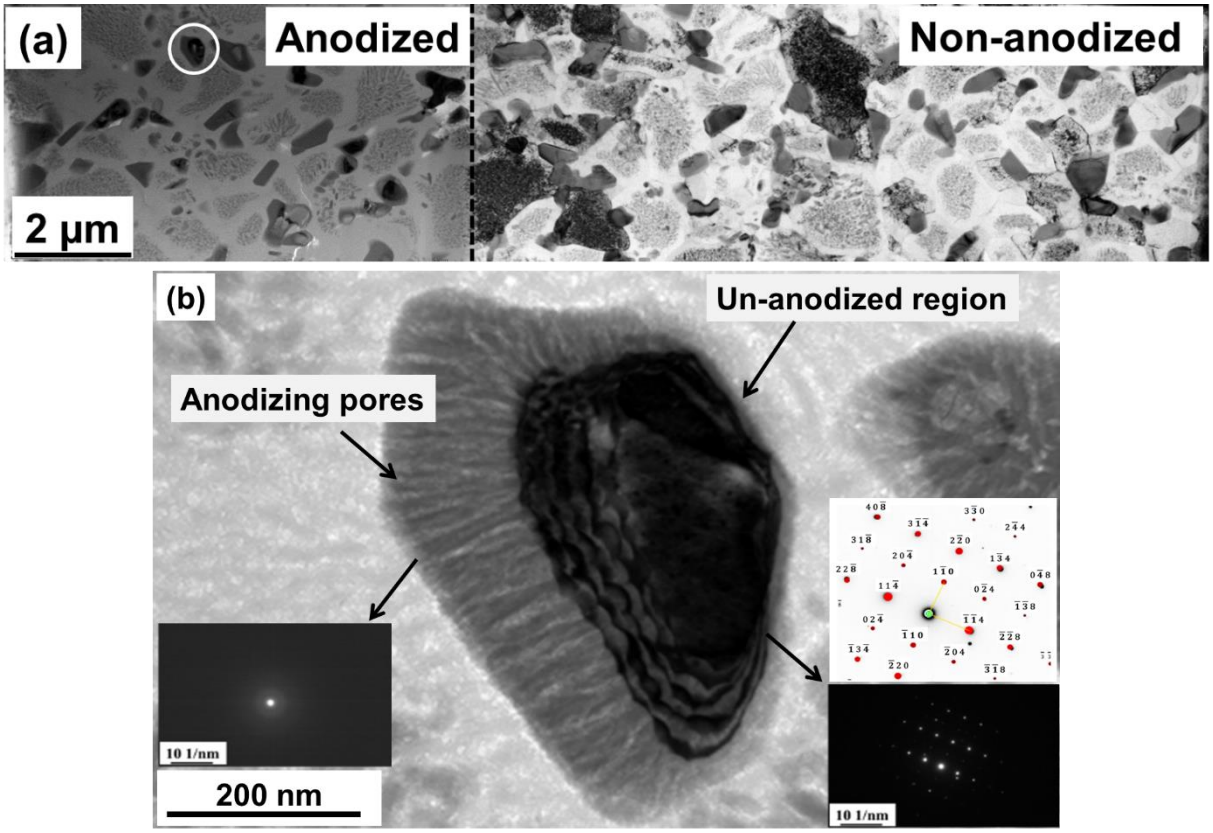

Figure 6.8: TEM bright field images of the Al-Zr sputtered coating after heat treatment and anodising: (a) cross section showing anodised and non-anodised region with SAED and (b) individual Al-Zr based second phase in anodised region with SAED.

Figure 6.8 (a) shows the TEM bright field image of a cross section lamella prepared by FIB milling and lift out from the heat treated and anodised sample. The anodised region (left of the image) shows the big, second phase precipitates which are partially anodised after the anodising process. The second kind of precipitates which are smaller in size (<100 nm) are fully oxidized. A typical, large second phase precipitate from the anodised region is shown in Figure 6.8 (b). It has been partially converted to oxide during the anodising process, while the core of the particle is intact in the metallic form. Pores created by the anodising process are clearly visible in the oxide crust oriented towards the surface showing the direction of anodising from left to right of the image. The SAED analysis from the un-anodised region of the big precipitate has been indexed to Al-Zr-Si crystalline phase perfectly matched with the I4/mmm space group with [221] as the zone axis, and the EDS analysis (Table 6.2) from anodised region of big precipitate show that it is partially oxidized and also converted to an amorphous phase after anodising.

Table 6.2: Representative EDS composition analysis of various phases in the anodised and un-anodised regions of the sample.

	Al (wt.%)	Zr (wt.%)	Si (wt.%)	O (wt.%)
Un-anodised big second phase	38.5 ± 0.23	52.3 ± 0.38	7.2 ± 0.10	1.9 ± 0.01
Anodised big second phase	21.1 ± 0.24	25.6 ± 0.41	6.3 ± 0.14	46.8 ± 0.51
Small second phase	42.8 ± 0.20	50.4 ± 0.32	6.7 ± 0.09	-
Anodised small second phase	18.0 ± 0.35	22.2 ± 0.67	3.7 ± 0.17	46.6 ± 0.86
Anodised matrix	31.7 ± 0.33	0.5 ± 0.09	0.5 ± 0.05	67.1 ± 0.67

6.3.7 Scanning Kelvin Probe Force Microscopy

The AFM surface topography map of the heat-treated coating is shown in Figure 6.9 (a) along with a back scattered electron image of same magnification in Figure 6.9 (b). The surface Volta potential map shown in Figure 6.9 (c) shows the distribution of potential values at the micro-scale of the Al matrix and the Al-Zr-Si precipitates at the location of Figure 6.9 (a). Line scan profiles in Figure 6.9 (d) of four lines show that the Volta potential for the Al-Zr-Si precipitates is lower than the surrounding Al matrix. This implies that the second phases are more noble compared to the surrounding Al matrix and the Volta potential difference between them is approx. 125-400 mV depending on the precipitate size. For very closely spaced precipitates, the measured Volta potential difference is highest (~400 mV) and the size is ~2 µm as they are scanned as one single precipitate. For individual precipitates the measured Volta potential difference is ~125 mV compared to the Al matrix. The dependence of measured potential values with size of the precipitates is due to the limited lateral resolution of the instrument during the Volta potential measurements.

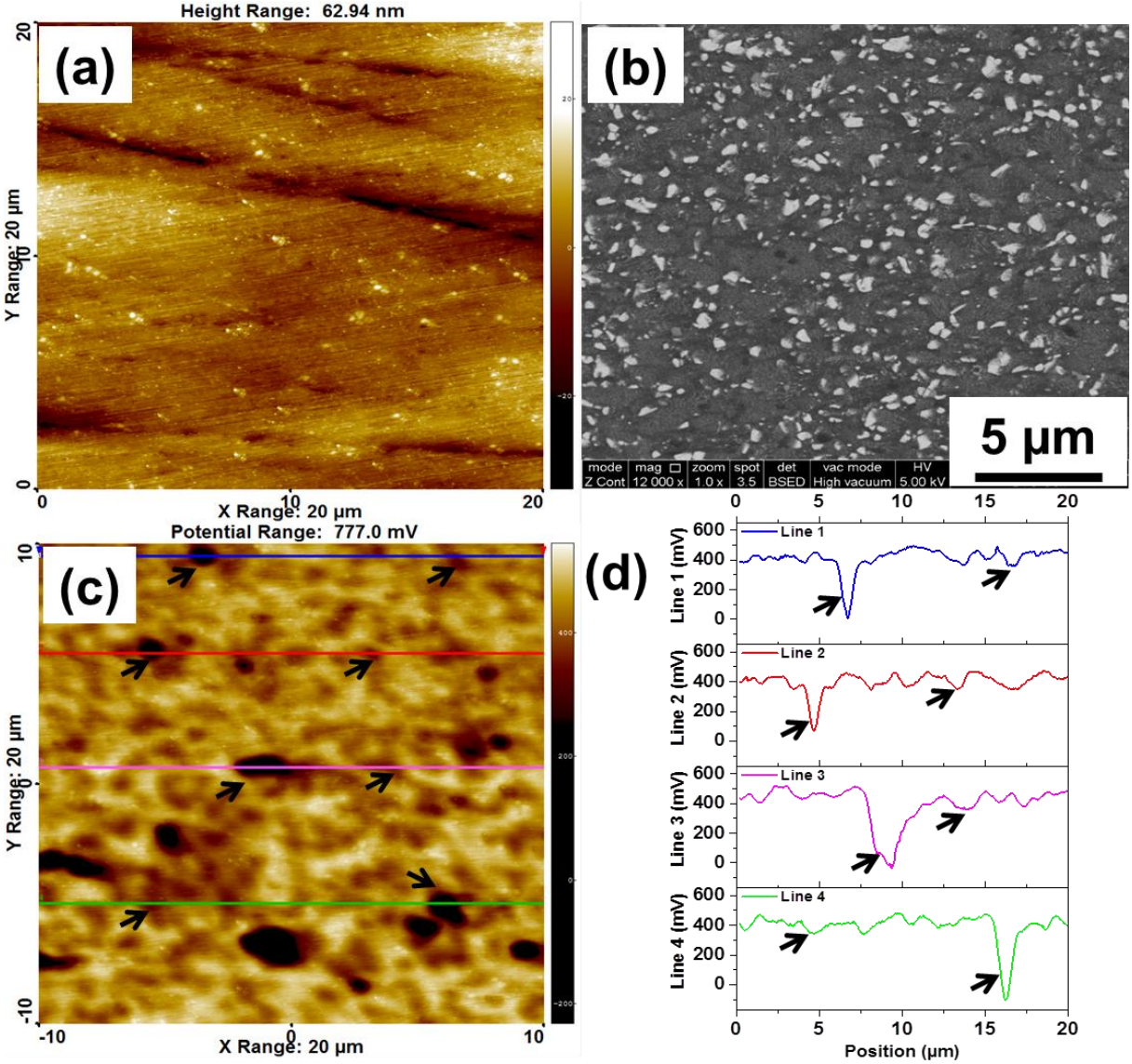

Figure 6.9: (a) AFM topography image, (b) back scattered electron image, (c) surface Volta potential map of (a) and (d) corresponding line scan section profiles of heat treated and mechanically polished Al-Zr coating surface.

6.4 Discussion

The results presented in this paper clearly elucidate the relationship between the substrate microstructural features in building the micro- and nano-scale morphology of the anodised layer in connection with the sputter coated Al-Zr system and the optical appearance of the anodised layer. The nano-layered Al/Al-Zr structure and columnar growth of the magnetron sputtered coating prior to heat treatment did not influence the optical appearance of the anodised layer significantly. This clearly shows that the major effect on optical appearance of the anodised layer is due to the presence of partially oxidized precipitates formed after heat treatment rather than the alloying elements themselves. The morphological, microstructural and compositional analysis, all indicate that the sputtered coating is polycrystalline in nature, composed of Zr dissolved in the Al matrix, and with the Zr composition varying within the layered structure. After anodising of these sputtered coatings, no metal is left un-oxidized in the anodised layer, although the anodised layer might be locally inhomogeneous with mixture of oxides as shown by the GI-XRD results. On the other hand, heat treatment generated a microstructure containing second phase precipitates (Figure 6.8 (a) & (b)) and upon anodising resulted in retention of these precipitates into the anodised layer in partially or fully oxidized form. The degree of oxidation of precipitates during anodising depends on their size and relative rates of anodising due to the differences in their chemical composition and electrochemical activity. The anodised layer consisting of partially oxidized metallic phases and the un-oxidized metallic part has profound influence on the optical appearance making the anodised surface appear dark and dull.

The layered structure for the sputter coating as shown in Figure 6.7 is due to the deposition geometry used during the sputter coating process. The configuration of the Al and Al-Zr sputter targets and the substrates in the sputter deposition chamber and rotation of specimen results in periodic difference in the flux of atoms approaching the surface. As the deposition process is a line-of-sight process, the substrates, when revolving around the central axis of the chamber, would be exposed to a varying sputtered atom flux from different targets which are alternatingly Al and Zr rich Al, resulting in layers of varying composition (Figure 6.7 (c)). Similar structures have also been reported by Asami et al. [59] for Al based sputtered coatings alloyed with heavy elements. Habazaki et al. [60] have studied similar layered magnetron sputtered coatings of Al valve metal binary alloys under barrier type anodising in pentaborate electrolytes. They observed that the anodised layer is an intimate mixture of oxides of Al and Zr and relative mobility of Al and Zr is within 10%.

As seen from Figure 6.2, heat treatment of the sputter coated samples gives a microstructure containing Al-Zr-Si phase with a dual size distribution, i.e., large second phase precipitates in the size range of 300-400 nm and small precipitates in the nanometre size range (<100 nm) (Figure 6.2 (c)). The Si diffusion from the substrate during heat treatment promotes formation of Al-Zr-Si phase instead of Al_3Zr. The Al-Zr-Si phase is a non-stoichiometric ternary phase of the general formula $Zr(Al_{1-x}Si_x)_3$ where the value of x varies from 0.1 to 0.14 and is referred to as τ_1 phase [61]. The relative composition of this phase formed at a temperature of 700 ˚C, 800 ˚C and 900 ˚C was reported by Jain et al. [62] by annealing diffusion couples of Zr and an Al-Si eutectic alloy. At an annealing temperature of 700 ˚C it was found that the τ_1 phase had formed closest to the diffusion interface in the Al-Si alloy which was then followed by layers of $ZrAl_3$, ZrSi, $ZrAl_2$, Zr_2Al_3, Zr_3Al and (Zr) in sequence. In the current case, Zr is distributed more evenly in the sputtered coating and hence we find the τ_1 phase throughout the coating after heat treatment. The formation of Al_3Zr is suppressed as Si diffuses readily in Al and has higher solubility in τ_1 phase (9-12.3 at.%) when compared to Al_3Zr phase (1.45 at.%) [62,63]. The dual size distribution of these precipitates might be attributed to the heterogeneous nature of the sputter coating. One possible hypothesis might be that during heat treatment, Zr from the Zr rich layer (dark fringe) of the coating diffuses into the adjacent Al layer and forms τ_1 phase which is thermodynamically more stable [64]. The Al-Zr-Si precipitates then grow in size until the Zr concentration in the dark fringe is reduced and reaches a value that is equivalent to that of the stable τ_1 phase. At this stage, precipitates containing remaining Zr from the dark fringe are formed and stabilized in the dark fringe region giving rise to smaller sizes distributions. This process of Zr diffusion from dark to adjacent bright fringes along with Si diffusion into the coating from the substrate would then result in the bi-modal size distribution of τ_1 precipitates after heat treatment. However, more detailed analysis is required to understand the exact local dynamics of the microstructural evolution after heat treatment.

During the anodising of heat treated samples, the precipitates with a larger size distribution are partially oxidized while the ones with a lower size distribution are completely oxidized (Figure 6.8). The SKPFM results (Figure 6.9) show that the τ_1 precipitates are cathodic when compared to the Al matrix. These are expected to have lower oxidation and dissolution kinetics due to passivating oxide films when compared to the surrounding matrix during anodising. Hence, as the anodising proceeds at a faster rate in the Al matrix than the precipitate, at one point the anodising front would have moved beyond the precipitate resulting in the enclosure of the precipitate in an anodised oxide matrix. After this, the access to the electrolyte for this precipitate and also the Al matrix metal below is cut off leading to even slower anodising rate. This results in partial anodising of the noble second phase precipitates in the Al matrix.

The un-anodised region of the large size precipitates (300-400 nm) is metallic in nature, while the anodised region is essentially an amorphous mixture of oxides of Al, Zr, and Si (Table 6.2). The refractive index of anodised Al is approximately 1.72 [57,65], ZrO_2 is 2.17 [66], and of SiO_2 is 1.52 [67] over the visible wavelength range respectively. Assuming that the refractive index of the anodised region of τ_1 precipitates is larger than that of the surrounding anodised Al and that they do not absorb light in visible region, more precipitates that are different from the matrix in terms of refractive index will result in more scattering of light. Homogenous distribution of such scattering centres in the anodised Al matrix results in multiple scattering of light, which disperses the incident light in all directions and creates a diffuse appearance of the surface [68]. However, the un-anodised region of the precipitates consisting of τ_1 phase is still crystalline and metallic. Metals and their alloys have a high extinction coefficient, which is responsible for their optical absorption characteristics. The extinction coefficient becomes prominent when the size range of the scattering medium is comparable to the wavelength of visible light. Metallic precipitates are highly absorbing in this size range [14,15,69]. This implies that multicomponent metallic precipitates containing τ_1 phase serve as centres of absorption for incoming light. The microstructure of the heat treated and anodised sputter coatings has large size precipitates whose anodised region scatters light due to higher refractive index than the anodised Al matrix, whereas the un-anodised region absorbs light owing to its metallic nature. Multiple scattering events thus result in an increased absorption of light and gives the overall diffused and grey appearance of the anodised layer.

An overview of the effect of various intermetallics on the anodised optical appearance was earlier reported by Timm et al. [36] who classified the different intermetallics into three categories based on their behaviour during anodising in sulphuric acid as shown in Table 6.3. From this, it can be stated that metallic second phase precipitates in Al alloys which are based on Fe, Mn, Ti and Si would behave in a similar fashion as the Zr based precipitates and would be present in an anodised Al matrix in an oxidized state.

Table 6.3: Behaviour of intermetallic compounds during anodising in sulphuric acid[36].

A	B	C
Unchanged an incorporated into oxide films	**Oxidised and incorporated (or dissolved) at a rate comparable or slower than Al**	**Oxidised and incorporated (or dissolved) at a rate faster than Al**
Si	$Al_{12}(Fe, Mn)_3$ Si *	$Al_{12}(Fe, Mn)_3$ Si *
$Al_6(Mn, Fe)$	Al_3Fe	Mg_2Al_3
Al_3Ti	Al_6Fe	Mg_5Al_8
	$Al_6(Fe, Mn)$	Mg_2Si
	$Al_9Fe_2Si_2$	Al_7Cr
		Al_2Cu

*** Depending on particle size**

For anodic films formed on pure aluminium, Saito et al. [70] have shown that presence of un-anodised metallic Al phase in anodised Al matrix leads to increased optical losses. Anodising at higher current densities resulted in the presence of higher amounts of un-anodised or metallic Al in anodic alumina and is shown to be the reason behind polarization dependent absorption characteristics of anodised Al films. Also, heat treatment of these Al containing anodic films showed decrease in optical loss with increasing treatment temperature, which has been attributed to the increased oxidation of remaining Al in the anodic film. Chang et al. [71] have carried out theoretical calculations for reflectance of anodic alumina films containing dispersed metallic Al phase taking the refractive index and extinction coefficient into consideration, and showed that the dark appearance is solely due to presence of absorbing metallic phase and speculated that it could be extended to any kind of dark films formed on metals. Hultquist [72] characterized brown to dark appearing “burned” anodic Al films obtained at high anodising current densities with the use of X-ray analysis and showed that presence of metallic Al in anodic film is the reason for their dark appearance as they act as pigmentation when present in an appropriate size range. Fratila-Apachitei et al. [31,73] have reported that precipitates based on Si anodise at a lower rate than the surrounding Al matrix resulting in occlusion of partially oxidized Si in the anodised film along with evolution of oxygen and formation of voids. The Fe and Si based second phases in a commercial AA1050 alloy have also been shown to display a similar behaviour of reduced oxidation rate and partial oxidation in the anodised film as was shown with the use of FIB-SEM by Jariyaboon et al. [74]. Difference in the oxidation rates of Al_3Fe and Al_6Fe intermetallics in Al matrix, studied by Shimizu et al. [27] showed that Al_3Fe intermetallics oxidize readily along with the adjacent Al matrix, whereas Al_6Fe intermetallics oxidize at approximately 0.44 times that of Al matrix. Also, the morphology of the anodic film is different in terms of pore density for the Fe based intermetallics compared to the Al matrix. In general, for Fe and Si based second phases, partial anodising is more probable as they are nobler than the Al matrix, whereas Cu and Mg based precipitates are more active compared to the Al matrix and hence they are expected to be anodised more readily [75]. This behaviour of second phases depending on their electrochemical behaviour along with the physical phenomenon of absorption of light by metallic particles in anodised Al agrees with the reported optical appearance of Al alloys, mainly AA1145, AA5005 and AA8014 studied by Timm [36]. AA1145 containing elemental Si appears dull as Si is not oxidized readily during anodising and metallic Si particles would absorb light while AA8014 extrusions containing $Al_6(Fe,Mn)$ precipitates show a bluish-grey appearance. They darken with depth of anodising which would increase the amount of absorbing particles in the anodised layer and hence the increased grey appearance. Another important finding was the size distribution of these Al-Fe-Mn precipitates on the specular gloss of the anodised surface. It was reported that the highest loss in specular gloss was observed when particle sizes were in the range of 0.4-1.5 µm. This, once again is a manifestation of the interaction of light with the metallic second phases where the scattering and absorption are highest for particle sizes which are comparable to wavelength of light [14,15]. The lower oxidizing rate of second phases may also cause the anodising front to move at a different rate at different locations, meaning the anodising front would not be a clearly lineated interface but would be rough. Regions with high concentration of particles would then have a rougher interface. This roughness at the interface if in the sub-micron range would increase the matte appearance of the anodised surface.

Mukhopadhyay et al. [76] studied the effect of Fe, Mn and Si on hard anodising of AA7075 extrusions and showed that $Al_{12}(Fe,Mn)_3Si$ based particles cause localized disruptions in the morphology of the anodic layer which is dependent on the orientation of the particles. If these disruptions are comparable to wavelength of light, they would modify the light scattering locally, both due to differing morphology and due to differing refractive index arising from different composition.

Depending on the size, distribution, electrochemical nature, anodising parameters (potential, time etc.) and the refractive index of respective oxides various second phases would alter the appearance of the anodised surface. If the distribution of these second phase precipitates is varying locally in the Al alloy due to deviations in manufacturing practice then upon anodising the localized difference would appear as a defect. On the other hand if they are distributed throughout the material then the effect would be an increase of dullness or cloudiness of the anodised surface. Future work in this area would be focused on the effect of

anodised layer thickness and anodising parameters such as voltage and time in altering the local morphology of particles influencing the decorative optical appearance.

As the phenomenon of scattering and/or absorption of light by partially anodised metallic precipitates in an anodised Al matrix are mainly dependent on optical properties of the material, such as refractive index and extinction coefficient, this study can be applied to explain the optical appearance of many commercial Al alloy systems, both primary and recycled, that contain various metallic second phases or intermetallics in their microstructures.

6.5 Conclusions

- Heat treatment of Al-Zr sputter coatings with varying Zr concentration showed precipitation of τ_1 phase (Al-Zr-Si). Diffusion of Silicon from the substrate contributed to the formation of Al-Zr-Si phase.
- High resolution SEM analysis of the coating showed a dual size distribution of the τ_1 phase after heat treatment. The dual size distribution is attributed to the initial layered structure of the plasma sputtered coating consisting of Zr rich layers as observed by TEM.
- High resolution SEM image of the anodised layer showed fully or partially oxidized τ_1 phases depending on the size. Partially oxidized τ_1 phase showed structure with oxide part on the top, while the bottom part was metallic due to the anodising direction and relative kinetics of oxidation between matrix and τ_1 phase.
- TEM bright field image of cross-section of the anodised layer showed local anodic film growth around the τ_1 phase with a partial metallic core depending on the size distribution of the particles. Further, the SAED shows that the oxidized part of the τ_1 phase is amorphous, while the un-oxidized part retains its crystallinity.
- Optical appearance of the anodised samples was dark due to the presence of partially oxidized Al-Zr-Si precipitates in the anodised layer. The un-oxidized metallic part act as absorption centres and leads to the dominantly absorbing behaviour of the sample surface and hence a darker appearance.

References

[1] H. Zhu, T. Wei, M.J. Couper, A.K. Dahle, Effect of Fe-rich particles on the formation of die streaks on anodized aluminum extrusions, Jom. 64 (2012) 337–345. doi:10.1007/s11837-012-0252-1.

[2] H. Zhu, X. Zhang, M.J. Couper, A.K. Dahle, Effect of primary intermetallic particles on surface microstructure and appearance of aluminium extrusions, Mater. Chem. Phys. 113 (2009) 401–406. doi:10.1016/j.matchemphys.2008.07.109.

[3] G. Vander Voort, B. Suárez Peña, J. Asensio Lozano, Microstructure Investigations of Streak Formation in 6063 Aluminum Extrusions by Optical Metallographic Techniques, Microsc. Microanal. 19 (2013) 276–284. doi:10.1017/S143192761300010X.

[4] H. Zhu, M.J. Couper, A.K. Dahle, Effect of process variables on the formation of streak defects on anodized aluminum extrusions: An overview, High Temp. Mater. Process. 31 (2012) 105–111. doi:10.1515/htmp-2012-0024.

[5] H. Zhu, X. Zhang, M.J. Couper, A.K. Dahle, Effect of initial microstructure on surface appearance of anodized aluminum extrusions, Metall. Mater. Trans. A Phys. Metall. Mater. Sci. 40 (2009) 3264–3275. doi:10.1007/s11661-009-9976-0.

[6] G. Gaustad, E. Olivetti, R. Kirchain, Improving aluminum recycling: A survey of sorting and impurity removal technologies, Resour. Conserv. Recycl. 58 (2012) 79–87. doi:10.1016/j.resconrec.2011.10.010.

[7] S.K. Das, Designing Aluminium Alloys for a Recycling Friendly World, Mater. Sci. Forum. 519-521 (2006) 1239–1244. doi:10.4028/www.scientific.net/MSF.519-521.1239.

[8] M. Mahfoud, D. Emadi, Aluminum Recycling - Challenges and Opportunities, Adv. Mater. Res. 83-86 (2009) 571–578. doi:10.4028/www.scientific.net/AMR.83-86.571.

[9] P.G. Sheasby, The Surface Treatment and Finishing of Aluminium and its Alloys, Finishing Publ,

Teddington, 1974. doi:10.1179/000705974798321639.
[10] J.D. Edwards, F. Keller, The structure of anodic oxide coatings, Trans. AIME, Inst. Met. Div. 156 (1944) 288–300. http://scholar.google.com/scholar?hl=en&btnG=Search&q=intitle:The+Structure+of+Anodic+Oxide+Coatings#4 (accessed November 8, 2013).
[11] S. Canulescu, K. Rechendorff, C.N. Borca, N.C. Jones, K. Bordo, J. Schou, et al., Band gap structure modification of amorphous anodic Al oxide film by Ti-alloying, Appl. Phys. Lett. 104 (2014) 121910. doi:10.1063/1.4866901.
[12] C.A. Grubbs, Anodizing of Aluminum, Met. Finish. 105 (2007) 397–412. doi:10.1016/S0026-0576(07)80359-X.
[13] G.. Thompson, Porous anodic alumina: fabrication, characterization and applications, Thin Solid Films. 297 (1997) 192–201. doi:10.1016/S0040-6090(96)09440-0.
[14] E. Hecht, Optics, Addison Wesley, 2002.
[15] R. Tilley, Colour and The Optical Properties of Materials: An Exploration of the Relationship Between Light, the Optical Properties of Materials and Colour, 2010. http://www.pilkington.com/products/bp/bybenefit/specialapplications/tecglass/ (accessed November 4, 2013).
[16] R. Silvennoinen, K. Peiponen, K. Muller, eds., Specular Gloss - Light Reflection From an Ideal Surface, Elsevier, Amsterdam, 2008. doi:http://dx.doi.org/10.1016/B978-008045314-9.50006-2.
[17] R. Silvennoinen, K. Peiponen, K. Muller, eds., Specular Gloss - Light Reflection From a Rough Surface, Elsevier, Amsterdam, 2008. doi:http://dx.doi.org/10.1016/B978-008045314-9.50007-4.
[18] F. Keller, M.S. Hunter, D.L. Robinson, Structural Features of Oxide Coatings on Aluminum, J. Electrochem. Soc. 100 (1953) 411. doi:10.1149/1.2781142.
[19] J.P. O'Sullivan, G.C. Wood, The Morphology and Mechanism of Formation of Porous Anodic Films on Aluminium, Proc. R. Soc. A Math. Phys. Eng. Sci. 317 (1970) 511–543. doi:10.1098/rspa.1970.0129.
[20] A.J. Dowell, Metal structure and composition effects in the alkaline etching of Aluminium, Trans. Inst. Met. Finish. 65 (1987) 147–151.
[21] N. Tabrizian, H.N. Hansen, P.E. Hansen, R. Ambat, P. Møller, Influence of annealing and deformation on optical properties of ultra precision diamond turned and anodized 6060 aluminium alloy, Surf. Coatings Technol. 204 (2010) 2632–2638. doi:10.1016/j.surfcoat.2010.02.002.
[22] I. Tsangaraki-Kaplanoglou, S. Theohari, T. Dimogerontakis, N. Kallithrakas-Kontos, Y.M. Wang, H.H. Kuo, et al., Effect of alloy types on the electrolytic coloring process of aluminum, Surf. Coatings Technol. 200 (2006) 3969–3979. doi:10.1016/j.surfcoat.2005.02.174.
[23] T.S. Shih, P.S. Wei, Y. Sen Huang, Optical properties of anodic aluminum oxide films on Al1050 alloys, Surf. Coatings Technol. 202 (2008) 3298–3305. doi:http://dx.doi.org/10.1016/j.surfcoat.2007.12.002.
[24] H. Habazaki, K. Shimizu, P. Skeldon, G.E. Thompson, G.C. Wood, X. Zhou, Effects of alloying elements in anodizing of aluminium, Trans. Inst. Met. Finish. 75 (1997) 18–23.
[25] X. Zhou, G.E. Thompson, H. Habazaki, K. Shimizu, P. Skeldon, G.C. Wood, Copper enrichment in Al-Cu alloys due to electropolishing and anodic oxidation, Thin Solid Films. 293 (1997) 327–332. doi:10.1016/S0040-6090(96)09117-1.
[26] M.A. Páez, T.M. Foong, C.T. Ni, G.E. Thompson, K. Shimizu, H. Habazaki, et al., Barrier-type anodic film formation on an Al-3.5 wt% Cu alloy, Corros. Sci. 38 (1996) 59–72. doi:10.1016/0010-938X(96)00102-3.
[27] K. Shimizu, G.M. Brown, K. Kobayashi, P. Skeldon, G.E. Thompson, G.C. Wood, Ultramicrotomy-a route towards the enhanced understanding of the corrosion and filming behaviour of aluminium and its alloys, Corros. Sci. 40 (1998) 1049–1072. doi:10.1016/S0010-938X(98)00006-7.
[28] V.C. Gudla, S. Canulescu, R. Shabadi, K. Rechendorff, J. Schou, R. Ambat, Anodization and Optical Appearance of Sputter Deposited Al-Zr Coatings, in: J. Grandfield, TMS (Eds.), Light Met. 2014, John Wiley & Sons, Inc., 2014: pp. 369–373. doi:10.1002/9781118888438.ch63.
[29] M. Aggerbeck, A. Junker-Holst, D.V. Nielsen, V.C. Gudla, R. Ambat, A.J. Holst, et al., Anodisation of Sputter Deposited Aluminium - Titanium Coatings : Effect of Microstructure on Optical Characteristics, Surf. Coatings Technol. 254 (2014) 138–144. doi:http://dx.doi.org/10.1016/j.surfcoat.2014.05.073.
[30] M. Saenz de Miera, M. Curioni, P. Skeldon, G.E. Thompson, The behaviour of second phase particles during anodizing of aluminium alloys, Corros. Sci. 52 (2010) 2489–2497. doi:10.1016/j.corsci.2010.03.029.
[31] L.E. Fratila-Apachitei, H. Terryn, P. Skeldon, G.E. Thompson, J. Duszczyk, L. Katgerman, Influence of substrate microstructure on the growth of anodic oxide layers, Electrochim. Acta. 49 (2004) 1127–1140. doi:10.1016/j.electacta.2003.10.024.

[32] Y. Ma, X. Zhou, G.E. Thompson, J.O. Nilsson, M. Gustavsson, A. Crispin, Anodizing of AA6063 aluminium alloy profiles: Generation of dark appearance, Surf. Interface Anal. 45 (2013) 1479–1484. doi:10.1002/sia.5219.
[33] M. Torkar, M. Godec, M. Lamut, Origin of stains on anodized aluminium profile, Eng. Fail. Anal. 16 (2009) 909–913. doi:10.1016/j.engfailanal.2008.08.021.
[34] F. Bijlhouwer, Why composition limits of popular extrusion alloys form an increasing obstacle for aluminium recycling, Mater. Technol. 24 (2009) 157–160. doi:10.1179/106678509X12475883285384.
[35] J.B. Hess, Physical metallurgy of recycling wrought aluminum alloys, Metall. Trans. A. 14 (1983) 323–327. doi:10.1007/BF02644210.
[36] J. Timm, Influence of Fe and Si Containing Phases on the Anodisation Behaviour, Key Eng. Mater. 44-45 (1990) 219–232. doi:10.4028/www.scientific.net/KEM.44-45.219.
[37] J.R. Scully, T.O. Knight, R.G. Buchheit, D.E. Peebles, Electrochemical characteristics of the Al2Cu, Al3Ta and Al3Zr intermetallic phases and their relevancy to the localized corrosion of Al alloys, Corros. Sci. 35 (1993) 185–195. doi:10.1016/0010-938X(93)90148-A.
[38] D. Kek Merl, P. Panjan, J. Kovač, Corrosion and surface study of sputtered Al-W coatings with a range of tungsten contents, Corros. Sci. 69 (2013) 359–368. doi:10.1016/j.corsci.2013.01.002.
[39] H. Yoshioka, H. Habazaki, A. Kawashima, K. Asami, K. Hashimoto, Anodic polarization behaviour of sputter-deposited Al-Zr alloys in a neutral chloride-containing buffer solution, Electrochim. Acta. 36 (1991) 1227–1233. doi:10.1016/0013-4686(91)85113-L.
[40] I.L. Soroka, J. Vegelius, P.T. Korelis, a. Fallberg, S.M. Butorin, B. Hjörvarsson, Structural stability and oxidation resistance of amorphous Zr-Al alloys, J. Nucl. Mater. 401 (2011) 38–45. doi:10.1016/j.jnucmat.2010.03.016.
[41] Y. Liu, M.A. Arenas, P. Skeldon, G.E. Thompson, P. Bailey, T.C.Q. Noakes, et al., Anodic behaviour of a model second phase: Al-20at.%Mg-20at.%Cu, Corros. Sci. 48 (2006) 1225–1248. doi:10.1016/j.corsci.2005.05.007.
[42] M. Saenz de Miera, M. Curioni, P. Skeldon, G.E. Thompson, Modelling the anodizing behaviour of aluminium alloys in sulphuric acid through alloy analogues, Corros. Sci. 50 (2008) 3410–3415. doi:10.1016/j.corsci.2008.09.019.
[43] H. Habazaki, K. Shimizu, P. Skeldon, G.E. Thompson, G.C. Wood, X. Zhou, Nanoscale enrichments of substrate elements in the growth of thin oxide films, Corros. Sci. 39 (1997) 731–737. doi:10.1016/S0010-938X(97)89339-0.
[44] P. Skeldon, G.E. Thompson, G.C. Wood, X. Zhou, H. Habazaki, K. Shimizu, Interactions of alloying elements during anodizing of dilute Al-Au-Cu and Al-W-Zn alloys and consequences for film growth, Corros. Sci. 41 (1998) 291–304. doi:10.1016/S0010-938X(98)00123-1.
[45] I. Felhosi, H. Habazaki, K. Shimizu, P. Skeldon, G.E. Thompson, G.C. Wood, et al., Void formation and alloy enrichment during anodizing of aluminium alloys containing cadmium, indium and tin, Corros. Sci. 40 (1998) 2125–2139. doi:10.1016/S0010-938X(98)00098-5.
[46] H. Habazaki, K. Shimizu, P. Skeldon, G.E. Thompson, G.C. Wood, The co-enrichment of alloying elements in the substrate by anodic oxidation of Al-Cu-W alloys, Corros. Sci. 39 (1997) 339–354. doi:10.1016/S0010-938X(97)83350-1.
[47] P.J. Kelly, R.D. Arnell, Magnetron sputtering: A review of recent developments and applications, Vacuum. 56 (2000) 159–172. doi:10.1016/S0042-207X(99)00189-X.
[48] H.H. Strehblow, C.M. Melliar-Smith, W.M. Augustyniak, Examination of Aluminum-Copper Films during the Galvanostatic Formation of Anodic Oxide, J. Electrochem. Soc. 125 (1978) 915. doi:10.1149/1.2131590.
[49] H. Habazaki, X. Zhou, K. Shimizu, P. Skeldon, G.E. Thompson, G.C. Wood, Mobility of copper ions in anodic alumina films, Electrochim. Acta. 42 (1997) 2627–2635. doi:10.1016/S0013-4686(96)00454-9.
[50] S.J. Garcia-Vergara, K. El Khazmi, P. Skeldon, G.E. Thompson, Influence of copper on the morphology of porous anodic alumina, Corros. Sci. 48 (2006) 2937–2946. doi:10.1016/j.corsci.2005.10.017.
[51] Y. Liu, P. Skeldon, G.. Thompson, H. Habazaki, K. Shimizu, Anodic film growth on an Al–21at.%Mg alloy, Corros. Sci. 44 (2002) 1133–1142. doi:10.1016/S0010-938X(01)00115-9.
[52] A.C. Crossland, G.E. Thompson, C.J.E. Smith, H. Habazaki, K. Shimizu, P. Skeldon, Formation of manganese-rich layers during anodizing of Al-Mn alloys, Corros. Sci. 41 (1999) 2053–2069. doi:10.1016/S0010-938X(99)00025-6.
[53] X. Zhou, H. Habazaki, K. Shimizu, P. Skeldon, G.E. Thompson, G.C. Wood, Enrichment-dependent anodic oxidation of zinc in Al-Zn alloys, Corros. Sci. 38 (1996) 1563–1577. doi:10.1016/0010-938X(96)00051-0.
[54] S. Van Gils, T. Dimogerontakis, G. Buytaert, E. Stijns, H. Terryn, P. Skeldon, et al., Optical properties

of magnetron-sputtered and rolled aluminum, J. Appl. Phys. 98 (2005). doi:10.1063/1.2085315.
[55] I. Lindseth, A. Bardal, R. Spooren, Reflectance measurements of aluminium surfaces using integrating spheres, Opt. Lasers Eng. 32 (1999) 419–435. doi:10.1016/S0143-8166(00)00010-5.
[56] P. Schmutz, Characterization of AA2024-T3 by Scanning Kelvin Probe Force Microscopy, J. Electrochem. Soc. 145 (1998) 2285. doi:10.1149/1.1838633.
[57] G.F. Pastore, Transmission interference spectrometric determination of the thickness and refractive index of barrier films formed anodically on aluminum, Thin Solid Films. 123 (1985) 9–17. doi:10.1016/0040-6090(85)90036-7.
[58] S. Van Gils, P. Mast, E. Stijns, H. Terryn, Colour properties of barrier anodic oxide films on aluminium and titanium studied with total reflectance and spectroscopic ellipsometry, Surf. Coatings Technol. 185 (2004) 303–310. doi:10.1016/j.surfcoat.2004.01.021.
[59] K. Asami, H. Yoshioka, K. Hashimoto, K. Shimizu, K. Kobayashi, Superlattice-like structure of sputter-deposited amorphous aluminum-heavy element alloys, J. Non. Cryst. Solids. 110 (1989) 258–264. doi:10.1016/0022-3093(89)90266-4.
[60] H. Habazaki, K. Shimizu, P. Skeldon, G.E. Thompson, G.C. Wood, Formation of amorphous anodic oxide films of controlled composition on aluminium alloys, Thin Solid Films. 300 (1997) 131–137. doi:http://dx.doi.org/10.1016/S0040-6090(96)09491-6.
[61] O. Schob, H. Nowotny, F. Benesovsky, Strukturbestimmung an einigen Phasen in den Systemen: Zr-Al-Si und Hf-Al-Si{ZrAl3(Si); ZrSi(Al), Hf(Si, Al); Zr3Si2; Hf3Si2}, Monatshefte fur Chemie. 92 (1961) 1218–1226. doi:10.1007/BF00914988.
[62] J.K. Jain, S.P. Gupta, Intermetallic compound formation in the Zr-Al-Si ternary system, Mater. Charact. 49 (2002) 139–148. doi:10.1016/S1044-5803(02)00343-1.
[63] A. Raman, K. Schubert, Uber den aufbau einiger zu TiAl3 verwandter legierungsreihen .2. Untersuchungen in einigen T-Al-Si und T4...6-in-systemen, Zeitschrift Fur Met. 56 (1965) 44–52.
[64] T. Hirano, H. Ohtani, M. Hasebe, Thermodynamic Analysis of the Al-Si-Zr Ternary System, High Temp. Mater. Process. 29 (2010) 347–371. doi:10.1515/HTMP.2010.29.5-6.347.
[65] I. Khan, J. Leach, N. Wilkins, The thickness and optical properties of films of anodic aluminium oxide, Corros. Sci. 6 (1966) 483–497. doi:10.1016/S0010-938X(66)80065-3.
[66] R.A. Synowicki, T.E. Tiwald, Optical properties of bulk c-ZrO2, c-MgO and a-As 2S3 determined by variable angle spectroscopic ellipsometry, Thin Solid Films. 455-456 (2004) 248–255. doi:10.1016/j.tsf.2004.02.028.
[67] E.D. Palik, Chapter 2 - Refractive Index, Handbook of Optical Constanst of Solids, in: Handb. Opt. Constants Solids, Academic Press, Burlington, 1997: pp. 5–114. doi:http://dx.doi.org/10.1016/B978-012544415-6.50149-7.
[68] R.J.D. Tilley, Colour due to Scattering, in: Colour Opt. Prop. Mater., John Wiley & Sons, Ltd, 2010: pp. 175–196. doi:10.1002/9780470974773.ch5.
[69] J.A. Perenboom, P. Wyder, F. Meier, Electronic properties of small metallic particles, Phys. Rep. 78 (1981) 173–292. doi:http://dx.doi.org/10.1016/0370-1573(81)90194-0.
[70] M. Saito, Unoxidized Aluminum Particles in Anodic Alumina Films, J. Electrochem. Soc. 140 (1993) 1907. doi:10.1149/1.2220737.
[71] R. Chang, W.F. Hall, On the correlation between optical properties and the chemical /metallurgical constitution of multi-phase thin films, Thin Solid Films. 46 (1977) L5–L8. doi:10.1016/0040-6090(77)90068-2.
[72] A.E. Hultquist, On the Nature of Burned Anodic Coatings, J. Electrochem. Soc. 111 (1964) 1302. doi:10.1149/1.2425989.
[73] L.. Fratila-Apachitei, F.D. Tichelaar, G.E. Thompson, H. Terryn, P. Skeldon, J. Duszczyk, et al., A transmission electron microscopy study of hard anodic oxide layers on AlSi(Cu) alloys, Electrochim. Acta. 49 (2004) 3169–3177. doi:10.1016/j.electacta.2004.02.030.
[74] M. Jariyaboon, P. Møller, R.E. Dunin-Borkowski, R. Ambat, FIB-SEM investigation of trapped intermetallic particles in anodic oxide films on AA1050 aluminium, Anti-Corrosion Methods Mater. 58 (2011) 173–178. doi:10.1108/00035591111148885.
[75] R.G. Buchheit, A Compilation of Corrosion Potentials Reported for Intermetallic Phases in Aluminum Alloys, J. Electrochem. Soc. 142 (1995) 3994. doi:10.1149/1.2048447.
[76] A.K. Mukhopadhyay, A.K. Sharma, Influence of Fe-bearing particles and nature of electrolyte on the hard anodizing behaviour of AA 7075 extrusion products, Surf. Coatings Technol. 92 (1997) 212–220. doi:10.1016/S0257-8972(97)00102-3.

7. Anodising of Al-Zr Coatings: Effect of Anodising Potential (Paper 3)

Anodising and Optical Appearance of Sputter Deposited Al-Zr Coatings*

Abstract

Anodised Al alloy components are extensively used in various applications like architectural, decorative and automobiles for corrosion protection and/or decorative optical appearance. However, tailoring the anodised layer for specific optical appearance is limited due to variation in composition and microstructure of the commercial alloys, and even more difficult with recycled alloys. Sputter coating methods promise to control the chemical composition of the Al alloy surfaces and eventually modify the microstructure of the surfaces with heat treatments thus enabling the freedom on the substrate quality. This paper evaluates the use of magnetron sputtered Al-Zr coatings on Al combined with heat treatment and anodising for obtaining required optical properties. Metallurgical and optical characterization was carried out to investigate the effect of coating microstructure and anodising parameters on appearance of the anodised layer. The microstructure of the coating is found to influence the appearance of anodised layer owing to the presence of completely or partially dissolved second phases during anodising process. Oxidation status of the second phase particles in the coatings affected the light absorption and scattering phenomenon there by imparting different appearances to the anodised alloy surfaces.

Keywords: Magnetron sputtering, Aluminium coating, Anodising, Appearance.

*Published as ***V.C. Gudla***, S. Canulescu, R. Shabadi, K. Rechendorff, J. Schou, R. Ambat, Anodization and Optical Appearance of Sputter Deposited Al-Zr Coatings, in: J. Grandfield, TMS (Eds.), Light Met. 2014, John Wiley & Sons, Inc., 2014: pp. 369–373.*

7.1 Introduction

Anodising is widely applied to Al alloy components used in various industrial segments such as architecture for outdoor profiles, windows, facades, electronic consumer goods for decorative packaging and transportation for automobile components either for corrosion protection, optical appearance or both [1]. Of the several kinds of electrolytes used in anodising of Al, sulphuric acid is the most commonly used for decorative anodising [2]. The anodised layer for decorative applications is a transparent oxide layer whose appearance depends on the anodising parameters and quality of the alloy surface being anodised [3,4]. Sulphuric acid anodising gives in certain cases an anodised layer with self-assembled nano porous structure. This structure is impregnated with organic or inorganic dyes and later sealed, imparting different colours to the surface [2]. Optical appearance of the anodised layer is sometimes difficult [5] to control due to the increased use of recycled Al alloys because of the increased intermetallic phases in recycled Al alloys [6] which behave differently from the Al matrix during the anodising process [1,7]. Many authors have reported the electrochemical behaviour of the second phases in various Al alloys during anodising [8–11], on the other hand not much has been reported on the influence of second phase particles on the optical appearance after anodising [12]. Recent studies show the potential use of sputtered coatings of binary and ternary alloy systems for understanding the anodising behaviour of Al based phases [13]. Sputter coating techniques provide surfaces with a wide range of compositions which cannot be obtained by conventional melt and cast techniques. Once the coating composition, heat treatment and the anodising processes are optimized, they can be deposited on any kind of Al alloy substrates, be it cast, wrought or recycled. By additional controlled heat treatments the microstructure could be varied to obtain desired second phase particles which upon anodising are expected to modify the interaction of light in terms of scattering and absorption, and thus alter the optical appearance. The anodising behaviour of several binary alloys systems like Al-Cu [14,15], Al-Mg [16], Al-Mn [17] and Al-Zn [18], prepared by sputter coating techniques, have been studied earlier in terms of morphology of anodised layer, migration of alloy species, adhesion and delamination of anodic films but their effect on optical appearance after anodising is not reported. Another important class of materials based on Al-Zr alloys has not been addressed in the literature. A high refractive index of 2.2 for ZrO_2 [19] which is larger than that of anodised aluminium (n=1.7) [20,21] makes it an ideal candidate for studying optical effects. This difference in refractive indices is expected to influence the optical appearance of the anodised surface. In order to understand and tailor the optical appearance of anodised surface, model Al-Zr alloy coatings on a pure aluminium surface with a varying concentration prepared by sputter coating technique is studied in detail. The effect of heat treatment and anodising voltage along with composition, microstructure and morphology of second phases on the optical appearance of the anodised layer is discussed.

7.2 Experimental

7.2.1 Materials and methods

Al substrates (Reinal™, 99.9 % purity) of dimensions 200 mm x 30 mm x 8 mm were prepared from billets obtained from Alcan rolled products, Germany. The Al-Zr coatings with a composition gradient from 6 wt.% to 23 wt.% Zr were deposited using DC magnetron sputtering (Model CemeCon 800/8) at Tribology Centre, Danish Technological Institute, Denmark. The deposition was performed with a starting pressure of 4 mPa, and with a bias voltage of -50 V. One commercial AA1050 and another AA1050 target with Zr inserts were used in the sputtering chamber for obtaining the desired Zr concentration gradient during the coating process. The thickness of the coatings obtained was approximately 15 µm.

Heat treatment of the coated samples was performed in a muffle furnace at a temperature of 550 ˚C for 4 h. The samples were then removed from the furnace and cooled in ambient air. The heat treated and as-received samples were then mechanically polished, buffed, and degreased in a mild Alficlean™ solution at 60 ˚C before being subjected to anodising. The samples were then subsequently de-smutted by immersing in diluted HNO_3 followed by rinsing with demineralised water. This process resulted in the removal of 5 - 6 µm of the coating thickness. Anodising was carried out in a 20 wt.% sulphuric acid bath maintained at 18 ˚C; potential used were 12.5 V and 20 V for different time periods aimed at achieving equal anodised layer thicknesses.

This was followed by rinsing with demineralized water. Sealing of the anodised layer was performed in water at 96 ˚C for 25 min followed by drying with hot air.

7.2.2 Spectrophotometry

Spectrally resolved optical reflectance of the coatings was measured using an integrating sphere-spectrophotometer setup. The samples were illuminated with a collimated beam from a deuterium tungsten-halogen light source (type DH2000 from Ocean Optics) at an angle of incidence of 8˚ with respect to normal. The reflected light was collected using an optical fibre coupled to an optical spectrometer (QE65000 from Ocean Optics). Each reflectance spectrum was acquired over the wavelength range from 350-750 nm and averaged over 4 s. Diffuse reflectance of a sample was measured directly using a gloss trap coated with a dark absorbing material in the specular light port of the sphere. The specular reflectance spectrum is obtained by subtracting the diffuse reflectance from total reflectance of each sample. The spectrophotometer was calibrated using high specular and high diffuse reflectance standards.

7.2.3 X-ray Diffraction

Grazing incidence X-ray diffraction (Model Bruker Discover D8™) analysis was performed using Cu K_α radiation at 40 kV and 40 mA for the phase analysis of as received and heat treated coatings before and after anodising. The XRD patterns were recorded in the 2θ range from 10° to 100° with an incidence angle of 0.25˚, step size of 0.01° and a scan step time of 3 s.

7.2.4 Electron Microscopy

The morphology and microstructure of sputtered coatings after heat treatment and anodising was observed using a scanning electron microscope (Model Quanta 200™ ESEM FEG, FEI) equipped with an EDS (Oxford Instruments 80 mm^2 X-Max™). The samples were mounted in an epoxy and polished to reveal the cross section. Transmission electron microscopy analysis was carried out on the sample cross section in the anodised as well as non-anodised regions using a TEM (Model Tecnai G2 20™) operating at 200 keV. The lamellas for TEM were prepared using focused ion beam milling and insitu lift out in the microscope (Model Quanta 200 3D™ DualBeam, FEI) which was further thinned in a FIB-SEM (Model Helios Nanolab™ DualBeam, FEI).

7.3 Results

7.3.1 Visual Appearance

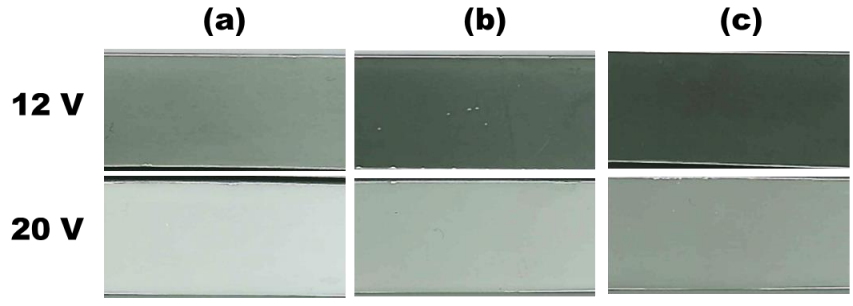

Figure 7.1: Optical images showing appearance of the anodised layer on Al-Zr coatings for Zr concentrations of: (a) 9 wt.%, (b) 15 wt.% and (c) 21 wt.% after heat treatment and anodising at different voltage.

The optical appearance of the samples which were heat treated and anodised at 12.5 V and 20 V is shown in Figure 7.1 for three surfaces with different Zr concentrations. Samples which are anodised at 20 V

are brighter than those anodised at 12.5 V for all the Zr concentration range. Also, the appearance darkens with increasing Zr concentration.

7.3.2 Spectrophotometry

The diffuse and total reflectance spectra of the samples taken at a location corresponding to a Zr concentration of 9 wt.% (low Zr end) are shown in Figure 7.2 (a). It can be seen that the as-received sample after polishing has a total reflectance and a diffuse reflectance value corresponding to approximately half of the total reflectance value. The specular reflectance is calculated as the difference between the total and diffuse reflectance. In the case of as received sample it can be seen that it is highly specular in nature, which is characteristic of a polished metal surface. After heat treatment, the total reflectance value reduces considerably and same is the case with the diffuse reflectance, however they are also highly specular. Anodising at 12.5 V after heat treatment reduces the total reflectance value to one third of the initial value for the as received and did not show significant difference between the diffuse and total reflectance value. On the other hand, the anodising at 20 V results in a reflectance value that is higher compared to 12.5 V and the diffuse reflectance is as high as the total reflectance. The specular reflectance for the anodised samples is minimal implying that the samples lose their glossy nature and appear matte and diffuse. This pattern is observed across all the Zr concentration values in the sample.

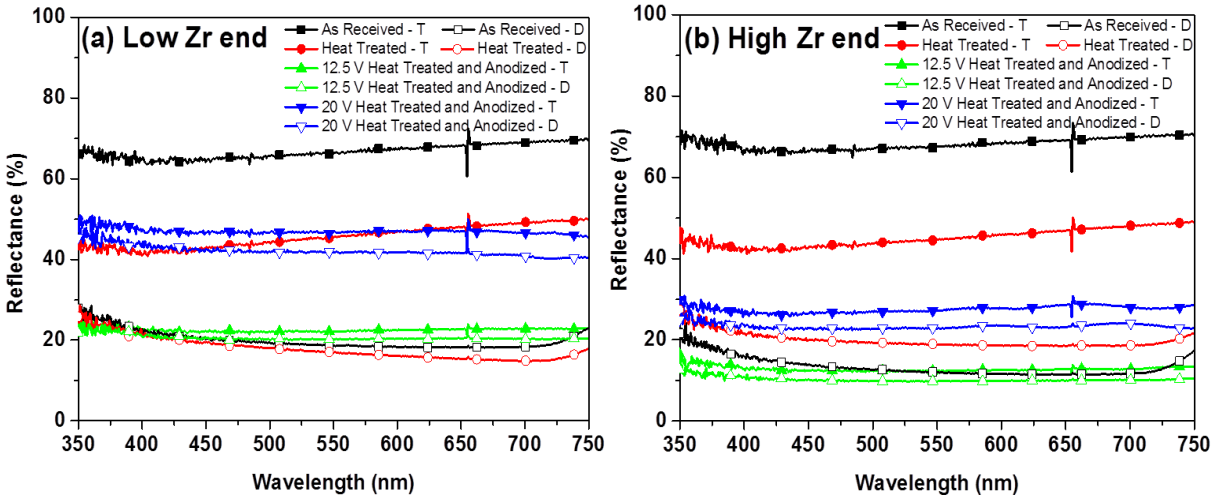

Figure 7.2: Reflectance spectra at visible wavelength region for Al-Zr coatings on pure Al in different conditions taken at location of: (a) Low Zr content and (b) High Zr content; T-Total reflectance and D-Diffuse reflectance.

Spectra taken from sample positions corresponding to a Zr concentration of 21 wt.% (high Zr end) are presented for comparison purpose in Figure 7.2 (b). The major difference observed when compared to spectra observed at high Zr is that the reflectance values are lower. This shows that the increase in Zr concentration makes the samples appear darker after anodising, which is consistent with the results on visual appearance.

7.3.3 X-Ray Diffraction

The GI-XRD pattern of the as-received, heat-treated, and anodised samples are shown in Figure 7.3. The diffraction pattern from the as-coated samples show peaks which correspond to the pure Al. There are no separate peaks which correspond to Zr or related phases, implying that all the Zr is dissolved in the Al matrix. The diffraction pattern of the heat treated samples shows peaks corresponding to Al and Al_3Zr phases. This is in accordance with the data obtained from the EDS results and the phase diagram for the Al-Zr binary system. The anodising process does not give rise to any new sharp peaks in the pattern as it transforms the surface to an amorphous structure. The intensity of the peaks from Al_3Zr phase is lower in the case of samples anodised at 20 V when compared to those at 12.5 V. This might be due to the higher degree of transformation to amorphous phase of the sample when anodised at 20 V.

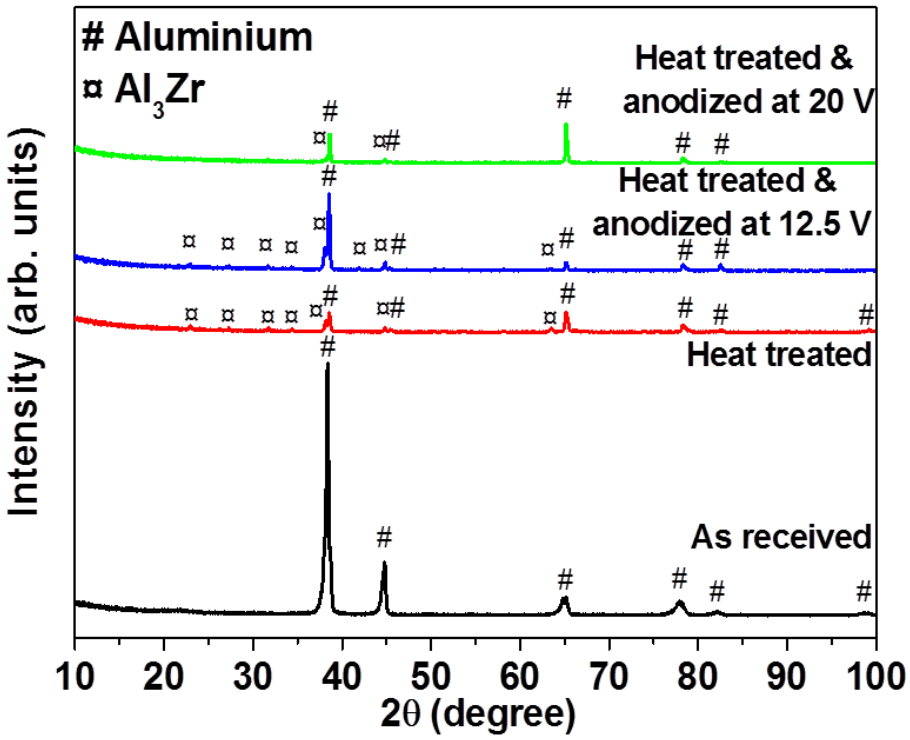

Figure 7.3: GI-XRD pattern for the as received, heat treated, and anodised samples at different voltages after heat treatment.

7.3.4 Scanning Electron Microscopy

Figure 7.4 (a) shows the cross section of the anodised layer and the underlying coating after heat treatment in back scattered imaging mode. The coating after heat treatment shows uniform distribution of the precipitates with long baton type morphology throughout the thickness along with some irregular shaped precipitates in some regions. These precipitates principally appear in the columnar structure arising out of the sputter deposition and growth process.

The EDS data (not shown) of the long baton shaped second phases show the presence of Al and Zr, and the relative concentrations of the elements relates to Al_3Zr phase, which is expected according to the binary alloy Al-Zr phase diagram. Anodising of the sputtered and heat treated coating has resulted in an anodised layer of approx. 2 µm thickness (Figure 7.4 (a), (b)), whereas the anodising at 20 V resulted in slightly thinner anodised layer (Figure 7.4 (c), (d)).

It can be observed in anodised zone that, the baton shaped second phases are only partially transformed by the anodising process at 12.5 V. The remaining non-anodised part of the precipitates appears to retain their contrast (shown with arrow) in the anodised layer (Figure 7.4 (b)). The EDS analysis (not shown) of these non-anodised part does not show any appreciable changes in the concentrations of the constituting elements, but presence of little oxygen. The samples anodised at 20 V show more or less a complete transformation of the second phases to oxide as there is no contrast in the brightness on individual particles (Figure 7.4 (d)). The structure and morphology of the coating was analysed for two other Zr concentrations and was observed to be similar.

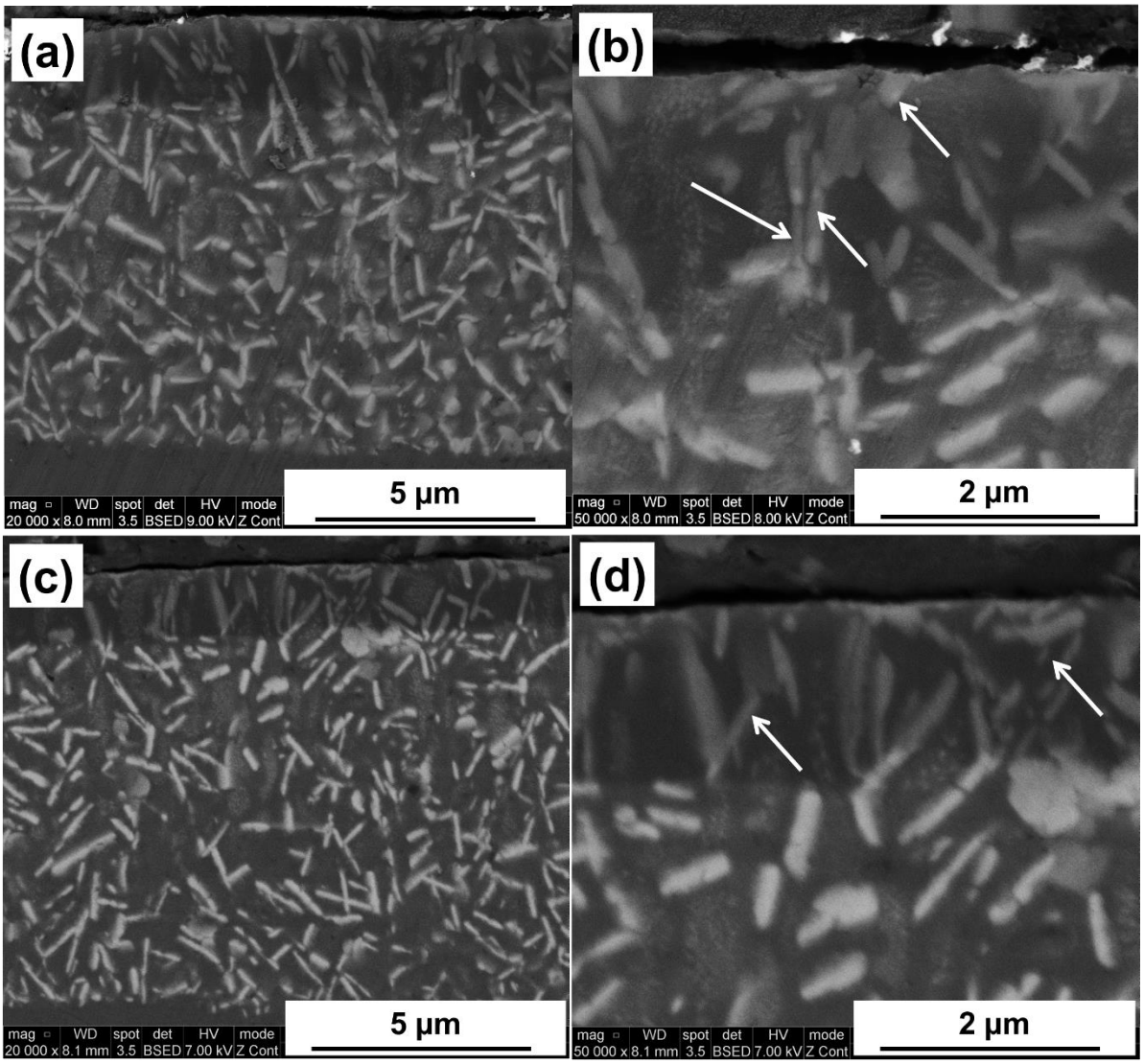

Figure 7.4: Back scattered electron images of Al-15 wt.% Zr coatings cross section on pure Al which were heat treated (550 ˚C for 4 h) and anodised at: (a), (b) 12.5 V and (c), (d) 20 V in sulphuric acid.

7.3.5 Transmission Electron Microscopy

Figure 7.5 (a) shows the bright field transmission electron micrograph in cross section of the sample heat treated and anodised at 12.5 V. The image shows the underlying heat treated sputtered coating containing big batons of Al_3Zr phases along with small precipitates. The anodising process has completely transformed the matrix into oxide; while the precipitates are completely or partially transformed (presence of pore structure can be seen both in the matrix and precipitates). Two partially transformed precipitates can be observed in the pictures which are marked by arrows. High magnification image of the partially transformed precipitate marked in circle in Figure 7.5 (a) is shown in Figure 7.5 (b). The anodised region of the precipitate is transformed into amorphous phase as confirmed by the selective area diffraction analysis and the EDS data shows that it contains Al, Zr and O (not shown), whereas the unaffected region is still crystalline.

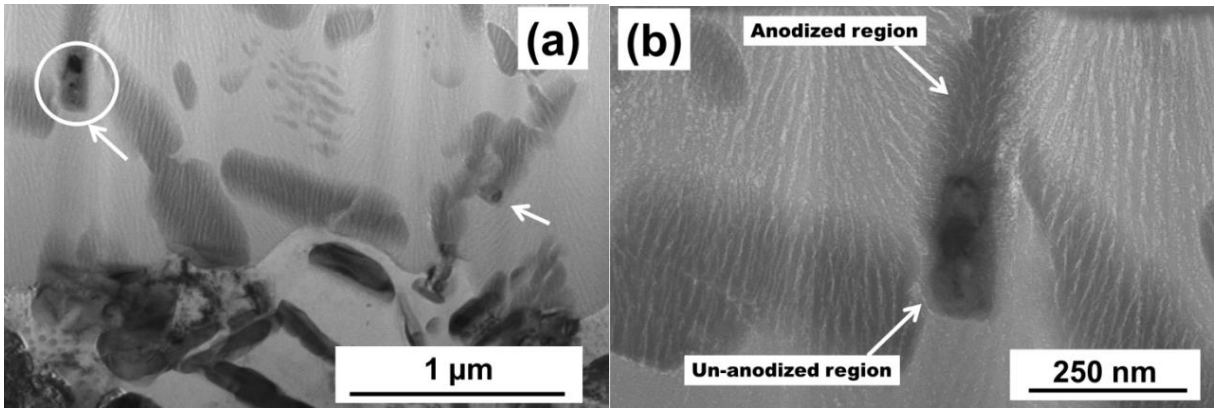

Figure 7.5: TEM bright field images of 12.5 V anodised sample showing: (a) anodised layer and underlying heat treated sputtered coating and (b) partially anodised Al_3Zr precipitate.

7.4 Discussion

The SEM (Figure 7.4) and XRD analysis (Figure 7.3) show that sputter deposition process of Al-Zr targets gives a coating which has Zr dissolved in the Al matrix. The coatings are crystalline and columnar in nature. Heat treatment of these coatings results in uniform precipitation of Al_3Zr phase in a matrix of Al. Two types of precipitate morphology are detected in the heat-treated coatings, one in the form of long batons and another fine precipitates. TEM analysis (Figure 7.5) shows that the baton shaped precipitates and the Al matrix are transformed to amorphous oxides upon anodising. The extent of transformation of the precipitates is dependent on their size and the voltage at which the anodising is carried out. Lower anodising voltages of 12.5 V only partially transform the precipitates whereas the anodising at 20 V transform to a larger extent. The un-anodised region of the precipitates retains their crystalline and metallic nature whereas the oxidized part of the particles is essentially an amorphous mixture of oxides/hydroxides of Al and Zr.

As mentioned earlier, the difference in the refractive index between anodised Al and mixed oxide of Al-Zr is responsible for multiple scattering of light. The larger the number of particles that differ from the matrix in terms of refractive index, the larger the scattering of light. Homogenous distribution of such scattering centres in the anodised Al matrix results in the multiple scattering of light, which disperses the incident light in different directions and creates a diffuse appearance of the surface.

However, the un-anodised region of the Al_3Zr precipitates is still metallic and metals alloys have a high extinction coefficient, which is responsible for their absorption characteristics. The extinction coefficient becomes a prominent factor when the size range of the metal particles is comparable to the wavelength of visible light resulting in high absorption [22]. The current microstructure and morphology of the anodised layer is made up of multi-component metallic particles like Al_3Zr of various sub-micron sizes and shapes, which serve as centres of absorption for the incoming light in an anodised Al surface and therefore induce a dark appearance of the heat-treated and anodised samples (Figure 7.1).

The intensity or fraction of the light that is absorbed depends on the number of absorptive events taking place, which in turn is dependent on the number of metallic absorptive centres in the anodised Al matrix. At low Zr content, increasing the anodising voltage from 12.5 V to 20 V results in fewer precipitates with metallic part in the anodised layer and hence the coatings appear brighter. The diffuse/total reflectance of the coatings (Figure 7.2) increases by factor of two with increasing anodisation voltage, and this is consistent with our observations across the Zr concentration range. At high Zr content, the fraction of un-anodised precipitates in the anodised layer for a given anodisation voltage is much larger and is the reason for the darker appearance with increasing Zr content.

7.5 Conclusions

Al-Zr coatings with Zr concentration varying from 6 wt.% to 23 wt.% on pure Al substrates are studied. The optical reflectivity of the anodised samples with heat treatment is found to be similar in response to

wavelength throughout the Zr composition except that it is slightly darker with increasing concentration of Zr. Heat treatment of the coated samples results in Al_3Zr formation with a dual size distribution. Upon heat treatment, smaller sized second phases (<100 nm) and larger baton shaped precipitates are formed. Anodising in sulphuric acid electrolyte at a voltage of 12.5 V, results in complete oxidation of small size second phase particles, while the larger particles are only partially oxidized. Upon increasing the anodising voltage to 20 V, the extent of oxidation is increased. Amorphous oxides of Al and Zr serve as scattering centres in anodised Al matrix, but as they are only partially anodised they still act as absorption centres and lead to the dominantly absorbing behaviour of the specimen. Anodising voltage of 20 V oxidizes the surface to a greater extent resulting in fewer absorption centres and hence the brighter appearance of the samples compared to those anodised at 12.5 V. From this study, it is shown that the optical appearance of anodised Al alloys can be tailored to obtain a bright appearance by addition of alloying elements that upon anodising would transform to oxides of high refractive index.

References

[1] P.G. Sheasby, The Surface Treatment and Finishing of Aluminium and its Alloys, Finishing Publ, Teddington, 1974. doi:10.1179/000705974798321639.

[2] C.A. Grubbs, Anodizing of Aluminum, Met. Finish. 105 (2007) 397–412. doi:10.1016/S0026-0576(07)80359-X.

[3] F. Keller, M.S. Hunter, D.L. Robinson, Structural Features of Oxide Coatings on Aluminum, J. Electrochem. Soc. 100 (1953) 411. doi:10.1149/1.2781142.

[4] J.P. O'Sullivan, G.C. Wood, The Morphology and Mechanism of Formation of Porous Anodic Films on Aluminium, Proc. R. Soc. A Math. Phys. Eng. Sci. 317 (1970) 511–543. doi:10.1098/rspa.1970.0129.

[5] H. Zhu, T. Wei, M.J. Couper, A.K. Dahle, Effect of Fe-rich particles on the formation of die streaks on anodized aluminum extrusions, Jom. 64 (2012) 337–345. doi:10.1007/s11837-012-0252-1.

[6] G. Gaustad, E. Olivetti, R. Kirchain, Improving aluminum recycling: A survey of sorting and impurity removal technologies, Resour. Conserv. Recycl. 58 (2012) 79–87. doi:10.1016/j.resconrec.2011.10.010.

[7] M. Saenz de Miera, M. Curioni, P. Skeldon, G.E. Thompson, The behaviour of second phase particles during anodizing of aluminium alloys, Corros. Sci. 52 (2010) 2489–2497. doi:10.1016/j.corsci.2010.03.029.

[8] H. Habazaki, K. Shimizu, P. Skeldon, G.E. Thompson, G.C. Wood, X. Zhou, Effects of alloying elements in anodizing of aluminium, Trans. Inst. Met. Finish. 75 (1997) 18–23.

[9] H. Habazaki, K. Shimizu, P. Skeldon, G.E. Thompson, G.C. Wood, X. Zhou, Nanoscale enrichments of substrate elements in the growth of thin oxide films, Corros. Sci. 39 (1997) 731–737. doi:10.1016/S0010-938X(97)89339-0.

[10] L.E. Fratila-Apachitei, H. Terryn, P. Skeldon, G.E. Thompson, J. Duszczyk, L. Katgerman, Influence of substrate microstructure on the growth of anodic oxide layers, Electrochim. Acta. 49 (2004) 1127–1140. doi:10.1016/j.electacta.2003.10.024.

[11] I. Tsangaraki-Kaplanoglou, S. Theohari, T. Dimogerontakis, N. Kallithrakas-Kontos, Y.M. Wang, H.H. Kuo, et al., Effect of alloy types on the electrolytic coloring process of aluminum, Surf. Coatings Technol. 200 (2006) 3969–3979. doi:10.1016/j.surfcoat.2005.02.174.

[12] Y. Ma, X. Zhou, G.E. Thompson, J.O. Nilsson, M. Gustavsson, A. Crispin, Anodizing of AA6063 aluminium alloy profiles: Generation of dark appearance, Surf. Interface Anal. 45 (2013) 1479–1484. doi:10.1002/sia.5219.

[13] Y. Liu, M.A. Arenas, P. Skeldon, G.E. Thompson, P. Bailey, T.C.Q. Noakes, et al., Anodic behaviour of a model second phase: Al-20at.%Mg-20at.%Cu, Corros. Sci. 48 (2006) 1225–1248. doi:10.1016/j.corsci.2005.05.007.

[14] H.H. Strehblow, C.M. Melliar-Smith, W.M. Augustyniak, Examination of Aluminum-Copper Films during the Galvanostatic Formation of Anodic Oxide, J. Electrochem. Soc. 125 (1978) 915. doi:10.1149/1.2131590.

[15] H. Habazaki, X. Zhou, K. Shimizu, P. Skeldon, G.E. Thompson, G.C. Wood, Mobility of copper ions in anodic alumina films, Electrochim. Acta. 42 (1997) 2627–2635. doi:10.1016/S0013-4686(96)00454-9.

[16] Y. Liu, P. Skeldon, G.. Thompson, H. Habazaki, K. Shimizu, Anodic film growth on an Al–21at.%Mg alloy, Corros. Sci. 44 (2002) 1133–1142. doi:10.1016/S0010-938X(01)00115-9.
[17] A.C. Crossland, G.E. Thompson, C.J.E. Smith, H. Habazaki, K. Shimizu, P. Skeldon, Formation of manganese-rich layers during anodizing of Al-Mn alloys, Corros. Sci. 41 (1999) 2053–2069. doi:10.1016/S0010-938X(99)00025-6.
[18] X. Zhou, H. Habazaki, K. Shimizu, P. Skeldon, G.E. Thompson, G.C. Wood, Enrichment-dependent anodic oxidation of zinc in Al-Zn alloys, Corros. Sci. 38 (1996) 1563–1577. doi:10.1016/0010-938X(96)00051-0.
[19] R.A. Synowicki, T.E. Tiwald, Optical properties of bulk c-ZrO2, c-MgO and a-As 2S3 determined by variable angle spectroscopic ellipsometry, Thin Solid Films. 455-456 (2004) 248–255. doi:10.1016/j.tsf.2004.02.028.
[20] G.F. Pastore, Transmission interference spectrometric determination of the thickness and refractive index of barrier films formed anodically on aluminum, Thin Solid Films. 123 (1985) 9–17. doi:10.1016/0040-6090(85)90036-7.
[21] I. Khan, J. Leach, N. Wilkins, The thickness and optical properties of films of anodic aluminium oxide, Corros. Sci. 6 (1966) 483–497. doi:10.1016/S0010-938X(66)80065-3.
[22] R.J.D. Tilley, Colour due to Scattering, in: Colour Opt. Prop. Mater., John Wiley & Sons, Ltd, 2010: pp. 175–196. doi:10.1002/9780470974773.ch5.

7.6 Appendix

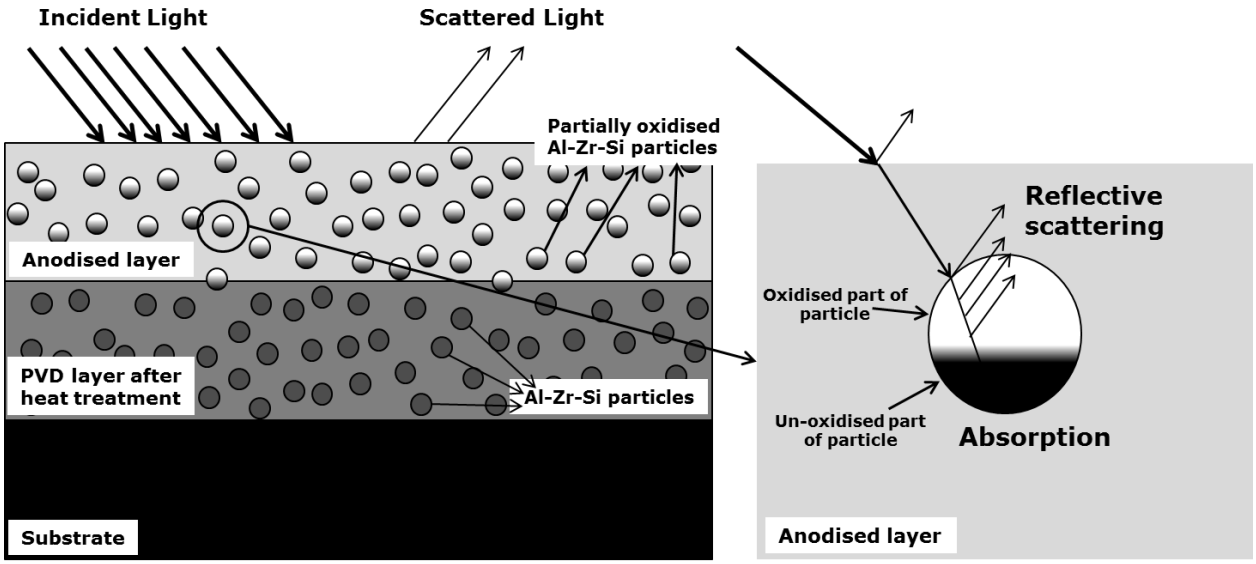

Figure 7.6: Schematic showing the proposed light scattering mechanism leading to darkening of anodised layer.

The schematic in Figure 7.6 shows the proposed mechanism for absorption of light from the anodised layer due to presence of partially anodised or completely un-anodised second phases or Al. In general, this mechanism is applicable to any kind of anodised layer that is optically transparent and contains incorporated metallic species that attenuate the incident light. Recycled Al alloys due to their higher content of intermetallic phases are more prone to such effects in their anodised layer and hence pose a difficulty in maintaining the quality and repeatability of the decorative anodised appearance.

8. Anodising of Al-Ti Coatings: Effect of Heat Treatment (Paper 4)

Anodising of Sputter Deposited Aluminium-Titanium Coatings: Effect of Microstructure on Optical Characteristics*

Abstract

Magnetron sputtered coatings of aluminium containing up to 18 wt.% titanium were deposited on aluminium substrates to study the effect of microstructure on the optical appearance of the anodised layer. The microstructure and morphology were studied using transmission electron microscopy (TEM), X-ray diffraction (XRD), and glow discharge optical emission spectroscopy (GDOES), while the optical appearance was investigated using photo-spectrometry. The microstructure of the coatings was varied by heat treatment, resulting in the precipitation of Al_3Ti phases. The reflectance of the anodised surfaces decreased with titanium content in the as-deposited, and heat-treated states, and after anodising of the as-deposited coatings. Specimens turned grey or black when anodising after heat treatment. Partially anodised Al_3Ti phases were found in the anodised layer, and the interface between substrate and anodised layer was rough, causing light trapping. Progressive darkening of the anodised layer is assumed to be due to the synergetic effect of morphology of incorporated intermetallics and substrate interface.

Keywords: Aluminium; Titanium; Anodising; Microstructure; Appearance; TEM.

Published as M. Aggerbeck, A. Junker-Holst, D.V. Nielsen, **V.C. Gudla, R. Ambat, Anodisation of sputter deposited aluminium-titanium coatings: Effect of microstructure on optical characteristics, Surf. Coatings Technol. 254 (2014) 138-144.*

8.1 Introduction

Anodised aluminium surfaces are widely used for decorative applications, often without colouring. The increased use of recycled aluminium alloys makes it difficult to predict the appearance of the anodised surface due to the presence of higher amounts of impurity elements and second phase particles in the aluminium matrix. Therefore, it is of great interest to understand the optical effect of various elements and second phase particles in the aluminium matrix, including those that are not highly soluble in aluminium.

Magnetron sputtering is a process that can be used for synthesis of non-equilibrium coating compositions, where the amount of various elements can be precisely controlled. Therefore, sputter coatings can be used as model systems for studying the effect of alloying elements and the resulting microstructure on various properties such as corrosion and wear resistance, and optical appearance. Both crystalline and amorphous TiO_2 is known to have high refractive indices, and therefore titanium has been deposited to create anodised aluminium layers containing TiO_2 constituents.

For as-deposited coatings containing up to 40 wt.% titanium it has been reported that the microstructure is comprised of a supersaturated α-Al [1–3]. Hampshire et al. [4,5] investigated the microstructure and mechanical properties of Al-Ti sputtered coatings in the as-deposited form and after heat treatment for 2 h at 600 °C. Additionally, many authors have studied the corrosion properties of Al-Ti coatings in saline [2,6,7], acidic [8–11] and alkaline environments [12].

Studies on the optical properties of a sputtered aluminium film show that both the index of refraction, *n*, and the extinction coefficient, k, are found to be affected by the sputtering parameters [13]. Wöltgens et al. [14] investigated optical properties of magnetron sputtered Al-Ti films of 80 nm thickness containing up to 13 wt.% titanium and found that the reflectance decreases with the titanium concentration both for the as-deposited film and after heat treatment.

Anodising of Al-Ti coatings have been done in several studies [3,15–18], finding the anodised layer to be amorphous with few inclusions of crystalline Al_2O_3 and TiO_2 [3,15,17]. The oxide layer has approximately the same Al-Ti ratio as the coating [3,15,17,18], and Ti^{4+} migrates at rates, which are max. 10 % lower than that of Al^{3+} [15]. Anodising of Al-Ti coatings showed that the pore diameters and pore distance for fixed potential [16,18] and the pore diameter for fixed current [3] increase with the titanium concentration both with and without hydrogen fluoride in the sulphuric acid electrolyte. The thickness of the anodised layer was found to decrease significantly with increasing titanium content when the anodising potential was kept constant [16,18].

The investigations in this paper use magnetron sputtered Al-Ti coatings containing up to 18 wt.% titanium as a model system to investigate the microstructural and optical effects of electrochemically stable titanium rich second phase particles. The as-deposited microstructure was altered by heat treatment and the coatings were anodised in sulphuric acid. Microstructural investigations were performed using transmission electron microscopy, X-ray diffraction and glow discharge optical emission spectroscopy, while optical investigations were performed with reflectance analysis using an integrating sphere spectrometer setup.

8.2 Materials and methods

8.2.1 Materials and heat treatments

All coatings were produced by DC magnetron sputtering on a commercial CemeCon 800/8 machine using two cathodes on each side of a centralised planetary rotating table. The setup and coating procedure are described in detail elsewhere [12].

Specimens of homogenous composition were produced on substrates of AA465.0 (8 wt.% - 11 wt.% silicon and 2 wt.% - 4 wt.% copper) with dimensions of 70 mm x 25 mm x 4 mm. For comparison, AA1050 coatings were produced using two AA1050 targets. Binary Al-Ti coatings were produced using an AA1050 target and a titanium target (grade 1, 99.5 % purity) with cylindrical pins of 1 cm in diameter of AA1050. The aluminium target was sputtered at a power of 2000 W, while the titanium-aluminium target was sputtered at 100 W, 200 W, 400 W, and 600 W achieving titanium concentrations of 3 wt.%, 6 wt.%, 13 wt.%, and 18 wt.% (measured with energy dispersive X-ray spectroscopy (EDS)). The coatings were 11-25 µm in thickness.

These coated specimens were heat-treated for 2 h at 200 °C, 300 °C, 400 °C and 500 °C and subsequently cooled in air.

Al-Ti gradient coatings were produced on substrates of AA6401 (0.35-0.7 wt.% magnesium and 0.25-0.7 wt.% silicon) with dimensions of 220 mm x 40 mm x 5 mm. The targets were displaced with respect to the centre of the sputter coating chamber. The aluminium target was sputtered at a power of 2000 W, while the Ti-Al target was sputtered at a power of 300 W giving a gradually varying composition along the length of the specimen. One specimen with titanium concentrations of 6.5-16.6 wt.% was obtained and cut into pieces, giving three specimens for each of four different concentration spans. The specimens were analysed in the as-deposited state and after heat treatment for 4 h at 500 °C and 4 h at 600 °C and subsequent air cooling. Another specimen was measured to contain 5.0-15.4 wt.% titanium and was anodised in the as-deposited state and subsequently analysed by photospectrometry.

8.2.2 Anodising

The specimens were rinsed with ethanol in an ultrasonic bath for 5 min before 2 min cleaning in 60 g/L AlfiClean™ from AluFinish at 60 °C. Desmutting was performed for 4 min in 69 % nitric acid at room temperature. Anodising was carried out for 20 min in 10 % sulphuric acid at 13-17 °C and a constant voltage of 18-19 V (the specimen containing 8.4-10.5 wt.% titanium, heat treated at 500 °C was instead unintentionally anodised at 20-23 V, but gave the same appearance). Subsequent sealing of the anodised specimens were carried out in demineralised water at 96 °C. All steps except sealing were followed by recurring rinsing in demineralised water.

The as-deposited 5.0-15.4 wt.% gradient sample was anodised for 30 min in sulphuric acid at 12.6 V and hot water sealed in one piece in an industrial setup described elsewhere [19].

8.2.3 Microstructural analysis

Phase identification was done by X-ray diffraction (XRD) measurements on a Bruker D8 Discover™ diffractometer with a copper $K_{\alpha 1}$ beam (1.54 Å) with grazing incidence at 2°. The measurements were performed in a 2θ range from 20° to 100° (only 20° to 85° is presented) with a step size of 0.03° and a step time of 4 s. Obtained diffraction patterns were indexed using the EVA™ Application software [20].

For detailed microstructural analysis, transmission electron microscopy (TEM) was performed using a Tecnai™ G2 20 from FEI operated at 200 keV. A Quanta 200 3D™ DualBeam microscope from FEI equipped with a micromanipulator was used for focused ion beam milling and in-situ lift out of a lamella of 2 µm thickness, followed by thinning in a Helios Nanolab™ DualBeam from FEI. The thickness of the TEM lamella made from the as-deposited coating was 175 nm, whereas the heat-treated and anodised specimen was milled to a thickness of 450 nm in the thickest area, while the oxide layer was milled away faster than the rest of the specimen and was therefore thinner. The final finishing of the lamella was performed by ion milling (2 keV) with low energy to avoid unintended damage from the beam.

Composition depth profiling was done using radio frequency Glow Discharge Optical Emission Spectrometry (GDOES) on a GD Profiler 2 from Horiba Scientific. The argon pressure was set to 650 Pa and the process ran at a power of 35 W. The module and phase was set to 7.6 V and 3.8 V respectively.

8.2.4 Photospectrometry

For optical reflectance measurements, an integrating sphere setup (described in details in [21]) with light from DH2000 from Ocean Optics using an optical fibre entering at 8° with respect to vertical was used. Reflections from the sample surface were integrated within the highly reflecting coated sphere and collected by an optical fibre connected to a photospectrometer (QE65000 from Ocean Optics). Measurements were performed across a wavelength range of 380-760 nm over an integration period of 3 s. All spectra were referenced against a NIST high reflectivity standard.

8.3 Results

8.3.1 Photographs

Figure 8.1shows the appearance of the anodised specimens of the lowest titanium concentrations for the as-deposited specimens and after heat treatment. For all titanium concentrations, anodising after heat treatment at 500 °C and 600 °C gave a homogenous dark grey, brown or even black appearance. The as-deposited specimens showed a more regular light appearance after anodising, and in some cases with colour bands due to thin film interference [22,23]. The concentrations shown in Figure 8.1 are the measured titanium content on the as-deposited specimens. Similar appearance was found for the other titanium concentrations.

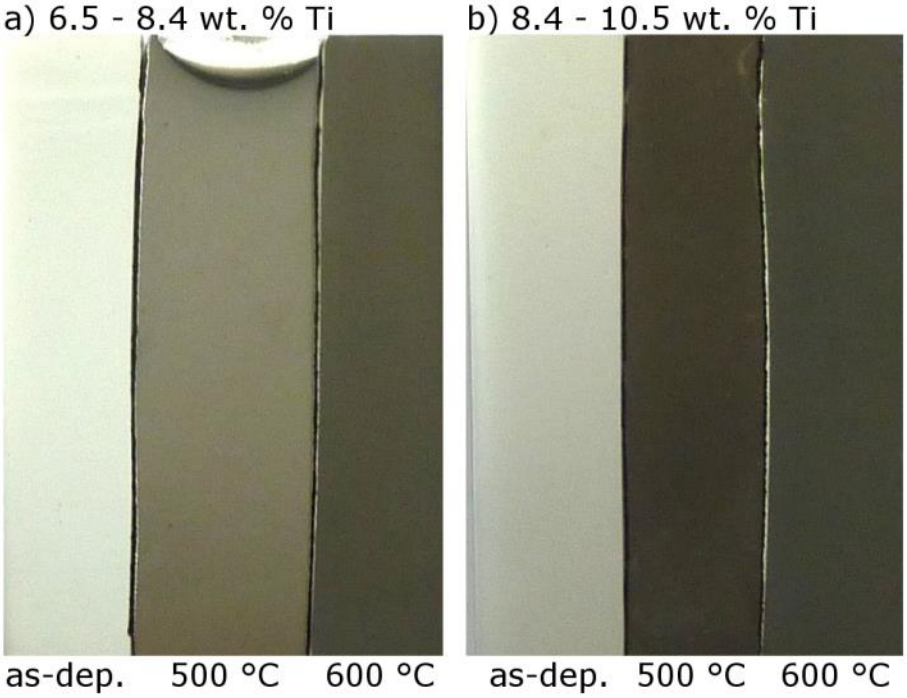

Figure 8.1: Photographs of anodised specimens for, left: as-deposited, middle: 500 °C, and right: 600 °C for specimens with a titanium concentrations of: (a) 6.5-8.4 wt.%, and (b) 8.4-10.5 wt.%.

8.3.2 Microstructural investigation

The TEM image of the as-deposited specimen containing 13 wt.% titanium (Figure 8.2 (a)) showed a layered structure with a general periodicity of 32 nm ± 4 nm due to the use of two different targets placed on opposite sides of the rotating specimen. Layers with bright appearance were mainly deposited from the AA1050 target with lower amounts of titanium, while the dark layers were rich in titanium. The bright layers of low titanium concentration were measured to be 22 nm – 30 nm and the dark titanium rich layers were measured to 2.5 nm – 9.5 nm depending on which layer was measured and how the layer boundaries were defined. Figure 8.2 (b) gives an overview of a specimen containing 10 wt.% titanium that was heat-treated for 4 h at 600 °C followed by anodising.

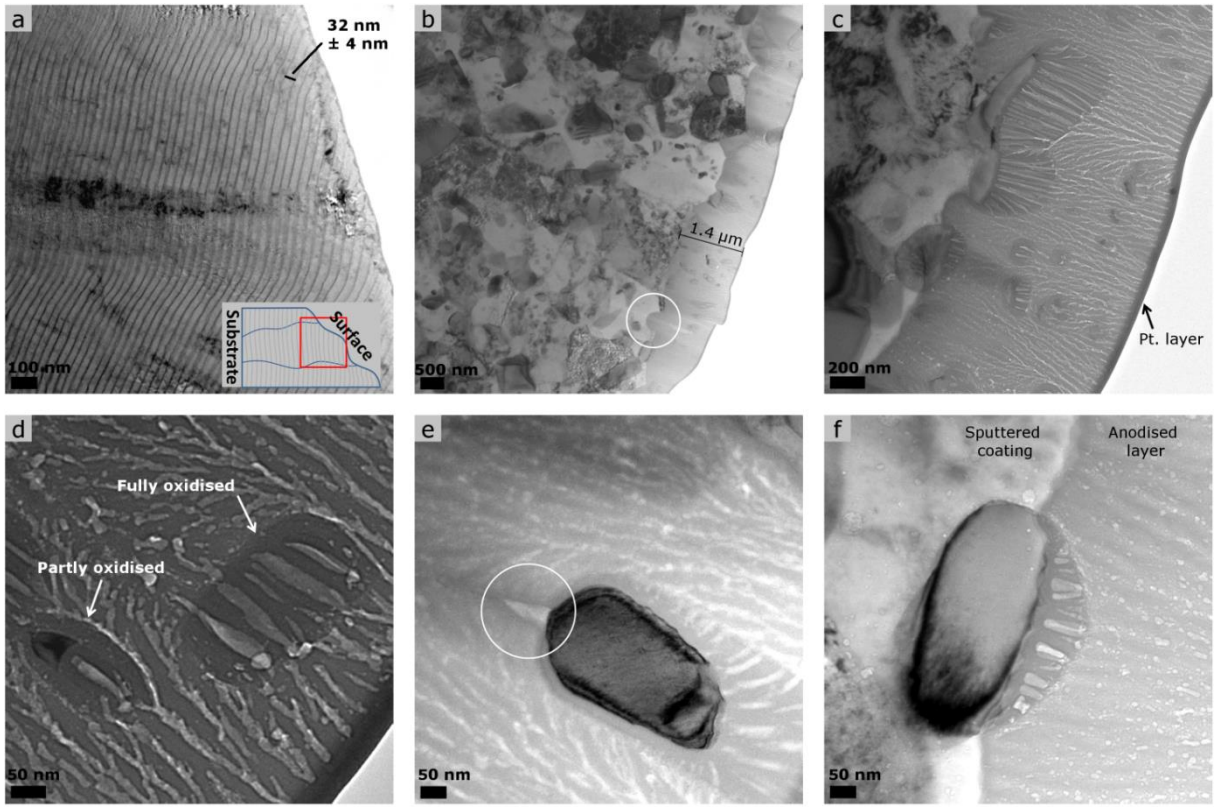

Figure 8.2: Cross section transmission electron microscopy images of: (a) as-deposited coating containing 13 wt.% Ti, and (b)-(f) heat-treated and anodised specimen containing approximately 10 wt.% Ti.

After heat treatment the layered structure was dissolved and a homogeneously appearing matrix containing precipitates with an average size of approximately 250 nm x 550 nm was formed. All precipitates were of the same composition, and the difference in contrast is due to the orientation with respect to the electron beam. The average thickness of the anodised layer was approximately 1.2 µm. The encircled part of Figure 8.2 (b) shows an area with no particles, where the anodising continued between two particles. The dark layer appearing at the oxide surface in Figure 8.2 (c) is the platinum layer deposited for protection during the milling and lift out process. Particles in the anodised layer were found to be partly or fully oxidised as presented in Figure 8.2 (c) and (d). The pores originated from the anodising process and were measured to be 8-10 nm in diameter in the aluminium matrix. The titanium-containing phases featured both narrow and wider pores with diameters of the wider pores of 25-35 nm. Furthermore, the pores in the aluminium collapsed during sealing, whereas both the narrow and the wide pores in the titanium-rich particles seemed unaffected by the sealing process. A bright region behind a particle (Figure 8.2 (e)), was expected to be un-anodised metallic aluminium [24–26], where Walmsley et al. [26] found similar areas behind partly oxidised particles and identified these as un-oxidised aluminium. Figure 8.2 (f) shows a partly anodised particle in the oxide-substrate interface.

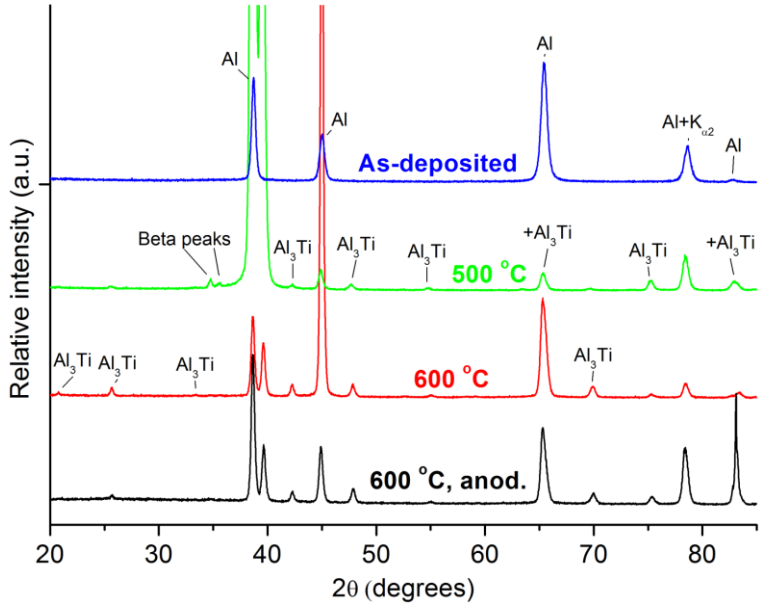

Figure 8.3: X-ray diffraction measurements for coatings containing approximately 12 wt.% Ti in the as-deposited and heat-treated condition.

XRD measurements (Figure 8.3) were used for phase identification of the as-deposited film containing 12 wt.% titanium, after heat treatment for 4 h at 500 °C and 600 °C, and for a heat-treated and anodised specimen. For the as-deposited specimen, only peaks for the α-Al phase were found, whereas for the specimens heat-treated at 500 °C and 600 °C, additional peaks corresponding to the Al_3Ti phase were found. No oxide containing phases were identified for the anodised specimen.

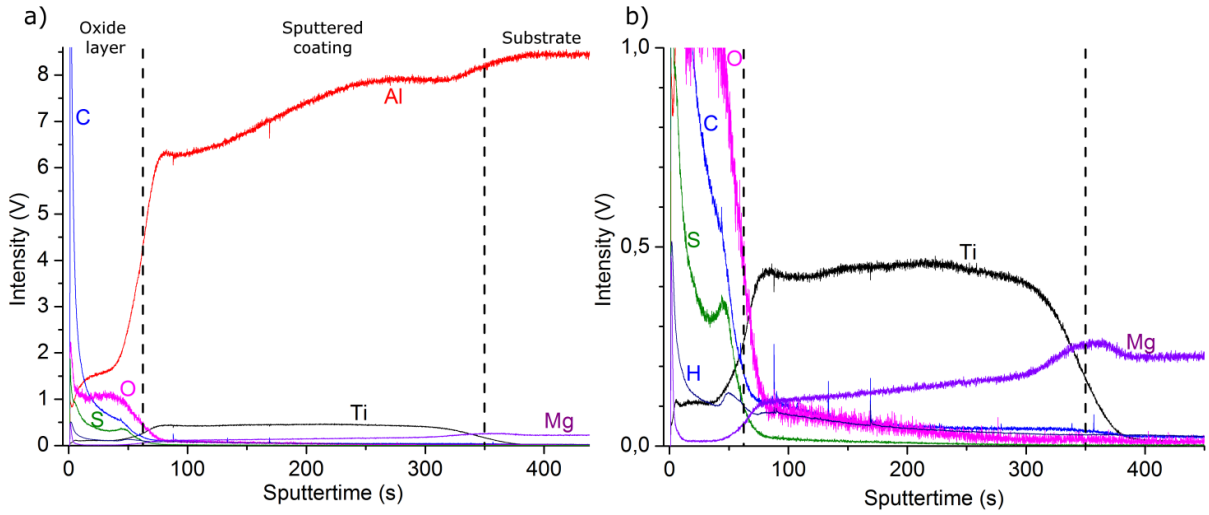

Figure 8.4: Glow discharge optical emission spectroscopy measurements of an anodised coating containing about 7 wt.% Ti on an AA6401 substrate: (a) overview, and (b) same measurement with magnified intensity scale.

The GDOES measurements of an anodised specimen containing 7 wt.% titanium are presented with an overview and magnified view of the lower intensity values (Figure 8.4 (a) and (b) respectively). From crater depth measurements (not presented) the sputter rate was calculated to be ~30 nm/s. In Figure 8.4 (a) and (b), dotted lines indicate the interface between the anodised layer and the sputtered coating and the coating-substrate interface. The oxide-coating interface was at about 1.9 µm (~63 s) from the surface, and the coating-substrate interface was at about 10.5 µm (~350 s) from the surface. It is found that the aluminium and oxygen

signals stabilised briefly within the oxide layer. This was followed by increasing signal for aluminium and decreasing signal for oxygen when closing in on the interface between the anodised layer and the sputtered coating. Presence of sulphur was attributed to the use of sulphuric acid in the anodising process and hydrogen containing species were expected to be incorporated into the film both during anodising and especially during sealing. The carbon peak at the surface was due to ethanol cleaning just before the measurement. Mainly aluminium and titanium was found in the sputtered coating. The oxygen concentration decreased and the magnesium concentration increased throughout the sputtered coating, due to diffusion from the AA6401 substrate during heat treatment.

8.3.3 Photospectrometry measurements

Photospectrometry measurements of the as-deposited coatings (Figure 8.5 (a)) showed that the total reflectance decreased with increasing titanium concentration. Additionally, it was found that the fraction of longer wavelengths increased with the titanium concentration i.e. the pure aluminium coating had a slight blue tint, whereas the coatings containing 13 wt.% and 18 wt.% titanium had a red tint. In Figure 8.5 (d) the reflectance of the as-deposited coatings are plotted at 600 nm as a function of titanium concentration (squares). Additionally, similar values for specimens heat-treated for 2 h at 300 °C are plotted (circles). In both cases the reflectance decreased with increasing titanium concentration. A series of specimens containing 13 wt.% titanium was heat-treated at different temperatures and the reflectance characteristics are presented in Figure 8.5 (b) and the reflectance at 600 nm in Figure 8.5 (e). The reflectance in general remains constant for specimens heat-treated for 2 h at 400 °C, while the reflectance decreased after heat treatment at 500 °C (Figure 8.5 (e)). Furthermore, as seen in Figure 8.5 (b), the reflectance of the anodised specimen heat treated at 500 °C was constant over the range of wavelengths, whereas for other specimens, reflectance has increased towards red.

The as-deposited and anodised specimen showed large interference fringes, making the plot harder to evaluate. Therefore, Figure 8.5 (c) presents curves, which are smoothed by adjacent averaging in Origin™, enabling comparison of the reflectance. A decrease in the reflectance was found from 450 nm towards lower wavelengths. The plot of reflectance at 600 nm (Figure 8.5 (f)) shows that the reflectance decreased with increasing titanium concentration from 8 wt.% titanium and more. The oxide thickness was measured by cross section SEM images (not presented) to be 3.8 µm for 5.0 wt.% titanium to 1.1 µm for 15.4 wt.% titanium.

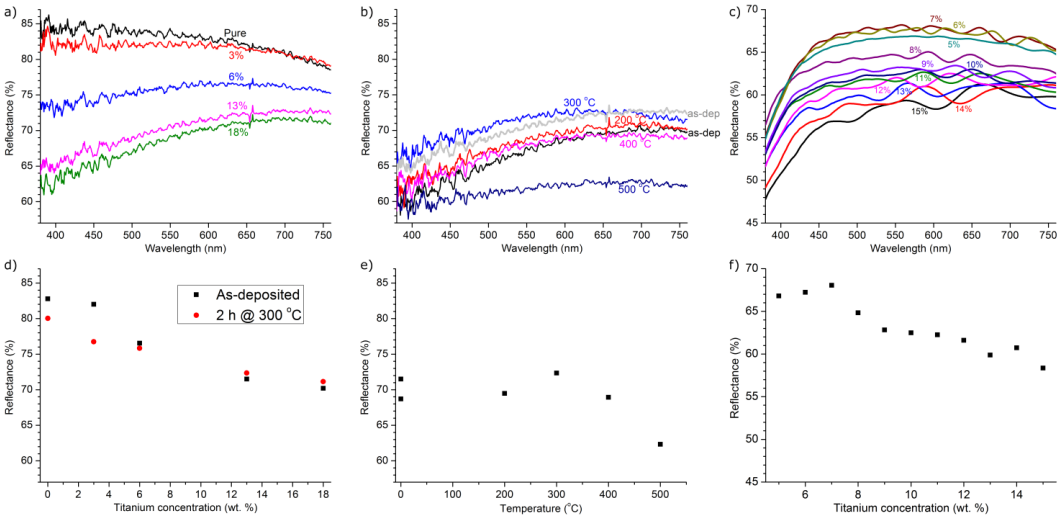

Figure 8.5: Photospectrometry measurements of: (a) as-deposited coatings, (b) reflectance as a function of heat-treatment temperature for specimens containing 13 wt.% Ti, (c) intensities measured on as-deposited, anodised specimen, smoothed by adjacent averaging in Origin. Reflectance values corresponding to 600 nm wavelength from (a), (b), and (c) are extracted and plotted in (d), (e) and (f) respectively.

8.4 Discussion

8.4.1 Microstructure and appearance of as-deposited coatings before and after anodising

The microstructure of the as-deposited coating was found to be alternating layers of low and high content of titanium (Figure 8.5 (a)), which is similar to the structure of magnetron sputtered coatings reported in the literature with similar configuration of targets and rotation of specimens [14,15]. Since no titanium-containing phases were formed during deposition (Figure 8.3), the coating is expected to be supersaturated α-Al, at least in the aluminium-rich layers [1–3]. The reflectance of the specimens is well correlated with the titanium concentration (Figure 8.5 (b)), which is not expected, as the layered structure should negate the effect of the titanium concentration. The penetration depth of light at 500 nm (the depth where the radiation intensity is ~37 % of the original incoming intensity) is calculated to be approximately 6.6 nm for pure aluminium and 16.5 nm for titanium. Furthermore, reflected light needs to return to the surface, doubling the optical path. Since the alternating layers had a period of 32 nm (Figure 8.5 (a)) for the specimen containing 13 wt.% titanium, it is not expected, that the light necessarily would be affected by both aluminium- and titanium-rich layers for all of the specimens. Furthermore, the measured layers are from different coatings produced in different processes, so that it is not expected that the same type of layer is at the surface for all specimens. The observed correlation between titanium concentration and the reflectance has not been explained. However, previous studies on Al-Ti coatings with a layered structure with a periodicity of only 1.6 nm [14] showed similar behaviour, where the reflectance also decreased with the titanium concentration.

After anodising of the as-deposited coating, wide colour fringes due to thin film interference [22,23] were observed (Figure 8.5 (c)). The oxide thickness was found to decrease with titanium concentration as previously reported [16,18]. The reflectance of the anodised specimen decreased with the titanium concentration (Figure 8.5 (c)), whereas for a regular aluminium alloy it is generally expected that the reflectance decreases with the thickness of the anodised layer [23].

8.4.2 Microstructure and appearance of heat-treated coatings before and after anodising

Heat treatment of the specimens modified the layered structure and resulted in the formation of Al_3Ti phases (Figure 8.2 (b) and Figure 8.3). Previous work identified Al_3Ti phases to form for heat treatment at 350 °C and more [5,12,14], which corresponds well with the XRD results presented in Figure 8.3. From the GDOES measurement it was found that the magnesium diffused from the substrate into the sputtered coating (Figure 8.4 (b)), however no magnesium containing phases were found in the XRD measurements (Figure 8.3), which might be due to the low concentration. Wöltgen et al. [14] found that the reflectance and the resistivity of the film decreased with the titanium concentration after heat treatments, as found in Figure 8.5 (d) (circles). In Figure 8.5 (b) and (e) it is found that the reflectance increases with heat treatment up to 300 °C followed by a decrease in the reflectance at higher heat treatment temperatures. The same trend was found for thin Al-Ti films [14], where the reflectance decrease from around 210 °C, due to the much lower thickness (80 nm) of the investigated films. It is therefore expected that the precipitation and growth of Al_3Ti phases, caused by the heat treatment, causes the resistivity and the reflectance to decrease.

Due to the passivating nature of titanium, Al_3Ti particles are in most cases only partially oxidised during anodising. This creates a structure with an oxidised upper part and a lower metallic core (Figure 8.2 (c) and (f)). It is known that anodised aluminium is amorphous [27] and that the anodised Al-Ti coatings are amorphous with low amounts of crystalline Al_2O_3 and TiO_2 phases [3,15,17]. This is well supported by the lack of oxide-containing phases in the XRD measurement of the anodised specimen (Figure 8.3). In general it is expected that the presence of intermetallic particles in the anodised layer causes darkening [24,25,28–30]. Furthermore, previous studies have shown that similar darkening effects can be created by holes within the oxide [31,32] and by very high substrate roughness before anodising [33]. Therefore, the darkening effect might be due to various effects for different specimens.

8.4.3 The darkening mechanism

The surface structure consists of a matrix of anodised and sealed aluminium. The matrix contains partially oxidized Al_3Ti particles with an oxide and an un-oxidised part. Furthermore, there is an interface between the anodised layer and the sputtered coating.

For the darkening effect to happen, some absorbing constituents are expected within the anodised layer. It has previously been reported that metallic parts such as the aluminium substrate [13], un-oxidised aluminium [24–26] and the un-oxidised part of intermetallic particles [34] all absorb light. The anodised and sealed aluminium matrix, and the oxidised part of the Al_3Ti particles are expected to have only little absorption.

Due to the low thickness of the oxide film (1.2 µm), additional effects are expected, causing the light to travel longer in the medium and thereby increasing the absorption of light. This can happen due to scattering, causing light to move inclined and parallel to the surface. Scattering is expected to happen as surface scattering at the interface between the anodised layer and the sputtered coating and in the metallic part of the particles. Furthermore, changes in refractive indices of the oxides will cause additional scattering. The interface between the anodised layer and the sputtered coating was quite rough as observed in Figure 8.2 (b) and (c). In comparison to a rough surface in air, the subsurface morphology appears optically larger when the background medium (the anodised layer) has a refractive index larger than air. Since we can expect a refractive index around 1.6 (the refractive index of the main constituents are $n_{Böhmite}$: ~1.65 and $n_{Gibbsite}$: ~1.57), the scattering effects at the interface are comparable to the same structure enlarged by 1.6 in air.

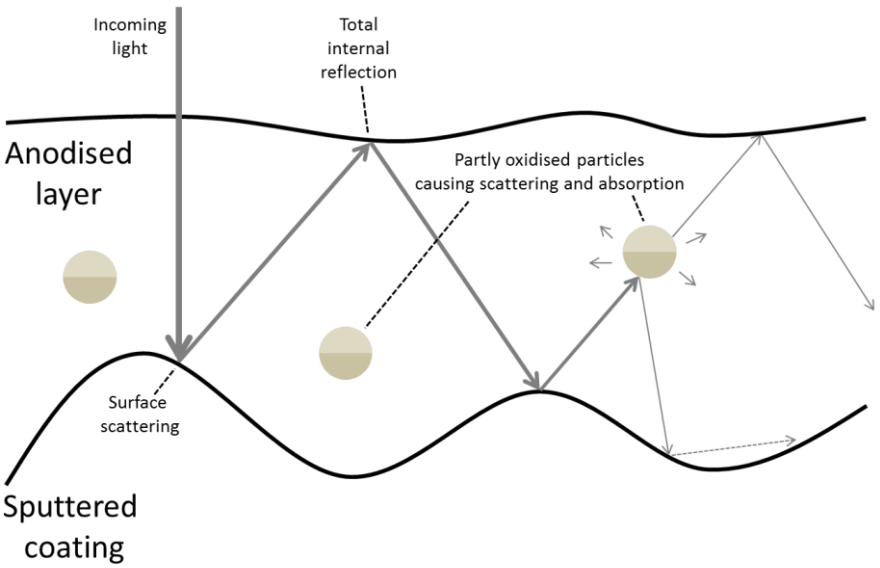

Figure 8.6: Schematic showing the possible reasons for oxide film darkening during anodising.

A preliminary suggestion to the darkening mechanism is presented in Figure 8.6, where incoming light hits the subsurface interface and is partly absorbed during surface scattering (reflection). For light returning to the surface at angles larger than the critical angle, ~38.7° to the surface normal ($n_{\text{anodised layer}}$ = 1.60), the light is experiencing total internal reflection in the interface of the anodised layer and the air without any loss. Subsequently, the light will again be reflected by the subsurface interface causing additional absorption. Most of the incoming light is therefore expected to reflect back and forth between the top surface of the anodised layer and the subsurface, denoted light trapping. Only light returning to the surface at an angle smaller than the critical angle will leave the oxide. Furthermore, the presented specimens contain absorbing particles inside the oxide causing the mean free path of a light wave to be even smaller, and thereby causing both more absorption and scattering.

The darkening effect is therefore expected to be caused by absorbing and scattering constituents in the oxide layer and the roughness of the interface between the anodised layer and the metallic sputtered

coating. The described mechanism is yet to be verified, but all these factors seem to contribute in a significant way.

The cross section TEM images (Figure 8.2) show evidence of the presence of local changes in oxide structures, metallic cores or shadow regions, which all support the mechanisms explained above. Similar partially oxidised intermetallics are found previously for silicon- [35,36], iron-rich [37,38], and unidentified particles in AA6060 [26]. Presence of impurities and alloying elements have been reported to darken the anodised layer [24,25,28,30], and the effect might be due to an undissolved part of the particles absorbing and scattering the light [34]. Electrochemical oxidation of intermetallics in the anodising bath depends on its electrochemical behaviour, and a number of intermetallics in commercial aluminium alloys are oxidised slower (e.g. Al_3Fe and $Al_9Fe_2Si_2$) or faster (e.g. Mg_2Al_3 and Mg_2Si) than the aluminium matrix [28,39]. It has been reported that Al_3Ti has a higher potential than the aluminium matrix [12] and that Al_3Ti particles are cathodic during etching [28,39] and remain unchanged and incorporated into the oxide film during anodising [28,39]. The parameters of the sulphuric anodising is not specified in [28,39] and therefore the rather high anodising voltage in this study might have caused the Al_3Ti particles to partly oxidise. Furthermore, it has been reported that the electrochemical behaviour of some intermetallic particles is highly dependent on the particle size [28,39]. Similarly, both fully and partly oxidised intermetallics are found in Figure 8.2, where the biggest particles are not fully oxidised. The pores are wider in the Al_3Ti particles as previously reported [3,16,18]. Habazaki et al. [15] found that the migration rate of Ti^{4+} are up to 10 % slower than the rate of Al^{3+}, which does not directly correlate with this picture, where there seems to be a bigger difference in the oxidation rate, however, this can be correlated to both particle size and the fact that this is Al_3Ti particles instead of metallic Ti as in [15].

It is known that surface structures such as grain boundary grooves [40–42] and surface scallops [36,43] are formed due to alloying elements and impurities, and that these cause a decrease in the reflectance of aluminium alloys. Since these surface structures are expected to cause a more diffuse reflection from the interface between the anodised layer and the sputtered substrate, it could also be caused by light trapping. Results presented elsewhere [19] show that the total reflectance of polished alloys are not decreased by anodising, whereas the total reflectance of etched specimens decreased with relation to the previous etching roughness [19]. This is in line with the proposed darkening mechanism.

The results presented in this paper show that the addition of titanium into aluminium based magnetron sputtered coatings decreases the reflectance of the specimen. After heat-treatment and anodising the specimens turned dark. It is suggested that the darkening mechanism is caused by partially oxidised Al_3Ti particles and a rough interface between the anodised layer and the sputtered coating. Controlling the subsurface roughness and the amount of partially oxidised particles in anodised layer of e.g. recycled aluminium alloys, might therefore be a way to achieve the desired appearance in spite of high amounts of impurities and alloying elements.

8.5 Conclusions

Magnetron sputtered coatings containing up to 18 wt.% titanium were investigated in the as-deposited form and after heat-treatment before and after anodising. It was found that:

- A structure of alternating layers containing low and high amounts of titanium was found, with α-Al as the only identified phase in the as-deposited coatings. After heat treatment for 4 h at 600 °C, a homogenous aluminium matrix and high concentrations of elongated Al_3Ti precipitates, with an average length of approximately 0.5 µm and an aspect ratio of about 1:2, appeared.
- Photospectrometry measurements showed that the reflectance decreases with increasing titanium concentration for the as-deposited specimens, for the specimens heat-treated for 2 h at 300 °C, and for the as-deposited and anodised specimens.
- Coatings containing 6-16 wt.% titanium that were heat-treated for 4 h at 500 °C and 600 °C all turned dark grey, brown or black during anodising.

- Transmission electron microscopy of a specimen containing 10 wt.% titanium showed an oxide film of 1.2 µm, containing many partially oxidised Al_3Ti particles with a metallic core. In some cases, expected un-oxidised aluminium was found behind the particles. Pores of 8-10 nm in diameter were found both in the aluminium matrix and in the Al_3Ti particles, where additional pores of 25-35 nm in diameter were also found.

References

[1] J.C. Oliveira, A. Manaia, J.P. Dias, A. Cavaleiro, D. Teer, S. Taylor, Structure and mechanical properties of Ti–Al films deposited by magnetron sputtering, Surf. Coatings Technol. 200 (2005) 395–398. doi:10.1016/j.surfcoat.2005.01.078.

[2] F. Sanchette, A. Billard, Main features of magnetron sputtered aluminium-transition metal alloy coatings, Surf. Coatings Technol. 142-144 (2001) 218–224.

[3] V.C. Nettikaden, H. Liu, P. Skeldon, G.E. Thompson, Porous anodic film formation on Al–Ti alloys in sulphuric acid, Corros. Sci. 57 (2012) 49–55. doi:10.1016/j.corsci.2011.12.035.

[4] J. Hampshire, P.J. Kelly, D.G. Teer, The tribological properties of co-deposited aluminium – titanium alloy coatings, Thin Solid Films. 447-448 (2004) 392–398. doi:10.1016/S0040-6090.

[5] J. Hampshire, P.J. Kelly, D.G. Teer, The structure of co-deposited aluminium–titanium alloy coatings, Thin Solid Films. 447-448 (2004) 418–424. doi:10.1016/j.tsf.2003.08.006.

[6] Q. Yan, H. Yoshioka, H. Habazaki, A. Kawashima, K. Asami, K. Hashimoto, Passivity and its breakdown on sputter-deposited amorphous Al-Ti alloys in a neutral aqueous solution with Cl-, Corros. Sci. 31 (1990) 401–406.

[7] H. Yoshioka, Q. Yan, K. Asami, K. Hashimoto, Pitting potential and structure of sputter-deposited Al-Ti alloys, Mater. Sci. Eng. A. 134 (1991) 1054–1057.

[8] K. Hashimoto, N. Kumagai, H. Yoshioka, J.H. Kim, E. Akiyama, H. Habazaki, et al., Corrosion-resistant amorphous surface alloys, Corros. Sci. 35 (1993) 363–370.

[9] Q. Yan, H. Yoshioka, H. Habazaki, A. Kawashima, K. Asami, K. Hashimoto, The corrosion behavior of sputter-deposited Al-Ti alloys in 1 N HCl, Corros. Sci. 32 (1991) 327–335.

[10] E. Akiyama, H. Habazaki, A. Kawashima, K. Asami, I.L. Hashimoto, K. Hashimoto, Corrosion-resistant amorphous aluminum alloys and structure of passive films, Mater. Sci. Eng. A. 226-228 (1997) 920–924.

[11] H. Yoshioka, Q. Yan, H. Habazaki, A. Kawashima, K. Asami, K. Hashimoto, Passivity and its breakdown on sputter-deposited amorphous Al-early transition metal alloys in 1 M HCl at 30°C, Corros. Sci. 31 (1990) 349–354. doi:10.1016/0010-938X(90)90130-W.

[12] M. Aggerbeck, K. Rechendorff, K. Dirscherl, R. Ambat, Saline and alkaline corrosion resistance of aluminium-titanium coatings prepared by plasma magnetron sputtering, Submitt. to Corros. Sci. (n.d.).

[13] S. Van Gils, T. Dimogerontakis, G. Buytaert, E. Stijns, H. Terryn, P. Skeldon, et al., Optical properties of magnetron-sputtered and rolled aluminum, J. Appl. Phys. 98 (2005). doi:10.1063/1.2085315.

[14] H.W. Wöltgens, I. Friedrich, W.K. Njoroge, W. Theiß, M. Wuttig, Optical, electrical and structural properties of Al-Ti and Al-Cr thin films, Thin Solid Films. 388 (2001) 237–244. doi:10.1016/S0040-6090(01)00807-0.

[15] H. Habazaki, K. Shimizu, P. Skeldon, G.E. Thompson, G.C. Wood, Formation of amorphous anodic oxide films of controlled composition on aluminium alloys, Thin Solid Films. 300 (1997) 131–137. doi:http://dx.doi.org/10.1016/S0040-6090(96)09491-6.

[16] S. Berger, H. Tsuchiya, P. Schmuki, Transition from nanopores to nanotubes : self-ordered anodic oxide structures on titanium-aluminides, Chem. Mater. 20 (2008) 3245–3247. doi:10.1016/j.cossms.2007.08.004.(22).

[17] A.N. Kamkin, L.A. Fishgoit, A.D. Davydov, Composition and structure of anodic oxide films on titanium–aluminum alloys by fast electron reflection diffraction, rutherford backscattering, and secondary neutral particle mass spectrometry, Russ. J. Electrochem. 39 (2003) 738–743.

[18] H. Tsuchiya, S. Berger, J.M. Macak, A. Ghicov, P. Schmuki, Self-organized porous and tubular oxide layers on TiAl alloys, Electrochem. Commun. 9 (2007) 2397–2402. doi:10.1016/j.elecom.2007.07.013.

[19] M. Aggerbeck, S. Canulescu, K. Dirscherl, V.E. Johansen, S. Engberg, J. Schou, et al., Appearance of anodised aluminium: Effect of alloy composition and prior surface finish, Surf. Coatings Technol. 254

(2014) 28–41. doi:10.1016/j.surfcoat.2014.05.047.
[20] SOCABIM, Software: EVA Application 6.0.0.1, (2000).
[21] S. Daviðsdóttir, S. Canulescu, K. Dirscherl, J. Schou, R. Ambat, Investigation of photocatalytic activity of titanium dioxide deposited on metallic substrates by DC magnetron sputtering, Surf. Coatings Technol. 216 (2013) 35–45. doi:10.1016/j.surfcoat.2012.11.015.
[22] S. Van Gils, P. Mast, E. Stijns, H. Terryn, Colour properties of barrier anodic oxide films on aluminium and titanium studied with total reflectance and spectroscopic ellipsometry, Surf. Coatings Technol. 185 (2004) 303–310. doi:10.1016/j.surfcoat.2004.01.021.
[23] T.S. Shih, P.S. Wei, Y. Sen Huang, Optical properties of anodic aluminum oxide films on Al1050 alloys, Surf. Coatings Technol. 202 (2008) 3298–3305. doi:http://dx.doi.org/10.1016/j.surfcoat.2007.12.002.
[24] M. Saito, Unoxidized Aluminum Particles in Anodic Alumina Films, J. Electrochem. Soc. 140 (1993) 1907. doi:10.1149/1.2220737.
[25] M. Saito, Y. Shiga, M. Miyagi, K. Wada, O. Sachiko, Optical Transmittance of Anodically Oxidized Aluminum Alloy, Jpn. J. Appl. Phys. 34 (1995) 3134. http://stacks.iop.org/1347-4065/34/i=6R/a=3134.
[26] J.C. Walmsley, C.J. Simensen, A. Bjørgum, F. Lapique, K. Redford, The Structure and Impurities of Hard DC Anodic Layers on AA6060 Aluminium Alloy, J. Adhes. 84 (2008) 543–561. doi:10.1080/00218460802161590.
[27] J.D. Edwards, F. Keller, The structure of anodic oxide coatings, Trans. AIME, Inst. Met. Div. 156 (1944) 288–300. http://scholar.google.com/scholar?hl=en&btnG=Search&q=intitle:The+Structure+of+Anodic+Oxide+Coatings#4 (accessed November 8, 2013).
[28] R. Akeret, H. Bichsel, E. Schwall, E. Simon, M. Textor, Influence of chemical composition and fabrication procedures on the properties of anodised aluminium surfaces, Trans. Inst. Met. Finish. 68 (1990) 20–28.
[29] L.F. Huang, M. Saito, M. Miyagi, Polarization characteristics of alumina films anodized at low temperature, Jpn. J. Appl. Phys. 32 (1993) 3169–3174. doi:10.1143/JJAP.32.3169.
[30] N. Tabrizian, H.N. Hansen, P.E. Hansen, R. Ambat, P. Møller, Influence of annealing and deformation on optical properties of ultra precision diamond turned and anodized 6060 aluminium alloy, Surf. Coatings Technol. 204 (2010) 2632–2638. doi:10.1016/j.surfcoat.2010.02.002.
[31] A. Junker-Holst, D. V Nielsen, Effect of Microstructure of Plasma Sputtered Coatings on Optical Appearance, Technical University of Denmark, 2012.
[32] Y. Ma, X. Zhou, G.E. Thompson, J.O. Nilsson, M. Gustavsson, A. Crispin, Anodizing of AA6063 aluminium alloy profiles: Generation of dark appearance, Surf. Interface Anal. 45 (2013) 1479–1484. doi:10.1002/sia.5219.
[33] M. Aggerbeck, Master thesis: Optical appearance of aluminium, 2010.
[34] V.C. Gudla, S. Canulescu, R. Shabadi, K. Rechendorff, J. Schou, R. Ambat, Anodization and Optical Appearance of Sputter Deposited Al-Zr Coatings, in: J. Grandfield, TMS (Eds.), Light Met. 2014, John Wiley & Sons, Inc., 2014: pp. 369–373. doi:10.1002/9781118888438.ch63.
[35] L.. Fratila-Apachitei, F.D. Tichelaar, G.E. Thompson, H. Terryn, P. Skeldon, J. Duszczyk, et al., A transmission electron microscopy study of hard anodic oxide layers on AlSi(Cu) alloys, Electrochim. Acta. 49 (2004) 3169–3177. doi:10.1016/j.electacta.2004.02.030.
[36] L.E. Fratila-Apachitei, H. Terryn, P. Skeldon, G.E. Thompson, J. Duszczyk, L. Katgerman, Influence of substrate microstructure on the growth of anodic oxide layers, Electrochim. Acta. 49 (2004) 1127–1140. doi:10.1016/j.electacta.2003.10.024.
[37] K. Shimizu, G.M. Brown, K. Kobayashi, P. Skeldon, G.E. Thompson, G.C. Wood, Ultramicrotomy-a route towards the enhanced understanding of the corrosion and filming behaviour of aluminium and its alloys, Corros. Sci. 40 (1998) 1049–1072. doi:10.1016/S0010-938X(98)00006-7.
[38] M. Jariyaboon, P. Møller, R.E. Dunin-Borkowski, R. Ambat, FIB-SEM investigation of trapped intermetallic particles in anodic oxide films on AA1050 aluminium, Anti-Corrosion Methods Mater. 58 (2011) 173–178. doi:10.1108/00035591111148885.
[39] J. Timm, Influence of Fe and Si Containing Phases on the Anodisation Behaviour, Key Eng. Mater. 44-45 (1990) 219–232. doi:10.4028/www.scientific.net/KEM.44-45.219.
[40] H. Zhu, X. Zhang, M.J. Couper, A.K. Dahle, Effect of primary intermetallic particles on surface microstructure and appearance of aluminium extrusions, Mater. Chem. Phys. 113 (2009) 401–406. doi:10.1016/j.matchemphys.2008.07.109.
[41] T. Hauge, K.F. Karhausen, Extrusion parameters influencing the anodising quality, Alum. Extrus. (1998) 32–37.
[42] T. Minoda, H. Yoshida, Effect of grain boundary characteristics on intergranular corrosion resistance of

6061 aluminum alloy extrusion, Metall. Mater. Trans. A. 33A (2002) 2891–2898.
[43] Y. Ma, X. Zhou, G.E. Thompson, J.-O. Nilsson, M. Gustavsson, A. Crispin, Origin of streaks on anodised aluminium alloy extrusions, Trans. Inst. Met. Finish. 91 (2013) 11–16. doi:10.1179/0020296712Z.00000000075.

9. Optical appearance of Polyurethae-TiO_2 composites (Paper 5)

Simulation of Reflectance from White Anodised Aluminium Surfaces Using Polyurethane-TiO_2 Composite Coatings*

Abstract

Theoretical calculations and experimental studies were carried out on Polyurethane-TiO_2 composite coatings on bright and matte aluminium surfaces with an aim to understand and tailor the light scattering from particles incorporated into an anodised layer for designing the optical appearance of anodised surfaces. Polyurethane (PU) matrix was selected for its matching refractive index (n=1.7) with anodic alumina layer. Three different TiO_2 particle size distributions were dispersed in polyurethane and spin coated onto bright high gloss (HG) and matte caustic etched (CE) aluminium substrates. The reflectance spectra of coated surfaces in the visible region were analysed using an integrating sphere-spectrophotometer. Data showed that the coated surfaces have a high diffuse reflectance due to the multiple scattering from TiO_2 particles and the coating-substrate interface. The diffuse reflectance spectra of the coated surfaces varied weakly with TiO_2 particle concentration and reached a steady state value at 1 wt.% but were dependent on the substrate type used. Using Kubelka Munk two-stream model, the scattering and absorption coefficient of TiO_2 in polyurethane was predicted. The studies presented in this paper provide insight into generating bright white anodised aluminium surfaces based on aluminium-TiO_2 composites.

Keywords: Anodised Aluminium; White; TiO_2; Reflectance; Etching; Gloss; Electrochemical Finishing; Polyurethane.

Published as **V.C. Gudla, V.E. Johansen, S. Canulescu, J. Schou, R. Ambat, Simulation of Reflectance from White Anodised Aluminium Surfaces Using Polyurethane-TiO_2 Composite Coatings, J. Mater. Sci. 50 (2015) 4565-4575.*

9.1 Introduction

White anodising of aluminium has been of great interest to the aluminium surface finishing industry for the past few decades as it finds applications in architecture and marine industry for structural profiles, automobile and consumer goods industry for its pleasing aesthetic appearance and in the aerospace industry due to its high reflectance along with good corrosion resistance [1–4]. However, achieving a bright white and glossy anodised Al surface has not been reported to date as the conventional dyeing and colouring process of anodised aluminium surfaces cannot be applied to achieve white appearance [5–9]. White appearance requires diffuse and broadband reflection of light generated from high refractive index scattering centres in a low refractive index medium. In nature, the white-bright beetle displays strong white appearance which arises from multiple scattering of light from a dense randomly structured anisotropic chitin network that has a very high refractive index [10]. But traditionally, these high refractive index scattering centres (white pigments) are an order of magnitude (approx. 150-200 nm) larger than the anodic alumina pore diameters (approx. 10-50 nm) and hence cannot be incorporated into them after anodising [11]. Consequently, various alternative techniques have been studied for achieving enhanced reflection of light from anodised surfaces like plasma electrolytic oxidation (PEO) or micro-arc oxidation (MAO). These processes result in a hard ceramic aluminium oxide surface that is used for applications requiring wear resistance and are not aesthetically pleasing as they are highly porous, rough and appear diffuse with no gloss [12,13]. Caustic etching of the Al substrates prior to anodising improves the scattering of light due to the microscopic surface roughness and also retains the surface gloss after anodising, but the obtained reflectance is not as high as that of surfaces obtained from PEO/MAO and also, there is a bluish metallic hue retained from the Al substrate [2,3,14,15].

One novel approach to obtain an white appearing anodised surface is to anodise an Al based composite that contains high refractive index light scattering particles that would be incorporated into the anodic alumina during anodising and allow multiple light scattering mimicking the structure of the white beetle [16]. Particles, for example, oxides that are inert allow them to be embedded in the anodised layer during anodising process and their high refractive index compared to anodic alumina provides diffuse scattering of light together with a glossy appearance from a smooth anodised surface. Using this approach, theoretically one could prepare white appearing anodised surfaces from using Al composites based on oxides like TiO_2 (n=2.6-2.9) [17–20] that are structurally similar to white paints. However, a fundamental understanding of different parameters, such as thickness of the anodised layer, size and distribution of the light scattering particles and their effect on the appearance is required so that the bluish metallic appearance from the Al substrate is masked and required multiple scattering of light is achieved within required anodised layer thickness.

In this paper we study multiple scattering of light from a model system that contains (i) TiO_2 particles having high refractive index for light scattering, (ii) a transparent medium based on polyurethane (PU) which mimics anodised Al in terms of lower refractive index (n=1.7) [21,22] and (iii) an Al substrate with a smooth and glossy appearance or rough and diffuse appearance to simulate the anodic layer-Al substrate interface. PU-TiO_2 composites were prepared and coated onto the Al substrates having different surface conditions. Scattering and absorption parameters are calculated for the above mentioned system using Kubelka-Munk two-stream model for different particle size distributions. The effect of particle size distribution and concentration of particles is experimentally investigated along with that of the initial Al surface condition. Reflectance measurements were performed in the visible wavelength region using an integrating sphere-spectrophotometer setup that measures the total and diffuse reflectance of a surface. The TiO_2 powders were characterized for size, shape and morphology using a laser particle analyser and a scanning electron microscope (SEM). Surface topography of Al substrates in terms of surface roughness was analysed with atomic force microscopy (AFM) [23]. Our studies serve as a model for understanding the interaction of light with high refractive index scattering particles in anodised aluminium matrix and facilitate designing of decorative anodised surfaces with required brightness and gloss.

9.2 Experimental

9.2.1 Materials & Methods

Aluminium (Al) substrates having high specular reflectance (high gloss) were obtained under cold rolled condition (Alcan Rolled Products, Germany). Substrates were subjected to ultrasonic etching in 10 wt. % NaOH at 60 ˚C for 10 min followed by demineralised water rinsing. The etched substrates were then desmutted in HNO_3 followed by demineralised water rinsing. A polyurethane (PU) clear coat based on acrylic resin (Sigmavar WS Satin™, Sigma coatings, the Netherlands) was used to mimic the anodic Al layer. TiO_2 particles in rutile phase of three different size distributions (DuPont™ Titanium Technologies, Belgium) were used. PU-TiO_2 dispersions with varying amount of TiO_2 (0.5, 1, 1.5, and 2 wt. %) were prepared by ultrasonic dispersion for 15 min. Coatings were deposited on as received high gloss and also on caustic etched Al substrates using a spin coater (Model WS-650Sz, Laurell Technologies Corporation, USA). Coating thickness of ~10 µm (measured using surface profilometry) was employed as most of the decorative anodising use an anodised layer thickness of ~10-15 µm [1]. The spin coated samples were dried in air.

9.2.2 Spectrophotometry

Optical appearance of the sample was analysed using an integrating sphere-spectrophotometer setup. The samples were illuminated with light from a Deuterium-Tungsten halogen light source (DH2000, Ocean optics) at an angle of incidence of 8˚. Reflected light was collected using a spectrometer (QE65000, Ocean Optics). The integrating sphere allows total or diffuse reflectance measurements. The wavelength range analysed was 350-750 nm and the integration time was 4 s. The spectrometer was calibrated using NIST high diffuse alumina standard.

9.2.3 Surface characterization

The surface topography and roughness of the Al substrates in high gloss and caustic etched condition were measured using an atomic force microscope (Bruker Multimode™ 5). A silicon tip (Nanosensors SSS-NCH) with a tip radius of < 2 nm was used in tapping mode. The scan range was 100 x 100 µm^2. Morphology of the TiO_2 powder was observed using scanning electron microscopy (Model Quanta 200™ ESEM FEG, FEI). Particle size analysis was performed on the TiO_2 powders using laser diffraction particle size analyser (Malvern Mastersizer™ 3000) coupled with a wet dispersion unit (Malvern Hydro SM).

9.3 Results

9.3.1 Particle Size Distribution

The particle size distribution of TiO_2 powders of different sizes measured with the laser diffraction particle analyser method are shown in Figure 9.1. Agglomerates were present when measuring particle size distributions due to incomplete dispersion in the wet medium that was used. The distribution observed at the lower end of particle size is as expected from the supplier of TiO_2 powders. Also from Figure 9.6, it is seen that there are no particles in the size range above 1 µm. Hence, the measured distributions were fit only to the first peak using a lognormal distribution [24] given by

$$N_p(r) = \frac{1}{r\beta\sqrt{2\pi}} e^{-(\ln(r)-\alpha)^2/(2\beta^2)}, \quad \textbf{(9.1)}$$

where the two parameters α, β can be found from the mean particle size $\bar{r}$ and its variance σ^2 as $\beta^2 = \ln(1 + \sigma^2/\bar{r}^2)$ and $\alpha = \ln(\bar{r}) - \frac{1}{2}\beta^2$. The obtained fit results and the original measured data are shown in Figure 9.1. An overview plot comparing the different distributions is also seen (Figure 9.1 (d)). The three different sized TiO_2 powders are named after their measured D_{50} values. The powder with D_{50} = 320 nm has

a smaller standard deviation and a slightly shifted peak compared to the two others of D_{50} = 390 nm and 500 nm.

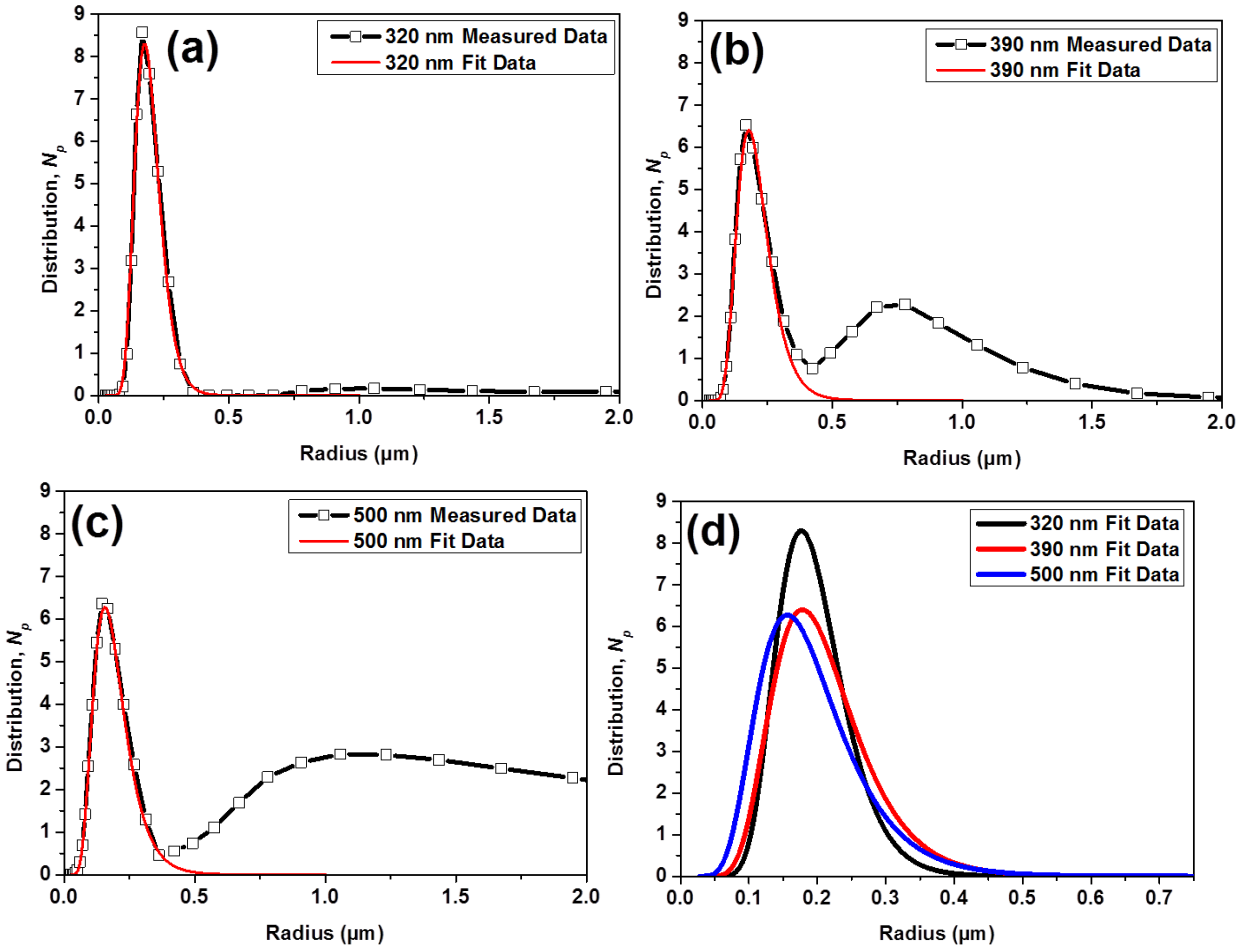

Figure 9.1: Particle size distribution as determined by the laser diffraction particle size analyser and respective lognormal fits for different TiO_2 powders: (a) D50 = 320 nm, $\bar{r} = 0.196$, $\sigma = 1.643$, (b) D50 = 390 nm, $\bar{r} = 0.210$, $\sigma = 1.342$, (c) D50 = 500 nm, $\bar{r} = 0.194$, $\sigma = 1.117$, and (d) comparison of the different distributions. Especially for powders of 390 nm and 500 nm, the agglomerates are clearly visible.

The nomenclature used for naming the prepared samples with and without PU-TiO_2 coatings is given in Table 9.1.

Table 9.1: Nomenclature given for naming the prepared samples.

Substrate		TiO_2 powder		Reflectance	
Type	**Designation**	**Type**	**Designation**	**Type**	**Designation**
Aluminium - High Gloss	HG	D_{50} = 320 nm	320	Total	T
Aluminium -Caustic Etched	CE	D_{50} = 390 nm	390	Diffuse	D
		D_{50} = 500 nm	500		

A sample termed as 'HG-320-0.5' would mean that the coating contained 0.5 wt.% TiO_2 of size distribution D_{50} of 320 nm in PU over an as received high gloss Al substrate. Samples coated with PU containing no TiO_2 were named as HG-PU-Ref and CE-PU-Ref. Samples without any coating were named as HG-Ref and CE-Ref.

9.4 Theory and Simulation

9.4.1 The Modified Kubelka-Munk model

In order to determine the best available particle distribution and highest obtainable reflection under optimal conditions, a two-stream Kubelka-Munk model has been used. This model predicts diffuse and specular reflectivity for a model like the one in Figure 9.2. This model considers top and bottom surface reflections assuming plane interfaces and ascribes some effective scattering and absorption parameters to the PU-TiO_2 system which converts collimated light to diffuse light as it travels in the medium.

The calculations were carried out using the approach presented in [25] – which is a modification of the classical Kubelka-Munk (KB) model [26]. As shown in [25], this model fits better for measurements using an integrating sphere which will be used to characterize the final samples. One shortcoming of the model is that is does not take the roughness of the Al surface into account, but this is seen as a small loss compared to the simplicity of the model and the purpose of getting a general understanding of optimal parameters. From [25] the specular (R_s) and diffuse (R_d) reflections are calculated as

$$\boldsymbol{R_s = r_{cc}^f}, \qquad \textbf{(9.2)}$$

$$\boldsymbol{R_d = \frac{(1-r_{cc}^f)(1-r_{dd}^b)R_{KM}}{1-r_{dd}^b R_{KM}}}, \qquad \textbf{(9.3)}$$

where r_{cc}^f is the collimated-collimated reflectance from the air-PU interface, r_{cd}^f is the collimated-to-diffuse reflection from the air-PU interface, r_{dd}^b is the diffuse-diffuse reflection from the medium and back into the medium, and R_{KM} is the traditional KB surface reflection coefficient given by

$$\boldsymbol{R_{KM} = \frac{1-r_{dd}^s[a-b\coth(bSh)]}{a+b\coth(bSh)-r_{dd}^s}}, \qquad \textbf{(9.4)}$$

Here, *S* and *K* are respectively the effective scattering and absorption coefficients used in the KB model, $a = (S+K)/S$, $b = \sqrt{a^2-1}$, *h* is the height of the PU layer, and r_{dd}^s is the diffuse-diffuse reflection from the Al substrate back into the medium.

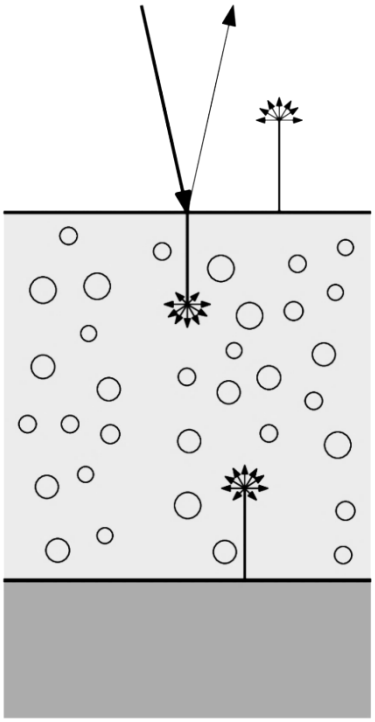

Figure 9.2: A model of an Al substrate with a PU-TiO_2 coating and plane interfaces. The incoming light (downwards thick arrow) is either reflected at the top surface or transported into the medium where it is scattered diffusely. The Al interface at the bottom reflects most of this diffuse light back, and in the end the diffuse light not absorbed leaves the PU coating again. The contribution from interface roughness is ignored in this model.

The reflection parameters are calculated using Fresnel reflection, and in particular the diffuse-diffuse reflection parameters are calculated as $r_{dd} = \int_0^{\frac{\pi}{2}} r(\theta) \cos\theta \, d\theta$, where r is the Fresnel reflection for the angle θ. This parameter is calculated using numerical integration and the results are seen in Figure 9.3 (a).

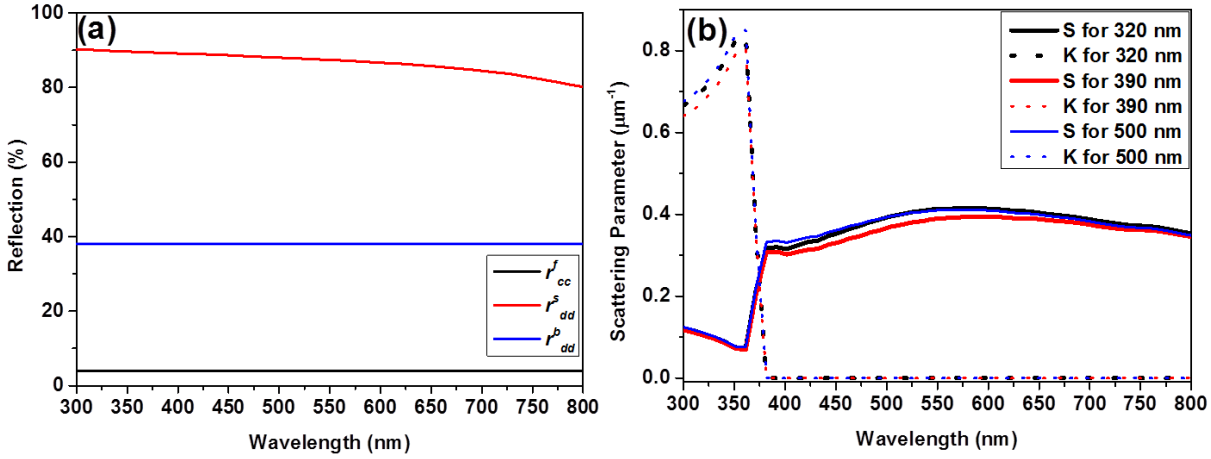

Figure 9.3: (a) Calculated reflection coefficients and (b) Calculated optical scattering parameters for different particle distributions (f = 10%).

9.4.2 Scattering and absorption parameters of particle distributions

Since S and K are heuristic parameters in the Kubelka-Munk model, there exist many ways of defining them, one method for spherical particles being [27]

$$S = \frac{3}{4} f \frac{C_{sca}(1-g)}{V_p}, \quad (9.5)$$

$$K = 2f \frac{C_{abs}}{V_p}, \quad (9.6)$$

where C_{sca}, C_{abs} are the particles scattering and absorption cross section respectively, f is the volume fraction of the particles in the PU, g is the so-called asymmetry parameter [28] and $V_p = \frac{4}{3}\pi r^3$ is the particle volume. Inherent in these expressions are (among others) that the particles act as single scatterers (they are optically far from each other), their size is in the Mie regime (which is controlled by the $\frac{3}{4}$ fraction), and that there is no depth (z) dependence on their scattering effect like seen in e.g. [29]. That the particles should be far from each other in turn means that the volume fraction, f, should be kept low as not to violate the validity of the scattering parameters calculation.

The parameters C_{sca}, C_{abs} can be calculated as explained in [28], and many computer implementations to do that exist. The freely available multiple spheres scattering tool MSTM 3.0 [30] was chosen. If only single particle scattering is of interest, then the programs BHMIE or BHCOAT that are based on code from [28] are available on the internet.

To be able to take size distribution of the particles into account, parameter calculation in [28] was generalized using the same procedure as in [27], which gives the average coefficients

$$< K >= 2f \frac{\int_0^\infty C_{abs}(r) N_p(r) dr}{\int_0^\infty V_p(r) N_p(r) dr}, \quad (9.7)$$

$$< S >= f \frac{3}{4} \frac{\int_0^\infty C_{sca}(r)(1-g(r)) N_p(r) dr}{\int_0^\infty V_p(r) N_p(r) dr}, \quad (9.8)$$

where r is the particle radius, and N_p is the normalized particle distribution, meaning that $\int_0^\infty N_p(r)dr = 1$. By using wavelength dependent optical data from [31] we calculated the S and K for the particle distributions and they can be seen in Figure 9.3 (b). To confirm that particle material and size are well-suited for our experiments, a contour plot of S for different choices of refractive index and size in a resin with a refractive index (n) of 1.7 was generated. The result is presented in Figure 9.4, and clearly shows a peak in scattering efficiency matching our particle properties. It is furthermore seen, that by decreasing the particle size (or refractive index), the scattering efficiency rolls off fast, and it is therefore important to have a small variation in particle distribution.

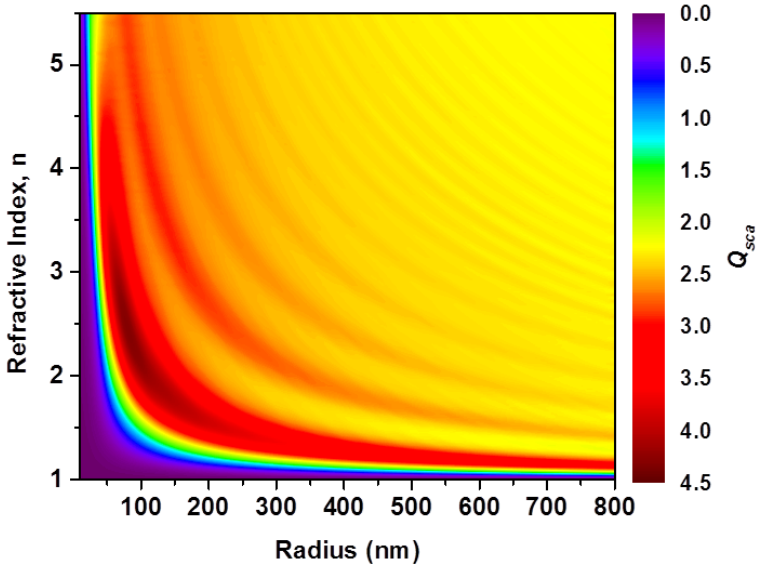

Figure 9.4: Scattering efficiency of a particle suspended in PU averaged over the visible spectrum.

9.4.3 Calculated Reflection

The above calculations show how r_{cc}^{f}, r_{dd}^{b}, r_{dd}^{s} are fixed due to the material properties of PU, and furthermore that *S*, *K* can be varied by choosing between our available particle distribution. Furthermore, the height of the coating, *h* and the particle volume fraction, *f*, is free parameters as well. We therefore studied total reflection for varying cases of these parameters. Since, *K* for all particle distributions is close to zero in the visible light range (~380 nm-750 nm); it does not influence visual appearance much. However, the scattering coefficient does influence the visual appearance and the 320 nm distribution is seen to be distinctly better than the two other powder size distributions used. For the overall reflection it was found that the difference is much less pronounced, and the three distributions are close to being of same quality. Therefore we only present results for the 320 nm distribution. By varying the height *h* in the modified Kubelka-Munk model and using the data presented above, the reflections presented in Figure 9.5 were obtained. The results show first of all that an almost flat spectral reflection should be obtainable and furthermore that a layer much thicker than traditional oxide thicknesses (~10−15 μm) is required for obtaining a good white reflection. From the formulas it is seen that the effect of varying volume fraction and height by a factor is the same. This means that if *f* = 20% was aimed at only half the heights from the plot would be needed to obtain the same effect. From this it can be concluded that a high volume fraction - still satisfying the single scattering assumption - is needed in order to obtain a good scattering effect within a reasonable height.

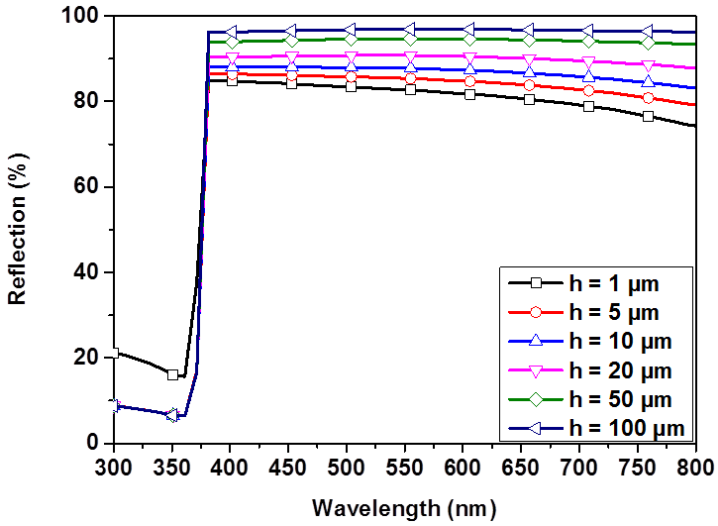

Figure 9.5: Calculated total reflectance (R_s+R_d) for different heights of an ideally coated sample with a filling fraction of *f* = 10% for TiO_2 powder of 320 nm size distribution.

9.5 Experimental Results

9.5.1 Scanning electron microscopy

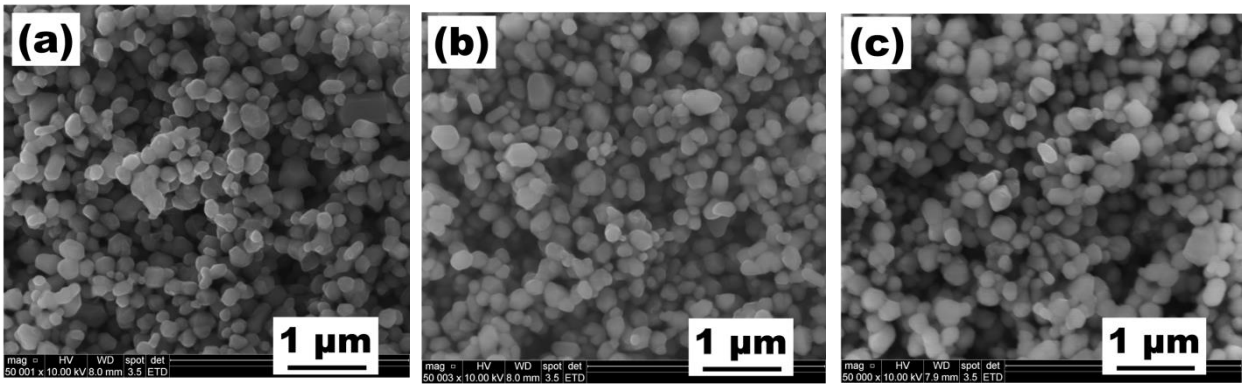

Figure 9.6: SEM micrographs of (a) TiO_2 powders-320 nm, (b) TiO_2 powders-390 nm and (c) TiO_2 powders-500 nm size distribution.

The SEM images of TiO_2 powders used for preparing the composite coatings are shown in Figure 9.6. It can be seen that the particles are spherical in shape and have a homogenous morphology. The size distribution (D_{50} value) measured using laser diffraction particle size analysis was found to be 320, 390, and 500 nm (Figure 9.1).

9.5.2 Surface morphology

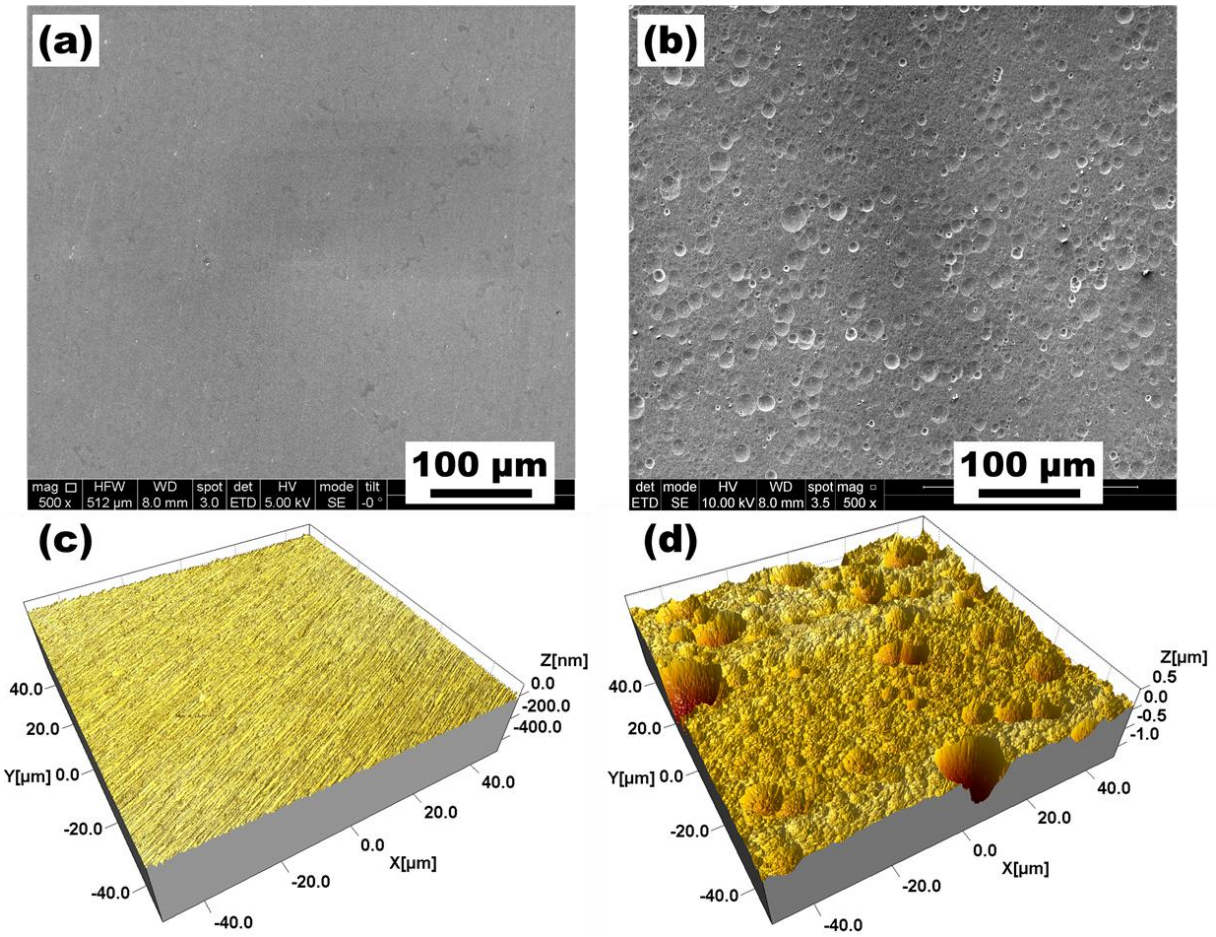

Figure 9.7: SEM micrographs of: (a) high gloss aluminium, (b) caustic etched aluminium and AFM surface topography images of (c) high gloss aluminium and (d) caustic etched aluminium.

The surface of as received high gloss Al substrate as shown in the SEM and AFM images (Figure 9.7 (a) & (c)) shows a typical rolled surface appearance with surface streaks in the rolling direction. The caustic etched aluminium surface (Figure 9.7 (b) & (d)) shows a homogenous attack by the etching agent which has resulted in the formation of hemi-spherical pits/scallops on the surface. Also, it can be seen that the prior rolled morphology of the surface is lost after caustic etching. Area roughness (S_a, measured from AFM topography data) of the high gloss substrate was measured to be ~8 nm which after caustic etching treatment increased to a value of ~158 nm.

9.5.3 Spectrophotometry

9.5.3.1 Coatings without TiO_2

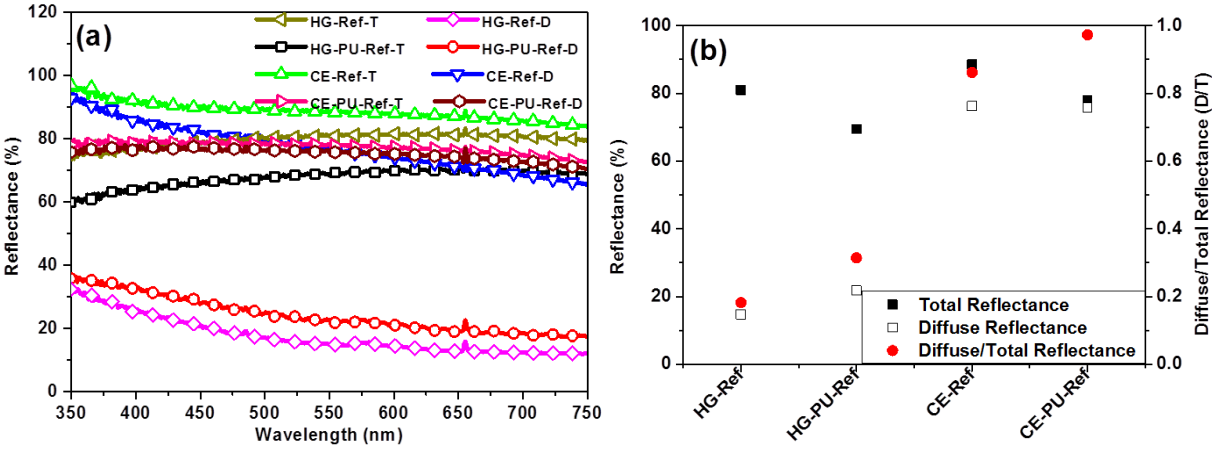

Figure 9.8: (a) Experimental reflectance spectra and (b) respective measured reflectance values at the wavelength of 555 nm of aluminium substrates (high gloss, HG and caustic etched, CE) with and without PU coating and D/T ratio (D- Diffuse and T-Total reflectance).

The magnitude of the reflectance spectra of the two different Al substrates showed little dependence on the wavelength (Figure 9.8 (a)), except for slight dependence at lower wavelengths. For the high gloss substrates, the reflectance was lower than average at lower wavelengths, but for etched substrate it was higher than average at lower wavelengths. Hence, the reflectivity of each coating at wavelength of 555 nm, where the human eye is most sensitive is summarized in Figure 9.8 (b). High gloss aluminium substrate (HG-Ref) has a total reflectance (Figure 9.8 (b)) of about 80% which upon etching increases to 90% (CE-Ref). The diffuse reflectance of high gloss aluminium is about 15% only whereas that for the caustic etched sample is 75%. The total and diffuse reflectance of high gloss substrates after being coated with PU (HG-PU-Ref) is 70% and 20%, respectively indicating that the PU coating reduces the reflectance of the sample and increases diffuse scattering of light. The reflectivity of the PU coating on caustic etched substrate reduces the total reflectance value to 80%, but does not affect the diffuse reflectance considerably. As can be seen from the diffuse to total reflectance ratio (right axis in Figure 9.8 (b)), the most diffuse appearing substrate surfaces are caustic etched with PU coating, but the brightest is caustic etched surface. The glossiest appearing surface is the as received HG aluminium surface.

9.5.3.2 Coatings with TiO_2

The reflectance spectra obtained from surfaces after coating with PU-TiO_2 showed absorption around 350-380 nm due to the TiO_2. There is no reflectance dependence on wavelength above this value up to 750 nm. Representative total reflectance spectra obtained from PU-TiO_2 coatings of size distribution 390 nm on high gloss substrates are shown in Figure 9.9 for reference.

The total and diffuse reflectance values at the wavelength of 555 nm for PU-TiO_2 coatings of different TiO_2 size distributions on high gloss and caustic etched Al substrates are shown in Figure 9.10. For high gloss substrates (HG), the total reflectance shows a very slight decrease with increasing TiO_2 content for all the powder size distributions. The diffuse reflectance however, shows a decreasing trend with increasing powder content for powders of 390 nm and 500 nm, while it increases for powder of 320 nm. For caustic etched surfaces (CE), the total reflectance value decreases with increasing TiO_2 for powders 320 nm and 500 nm, while it shows a maximum at 1 wt.% for powder 390 nm. The diffuse reflectance decreases with increasing TiO_2 for powder 320 nm and is not intensely affected for powders 390 nm and 500 nm.

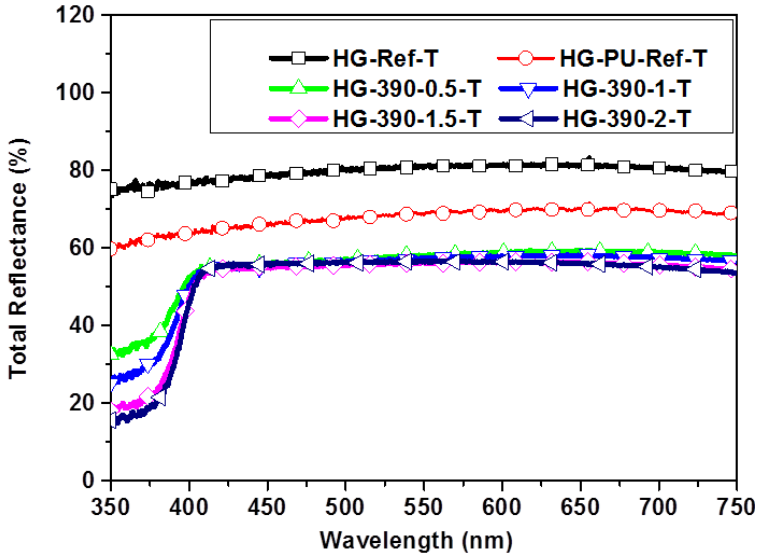

Figure 9.9: Experimental total reflectance spectra of PU-TiO_2 (390 nm) coatings on high gloss substrates with varying TiO_2 content.

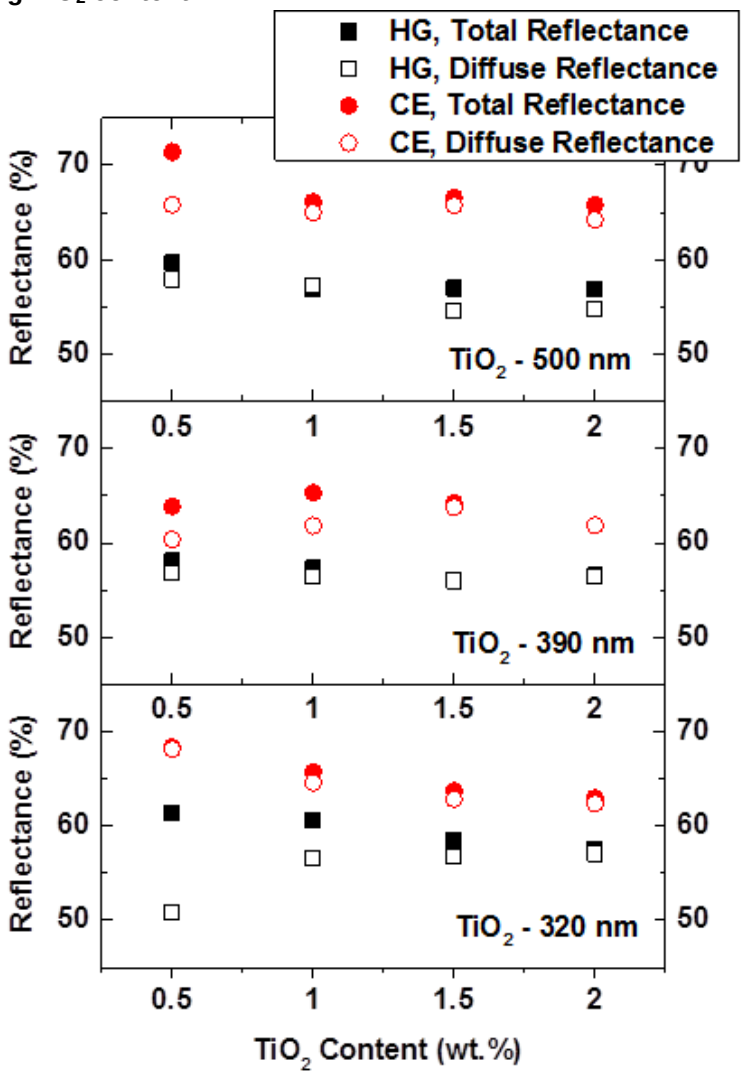

Figure 9.10: Reflectance values at 555 nm obtained for high gloss (HG) and caustic etched (CE) Al substrates coated with PU containing TiO_2 powders of different size distributions.

The ratio of diffuse to total reflectance (D/T) is presented in Figure 9.11 for PU coatings with different powders on high gloss as well as caustic etched substrates. For coatings containing 320 nm sized powders on high gloss substrates, the D/T ratio increases with increasing TiO_2 content. For caustic etched substrates, the D/T ratio does not vary significantly with increasing TiO_2. For powders of 390 nm, the D/T ratio increases with increasing TiO_2 on high gloss as well as caustic etched substrates. Saturation is observed for caustic substrates at 1.5 wt.% TiO_2. For 500 nm powder, the D/T ratio does not show any observable trend on high gloss substrates, but increases with increasing TiO_2 content on caustic etched substrates. Of all the coatings prepared the most diffuse appearing on high gloss substrates is for 500 nm powder at 1 wt.% (HG-500-1) and on caustic etched substrates is for 320 nm powder at 0.5 wt.% (CE-320-0.5) and 390 nm at 2 wt.% (CE-390-2). The least diffuse appearing surfaces are 320 nm powder at 0.5 wt.% on high gloss (HG-320-0.5) and 500 nm powder at 0.5 wt.% on caustic etched substrates (CE-500-0.5).

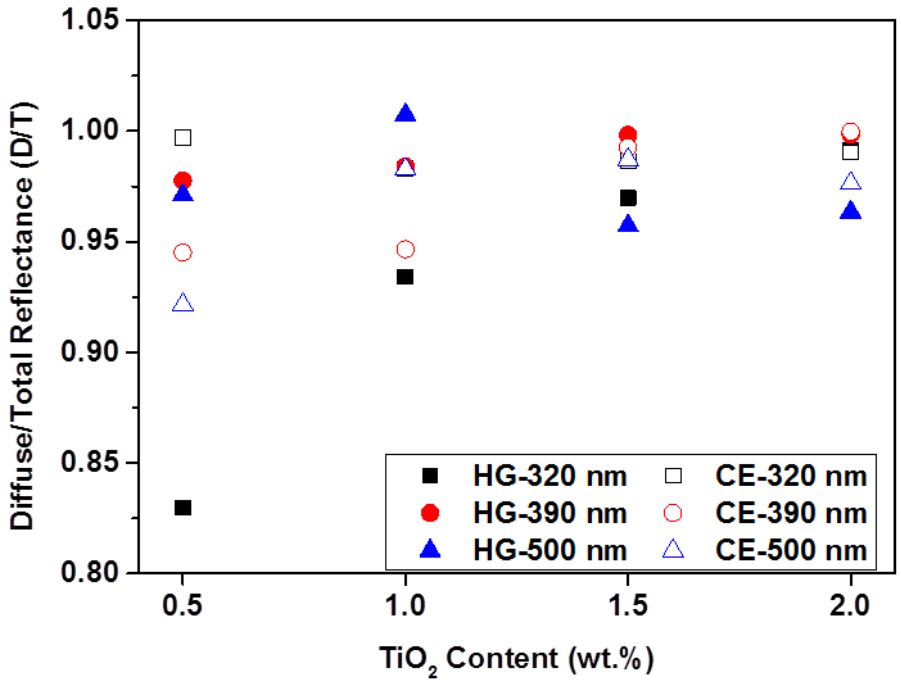

Figure 9.11: Diffuse to total reflectance ratio of the Al substrates coated with PU containing TiO_2 powders of different size distributions.

9.6 Discussion

The theoretical calculations show that the best scattering efficiency for a single sphere in PU is achieved when the particle size has a diameter of ~190-240 nm and a refractive index of ~2.2-2.9 (Figure 9.4). The efficiency of scattering and hence reflectance also increases with increasing thickness (Figure 9.5). However, an anodised layer of thickness higher than 15-20 µm is not feasible for decorative applications due to mechanical integrity issues like hardness and density mismatch between the anodised layer and the Al substrate [2,5]. A lower film thickness (of ~10 µm) would require more scattering centres implying a larger particle concentration which might lead to optical crowding. For the powder size distributions used for preparing the coatings in the present study, theoretical calculations (Figure 9.3 (b)) show that there is not much difference in the scattering parameters for the three different powder distributions. However, the experimentally measured reflectance values on high gloss Al substrates show that there is better reflectance obtained for surfaces containing powder of 320 nm compared to that measured for powders of 390 nm and 500 nm (see Figure 9.10).

The measured reflectance values of PU- TiO_2 coatings on high gloss substrates are about 60 %. However, caustic etching treatment of the Al substrates increases the total reflectance and decreases the

specular reflectance of the PU-TiO_2 coatings. The highest reflectance measured is 70 % and is for the coatings on caustic etched substrate. Also, the most diffuse appearing surfaces are achieved by caustic etching of the surfaces and at 2 wt.% of 390 nm powder (CE-390-2) and at 0.5 wt.% for 320 nm powder (CE-320-0.5).

Theoretical calculations based on Kubelka Munk two-stream model predict an enhancement of the diffuse reflectance with increasing thickness or particle concentration (see Figure 9.5). This trend is observed for particles which exhibit the largest scattering efficiency (320 nm) coated on highly reflective substrates. Indeed, the largest reflectance of the TiO_2-PU coating on high gloss substrates is observed at a concentration of 2 wt. %. However, for 390 nm and 500 nm TiO_2 powders, the diffuse reflectance decreases slightly with increasing particle concentration. A reason for this trend can be the agglomeration of the TiO_2 particles in the composite coatings. Agglomerated TiO_2 particles behave as a single larger particle rather than a smaller one, and the scattering efficiency is therefore moved away from the optimum [11]. Also, concentration of TiO_2 in the prepared composites that are higher than the critical pigment volume concentration would lead to a reduced gloss and contribute to lower reflectance [11,32,33].

White anodising of Al using PEO and MAO techniques have typically reflectance values up to 80% [2], but the resulting anodised surfaces are totally diffuse. On the other hand, the physically simulated coatings prepared on the etched Al substrates in the current study have a reflectance of ~70 % with a specular component of about 5%. The PU coating when applied onto the high gloss and caustic etched substrates shows a reduction in the total reflectance value by 10-15 percentage points. This reduction in reflectance would however not be the case for decorative anodised pure Al as the anodic layer shows reduction in reflectance of only up to 5 percentage points [34]. So, under the optimum size, distribution and concentration of TiO_2 particles, the reflectance for anodised Al with light scattering particles would be expected to be 5-10 percentage points higher (approx. 75-80 % total reflectance) than the measured values for the PU-TiO_2 coated surfaces. Therefore, for anodic alumna with TiO_2 powders of 390 nm on a caustic etched substrate the total reflectance would be about 80% (with more than 90% of it as diffuse component). This reflectance value is comparable to the surfaces obtained by PEO or MAO techniques and is suitable for decorative applications due to the specular component which gives the surface gloss. [35]. Gudla et al. have applied this approach to anodise Al-TiO_2 composites and have reported reflectance values of 50 % for white appearing anodised surfaces. The low value of reflectance when compared to the calculated value here is shown to be due to lower particle concentration in the anodic layer [16].

9.7 Conclusions

- Kubelka-Munk two stream model serves as an effective tool to simulate and estimate the optical reflectance of anodic alumina containing light scattering centres.
- Model systems based on PU-TiO_2 coatings of various size distributions and concentrations over Al substrates are successfully prepared and used to tailor and predict the optical appearance of anodised aluminium.
- Caustic etching of Al substrates increases the diffuse reflectance of the substrates, while PU coating reduces the total reflectance and increases the diffuse reflectance. Increase in the amount of light scattering TiO_2 particles decreases the specular reflectance thus making the surface appear more diffuse.
- The TiO_2 particle size distribution for achieving the maximum diffuse reflectance in the current tested range is observed to be 2 wt.% for PU-TiO_2 (390 nm) on caustic etched Al, but theoretical calculations predict an even higher content of TiO_2 is required.

References

[1] S. Mohagheghi, A. Hatefi, A. Kianvash, Effect of H3PO4 Anodising variations on Al-epoxy adhesion strength, Surf. Eng. 29 (2013) 737–742. doi:10.1179/1743294413Y.0000000158.

[2] P.G. Sheasby, The Surface Treatment and Finishing of Aluminium and its Alloys, Finishing Publ, Teddington, 1974. doi:10.1179/000705974798321639.

[3] C.A. Grubbs, Decorative and architectural anodizing, Met. Finish. 93 (1995) 449–459. doi:10.1016/0026-0576(95)93394-H.

[4] H.J. Spies, Surface engineering of aluminium and titanium alloys: an overview, Surf. Eng. 26 (2010) 126–134. doi:10.1179/174329409X451146.

[5] C.A. Grubbs, Anodizing of Aluminum, Met. Finish. 105 (2007) 397–412. doi:10.1016/S0026-0576(07)80359-X.

[6] G.E. Thompson, G.C. Wood, Porous anodic film formation on aluminium, Nature. 290 (1981) 230–232. doi:10.1038/290230a0.

[7] P.G. Sheasby, The weathering of anodized aluminium, Alum. 2000. (1990) 8–28.

[8] M. Selvam, Colouring of anodised aluminium by electroless method, Surf. Eng. 27 (2011) 711–718. doi:10.1179/1743294411Y.0000000022.

[9] H. Rezagholi, K. Zangeneh-Madar, M. Mirjani, M. Ahangarkani, Study on electropolished/anodised aluminium foil before and after dyeing., Surf. Eng. 30 (2014) 165–171. doi:10.1179/1743294413Y.0000000243.

[10] M. Burresi, L. Cortese, L. Pattelli, M. Kolle, P. Vukusic, D.S. Wiersma, et al., Bright-white beetle scales optimise multiple scattering of light., Sci. Rep. 4 (2014) 6075. doi:10.1038/srep06075.

[11] DuPont, DuPont ™ Ti-Pure titanium dioxide - Titanium Dioxide For Coatings, 2007.

[12] A.L. Yerokhin, X. Nie, A. Leyland, A. Matthews, S.J. Dowey, Plasma electrolysis for surface engineering, Surf. Coatings Technol. 122 (1999) 73–93. doi:10.1016/S0257-8972(99)00441-7.

[13] J.A. Curran, T.W. Clyne, Thermo-physical properties of plasma electrolytic oxide coatings on aluminium, Surf. Coatings Technol. 199 (2005) 168–176. doi:10.1016/j.surfcoat.2004.09.037.

[14] S. Bagheri, M. Guagliano, Review of shot peening processes to obtain nanocrystalline surfaces in metal alloys, Surf. Eng. 25 (2009) 3–14. doi:10.1179/026708408X334087.

[15] R. Priestner, D.M. Priestner, Importance of substrate in surface engineering, Surf. Eng. 7 (1991) 53–59.

[16] V.C. Gudla, F. Jensen, A. Simar, R. Shabadi, R. Ambat, Friction stir processed Al–TiO2 surface composites: Anodising behaviour and optical appearance, Appl. Surf. Sci. 324 (2015) 554–562. doi:http://dx.doi.org/10.1016/j.apsusc.2014.10.151.

[17] U. Diebold, The surface science of titanium dioxide, Surf. Sci. Rep. 48 (2003) 53–229. doi:10.1016/S0167-5729(02)00100-0.

[18] J. Winkler, Titanium dioxide, Vincentz Verlag, Hannover, 1992. doi:10.1016/S0306-3747(05)80006-5.

[19] J.K. Yao, H.L. Huang, J.Y. Ma, Y.X. Jin, Y. a. Zhao, J.D. Shao, et al., High refractive index TiO2 film deposited by electron beam evaporation, Surf. Eng. 25 (2009) 257–260. doi:10.1179/026708408X329498.

[20] W.X. Dai, X. Chen, E. Li, X.X. Wang, P. Liu, X.Z. Fu, Influence of pH value of TiO2 sol on surface gloss of corresponding TiO2 film coated on ceramic tiles, Surf. Eng. 25 (2009) 106–110. doi:10.1179/174329408X326498.

[21] I. Khan, J. Leach, N. Wilkins, The thickness and optical properties of films of anodic aluminium oxide, Corros. Sci. 6 (1966) 483–497. doi:10.1016/S0010-938X(66)80065-3.

[22] G.F. Pastore, Transmission interference spectrometric determination of the thickness and refractive index of barrier films formed anodically on aluminum, Thin Solid Films. 123 (1985) 9–17. doi:10.1016/0040-6090(85)90036-7.

[23] J.T. Thornton, Metal surface investigation by scanning probe microscopy, Surf. Eng. 16 (2000) 287–293. doi:10.1179/026708400101517224.

[24] R.A. Johnson, I. Miller, J.E. Freund, Miller & Freund's Probability and Statistics for Engineers, Prentice Hall, 2011. https://books.google.dk/books?id=EjCVQAAACAAJ.

[25] A.B. Murphy, Modified Kubelka–Munk model for calculation of the reflectance of coatings with optically-rough surfaces, J. Phys. D. Appl. Phys. 39 (2006) 3571–3581. doi:10.1088/0022-3727/39/16/008.

[26] P. Kubelka, F. Munk, An article on optics of paint layers, Z. Tech. Phys. 12 (1931) 593–601.

http://www.graphics.cornell.edu/~westin/pubs/kubelka.pdf.
[27] J.C. Auger, R.G. Barrera, B. Stout, Scattering efficiency of clusters composed by aggregated spheres, J. Quant. Spectrosc. Radiat. Transf. 79-80 (2003) 521–531. doi:10.1016/S0022-4073(02)00305-9.
[28] C.F. Bohren, D.R. Huffman, Absorption and scattering of light by small particles, Wiley-VCH, 1983. doi:10.1002/9783527618156.
[29] W.E. Vargas, G. a Niklasson, Generalized method for evaluating scattering parameters used in radiative transfer models, J. Opt. Soc. Am. A. 14 (1997) 2243–2252. doi:10.1364/JOSAA.14.002243.
[30] http://www.eng.auburn.edu/users/dmckwski/scatcodes/, (n.d.).
[31] E.D. Palik, Chapter 2 - Refractive Index, Handbook of Optical Constanst of Solids, in: Handb. Opt. Constants Solids, Academic Press, Burlington, 1997: pp. 5–114. doi:http://dx.doi.org/10.1016/B978-012544415-6.50149-7.
[32] W.K. Asbeck, M. Van Loo, Critical Pigment Volume Relationships., Ind. Eng. Chem. 41 (1949) 1470–1475. doi:10.1021/ie50475a042.
[33] G.P. Bierwagen, D.C. Rich, The critical pigment volume concentration in latex coatings, Prog. Org. Coatings. 11 (1983) 339–352. doi:10.1016/0033-0655(83)85007-9.
[34] S. Canulescu, K. Rechendorff, C.N. Borca, N.C. Jones, K. Bordo, J. Schou, et al., Band gap structure modification of amorphous anodic Al oxide film by Ti-alloying, Appl. Phys. Lett. 104 (2014) 121910. doi:10.1063/1.4866901.
[35] S. Van Gils, P. Mast, E. Stijns, H. Terryn, Colour properties of barrier anodic oxide films on aluminium and titanium studied with total reflectance and spectroscopic ellipsometry, Surf. Coatings Technol. 185 (2004) 303–310. doi:10.1016/j.surfcoat.2004.01.021.

10. Anodising of Al-Metal Oxide Composites (Paper 6)

Friction Stir Processed Al-Metal Oxide Surface Composites: Anodising and Optical Appearance*

Abstract

Multiple-pass friction stir processing (FSP) was employed to impregnate metal oxide (TiO_2, Y_2O_3 and CeO_2) particles into the surface of an Aluminium alloy. The surface composites were then anodised in a sulphuric acid electrolyte. The effect of anodising parameters on the resulting optical appearance was studied. Microstructural and morphological characterization was performed using transmission electron microscopy (TEM). The surface appearance was analysed using an integrating sphere-spectrometer setup. Increasing the anodising potential changed the surface appearance of the composites from dark to greyish white. This is attributed to the localized microstructural and morphological differences around the metal oxide particles incorporated into the anodic alumina matrix. The metal oxide particles in the FSP zone electrochemically shadowed the underlying Al matrix and modified the local morphology of the anodic layer as well as changed the light interaction phenomenon.

Keywords: Aluminium, Friction Stir Processing, Spectrophotometry, Optical appearance, TiO_2, Y_2O_3, CeO_2, Reflectance, Electrochemical Finishing, Transmission Electron Microscopy, Composites, Decorative Anodising, Sulphuric Acid, Focused Ion Beam.

Published as **V.C. Gudla, F. Jensen, S. Canulescu, A. Simar, R. Ambat, Friction Stir Processed Al-Metal Oxide Surface Composites: Anodising and Optical Appearance, in: T.S. Sudarshan, P. Vuoristo, H. Koivuluoto (Eds.), Surf. Modif. Technol. XXVIII, ValarDocs, Tampere, Finland, 2014: pp. 375–384.*

10.1 Introduction

Aluminium alloys are used in various applications due to their high mechanical strength to weight ratio. Surface finishing of Al by anodising improves its corrosion and wear resistance and also adhesion to subsequent paint layers [1–3]. Sulphuric acid anodising (SAA) provides a clear and transparent anodic oxide layer on the surface of Al which comprises a self-organized hexagonal porous structure (20-30 nm pore diameter) [4,5]. This porous structure is usually filled with dyes using capillary effect and later sealed in boiling water to impart colours to the anodised surface [6–8]. A wide range of colours, including black have been produced over the years but achieving a white glossy anodised Al surface is difficult. This is because white appearance is generated by scattering of light by particles that are bigger than the pores while colours are generated by selective absorption of particular wavelengths [9,10].

White anodised Al finds application in the aerospace and architectural industry where a low solar absorptance is preferred to prevent temperature rise and related thermal expansion of structural components [11,12]. Also, it is of great interest for aesthetic purposes and decorative applications in the architectural industry for facades, window profiles etc. White anodised Al has been reported earlier using a mixture of electrolytes, but the reflectance from these surfaces is not very high [13,14]. Alternate processes based on Plasma Electrolytic Oxidation (PEO) and Micro Arc Oxidation (MAO), which are commercially available reported grey to white anodised surfaces. However the surfaces generated by these methods are not glossy and have a very high surface roughness [15–18].

The glossy white anodised surface requires scattering of incident light within the anodic layer and also generate a surface gloss due to specular reflectance from a smooth surface without any absorption in the visible wavelength region [19–21]. One approach for achieving this is to mimic the optical scattering phenomenon from white paints which contain a pigment in a polymer matrix. The pigments used should have a high refractive index difference with the surrounding polymer matrix and enable very efficient scattering. Similar scattering effects can be achieved using high refractive index metal oxides (based on Ti, Y and Ce) in anodic alumina which has a refractive index similar to polymer matrix of paints [22–24]. To obtain such a structure on the anodised Al surface, metal oxide particles need to be incorporated into the Al matrix prior to anodising and the obtained composite be later anodised to reveal these particles in a transparent anodic alumina matrix (similar to paints).

Incorporation of metal oxide powders into metal matrices has been of interest to many researchers due to the enhanced mechanical properties of the obtained composites by particle reinforcement. Various techniques have been employed to prepare many composite systems [25–30]. Friction stir processing (FSP) is one such technique that has been extensively used for preparation of composites [31–35]. FSP allows for semi solid state mixing of the involved phases and the maximum temperature involved for Al based composites processing is up to 450 °C-500 °C [36]. However, use of this technique to obtain composite surfaces for white anodising of Al has not yet been attempted.

In the current work we present the initial findings on use of metal oxides incorporation into anodic alumina for white anodised surface finish. The effect of anodising parameters on the obtained optical appearance is studied. Transmission electron microscopy (TEM) was used to investigate the structure and morphology of the anodised composites. Surface appearance was characterized using reflectance spectroscopy and the obtained surface appearance is explained in terms of morphological features of the anodic layer.

10.2 Experimental

10.2.1 Materials

Aluminium substrates (Peraluman™ 853, Alcan rolled products, Germany) with dimensions 200 mm x 60 mm x 6 mm were obtained in rolled condition. Commercial metal oxide powders TiO_2 (300 nm, Ti-Pure™ R796, DuPont Titanium Technologies, Belgium), Y_2O_3 (0.5-1 µm, SkySpring Nanomaterials, Inc., USA) and CeO_2 (200-300 nm, Nano-Oxides, Inc, USA) were used. Particle size distributions were chosen based on the refractive index and their related light scattering power.

10.2.2 Friction Stir Processing

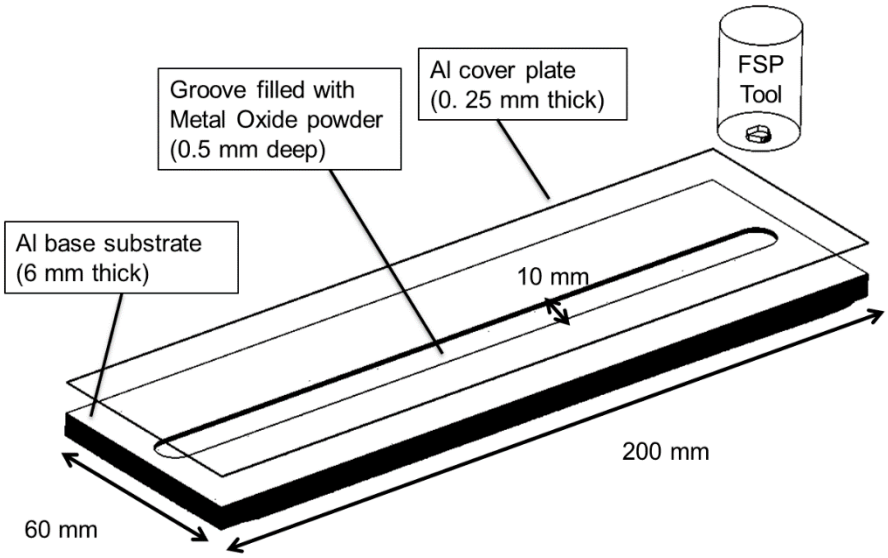

Figure 10.1: Schematic showing the setup with sample substrate and groove used for friction stir processing of Al- Metal Oxide surface composites.

FSP was performed using a Hermle milling machine equipped with a steel tool having 20 mm shoulder diameter, 1.5 mm pin length with a M6 thread and three flats. The backwards tilt angle of the tool was maintained at 1°. A groove 0.5 mm deep, 10 mm wide and 180 mm long in the substrates was filled with the powders (see Figure 10.1). The filled substrates were then covered by the same Al sheet rolled down to a thickness of 0.25 mm to prevent loss of powders during the initial FSP pass. Rotational speed of the tool was 1000 rpm and the advancing speed was 200 mm/min for the first pass and 1000 mm/min for the next six passes. A surface of 175 mm long x 20 mm wide was processed for each pass with a total processing time of roughly 2 min. All seven passes were performed one over the other without any shift.

10.2.3 Anodising

The processed composite surfaces were polished and buffed to a mirror finish and subsequently degreased in a mild Alficlean™ solution at 60 ˚C. Desmutting was performed by immersing in dilute HNO_3 followed by demineralised water rinsing. Anodising was carried out in a 20 wt.% sulphuric acid bath maintained at 18 ˚C. Three different anodising voltages of 10 V, 15 V, and 19 V were used to obtain approx. 5 µm of anodised layer. After anodising, the samples were rinsed with demineralized water. Sealing of the anodised layer was performed in water at 96 ˚C for 25 min followed by drying with hot air.

10.2.4 Reflectance Spectroscopy

Optical appearance of the processed composites after anodising was analysed using an integrating sphere-spectrometer setup. The samples were illuminated at 8° incidence, with light from a Deuterium-Tungsten halogen light source (DH2000, Ocean optics). Reflected light from the samples was collected and analysed for diffuse and total reflectance using a spectrometer (QE65000, Ocean Optics). The wavelength range analysed was 350-750 nm and was integrated over a period of 4 s. The spectrophotometer was calibrated using NIST standards.

10.2.5 Transmission Electron Microscopy

Transmission electron microscopy was carried out on the sample cross section in the anodised as well as non-anodised regions using a TEM (Model Tecnai G2 20™) operating at 200 keV. The lamella for TEM were prepared using FIB-SEM in situ lift out (Model Quanta 200 3D™ DualBeam, FEI) and further thinned for electron transparency in a FIB-SEM (Helios Nanolab™ DualBeam, FEI).

10.3 Results

10.3.1 Visual Appearance

The visual appearance of the FSP samples after anodising is shown in Figure 10.2. The FSP zone shows a different appearance for all three powders when compared to the adjacent unprocessed Al. The processed zone can be clearly identified (region between dotted lines) as it shows macroscopic semi-circular striations. For all the three powders types used, the anodised appearance shifts from dark to greyish white as the anodising voltage is increased from 10 V to 19 V. This effect is most prominent in the case of surface containing TiO_2 powders where there is a clear difference between the surfaces anodised at 10 V and 15 V.

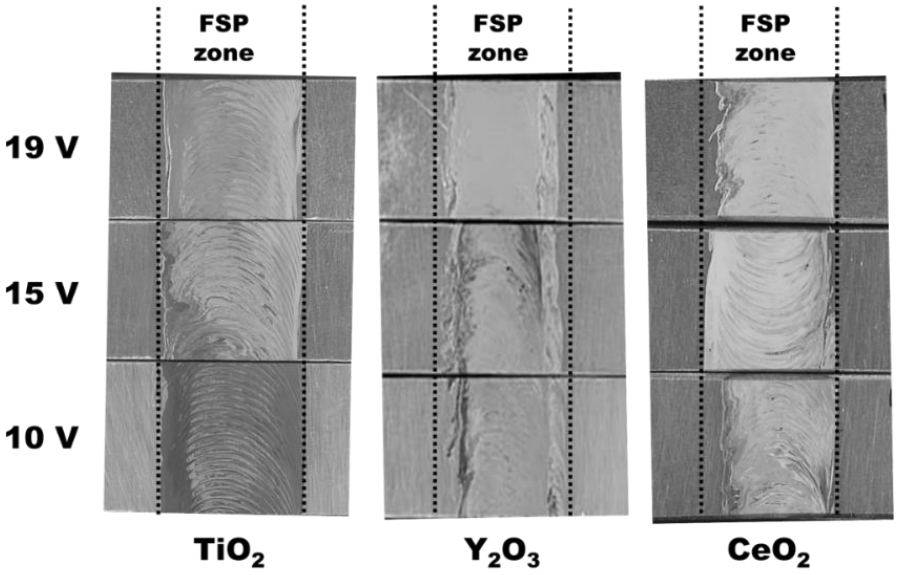

Figure 10.2: Visual appearance of the friction stir processed samples with different powders after sulphuric acid anodising at different voltages.

10.3.2 Reflectance Spectroscopy

The reflectance values (at 555 nm) obtained from the spectrophotometry data are presented in Figure 10.3 (a). It can be seen that the total reflectance of the anodised surface increases from anodising at 10 V to 15 V and then slightly reduces at 19 V for TiO_2 and CeO_2. However, for samples containing Y_2O_3, the total reflectance is lower at 15 V anodising when compared to the 10 V and 19 V anodising. The diffuse to total reflectance ratio which is a measure of how well the surface scatters light is shown in Figure 10.3 (b). It can be observed that the diffuse reflectance component for the Y_2O_3 containing surfaces is lower than that for TiO_2 and CeO_2 even though their total reflectance value is lower.

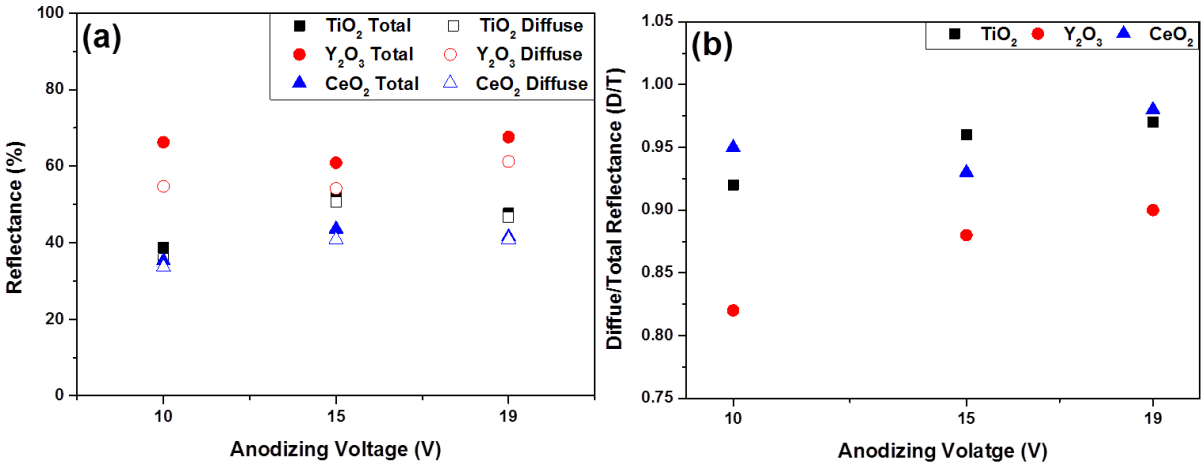

Figure 10.3: (a) Total and diffuse reflectance values (wavelength ~ 555 nm) and (b) Diffuse to Total reflectance (D/T) ratio obtained from the FSP surfaces after sulphuric acid anodising at different voltages.

10.3.3 Transmission Electron Microscopy

The anodised layer on FSP surface containing TiO_2 at19 V anodising (Figure 10.4 (a)) shows different morphological features for the TiO_2 particles. In this case, the particles present in the anodised layer are fully or partially transformed. Typical features of the TiO_2 particle in Figure 10.4 (b) show that the particle is partially affected (top region of the particle) by the anodising process. Also, the picture shows a bright region below the TiO_2 particle.

Elemental analysis of the bright regions using energy dispersive spectroscopy (EDS) technique, show presence of very high content of Al compared to surrounding regions which showed Al, Ti and O. The anodised layer on the sample containing Y_2O_3 particles is shown in Figure 10.4 (c). Unlike the TiO_2 containing sample, the Y_2O_3 particles are not present in the anodised layer. The anodised layer shows large number of voids, although the FSP substrate shows good distribution of Y_2O_3 particles (Figure 10.4 (d)). The voids are expected to be the result of expulsed Y_2O_3 particles during the anodising process. For the samples containing CeO_2, anodising at 10 V showed similar morphological features as for the TiO_2 particles (Figure 10.4 (e)). One of the CeO_2 particles shown in Figure 10.4 (f) appears affected (top region of the particle) by the anodising process. However, regions of high Al content like those observed beneath the TiO_2 particles have not been observed in the anodised layer of CeO_2 containing samples.

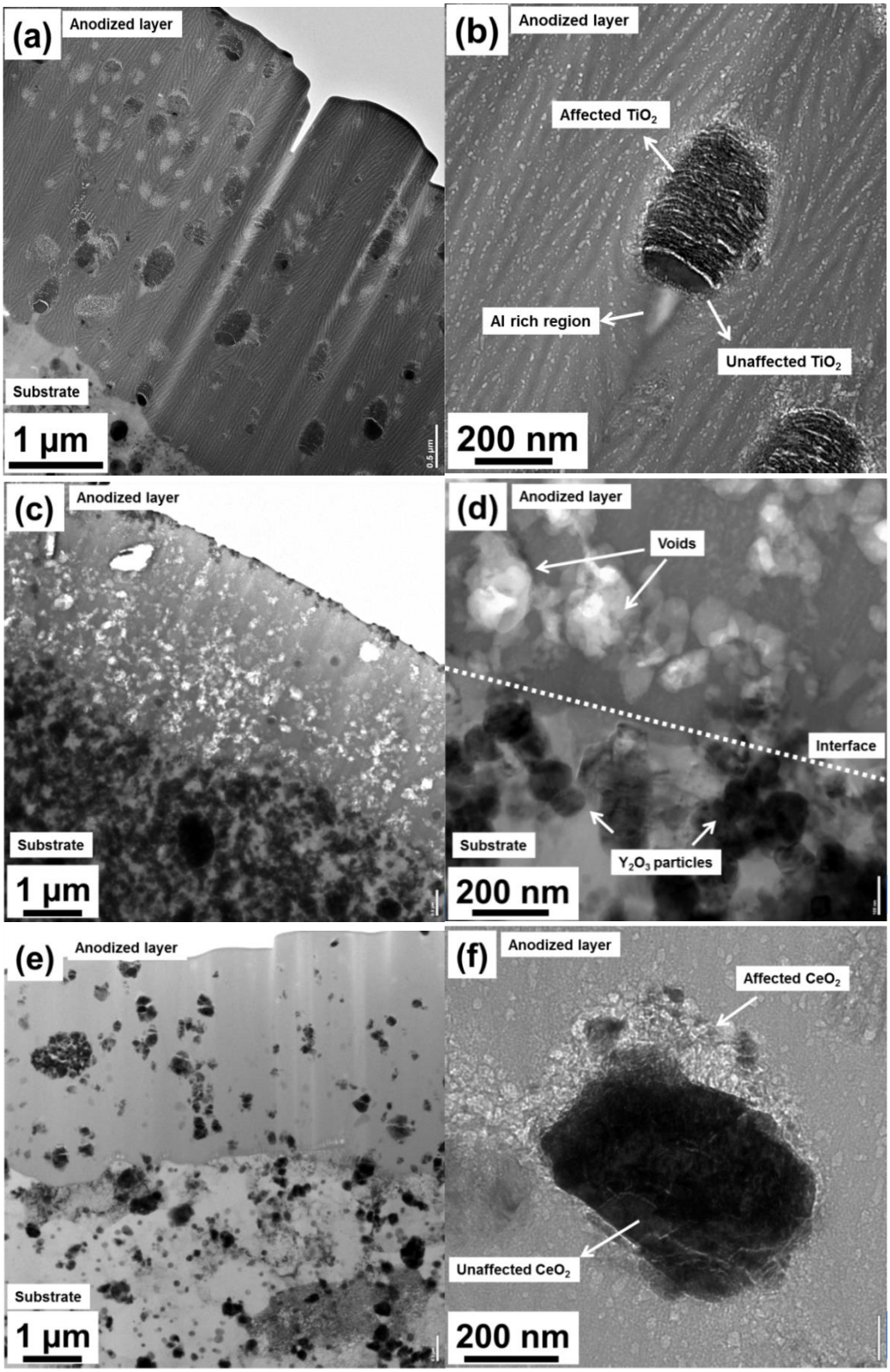

Figure 10.4: TEM bright field image showing anodised layer cross section of FSP and anodised samples with (a), (b) TiO_2, 19 V, (c), (d) Y_2O_3, 10 V and (e), (f) CeO_2 10 V.

10.4 Discussion

Friction stir processing (FSP) of Al substrate with metal oxide powders resulted in a surface composite with good distribution of particles in the processed zone. Anodising of these composite surfaces visually revealed macroscopic inhomogeneity in the processed zone in terms of semi-circular striations (Figure 10.2).

The striations are caused by the forward movement of the tool that generates a trail behind it. Overall distribution of particles in the FSP zone is uniform without any significant agglomeration (Figure 10.4). In all the cases, upon visual observation the surface appearance changed from dark to greyish white with increasing anodising voltage. Reflectance spectroscopy data (Figure 10.3) measured by the integrating sphere setup showed that the reflectance values are highest for the Y_2O_3 containing surfaces when compared to the TiO_2 and CeO_2 containing surfaces irrespective of the anodising voltage used. For anodised surfaces containing TiO_2 and CeO_2 the reflectance increased from 10 V to 15 V anodising and later decreased from 15 V to 19 V anodising. However for the Y_2O_3 containing samples, the reflectance was lowest for anodising at 15 V. The TEM images shown in Figure 10.4 reveal that the morphology of the anodic layer and particles is different for different powders used. For Y_2O_3 powders the anodised layer showed very little presence of the particles. Surfaces containing TiO_2 and CeO_2 showed partially affected particles in the anodic layer. Also, un-anodised Al rich regions were observed beneath the TiO_2 particles in the anodised layer.

The difference in reflectance values measured from the anodised surfaces containing different powders is a manifestation of various factors like the refractive index of the powders, the distribution and concentration of the powders, the roughness of the surface and the interface between anodised layer and substrate, morphology of the anodised layer as well as of the powder particles [9,10]. High refractive index particles in a visibly transparent medium scatter light and increase the diffuse reflectance. The increased scattering is due to the refractive index difference between the particle and the surrounding medium. In the present case, the metal oxide particles have a higher refractive index when compared to anodic alumina (n=1.6-1.7) [37,38] and hence result in a high diffuse reflectance value. However, the total reflectance value measured is only 40-60% of the incident light intensity. The loss of intensity can be explained by the morphological features observed in the anodic layer. In the case of anodised layer with TiO_2, regions of high Al content observed beneath the particles act as absorption centres for light. Anodic alumina is a transparent medium under visible light, but Al as a metal has a very high optical extinction coefficient. This coupled with the sub-micron size of the metallic Al region leads to an effective extinction of light and hence the reduced loss of reflected intensity [39–43]. The presence of these metallic Al regions in anodic alumina depends on the anodising voltage as the oxidation power of the process increases with anodising voltage [44,45]. At lower anodising voltages the oxidative power is not sufficient to fully anodise the Al beneath the insulating TiO_2 particles owing to the current field distribution [46]. Hence, an increased amount of such metallic Al in anodised layer results in higher absorption of light and thus the reduced reflectance values. As the anodising voltage increases, it is assumed that the Al surrounding the TiO_2 particle gets completely anodised increasing the reflectance.

The Y_2O_3 containing anodised surfaces show no such Al rich regions and also have a higher reflectance values. This is due to the absence of any insulating particles in the anodised layer as seen in Figure 10.4 (c). Also, as the particles have been removed from the matrix during the anodising process, the diffuse reflectance obtained in this case is due to the scattering from voids rather than the particles themselves. A lower diffuse reflectance component observed for the Y_2O_3 containing surfaces (Figure 10.3 (b)) is due to the fact that the incident light is now reflected from the anodised layer – metal substrate interface, which is similar to the reflection from a smooth metal surface which appears glossy (specular). The phenomenon of transformation of crystalline TiO_2 and CeO_2 particles to amorphous phase and also the removal of Y_2O_3 particles after anodising of these composites is yet to be understood and requires more detailed analysis. One possible explanation for the visible transformation of TiO_2 to amorphous phase is that it is known to be soluble in sulphuric acid, and the combined effect of the acid with the external applied anodising voltage can cause dissolution and re-precipitation in amorphous phase of the oxide. For the Y_2O_3 particles it was observed that their morphology is very porous and this can be the reason for their leaching out into the electrolyte from the matrix due to the acid and voltage applied.

Refractive index of TiO_2 (n=2.6-2.9) [47] is higher than that of CeO_2 (n=2.2-2.4) [48] and hence the scattering efficiency of the anodised Al-TiO_2 system would be better than that of anodised Al-CeO_2 system. However, from the reflectance values, only slight difference was observed at a given voltage. This could be attributed to the transformation of TiO_2 to amorphous phase in the anodic alumina with a reduced refractive index (n=2.42) [49,50].

A white glossy anodised Al surface would have a total reflectance of 80-90% with a very high diffuse reflectance component. The values obtained for such surfaces using metal oxide incorporation into Al matrix before anodising have been shown to be max. 50%. Use of Y_2O_3 gives higher reflectance value, but the voids generated reduce the mechanical properties of the anodic alumina layer. When comparing between TiO_2 and CeO_2, it has been observed that the reflectance values do not differ considerably. However high values of reflectance would be achieved if higher particle concentrations are used and the crystalline nature of the oxide particles is retained after anodising.

10.5 Conclusions

- Friction stir processing was employed to prepare Al with Ti, Y and Ce oxide surface composites with little or no agglomerations of particles.
- Sulphuric acid anodising of the prepared surface composites showed an increase in surface brightness with increasing anodising voltage.
- High resolution TEM analysis show that the anodising process transformed the TiO_2 and CeO_2 particles to an amorphous state, while the Y_2O_3 particles were removed from the Al matrix during anodising.
- Anodising at lower voltages showed the presence of un-anodised crystalline Al regions below the TiO_2 particles.
- Presence of metallic Al in the anodic alumina along with the reduced refractive index of TiO_2 and CeO_2 particles resulted in reduced reflectance of anodised surface.
- The Y_2O_3 containing surfaces showed higher reflectance due to scattering from the voids in the anodic layer and reflection from the anodic layer-metal substrate interface.

References

[1] P.G. Sheasby, The Surface Treatment and Finishing of Aluminium and its Alloys, Finishing Publ, Teddington, 1974. doi:10.1179/000705974798321639.

[2] S. Mohagheghi, A. Hatefi, A. Kianvash, Effect of H3PO4 Anodising variations on Al-epoxy adhesion strength, Surf. Eng. 29 (2013) 737–742. doi:10.1179/1743294413Y.0000000158.

[3] H.J. Spies, Surface engineering of aluminium and titanium alloys: an overview, Surf. Eng. 26 (2010) 126–134. doi:10.1179/174329409X451146.

[4] C.A. Grubbs, Anodizing of Aluminum, Met. Finish. 105 (2007) 397–412. doi:10.1016/S0026-0576(07)80359-X.

[5] S. Canulescu, K. Rechendorff, C.N. Borca, N.C. Jones, K. Bordo, J. Schou, et al., Band gap structure modification of amorphous anodic Al oxide film by Ti-alloying, Appl. Phys. Lett. 104 (2014) 121910. doi:10.1063/1.4866901.

[6] G.E. Thompson, G.C. Wood, Porous anodic film formation on aluminium, Nature. 290 (1981) 230–232. doi:10.1038/290230a0.

[7] M. Selvam, Colouring of anodised aluminium by electroless method, Surf. Eng. 27 (2011) 711–718. doi:10.1179/1743294411Y.0000000022.

[8] H. Rezagholi, K. Zangeneh-Madar, M. Mirjani, M. Ahangarkani, Study on electropolished/anodised aluminium foil before and after dyeing., Surf. Eng. 30 (2014) 165–171. doi:10.1179/1743294413Y.0000000243.

[9] E. Hecht, Optics, Addison Wesley, 2002.

[10] R. Tilley, Colour and The Optical Properties of Materials: An Exploration of the Relationship Between Light, the Optical Properties of Materials and Colour, 2010. http://www.pilkington.com/products/bp/bybenefit/specialapplications/tecglass/ (accessed November 4, 2013).
[11] W. Kaysser, Surface Modifications in Aerospace Applications, Surf. Eng. 17 (2001) 305–312. doi:10.1179/026708401101517926.
[12] A.K. Sharma, Surface engineering for thermal control of spacecraft, Surf. Eng. 21 (2005) 249–253. doi:10.1179/174329405X50118.
[13] C. Siva Kumar, S.M. Mayanna, K.N. Mahendra, A.K. Sharma, R. Uma Rani, Studies on white anodizing on aluminum alloy for space applications, Appl. Surf. Sci. 151 (1999) 280–286. doi:10.1016/S0169-4332(99)00290-1.
[14] C. Siva Kumar, A.K. Sharma, K.N. Mahendra, S.M. Mayanna, Studies on anodic oxide coating with low absorptance and high emittance on aluminum alloy 2024, Sol. Energy Mater. Sol. Cells. 60 (2000) 51–57. doi:10.1016/S0927-0248(99)00062-8.
[15] A.L. Yerokhin, X. Nie, A. Leyland, A. Matthews, S.J. Dowey, Plasma electrolysis for surface engineering, Surf. Coatings Technol. 122 (1999) 73–93. doi:10.1016/S0257-8972(99)00441-7.
[16] J.M. Wheeler, J.A. Curran, S. Shrestha, Microstructure and multi-scale mechanical behavior of hard anodized and plasma electrolytic oxidation (PEO) coatings on aluminum alloy 5052, Surf. Coatings Technol. 207 (2012) 480–488. doi:10.1016/j.surfcoat.2012.07.056.
[17] U. Malayoglu, K.C. Tekin, U. Malayoglu, S. Shrestha, An investigation into the mechanical and tribological properties of plasma electrolytic oxidation and hard-anodized coatings on 6082 aluminum alloy, Mater. Sci. Eng. A. 528 (2011) 7451–7460. doi:10.1016/j.msea.2011.06.032.
[18] V.J. Kharanagh, M.A.F. Sani, E. Rafizadeh, Effect of current frequency on coating properties formed on aluminised steel by plasma electrolytic oxidation., Surf. Eng. 30 (2014) 224–228. doi:10.1179/1743294413Y.0000000190.
[19] K. Muller, R. Silvennoinen, K.E. Peiponen, Specular Gloss, 2008. doi:10.1520/D0523-08.2.
[20] R. Silvennoinen, K. Peiponen, K. Muller, eds., Specular Gloss - Light Reflection From an Ideal Surface, Elsevier, Amsterdam, 2008. doi:http://dx.doi.org/10.1016/B978-008045314-9.50006-2.
[21] R. Silvennoinen, K. Peiponen, K. Muller, eds., Specular Gloss - Light Reflection From a Rough Surface, Elsevier, Amsterdam, 2008. doi:http://dx.doi.org/10.1016/B978-008045314-9.50007-4.
[22] U. Diebold, The surface science of titanium dioxide, Surf. Sci. Rep. 48 (2003) 53–229. doi:10.1016/S0167-5729(02)00100-0.
[23] J. Winkler, Titanium dioxide, Vincentz Verlag, Hannover, 1992. doi:10.1016/S0306-3747(05)80006-5.
[24] J.K. Yao, H.L. Huang, J.Y. Ma, Y.X. Jin, Y. a. Zhao, J.D. Shao, et al., High refractive index TiO2 film deposited by electron beam evaporation, Surf. Eng. 25 (2009) 257–260. doi:10.1179/026708408X329498.
[25] B.S.B. Reddy, K. Das, S. Das, A review on the synthesis of in situ aluminum based composites by thermal, mechanical and mechanical-thermal activation of chemical reactions, J. Mater. Sci. 42 (2007) 9366–9378. doi:10.1007/s10853-007-1827-z.
[26] P.C. Maity, S.C. Panigrahi, P.N. Chakraborty, Preparation of aluminium-alumina in-situ particle composite by addition of titania to aluminium melt, Scr. Metall. Mater. 28 (1993) 549–552. doi:10.1016/0956-716X(93)90194-W.
[27] P.C. Maity, P.N. Chakraborty, S.C. Panigrahi, Processing and properties of Al□Al2O3 (TiO2) in situ particle composite, J. Mater. Process. Technol. 53 (1995) 857–870. doi:10.1016/0924-0136(94)01757-R.
[28] C.F. Feng, L. Froyen, Formation of Al3Ti and Al2O3 from an Al–TiO2 system for preparing in-situ aluminium matrix composites, Compos. Part A Appl. Sci. Manuf. 31 (2000) 385–390. doi:10.1016/S1359-835X(99)00041-X.
[29] D.Y. Ying, D.L. Zhang, M. Newby, Solid-state reactions during heating mechanically milled Al/TiO2 composite powders, Metall. Mater. Trans. A. 35 (2004) 2115–2125. doi:10.1007/s11661-004-0160-2.
[30] C.F. Chen, P.W. Kao, L.W. Chang, N.J. Ho, Effect of Processing Parameters on Microstructure and Mechanical Properties of an Al-Al11Ce3-Al2O3 In-Situ Composite Produced by Friction Stir Processing, Metall. Mater. Trans. A. 41 (2010) 513–522. doi:10.1007/s11661-009-0115-8.
[31] H.S. Arora, H. Singh, B.K. Dhindaw, Composite fabrication using friction stir processing - A review, Int. J. Adv. Manuf. Technol. 61 (2012) 1043–1055. doi:10.1007/s00170-011-3758-8.
[32] Z.Y. Ma, Friction Stir Processing Technology: A Review, Metall. Mater. Trans. A. 39 (2008) 642–658. doi:10.1007/s11661-007-9459-0.
[33] R.S. Mishra, Z.Y. Ma, I. Charit, Friction stir processing: A novel technique for fabrication of surface

composite, Mater. Sci. Eng. A. 341 (2003) 307–310. doi:10.1016/S0921-5093(02)00199-5.
[34] I.S. Lee, P.W. Kao, N.J. Ho, Microstructure and mechanical properties of Al-Fe in situ nanocomposite produced by friction stir processing, Intermetallics. 16 (2008) 1104–1108. doi:10.1016/j.intermet.2008.06.017.
[35] C.J. Hsu, C.Y. Chang, P.W. Kao, N.J. Ho, C.P. Chang, Al-Al3Ti nanocomposites produced in situ by friction stir processing, Acta Mater. 54 (2006) 5241–5249. doi:10.1016/j.actamat.2006.06.054.
[36] R.S. Mishra, Z.Y. Ma, Friction stir welding and processing, Mater. Sci. Eng. R Reports. 50 (2005) 1–78. doi:10.1016/j.mser.2005.07.001.
[37] G.F. Pastore, Transmission interference spectrometric determination of the thickness and refractive index of barrier films formed anodically on aluminum, Thin Solid Films. 123 (1985) 9–17. doi:10.1016/0040-6090(85)90036-7.
[38] I. Khan, J. Leach, N. Wilkins, The thickness and optical properties of films of anodic aluminium oxide, Corros. Sci. 6 (1966) 483–497. doi:10.1016/S0010-938X(66)80065-3.
[39] R. Chang, W.F. Hall, On the correlation between optical properties and the chemical /metallurgical constitution of multi-phase thin films, Thin Solid Films. 46 (1977) L5–L8. doi:10.1016/0040-6090(77)90068-2.
[40] M. Saito, Unoxidized Aluminum Particles in Anodic Alumina Films, J. Electrochem. Soc. 140 (1993) 1907. doi:10.1149/1.2220737.
[41] V.C. Gudla, S. Canulescu, R. Shabadi, K. Rechendorff, J. Schou, R. Ambat, Anodization and Optical Appearance of Sputter Deposited Al-Zr Coatings, in: J. Grandfield, TMS (Eds.), Light Met. 2014, John Wiley & Sons, Inc., 2014: pp. 369–373. doi:10.1002/9781118888438.ch63.
[42] M. Aggerbeck, A. Junker-Holst, D.V. Nielsen, V.C. Gudla, R. Ambat, A.J. Holst, et al., Anodisation of Sputter Deposited Aluminium - Titanium Coatings : Effect of Microstructure on Optical Characteristics, Surf. Coatings Technol. 254 (2014) 138–144. doi:http://dx.doi.org/10.1016/j.surfcoat.2014.05.073.
[43] V.C. Gudla, S. Canulescu, R. Shabadi, K. Rechendorff, K. Dirscherl, R. Ambat, Structure of anodized Al-Zr sputter deposited coatings and effect on optical appearance, Appl. Surf. Sci. 317 (2014) 1113–1124. doi:http://dx.doi.org/10.1016/j.apsusc.2014.09.037.
[44] J.C. Walmsley, C.J. Simensen, A. Bjørgum, F. Lapique, K. Redford, The Structure and Impurities of Hard DC Anodic Layers on AA6060 Aluminium Alloy, J. Adhes. 84 (2008) 543–561. doi:10.1080/00218460802161590.
[45] K. Shimizu, G.M. Brown, K. Kobayashi, P. Skeldon, G.E. Thompson, G.C. Wood, Ultramicrotomy-a route towards the enhanced understanding of the corrosion and filming behaviour of aluminium and its alloys, Corros. Sci. 40 (1998) 1049–1072. doi:10.1016/S0010-938X(98)00006-7.
[46] D. Regonini, V. Adamaki, C.R. Bowen, S.R. Pennock, J. Taylor, A.C.E. Dent, AC electrical properties of TiO2 and Magnéli phases, TinO2n−1, Solid State Ionics. 229 (2012) 38–44. doi:10.1016/j.ssi.2012.10.003.
[47] E.D. Palik, Chapter 2 - Refractive Index, Handbook of Optical Constanst of Solids, in: Handb. Opt. Constants Solids, Academic Press, Burlington, 1997: pp. 5–114. doi:http://dx.doi.org/10.1016/B978-012544415-6.50149-7.
[48] G. Hass, J.B. Ramsey, R. Thun, Optical Properties and Structure of Cerium Dioxide Films, J. Opt. Soc. Am. 48 (1958) 324. doi:10.1364/JOSA.48.000324.
[49] J.D.B. Bradley, C.C. Evans, J.T. Choy, O. Reshef, P.B. Deotare, F. Parsy, et al., Submicrometer-wide amorphous and polycrystalline anatase TiO2 waveguides for microphotonic devices, Opt. Express. 20 (2012) 23821. doi:10.1364/OE.20.023821.
[50] E.T. Fitzgibbons, K.J. Sladek, W.H. Hartwig, TiO2 Film Properties as a Function of Processing Temperature, J. Electrochem. Soc. 119 (1972) 735–739. http://jes.ecsdl.org/content/119/6/735.abstract.

11. Anodising of Al-TiO_2 Composites: Effect of Potential (Paper 7)

Friction Stir Processed Al-TiO_2 Surface Composites: Anodising Behaviour and Optical Appearance*

Abstract

Multiple-pass friction stir processing (FSP) was employed to impregnate TiO_2 (rutile) particles into the surface of an Aluminium alloy. The surface composites of Al-TiO_2 were then anodised in a sulphuric acid electrolyte. The effect of anodising parameters on the resulting optical appearance was investigated. Microstructural and morphological characterization was performed using scanning (SEM) and transmission electron microscopy (TEM), and X-ray diffraction (XRD). The surface appearance was analysed using an integrating sphere-spectrophotometer setup which measures the diffuse and total reflectance of light from the surface. Compared to samples without TiO_2, surface appearance after anodising of samples with TiO_2 changed from dark to greyish white upon increasing the anodising voltage. This is attributed to the localized microstructural and morphological differences around the TiO_2 powder particles incorporated into the anodic alumina matrix. The TiO_2 powder particles in the FSP zone were partially or completely amorphized during the anodising process, and also electrochemically shadowed the anodising of underlying Al matrix.

Keywords: Aluminium; TiO_2; Anodising; Friction stir processing; Spectrophotometry; TEM; Optical Appearance; White.

*Published as ***V.C. Gudla***, F. Jensen, A. Simar, R. Shabadi, R. Ambat, Friction stir processed Al-TiO_2 surface composites: Anodising behaviour and optical appearance, Appl. Surf. Sci. 324 (2015) 554-562.*

11.1 Introduction

Aluminium and its alloys are widely used in various engineering applications due to their light weight coupled with high level of mechanical properties. Anodising of Al enhances its corrosion and wear resistance as well as improves its aesthetic appearance for use in architectural, decorative, and automobile industries [1]. Over the years, sulphuric acid anodising (SAA) has been carried out as a preferred surface finishing technique as it provides an anodised layer with excellent decorative properties [2]. The anodised layer formed after SAA is optically transparent in visible wavelength region and the thickness of such a layer for best decorative appearance is in the range of 10-15 μm. The anodised layer contains a self-organized nano-porous structure (20-30 nm diameter), which can be used for colouring by impregnating with organic or inorganic dyes followed by a sealing process [2,3]. Nearly all colours including black can be produced by the dyeing process, while achieving a white anodised Al surface is difficult. This is due to the fact that the white appearance is related to optical scattering of light achieved by pigments that are too big to be impregnated into the pores of anodised Al. However, individual colours (like red, green, blue etc.) are produced by the absorption of a specific or group of wavelengths by the dye molecules that are easily impregnated as they are smaller than the pores in anodic alumina.

Previously, white anodising of Al has been studied for use in applications like aerospace, where a mixture of sulphuric acid, lactic acid, glycerol and sodium molybdate were used for obtaining anodised Al surface with improved reflectance [4,5]. Other anodising processes like Plasma Electrolytic Oxidation (PEO) and Micro Arc Oxidation (MAO) have also been reported to generate surfaces from grey to white appearance, but the thickness of these anodic coatings is higher than those used for the decorative anodised surfaces. Also, the surface gloss of these oxide coatings is very low owing to their very high surface roughness [6–10]. For the anodised layer to appear white and glossy, it needs to facilitate effective scattering of light along with a smooth surface to retain its gloss [11,12]. One approach for achieving this is by incorporation of high refractive index particles in the transparent anodised layer that would scatter the incident light, while the smooth anodised surface would generate the glossy appearance. Titanium dioxide (TiO_2) in rutile phase has a refractive index of 2.6-2.9 [13] and is widely used as a white pigment in many commercial applications [14,15]. Thus, the use of TiO_2 as scattering medium in anodic layer for achieving white surfaces after SAA of Al is very promising and needs understanding in terms of incorporation into Al matrix, anodising behaviour, and optical appearance.

The TiO_2 incorporation into Al matrix has been studied extensively to understand the effect on mechanical properties. Techniques like reactive hot pressing (RHP), reactive squeeze casting (RSC), and mechanical alloying have been used for dispersing the TiO_2 powders into the Al matrix [16–19]. Friction stir processing (FSP) [20] is one mechanical alloying technique which has been widely used to obtain metal matrix composites (MMCs) of various combinations [21–25]. MMCs using TiO_2 powders [26–28] and nanofibers [29] have been prepared by FSP to reinforce the Al matrix by allowing for reactive processing between Al and TiO_2 to form Al-Ti based intermetallic phases. However, the use of this technique to obtain tailored surfaces that can be further functionalized by anodising still needs to be investigated.

In this paper we evaluate the use of FSP of Al-TiO_2 to obtain surface composites which are further anodised to achieve light scattering by TiO_2 in a transparent anodised Al matrix. The effect of FSP and anodising parameters on the optical appearance of anodised layer is studied. Scanning (SEM) and transmission electron microscopy (TEM) was used to observe the microstructure of the anodised composite surfaces in terms of morphology and incorporation of TiO_2 particles. Focused ion beam milling (FIB) was used to lift out lamella in-situ from the anodised surface for TEM analysis. Grazing incidence X-ray diffraction (GI-XRD) was performed to characterize the phases in the prepared composite surfaces before and after anodising. The surface appearance was evaluated using an integrating sphere-spectrophotometer setup and the obtained data was correlated with the observed microstructure and phases to explain the appearance.

11.2 Experimental

11.2.1 Materials

Aluminium plates (Peraluman™ 853, Alcan rolled products, Germany) were obtained with dimensions 200 mm x 60 mm x 6 mm for FSP. Commercial TiO_2 powder (Ti-Pure™ R900, DuPont Titanium Technologies, Belgium) in rutile phase was used. The median diameter of the powder particles was 210 nm.

11.2.2 Friction Stir Processing

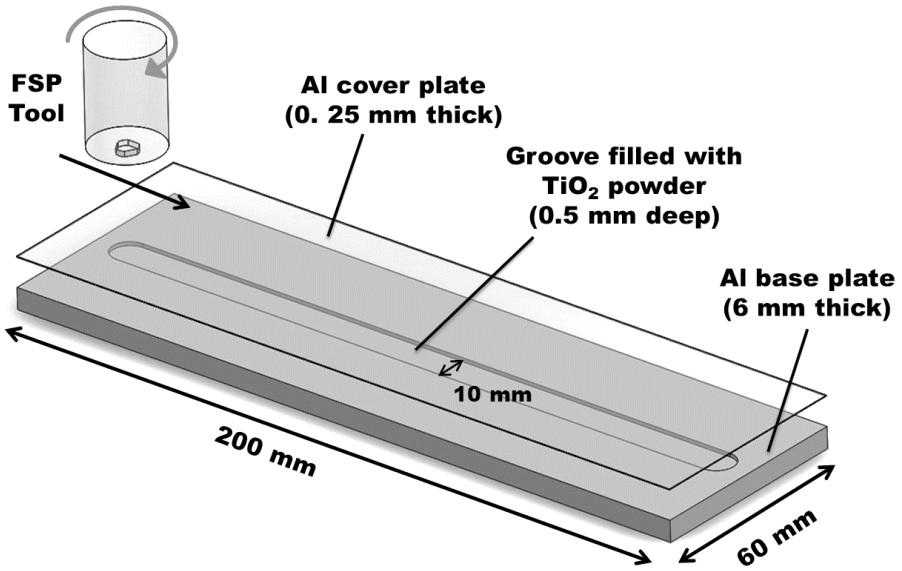

Figure 11.1: Schematic of the sample geometry with groove used for FSP process.

The FSP process was performed using a Hermle milling machine equipped with a steel tool having 20 mm shoulder diameter, 1.5 mm pin length with a M6 thread (see Figure 11.1). The backwards tilt angle of the tool was maintained at 1˚. A groove 0.5 mm deep, 10 mm wide, and 180 mm long (see Figure 11.1) in the Al plates which was compactly filled with TiO_2 powder. The filled plates were then covered by the same Al sheet rolled down to a thickness of 0.25 mm to prevent loss of TiO_2 powder during the initial FSP pass. Rotational speed of the tool was 1000 rpm and the advancing speed was 200 mm/min for the first pass to ensure correct closure of the groove and 1000 mm/min for the next six passes. A surface of 175 mm long x 20 mm wide was processed for each pass with a total processing time of roughly 2 min. All seven passes were performed one over the other without any shift. For comparison, reference samples without any TiO_2 powder were also produced using the same FSP parameters.

11.2.3 Anodising

The processed samples with and without TiO_2 powder were then mechanically polished, buffed to a mirror finish and then degreased in a mild Alficlean™ solution at 60 ˚C. The samples were subsequently desmutted by immersing in diluted HNO_3 followed by demineralised water rinsing. Anodising was carried out in a 20 wt.% sulphuric acid bath maintained at 18 ˚C. Four different anodising voltages of 4.8 V, 9.6 V, 15.1 V, and 18.9 V were used (approx. anodising times are 90 min, 55 min, 35 min and 18 min respectively). After anodising, the samples were rinsed with demineralized water. Sealing of the anodised layer was performed in water at 96 ˚C for 25 min followed by drying with hot air.

11.2.4 Spectrophotometry

Optical appearance of the FSP samples in polished condition before and after anodising was analysed using an integrating sphere-spectrophotometer setup. The samples were illuminated at 8˚ incidence, with light from a Deuterium-Tungsten halogen light source (DH2000, Ocean optics). Reflected light from the samples was collected and analysed for diffuse and total reflectance using a spectrometer (QE65000, Ocean Optics). The wavelength range analysed was 350-750 nm and was integrated over a period of 4 s. The spectrophotometer was calibrated using NIST standards.

11.2.5 Electron Microscopy

The morphology, microstructure, and compositional analysis of the samples was performed using SEM (Model Quanta 200™ ESEM FEG, FEI) equipped with EDS (Oxford Instruments 80 mm^2 X-Max™). The samples were mounted in epoxy resin and mechanically polished to reveal the cross section. Transmission electron microscopy analysis was carried out on the sample cross section in the anodised as well as non-anodised regions using a TEM (Model Tecnai™ G2 20) operating at 200 keV. The lamellas for TEM were prepared using FIB-SEM in-situ lift out (Model Quanta 200 3D™ DualBeam, FEI) and further thinned for electron transparency in a FIB-SEM (Helios Nanolab™ DualBeam, FEI).

11.2.6 X-ray Diffraction

Grazing incidence X-ray diffraction (Model Bruker Discover D8™) analysis was performed using Cu-K_α radiation at 40 kV and 40 mA for phase analysis of the samples after FSP and anodising. Diffraction data was recorded in the 2θ range from 20° to 70° with an incidence angle of 0.25°, step size of 0.03° and a scan step time of 4 s.

11.3 Results

11.3.1 Visual Appearance

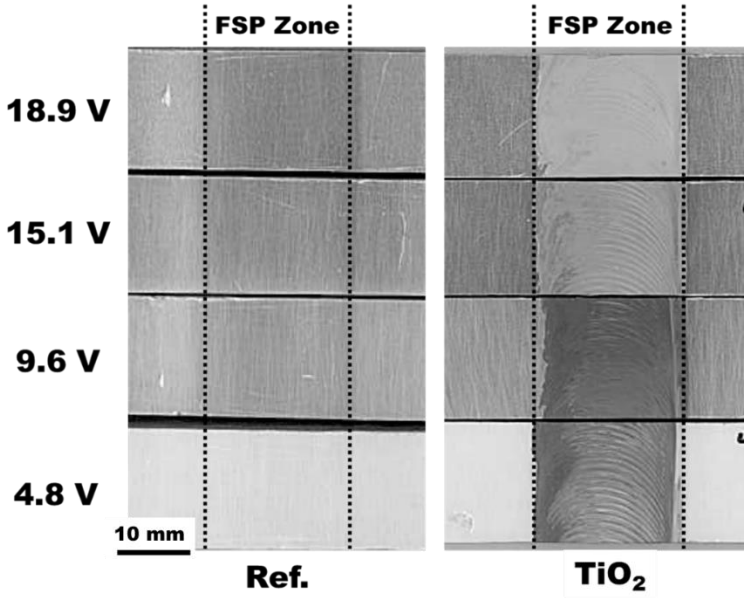

Figure 11.2: Visual appearance of the FSP samples without (Ref., left-hand column) and with TiO_2 particles (right-hand column) after sulphuric acid anodising at different voltages. The region between the dotted lines is the FSP zone.

The visual appearance of the FSP samples with and without TiO_2 after SAA is shown in Figure 11.2. The FSP zone without TiO_2 powder does not show any major difference compared to adjacent un-processed

aluminium after anodising at different voltages. However, the FSP samples with TiO_2 after anodising at different voltages show a difference in their appearance. The samples anodised at 4.8 V looks dark, while up on increasing the anodising voltage to 18.9 V, the appearance has changed gradually from dark to greyish white.

11.3.2 Spectrophotometry

The total and diffuse reflectance spectra recorded using the integrating sphere-spectrophotometer setup of the anodised FSP surface with and without TiO_2 powder are shown in Figure 11.3. It can be seen in Figure 11.3 (a) that total reflectance of the anodised surface without TiO_2 in the FSP zone remains the same independent of the anodising voltage used. However, the diffuse reflectance is lower for the surface anodised at 9.6 V and 15.1 V when compared to those anodised at 4.8 V and 18.9 V. On the other hand, the total reflectance values for processed surfaces containing TiO_2 after anodising show a clear dependence on the anodising voltage used as seen in Figure 11.3 (b).

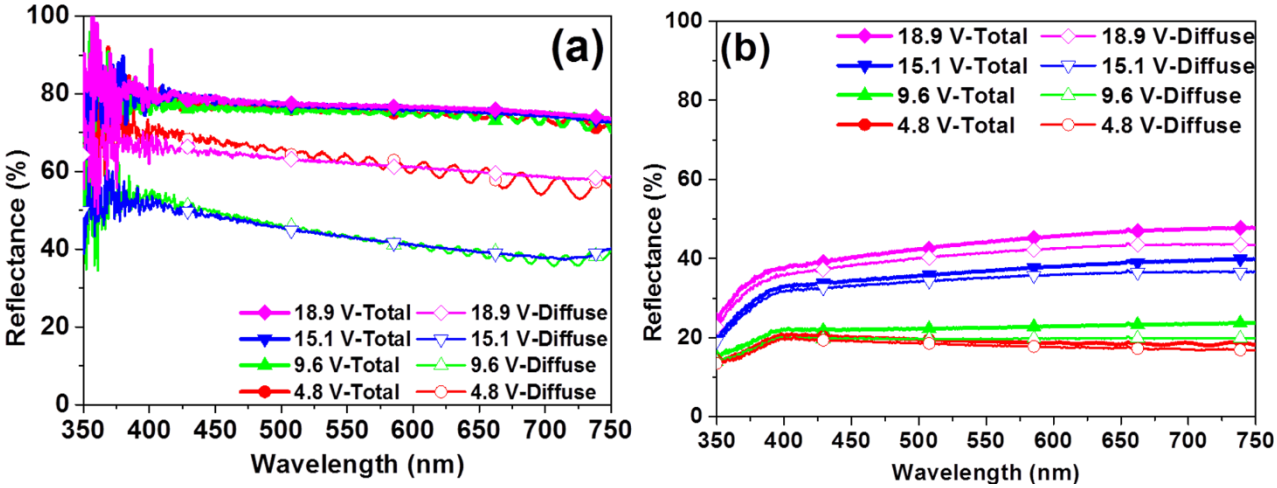

Figure 11.3: Reflectance spectra from the friction stir processed samples: (a) without and (b) with TiO_2 particles after sulphuric acid anodising at different voltages.

The total and diffuse reflectance of the surface increases with increasing anodising voltage. The specular reflectance which is a measure of glossiness of the surface is the difference between total and diffuse reflectance. For the samples anodised at 4.8 V, the specular reflectance is lowest and increases with increasing anodising voltage. This means that the surfaces appear glossier as the anodising voltage increases. Also, comparing the reflectance spectra of the anodised surfaces with and without TiO_2, it can be seen that the samples containing TiO_2 show an absorption region in the lower wavelengths, whereas for surfaces without TiO_2 there is no absorption regions.

11.3.3 Scanning Electron Microscopy

Figure 11.4 shows cross section of the samples after anodising, showing part of the FSP region and the anodised layer. The FSP region shows that the TiO_2 powder is well distributed in the Al matrix without any agglomeration with a surface fraction estimated to be equal to 1.5% which translates to 2.3 wt.% TiO_2. The average particle diameter calculated from the image analysis is 170 nm. The sample anodised at 4.8 V (Figure 11.4 (a)) shows an anodised layer which is disintegrated at various locations whereas the samples anodised at 9.6 V, 15.1 V, and 18.9 V appear intact. The TiO_2 particles in the anodised layer of the 4.8 V anodised sample appear unaffected as they do not show any brightness contrast in back scatter electron (BSE) detection mode when compared to the particles in the aluminium plate matrix. However, as the anodising voltage is increased, it is clearly visible that the particles are affected by the anodising process in an increasing manner, which is apparent from the difference in brightness contrast of the particles (marked with arrows) in the matrix to the particles in the anodised layer. After anodising at 9.6 V (Figure 11.4 (c) & (d)), the particles are only partially affected by the anodising process, while they were completely modified when the anodising is

performed at 18.9 V (Figure 11.4 (g) & (h)). Also, the affected region of the particles is always facing the surface (i.e. on top of the particle in Figure 11.4) which is being anodised. The anodised layer thickness is nearly the same for all the samples as the anodising time was varied to maintain the thickness at different voltages.

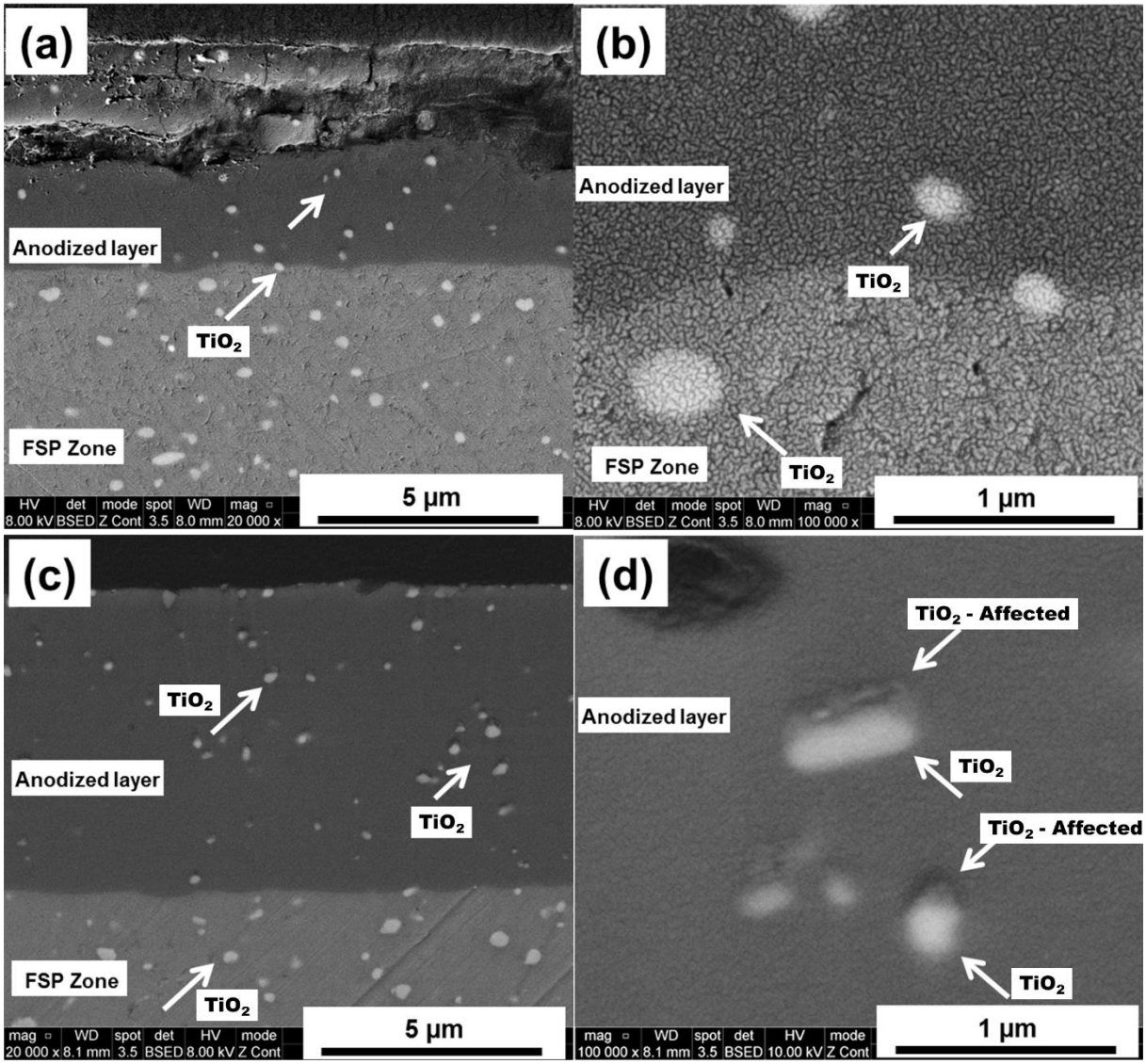

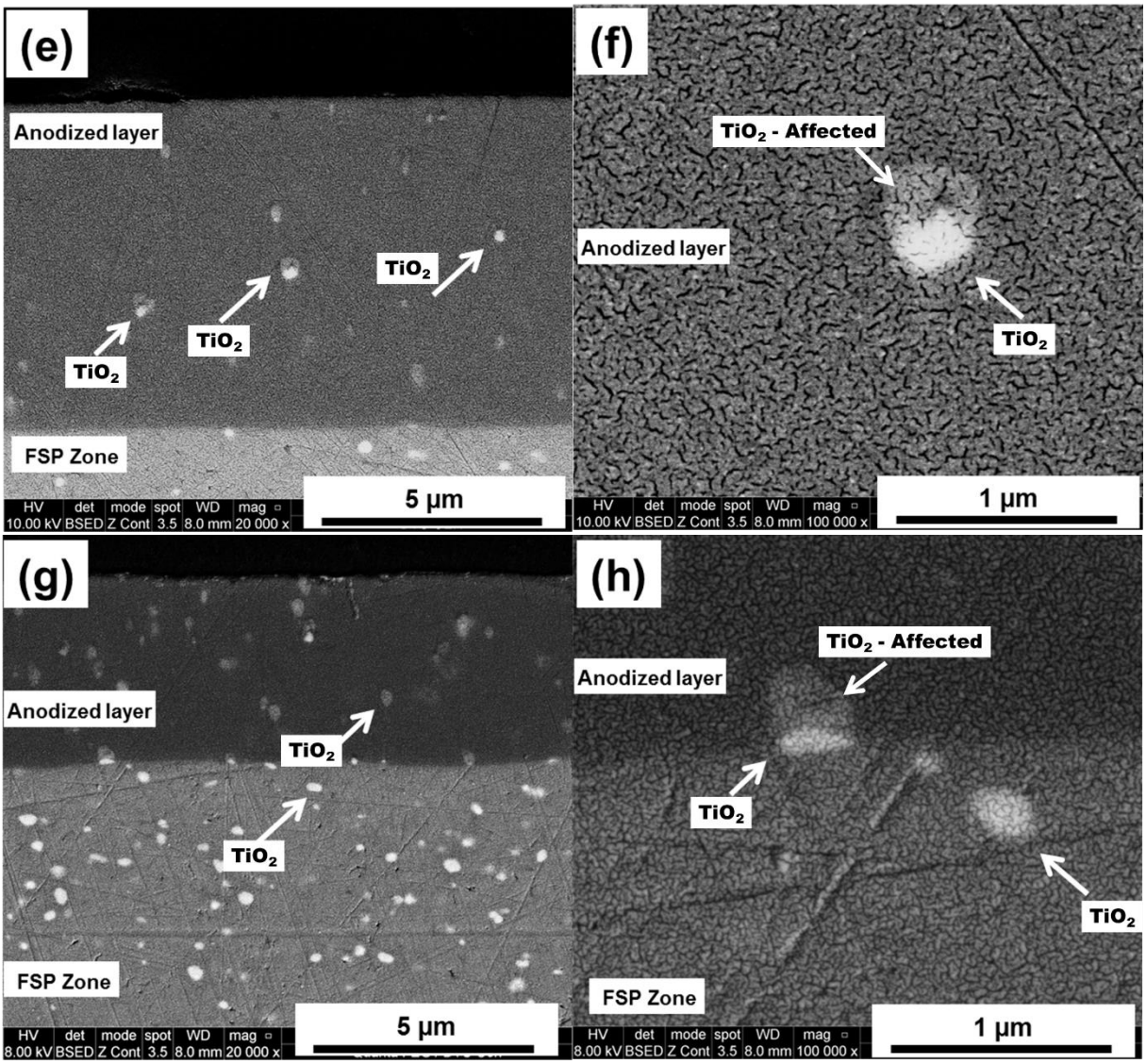

Figure 11.4: SEM-BSE cross section images of processed samples with TiO_2 after anodising: (a), (b) 4.8 V, (c), (d) 9.6 V, (e), (f) 15.1 V and (g), (h) 18.9 V. The grainy topography of the surfaces at high magnification is from the conductive Au sputter coating.

11.3.4 Grazing Incidence X-ray Diffraction

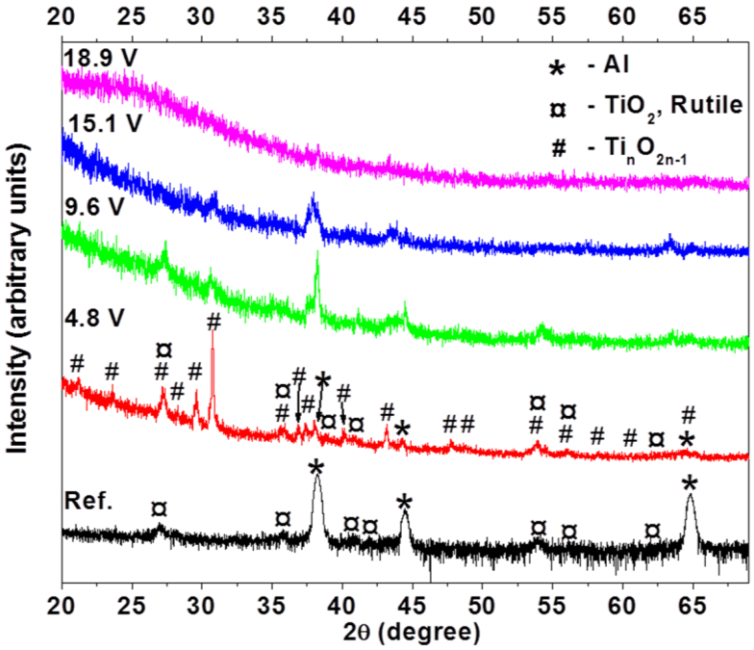

Figure 11.5: GI-XRD pattern from the processed surface of samples with TiO_2 before (Ref.) and after anodising at different voltages.

GI-XRD patterns from the FSP samples with TiO_2 before and after anodising are shown in Figure 11.5. The diffraction pattern from the FSP surface shows peaks for Al and rutile phase TiO_2, implying that the powder has not transformed or reacted considerably with the Al matrix under the FSP conditions. The diffraction pattern from the sample anodised at 18.9 V shows a broad peak around 25°, characteristic of amorphous anodic alumina layer. However, the samples anodised at lower voltages show several diffraction peaks other than rutile, which were indexed to a family of oxygen deficient titanium based oxides which are represented by the general formula Ti_nO_{2n-1} (like Ti_2O_3, Ti_4O_7 etc.). The diffraction peaks corresponding to these oxygen deficient phases decrease in intensity along with the Al peaks as the anodising voltage increases and are almost not present for the sample anodised at 18.9 V.

11.3.5 Transmission Electron Microscopy

The cross section TEM bright field image of FSP sample anodised at 9.6 V is shown in Figure 11.6 (a). Typical feature of the TiO_2 particle in the image shows that the particles are partially affected by the anodising treatment. A closer look reveals three regions namely the modified region on the top, while the interior part of the TiO_2 is unaffected, and a shadow region below the particle indicating un-anodised aluminium. The selective area electron diffraction (SAED) pattern from the modified region of the particle (inset top right) have diffuse diffraction rings indicating that it is transformed to amorphous phase, whereas the unaffected region (inset bottom left) shows sharp diffraction patterns, indicating that the crystalline structure of rutile TiO_2 is maintained. The TiO_2 particles in the 18.9 V anodised layer are completely modified, as shown in Figure 11.6 (b).

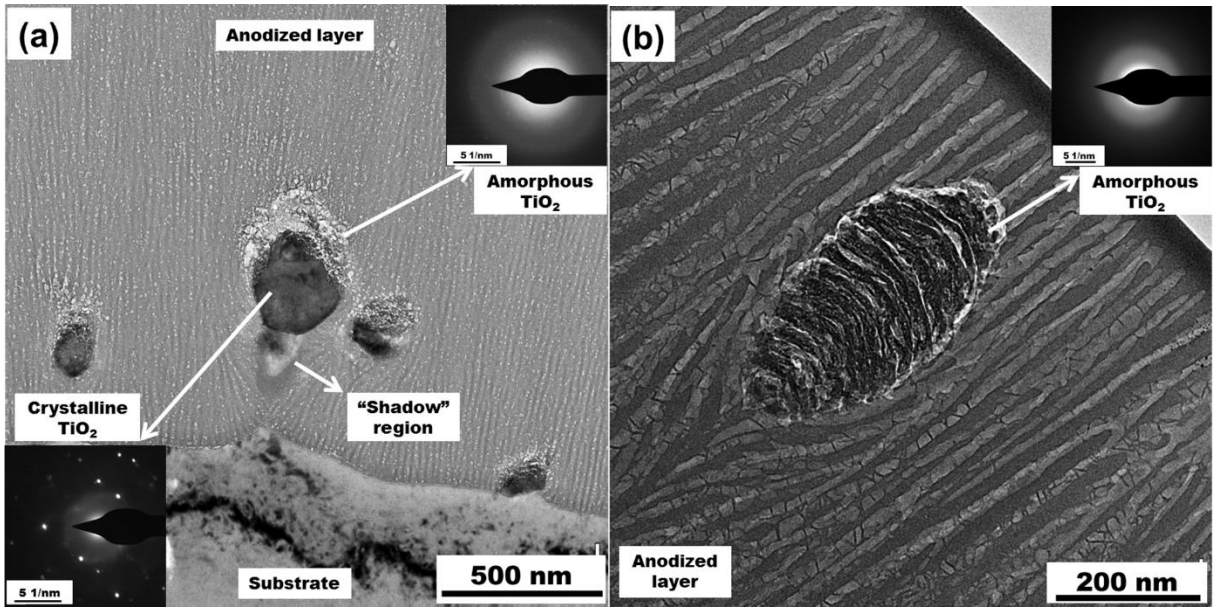

Figure 11.6: TEM bright field image and selected area electron diffraction (SAED) showing anodised layer cross section of the samples anodised at: (a) 9.6 V and (b) 18.9 V.

The SAED analysis from this particle shows diffuse diffraction rings meaning that the anodising process has completely transformed the rutile phase into an amorphous phase. The EDS data (not shown) indicate that there is no considerable change in the composition of these particles in the affected and unaffected region. The shadow region below the affected TiO_2 in the 9.6 V anodised sample (Figure 11.6 (a)) reveals a higher content of Al than the surrounding anodised Al matrix and the SAED pattern showed that it is crystalline. Similar shadow regions were observed for many particles in the anodised layer, however the samples anodised at 18.9 V (Figure 11.6 (b)) did not show any such shadow regions. Another difference in the samples anodised at different voltages is the morphology of the affected region of the TiO_2 particles. The 9.6 V anodised particle has been transformed into an amorphous state and appears powdery compared to the particle anodised at 18.9 V which appears to be transformed to an amorphous phase with a lamellar structure. It can also be seen that the particle anodised at 18.9 V, has elongated slightly in the direction of anodising compared to the partially affected particles anodised at 9.6 V. Similar features of partial amorphized TiO_2 and un-anodised Al "shadow region" were observed at various locations for the 9.6 V and 4.8 V anodised sample.

11.4 Discussion

11.4.1 Investigation of Al-TiO_2 surface composites

The FSP of Al surface together with TiO_2 powder resulted in a surface composite with uniform distribution of TiO_2 powder without any significant agglomerations. The forward movement of the tool during the overlapping passes has introduced striations on the FSP surface which is preserved and revealed clearly after anodising. The FSP process allows mixing of the involved phases in a semi-solid state of at least one phase due to frictional heat and pressure [30]. The temperatures involved during the friction stir welding (FSW) of Al have been reported to be as high as 500 ˚C at the centre of the stir zone and gradually reduced at locations away from the centre [20]. Similar temperatures would be involved in the friction stir processing of Al based MMC's when no external heating or cooling is applied as in the present case. At the peak processing temperatures, as the Gibb's free energy predicts, Al and TiO_2 react to form Al_3Ti and Al_2O_3 and the reaction is thermodynamically favourable at temperatures up to 3200 ˚C [31]. This reaction between Al and metal oxides has been exploited by many researchers to reinforce the Al matrix with intermetallic phases [16,18,32,33]. However, in the present work, phase analysis from the processed zone using GI-XRD (Figure 11.5) shows

that under the current processing conditions TiO_2 does not react with Al considerably as any diffraction peaks from reaction products like Al_3Ti are not detected.

11.4.2 Anodising behaviour

The anodising of FSP Al-TiO_2 surface composites in sulphuric acid resulted in the formation of different Ti-O based phases in the anodised layer along with amorphous anodic alumina. Diffraction peaks corresponding to several new phases that appear after 4.8 V anodising are indexed to the oxygen deficient TiO_2 phases. The phase diagram of Ti-O shows several phases of general formula Ti_nO_{2n-1} which exist between TiO_2 and Ti_2O_3 and are termed as Magneli phases [14,34–36]. As the anodising voltage is increased the diffraction peak intensities from these Magneli phases decreases and are almost absent when anodised at 18.9 V. This might be due to the increased oxidative power of the anodising process which is sufficient to annihilate the oxygen deficiency of these phases. Another possible explanation might be that these phases are present in the anodic layer even after high voltage anodising, but are amorphous and do not give any distinct diffraction peaks. The SEM images (Figure 11.4) and SAED analysis from TEM (Figure 11.6 (a) & (b)) of the anodised layer from the processed zone confirm the GI-XRD results that upon increasing the anodising voltage the TiO_2 is gradually transformed to the amorphous phase. The difference in morphology of the amorphous regions of TiO_2 particles between the samples anodised at 9.6 V and 18.9 V seen in the TEM images (Figure 11.6) is not understood currently and needs further investigation.

The mechanism of transformation from crystalline to amorphous for TiO_2 powder and formation of oxygen deficient phases can be explained by the instability of TiO_2 in sulphuric acid. TiO_2 is known to react with sulphuric acid to form $TiOSO_4$(aq.) and the reaction proceeds in forward direction up to a temperature of 130 ˚C [31]. Under the anodising conditions, the TiO_2 powder is expected to react with sulphuric acid in the electrolyte as the anodising is carried out at 18 ˚C. But, due to the imposed anodising voltage and presence of water, the aqueous $TiOSO_4$ phase is expected to hydrolyse and re-oxidize to form hydrated TiO_2. Another process of reduction and oxidation which takes place in parallel is that of Al. The Al matrix too, along with TiO_2 is dissolved into the electrolyte and reoxidized due to imposed anodising voltage. In the aqueous state it is easier for Al to oxidize than Ti as it has more affinity for oxygen and this would result in not enough oxygen for TiO_2 re-deposition from aqueous media and hence the presence of oxygen deficient TiO_2 phases. As the anodising voltage is increased from 4.8 V to 18.9 V, the oxidation potential is high and Al as well as Ti from aqueous media are more readily and completely oxidized and as a result we see lesser or negligible amount of oxygen deficiency in the re-deposited TiO_2 phases. This is also the reason why we see an increase in the amount of amorphous phases, as the re-deposited TiO_2 is mostly hydrated and amorphous.

Another feature observed in the microstructure of these anodised composites is that for 9.6 V anodising, the anodising pores are progressing around the TiO_2 powder particle but do not completely surround it and leave behind some Al below it. This can be seen in Figure 11.6 (a) where a “shadow region” of un-anodised Al is visible below the partially affected TiO_2 powder particle. However, as the anodising voltage is increased to 18.9 V, it is visible that the anodising pores are covering the whole TiO_2 powder particle and there is no un-anodised Al “shadow region” below the particle (Figure 11.6 (b)). This is due to the insulating nature of TiO_2 under DC anodising conditions which would require a higher anodising voltage to allow for complete oxidation of the underlying Al matrix [37]. Also, as the Al matrix is more active than the TiO_2 it would preferentially oxidize than the TiO_2 powder particles. As the anodising progresses, the anodic oxide-metal interface in the Al matrix around the TiO_2 powder particle would advance faster and at some point the interface would move beyond the particle resulting in incorporation of a partially affected TiO_2 powder particle in anodised Al matrix. When this happens, the access of electrolyte species to the TiO_2 powder particle and the Al below it would be reduced and the oxidation would reduce to an even slower rate. Similar behaviour of slower anodising of different second phases in Al alloys and presence of un-anodised Al matrix in the anodised regions has been reported earlier by Walmsley et al. [38] and Shimizu et al. [39].

11.4.3 Optical appearance

The optical appearance of a material is a function of its physical properties like refractive index as well as the surface, sub-surface structure, and morphology. It can be quantified in terms of the brightness or reflectance, and be qualitatively determined in terms of diffuse and gloss appearance. The surface gloss or specular gloss of a surface is mostly determined by the smoothness of the surface. Highly smooth surfaces have a very high specular gloss like mirrors, while diffuse appearance or diffuse reflectance is determined by how well the incident light is scattered from the surface. The total of diffuse and specular reflectance is equal to the incident light intensity (in an ideal case and without any transmission). A bright white, glossy anodised Al surface should have a high diffuse reflectance along with a considerable amount of specular reflectance. In the current case, TiO_2 powder of refractive index 2.6-2.9 is present in a transparent anodised Al matrix of refractive index 1.6-1.7. For incoming light, the TiO_2 powder acts as very efficient light scattering centres and would increase the diffuse reflectance of the sample. However, the anodising at lower voltages in the present investigation has resulted in dark appearance of the surfaces and also a low diffuse reflectance which increases with anodising voltage (Figure 11.3).

For non TiO_2 containing surfaces, the FSP zone has a slightly different appearance when compared to the adjacent Al after anodising (Figure 11.2). This is due to the difference in their respective grain sizes, as the FSP zone has a refined grain structure and different morphology compared to the initial Al matrix [20]. The surface of non-TiO_2 containing FSP sample surfaces look cloudy and porous after 4.8 V anodising, while it changes to clear and transparent as the anodising voltage increases to 18.9 V. The cloudy appearance of the 4.8 V anodised surface is due to prolonged anodising time of ~120 min used to achieve a 5 µm anodised layer thickness whereas for the samples anodised at 18.9 V, the same thickness was achieved in ~6 min of anodising. During anodising, the sulphuric acid electrolyte is dissolving the aluminium oxide and the external applied voltage is actively oxidizing it [3,40]. When the surface is exposed to the anodising electrolyte for a prolonged period, a “powdering” effect [1] due to oxide dissolution is usually observed which weakens the anodised layer and also makes it cloudy and porous. Same reason could be attributed for the observed cracking and disintegration at various locations of the anodised surface in the SEM images (Figure 11.4 (a), (b)).

Optical appearance of the anodised Al-TiO_2 samples clearly shows that the FSP process alone did not affect the appearance as the incorporation of TiO_2 has significant influence depending on the anodising voltage. The change in appearance is most prominent when the anodising voltage is increased from 9.6 V to 15.1 V. The reflectance measurements (Figure 11.3) show that the total reflectance and gloss of the samples also increases with increasing anodising voltage. The low gloss values obtained at 4.8 V anodising is due to the “powdering effect” caused by extended exposure to the sulphuric acid electrolyte.

The darkening of the anodised layer at lower anodising voltages can be attributed to two factors. Firstly, the reduced state of TiO_2, such as formation of Magneli phases has oxygen defects which act as colour centres. These defects have been shown to generate colours ranging from light to dark blue for TiO_2 crystals which are otherwise transparent [41,42]. Presence of these phases in the anodised Al matrix, confirmed by GI-XRD (Figure 11.5), gives rise to colouration of the surface as the anodised Al matrix alone is transparent [2,43]. As the anodising voltage is increased, the colour centres disappear from the TiO_2 as no XRD peak was observed, and this might lead to the observed change in appearance from dark to greyish white (Figure 11.5).

The second reason for darkening of anodised layer is the “shadow regions” of un-anodised Al under the TiO_2 particles (Figure 11.6 (a)). The left over metallic regions contribute to absorption of incident light in the otherwise transparent anodic layer. Chang et al. [44] and Saito et al. [45] using theoretical calculations have shown that the presence of dispersed metallic phases like Al in the transparent anodised Al matrix would lead to absorption of light as the metallic part has high extinction coefficient (refractive index of Al, n= 1.23 and extinction co-efficient k = 13.2). Gudla et al. [46] have used Al-Zr binary sputter coatings, which were then microstructurally modified using heat treatment to generate Al_3Zr intermetallics in the coating matrix. Subsequent anodising of the coating with Al_3Zr intermetallic particles at different voltages reported to show a direct correlation between the presence of un-anodised metallic phases and the reflectance of the surface. The surfaces were reported to be dark when there is un-anodised Al_3Zr in the anodised matrix, while the

surface became brighter by complete oxidation of the phases at higher anodising voltages. Both theoretical and experimental results reported are in clear agreement with the present observations of Al shadow regions and their effect on appearance. As the anodising voltage is increased the colour centres are annihilated due to complete oxidation and the high oxidative power reduces the level of un-anodised metallic Al phase. Further, the absorption/scattering phenomenon becomes more prominent when the scattering medium (in this case TiO_2 particles as well as un-anodised metallic Al) is in a size range half that of visible light wavelength (~ 200-350 nm) [47]. So, even a very low amount of un-anodised metallic Al in the right size would lead to a very high degree of absorptive scattering in the anodised layer.

The total reflectance values obtained at anodising voltage of 18.9 V is about 45 %. For white anodised aluminium used in space applications, reflectance values of up to 80 % have been reported [1]. The lower values of reflectance even at higher anodising voltage can be explained due to transformation of the TiO_2 particles from crystalline to amorphous phase upon anodising. The TiO_2 in crystalline state has a refractive index of 2.87, whereas in amorphous state the refractive index value drops to 2.42 (λ = 632.8 nm) [48,49]. The reduced refractive index results in lowering of light scattering efficiency by the pigments in anodic alumina and therefore might influence the reflectance value [50,51]. Further, volume fraction of TiO_2 has a direct influence as the coverage reduces, Al surface at the interface will be visible through the anodised layer.

11.5 Conclusions

- The friction stir processing of Al surface with TiO_2 particles produced surface composites with little or no agglomerations of TiO_2 particles.
- Optical appearance of the anodised Al-TiO_2 surface composites was found to be function of the anodising voltage due to the interaction of TiO_2 particles with the anodising bath and presence of un-anodised Al shadow regions below the particles.
- The SEM, TEM and GI-XRD analysis show that at lower anodising voltages (4.8 V and 9.6 V), TiO_2 particles are partially modified producing oxygen deficient Magneli phases, while higher anodising voltage has changed the TiO_2 to fully amorphous state.
- Presence of un-anodised Al part and Magneli phases at low voltage anodising makes the anodised surface darker with less diffuse reflectance, while the high voltage anodising results in brighter appearance with high diffuse reflectance due to removal of un-anodised Al and modification of TiO_2 to amorphous phase with lower refractive index than crystalline TiO_2.

References

[1] P.G. Sheasby, The Surface Treatment and Finishing of Aluminium and its Alloys, Finishing Publ, Teddington, 1974. doi:10.1179/000705974798321639.

[2] C.A. Grubbs, Anodizing of Aluminum, Met. Finish. 105 (2007) 397–412. doi:10.1016/S0026-0576(07)80359-X.

[3] G.E. Thompson, G.C. Wood, Porous anodic film formation on aluminium, Nature. 290 (1981) 230–232. doi:10.1038/290230a0.

[4] C. Siva Kumar, S.M. Mayanna, K.N. Mahendra, A.K. Sharma, R. Uma Rani, Studies on white anodizing on aluminum alloy for space applications, Appl. Surf. Sci. 151 (1999) 280–286. doi:10.1016/S0169-4332(99)00290-1.

[5] C. Siva Kumar, A.K. Sharma, K.N. Mahendra, S.M. Mayanna, Studies on anodic oxide coating with low absorptance and high emittance on aluminum alloy 2024, Sol. Energy Mater. Sol. Cells. 60 (2000) 51–57. doi:10.1016/S0927-0248(99)00062-8.

[6] A.L. Yerokhin, X. Nie, A. Leyland, A. Matthews, S.J. Dowey, Plasma electrolysis for surface engineering, Surf. Coatings Technol. 122 (1999) 73–93. doi:10.1016/S0257-8972(99)00441-7.

[7] J.M. Wheeler, J.A. Curran, S. Shrestha, Microstructure and multi-scale mechanical behavior of hard anodized and plasma electrolytic oxidation (PEO) coatings on aluminum alloy 5052, Surf. Coatings

Technol. 207 (2012) 480–488. doi:10.1016/j.surfcoat.2012.07.056.
[8] U. Malayoglu, K.C. Tekin, U. Malayoglu, S. Shrestha, An investigation into the mechanical and tribological properties of plasma electrolytic oxidation and hard-anodized coatings on 6082 aluminum alloy, Mater. Sci. Eng. A. 528 (2011) 7451–7460. doi:10.1016/j.msea.2011.06.032.
[9] J.A. Curran, T.W. Clyne, Thermo-physical properties of plasma electrolytic oxide coatings on aluminium, Surf. Coatings Technol. 199 (2005) 168–176. doi:10.1016/j.surfcoat.2004.09.037.
[10] L. Rama Krishna, K.R.. Somaraju, G. Sundararajan, The tribological performance of ultra-hard ceramic composite coatings obtained through microarc oxidation, Surf. Coatings Technol. 163-164 (2003) 484–490. doi:10.1016/S0257-8972(02)00646-1.
[11] R. Silvennoinen, K. Peiponen, K. Muller, eds., Specular Gloss - Light Reflection From a Rough Surface, Elsevier, Amsterdam, 2008. doi:http://dx.doi.org/10.1016/B978-008045314-9.50007-4.
[12] R. Silvennoinen, K. Peiponen, K. Muller, eds., Specular Gloss - Light Reflection From an Ideal Surface, Elsevier, Amsterdam, 2008. doi:http://dx.doi.org/10.1016/B978-008045314-9.50006-2.
[13] E.D. Palik, Chapter 2 - Refractive Index, Handbook of Optical Constanst of Solids, in: Handb. Opt. Constants Solids, Academic Press, Burlington, 1997: pp. 5–114. doi:http://dx.doi.org/10.1016/B978-012544415-6.50149-7.
[14] U. Diebold, The surface science of titanium dioxide, Surf. Sci. Rep. 48 (2003) 53–229. doi:10.1016/S0167-5729(02)00100-0.
[15] J. Winkler, Titanium dioxide, Vincentz Verlag, Hannover, 1992. doi:10.1016/S0306-3747(05)80006-5.
[16] P.C. Maity, S.C. Panigrahi, P.N. Chakraborty, Preparation of aluminium-alumina in-situ particle composite by addition of titania to aluminium melt, Scr. Metall. Mater. 28 (1993) 549–552. doi:10.1016/0956-716X(93)90194-W.
[17] P.C. Maity, P.N. Chakraborty, S.C. Panigrahi, Processing and properties of Al□Al2O3 (TiO2) in situ particle composite, J. Mater. Process. Technol. 53 (1995) 857–870. doi:10.1016/0924-0136(94)01757-R.
[18] C.F. Feng, L. Froyen, Formation of Al3Ti and Al2O3 from an Al–TiO2 system for preparing in-situ aluminium matrix composites, Compos. Part A Appl. Sci. Manuf. 31 (2000) 385–390. doi:10.1016/S1359-835X(99)00041-X.
[19] D.Y. Ying, D.L. Zhang, M. Newby, Solid-state reactions during heating mechanically milled Al/TiO2 composite powders, Metall. Mater. Trans. A. 35 (2004) 2115–2125. doi:10.1007/s11661-004-0160-2.
[20] R.S. Mishra, Z.Y. Ma, Friction stir welding and processing, Mater. Sci. Eng. R Reports. 50 (2005) 1–78. doi:10.1016/j.mser.2005.07.001.
[21] H.S. Arora, H. Singh, B.K. Dhindaw, Composite fabrication using friction stir processing - A review, Int. J. Adv. Manuf. Technol. 61 (2012) 1043–1055. doi:10.1007/s00170-011-3758-8.
[22] Z.Y. Ma, Friction Stir Processing Technology: A Review, Metall. Mater. Trans. A. 39 (2008) 642–658. doi:10.1007/s11661-007-9459-0.
[23] R.S. Mishra, Z.Y. Ma, I. Charit, Friction stir processing: A novel technique for fabrication of surface composite, Mater. Sci. Eng. A. 341 (2003) 307–310. doi:10.1016/S0921-5093(02)00199-5.
[24] I.S. Lee, P.W. Kao, N.J. Ho, Microstructure and mechanical properties of Al-Fe in situ nanocomposite produced by friction stir processing, Intermetallics. 16 (2008) 1104–1108. doi:10.1016/j.intermet.2008.06.017.
[25] C.J. Hsu, C.Y. Chang, P.W. Kao, N.J. Ho, C.P. Chang, Al-Al3Ti nanocomposites produced in situ by friction stir processing, Acta Mater. 54 (2006) 5241–5249. doi:10.1016/j.actamat.2006.06.054.
[26] Q. Zhang, B.L. Xiao, W.G. Wang, Z.Y. Ma, Reactive mechanism and mechanical properties of in situ composites fabricated from an Al–TiO2 system by friction stir processing, Acta Mater. 60 (2012) 7090–7103. doi:10.1016/j.actamat.2012.09.016.
[27] Q. Zhang, B.L. Xiao, Q.Z. Wang, Z.Y. Ma, In situ Al3Ti and Al2O3 nanoparticles reinforced Al composites produced by friction stir processing in an Al-TiO2 system, Mater. Lett. 65 (2011) 2070–2072. doi:10.1016/j.matlet.2011.04.030.
[28] Q. Zhang, B.L. Xiao, D. Wang, Z.Y. Ma, Formation mechanism of in situ Al3Ti in Al matrix during hot pressing and subsequent friction stir processing, Mater. Chem. Phys. 130 (2011) 1109–1117. doi:10.1016/j.matchemphys.2011.08.042.
[29] L. Zhang, R. Chandrasekar, J.Y. Howe, M.K. West, N.E. Hedin, W.J. Arbegast, et al., A metal matrix composite prepared from electrospun TiO2 nanofibers and an Al 1100 alloy via friction stir processing., ACS Appl. Mater. Interfaces. 1 (2009) 987–991. doi:10.1021/am900095x.
[30] P.B. Berbon, W.H. Bingel, R.S. Mishra, C.C. Bampton, M.W. Mahoney, Friction stir processing: A tool to homogenize nanocomposite aluminum alloys, Scr. Mater. 44 (2001) 61–66. doi:10.1016/S1359-6462(00)00578-9.

[31] OutoKumpu, HSC Chemistry, (2002).
[32] P. Yu, C.J. Deng, N.G. Ma, M.Y. Yau, D.H.L. Ng, Formation of nanostructured eutectic network in ??-Al2O3 reinforced Al-Cu alloy matrix composite, Acta Mater. 51 (2003) 3445–3454. doi:10.1016/S1359-6454(03)00165-4.
[33] D. Roy, S. Ghosh, a. Basumallick, B. Basu, Preparation of Fe-aluminide reinforced in situ metal matrix composites by reactive hot pressing, Mater. Sci. Eng. A. 415 (2006) 202–206. doi:10.1016/j.msea.2005.09.100.
[34] G. V Samsonov, The Oxide Handbook, IFI/Plenum, London, 1973. doi:10.1016/0040-6031(83)80052-5.
[35] P.G. Wahlbeck, P.W. Gilles, Reinvestigation of the Phase Diagram for the System Titanium–Oxygen, J. Am. Ceram. Soc. 49 (1966) 180–183. doi:10.1111/j.1151-2916.1966.tb13229.x.
[36] S. Andersson, A. Magnéli, Diskrete Titanoxydphasen im Zusammensetzungsbereich TiO1,75-TiO1,90, Naturwissenschaften. 43 (1956) 495–496. doi:10.1007/BF00632520.
[37] D. Regonini, V. Adamaki, C.R. Bowen, S.R. Pennock, J. Taylor, A.C.E. Dent, AC electrical properties of TiO2 and Magnéli phases, TinO2n−1, Solid State Ionics. 229 (2012) 38–44. doi:10.1016/j.ssi.2012.10.003.
[38] J.C. Walmsley, C.J. Simensen, A. Bjørgum, F. Lapique, K. Redford, The Structure and Impurities of Hard DC Anodic Layers on AA6060 Aluminium Alloy, J. Adhes. 84 (2008) 543–561. doi:10.1080/00218460802161590.
[39] K. Shimizu, G.M. Brown, K. Kobayashi, P. Skeldon, G.E. Thompson, G.C. Wood, Ultramicrotomy-a route towards the enhanced understanding of the corrosion and filming behaviour of aluminium and its alloys, Corros. Sci. 40 (1998) 1049–1072. doi:10.1016/S0010-938X(98)00006-7.
[40] G.D. Sulka, Highly Ordered Anodic Porous Alumina Formation by Self-Organized Anodizing, in: Nanostructured Mater. Electrochem., Wiley-VCH Verlag GmbH & Co. KGaA, 2008: pp. 1–116. doi:10.1002/9783527621507.ch1.
[41] M. Li, W. Hebenstreit, U. Diebold, A.M. Tyryshkin, M.K. Bowman, G.G. Dunham, et al., The influence of the bulk reduction state on the surface structure and morphology of rutile TiO2(110) single crystals, J. Phys. Chem. B. 104 (2000) 4944–4950. doi:Doi 10.1021/Jp9943272.
[42] U. Diebold, M. Li, O. Dulub, E.L.D. Hebenstreit, W. Hebenstreit, The relationship between bulk and surface properties of rutile TiO2 (110), Surf. Rev. Lett. 07 (2000) 613–617. doi:10.1142/S0218625X0000052X.
[43] S. Canulescu, K. Rechendorff, C.N. Borca, N.C. Jones, K. Bordo, J. Schou, et al., Band gap structure modification of amorphous anodic Al oxide film by Ti-alloying, Appl. Phys. Lett. 104 (2014) 121910. doi:10.1063/1.4866901.
[44] R. Chang, W.F. Hall, On the correlation between optical properties and the chemical /metallurgical constitution of multi-phase thin films, Thin Solid Films. 46 (1977) L5–L8. doi:10.1016/0040-6090(77)90068-2.
[45] M. Saito, Unoxidized Aluminum Particles in Anodic Alumina Films, J. Electrochem. Soc. 140 (1993) 1907. doi:10.1149/1.2220737.
[46] V.C. Gudla, S. Canulescu, R. Shabadi, K. Rechendorff, J. Schou, R. Ambat, Anodization and Optical Appearance of Sputter Deposited Al-Zr Coatings, in: J. Grandfield, TMS (Eds.), Light Met. 2014, John Wiley & Sons, Inc., 2014: pp. 369–373. doi:10.1002/9781118888438.ch63.
[47] R.J.D. Tilley, Colour due to Scattering, in: Colour Opt. Prop. Mater., John Wiley & Sons, Ltd, 2010: pp. 175–196. doi:10.1002/9780470974773.ch5.
[48] J.D.B. Bradley, C.C. Evans, J.T. Choy, O. Reshef, P.B. Deotare, F. Parsy, et al., Submicrometer-wide amorphous and polycrystalline anatase TiO2 waveguides for microphotonic devices, Opt. Express. 20 (2012) 23821. doi:10.1364/OE.20.023821.
[49] E.T. Fitzgibbons, K.J. Sladek, W.H. Hartwig, TiO2 Film Properties as a Function of Processing Temperature, J. Electrochem. Soc. 119 (1972) 735–739. http://jes.ecsdl.org/content/119/6/735.abstract.
[50] E. Hecht, Optics, Addison Wesley, 2002.
[51] R. Tilley, Colour and The Optical Properties of Materials: An Exploration of the Relationship Between Light, the Optical Properties of Materials and Colour, 2010. http://www.pilkington.com/products/bp/bybenefit/specialapplications/tecglass/ (accessed November 4, 2013).

12. HF Anodising of Al-TiO_2 Composites: Microstructure (Paper 8)

Effect of High Frequency Pulsing on the Interfacial Structure of Anodised Aluminium-TiO_2*

Abstract

High frequency anodising of friction stir processed Al-TiO_2 surface composites was investigated. The effect of anodising parameters on the structure and morphology of the anodic layer including the incorporation of the TiO_2 particles into the anodic layer is studied. Anodising process was carried out using a high frequency pulse and pulse reverse pulse technique at a fixed frequency in a sulphuric acid bath. The structure of the composites and the anodised layer was studied using scanning and transmission electron microscopy. The pulse reverse pulse anodising technique, using a negative potential on the low voltage cycle, showed extensive pore branching at the TiO_2 particle-anodic alumina matrix interface. However, the pulse anodising technique using zero potential during the low voltage cycle showed no such features in the pore morphology, but only entrapment of TiO_2 particles into the anodic alumina. Lower electrical resistance of the TiO_2 arising from oxygen defects, combined with applied negative potential during the low voltage cycle, are found to be responsible for the observed morphological features in the anodic alumina.

Keywords : Pulse Anodising; TiO_2; Aluminium; TEM; Microstructure.

*Published as ***V.C. Gudla***, F. Jensen, K. Bordo, A. Simar, R. Ambat, Effect of High Frequency Pulsing on the Interfacial Structure of Anodized Aluminium-TiO_2, J. Electrochem. Soc. 162 (2015) C303-C310.*

12.1 Introduction

Anodising is a widely applied surface finishing technique for Al and its alloys used in automobile, architecture, and aerospace industry. Anodised Al surfaces provide improved corrosion and wear resistance and more importantly pleasing aesthetics [1,2]. Different optical appearances for decorative purposes by colouring of the anodised layer are produced by pore filling using organic or inorganic dyes [3–5]. Recently attempts have been made for less intense optical shades using magnetron sputtered binary coatings of specific compositions [6–8] and anodising of Al based metal matrix composites like Al-TiO_2 [9]. Varying levels of bright and white anodised appearance was generated with the help of light scattering from the incorporated TiO_2 in an otherwise transparent anodic alumina matrix. However, the anodic layer obtained for magnetron sputtered coatings as well as for Al-TiO_2 composites under conventional DC anodising conditions was non-uniform in terms of completeness of the oxidation of different phases and the morphology of the anodic structure. These non-uniformities are attributed to the inherent electrochemical heterogeneity of the multiphase surfaces being anodised, which leads to an anodised layer with un-anodised or partially anodised Al based second phases as reported for commercial aluminium alloys [10–12]. In the case of Al-TiO_2 composites, the morphology of TiO_2 was altered, while electrochemical shadowing of the underlying Al by TiO_2 caused the presence of un-anodised Al beneath the particles [9]. Overall the presence of heterogeneities in the metallic form in the anodised layer cause darkening and dull appearance of the anodised layer [13–16].

The Al-Si cast alloys, due to their heterogeneity, and passivating nature of primary Si phase pose similar challenges during conventional DC anodising. Ono et al. [17] used high frequency electrolysis technique to investigate the effect on uniformity of the anodised surface of a cast Al-Si (AC8A) alloy. It has been found that the high frequency pulsing provides effective anodising of Al even below the incorporated primary Si phase due to pore branching, which otherwise is shadowed in conventional DC anodising. Kanagaraj et al. [18,19] studied the effect of pulse frequency and duty cycle on the anodising of AA1100 and reported that better quality anodic films are obtained at higher frequencies when compared to lower frequencies.

Juhl et al. [20] have examined pulse anodised Al alloys (both extruded and cast) and investigated different pulsing techniques namely: (i) low frequency pulsing [21], (ii) high frequency pulsing [22], and (iii) pulse reverse pulsing technique [23,24]. The hardness of the anodic layers was found to be lower for the pulse reverse pulse anodised samples when compared to the other two techniques. However, the structure of the anodic layers obtained did not show considerable differences as observed using scanning electron microscopy. Also, the ability to colour the anodic layer was lower for low frequency pulse anodised samples. Komisarov et al. [25] have studied the structure of pulse anodised AA6063 and AA7075 alloys and observed variations in the pore morphology. Extensive pore branching in the anodic layer was observed for AA7075 compared to AA6063. Also, the regions of oxide growth under high current regime and low current regime could be differentiated when the difference between the high and low pulse amplitudes was high. However, for decorative applications, pulse anodising and AC anodising is traditionally not recommended due to the danger of deposition of sulphur and sulphur compounds in the anodic pores during the cathodic reaction and subsequent yellowness of the anodic layer [26,27]. Nevertheless, with addition of heavy metals during anodising, the colours that can be imparted to the AC anodised surfaces showed very good light fastness [28–30]. Balasubramanian et al. [31] have studied the effect of Na_2SO_4 additive to sulphuric acid electrolyte for decorative AC anodising and particularly on the deposition of sulphur into the anodic matrix. Results showed that the alloys which cannot be easily anodised under DC conditions can be anodised effectively under AC conditions.

Based on the above investigations, the present work focuses on investigating the high frequency pulse and pulse reverse pulse technique for anodising the Al-TiO_2 surface composites. The effect of high frequency anodising using a zero (pulse technique) or negative (pulse reverse pulse) potential during cathodic cycle (low voltage cycle) is investigated on the resulting microstructure and optical appearance of the anodic layer. Transmission electron microscopy (TEM) was employed for observing the cross sections prepared using focused ion beam scanning electron microscope (FIB-SEM) in-situ lift-out technique. Various microstructural and morphological features of the anodised layer are presented and the underlying mechanism during anodising is discussed.

12.2 Experimental

12.2.1 Surface Composite Preparation

Aluminium substrates of dimensions 200 mm x 60 mm x 6 mm (Peraluman™ 853, Alcan rolled products, Germany) were obtained in the rolled condition. Commercial powders of TiO_2 (D_{50} = 210 nm, Ti-Pure™ R900, DuPont Titanium Technologies, Belgium) were used for making the surface composites. Friction stir processing was performed to generate Al-TiO_2 surface composites. The experimental details of the process are described elsewhere [9]. The processed composite surfaces were mechanically polished to a mirror finish and were subsequently degreased in a mild alkaline solution. Desmutting was performed by immersing in dilute HNO_3 followed by demineralised water rinsing. Finally the samples were ultrasonically cleaned in acetone for 15 min and dried in warm air.

12.2.2 High Frequency Anodising

The polished surface composites were anodised in a 20 wt.% sulphuric acid bath maintained at 10 °C. Anodising was performed by applying square voltage pulses (see Figure 12.1) from a function generator (33120A, Agilent Technologies). Waveforms of the voltage and current during the anodising were monitored with the help of a digital oscilloscope (TDS3034B, Tektronix). The anodised area was approx. 2 cm^2. The potential during anodic cycle (V_1, high voltage cycle) was either 10 V or 20 V and during cathodic cycle (V_2, low voltage cycle) was either -2 V (pulse reverse pulse, called PRPA) or 0 V (pulse, called PA). The pulse frequency was fixed at 2 kHz and the duty cycle (i.e. the ratio between the anodic cycle duration and the time interval between two subsequent pulses) was fixed at 50 % (i.e. t_1=t_2=500 µs). The total anodising time was adjusted for each sample so as to achieve an anodic layer thickness of approx. 10 µm.

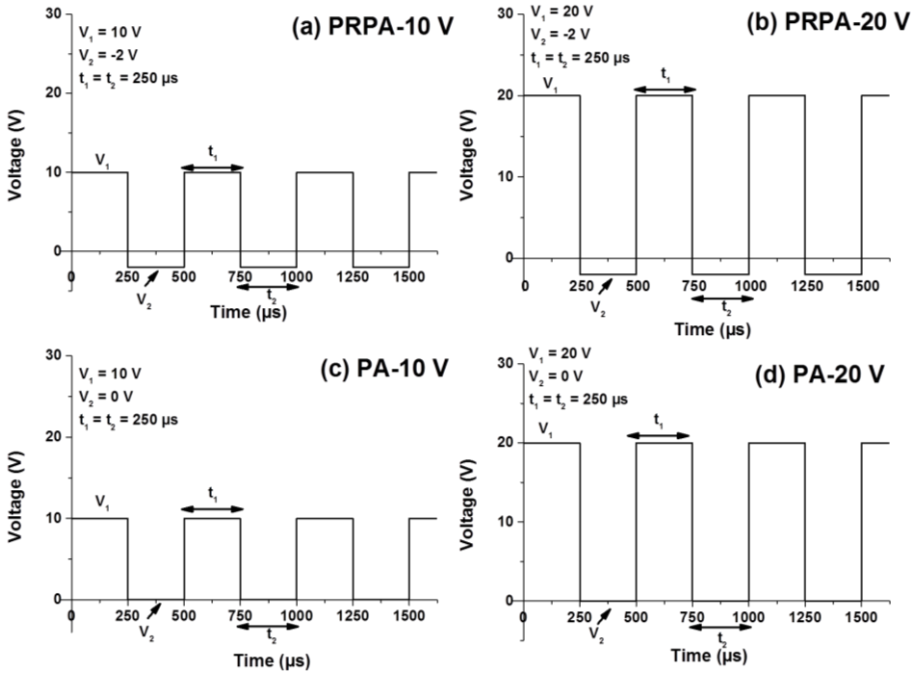

Figure 12.1: Voltage profiles used for high frequency Pulse Reverse Pulse Anodising: (a) PRPA-10 V, (b) PRPA-20 V; and Pulse anodising (c) PA-10 V, (d) PA-20 V.

12.2.3 Microstructural Characterization

The microstructure and morphology of the Al-TiO_2 composites and the obtained anodic layers were studied by a scanning electron microscope (Quanta 200™ ESEM FEG, FEI) equipped with a back scatter electron detector (BSED) and energy dispersive spectroscopy (EDS) capability (80 mm^2 X-Max™ Silicon drift detector, Oxford Instruments). The SEM was typically operated at an acceleration voltage of 10 keV. For cross-sectional imaging, the samples were mounted in an epoxy and polished in cross-section. In order to minimize

charging, the samples were coated with 2-3 nm Au layer by magnetron sputtering (Cressington 208HR sputter coater). Transmission electron microscopy (TEM) analysis was carried out on the FSP and anodised sample cross section using a TEM (Model Tecnai™ G2 20) operating at 200 keV. The lamella for TEM were prepared using FIB-SEM in-situ lift-out (Model Quanta 200 3D™ DualBeam, FEI) and further thinned for electron transparency in a FIB-SEM (Helios Nanolab™ DualBeam, FEI).

12.3 Results

12.3.1 Visual Appearance of Anodised Surface

The visual appearance of the anodised surfaces using different anodising parameters is shown in Figure 12.2. The samples anodised using PRPA appear slightly brighter than the specimens anodised using PA irrespective of the potential during the anodic cycle. However, there is no significant difference in the brightness of the surfaces anodised with different anodic pulse amplitude. The striations observed in the anodised FSP Al-TiO_2 region are due to the forward movement of the FSP tool. The non-homogeneities in the distribution of the TiO_2 particles after FSP are revealed visually as striations after anodising.

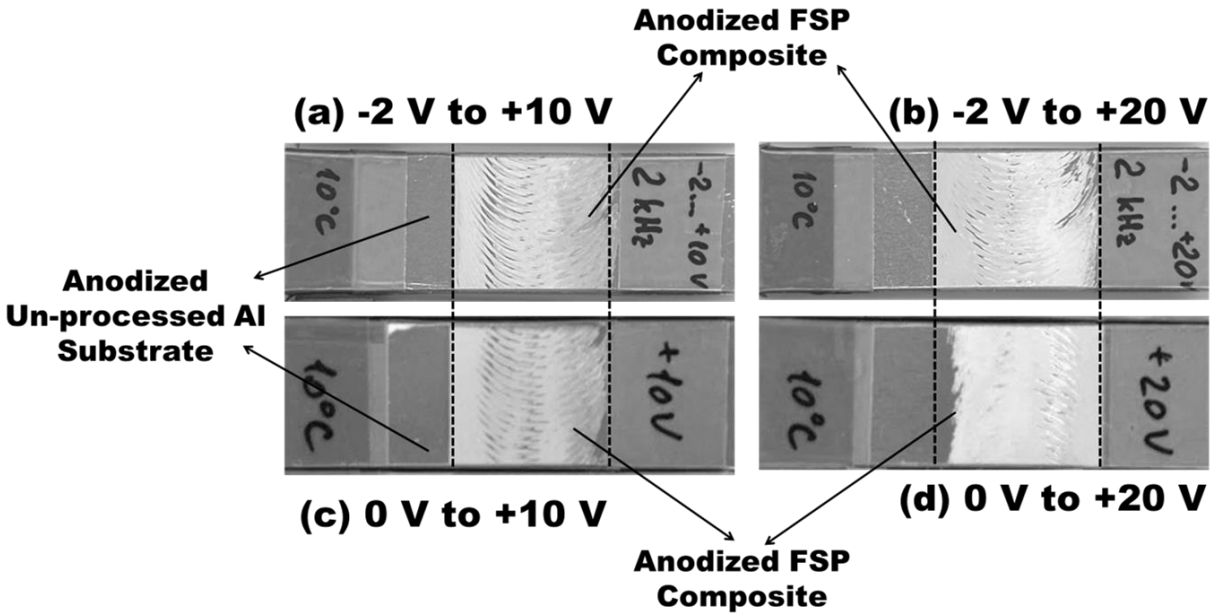

Figure 12.2: Optical images of anodised FSP Al-TiO_2 samples using: (a) PRPA-10 V (b) PRPA-20 V (c) PA-10 V and (d) PA-20 V.

12.3.2 Microstructure of Al-TiO_2 Surface Composites

Bright field TEM image(s) of the FSP Al-TiO_2 composite, in cross section is shown in Figure 12.3 (a) and (b). The TiO_2 particles have not disintegrated during the FSP process and retained their spherical shape. The average size of the TiO_2 particles is approx. 200 nm. The particles are homogenously distributed in the Al matrix, and are found both within the grains and at the grain boundaries of the Al matrix. Further, there is no observable evidence of any porosity or voids near the TiO_2-Al matrix interface. There is no visible contrast at the interface hinting that there is very little reaction products at the interface due to chemical interactions between Al-TiO_2 during FSP (Figure 12.3 (b)).

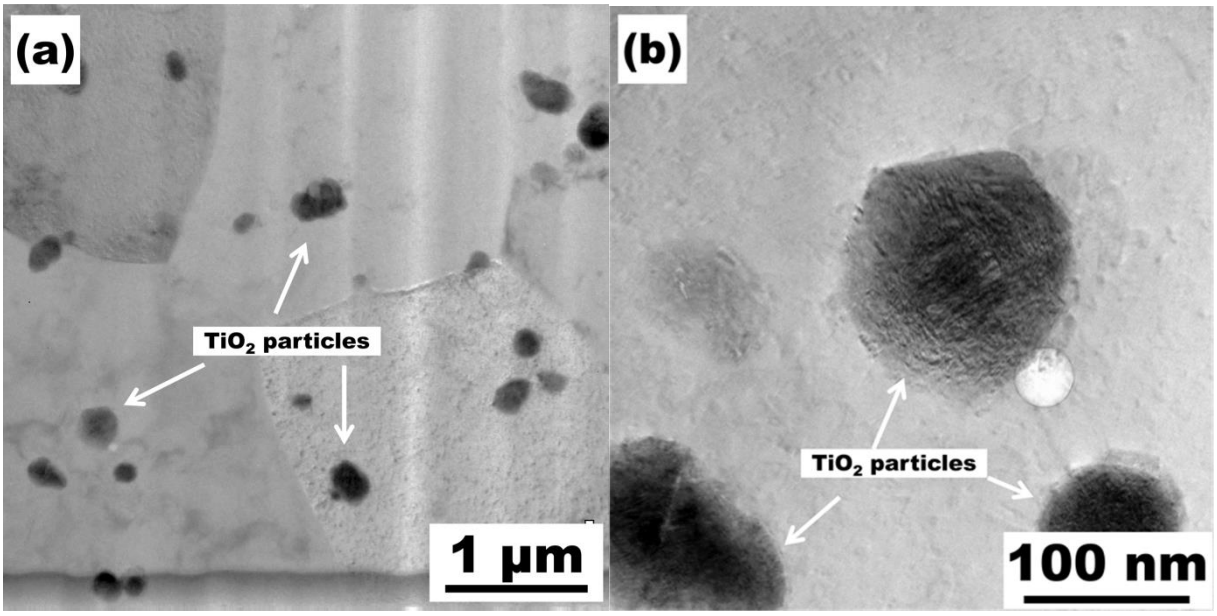

Figure 12.3: Bright field TEM cross section images of: (a) FSP Al-TiO_2 surface composites and (b) incorporated TiO_2 particle into the Al matrix, the circular hole at the edge of the particle is due to e-beam damage.

12.3.3 Microstructure of the Anodised Layer

12.3.3.1 Scanning Electron Microscopy

Figure 12.4 (a) shows the cross-sectional image of the anodised layer after PRPA-10 V. The image shows dark spots on upper part of the anodised layer, while bottom part of the layer shows bright spots. The thickness of the whole anodised layer was approx. 10 µm. It is observed that an increase in the anodic cycle potential to +20 V (PRPA-20 V) results in the appearance of these dark spots throughout the thickness of the anodic layer (see Figure 12.4 (b)). EDS analysis (not shown here) of the bright and dark spots reveals the presence of Ti and O, suggesting that it corresponds to the TiO_2 particles incorporated in the anodised layer. However, for PA-10 V (see Figure 12.4 (c)), the TiO_2 particles are present mostly as bright spots and increase of anodic cycle potential to +20 V (PA-20 V) caused more dark spots (see Figure 12.4 (d)).

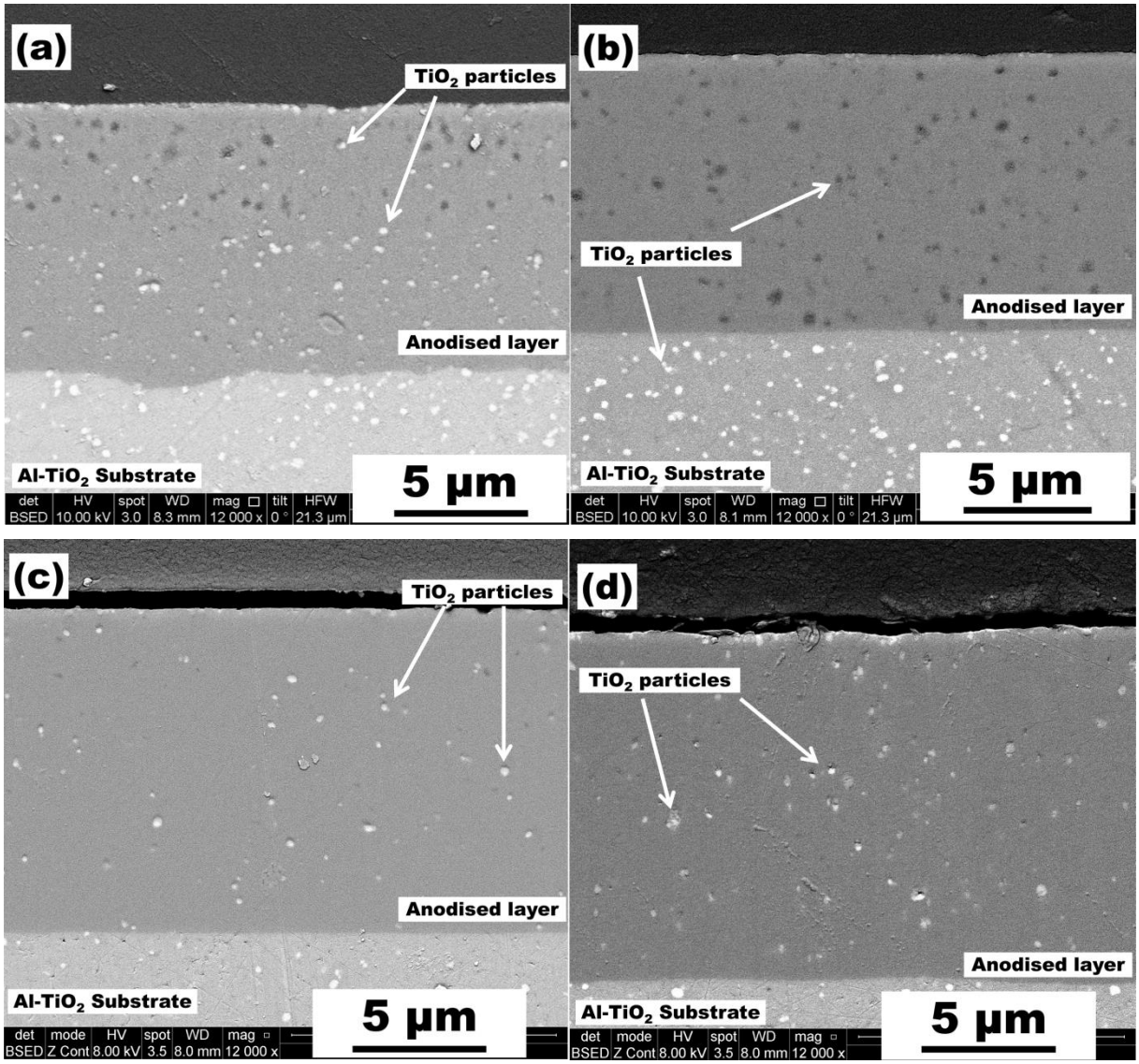

Figure 12.4: SEM-BSE cross-section image of the FSP Al-TiO_2 sample anodised using: (a) PRPA-10 V, (b) PRPA-20 V, (c) PA-10 V, and (d) PA-20 V at 2 kHz. (The TiO_2 particles can be seen in the Al-TiO_2 composite substrate and in the anodised layer as both bright and dark spots.)

12.3.3.2 Transmission Electron Microscopy

12.3.3.2.1 High Frequency Pulse Reverse Pulse Anodising

TEM bright field image of PRPA-10 V anodic layer cross-section is shown in the Figure 12.5 (a). It can be seen that the bright as well as dark spots that were observed in the SEM-BSE cross-section image (Figure 12.4 (a)) are TiO_2 particles in the anodic layer that are different in their morphology. The dark spots in the SEM-BSE image (Figure 12.4 (a)) at the top half of the anodic layer correspond to TiO_2 particles in Figure 12.5 (a) which are transformed to a porous morphology in the anodic matrix during anodizing or in some cases are completely lost leaving behind a void (Figure 12.5 (b)). The brighter spots observed in the SEM-BSE image at the bottom of the anodic layer correspond to denser TiO_2 particles, which are transformed to a lesser extent or are preserved in their crystalline state.

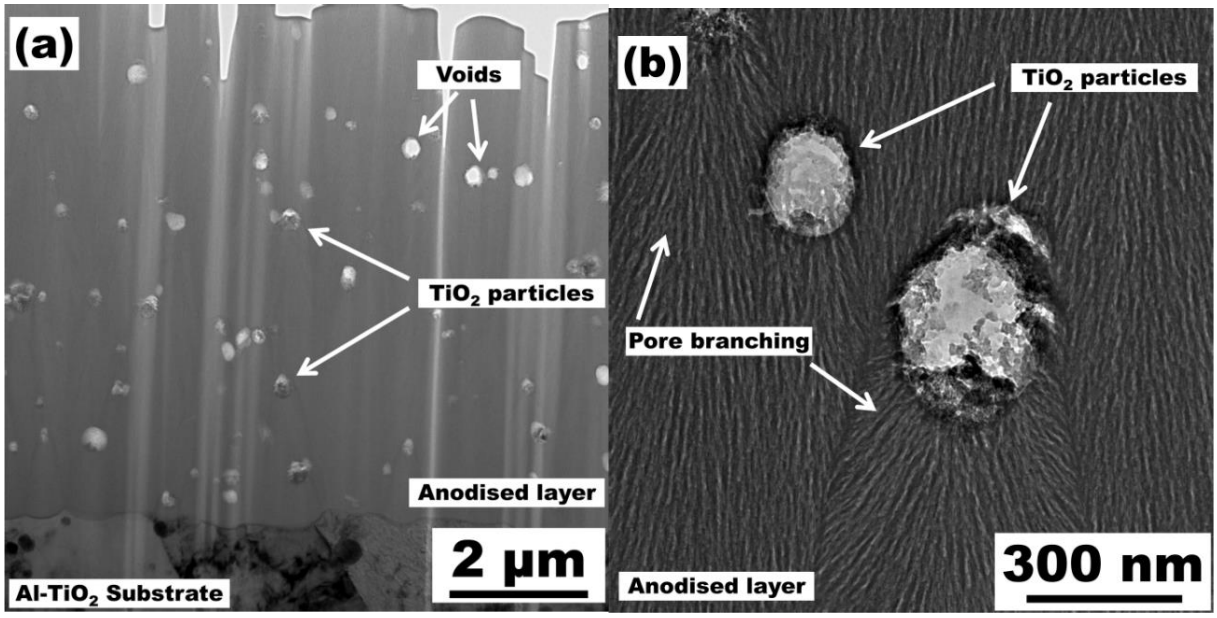

Figure 12.5: Bright field TEM cross-section images of FSP Al-TiO_2 sample anodised using: (a) PRPA-10 V at 2 kHz showing (b) transformed TiO_2 particles in the anodic matrix and preferential origin of anodic pores from the TiO_2 particle-Al interface.

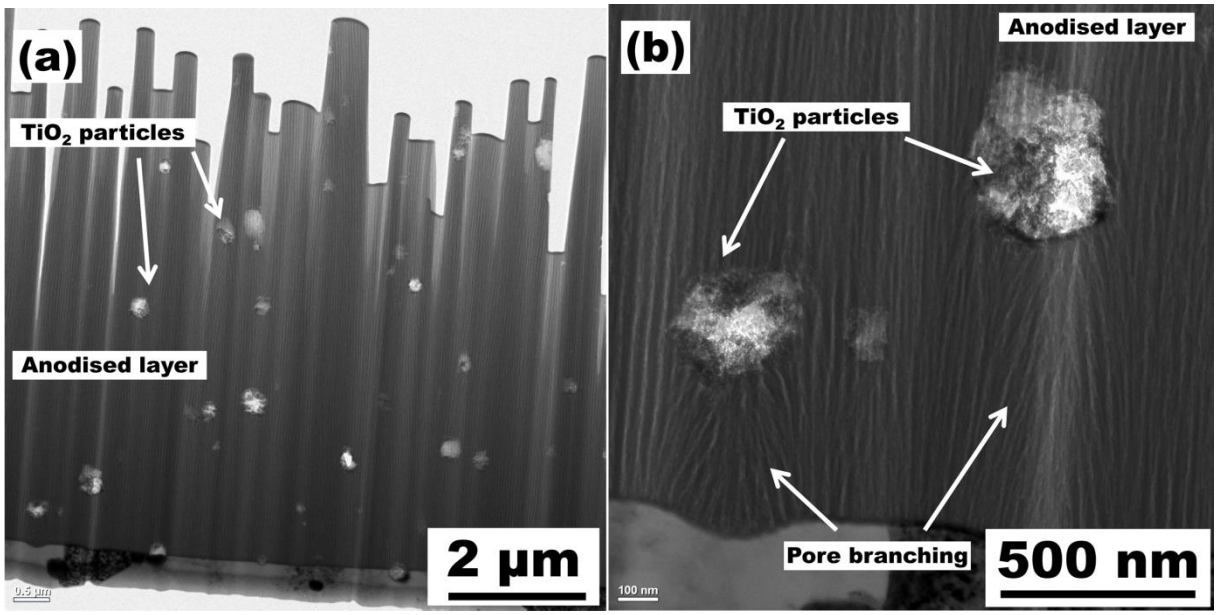

Figure 12.6: Bright field TEM cross-section image of FSP Al-TiO_2 sample anodised using: (a) PRPA-20 V at 2 kHz showing (b) transformed TiO_2 particles in the anodic matrix and preferential origin of anodic pores from the TiO_2 particle-Al interface.

Higher magnification image shows that the anodising pores originate preferentially from the bottom of the TiO_2 particles (marked as pore branching), whereas in the surrounding matrix they appear continuous (Figure 12.5 (b)). Further, the anodic layer-substrate interface has grown more inward into the substrate compared to the surrounding areas (Figure 12.5 (a)). Similar morphological features are also observed for samples anodised using PRPA-20 V at 2 kHz as seen in Figure 12.6 (a) and (b).

12.3.3.2.2 High Frequency Pulse Anodising

Figure 12.7 shows the bright field TEM images of the sample anodised using PA-10 V in cross section. The TiO_2 particles are intact in the anodic Al matrix and there is little observable transformation to porous morphology of the TiO_2 particles. These particles are observed as bright spots in the SEM-BSE image in Figure 12.4 (c). Voids on the top of the TiO_2 particles are seen in the anodic matrix. The anodised pore structure in this case is different from the structure observed for pulse reverse pulse anodising technique (Figure 12.5 and Figure 12.6). The anodised pores appear to be growing around the TiO_2 particle unlike originating below the particle as in the case of PRPA-10 V and PRPA-20 V. Further, a clear discontinuity is observed in the anodic pore structure. Careful observation of the pore structure shows that the anodising process has not completely progressed under the TiO_2 particles (marked as incomplete anodising in Figure 12.7 (a) and (b)).

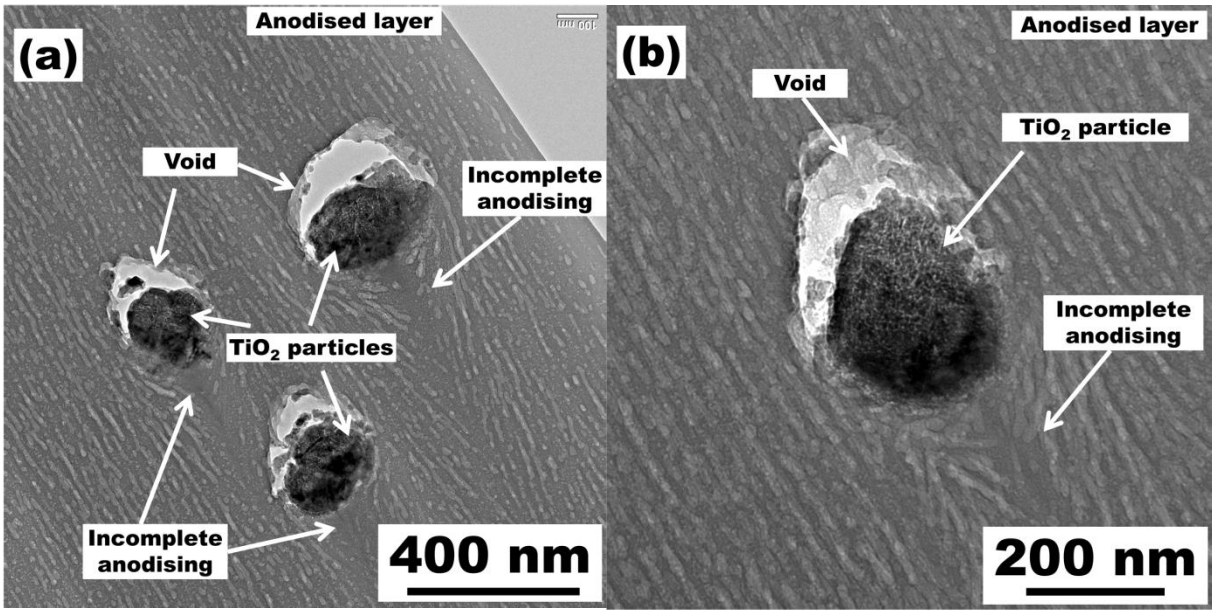

Figure 12.7: Bright field TEM cross-section image of FSP Al-TiO_2 sample anodised using: (a) PA-10 V at 2 kHz showing (b) TiO_2 particles with voids on the top that are incorporated into the anodic layer and incomplete progress of anodic pores below the particles.

The bright field TEM images of sample anodised with PA-20 V at 2 kHz in cross section is shown in Figure 12.8. The effect of increasing the anodic cycle voltage can be clearly observed in terms of the progress of the pores under the TiO_2 particles. The TiO_2 particles are completely surrounded by pores unlike the features observed in Figure 12.7 but are not originating from the TiO_2 particle-anodic matrix interface like seen in Figure 12.5 and Figure 12.6. The anodic pore structure observed is intermittent and discontinuous similar to that observed for the PA-10 V sample.

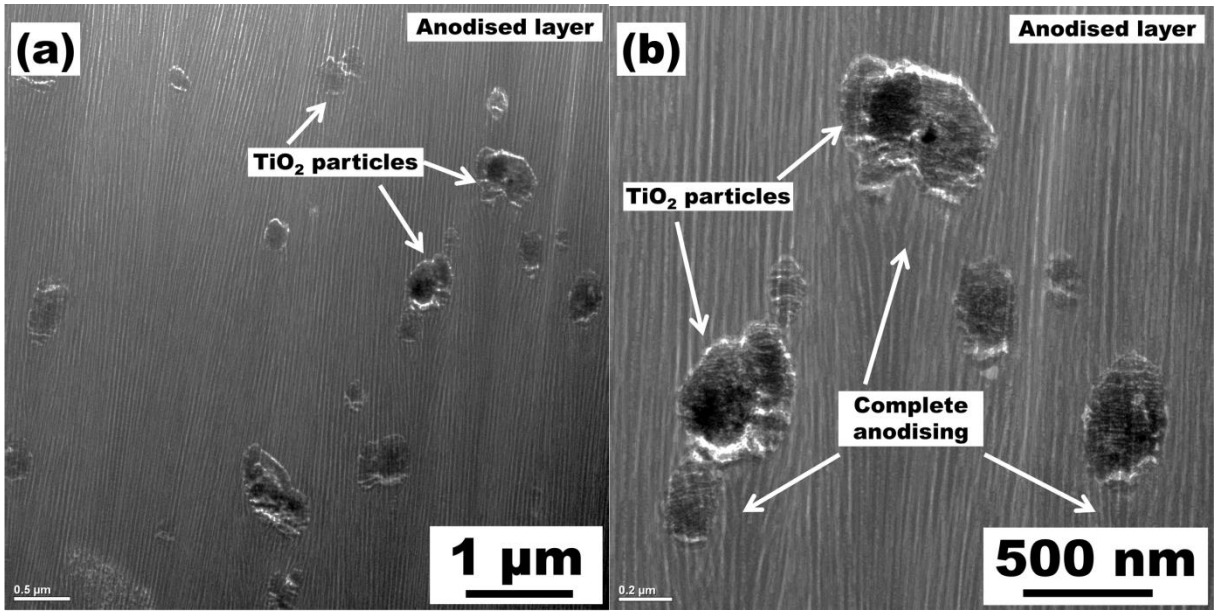

Figure 12.8: Bright field TEM cross-section image of FSP Al-TiO_2 sample anodised using: (a) PA-20 V at 2 kHz showing (b) TiO_2 particles that are incorporated into the anodic layer and coverage of anodic pores below the particles.

12.4 Discussion

Friction stir processing of Al with TiO_2 provided surface composites with little or no degradation of the TiO_2 particles. There are no observable voids or discontinuity between the TiO_2 particles and the Al matrix, and no bulk reaction products are observed (see Figure 12.3). The temperature involved during FSP of Al is reported to be between 400-450 °C [32]. Although the increase in temperature during the FSP process is enough for the formation of Al-Ti intermetallic phases [33–35], the quenching effect provided by high cooling rate of the thick Al base plate might have reduced the reaction kinetics. Gudla et al. [9], using grazing incidence X-ray diffraction, showed that the FSP process itself does not cause any considerable formation of Al-Ti based phases under the same processing conditions.

Anodising using pulse reverse pulse technique (PRPA) shows visually brighter surfaces when compared to pulse anodising (PA) (see Figure 12.2). The microstructure of the anodic layer obtained using PRPA shows transformation to porous morphology and subsequent loss of TiO_2 particles in the anodic matrix and the effect is increased with increase in the anodic cycle potential (Figure 12.4 (a) and (b)). However, when only PA is used, the TiO_2 particles are incorporated and retained in the anodic layer to a higher extent (Figure 12.7 and Figure 12.8) both in transformed and non-transformed states. The other main difference in the morphology of the anodic layer is that of the observed anodic pore structure. The PRPA technique shows pores originating from the bottom of the TiO_2 particles (Figure 12.5 and Figure 12.6) whereas the anodic pores are observed to be growing around the TiO_2 particles under PA conditions (Figure 12.7 and Figure 12.8). Also, the completeness of the anodising beneath the particles is observed to be higher for PA-20 V when compared to PA-10V.

Gudla et al. [9], using grazing incidence X-ray diffraction, have reported the existence of various kinds of Ti-O phases of general formula Ti_nO_{2n-1} (magneli phases) in the anodic layer of Al-TiO_2 surface composites after being subjected to conventional DC sulphuric acid anodising. This generation of oxygen defects in the TiO_2 was attributed to the combined effect of sulphuric acid electrolyte and the applied anodising potential. The presence of Magneli phases [36] increases the electrical conductivity of the TiO_2 [37,38]. The electrical properties of the Ti-O phases under AC conditions are frequency and temperature dependent as shown by Regonini et al. [39]. The conductivity of the phases is observed to be six orders of magnitude higher than TiO_2 (rutile) at room temperature measured at 2 kHz AC frequency [40]. This increased conductivity makes the Ti-

O Magneli phases in the anodic layer more conductive under AC/pulse conditions at high frequency compared to the conventional DC anodising.

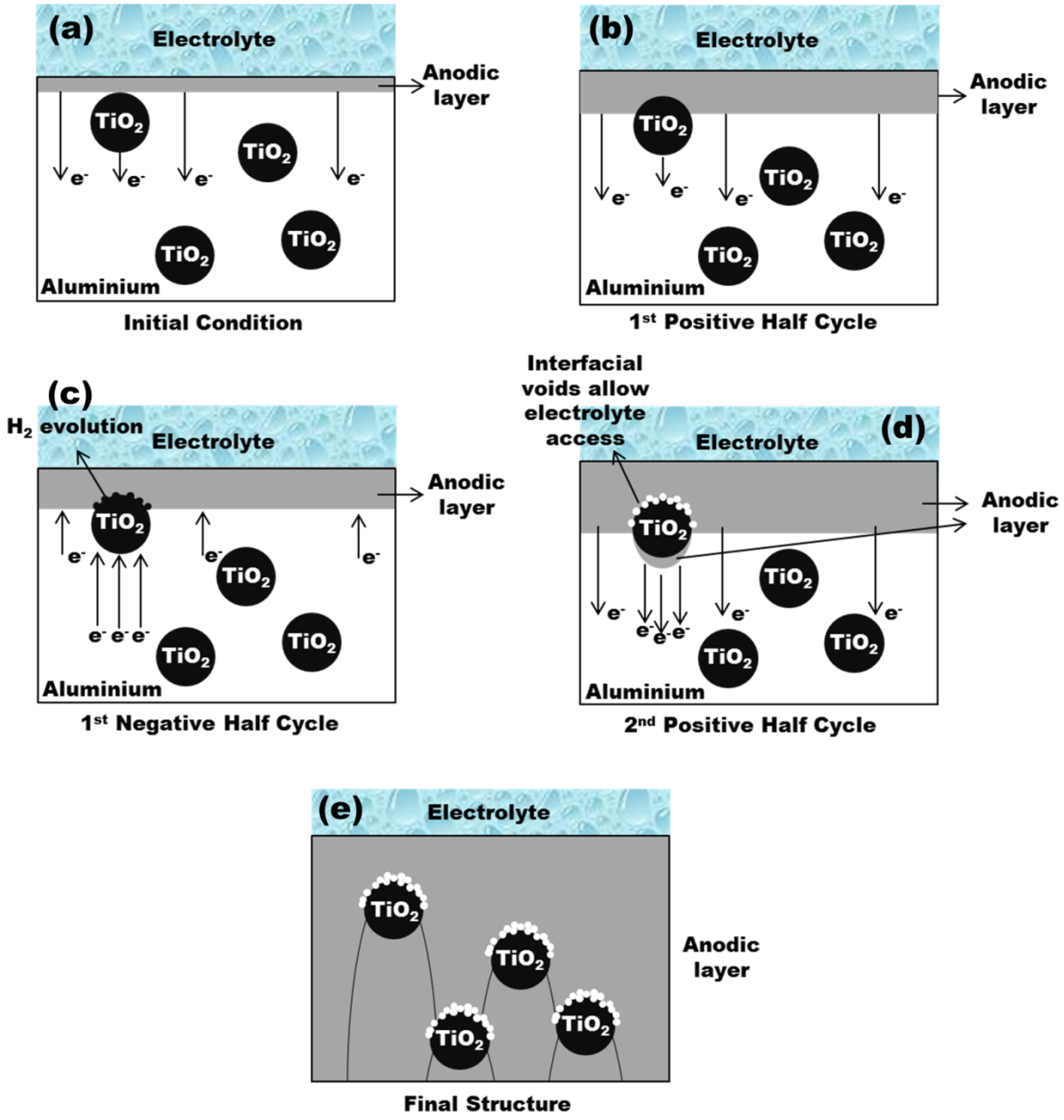

Figure 12.9: Schematic showing the: (a) to (e) stepwise anodic film growth on Al-TiO_2 composite and successive incorporation of TiO_2 particles during high frequency pulse reverse pulse anodising (PRPA).

The observed morphology and structure of the anodic layer for high frequency PRPA and PA of Al-TiO_2 composites can be explained as below and is also schematically shown in Figure 12.9 as sequence of possible steps. Under PRPA, anodic oxidation of Al and consequent film growth takes place under the applied positive potential (+10 V or +20 V). The film grows uniformly over the particle free Al matrix and in the surrounding areas of the TiO_2 particles, which are at the anodic oxide-substrate interface. The TiO_2 particles are assumed to remain chemically inert during the anodic or positive cycle. At the end of positive cycle, the TiO_2 particles are partially surrounded by the anodic Al-oxide that is formed (Figure 12.9 (b)). The possibility of formation of a barrier type anodic alumina layer over the TiO_2 particles is not clear yet. During the cathodic

or negative cycle of PRPA, the anodic film on Al ceases to grow and cathodic reactions like hydrogen gas evolution (and cathodic deposition of elements such as Sulphur) take place [41] if there is sufficient negative potential applied to allow for current through the barrier layer. In the present situation, the applied negative cycle is only -2 V and is not sufficient for current flow through the barrier layer.

However, as the TiO_2 (containing Magneli phases) is more electrically conducting than the barrier anodic Al oxide, the cathodic current gets localised (due to lower electrical resistance) at the particles that are partially in the substrate Al metal matrix and partially surrounded by the anodic Al oxide. As a result, the cathodic reactions like hydrogen gas evolution take place more vigorously at the TiO_2 particle-electrolyte interface when compared to that at the barrier layer-electrolyte interface (Figure 12.9 (c)). This localised vigorous gas evolution causes the barrier anodic Al oxide (if formed during the previous anodic cycle) over the TiO_2 particles and the surrounding porous anodic alumina to get mechanically weakened or completely disintegrated generating porosity and voids at the TiO_2 particle-anodic layer interface. Other factors that might contribute to porosity at the interface are the formation of oxygen during the anodic oxidation [42–45] and density mismatch between the growing anodic oxide and the TiO_2 particle. However, hydrogen evolution during cathodic cycle is very vigorous, therefore expected to be a greater contributing factor. As a result of this porosity, the electrical resistance at the interface of the TiO_2 particles-anodic layer-Al substrate junctions is further reduced [46]. In parallel, during the cathodic cycle, the anodic barrier layer on the particle free interface is also expected to be reduced in thickness due to chemical dissolution by the anodising electrolyte. But, in the present scenario the cathodic cycle time is only 250 µs and according to the dissolution rates reported by Zhang et al. [47] for anodic barrier oxides in sulphuric acid thinning of barrier layer can be neglected.

During the next positive or anodic cycle, the anodic film growth takes place evenly on the particle free Al areas (Figure 12.9 (d)). Since the TiO_2 is conducting and also the electrical resistance is lowered at the particle locations due to hydrogen evolution and subsequent mechanical weakening of the anodic oxide, the anodic current is localised to a higher extent at the TiO_2 particle-substrate interface. The generated porosity or voids in the cathodic cycle at the TiO_2 particle-Al matrix allows easy access for the anodising electrolyte and porous anodic film growth begins at the interface. The result of this phenomenon can be observed in Figure 12.5 and Figure 12.6, where the anodising pores are originating from the TiO_2 particle-matrix interface. This localisation of anodic current at the TiO_2 particles results in a faster anodic film growth beneath the particles and leads to the anodic structure as observed in Figure 12.9 (e).

Under high frequency pulse anodising conditions (PA), the applied potential during the cathodic cycle is only 0 V and hence the corresponding cathodic reactions will not take place. When the second cycle of anodic potential is impressed upon the system, the anodic film continues to grow more or less at the same rate in particle free areas and also around the particles. Once the TiO_2 particles are embedded into the anodic oxide, they lose electrical contact from the substrate matrix and hence the anodic layer does not show any pores generated at the TiO_2 particle-anodised matrix interface (Figure 12.7 and Figure 12.8). The extent of coverage of the TiO_2 particles by the anodic alumina matrix is observed to be dependent on the amplitude of the anodic cycle potential that is applied (+10 V or +20 V). The higher the potential applied, better the anodic pores surrounding the TiO_2 particle (Figure 12.8). Gudla et al. [7–9] have shown with the use of sputter deposited Al-Zr coatings that un-anodised metallic phases and left over aluminium matrix in an anodic layer contribute to darkening of the anodic layer. This phenomenon may be one of the reasons behind the slightly darker appearance of pulse anodised (PA) surfaces when compared to pulse reverse pulse anodised (PRPA) surfaces (see Figure 12.2) as there is more probability of presence of un-anodised Al under the TiO_2 particles for PA technique (especially PA-10 V)

In Figure 12.5 there are locations where the TiO_2 particles are lost from the anodic matrix leaving behind voids. This is assumed to be due to the vigorous hydrogen gas evolution during the cathodic cycle. Factors like reduction in mechanical integrity of the interface and volume expansion as well as dissolution of the surrounding Al oxide combine to expulse the TiO_2 particles.

12.5 Conclusions

- High frequency pulse reverse pulse (PRPA) and pulse anodising (PA) of friction stir processed Al-TiO_2 surface composites showed that the potential applied during the cathodic cycle has significant effect on the resulting anodic pore structure.
- Pulse reverse pulse anodising caused anodic pores to nucleate and grow under the TiO_2 particles and at the particle-Al matrix interface due to cathodic current localisation caused by combined effect of increased electrical conductivity of TiO_2 and mechanical weakening of anodic oxide at particle-oxide interface.
- High frequency pulse anodising resulted in the anodic pores to grow normally and uniformly around the TiO_2 particles.
- Increase in anodic cycle potential does not affect the structure of the anodic layer considerably in case of pulse reverse pulse anodising (PRPA), but for pulse anodising (PA) the uniformity of coverage of TiO_2 particles with anodic pores is improved.

References

[1] P.G. Sheasby, R. Pinner, The Surface Treatment and Finishing of Aluminium and Its Alloys, Volume 1, 6th ed., ASM International; Finishing Publications, 2001.

[2] P.G. Sheasby, R. Pinner, The Surface Treatment and Finishing of Aluminium and Its Alloys, Volume 2, 6th ed., ASM International; Finishing Publications, 2001.

[3] C.A. Grubbs, Anodizing of Aluminum, Met. Finish. 105 (2007) 397–412. doi:10.1016/S0026-0576(07)80359-X.

[4] C.A. Grubbs, Decorative and architectural anodizing, Met. Finish. 93 (1995) 449–459. doi:10.1016/0026-0576(95)93394-H.

[5] G.E. Thompson, G.C. Wood, Porous anodic film formation on aluminium, Nature. 290 (1981) 230–232. doi:10.1038/290230a0.

[6] M. Aggerbeck, A. Junker-Holst, D.V. Nielsen, V.C. Gudla, R. Ambat, Anodisation of sputter deposited aluminium-titanium coatings: Effect of microstructure on optical characteristics, Surf. Coatings Technol. 254 (2014) 138–144. doi:10.1016/j.surfcoat.2014.05.073.

[7] V.C. Gudla, S. Canulescu, R. Shabadi, K. Rechendorff, J. Schou, R. Ambat, Anodization and Optical Appearance of Sputter Deposited Al-Zr Coatings, in: J. Grandfield, TMS (Eds.), Light Met. 2014, John Wiley & Sons, Inc., 2014: pp. 369–373. doi:10.1002/9781118888438.ch63.

[8] V.C. Gudla, S. Canulescu, R. Shabadi, K. Rechendorff, K. Dirscherl, R. Ambat, Structure of anodized Al-Zr sputter deposited coatings and effect on optical appearance, Appl. Surf. Sci. 317 (2014) 1113–1124. doi:http://dx.doi.org/10.1016/j.apsusc.2014.09.037.

[9] V.C. Gudla, F. Jensen, A. Simar, R. Shabadi, R. Ambat, Friction stir processed Al–TiO2 surface composites: Anodising behaviour and optical appearance, Appl. Surf. Sci. 324 (2015) 554–562. doi:http://dx.doi.org/10.1016/j.apsusc.2014.10.151.

[10] K. Shimizu, G.M. Brown, K. Kobayashi, P. Skeldon, G.E. Thompson, G.C. Wood, Ultramicrotomy-a route towards the enhanced understanding of the corrosion and filming behaviour of aluminium and its alloys, Corros. Sci. 40 (1998) 1049–1072. doi:10.1016/S0010-938X(98)00006-7.

[11] M. Jariyaboon, P. Møller, R.E. Dunin-Borkowski, R. Ambat, FIB-SEM investigation of trapped intermetallic particles in anodic oxide films on AA1050 aluminium, Anti-Corrosion Methods Mater. 58 (2011) 173–178. doi:10.1108/00035591111148885.

[12] J.C. Walmsley, C.J. Simensen, A. Bjørgum, F. Lapique, K. Redford, The Structure and Impurities of Hard DC Anodic Layers on AA6060 Aluminium Alloy, J. Adhes. 84 (2008) 543–561. doi:10.1080/00218460802161590.

[13] M. Saito, Unoxidized Aluminum Particles in Anodic Alumina Films, J. Electrochem. Soc. 140 (1993) 1907. doi:10.1149/1.2220737.

[14] J. Timm, Influence of Fe and Si Containing Phases on the Anodisation Behaviour, Key Eng. Mater. 44-45 (1990) 219–232. doi:10.4028/www.scientific.net/KEM.44-45.219.

[15] A.E. Hultquist, On the Nature of Burned Anodic Coatings, J. Electrochem. Soc. 111 (1964) 1302. doi:10.1149/1.2425989.

[16] R. Chang, W.F. Hall, On the correlation between optical properties and the chemical /metallurgical constitution of multi-phase thin films, Thin Solid Films. 46 (1977) L5–L8. doi:10.1016/0040-6090(77)90068-2.
[17] T. Yamamoto, H. Tanaka, M. Fujita, H. Asoh, S. Ono, Effect of high-frequency switching electrolysis on film thickness uniformity of anodic oxide film formed on AC8A Aluminum alloy, J. Japan Inst. Light Met. 60 (2010) 602–607. doi:10.2464/jilm.60.602.
[18] D. Kanagaraj, V. Raj, S. Vincent, S.V. Iyer, Effect of Pulse Frequency on Pulse Anodising of AA1100 Aluminium Alloy in Sulphamic Acid, Bull. Electrochem. 17 (2001) 523–526.
[19] D. Kanagaraj, V. Raj, S. Vincent, B.P. Kumar, A.S. Kumar, S.V. Iyer, Pulse anodizing of AA1100 aluminium alloy in oxalic acid electrolyte, Bull. Electrochem. 17 (2001) 285–288. http://cecri.csircentral.net/1232/ (accessed May 22, 2014).
[20] A. Deacon Juhl, Pulse anodising of extruded and cast aluminium alloys, Technical University of Denmark, 1999.
[21] K. Yokoyama, H. Konno, H. Takahashi, M. Nagayama, Advantages of Pulse Anodizing, Plat. Surf. Finish. 69 (1982) 62–65.
[22] C. Colombini, Using Pulse Rectifiers for Aluminium Anodizing, Finishing. 12 (1988) 34–38.
[23] K. Okubo, S. Toba, Y. Sakura, Studies of High-Temperature, High Speed Anodic Oxidation on Aluminum by the Pulse Current With Negative Current Component, J. Met. Finish. Soc. Japan. 39 (1988) 512–516. doi:10.4139/sfj1950.39.512.
[24] K. Okubo, S. Suyama, Y. Sakura, Studies of Microstructure of Anodic Oxide Films on Aluminum by Pulse Current with a Negative Component, J. Surf. Finish. Soc. Japan. 40 (1989) 1366–1371. doi:10.4139/sfj.40.1366.
[25] V. Komisarov, A.R. Thölén, TEM investigation of pulse anodized porous films formed on aluminium alloys, Mater. Sci. Eng. A. 151 (1992) 197–203. doi:10.1016/0921-5093(92)90208-I.
[26] I. De Graeve, H. Terryn, G.E. Thompson, AC-Anodising of Aluminium: Contribution to Electrical and Efficiency Study, Electrochim. Acta. 52 (2006) 1127–1134. doi:10.1016/j.electacta.2006.07.010.
[27] J.M. Kape, AC Anodizing, Met Finish J. 20 (1974) 80–84.
[28] J.M. Kape, Anodising with Alternating Current, Trans. Inst. Met. Finish. 55 (1977) 25–30.
[29] J.M. Kape, Comparison of AC and DC sulphuric acid based anodizing processes, Trans. Inst. Met. Finish. 66 (1988) 41–46.
[30] J.M. Kape, Further developments in the AC anodizing of aluminium in sulphuric acid electrolytes, Trans. Inst. Met. Finish. 63 (1985) 90–97.
[31] V. Balasubramanian, S. John, B.A. Shenoi, Influence of Addition Agents for A.C. Anodizing in Sulphuric Acid Electrolytes, Surf. Technol. 19 (1983) 293–303. doi:10.1016/0376-4583(83)90034-1.
[32] R.S. Mishra, Z.Y. Ma, I. Charit, Friction stir processing: A novel technique for fabrication of surface composite, Mater. Sci. Eng. A. 341 (2003) 307–310. doi:10.1016/S0921-5093(02)00199-5.
[33] Q. Zhang, B.L. Xiao, D. Wang, Z.Y. Ma, Formation mechanism of in situ Al3Ti in Al matrix during hot pressing and subsequent friction stir processing, Mater. Chem. Phys. 130 (2011) 1109–1117. doi:10.1016/j.matchemphys.2011.08.042.
[34] Q. Zhang, B.L. Xiao, Q.Z. Wang, Z.Y. Ma, In situ Al3Ti and Al2O3 nanoparticles reinforced Al composites produced by friction stir processing in an Al-TiO2 system, Mater. Lett. 65 (2011) 2070–2072. doi:10.1016/j.matlet.2011.04.030.
[35] C.J. Hsu, C.Y. Chang, P.W. Kao, N.J. Ho, C.P. Chang, Al-Al3Ti nanocomposites produced in situ by friction stir processing, Acta Mater. 54 (2006) 5241–5249. doi:10.1016/j.actamat.2006.06.054.
[36] G. V Samsonov, The Oxide Handbook, IFI/Plenum, London, 1973. doi:10.1016/0040-6031(83)80052-5.
[37] M. Li, W. Hebenstreit, U. Diebold, A.M. Tyryshkin, M.K. Bowman, G.G. Dunham, et al., The influence of the bulk reduction state on the surface structure and morphology of rutile TiO2(110) single crystals, J. Phys. Chem. B. 104 (2000) 4944–4950. doi:Doi 10.1021/Jp9943272.
[38] U. Diebold, The surface science of titanium dioxide, Surf. Sci. Rep. 48 (2003) 53–229. doi:10.1016/S0167-5729(02)00100-0.
[39] D. Regonini, A.C.E. Dent, C.R. Bowen, S.R. Pennock, J. Taylor, Impedance spectroscopy analysis of TinO2n-1 Magneli phases, Mater. Lett. 65 (2011) 3590–3592. doi:10.1016/j.matlet.2011.07.094.
[40] D. Regonini, V. Adamaki, C.R. Bowen, S.R. Pennock, J. Taylor, A.C.E. Dent, AC electrical properties of TiO2 and Magnéli phases, TinO2n−1, Solid State Ionics. 229 (2012) 38–44. doi:10.1016/j.ssi.2012.10.003.
[41] G.E. Thompson, R.C. Furneaux, G.C. Wood, Electron microscopy of ion beam thinned porous anodic films formed on aluminium, Corros. Sci. 18 (1978) 481–498.

http://www.sciencedirect.com/science/article/pii/S0010938X78800419 (accessed May 21, 2014).
[42] L. Kompotiatis, I. Kaplanoglou, Oxygen Evolution During the Formation of Barrier Type Anodic Film on 2024-T3 Aluminium Alloy, Corosion Sci. 40 (1998) 1939–1951. doi:http://dx.doi.org/10.1016/S0010-938X(98)00114-0.
[43] M. Saenz De Miera, M. Curioni, P. Skeldon, G.E. Thompson, Preferential anodic oxidation of second-phase constituents during anodising of AA2024-T3 and AA7075-T6 alloys, Surf. Interface Anal. 42 (2010) 241–246. doi:10.1002/sia.3191.
[44] X. Zhu, L. Liu, Y. Song, H. Jia, H. Yu, X. Xiao, et al., Oxygen evolution and porous anodic alumina formation, Mater. Lett. 62 (2008) 4038–4040. doi:10.1016/j.matlet.2008.05.062.
[45] X.F. Zhu, D.D. Li, Y. Song, Y.H. Xiao, The study on oxygen bubbles of anodic alumina based on high purity aluminum, Mater. Lett. 59 (2005) 3160–3163. doi:10.1016/j.matlet.2005.05.038.
[46] J. Zahavi, A-C Anodizing Processes of Aluminum Alloys, J. Electrochem. Soc. 129 (1982) 1572. doi:10.1149/1.2124211.
[47] L. Zhang, G.E. Thompson, M. Curioni, P. Skeldon, Anodizing of Aluminum in Sulfuric Acid/Boric Acid Mixed Electrolyte, J. Electrochem. Soc. 160 (2013) C179–C184. doi:10.1149/2.032306jes.

13. HF Anodising of Al-TiO_2 Composites: Optical Appearance (Paper 9)

Optical Appearance of High Frequency Pulse Reverse Pulse Anodised Aluminium-TiO_2 Surface Composites*

Abstract

High frequency anodising of Al-TiO_2 composites using pulse reverse pulse technique was investigated with an aim to understand the effect of the anodising parameters on the optical appearance, microstructure, and growth rate of the anodic layer. Friction stir processing was employed to prepare the Al-TiO_2 surface composites, which were anodised in a 20 wt.% sulphuric acid bath at 10 °C as a function of pulse frequency, pulse duty cycle, and anodic cycle voltage amplitudes. The optical appearance of the films was characterized and quantified using an integrating sphere-spectrometer setup, which measures the total and diffuse reflectance from the surface. The change in optical reflectance spectra from the anodised layer was correlated to the applied anodising parameters and microstructure of the anodic layer as well as the composite substrate. Change in hardness of the anodised layer was also measured as a function of various anodising parameters. Anodic film growth, hardness, and total reflectance of the surface were found to be highly dependent on the anodising frequency and the anodic cycle potential. Longer exposure times to the anodising electrolyte at lower growth rates resulted in lowering of the reflectance due to TiO_2 particle degradation and low hardness due to increased dissolution of the anodised layer during the process.

Keywords: Pulse anodising; Aluminium; TiO_2; Hardness; Reflectance; SEM; TEM.

Published as **V.C. Gudla, K. Bordo, F. Jensen, S. Canulescu, S. Yuksel, A. Simar, R. Ambat, High Frequency Anodising of Aluminium-TiO_2 Surface Composites: Anodising Behaviour and Optical Appearance, Surf. Coatings Technol. 277 (2015) 67–73.*

13.1 Introduction

Anodising of aluminium is widely used in different fields of industry for corrosion protection, wear resistance, and appealing decorative/cosmetic appearances [1,2]. Decorative anodised surfaces are commonly produced by direct current (DC) anodising of aluminium in a sulphuric acid bath [3]. The resulting anodic alumina layers are usually transparent to the visible light; however, their optical appearance depends on the anodising parameters as well as on the composition and surface morphology of the specimen being anodised [4,5]. White appearing anodised Al surfaces have found applications in the aerospace industry for their high solar reflectance [6,7]. Gudla et al. [8] have shown that different kinds of light-grey to white appearance can be obtained by introducing the metal oxide particles into the Al matrix and further anodising the Al-metal oxide composite. The reflectance values obtained were highly dependent on the microstructural aspects of the anodic layer resulting from the differences in anodising parameters [9]. It was shown that the presence of un-anodised Al in the anodic alumina matrix can result in absorption of light resulting in reduced reflectance from the anodised surfaces [10–12].

Recently high-frequency anodising of cast Al-Si alloys containing primary Si phases was reported [13]. The microstructure of the obtained porous anodic films is different compared to the anodic layers produced by conventional DC anodising [14]. In particular, the high frequency anodising was accompanied by branching of the anodic pores and effective oxidation of the Al below the primary Si phases [15]. Applying the technique of high frequency anodising to Al-TiO_2 composites is expected to completely oxidize the Al phase (which absorbs light in anodic layer) surrounding the TiO_2 particles and improve the reflectance of the resulting anodised surfaces.

Friction stir processing (FSP) [16,17] is a rapid solid state processing technique, which has been extensively used for preparation of various types of surface composites. The objective of the present work is to study the high frequency anodising of FSP surface composites of Al-TiO_2 and to determine the effect of the anodising parameters on the growth behaviour, surface reflectance, microstructure, and hardness of the anodic films. The TiO_2 particles were used to prepare the Al-TiO_2 composites via friction stir processing. Rutile form of TiO_2 was chosen for its high refractive index compared to the anodic alumina [18]. Average particle size of 210 nm was chosen for optimum scattering efficiency [19]. Integrating sphere setup was used for characterising the surface reflectance and high resolution SEM and TEM were employed to observe the anodised layers structure.

13.2 Experimental

13.2.1 Composites and Surface Preparation

Aluminium substrates with dimensions of 200 x 60 x 6 mm were obtained in rolled condition and commercial powders of TiO_2 (Ti-Pure™, DuPont R900, Rutile, D_{50}= 210 nm) were used. The Friction stir processing (FSP) was performed using a Hermle milling machine equipped with a steel tool having 20 mm shoulder diameter, 1.5 mm pin length with a M6 thread, and three flats. The TiO_2 powder is placed in grooves and the friction stir process distributes it in the aluminium surface. The friction stir processing parameters are discussed in detail elsewhere [9]. The processed composite surfaces were mechanically polished to a mirror finish and were subsequently degreased in a mild alkaline solution (30 g/L, Alficlean™, Alufinish, Germany). Desmutting was performed by immersing in a 100 g/L HNO_3 solution followed by demineralised water rinsing. Finally the samples were cleaned by ultra-sonication in acetone for 15 min and dried in air flow.

13.2.2 High Frequency Anodising

The FSP composites were then anodised in a 20 wt.% sulphuric acid bath maintained at 10 °C. Anodising was performed by applying square voltage pulses from a function generator (33120A, Agilent) as shown in Figure 13.1. The waveforms of voltage and current during the anodising were monitored with the help of a digital oscilloscope (TDS3034B, Tektronix). The anodised area was approximately 2 cm^2. The potential at the cathodic cycle was -2 V (low voltage cycle, V_2), while the potential during the anodic cycle was either +10 V or +20 V (high voltage cycle, V_1). The pulse frequency was varied between 0.1 kHz and 10 kHz.

The duty cycle (i.e. the ratio between the anodic cycle duration, t_1 and the time interval between two subsequent pulses, $t_1 + t_2$ was 30 %, 50 % or 70 %. The thickness of the obtained anodic layers was measured using a capacitance probe (Omniprobe™, Fischer).

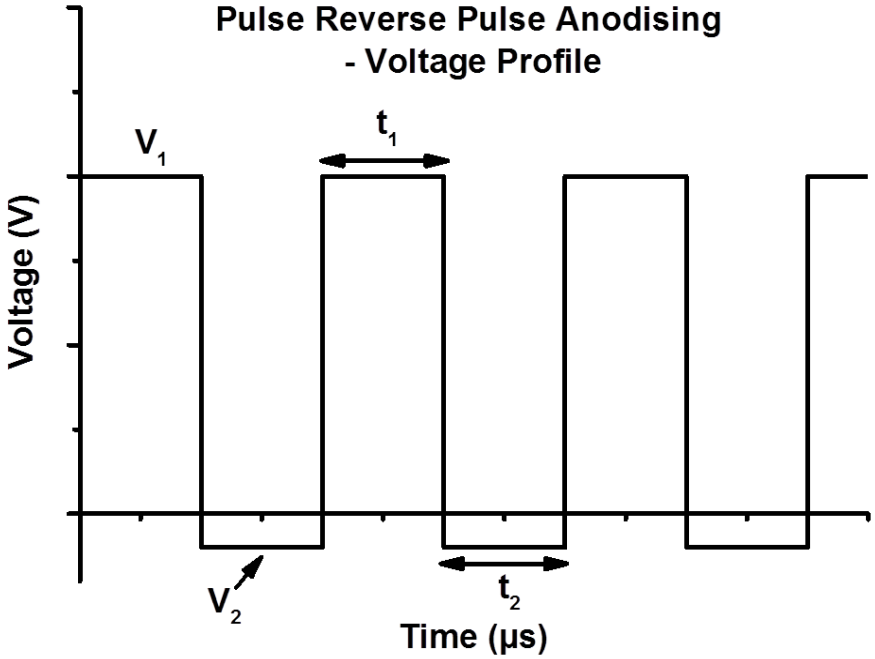

Figure 13.1: Voltage profile used for high frequency pulse reverse pulse anodising (PRPA) of FSP Al-TiO_2 surface composites.

13.2.3 Optical Appearance

Surface appearance of the FSP surface composites after anodising was analysed using an integrating sphere-spectrometer setup. The samples were illuminated with white light from a deuterium tungsten halogen light source (DH2000, Ocean Optics). Reflected light from the samples was collected using an integrating sphere and analysed for diffuse and total reflectance with a fibre optic spectrometer (QE65000, Ocean Optics) in the wavelength range from 300 nm to 750 nm. The spectrometer was calibrated using NIST standards.

13.2.4 Microstructural Characterization

The microstructure and surface morphology of the obtained anodic layers were studied using SEM (Quanta 200™ ESEM FEG, FEI) having EDS capability (80 mm^2 X-Max™ silicon drift detector, Oxford Instruments). The SEM was typically operated at an acceleration voltage of 10 keV. For cross-sectional imaging, the samples were machined through thickness, mounted in an epoxy and mechanically polished. In order to minimize charging, the samples were coated with a 2-3 nm Au layer by magnetron sputtering (Cressington 208HR sputter coater). Transmission electron microscopy was employed to obtain high resolution images of the anodic layer cross-sections. A TEM (Tecnai™ G2 20), operating at 200 keV was used for generating bright field images. The sample lamella from the anodised surfaces were prepared using in-situ focused ion beam lift out and subsequent thinning using FIB-SEM (Helios Nanolab™ Dualbeam, FEI). The micro-Vickers hardness of the anodised surfaces was measured using a Future-Tech FM 700 micro-hardness tester with a load of 10 g – 25 g for 5 s. For each sample, a minimum of 20 measurements were performed to get a reliable average value.

13.3 Results and Discussion

13.3.1 Rate of the anodic film growth

The growth of anodic films on FSP-treated composite layer was found to be strongly dependent on the anodising conditions, namely the anodic cycle potential and the pulse frequency. Figure 13.2 shows the effect of the anodic cycle potential, pulse frequency, and duty cycle on the rate of anodic film growth. Increasing the pulse frequency from 0.1 kHz to 10 kHz leads to a significant increase in the growth rate across all duty cycles (Figure 13.2 (a)). The growth rate increases rapidly up to a frequency of 2 kHz, while from 2 kHz to 10 kHz the increase in the growth rate is less significant. Further, the anodic growth rate is high for higher anodic cycle potential values. When the anodic cycle voltage increases from +10 V to +20 V, the growth rate increases from 0.9 µm/min to 2.1 µm/min at an anodising frequency of 2 kHz. On the other hand, changing the duty cycle does not show any notable effect on the growth rate (Figure 13.2 (b)) at lower anodic cycle potential values (+10 V). A mixed dependence on duty cycle is observed for higher anodic cycle potential values (+20 V). Further, the rate of anodic film growth for high-frequency pulse reverse pulse anodising of FSP composites was found to be significantly higher than that for conventional DC anodising at the same value of anodic potential. For example, pulse reverse pulse anodising of the composite surfaces at 2 kHz and at an anodic potential of +10 V proceeds at a rate 4-5 times faster than DC anodising at +10 V (see Appendix 13.5) [1,2]. Therefore, the high-frequency anodising can be advantageous for composite films compared to the conventional DC anodising when thick anodic layer coatings are required.

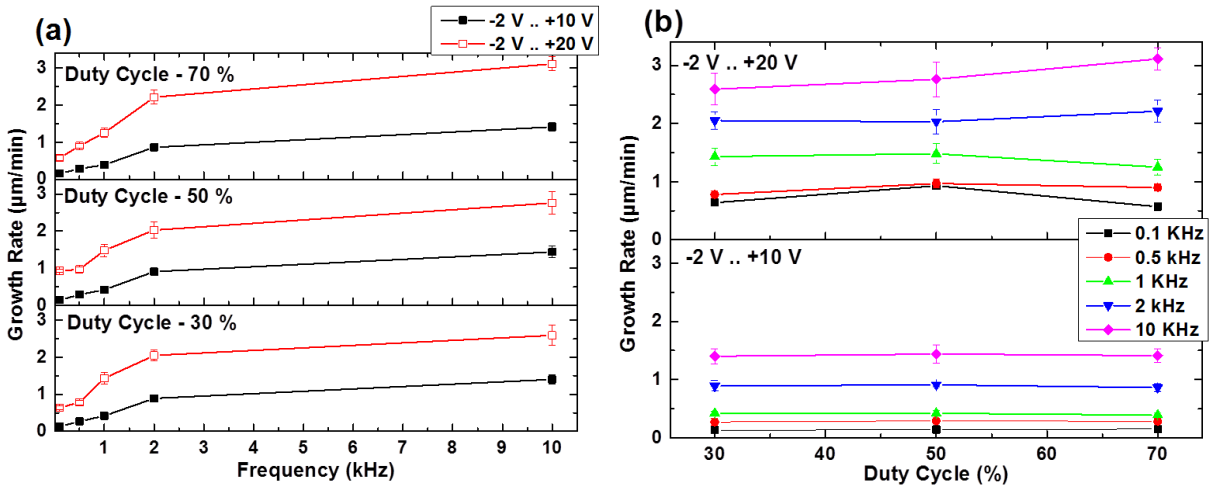

Figure 13.2: Rate of the anodic film growth as a function of: (a) pulse frequency and (b) duty cycle.

Kanagaraj et al. [20] have reported that the thickness of the anodic layer increased for a given anodising time by increasing the pulse frequency from 0.01 Hz to 100 Hz. Similarly, increasing the duty cycle or the anodising current density also resulted in increased anodic layer thickness. This increase in anodic growth rate and better quality of anodic films was attributed to the amount of time allowed for the dissipation of heat, which is generated during anodising cycle. The optimum duty cycle for best anodic film properties on AA1100 was stated as 75 % - 80 %, but the corresponding pulse frequency was not reported [21]. Inferior properties measured on the anodic films obtained above this duty cycle level was attributed to the higher heat generated during longer anodic pulse cycle and subsequent lower 'off' time that does not allow effective heat dissipation. However, a clear explanation and correlation between the heat dissipation and anodic film growth rate was not reported. Yokoyama et al. [22] in their initial studies on advantages of pulse anodising emphasize that the recovery effect (chemical dissolution of anodic oxide) during the low voltage cycle or the 'off' cycle will enhance the rate of anodic film growth. However, the pulse frequencies in those studies were lower than 100 Hz.

In the current work, the positive effect of increasing pulse frequency on the anodising growth rate could signify the contribution of recovery effect and also the heat dissipation during the cathodic cycle. However, too

low cathodic cycle period (50 µs at 10 kHz) will be insufficient for the recovery to take place due to negligible dissolution of the anodic oxide [23]. Therefore, the observed higher growth rates can be attributed to the lower heat generation during the short anodic cycle and the effective dissipation of this heat during the cathodic cycle.

The weak dependence of anodic growth rate on the duty cycle at +10 V anodic cycle potential shows that the effect of 'off' time or cathodic cycle time is minimal. One can speculate that the heat generated during the anodic cycle is effectively removed during the subsequent cathodic cycle for all duty cycles investigated. Also, the higher growth rates observed for higher anodic cycle potential values result in the observed differences in duty cycle dependence for +10 V and +20 V anodic cycle potential. However, additional investigations are necessary to fully elucidate the effect of high frequency pulse anodising of Al-TiO_2 composites and the effect of duty cycle.

13.3.2 Microstructure and Morphology

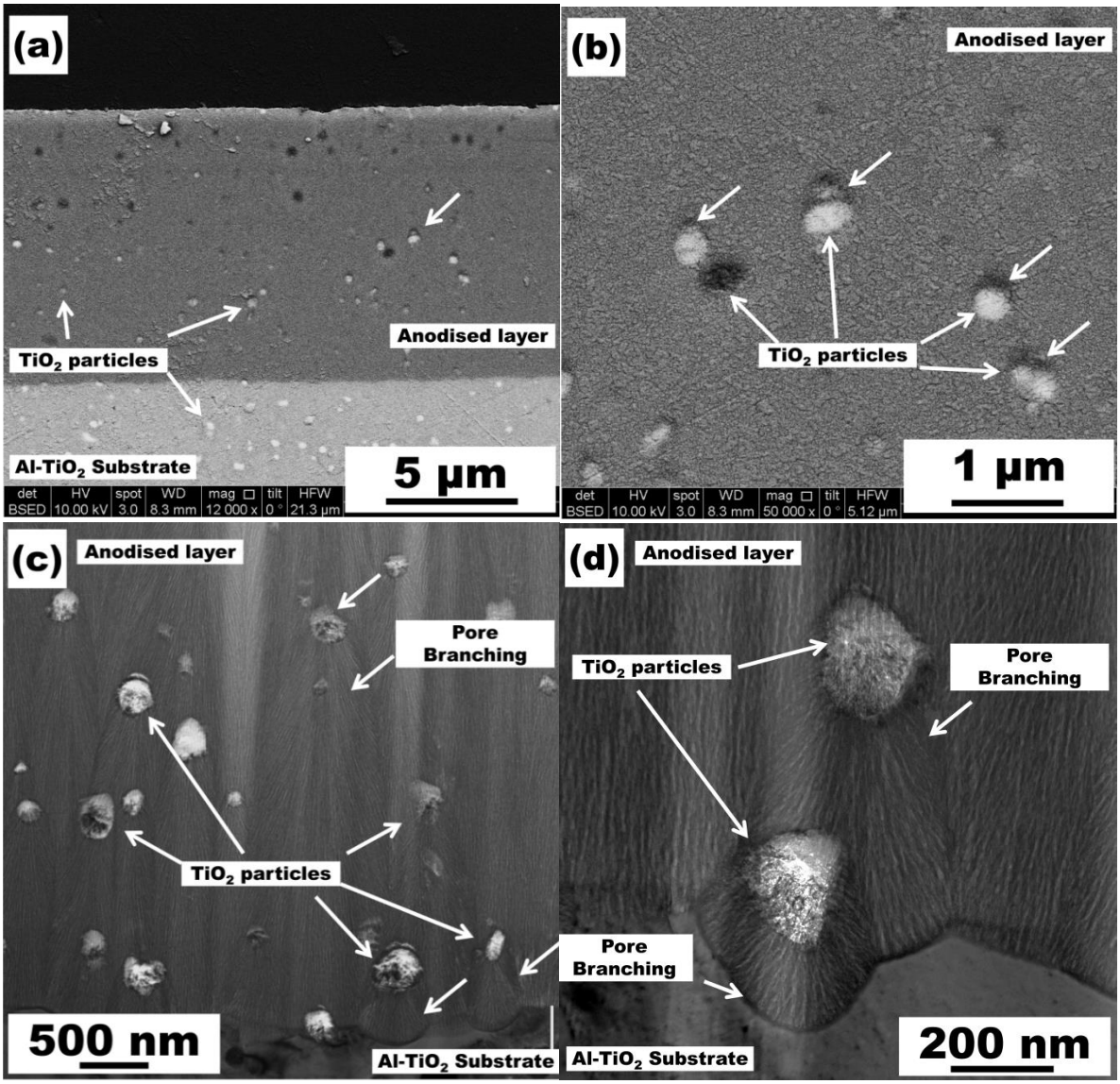

Figure 13.3: Cross section of anodic layer obtained at anodic cycle potential of + 10 V, 2 kHz, 50% duty cycle; SEM-BSE images showing: (a) TiO_2 particles incorporated into anodic layer, (b) difference in contrast within TiO_2 particles, and bright field TEM images showing: (c) porous nature of the TiO_2 particles in anodic layer and (d) anodic pore branching at TiO_2 particle locations.

The representative microstructure and morphology of the anodic layers obtained after high frequency anodising using +10 V as anodic cycle potential is shown in Figure 13.3. The SEM-BSE images show that the particles are uniformly dispersed in the Al matrix and similarly are uniformly incorporated into the anodic layer after anodising. There is an observable difference in the contrast of the TiO_2 particles at the top of the anodised layer compared to the ones close to the substrate interface (see Figure 13.3 (a)). High magnification image shows a contrast within the TiO_2 particles in the anodic layer as shown in Figure 13.3 (b). This difference in contrast in back scatter detection mode was shown to be due to transformation of the morphology of the TiO_2 particles [9].

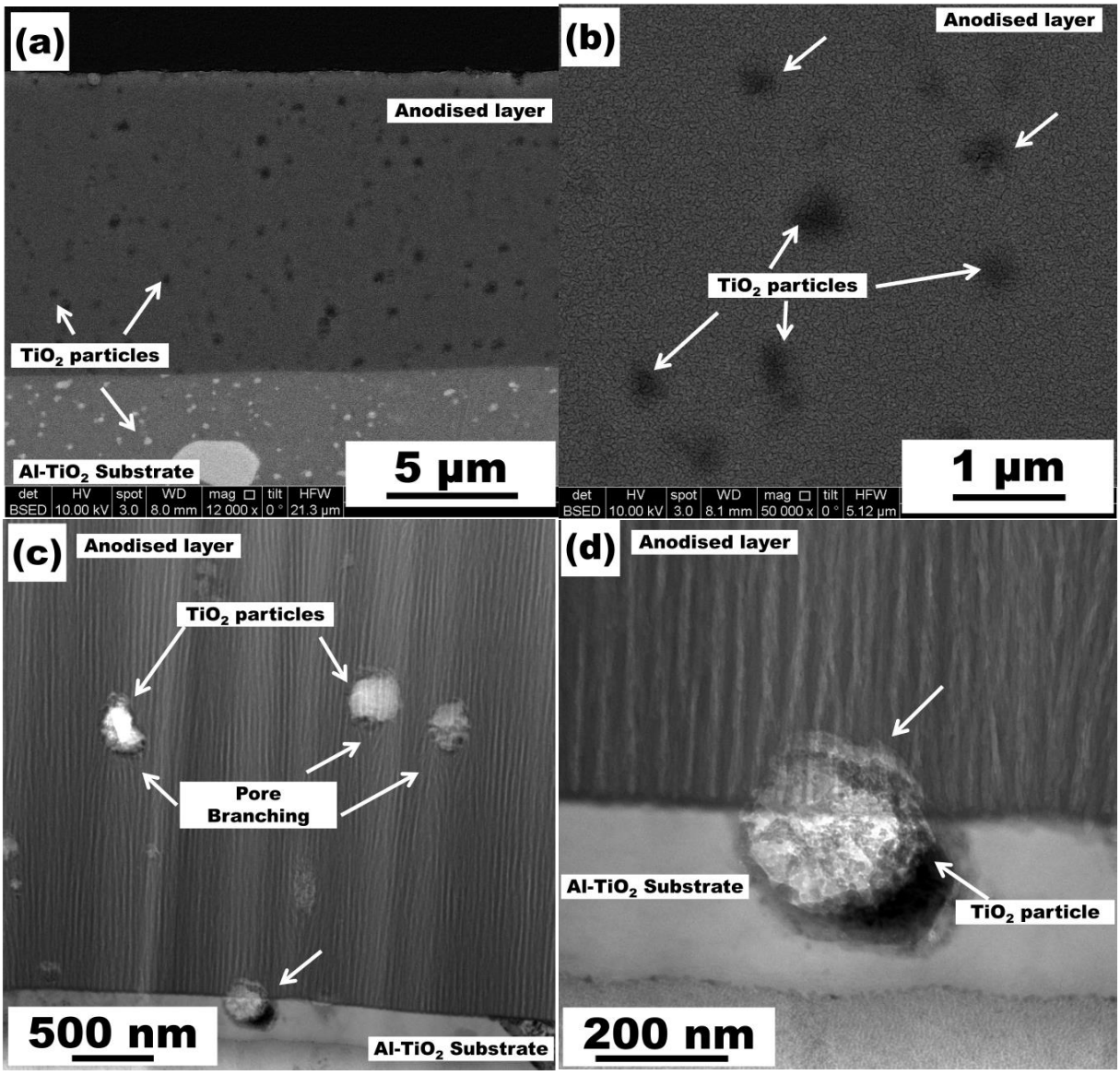

Figure 13.4: Cross section of anodic layer obtained at anodic cycle potential of + 20 V, 2 kHz, 50% duty cycle; SEM-BSE images showing: (a), (b) TiO_2 particles incorporated into anodic layer with difference in contrast between TiO_2 particles in Al substrate and anodic layer, and bright field TEM images showing: (c) porous nature of the TiO_2 particles and pore branching in anodic layer and (d) porosity of TiO_2 particles.

Bright field TEM images (see Figure 13.3 (c) and (d)) of the anodic layer cross sections show change in morphology of the TiO_2 particles from crystalline to porous- amorphous phase, and hence appear dark in the SEM-BSE images. In some cases, voids are present at TiO_2 particle locations. A closer look shows an

associated change in the structure of the anodic pores at the TiO_2 particle locations. Figure 13.3 (d) shows 'pore branching' in the anodic layer and at the anodic layer-Al metal interfaces, and the anodic pores preferentially grow more inwards into the substrate. This could be due to the ease of access for the anodising electrolyte at the locations where TiO_2 particles have changed their morphology.

The structure of the anodic layers obtained after anodising with an anodic cycle potential of +20 V is shown in Figure 13.4. Features that were observed in Figure 13.3 for the + 10 V anodic cycle potential can also be seen here. The dark appearance of the TiO_2 particles in this case extends throughout the anodic layer thickness (see Figure 13.4 (a)). Also, there is no difference in contrast within the TiO_2 particles in the anodic layer (see Figure 13.4 (b)). Bright field TEM image confirms that the TiO_2 particles are completely transformed in morphology to porous- amorphous phase (Figure 13.4 (c)), and also shows the presence of voids at TiO_2 particle locations. High magnification image of the anodic layer-Al substrate interface shows a TiO_2 particle situated at the interface showing porous nature for the region in the anodic layer and a remnant dense crystalline TiO_2 in the Al substrate (see Figure 13.4 (d)).

Summarising the observations from Figure 13.3 and Figure 13.4, it is clear that the increase in anodic cycle potential from +10 V to + 20 V increases the fraction of structurally transformed TiO_2 particles from crystalline rutile phase to amorphous phase. The presence of voids at TiO_2 particle locations can be due to two factors: (i) the particles may have been completely transformed, i.e. dissolved, and subsequently lost into the anodising electrolyte, or (ii) they are loosely bound to the matrix so that they are lost during the mechanical preparation of the cross sections of the samples. However, from the reflectance spectra shown in Figure 13.6, at a wavelength of 300-350 nm, the absorption edge of TiO_2 still exists for both the samples [24,25]. This implies that the surfaces generated at +10 V and at +20 V anodic cycle potentials contain incorporated TiO_2 in the anodic layer, ruling out the loss of TiO_2 into the anodising electrolyte under the anodising conditions. The pore branching observed at TiO_2 particle locations is more severe in the case of +10 V than +20 V. A detailed analysis of the generation of these microstructures and observed features in the morphology of the high frequency anodised FSP composite surfaces was recently reported by Gudla et al. [26]. The specific features of pore branching was explained to be due to the increased conductivity of the oxygen deficient TiO_2 under the high frequency pulse reverse pulse conditions. This results in current localisation during the cathodic cycle at the particle locations leading to the localised pore branching.

13.3.3 Reflectance measurements

Optical reflectance of the anodised FSP composite surfaces was measured as a function of anodic layer thickness, anodic cycle potential, and pulse frequency. Figure 13.5 shows the effect of the anodic layer thickness on the optical reflectance. Overall the total and diffuse reflectance showed decreasing trend with increasing anodic layer thickness. This is expected since the light absorption increases with the thickness of the anodic oxide layer. At higher anodic layer thicknesses (approx. 23 µm and 36 µm), the reflectance values show a high dependence on the wavelength. The total and diffuse reflectance values observed are lower at lower wavelengths and gradually increase with increasing wavelength. However, the wavelength dependence is less pronounced at lower anodic layer thicknesses.

The reflectance spectra in Figure 13.6 shows that the increasing potential in the anodic cycle from +10 V to +20 V (at 2 kHz frequency, 50 % duty cycle) leads to an increase in both the diffuse and total reflectance. The total reflectance of the samples in the visible range also increases monotonically with the increase in the pulse frequency from 0.1 kHz to 10 kHz (see Figure 13.7 (a)) for a given anodic layer thickness at +10 V anodic cycle potential. However, this dependence on anodising frequency is almost negligible when the anodic cycle potential is increased to +20 V (see Figure 13.7(b)) and the maximum reflectance observed is approx. 60 % (at 10 kHz frequency) for both the surfaces. The wavelength dependence of reflectance is less pronounced with increase in anodic cycle voltage or with increase in pulse frequency compared to results for thicker films (Figure 13.5). Although not shown here, duty cycle did not show significant effect on reflectance.

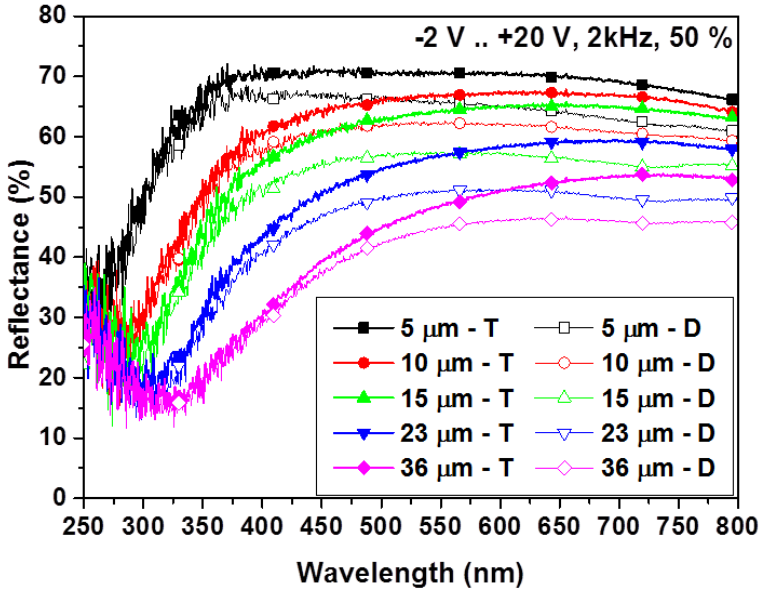

Figure 13.5: Total and diffuse reflectance of the high frequency anodised surfaces as a function of the anodic layer thickness (T- Total reflectance, D – Diffuse reflectance).

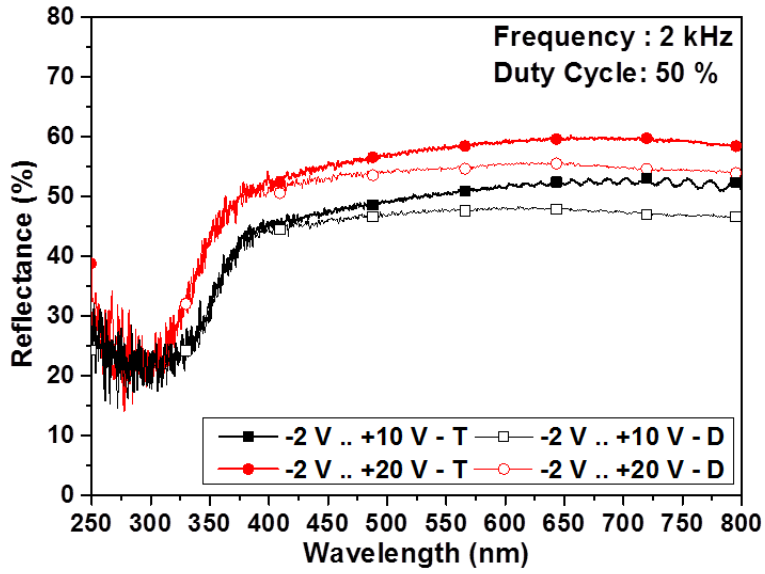

Figure 13.6: Optical reflectance of high frequency anodised FSP-treated samples as a function of the anodic cycle voltage (T- Total reflectance, D – Diffuse reflectance).

The reflectance spectra of the high frequency anodised samples (see Figure 13.6) show increasing reflectance with increasing anodic cycle potential. The anodised layers contain light scattering TiO_2 particles in either partially crystalline and/or completely amorphous phase as seen from the SEM and TEM images (see Figure 13.3 and Figure 13.4). The refractive index for crystalline phase TiO_2 is higher than the amorphous phase and hence better light scattering is expected where partial crystallinity is still maintained for TiO_2 particles in the anodic layer. This implies that better reflectance should be observed for samples anodised at +10 V compared to +20 V. As this is not the case, the lower reflectance for +10 V anodised surface might be arising from other factors such as the presence of light absorbing phases in the anodic layer. It has been previously reported that the presence of un-anodised metallic phases in the anodic layer leads to absorption of light and darkening of the anodised surfaces [11,12, 27–29]. Anodising at low voltage results in a large

fraction of incomplete anodising of Al leading to more pronounced absorption of light and lower reflectance values [9,10]. Also, for TiO_2 containing DC anodised layers, anodising at lower potentials resulted in the formation of light absorbing Magneli phases in the incorporated TiO_2 [9]. However, in the present study no evidence of un-anodised Al was found during the microstructural investigations as shown in Figure 13.3 and Figure 13.4.

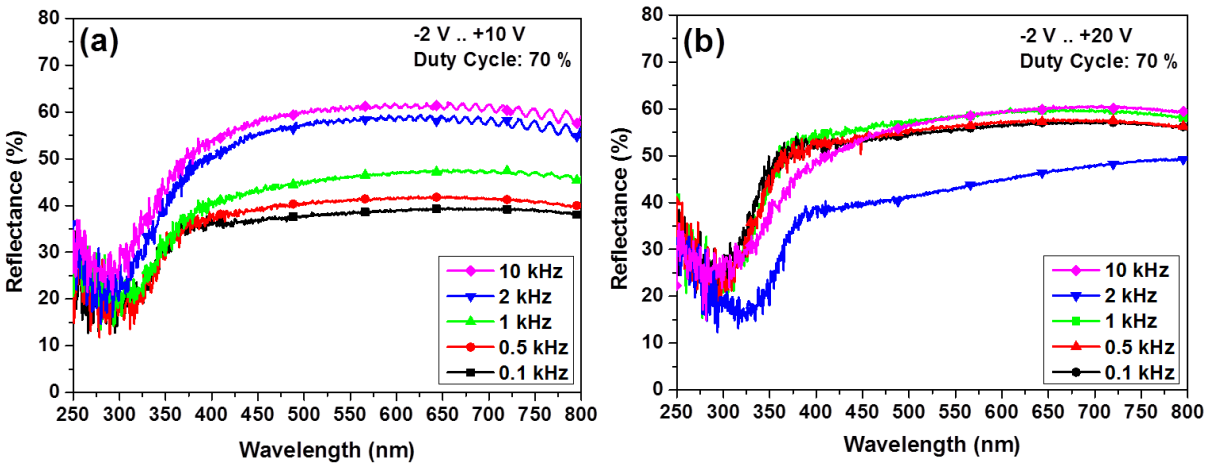

Figure 13.7: Optical reflectance of high frequency anodised FSP-treated samples as a function of the pulse frequency with: (a) +10 V and (b) +20 V as the anodic cycle potential.

The thickness and frequency dependence of reflectance values (see Figure 13.5 and Figure 13.7) can also be explained by the formation of light absorbing Magneli phases in the incorporated TiO_2. The anodising time for obtaining higher anodic layer thickness increases gradually with required thickness. This results in longer exposure of the TiO_2 particles in the anodic layer to the sulphuric acid anodising electrolyte. It is known, both from the manufacturing of TiO_2 and also from thermodynamic calculations [30] that TiO_2 dissolves in sulphuric acid to form Titanyl Sulphate ($TiOSO_4$(aq.)). Aqueous titanyl sulphate in the presence of reducing agents like Al, results in reduction of Ti^{4+} to Ti^{3+}, showing a deep blue colour corresponding to light absorbing Magneli phases [31,32]. The higher reflectance values observed with increasing anodising frequency and increased anodic cycle potential can also be explained in a similar fashion due to the reduced anodising time for a given anodic layer thickness (see Figure 13.2 (a)).

13.3.4 Hardness measurements

The micro-Vickers hardness values of the high frequency anodised surfaces (see Figure 13.8) show a decreasing trend with increasing anodic layer thickness. With increasing anodising frequency, the hardness values show an increase initially up to a frequency of 2 kHz, but appear to be slightly lower at 10 kHz for all duty cycles (Figure 13.9 (a)). The hardness values show a slightly increasing trend with increasing duty cycle for all the anodising frequencies investigated for +10 V and +20 V anodic cycle potential values (see Figure 13.9 (b)). The reduction in hardness with increase in thickness is due to the dissolution of the pore inner walls and subsequent weakening of the anodised layer formed in the initial stages of anodising [33]. Higher anodised layer thicknesses obtained by longer anodising times result in the ‘powdering’ of the anodised layer due to chemical dissolution by the sulphuric acid electrolyte [34,35]. Similarly, higher anodising times required for obtaining a specific anodic layer thickness at lower anodising frequencies also result in lower mechanical hardness of the anodised surfaces. Increasing the duty cycle slightly improves the growth rate of the anodic films and reduces the ‘off’ time that contributes to dissolution and mechanical weakening of the anodised surface. Thus higher mechanical hardness is expected at higher duty cycles. However, duty cycle values reaching DC conditions (approx. 80 % - 90 %) result in higher heat generation and lower heat dissipation causing increased dissolution due to temperature effects and hence lower the mechanical hardness [21].

Overall, it was observed that the higher anodic cycle potentials give better growth rates for high frequency anodising of the Al-TiO_2 composites. Similar behaviour is also observed with increasing pulse

frequency. Surface reflectance as well as hardness of the anodised surfaces also showed an improving trend with increasing the anodic cycle potential and pulse frequency.

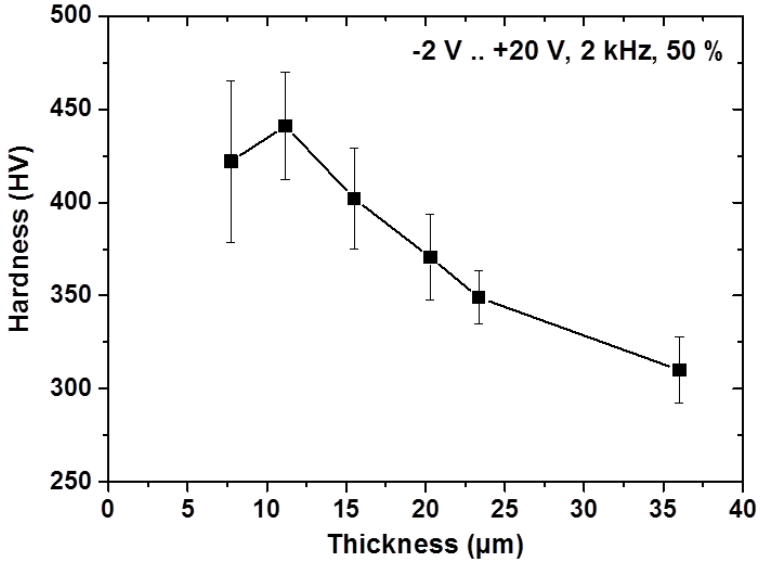

Figure 13.8: Hardness of high frequency anodised surfaces measured as a function of anodised layer thickness.

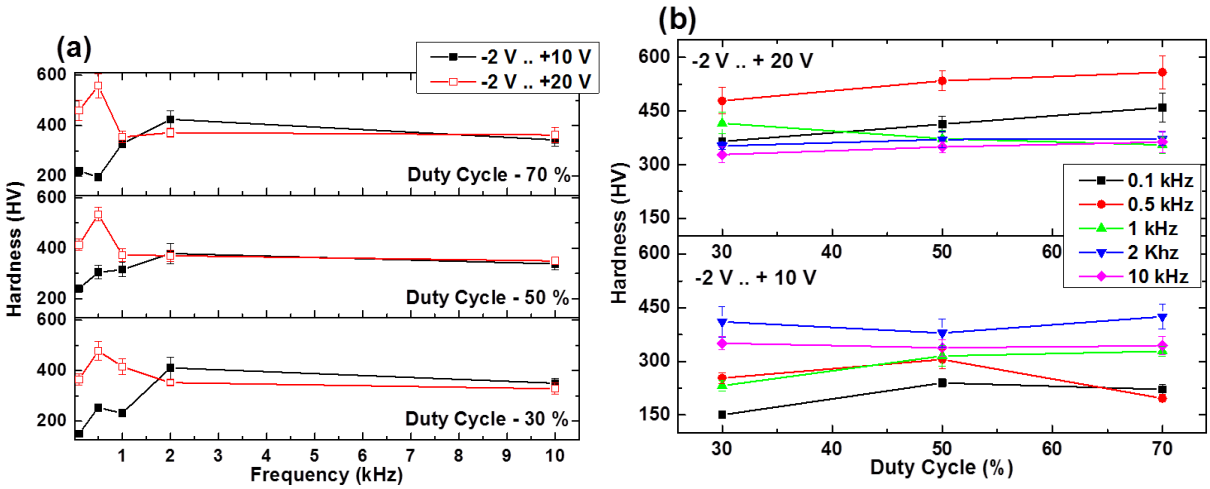

Figure 13.9: Hardness of high frequency anodised surfaces measured as a function of: (a) duty cycle and (b) anodising frequency.

13.4 Conclusions

- High frequency pulse reverse pulse anodising was shown to be an effective technique for obtaining high reflectance anodised surfaces over FSP surface composites of Al-TiO_2.
- The growth rate of anodic layer increases with an increase in the anodic cycle voltage and anodising frequency, but it is almost independent of the duty cycle at +10 V and slightly increases at +20 V anodic cycle potential.
- The total optical reflectance of the anodised FSP-processed samples depends on the anodic cycle voltage, frequency, and the duty cycle. In general, increasing the anodic cycle voltage and frequency leads to an increase in the total reflectance.
- High frequency anodising of the as-prepared samples with voltage amplitude of -2 V to +10 V is accompanied by pore branching and allows complete oxidation of Al in the regions below the embedded

TiO_2 particles. At the higher positive cycle voltage (+20 V), all of the embedded particles are disintegrated during the anodising.

- Micro-hardness of the anodised surfaces increases with anodising frequency and duty cycle, and reduces with the anodic layer thickness.

References

[1] P.G. Sheasby, R. Pinner, The Surface Treatment and Finishing of Aluminium and Its Alloys, Volume 1, 6th ed., ASM International; Finishing Publications, 2001.

[2] P.G. Sheasby, R. Pinner, The Surface Treatment and Finishing of Aluminium and Its Alloys, Volume 2, 6th ed., ASM International; Finishing Publications, 2001.

[3] C.A. Grubbs, Anodizing of Aluminum, Met. Finish. 105 (2007) 397–412. doi:10.1016/S0026-0576(07)80359-X.

[4] G.E. Thompson, G.C. Wood, Porous anodic film formation on aluminium, Nature. 290 (1981) 230–232. doi:10.1038/290230a0.

[5] S. Canulescu, K. Rechendorff, C.N. Borca, N.C. Jones, K. Bordo, J. Schou, et al., Band gap structure modification of amorphous anodic Al oxide film by Ti-alloying, Appl. Phys. Lett. 104 (2014) 121910. doi:10.1063/1.4866901.

[6] C. Siva Kumar, S.M. Mayanna, K.N. Mahendra, A.K. Sharma, R. Uma Rani, Studies on white anodizing on aluminum alloy for space applications, Appl. Surf. Sci. 151 (1999) 280–286. doi:10.1016/S0169-4332(99)00290-1.

[7] C. Siva Kumar, A.K. Sharma, K.N. Mahendra, S.M. Mayanna, Studies on anodic oxide coating with low absorptance and high emittance on aluminum alloy 2024, Sol. Energy Mater. Sol. Cells. 60 (2000) 51–57. doi:10.1016/S0927-0248(99)00062-8.

[8] V.C. Gudla, F. Jensen, S. Canulescu, A. Simar, R. Ambat, Friction Stir Processed Al-Metal Oxide Surface Composites: Anodising and Optical Appearance, in: T.S. Sudarshan, P. Vuoristo, H. Koivuluoto (Eds.), Surf. Modif. Technol. XXVIII, ValarDocs, Tampere, Finland, 2014: pp. 375–384. www.valardocs.com.

[9] V.C. Gudla, F. Jensen, A. Simar, R. Shabadi, R. Ambat, Friction stir processed Al–TiO2 surface composites: Anodising behaviour and optical appearance, Appl. Surf. Sci. 324 (2015) 554–562. doi:http://dx.doi.org/10.1016/j.apsusc.2014.10.151.

[10] V.C. Gudla, S. Canulescu, R. Shabadi, K. Rechendorff, J. Schou, R. Ambat, Anodization and Optical Appearance of Sputter Deposited Al-Zr Coatings, in: J. Grandfield, TMS (Eds.), Light Met. 2014, John Wiley & Sons, Inc., 2014: pp. 369–373. doi:10.1002/9781118888438.ch63.

[11] V.C. Gudla, S. Canulescu, R. Shabadi, K. Rechendorff, K. Dirscherl, R. Ambat, Structure of anodized Al-Zr sputter deposited coatings and effect on optical appearance, Appl. Surf. Sci. 317 (2014) 1113–1124. doi:http://dx.doi.org/10.1016/j.apsusc.2014.09.037.

[12] M. Aggerbeck, A. Junker-Holst, D.V. Nielsen, V.C. Gudla, R. Ambat, Anodisation of sputter deposited aluminium-titanium coatings: Effect of microstructure on optical characteristics, Surf. Coatings Technol. 254 (2014) 138–144. doi:10.1016/j.surfcoat.2014.05.073.

[13] T. Yamamoto, H. Tanaka, M. Fujita, H. Asoh, S. Ono, Effect of high-frequency switching electrolysis on film thickness uniformity of anodic oxide film formed on AC8A Aluminum alloy, J. Japan Inst. Light Met. 60 (2010) 602–607. doi:10.2464/jilm.60.602.

[14] L.. Fratila-Apachitei, F.D. Tichelaar, G.E. Thompson, H. Terryn, P. Skeldon, J. Duszczyk, et al., A transmission electron microscopy study of hard anodic oxide layers on AlSi(Cu) alloys, Electrochim. Acta. 49 (2004) 3169–3177. doi:10.1016/j.electacta.2004.02.030.

[15] M. Fujita, H. Tanaka, H. Muramatsu, T. Yamamoto, H. Asoh, S. Ono, Effect of High Frequency Switching Electrolysis on Structure of Anodic Oxide Film Formed on Aluminum Alloy, J. Surf. Finish. Soc. Japan. 62 (2011) 346–350.

[16] H.S. Arora, H. Singh, B.K. Dhindaw, Composite fabrication using friction stir processing - A review, Int. J. Adv. Manuf. Technol. 61 (2012) 1043–1055. doi:10.1007/s00170-011-3758-8.

[17] R.S. Mishra, Z.Y. Ma, I. Charit, Friction stir processing: A novel technique for fabrication of surface composite, Mater. Sci. Eng. A. 341 (2003) 307–310. doi:10.1016/S0921-5093(02)00199-5.

[18] E.D. Palik, Chapter 2 - Refractive Index, Handbook of Optical Constanst of Solids, in: Handb. Opt. Constants Solids, Academic Press, Burlington, 1997: pp. 5–114. doi:http://dx.doi.org/10.1016/B978-

012544415-6.50149-7.
[19] V.C. Gudla, V.E. Johansen, S. Canulescu, J. Schou, R. Ambat, Simulation of Reflectance from White Anodised Aluminium Surfaces Using Polyurethane-TiO2 Composite Coatings, J. Mater. Sci. 50 (2015) 4565–4575. doi:DOI: 10.1007/s10853-015-9005-1.
[20] D. Kanagaraj, V. Raj, S. Vincent, S.V. Iyer, Effect of Pulse Frequency on Pulse Anodising of AA1100 Aluminium Alloy in Sulphamic Acid, Bull. Electrochem. 17 (2001) 523–526.
[21] D. Kanagaraj, V. Raj, S. Vincent, B.P. Kumar, A.S. Kumar, S.V. Iyer, Pulse anodizing of AA1100 aluminium alloy in oxalic acid electrolyte, Bull. Electrochem. 17 (2001) 285–288. http://cecri.csircentral.net/1232/ (accessed May 22, 2014).
[22] K. Yokoyama, H. Konno, H. Takahashi, M. Nagayama, Advantages of Pulse Anodizing, Plat. Surf. Finish. 69 (1982) 62–65.
[23] L. Zhang, G.E. Thompson, M. Curioni, P. Skeldon, Anodizing of Aluminum in Sulfuric Acid/Boric Acid Mixed Electrolyte, J. Electrochem. Soc. 160 (2013) C179–C184. doi:10.1149/2.032306jes.
[24] T. Ohno, K. Sarukawa, K. Tokieda, M. Matsumura, Morphology of a TiO2 photocatalyst (Degussa, P-25) consisting of anatase and rutile crystalline phases, J. Catal. 203 (2001) 82–86. doi:10.1006/jcat.2001.3316.
[25] E. Kowalska, O.O.P. Mahaney, R. Abe, B. Ohtani, Visible-light-induced photocatalysis through surface plasmon excitation of gold on titania surfaces, Phys. Chem. Chem. Phys. 12 (2010) 2344–2355. doi:10.1039/B917399D.
[26] V.C. Gudla, F. Jensen, K. Bordo, A. Simar, R. Ambat, Effect of High Frequency Pulsing on the Interfacial Structure of Anodized Aluminium-TiO2, J. Electrochem. Soc. 162 (2015) C303–C310. doi:10.1149/2.0311507jes.
[27] M. Saito, Unoxidized Aluminum Particles in Anodic Alumina Films, J. Electrochem. Soc. 140 (1993) 1907. doi:10.1149/1.2220737.
[28] A.E. Hultquist, On the Nature of Burned Anodic Coatings, J. Electrochem. Soc. 111 (1964) 1302. doi:10.1149/1.2425989.
[29] R. Chang, W.F. Hall, On the correlation between optical properties and the chemical /metallurgical constitution of multi-phase thin films, Thin Solid Films. 46 (1977) L5–L8. doi:10.1016/0040-6090(77)90068-2.
[30] OutoKumpu, HSC Chemistry, (2002).
[31] M. Li, W. Hebenstreit, U. Diebold, A.M. Tyryshkin, M.K. Bowman, G.G. Dunham, et al., The influence of the bulk reduction state on the surface structure and morphology of rutile TiO2(110) single crystals, J. Phys. Chem. B. 104 (2000) 4944–4950. doi:Doi 10.1021/Jp9943272.
[32] U. Diebold, M. Li, O. Dulub, E.L.D. Hebenstreit, W. Hebenstreit, The relationship between bulk and surface properties of rutile TiO2 (110), Surf. Rev. Lett. 07 (2000) 613–617. doi:10.1142/S0218625X0000052X.
[33] R.C. Furneaux, W.R. Rigby, B.G. Carter, Mechanisms of Short-Term Superficial Weathering of Anodized Aluminium, Proc. - INTERFINISH 84, 11th World Congr. Met. Finish. (1984) 376–384.
[34] M. Nagayama, K. Tamura, Dissolution of the anodic oxide film on aluminium in a sulphuric acid solution, Electrochim. Acta. 12 (1967) 1097–1107. doi:http://dx.doi.org/10.1016/0013-4686(67)80105-1.
[35] M. Nagayama, K. Tamura, H. Takahashi, Dissolution of porous anodic oxide films on Al in (COOH)2 solutions, Corros. Sci. 10 (1970) 617–627. doi:http://dx.doi.org/10.1016/S0010-938X(70)80055-5.

13.5 Appendix

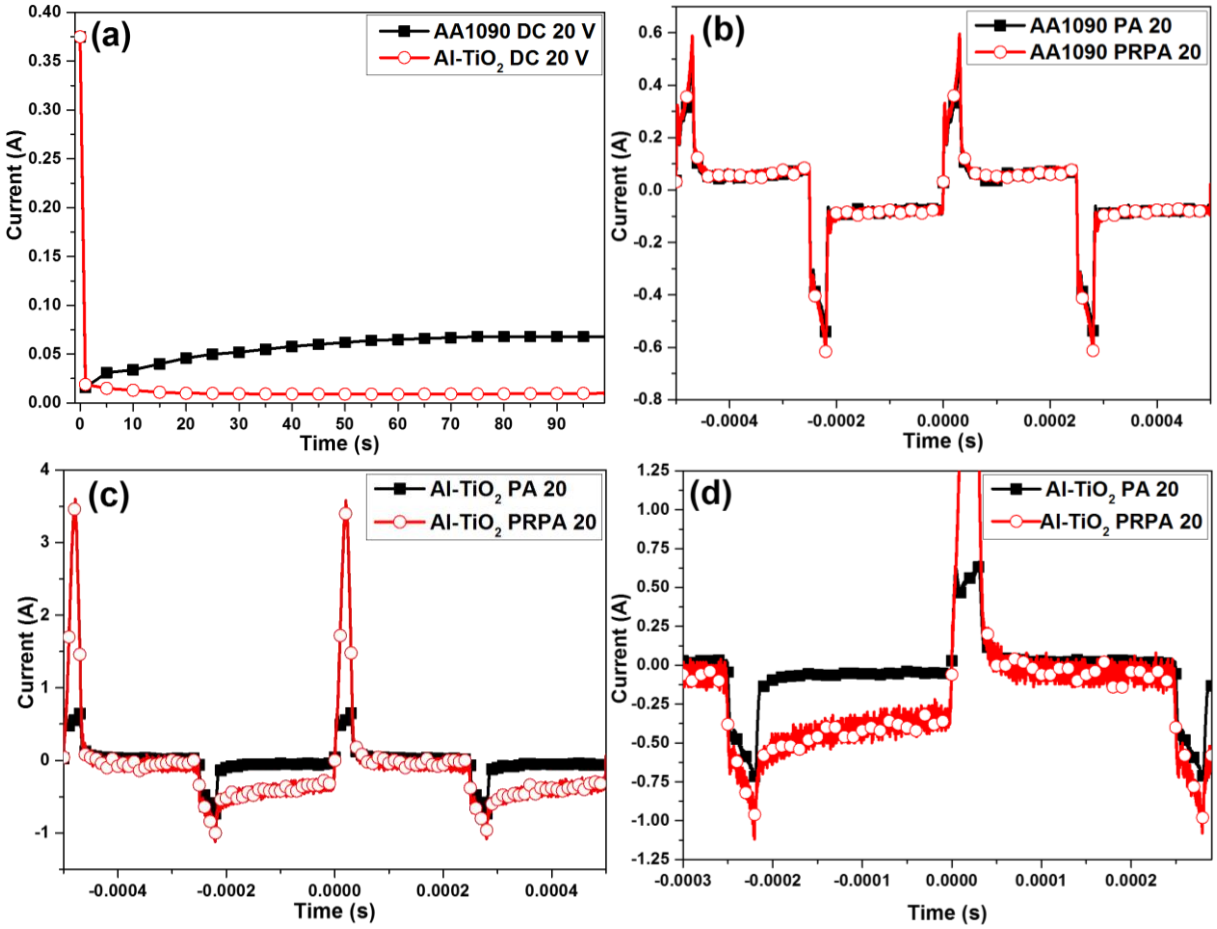

Figure 13.10: Current profiles recorded for (a) DC anodising and (b), (c) and (d) high frequency pulse and pulse reverse pulse anodising of pure Al and Al-TiO_2 surface composites.

The current profiles during DC and high frequency anodising of Al and Al-TiO_2 composites are shown in Figure 13.10. For a fixed surface area, the DC anodising current is lower for Al-TiO_2 composites when compared to pure Al. High frequency PA 20 and PRPA 20 for pure Al do not show significant difference in the current profiles. However, for the Al-TiO_2 composites there is a higher plateau current (negative value) during the 'off' cycle of the PRPA 20 in addition to the higher peak current (positive value) during the 'on' cycle. Comparing the steady state anodising current values for DC 20, PA 20 and PRPA 20 for Al-TiO_2 composites, we can see that the current value is the lowest for DC 20.

14. HF Anodising of Al-Zr, Al-Ti Coatings (Paper 10)

High Frequency Pulse Anodising of Magnetron Sputtered Al-Zr and Al-Ti Coatings*

Abstract

High frequency pulse anodising of Al-Zr and Al-Ti coatings is studied and compared to conventional decorative DC anodising. The coatings were deposited using magnetron sputtering and were heat treated after deposition to generate a multiphase microstructure with Al_3Zr and Al_3Ti intermetallic phases in an α-Al matrix. The effect of the Zr/Ti concentration content and the anodising potential on the anodising rate, the optical appearance and the microstructure is investigated. Characterization of the surfaces was performed using transmission electron microscopy, grazing incidence X-ray diffraction and the optical appearance was quantified using an integrating sphere – spectrometer setup. The anodising rate and the surface total reflectance was found to be highly dependent on the anodising potential. Anodised layer was more homogenous for high frequency pulse anodised surfaces when compared to DC anodising.

Keywords: Anodising, Aluminium, Zirconium, Titanium, Pulse, TEM, Appearance, XRD, Intermetallic, Sulphuric Acid.

* ***V.C. Gudla***, *K. Bordo, S. Engberg, K. Rechendorff, R. Ambat, High frequency pulse anodising of magnetron sputtered Al-Zr and Al-Ti Coatings, Mater. Des. 95 (2016) 340–347.*

14.1 Introduction

Anodising has been extensively applied as a surface finishing technique for aluminium alloys used in the automobile, architecture, and aerospace industry. This process is mainly used as a finishing method for applications involving corrosion and wear resistance, aesthetic, and decorative appearance [1,2]. The applications of anodising process to generate surfaces for decorative, aesthetic, and design purposes demand uniformity and homogeneity of the anodised layer in order to obtain a clear, transparent, and visually appealing surface layer [3–11].

Recent studies on electrochemical behaviour of Al alloys have focused on the use of magnetron sputtered coatings as model alloy systems. Various magnetron sputtered coatings based on Al-Mg [12,13], Al-Cu [14], Al-Mn [15], Al-Mo [16], Al-Ta [17], Al-W [18], Al-Fe [19], Al-Zr [20,21], and Al-Ti [22,23] systems have been investigated for understanding the electrochemical behaviour including the effect of anodising. Magnetron sputtered coatings provide the advantage of using selective constituents in the model alloys as binary or ternary compositions with controlled composition and high purity [24–26]. They can also be deposited on different kinds of substrates, and therefore used as model systems for studying the optical appearance of alloys before and after anodising [27,28]. Gudla et al. [20,21] and Aggerbeck et al. [22] have studied the anodising behaviour and resulting optical appearance of magnetron sputtered Al-Zr and Al-Ti coatings after heat treatment. It was observed that the applied DC voltage was not effective in completely anodising the multi-phase heterogeneous structures, which resulted in the darkening of the anodised layer [29–31]. The studies also help in understanding the optical appearance of anodised recycled Al alloys, which usually contain higher amount of intermetallic particles of varying electrochemical behaviour [32–36].

In order to reduce the heterogeneity in the structure of the anodic layer resulting from the different electrochemical behaviour of the constituting phases in the commercial Al alloys, various studies based on the effect of alternating or pulse voltage for anodising were performed [37]. Fujita et al. [38], Yamamoto et al. [39], and Juhl et al. [40] have used high frequency electrolysis technique and pulse anodising technique to anodise cast (Al-Si) as well as wrought aluminium alloy surfaces that have highly heterogeneous microstructures. The uniformity of the obtained anodic layers was improved compared to the DC anodising. The parameters such as pulse frequency and duty cycle effected the properties and structure of the obtained anodic layers. Also, the high frequency anodising provided better quality anodic films compared to the low frequency anodising [41,42]. Pulsing the applied voltage from positive to negative potential (pulse reverse pulse anodising, PRPA) resulted in a lower hardness of the anodic film compared to the pulsing from positive to zero potential (pulse anodising, PA) [40].

In this study we have investigated the effect of high frequency pulse anodising on the heterogeneous microstructure of magnetron sputtered and heat treated Al-Zr and Al-Ti coatings. Anodising was carried out in a sulphuric acid electrolyte. The effect of the anodic potential in the pulse cycle was investigated and compared with the conventional DC anodising in terms of growth rate, optical appearance, and structure of the anodised layer. The anodic layers obtained were characterized using high resolution transmission electron microscopy and the optical appearance was investigated using an integrating sphere spectrometer setup.

14.2 Experimental

14.2.1 Magnetron Sputter Deposition

Aluminium substrates (Reinal™, AA1090) were obtained in dimensions of 100 mm x 25 mm x 5 mm from Alcan Rolled Products, Germany. The samples were mechanically polished and degreased prior to the magnetron sputter deposition. The DC magnetron sputtering was performed in a CemeCon 800/9 sputter chamber at Tribology Centre, Danish Technological Institute. Binary coatings with a fixed concentration of Zr or Ti were deposited using two AA1090 targets and either two Zr targets (99.9 % purity) or two Ti targets (99.9 % purity), an AA1090 target with cylindrical Zr or Ti inserts (99.9 % purity). By varying the relative power on the Al to the Zr or Ti sputter targets, keeping the total power constant at 700 W, coatings were produced with four different concentrations of Zr or Ti (aiming at 4 wt.%, 8 wt.%, 12 wt.% and 16 wt.%). Substrates were on -80 V DC bias, and Ar flow was 200 mL/min, resulting in a pressure of about 180 mPa during deposition. Start

pressure was 1 mPa. Thickness of the deposited coatings was approx. 15 µm. The sputter deposited samples were heat treated at 550 °C for 4 h and then air cooled.

14.2.2 Anodising

The heat treated samples were then mechanically polished to a mirror finish and degreased in a mild alkaline solution (Alficlean™) prior to the anodising process. The conventional DC anodising as well as the high frequency pulse anodising (PA) was performed in a 20 wt. % sulphuric acid bath maintained at 15 °C. The bath was mechanically stirred, and the distance between the electrodes was kept around 5 cm. The total anodised area was approx. 2 cm^2. The parameters used for the anodising are presented in Table 14.1.

Table 14.1: Anodising parameters used for the heat treated magnetron sputter coated samples.

Sample name	Anodising Type	Anodic Voltage (V)	Cathodic Voltage (V)	Frequency (kHz)	Duty Cycle (%)
DC-10	DC	10	-	-	-
DC-20	DC	20	-	-	-
PA-10	Pulse	10	0	2	50
PA-20	Pulse	20	0	2	50

The high frequency anodising was performed by applying square voltage pulses from a function generator (Agilent 33120A) and the waveforms of voltage and current during the anodising were monitored with the help of a digital oscilloscope (TDS3034B, Tektronix). The thickness of the obtained anodic layers at regular intervals was determined by a capacitance probe (Omniprobe™, Fischer) with a precision of ± 1 µm. The hydrothermal sealing of the anodised surfaces was performed by immersing the samples in a water bath maintained at 98 °C and all the samples were dried later in warm air.

14.2.3 Reflectance Spectroscopy

The optical appearance of the anodised surfaces was analysed using spectrophotometry technique [43]. An integrating sphere-spectrometer setup equipped with deuterium tungsten and a halogen light source (DH2000, Ocean Optics) was used. Samples were illuminated with collimated light at an angle of incidence of 8° to the normal. The scattered light from the sample surface and after multiple scattering from the inner surface of the integrating sphere was collected using an optical fibre coupled to a spectrometer (QE65000, Ocean Optics). Each measurement was integrated over 30 s in the wavelength range of 350-750 nm and the data is reported in terms of the total and diffuse reflectance from the surface at a wavelength of 555 nm. The spectrometer was aligned using a high total reflectance standard and calibrated using a highly diffuse reflectance standard.

14.2.4 Microstructural and Phase Analysis

The phase analysis of the sputter coated surfaces before and after anodising was performed using grazing incidence X-ray diffraction (GI-XRD, Discover D8™, Bruker). A radio frequency glow discharge optical emission spectrometer (RF-GDOES, GD-Profiler 2, Horiba Jobin Yvon) was used for the compositional depth profiling. The microstructure and morphology of the pulse anodised surfaces was characterized using transmission electron microscopy (TEM, Tecnai™ G2 20, FEI) equipped with energy dispersive X-ray spectroscopy (EDS, Oxford Instruments 80 mm^2 X-Max™ silicon drift detector). The focused ion beam - scanning electron microscope (FIB-SEM, Quanta 200 3D™ DualBeam, FEI) was employed to prepare the lamella from the anodised surfaces using in-situ lift out technique and further thinning for electron transparency was performed in a dual beam FIB-SEM (Helios Nanolab™ DualBeam, FEI) .

14.3 Results

14.3.1 Phase Analysis

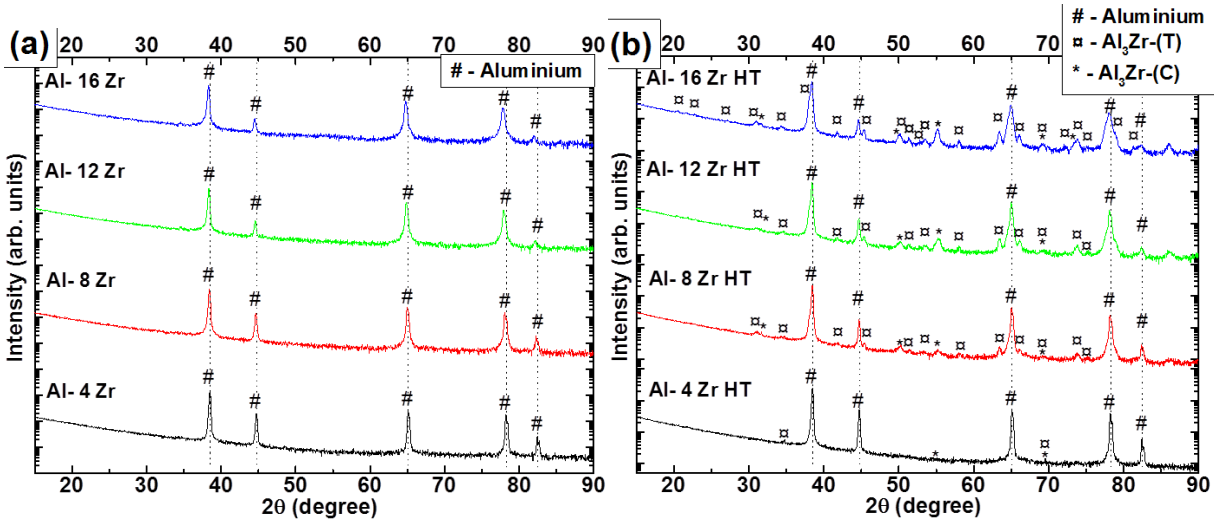

Figure 14.1: Grazing incidence X-ray diffraction patterns of Al-Zr sputtered coatings in: (a) as-received and (b) heat treated condition. Al_3Zr-(T) corresponds to tetragonal phase and Al_3Zr-(C) corresponds to cubic phase.

Figure 14.1 and Figure 14.2 show the X-ray diffraction patterns recorded from the magnetron sputtered coatings in as-received condition and after heat treatment. In the as-received condition, peaks from aluminium phase are observed for both Al-Zr and Al-Ti sputter coatings. As the concentration of Zr or Ti increases from 4 wt. % to 16 wt. %, the peaks for Al shift from their actual positions for both types of coatings (Figure 14.1 (a) and Figure 14.2 (a)). The absence of peaks from any other phases indicates that the Zr or Ti have completely dissolved in the Al matrix or are deposited as an amorphous phase. Heat treatment of the sputter coated samples gives rise to different phases. Figure 14.1 (b) and Figure 14.2 (b) show that the heat treatment produces tetragonal Al_3Zr and Al_3Ti phases in the sputtered coating. For Al-Zr coating, an additional phase with a structure corresponding to cubic-Al_3Zr was also found after the heat treatment. In addition, heat treatment of the coating removes the peak shift observed for Al in the as-received condition.

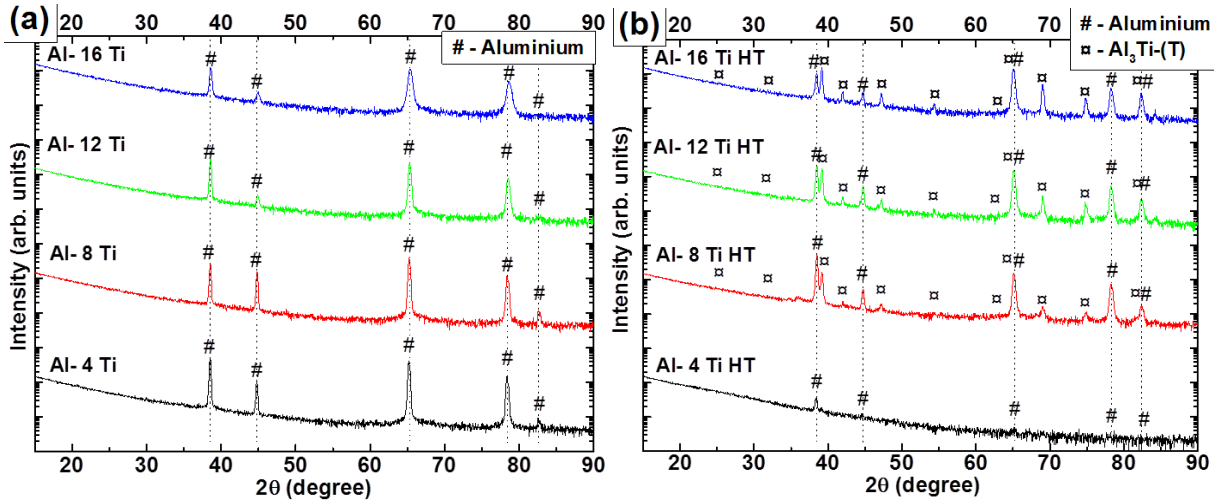

Figure 14.2: Grazing incidence X-ray diffraction patterns of Al-Ti sputtered coatings in: (a) as-received and (b) heat treated condition. Al_3Ti-(T) corresponds to tetragonal phase.

14.3.2 Anodising behaviour

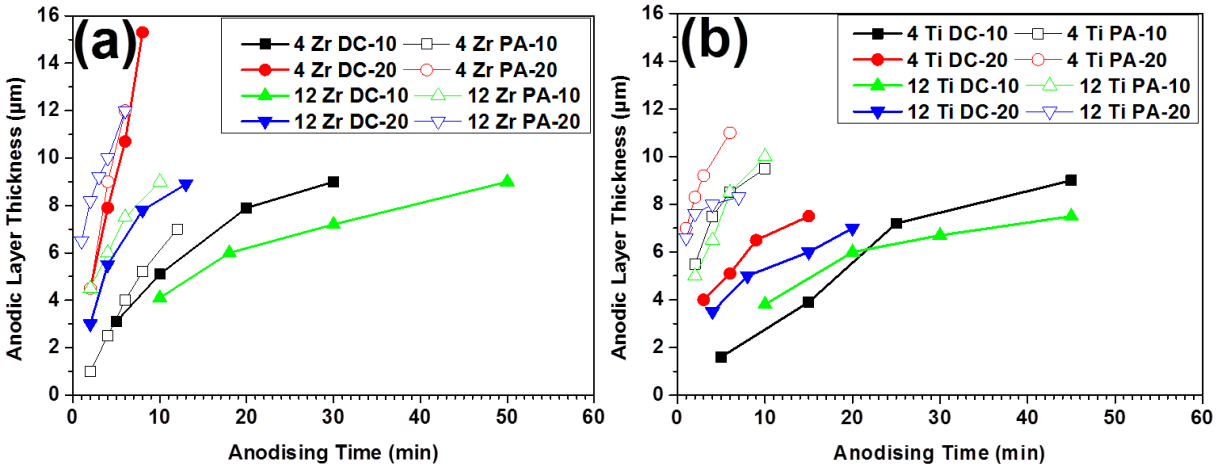

Figure 14.3: Anodic film thickness vs. anodising time for: (a) 4 wt. % and 12 wt. % Zr and (b) 4 wt. % and 12 wt. % Ti containing magnetron sputtered coatings under DC and high frequency pulse anodising.

The anodic film thickness measured after different anodising time intervals for the heat treated sputter coatings containing 4 wt. % and 12 wt. % of Zr and Ti is shown in Figure 14.3 (a) and (b). In general, the growth rate of the anodic film is high initially and then stabilises with progress of the anodising time. The anodic film grows very fast under high frequency pulse anodising compared to the conventional DC anodising. This trend is clearly observed for the Ti containing coatings (see Figure 14.3 (b)). By increasing the anodic cycle voltage from 10 V to 20 V, the anodic film grows at a faster rate both for conventional DC and high frequency pulse anodising. For coatings containing 4 wt. % Zr, the growth rate observed for DC-20 is as high as that observed for PA-20. The growth rate as measured from the obtained thickness for a given total anodising time for the sputter coated samples is presented in Figure 14.4. Under the DC-10 anodising conditions, the growth rate is similar for Zr and Ti containing sputter coatings. However, when the anodising potential is increased to 20 V (DC-20), the Zr containing samples anodise at a faster rate than the Ti containing sputter coatings. The general trend for anodising rate is PA-20 > PA-10 > DC-20 > DC-10 excluding the behaviour of 4 wt. % Zr containing coatings (especially DC-20). Also, the growth rate for DC-20 and PA-20 is lower for higher alloy concentration. However, the effect is reversed for the PA-10 anodising.

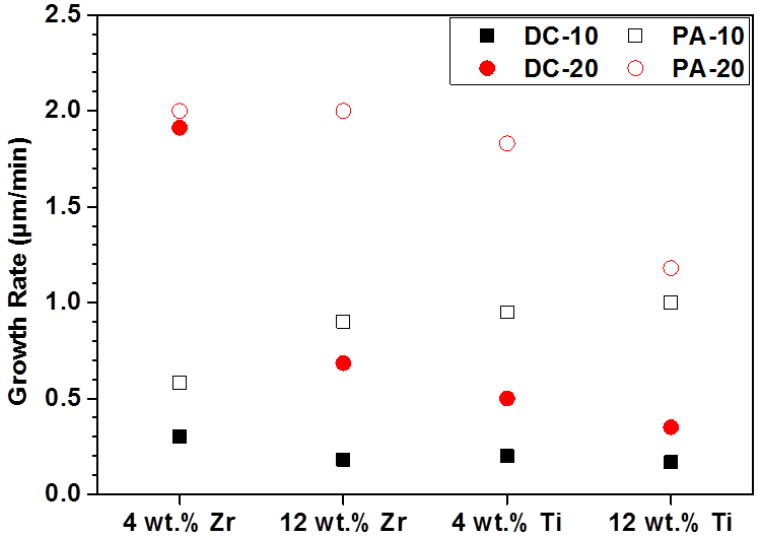

Figure 14.4: Anodic film growth rate of magnetron sputtered and heat treated Al-Zr and Al-Ti surfaces during conventional DC and high frequency pulse anodising in sulphuric acid.

14.3.3 Reflectance spectroscopy

The percentage of reflected light from the various anodised surfaces measured using integrating sphere-spectrometer technique is presented in Figure 14.5. Although, not presented here, the intensity dependence of total and diffuse components of reflected light on the wavelength in the range of 350-700 nm was very weak. Hence, only the total reflectance values at a wavelength of 555 nm are presented here. For the Zr and Ti containing sputtered coatings, the reflectance value decreased with increase in the concentration of Zr and Ti. The dependence of reflectance on the alloy composition is stronger for Zr containing coatings compared to the Ti coatings, and the reflectance values are higher for the Zr containing coating as a function of all respective anodising parameters compared to the Ti containing surfaces. Higher reflecting surfaces are achieved after the high frequency pulse anodising compared to the DC anodising at lower alloy concentrations. High concentrations of alloying elements did not show a prominent effect of pulse anodising and therefore no observable trend was found.

The diffuse/total reflectance ratio (D/T) of the anodised surfaces, which is a measure of the specular (gloss) or diffuse nature of the surfaces, is shown in Figure 14.6. For Ti containing sputter coatings, the D/T ratio is close to unity for most of the anodised surfaces indicating a highly diffuse appearing surface. On the other hand, the Zr containing sputter coatings show a D/T ratio in the range of 0.6-0.9 indicating some level of surface gloss or specular reflectance. The coatings are more glossy or specular at lower Zr concentrations and become more diffuse as the Zr concentration increases. For Ti containing surfaces, anodising at 10 V gives somewhat glossier surfaces compared to anodising at 20 V both for DC and high frequency pulse anodising. Similar trend is observed for Zr containing surfaces, but there is a mixed behaviour at lower Zr concentrations.

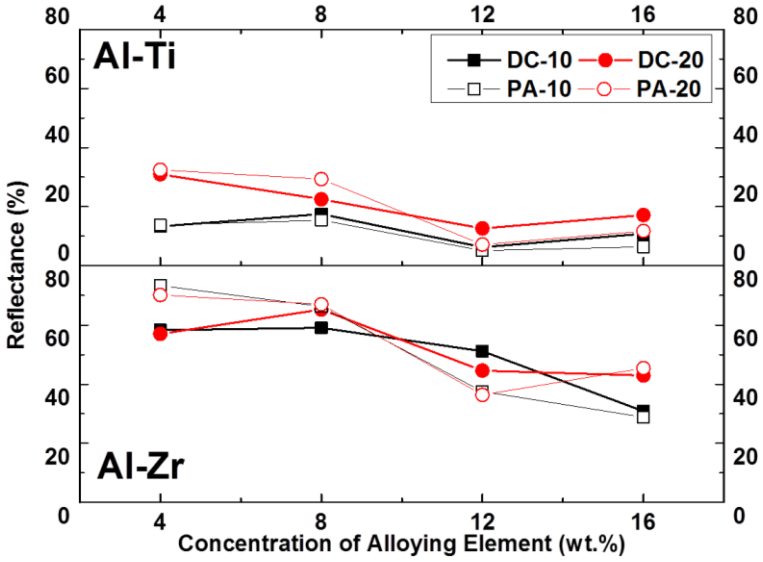

Figure 14.5: Total reflectance values at 555 nm from the Al-Zr and Al-Ti heat treated and anodised sputter coatings after DC and high frequency pulse anodising.

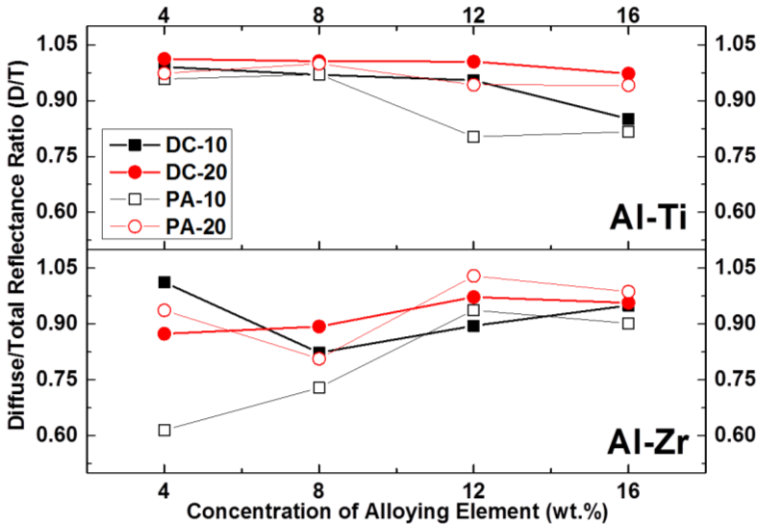

Figure 14.6: Diffuse to total reflectance ratio at 555 nm from the Al-Zr and Al-Ti heat treated and anodised sputter coating surfaces after DC and high frequency pulse anodising.

14.3.4 Microstructure

The structure of the anodic layer on Al-12 Zr with PA-20 anodising is shown in Figure 14.7 (a). The morphology of the Al_3Zr precipitates is needle like. However, other crystalline intermetallic particles were incorporated in the anodic layer as shown in Figure 14.7 (a) and (b). The elemental composition analysis using EDS showed the presence on mainly Al and Fe suggesting that they are Al-Fe based intermetallic particles. The representative compositions of various features observed in the anodic layer cross-section is summarized in Table 14.2.

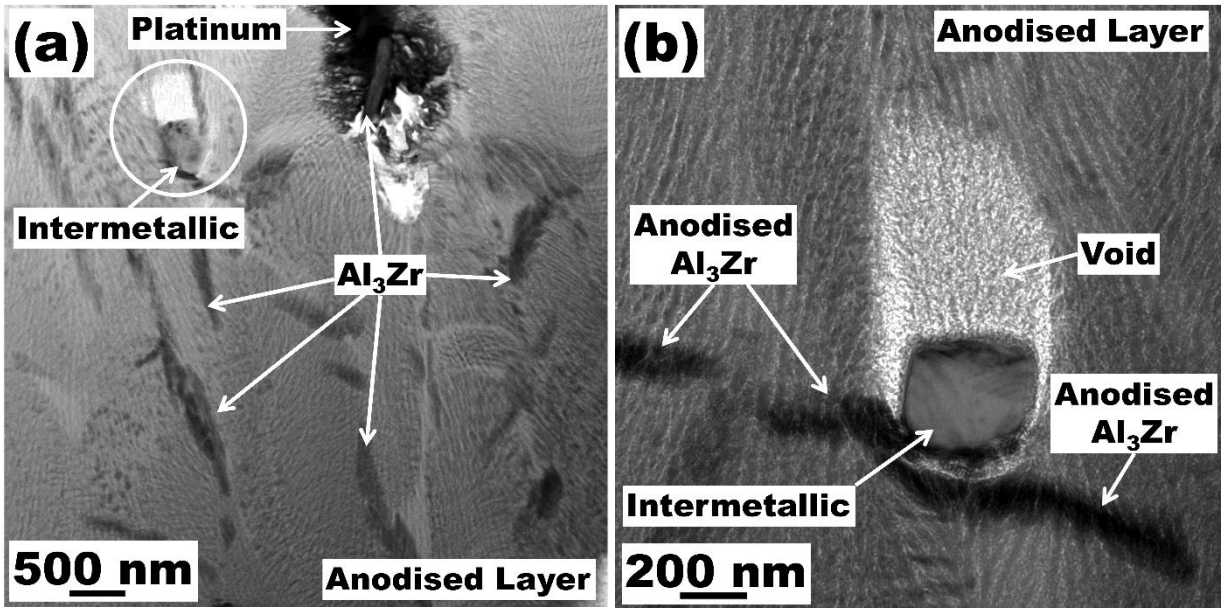

Figure 14.7: (a) Bright field TEM image of Al-12 Zr PA-20 anodic layer in cross section, and (b) showing a partially anodised intermetallic particle and completely anodised Al_3Zr particles.

The anodic layer in the vicinity of the Al-Fe intermetallic particle appears to be less dense compared to other locations (appear bright in the TEM image) suggesting the presence of voids or porosity. In Figure 14.7 (a), an Al_3Zr particle is observed in the un-anodised state incorporated in the anodic layer close to the top surface of the sample. Overall, the Al_3Zr particles appear to be completely anodised in the anodic layer as

there is no evidence of partial anodising. The anodic pore morphology does not show a considerable difference between the matrix and Al_3Zr precipitate. However, the pores do not extend perpendicularly to the substrate and appear to grow in oblique directions. Apart from the presence of Al and Zr, the anodic layer also contained considerable quantities of sulphur, which was not present in the sputtered coating. The dark appearing area in Figure 14.7 (a) is the platinum deposited as a protective layer during the sample preparation process in the FIB-SEM to prevent damage to the region of interest by the Ga ion beam.

Table 14.2 Representative EDS compositional analysis (in wt. %) of different features observed in the anodised layer of Al-12 Zr PA-20 sample.

	Al	Zr	S	O	Fe	Others (Cu, Mn, Cr, Si, Pt etc)
Sputtered Coating	86.22 ± 0.12	13.36 ± 0.11	0.03 ± 0.02	0.65 ± 0.03	0.03 ± 0.01	0.03 ± 0.01
Anodised Sputtered Coating	41.77 ± 1.01	8.34 ± 1.60	4.42 ± 0.40	45.40 ± 0.45	0.34 ± 0.43	0.105 ± 0.02
Anodised Al_3Zr particle	37.16 ± 0.12	20.54 ± 0.14	3.85 ± 0.04	38.72 ± 0.12	0.05 ± 0.01	0.021 ± 0.01
Un-Anodised Al_3Zr particle	18.63 ± 0.11	37.89 ± 0.23	2.17 ± 0.05	22.45 ± 0.16	0.05 ± 0.03	18.82 ± 0.02
Al_3Zr particle in coating after HT	63.95 ± 3.32	35.90 ± 3.38	0.11 ± 0.02	0.59 ± 0.08	0.09 ± 0.05	0.02 ± 0.01
Intermetallic Particle	71.66 ± 1.94	0.75 ± 0.64	0.17 ± 0.18	4.79 ± 2.58	21.95 ± 1.12	1.08 ± 0.01

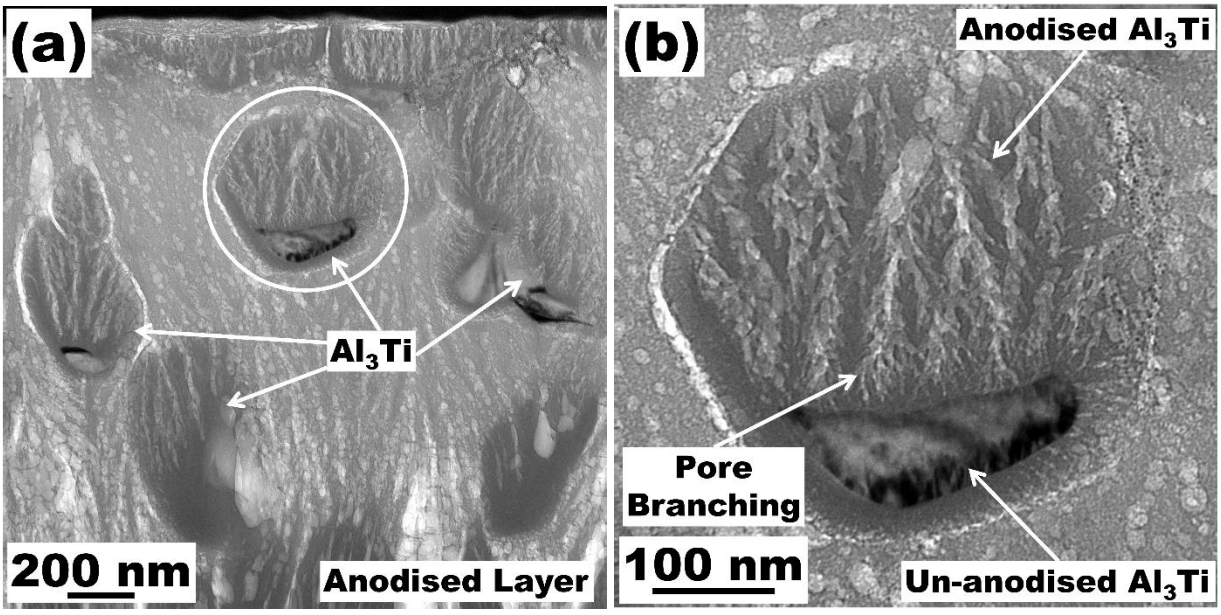

Figure 14.8: (a) Bright field TEM image of Al-12 Ti PA-20 anodic layer in cross section and (b) showing partially anodised Al_3Ti particle and pore branching within the anodised region of Al_3Ti particle.

The anodic layer formed on Al-12Ti PA-20 showed features corresponding to partially anodised phases in the anodic layer (Figure 14.8). The microstructure of the Al-12Ti coating after the heat treatment

was a dual phase structure with spheroidal Al_3Ti particles in the Al matrix. The pulse anodising at 20 V resulted in complete anodising of the Al matrix, but the Al_3Ti particles are only partially anodised as seen in Figure 14.8 (a). Higher magnification image (Figure 14.8 (b)) shows a considerable difference in the pore structure within the anodised Al_3Ti particle compared to the surrounding anodised Al matrix. The anodic pores within the particle appear to be finer than those in the Al matrix. Further, pores within the particles showed intense pore branching within the anodised region of the particle (marked in Figure 14.8 (b)). Similar to that observed for the Al-12 Zr PA-20 (Figure 14.7), the anodic pores are not extending perpendicularly towards the Al substrate. The composition of various features present in the microstructure of the anodised layer measured using EDS is summarised in Table 14.3. Similar to Al-12 Zr PA-20, the anodised layer also showed the presence of high levels of sulphur.

Table 14.3 Representative EDS compositional analysis (in wt. %) of different features observed in the anodised layer of Al-12 Ti PA-20 sample.

	Al	Ti	S	O	Others (Cu etc)
Sputtered Coating	84.54 ± 0.84	9.79 ± 0.19	-	0.84 ± 0.16	4.84 ± 0.16
Anodised Sputtered Coating	32.65 ± 0.1	15.08 ± 0.07	2.55 ± 0.04	43.38 ± 0.12	6.35 ± 0.05
Anodised Al Matrix	38.52 ± 0.1	6.36 ± 0.05	3.32 ± 0.04	46.57 ± 0.12	5.23 ± 0.05
Anodised Al_3Ti particle	46.65 ± 0.1	22.14 ± 0.07	0.77 ± 0.02	24.53 ± 0.11	5.91 ± 0.05
Un-anodised Al_3Ti Particle	65.05 ± 0.08	28.55 ± 0.07	-	0.85 ± 0.04	5.58 ± 0.04
Al_3Ti particle in coating after HT	63.62 ± 0.34	30.34 ± 0.3	-	0.8 ± 0.19	5.26 ± 0.17

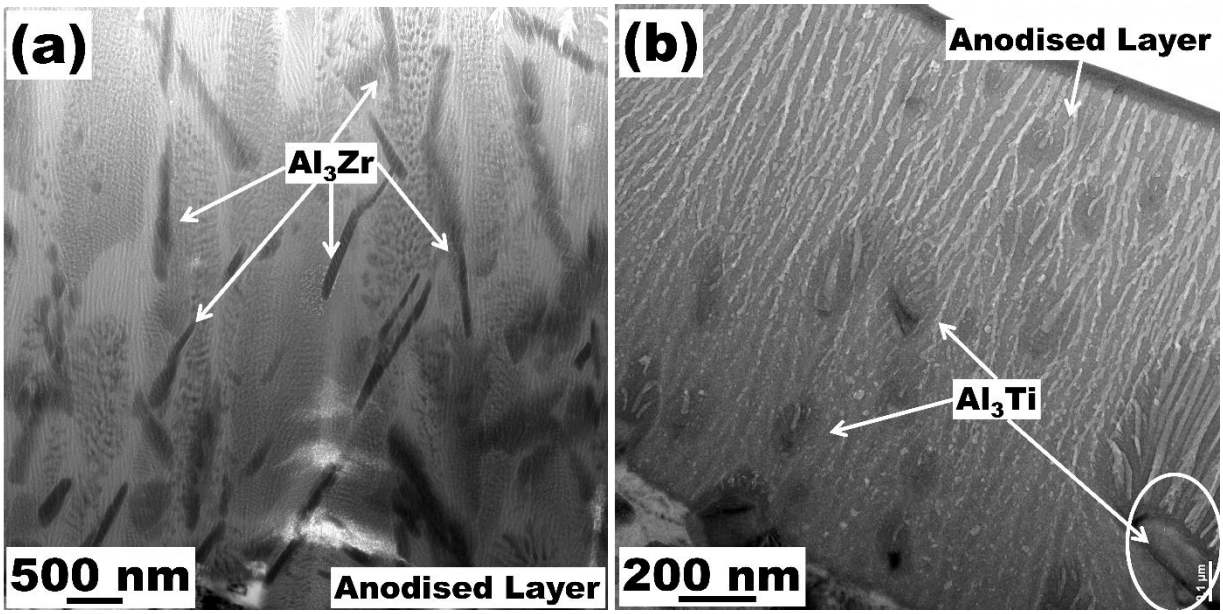

Figure 14.9: Bright field TEM images of anodic layers generated by: (a) Al-12 Zr DC-20 showing completely anodised Al_3Zr precipitates and (b) Al-12 Ti DC-20 showing partially anodised Al_3Ti precipitates. Note the larger pore diameter in the anodised region of Al_3Ti intermetallic precipitate.

The anodic layers obtained by conventional DC anodising for 12 wt. % Zr and 12 wt. % Ti containing coatings are shown in Figure 14.9 (a) and (b) for comparison. The Zr containing anodic layer showed complete anodising of the Al_3Zr precipitates without any un-anodised regions. The anodic pore structure is homogenous and extends perpendicularly towards the substrate. There is no observable difference in the pore structure in the anodised region of the Al_3Zr precipitate and the surrounding matrix (Figure 14.9 (a)). For the Ti containing coatings, the anodised layer showed evidence of un-anodised Al_3Ti precipitates. The anodic pore structure showed branching of the pores and also the anodic pores were of higher diameter in the anodised region of Al_3Ti precipitates compared to the surrounding matrix. Further, compared to the pore structure seen in Figure 14.8 (b), no pore branching was observed within the anodised region of Al_3Ti precipitates for Al-12 Ti DC-20 (Figure 14.9 (b)). The anodic pores are observed to be extending perpendicularly to the substrate.

14.4 Discussion

The as-received magnetron sputtered coatings of Al-Zr and Al-Ti showed primarily Al phase and did not show any evidence of the phases based on Al-Zr or Al-Ti (Figure 14.1 (a) and Figure 14.2 (a)). After heat treatment, the Al-Zr sputtered coatings showed the presence of a cubic and a tetragonal Al_3Zr phase. The Al-Ti coating after heat treatment showed the formation of tetragonal Al_3Ti phase (Figure 14.1 (b) and Figure 14.2 (b)). The Al-Zr phase diagram shows the tetragonal Al_3Zr phase as the equilibrium phase, whereas the cubic phase is found to be a metastable phase [44]. The crystal structures for the cubic Al_3Zr phase are reported to be based on $L1_2$ structure, while the tetragonal system is based on the DO_{23} system [45]. For the tetragonal Al_3Ti system, the crystal structure is based on DO_{22} structure [46]. The EDS analysis performed on the intermetallic phases for the heat treated Al-Zr and Al-Ti coatings confirms that the phases correspond to The Al_3Zr and Al_3Ti.

Anodising using high frequency pulse technique (PA) of the heat treated coatings showed clear effect of the alloying element, content, and heat treated microstructure on the anodised layer growth (Figure 14.3 and Figure 14.4). In general, the anodising rate decreased with increasing anodising time both for the Al-Zr and Al-Ti sputtered coatings. Also, an increase in the anodic potential resulted in an increase in the anodising rate. High frequency anodising showed a higher anodising rate compared to the conventional DC anodising. The measured total reflectance values show a mixed dependence on the alloy concentration (Figure 14.5). The reflectance values in general reduce with increasing the alloy content both for Al-Zr and Al-Ti coatings after heat treatment and anodising. A clear trend was not observed for the reflectance values for conventional DC and high frequency pulse anodised surfaces. However, better reflectance values were observed for anodising at higher anodising potentials. The surfaces obtained for the Al-Ti coatings were very diffuse and those for Al-Zr showed some gloss at lower Zr concentrations (Figure 14.5).

The microstructure of the anodised surfaces showed various features using bright field transmission electron microscopy (Figure 14.7, Figure 14.8 and Figure 14.9). For the Al-Zr coatings, the anodic layer showed complete oxidation of the DO_{23}-Al_3Zr precipitates. However, the intermetallic particles based on Al-Fe were present in the anodised layer in the un-anodised state (Figure 14.7 (b)). For the Al-Ti coatings, DO_{22}-Al_3Ti intermetallic phases are incorporated in a partially anodised state in the anodic layer (Figure 14.8 (b)). The higher anodising rates observed for Al-Zr compared to Al-Ti coatings might be due to the higher passivating nature of Ti compared to Zr. Titanium as a metal during anodising produces an adherent dense barrier type anodic layer which thickens as the anodising potential increases [47]. On the other hand, anodising of aluminium proceeds with the formation of the porous type anodic layer, which continues to grow under applied potential [1]. For mixed phases similar to Al_3Ti, upon anodising at a certain potential, either a porous type or a barrier type anodic layer can form depending on the concentration of Ti [23]. At lower concentrations of Ti, porous anodic films are observed and barrier type films are observed for coatings containing Ti concentrations above 45 at.%. Hence, the type of anodic film formed over Al_3Ti intermetallics would be of porous type as the Ti concentration in the intermetallic particle is approx. 25 at.%. The rate of anodising of the Al_3Ti intermetallic depends on the anodising potential applied. At lower anodising potential, the kinetics is slower due to the reduced ionic mobility of Al/Ti. As a result, the Al_3Ti intermetallic particles anodise only partially, whereas the surrounding Al matrix anodises at a faster rate resulting in incorporation of the partially

oxidised phases into the anodic layer (Figure 14.8 (b) and Figure 14.9 (b)). However, this also depends on the size of the intermetallic particles. Larger intermetallic phases of cathodic or passivating nature require longer anodising times compared to the surrounding Al matrix. The Al-Zr phases also behave in a similar fashion as shown by Gudla et al. [20] for which the Al-Zr-Si based intermetallic phases were found to be incorporated into the anodic layer. However, in the current study Al_3Zr phases are needle like in morphology, therefore lower cross sectional area compared to the spherical Al-Zr-Si intermetallic phases. This has led to the complete oxidation of the Al_3Zr phases as seen in Figure 14.7.

The high frequency pulse anodising has been shown to be very effective in achieving a uniform anodic layer for cast Al-Si alloys [38,39]. This is due to the fact that the cathodic cycle during the anodising process allows for the dissolution and mechanical weakening of the formed anodic oxide at the substrate interface thus increasing the anodising rate in the subsequent anodic cycle [48]. This process is clearly seen in the TEM images for Al-Ti coatings shown in Figure 14.8 (b) where the observed pore branching within the intermetallic particle is a result of the high frequency pulsing. During the cathodic cycle (0 V), the anodic layer formed in the Al_3Ti intermetallic (Al-Ti-O) is reduced in thickness and/or is mechanically weakened. This reduction in barrier layer thickness causes current localisation in the subsequent anodic cycle and also facilitates faster anodising kinetics. This results in the initiation of a new set of pores causing pore branching [49]. Under the current anodising parameters, the voltage pulses are applied from zero to a positive value of 10 V or 20 V. This is expected to reduce the level of any cathodic reactions significantly. However, there will be a current spike due to rapid change in the potential both while switching from 0 V to 10 or 20 V and from 10 or 20 V to 0 V. This will cause an effective current measured in the 0 V pulse cycle. This short pulse of high current causes cathodic reactions like electrolysis of water and generation of hydrogen. The vigorous evolution of hydrogen causes mechanical weakening of the anodic oxide at the interface and is known to be one of the contributing factors for higher uniformity of the anodic layers on heterogeneous microstructures.

In summary, shape of the second phase particles influence of the extent of oxidation of the particles during the anodising process. The Al_3Zr phase provides a smaller cross-section for anodising and hence the possibility of partial anodising and subsequent incorporation is very low compared to the Al_3Ti intermetallics. The tendency for partial anodising and incorporation, however, increases with increasing the alloy concertation both for Zr and Ti containing coatings. Similarly, due to the better anodising, more uniformity is achieved by high frequency pulsing and at higher anodic potential values. The DC anodising would lead to higher un-anodised intermetallic phases in the anodic layer. The presence of un-anodised metallic phases in an anodic alumina matrix contributes to the darkening of the anodic layer due to the attenuation of light [31,50–52]. This phenomenon has been systematically investigated by Gudla et al. [20,21], Aggerbeck et al. [22] and also theoretically handled by Saito et al. [29] and Chang et al. [30]. In view of this phenomenon, and the observed anodising response of the Al_3Zr and Al_3Ti intermetallic phases under the DC and high frequency pulse anodising, it can be stated that the increasing the Zr/Ti alloy content, use of lower anodising potentials (10 V vs. 20 V) and DC anodising (vs. PA) would lead to darker anodic films. In addition, as Al_3Zr intermetallic phases are more readily anodised compared to Al_3Ti phases, the reflectance values obtained (Figure 14.5) from the surfaces containing Zr as alloying element are brighter than those containing Ti. In general, the understanding from this study can be used for explaining the darkening behaviour of the anodic layer during anodising of commercial aluminium alloys depending on the nature of intermetallic particles that are cathodic or passivating.

14.5 Conclusions

- High frequency pulse anodising provides uniform anodised surfaces for the heat-treated magnetron sputtered Al-Zr and Al-Ti coatings.
- Heat treatment of Al-Zr and Al-Ti coatings showed formation of a tetragonal and cubic Al_3Zr, and tetragonal Al_3Ti intermetallic phases in the sputtered coatings.
- Increasing the anodising potential under DC or high frequency pulsing improved the anodising rate and the total reflectance of the anodised surfaces.
- High frequency pulse anodising showed higher uniformity in the microstructure of the anodised layer compared to the conventional DC anodising of surfaces.

- The negative current during high frequency pulsing causes pore branching due to the mechanical weakening and anodic layer dissolution resulting in better uniformity in the anodic layers.
- Partial anodising of intermetallic phases and subsequent incorporation into the anodised layer causes darkening of the anodic layer.

References

[1] P.G. Sheasby, R. Pinner, The Surface Treatment and Finishing of Aluminium and Its Alloys, Volume 1, 6th ed., ASM International; Finishing Publications, 2001.

[2] P.G. Sheasby, R. Pinner, The Surface Treatment and Finishing of Aluminium and Its Alloys, Volume 2, 6th ed., ASM International; Finishing Publications, 2001.

[3] C.A. Grubbs, Decorative and architectural anodizing, Met. Finish. 93 (1995) 449–459. doi:10.1016/0026-0576(95)93394-H.

[4] Steiger A. J., Decorative Dyeing of Aluminium and Its Alloys, Met. Finish. J. September (1960) 368–369.

[5] Y. Ma, X. Zhou, G.E. Thompson, J.O. Nilsson, M. Gustavsson, A. Crispin, Anodizing of AA6063 aluminium alloy profiles: Generation of dark appearance, Surf. Interface Anal. 45 (2013) 1479–1484. doi:10.1002/sia.5219.

[6] J. Timm, Influence of Fe and Si Containing Phases on the Anodisation Behaviour, Key Eng. Mater. 44-45 (1990) 219–232. doi:10.4028/www.scientific.net/KEM.44-45.219.

[7] N. Tabrizian, H.N. Hansen, P.E. Hansen, R. Ambat, P. Møller, Influence of annealing and deformation on optical properties of ultra precision diamond turned and anodized 6060 aluminium alloy, Surf. Coatings Technol. 204 (2010) 2632–2638. doi:10.1016/j.surfcoat.2010.02.002.

[8] M. Aggerbeck, S. Canulescu, K. Dirscherl, V.E. Johansen, S. Engberg, J. Schou, et al., Appearance of anodised aluminium: Effect of alloy composition and prior surface finish, Surf. Coatings Technol. 254 (2014) 28–41. doi:10.1016/j.surfcoat.2014.05.047.

[9] H. Zhu, X. Zhang, M.J. Couper, A.K. Dahle, Effect of primary intermetallic particles on surface microstructure and appearance of aluminium extrusions, Mater. Chem. Phys. 113 (2009) 401–406. doi:10.1016/j.matchemphys.2008.07.109.

[10] H. Zhu, T. Wei, M.J. Couper, A.K. Dahle, Effect of extrusion profile on surface microstructure and appearance of aluminum extrusions with different Fe contents, JOM. 65 (2013) 618–624. doi:10.1007/s11837-013-0581-8.

[11] H. Zhu, X. Zhang, M.J. Couper, A.K. Dahle, Effect of initial microstructure on surface appearance of anodized aluminum extrusions, Metall. Mater. Trans. A Phys. Metall. Mater. Sci. 40 (2009) 3264–3275. doi:10.1007/s11661-009-9976-0.

[12] Y. Liu, P. Skeldon, G.. Thompson, H. Habazaki, K. Shimizu, Anodic film growth on an Al–21at.%Mg alloy, Corros. Sci. 44 (2002) 1133–1142. doi:10.1016/S0010-938X(01)00115-9.

[13] X. Zhou, G.E. Thompson, P. Skeldon, G.C. Wood, K. Shimizu, H. Habazaki, Film formation and detachment during anodizing of Al-Mg alloys, Corros. Sci. 41 (1999) 1599–1613. doi:10.1016/S0010-938X(99)00007-4.

[14] S.J. Garcia-Vergara, K. El Khazmi, P. Skeldon, G.E. Thompson, Influence of copper on the morphology of porous anodic alumina, Corros. Sci. 48 (2006) 2937–2946. doi:10.1016/j.corsci.2005.10.017.

[15] A.C. Crossland, G.E. Thompson, C.J.E. Smith, H. Habazaki, K. Shimizu, P. Skeldon, Formation of manganese-rich layers during anodizing of Al-Mn alloys, Corros. Sci. 41 (1999) 2053–2069. doi:10.1016/S0010-938X(99)00025-6.

[16] H. Habazaki, P. Skeldon, K. Shimizu, Anodic film formation on a sputter-deposited Al-30at% Mo alloy, Corros. Sci. 31 (1995) 1497–1509. http://www.sciencedirect.com/science/article/pii/0010938X9500061N (accessed May 22, 2014).

[17] G. Alcalá, S. Mato, P. Skeldon, G.E. Thompson, P. Bailey, T.C.Q. Noakes, et al., Anodic film growth in the Al-Ta alloy system, Corros. Sci. 45 (2003) 1803–1813. doi:10.1016/S0010-938X(02)00252-4.

[18] S.J. Garcia-Vergara, P. Skeldon, G.E. Thompson, H. Habazaki, Pore development during anodizing of Al – 3.5 at.% W alloy in phosphoric acid, Technology. 201 (2007) 9506–9511. doi:10.1016/j.surfcoat.2007.04.015.

[19] H. Habazaki, K. Shimizu, P. Skeldon, G.E. Thompson, G.C. Wood, The behaviour of iron during anodic oxidation of sputtering-deposited Al-Fe alloys, Corros. Sci. 43 (2001) 1393–1402. doi:10.1016/S0010-

938X(00)00151-7.
[20] V.C. Gudla, S. Canulescu, R. Shabadi, K. Rechendorff, K. Dirscherl, R. Ambat, Structure of anodized Al-Zr sputter deposited coatings and effect on optical appearance, Appl. Surf. Sci. 317 (2014) 1113–1124. doi:http://dx.doi.org/10.1016/j.apsusc.2014.09.037.
[21] V.C. Gudla, S. Canulescu, R. Shabadi, K. Rechendorff, J. Schou, R. Ambat, Anodization and Optical Appearance of Sputter Deposited Al-Zr Coatings, in: J. Grandfield, TMS (Eds.), Light Met. 2014, John Wiley & Sons, Inc., 2014: pp. 369–373. doi:10.1002/9781118888438.ch63.
[22] M. Aggerbeck, A. Junker-Holst, D.V. Nielsen, V.C. Gudla, R. Ambat, A.J. Holst, et al., Anodisation of Sputter Deposited Aluminium - Titanium Coatings : Effect of Microstructure on Optical Characteristics, Surf. Coatings Technol. 254 (2014) 138–144. doi:http://dx.doi.org/10.1016/j.surfcoat.2014.05.073.
[23] V.C. Nettikaden, H. Liu, P. Skeldon, G.E. Thompson, Porous anodic film formation on Al-Ti alloys in sulphuric acid, Corros. Sci. 57 (2012) 49–55. doi:10.1016/j.corsci.2011.12.035.
[24] R.. Arnell, P.. Kelly, Recent advances in magnetron sputtering, Surf. Coatings Technol. 112 (1999) 170–176. doi:10.1016/S0257-8972(98)00749-X.
[25] I. Safi, Recent aspects concerning DC reactive magnetron sputtering of thin films: a review, Surf. Coatings Technol. 127 (2000) 203–218. doi:10.1016/S0257-8972(00)00566-1.
[26] P.J. Kelly, R.D. Arnell, Magnetron sputtering: A review of recent developments and applications, Vacuum. 56 (2000) 159–172. doi:10.1016/S0042-207X(99)00189-X.
[27] S. Van Gils, T. Dimogerontakis, G. Buytaert, E. Stijns, H. Terryn, P. Skeldon, et al., Optical properties of magnetron-sputtered and rolled aluminum, J. Appl. Phys. 98 (2005). doi:10.1063/1.2085315.
[28] S. Canulescu, K. Rechendorff, C.N. Borca, N.C. Jones, K. Bordo, J. Schou, et al., Band gap structure modification of amorphous anodic Al oxide film by Ti-alloying, Appl. Phys. Lett. 104 (2014) 121910. doi:10.1063/1.4866901.
[29] M. Saito, Unoxidized Aluminum Particles in Anodic Alumina Films, J. Electrochem. Soc. 140 (1993) 1907. doi:10.1149/1.2220737.
[30] R. Chang, W.F. Hall, On the correlation between optical properties and the chemical /metallurgical constitution of multi-phase thin films, Thin Solid Films. 46 (1977) L5–L8. doi:10.1016/0040-6090(77)90068-2.
[31] A.E. Hultquist, On the Nature of Burned Anodic Coatings, J. Electrochem. Soc. 111 (1964) 1302. doi:10.1149/1.2425989.
[32] J.B. Hess, Physical metallurgy of recycling wrought aluminum alloys, Metall. Trans. A. 14 (1983) 323–327. doi:10.1007/BF02644210.
[33] R.G. Buchheit, A Compilation of Corrosion Potentials Reported for Intermetallic Phases in Aluminum Alloys, J. Electrochem. Soc. 142 (1995) 3994. doi:10.1149/1.2048447.
[34] J.R. Scully, T.O. Knight, R.G. Buchheit, D.E. Peebles, Electrochemical characteristics of the Al2Cu, Al3Ta and Al3Zr intermetallic phases and their relevancy to the localized corrosion of Al alloys, Corros. Sci. 35 (1993) 185–195. doi:10.1016/0010-938X(93)90148-A.
[35] N. Birbilis, R.G. Buchheit, Electrochemical Characteristics of Intermetallic Phases in Aluminum Alloys: An Experimental Survey and Discussion, J. Electrochem. Soc. 152 (2005) B140–B151. doi:10.1149/1.1869984.
[36] R.G. Buchheit, R.K. Boger, M.C. Carroll, R.M. Leard, C. Paglia, J.L. Searles, The electrochemistry of intermetallic particles and localized corrosion in Al alloys, JOM. 53 (2001) 29–33. doi:10.1007/s11837-001-0084-x.
[37] I. De Graeve, H. Terryn, G.E. Thompson, AC-Anodising of Aluminium: Contribution to Electrical and Efficiency Study, Electrochim. Acta. 52 (2006) 1127–1134. doi:10.1016/j.electacta.2006.07.010.
[38] M. Fujita, H. Tanaka, H. Muramatsu, T. Yamamoto, H. Asoh, S. Ono, Effect of High Frequency Switching Electrolysis on Structure of Anodic Oxide Film Formed on Aluminum Alloy, J. Surf. Finish. Soc. Japan. 62 (2011) 346–350.
[39] T. Yamamoto, H. Tanaka, M. Fujita, H. Asoh, S. Ono, Effect of high-frequency switching electrolysis on film thickness uniformity of anodic oxide film formed on AC8A Aluminum alloy, J. Japan Inst. Light Met. 60 (2010) 602–607. doi:10.2464/jilm.60.602.
[40] A. Deacon Juhl, Pulse anodising of extruded and cast aluminium alloys, Technical University of Denmark, 1999.
[41] D. Kanagaraj, V. Raj, S. Vincent, S.V. Iyer, Effect of Pulse Frequency on Pulse Anodising of AA1100 Aluminium Alloy in Sulphamic Acid, Bull. Electrochem. 17 (2001) 523–526.
[42] D. Kanagaraj, V. Raj, S. Vincent, B.P. Kumar, A.S. Kumar, S.V. Iyer, Pulse anodizing of AA1100 aluminium alloy in oxalic acid electrolyte, Bull. Electrochem. 17 (2001) 285–288. http://cecri.csircentral.net/1232/ (accessed May 22, 2014).

[43] I. Lindseth, A. Bardal, R. Spooren, Reflectance measurements of aluminium surfaces using integrating spheres, Opt. Lasers Eng. 32 (1999) 419–435. doi:10.1016/S0143-8166(00)00010-5.
[44] ASM Handbook - Alloy Phase Diagrams - Volume 3, ASM International, 1992.
[45] K.E. Knipling, D.C. Dunand, D.N. Seidman, Precipitation evolution in Al–Zr and Al–Zr–Ti alloys during aging at 450–600 °C, Acta Mater. 56 (2008) 1182–1195. doi:http://dx.doi.org/10.1016/j.actamat.2007.11.011.
[46] S.Z. Han, S.I. Park, J.-S. Huh, Z.-H. Lee, H.M. Lee, Lattice matching of D023 and D022 phases in Al-6at.%(Ti,V,Zr) systems, Mater. Sci. Eng. A. 230 (1997) 100–106. doi:http://dx.doi.org/10.1016/S0921-5093(96)10857-1.
[47] P. Møller, L. Pleth Nielsen, Advanced surface technology Vol. 1-2, Møller & Nielsen, 2013.
[48] V.C. Gudla, F. Jensen, K. Bordo, A. Simar, R. Ambat, Effect of High Frequency Pulsing on the Interfacial Structure of Anodized Aluminium-TiO2, J. Electrochem. Soc. 162 (2015) C303–C310. doi:10.1149/2.0311507jes.
[49] J. Zahavi, A-C Anodizing Processes of Aluminum Alloys, J. Electrochem. Soc. 129 (1982) 1572. doi:10.1149/1.2124211.
[50] R. Tilley, Colour and The Optical Properties of Materials: An Exploration of the Relationship Between Light, the Optical Properties of Materials and Colour, 2010. http://www.pilkington.com/products/bp/bybenefit/specialapplications/tecglass/ (accessed November 4, 2013).
[51] E. Hecht, Optics, Addison Wesley, 2002.
[52] V.C. Gudla, F. Jensen, A. Simar, R. Shabadi, R. Ambat, Friction stir processed Al–TiO2 surface composites: Anodising behaviour and optical appearance, Appl. Surf. Sci. 324 (2015) 554–562. doi:http://dx.doi.org/10.1016/j.apsusc.2014.10.151.

15. White Anodised, and Pastel Coloured Aluminium Surfaces

This chapter summarizes the outcome of the research work carried out in the PhD project. Incorporating the key learnings and findings from the previous chapters, a novel white anodising process platform was invented and several white anodised surfaces were generated for the first time. In addition, a new generation of pastel colours were imparted to anodised Al surfaces using the white anodised surfaces as precursors. Different pastel appearing anodised surfaces are also prepared and presented. Due to the confidentiality and intellectual property rights related to this new white anodising process, only selected results and details are presented and discussed.

15.1 Introduction

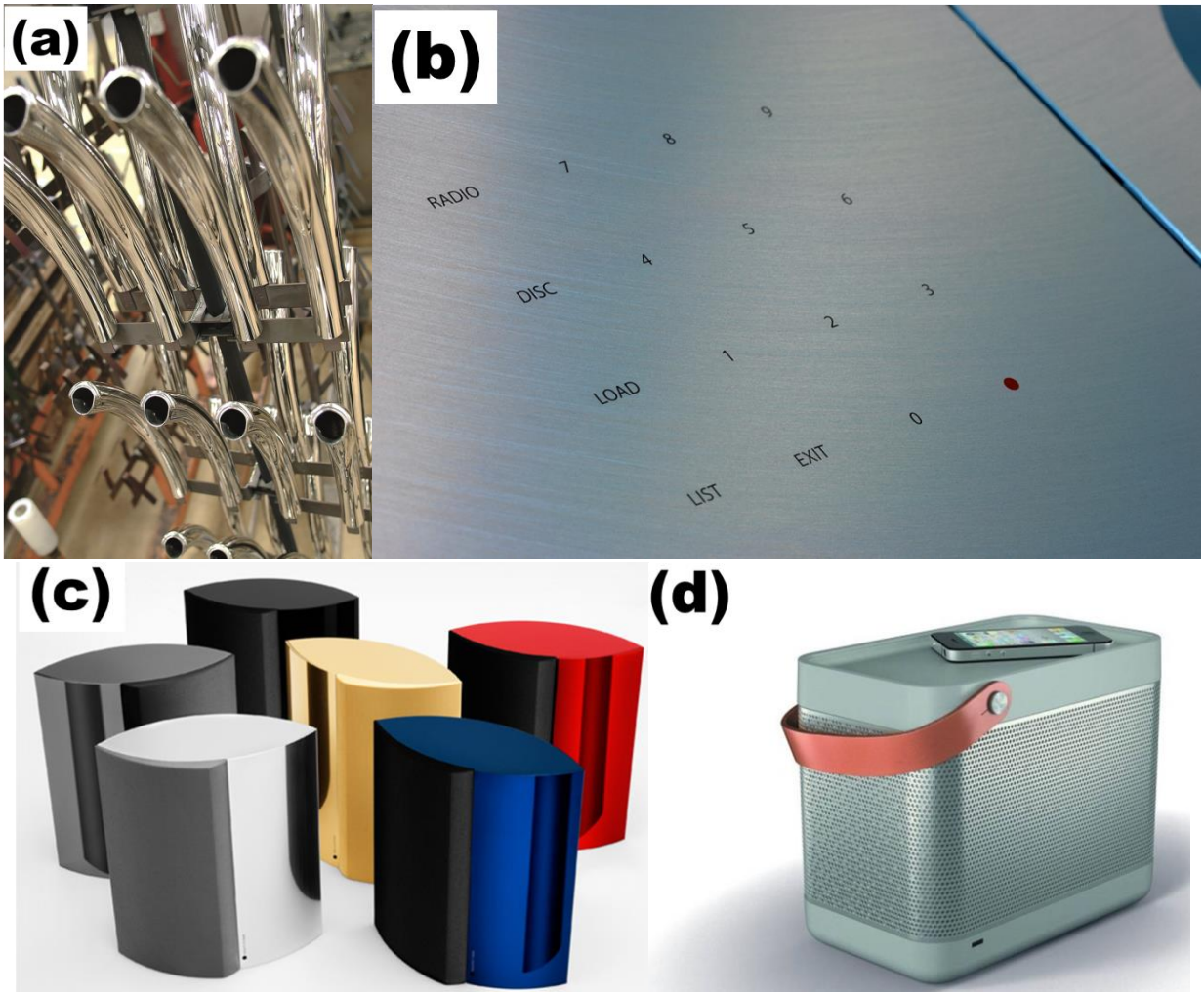

Figure 15.1: Some of the high-end design products and surfaces produced by Bang and Olufsen A/S, Denmark: (a) very bright glossy Aluminium profiles, (b) machined appearance of anodised Al surface, (c) BeoLab 4000 speakers of various colours produced by dyeing after anodising, and (d) BeoLit 12 audio system.

The focus and vision of the current PhD project and the overall 'ODAAS' project is to achieve white anodised Al surfaces with high gloss and diffuse reflectance. It is the wish of the project partner, Danish

industry Bang and Olufsen A/S, to obtain these white anodised surfaces for extending their design possibilities beyond their current limitations. Such anodised Al surfaces would inherently exhibit a white appearance, and also possess a decorative and aesthetically pleasing appearance along with high scratch and wear resistance. Current design capabilities of the industrial partner include generating surfaces from a very bright glossy appearance to a matte etched appearing surface (Figure 15.1). Apart from being decorative, the white anodising process would be environmentally friendly as there are no organic paints involved to generate the white colour, which also leads to a higher scrap value for the material.

15.2 White Anodising

Various kinds of surface appearances or visual effects are imparted to the anodised Aluminium surfaces by pre-treating the aluminium surface using different techniques [1,2]. The caustic etching by immersion in 10 wt. % NaOH solution at 60 °C in an ultrasonic bath for 10 min provides a rough and matte appearing anodised surface due to the etch pits and scallops produced on the aluminium surface, which scatter light in a very diffuse manner [3,4]. Similar appearances can be achieved using blasting of the surface by hard abrasive particles or glass beads, which impart the scalloped topography to the aluminium surface [5,6]. Rough grinding using an abrasive wheel or a tool generates a unique appearance which displays grinding marks on the surface, which are retained at the anodised aluminium-substrate interface after anodising [7]. The direction and manner of grinding play an important role in the final visual appearance. Wire brushing of the surface results in similar appearance, displaying optical effects due to the deep gouging marks on the soft aluminium substrate by the tips of the wire brush [8]. The pressure applied on the surface and the stiffness of the wire brush play a very important role in the roughness achieved on the aluminium surface [9].

A new set of colours for anodised Aluminium surfaces based on pastel colours is also investigated. Pastels or pastel colours are the family of colours which have ‘high value’ and ‘low to intermediate saturation’ [10,11]. They are usually defined as colours that are obtained by adding white to saturated colours. Such colours to date have not been imparted to anodised aluminium due to the high intensity of the dyes used for colouring anodised aluminium. Unique approach to achieve pastel colouring of anodised aluminium is to conventionally dye a bright white anodised aluminium surface. The dye would provide the colour and the white from the anodised surface would reduce the saturation resulting in pastel appearance.

In this chapter, the optical appearance (characterized using CIE-Lab measurements) of bright white anodised as well as different pastel coloured anodised aluminium surfaces is presented. The white anodised surfaces of varying anodic layer thickness were prepared using Al-TiO_2 composites. Certain details related to processing of the white anodised layer using anodising process is not discussed due to confidentiality related to the invention, which is not yet patented.

15.3 Materials and Methods

The starting material used is Al-TiO_2 composite with TiO_2 (rutile) particles in the size range of 320 nm to 500 nm. The surface of the composites is polished to a fine surface finish using the traditional coarse grinding followed by the wheel polishing using an alumina abrasive paste of different size grades. Fine polishing was performed using a soft polishing disc for obtaining a high gloss surface. The prepared surface of the composite was then cleaned using ethanol for removing the polishing residues. To obtain rough matte appearing surfaces, blasting with glass beads was performed. Ground finish was obtained by brushing the sample surfaces with a wire brush. Degreasing of the composite surfaces after surface treatement was performed by immersing in a commercial AlfiClean™ solution from AluFinish at 60 °C for 2 min – 7 min with rough agitation. Desmutting of the degreased surfaces was performed by dipping in 6 wt. % HNO_3 at 27-28 °C for approx. 4 min followed by rinsing in demineralized water. The specimens were then subjected to white anodising process based on the research findings presented earlier for various time intervals to achieve an anodised surface with varying anodic layer thickness. Hydrothermal sealing of the white anodised surfaces was performed by immersing in a water bath containing 2-3 g/L AlfiSeal™ from AluFinish maintained at 96 °C. The sealing time was varied depending on the anodised layer thickness and was approx. 2-3 min/µm of the anodised layer.

The pastel colouring of the surface was achieved by dyeing the white anodised surfaces using the commercially available dyes. The white anodised surfaces prior to sealing were immersed in a solution containing the dye followed by using the hydrothermal process. The dyeing time was varied depending on the anodised layer thickness, and also the intensity and depth of the colour that was required. Optical characterization of the anodised surfaces was performed using a spectral analyser (Datacolor Check II™, Datacolor, Belgium) with a pulsed Xenon light source. The instrument was calibrated using a set of coloured tiles (British Ceramic Research, BCRA). The reflectance was measured in the wavelength range of 400-700 nm and CIE-L, a, b values are reported [12].

15.4 Results and Discussion

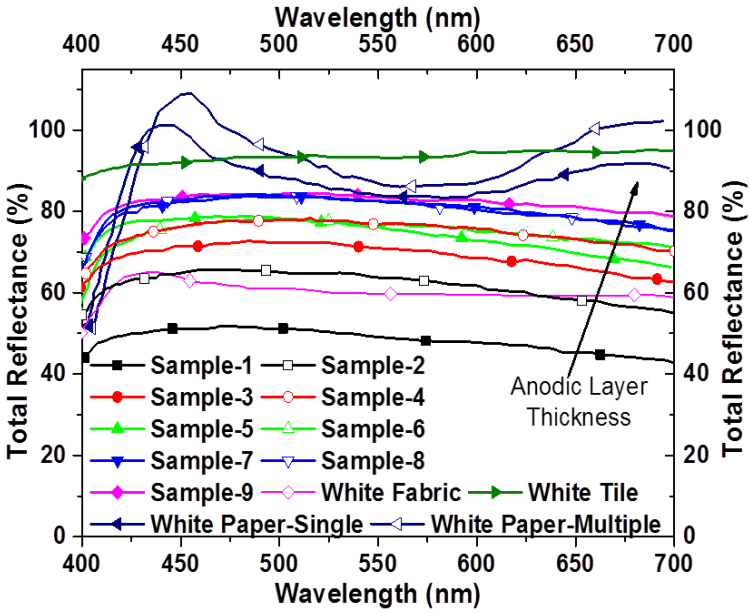

Figure 15.2: Total reflectance spectra obtained from different white anodised surfaces, white printing paper, white fabric, and a white calibration tile.

The total surface reflectance of various white anodised surfaces is shown in Figure 15.2. The reflectance values are compared with those measured from a white calibration tile, white printing paper, and a white fabric. For the white anodised surface (Sample-1 to Sample-9) the dependence of the reflectance over the entire wavelength is minimal and only a slight reduction with increasing wavelength is observed. The reflectance increases with increasing anodic layer thickness (marked with an arrow). Reflectance values of the order of 85 % can be observed for Sample-9, which has the highest thickness among the eight samples. The white calibration tile has a total reflectance of about 95 %. Plain white printing paper has a total reflectance which is not only highly dependent on the wavelength, but also shows a value higher than 100 % at lower wavelengths. The reflectance values above 100% for the white paper at lower wavelength region is due to the fluorescence from the optical brighteners, which are used to increase the reflectance of the paper [13,14]. The compounds in the optical brightener absorb UV radiation in the wavelength range of 300 nm - 430 nm, which is invisible to human eye and re-emit it as fluorescence in the visible region of 400 nm - 500 nm range [15].

The effect of increasing anodised layer thickness on the total surface reflectance for white anodised surfaces (Sample-1 to Sample-9) is shown in Figure 15.3. The total reflectance shows an increasing trend with increasing anodised layer thickness and appears to saturate at higher anodic layer thickness.

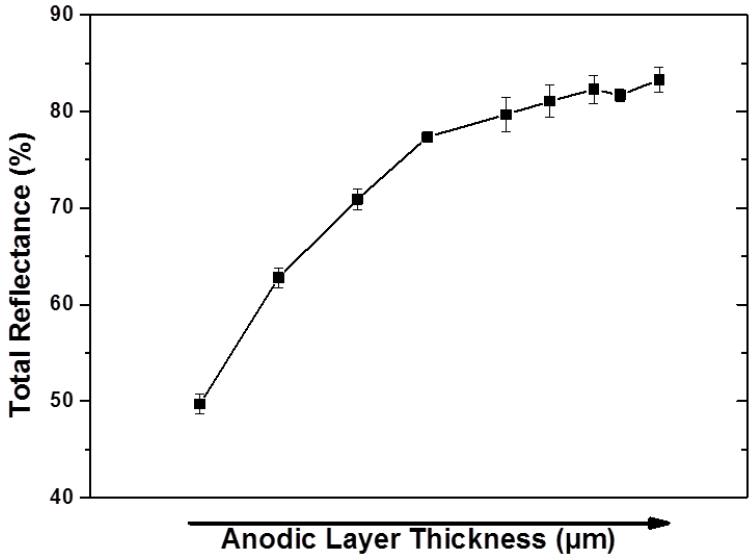

Figure 15.3: Total reflectance from white anodised surfaces measured as a function of increasing anodic layer thickness (Sample-1 to Sample-9; Wavelength is 55 nm).

The CIE-Lab values for the white anodised surfaces are presented in Table 15.1 and plotted in Figure 15.4 (a) and (b) along with the values for other white surfaces. The values for CIE-a and b are very close to zero and the CIE-L is increasing with increasing anodic layer thickness. This implies that there is little colour to the surfaces and they are very bright. The values for the white calibration tile are slightly higher than those for the white anodised surfaces. Also, for single and multiple white papers, the CIE-L value is higher than the white anodised surfaces, however the CIE-a and b are higher due to the bluish tinge caused by the optical brighteners. The colour difference between the eight white anodised surfaces is very little as can be seen from the scatter in their CIE-a and b values in Figure 15.4 (b) and also their chromaticity values in Table 15.1.

Table 15.1: Measured CIE-L, a, and b values from different white anodised surfaces, white printing paper, white fabric, and a white calibration tile.

Sample	CIE-L	CIE-a	CIE-b	Chromaticity
Sample-1	76.15	-2.26	-1.33	2.62
Sample-2	83.10	-2.41	-0.61	2.48
Sample-3	87.05	-2.34	0.15	2.34
Sample-4	90.34	-2.12	0.48	2.17
Sample-5	90.64	-2.29	-1.58	2.79
Sample-6	92.08	-2.04	0.14	2.10
Sample-7	90.26	-2.33	0.31	2.51
Sample-8	92.39	-1.95	-0.98	2.37
Sample-9	91.96	-1.96	0.31	2.15
White Paper-Multiple	96.29	2.13	-9.82	10.05
White Paper-Single	94.65	1.80	-8.51	8.70
White Fabric	81.85	0.36	-2.82	2.84
White Tile	96.67	-0.33	1.29	1.33
Pastel-Red	77.68	17.55	-1.84	17.65
Pastel-Blue	62.04	-9.43	-25.90	27.56
Pastel-Grey	62.31	-3.70	-2.01	4.21

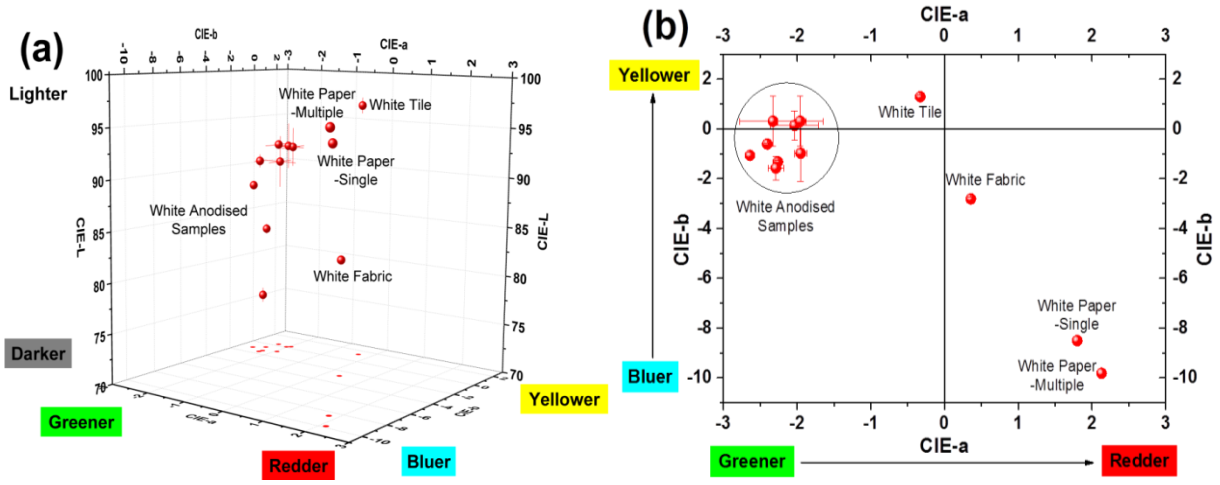

Figure 15.4: (a) CIE-L, a and b values plotted in 3D space showing the reflectance values of several surfaces, and (b) CIE-a and b plotted in 2D space for various white surfaces showing the colour of different surfaces.

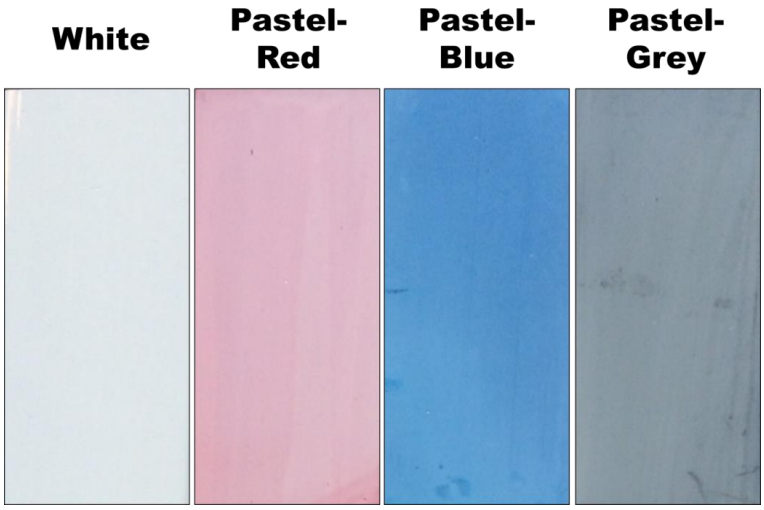

Figure 15.5: Optical images of white anodised aluminium surface and pastel colours obtained after conventional dyeing of the white anodised surfaces.

The CIE-L, a and b values for the pastel colours generated by dyeing the white anodised aluminium surfaces shows CIE-L values in the range of 60-70 (Table 15.1) . The optical images of the surfaces are shown in Figure 15.5. The surfaces appear very diffuse and are similar to the appearance of water colours. Such surfaces for anodised aluminium have not been reported earlier. The CIE-L, a and b values are also plotted in 3D and 2D space in Figure 15.6, which shows that the values are far away from those measured for the white anodised surfaces.

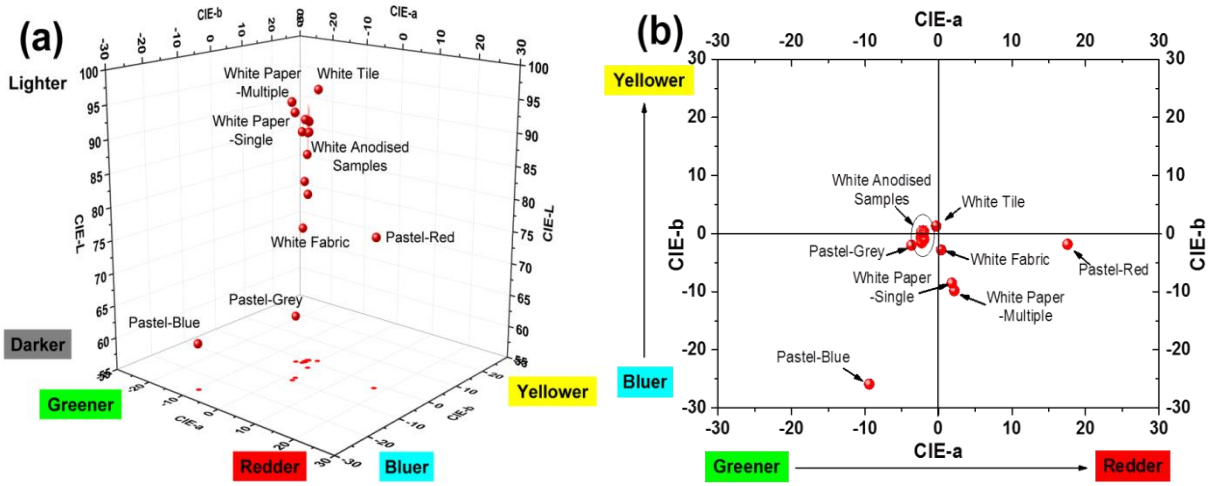

Figure 15.6: (a) CIE-L, a and b values plotted in 3D space showing the reflectance values of several surfaces, and (b) CIE-a and b plotted in 2D space for various white surfaces and pastel colours (Pastel-Red, Blue and Grey) showing the colour of different surfaces.

The total reflectance spectra from the pastel coloured surfaces is presented in Figure 15.7 and compared with the thinnest and thickest white anodised surfaces (Sample-1 and Sample-9). The total reflectance for Pastel-Grey is lower than that observed for the thinnest white anodised surface, whereas for Pastel-Red and Pastel-Blue, the maximum reflectance is higher than the thinnest white anodised surface. However, this is only an example and the values can be tailored depending on the requirement by varying the extent of white anodising of the Aluminium surface in combination with the intensity of the dye or the depth of colouration (dye concentration and dyeing time).

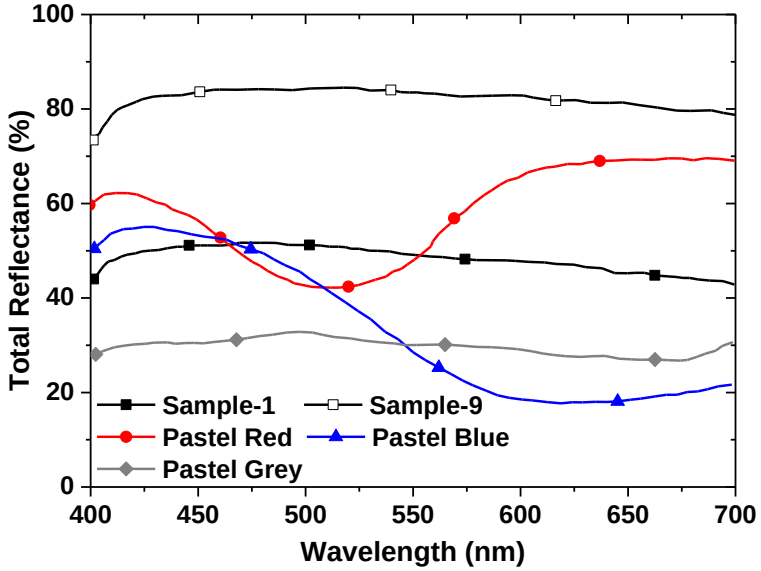

Figure 15.7: Total reflectance spectra obatined from Pastel-Red, Blue, and Grey surfaces compared with that from thinnest and thickest white anodised surfaces.

Overall, the newly developed white anodised surfaces and pastel coloured surfaces extend the design possibility of various consumer goods which use decorative surfaces. The level of whiteness and reflectance required can be tuned as required by varying the material properties and also the anodising thickness. The high reflectance, diffuse nature, and inherent UV resistance of these surfaces allow them to be used in various applications in the architecture, automotive, and shipping industry where currently used white surfaces involve an organic paint or lacquer.

15.5 Conclusions

- Anodising of Al-TiO_2 composites with TiO_2 particles in the size range of 320 nm to 500 nm has been shown to be effective in generating white anodised surfaces.
- White anodised surfaces with reflectance values of up to 85% have been achieved by this approach and the degree of whiteness can be varied depending on the layer thickness.
- The CIE-a and b values for the white anodised surfaces are close to zero and the CIE-L values depend on the anodising thickness, and the total reflectance showed an increase with increasing layer thickness.
- Anodised surface with pastel colours are produced using the conventional colouring of the white anodised layer followed by the sealing process.

References

[1] P.G. Sheasby, R. Pinner, The Surface Treatment and Finishing of Aluminium and Its Alloys, Volume 1, 6th ed., ASM International; Finishing Publications, 2001.

[2] P.G. Sheasby, R. Pinner, The Surface Treatment and Finishing of Aluminium and Its Alloys, Volume 2, 6th ed., ASM International; Finishing Publications, 2001.

[3] C.A. Grubbs, Anodizing of Aluminum, Met. Finish. 105 (2007) 397–412. doi:10.1016/S0026-0576(07)80359-X.

[4] V.C. Gudla, V.E. Johansen, S. Canulescu, J. Schou, R. Ambat, Simulation of Reflectance from White Anodised Aluminium Surfaces Using Polyurethane-TiO2 Composite Coatings, J. Mater. Sci. 50 (2015) 4565–4575. doi:DOI: 10.1007/s10853-015-9005-1.

[5] W. Possart, C. Bockenheimer, B. Valeske, The state of metal surfaces after blasting treatment Part I: Technical aluminium, Surf. Interface Anal. 33 (2002) 687–696. doi:10.1002/sia.1436.

[6] G. Kuppinger, Uebersicht Ueber Stahlmittel Und Strahlanlagen Fuer Formteile Aus Aluminium. (Survey of Shot Blasting Materials and Equipment for the Treatment of Formed Aluminum Parts), Aluminium. 54 (1978) 645–647.

[7] Y.D. Gong, C. Wang, J. Cheng, X.L. Wen, G.Q. Yin, Influence of Processing Parameters on Surface Roughness in Micro Mill-Grinding Aluminium Alloy 6061, Adv. Mater. Res. 3410 (2014) 495–499. doi:10.4028/www.scientific.net/AMR.1017.495.

[8] A. Selwood, J. Molgaard, Wire brushing of Aluminium -- Mechanism of “orange peeling,” Wear-Usure-Verschleiss. 3 (1960) 394–400.

[9] R. Jamaati, M.R. Toroghinejad, The role of surface preparation parameters on cold roll bonding of aluminum strips, J. Mater. Eng. Perform. 20 (2011) 191–197. doi:10.1007/s11665-010-9664-7.

[10] B. Gilbert, Beaded Colorways: Freeform Beadweaving Projects and Palettes, North Light Books, 2009. http://books.google.dk/books?id=D_NyRs8daJ8C.

[11] J.C. Whitaker, ed., The Electronics Handbook, CRC Press, 2005.

[12] Y. Ohno, CIE fundamentals for color measurements, IS&T’S NIP16 Int. Conf. Digit. Print. Technol. (2000) 540–545.

[13] E. Smulders, W. Von Rybinski, A. Nordskog, Laundry Detergents, 1. Introduction, in: Ullmann’s Encycl. Ind. Chem., Wiley-VCH Verlag GmbH & Co. KGaA, 2000. doi:10.1002/14356007.a08_315.pub3.

[14] E. Smulders, E. Sung, Laundry Detergents, 2. Ingredients and Products, in: Ullmann’s Encycl. Ind. Chem., Wiley-VCH Verlag GmbH & Co. KGaA, 2000. doi:10.1002/14356007.o15_o13.

[15] A.E. Siegrist, C. Eckhardt, J. Kaschig, E. Schmidt, Optical Brighteners, in: Ullmann’s Encycl. Ind. Chem., Wiley-VCH Verlag GmbH & Co. KGaA, 2000. doi:10.1002/14356007.a18_153.

16. General Discussion

The appended papers (Chapter 5-14) and chapter 15 (white anodising) present detailed discussion on specific investigations carried out in this thesis. Therefore this section presents only a short general discussion based on the observations made from studies performed in relation with the anodising and characterization of the Al-Zr and Al-Ti sputter coating systems and Al metal matrix composites that are presented as appended papers and chapters in the thesis. The behaviour of these systems during conventional DC anodising and high frequency anodising in terms of their properties, growth behaviour, and the obtained optical appearance is presented in view of the final goal of achieving white appearing anodised Al surfaces.

The white anodised Al requires efficient scattering of light and hence a heterogeneous structure in the anodised layer for scattering the incident light is necessary. Use of Al-Zr sputtered coatings for generating such heterogeneous microstructures proved to be promising. The heat treated structure showed intermetallics of Al_3Zr in an α-Al matrix [1], which is an essential precursor structure for anodising in order to generate high refractive index Al-Zr-O phases in a low refractive index anodised Al matrix. Similar structures were also obtained by heat treating Al-Ti sputtered coatings. Conventional sulphuric acid anodising resulted in darkening of the anodised layer due to partial anodising of the second phases owing to their varying electrochemical nature compared to Al [2]. The metallic nature of these un-anodised phases leads to the effective attenuation of incident light leading to the darkening of anodised layer [3,4]. Modifying the anodising parameters by increasing the anodising potential resulted in a higher degree of oxidation of the intermetallics and consequently a brighter anodised surface. However, the reflectance values measured are not high enough to provide a bright appearing surface.

Theoretical and physical simulation studies performed showed that the optimum scattering particle size for light scattering is in the range of 150-250 nm and requires a high refractive index of 2.4-2-6. Also, the diffuse and specular reflection of the surfaces could be tuned by varying the scattering particle concentration and the Al substrate morphology. Initial studies on the metal oxide surface composites prepared using FSP of Y_2O_3, CeO_2, and TiO_2 showed an increasing trend of total reflectance with increasing anodising potential under conventional DC anodising conditions. However, various morphological features were observed for the incorporated particles in the anodic layer as observed using TEM. Use of TiO_2 as light scattering medium in anodic alumina showed promising results. Reflectance values as high as 45 % were achievable using this approach at higher anodising potentials as opposed to very low values that were observed for the Al-Zr and Al-Ti sputtered coatings. However, difficulties in maintaining the crystallinity of the TiO_2 particles at higher anodising potentials and complete anodising of Al at lower anodising potentials posed challenges in optimising the anodising process and also increasing the total reflectance from the anodised surface. In addition, formation of oxygen deficient dark appearing magneli phases in the anodic layer due to the reaction of TiO_2 with the anodising electrolyte lead a loss of total reflectance [5,6].

The un-oxidised Al phase incorporated into the anodic layer due to electrochemical shadowing by TiO_2 under DC anodising conditions was responsible for the low reflectance values at lower anodising potentials. In order to completely anodise the Al phase, high frequency pulse and pulse reverse pulse anodising were employed. Reversing of the polarity in pulse reverse pulse anodising resulted in the complete oxidation of the Al phase in the anodic layer due to various factors. Cathodic reactions such as the formation of hydrogen and also the current localisation, and subsequent weakening of the anodic layer in the reverse cycle at highly conducting oxygen deficient magneli phases in the anodic layer were found to be the main factors for increased reflectance of the anodic layer [7]. The anodic cycle potentials and the pulse frequency showed greatest effect on the total reflectance and the anodising growth rate. Duty cycle of the pulse showed minimum effect on the anodising behaviour.

The duty cycle, anodising potential, polarity of the pulses during anodising, and temperature of the electrolyte were optimized and various white anodised surfaces were generated. The total reflectance of the anodised surfaces could be varied by varying the anodic layer thickness and reflectance values as high as 85% were achieved. Increase in the anodic layer thickness increases the scattering of light within the anodic layer leading to enhanced surface reflectance. The CIE-Lab analysis of the surfaces showed that the chromaticity of the surfaces was very low indicating they have no colour and the high values of CIE-L of 90

showed that the surfaces are very bright and white appearing. Conventional dyeing of the white anodised surfaces showed that a new appearance based on pastel colours could be imparted to the anodised surfaces using white anodic surfaces as precursors.

References

[1] ASM Handbook - Alloy Phase Diagrams - Volume 3, ASM International, 1992.
[2] R.G. Buchheit, A Compilation of Corrosion Potentials Reported for Intermetallic Phases in Aluminum Alloys, J. Electrochem. Soc. 142 (1995) 3994. doi:10.1149/1.2048447.
[3] R. Tilley, Colour and The Optical Properties of Materials: An Exploration of the Relationship Between Light, the Optical Properties of Materials and Colour, 2010. http://www.pilkington.com/products/bp/bybenefit/specialapplications/tecglass/ (accessed November 4, 2013).
[4] M. Saito, Unoxidized Aluminum Particles in Anodic Alumina Films, J. Electrochem. Soc. 140 (1993) 1907. doi:10.1149/1.2220737.
[5] M. Li, W. Hebenstreit, U. Diebold, A.M. Tyryshkin, M.K. Bowman, G.G. Dunham, et al., The influence of the bulk reduction state on the surface structure and morphology of rutile TiO2(110) single crystals, J. Phys. Chem. B. 104 (2000) 4944–4950. doi:Doi 10.1021/Jp9943272.
[6] U. Diebold, M. Li, O. Dulub, E.L.D. Hebenstreit, W. Hebenstreit, The relationship between bulk and surface properties of rutile TiO2 (110), Surf. Rev. Lett. 07 (2000) 613–617. doi:10.1142/S0218625X0000052X.
[7] T. Yamamoto, H. Tanaka, M. Fujita, H. Asoh, S. Ono, Effect of high-frequency switching electrolysis on film thickness uniformity of anodic oxide film formed on AC8A Aluminum alloy, J. Japan Inst. Light Met. 60 (2010) 602–607. doi:10.2464/jilm.60.602.

17. General Conclusions

Various conclusions related to the individual studies are available in the appended papers; therefore, this section focuses only on the general overall conclusions from the findings of this thesis. The conclusions provided here are divided into two main aspects based on the anodising of: (i) magnetron sputtered coatings and (ii) Al based metal matrix composites.

17.1 Magnetron Sputtered Coatings

In general, the work performed shows that magnetron sputtered coatings can be used effectively as model alloys to study the microstructural effect on anodising behaviour with controlled chemical composition and microstructural evolution during heat treatment. Various chemical compositions can be synthesized including non-equilibrium compositions and subsequent phase transformation to understand, as focussed in this thesis, on the optical appearance after anodising and for tailoring appearance of anodised surfaces. Present investigation shows:

- Studies on the Al-Zr and Al-Ti magnetron sputtered coatings with subsequent heat treatment for controlled phase transformation and anodising shows the feasibility of tailoring optical appearance after anodising by optimizing the chemical composition, microstructure and anodising parameters.
- Microstructural evolution studies on magnetron sputtered Al-Zr coatings showed formation of DO_{23}-tetragonal Al_3Zr phase with needle like morphology in an α-Al matrix.
- Addition of Si to the sputtered coating promotes the formation of $Al_{2.6}Si_{0.4}Zr$ phase based on the DO_{22}-tetragonal system with nodular morphology, which is similar to the Al_3Ti phase in heat treated Al-Ti sputtered coatings.
- Electrochemical heterogeneity of the intermetallic phases results in incorporation of partially or fully oxidised intermetallic particles in the anodised layer. Oxidation of intermetallic particles during anodising was also a function of the morphology of the particles. The Al_3Zr phase with needle like morphology is easily oxidized during anodising compared to the $Al_{2.6}Si_{0.4}Zr$ phase with nodular morphology.
- Modification of the light scattering phenomenon and subsequent darkening of the anodised layer by efficient light extinction is caused by the un-anodised metallic part of the intermetallic phases in the anodised layer. Therefore the optical appearance can be controlled and modified by optimization of anodising process resulting in complete oxidation.
- Increase of anodising potential in DC anodising shows increase in total reflectance due to the lower amount of un-anodised metallic phases in the anodised layer.
- Application of high frequency pulse anodising to the heat treated Al-Ti and Al-Zr sputtered coatings improves the anodising growth rate and total reflectance when compared to DC anodising due to the increased oxidation of particles in the anodised layer.

17.2 Aluminium Based Metal Matrix Composites

The use of Al-metal matrix composites for embedding light scattering particles to the anodised layer to impart optical appearance based on scattered and diffused reflection in general is shown to be an effective method. Investigations carried out on model surface composites prepared using FSP process showed the possibility of using various composites and anodising process for achieving desired optical appearances based on light scattering principle. Further, the investigations show the following:

- Theoretical calculations and experimental studies showed that the light scattering particles of refractive index (*n*) 2.4-2.6 with a particle size of 150-250 nm is optimum for highest scattering from a given anodic layer thickness for diffused reflection and obtaining white appearance.
- Anodising of Al-TiO_2 surface composites in sulphuric acid showed increase in surface reflectance with increasing anodising potential and the optical appearance varied from dark to light grey. The variation in optical appearance was due to the modification of the crystallinity and structure of the TiO_2 particles.
- Lower anodising potential showed formation of magneli phases (Ti_nO_{2n-1}) and presence of un-oxidised Al below the TiO_2 particles due to the electrochemical shadowing by TiO_2. Presence of un-oxidised Al had the greatest effect on the optical appearance in this case providing dark appearance to the anodic layer.
- At higher anodising potentials, morphological transformation of the TiO_2 particles to an amorphous phase with reduced refractive index was observed. The reduced refractive index of the particles in the anodised matrix has reduced the scattering power resulting in lower degree of whiteness of the anodised layer.
- Use of high frequency pulse anodising resulted in the complete oxidation of the Al phase in the anodic layer, however various other effects were observed at the TiO_2 particles depending on the nature of pulsing used for anodising.
- Transformation of TiO_2 particles into the oxygen deficient highly conducting Magneli phases under pulse anodising resulted in intense pore branching in the anodic layer due to current localisation in the reverse cathodic pulse cycle. However, the effect was dependant on the cathodic pulse potential.
- Use of pulse anodising with only 0 V at low potential cycle showed no pore branching and subsequent incomplete anodising of Al phase below the TiO_2 particles in the anodic layer. However, the crystallinity of the TiO_2 particles was more or less retained after anodising.
- The anodising pulse frequency and anodic cycle potential had the highest impact on the anodising growth rate, total reflectance and hardness.

17.3 Anodised aluminium surface appearing white

Optimising the decorative anodising parameters for the Al-TiO_2 composites has resulted in novel highly reflecting and white appearing anodised surfaces. The surface total reflectance values as high as 85 %, and CIE-L values as high as 90 were achieved for the prepared white anodised surfaces. Conventional dyeing of the white anodised surfaces prior to hydrothermal sealing generates new surfaces based on pastel colours.

18. Future Work

- The technique of high frequency pulse anodising for decorative anodising of Al-TiO_2 composites and magnetron sputtered coatings has been studied. Further work based on this promising technique to anodise low quality recycled Al alloys with high amount of intermetallic particles will be of interest.
- Use of pulse anodising method has resulted in faster anodising times compared to conventional DC anodising technique. Detailed investigations based on the efficiency of the process and improvement in the anodising performance for traditional Al alloys could be useful.
- Cast Al alloys based on Al-Si system that are difficult to decorative anodise using conventional techniques can be anodised using the pulse anodising technique. Investigations for the anodising behaviour, optical appearance, and ability to colour such anodised surfaces could be tried.
- For obtaining white anodised surfaces, FSP process was used to generate model Al-TiO_2 composite surfaces. However, upscaling of this process is necessary to obtain Al-TiO_2 composites on a large scale, which can be anodised further. Light fastness, weathering resistance, and mechanical property testing for white anodised surfaces needs to be investigated.
- The applicability of various pre-treatment techniques to impart various artistic surface finishes to white anodised surfaces can be explored.
- Other anodised surfaces with novel functional properties can be prepared using the process of incorporation using FSP into Al matrix and further anodising.

DTU Mechanical Engineering
Section of Materials and Surface Engineering
Technical University of Denmark

Produktionstorvet, Bld. 425
DK-2800 Kgs. Lyngby
Denmark
Phone (+45) 4525 2205
Fax (+45) 4593 6213
www.mek.dtu.dk
ISBN: 978-87-7475-448-0